Processing and analysis of Electrical Impedance Epigastrography signals for investigation and modelling of gastric motility in humans

by

M Freedman

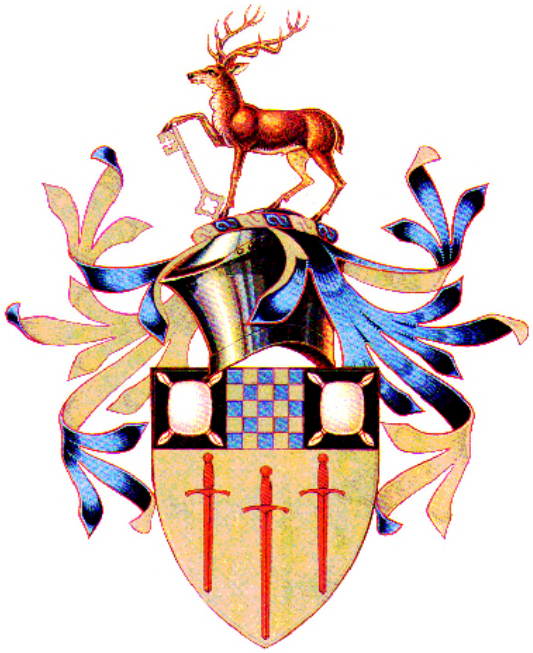

A thesis submitted to the University Of Surrey for the degree of Doctor of Philosophy

Department of Physics
School of Electronics and Physical Sciences
University of Surrey

August 2004

ABSTRACT

Electrical Impedance Epigastrography (EIE) has been used for many years to detect gastric emptying rates in humans. Previous work has found that the EIE signals also contain information relating to the contractility of the stomach that could additionally provide valuable information regarding the nature of gastric function. The electrical field generated by EIE was modelled using sets of equations based on representing the human torso as an elliptical cylinder. The equipotentials were plotted using a computer program to solve these equations. A software package called ACCESS (Analysis, Characterisation and Classification of Epigastrographic SignalS) was produced to provide comprehensive processing and analysis of EIE signals to extract several gastro-physiological parameters.

The software was tested using 'pseudo-EIE' signals that represent typical signals produced by EIE, made by superimposing pure sine waves and other mathematical functions. Furthermore, pure waveforms such as sinusoidal and chirp functions were examined by the software to assess the efficacy of the various signal processing and analysis functions and identify faults and weaknesses. Experiments to determine whether EIE could detect differences relating to the gastrointestinal processing of three liquid and semi-solid meals were carried out with 54 healthy volunteers (18 in each group). The meals were: meal A (mineral water), meal B (low fat semi-solid meal) and meal C (high fat semi-solid meal).

The results from these studies indicated that gastric emptying rates were increasingly delayed by the presence of fat in the meal. The power of gastric contractions and duration of motile events decreased with fat content while the measurements of the frequency and velocity of the flow of gastric chyme increased. Following an extensive literature review, these data indicate that EIE is able to detect the half emptying time of liquid and semi-solid meals together with the power, frequency and velocity of gastric motile events but that EIE predominantly measures the flow of gastric chyme rather than the propagation of antral contractions. Since delayed gastric emptying and changes in the distribution of the ingested meal indicate gastric dysfunction, it is possible that EIE, in conjunction with ACCESS provides a novel and valuable contribution to the assessment of gastric function which could lead to the development of a safe, comprehensive, portable and inexpensive diagnostic test for gastric dysmotility disorders.

בסיעתא דשמיה

With sincere gratitude to הקב"ה

ברוך אתה ה' חונן הדעת

To my parents, for their unconditional love, support, encouragement and continuous faith in me.

To my brothers and sisters–in–law who have not only encouraged me and given me confidence during the last four years, but who have made me an uncle and in doing so, have provided me with a wonderful and necessary distraction from my work.

'A man's joy is greatest when his family is with him'

Rabbi Shlomo Ephraim Lunshitz, 1550 – 1619

ACKNOWLEDGMENTS

I wish to firstly express my sincere gratitude to my supervisor, Professor Nicholas Spyrou for his valuable and continuous support throughout my time at the University of Surrey. His patient advice, direction and encouragement have inspired me to produce research, culminating in this thesis that has exceeded my most positive expectations.

Sincere thanks to Dr. Andrew Sutton of Guildford Clinical Pharmacology for his invaluable suggestions in matters regarding gastric physiology, dysfunction and pharmacology. His support and enthusiasm was always encouraging. I would also like to also thank Dr. Richard Bacon for his help and advice in matters regarding computer programming and mathematics.

I am especially indebted to Dr. Nadia Hadi for allowing me to use data from previous studies carried out at the Kuwait Cancer Research Centre, for her help in carrying out EIE experiments, for her suggestions related to the production of the analysis software and especially for her continued academic advice and friendship during the last four years. I am also grateful to Dr. Anastasia Giovanoudi and Dr. Behin Amaee for their advice during the early stages of my work.

I wish to also thank Miss. Imane Bouallal for her assistance in carrying out EIE experiments and testing of the analysis software for her own work. I am also grateful to Mr. Abdulrahman Alfuriah for his suggestions regarding bioimpedance, programming and signal processing, Mr. Ali Alghamdi, Mr. Andy Ma, Miss. Loretta Admans, Mr. Elafatih Abuelhia, Mr. Daniel Beasley and all of my colleagues at the University of Surrey for their patient support and assistance when I have pestered them with my problems. I am grateful to Eric Worpe for his important suggestions in issues related to the Epigastrograph and particularly for his suggestions for the future development of the hardware and to Liz Griffiths, Dennis Libaert, Dave Munro and Jeff Dahlke. In addition I must express sincere gratitude to Val Newey at the Clinical Physics Department of St. George's Hospital for helping to maintain the Epigastrograph in good working order. I wish to acknowledge the support of the EPSRC and the Grundy Educational Trust for awarding me one of their prestigious scholarships.

Lastly, I wish thank all of the volunteers who took part in EIE studies, without whom this work would not have been possible.

CONTENTS

LIST OF FIGURES

LIST OF TABLES

1 INTRODUCTION

The billions of cells in the human body require oxygen and energy to function properly but are completely isolated from direct contact with the outside world. Just as our respiratory system extracts oxygen from the gaseous environment in which we live, energy must also be extracted from food in some way and absorbed into the bloodstream. To complicate matters, we eat food of many different varieties which consist of large and complex molecules and in order to provide nourishment, molecules must be small and simple so that they can be dissolved and absorbed into the bloodstream, carried through the body and easily taken in by the cells. For example, the proteins found in animals and plants are not always the same as human proteins. There are also elements within the food that can not be absorbed by humans and so these parts must be discarded.

The digestive system is responsible for the processing of food into a useable form allowing the body to absorb it while discarding the waste. The stomach plays a critical role in the digestive process; while acting as a reservoir for ingested food, the stomach triturates and macerates the chyme to facilitate the absorption of nutrients throughout the gastrointestinal tract.

Many conditions adversely affect gastric function, either directly or indirectly. Currently, there are a number of techniques used for the diagnosis of gastric dysfunction most of which measure the rates of gastric emptying, contractility or the distribution of the ingested meal. The most widely used techniques in Gastroenterology clinics include nuclear medicine imaging of the stomach using scintigraphy for the determination of gastric emptying rates or endoscopy that allows the Gastroenterologist to observe the inside of the stomach and perform surgical procedures.

Dyspepsia is the general term that describes a set of symptoms related to disordered digestion given to patients complaining of early satiety, nausea or vomiting after eating, often accompanied by pain and discomfort in the abdominal region. In the Western world, the annual prevalence of Dyspepsia is approximately 25% and the condition accounts for between 2% and 5% of all primary care consultations [Talley NJ, 2002].

However, more than half of dyspeptic patients referred by their general practitioner for gastroenterological assessment undergo conventional diagnostic tests that do not reveal any pathological cause for their symptoms [Bennett EJ, 1999]. In the absence of an identifiable organic cause these clinical conditions are labelled as 'functional' gastrointestinal disorders or Non-Ulcerative Dyspepsia (NUD).

There has been much interest into the aetiology of NUD and hitherto abnormalities associated with NUD include delayed gastric emptying rates [Waldron B, 1991], abnormal distribution of food in the stomach [Troncon LEA, 1994] and several neuromuscular abnormalities including visceral hypersensitivity [Kanazawa M, 2000 and Coffin B, 1994] and impaired smooth muscle function [Koch KL, 1996]. Nevertheless, the diagnosis of NUD is controversial and its management remains the subject of considerable debate [Talley NJ, 2002]. These facts demonstrate that a multifaceted, comprehensive and reliable test that can be repeated at no risk to the patient is needed for the assessment of gastric function. If such a diagnostic tool was available, it would not only provide clinicians with a means of diagnosis, but it would facilitate the monitoring of treatment and help to determine the most effective management protocol while providing a better understanding of the nature of gastric dysfunction and the causes of dyspeptic symptoms.

Electrical Impedance Epigastrography (EIE) has been used for almost 20 years to measure gastric emptying rates [Pickworth MJW, 1984, Sutton JA, 1985, McClelland GR, 1985 and Sutton JA, 1987]. Nevertheless, even in its early stages, researchers became aware that the measurements were also detecting changes in the signal that appeared to represent gastric contractility. Previously, there have been studies investigating the possibility of measuring contractility from EIE signals [Castillo FD, 1987; Ching EJ, 1992; and Giouvanoudi A, 2000]. However, these studies did not significantly advance the prospect of EIE becoming a useful diagnostic tool.

EIE operates by passing an alternating current with a frequency of 32kHz through the epigastric region of the abdomen, over the antral region of the stomach. The current can be varied by the operator to apply between 1mA and 4mA. Changes in the impedance of the abdomen will give rise to variations of potential difference, detected by the same six electrodes using digital multiplexing. These changes in impedance are caused by the change in conductivity of the measured area and volume changes in the stomach.

The ultimate goal of this work is to demonstrate that EIE could become a valuable diagnostic tool. The primary aim is to create a novel, effective and multifaceted software package that will provide a comprehensive analysis of EIE signals in order to extract valuable gastro-physiological information, while remaining accessible and user friendly.

Rigorous testing of the software is critical and so modelling of the electrical field produced by EIE and the generation of pseudo-EIE signals will help to determine the limitations of the system as a whole and uncover faults and flaws in the software. The verification of the EIE system's ability to detect gastro-physiological phenomena will be achieved by analysis of the EIE signals produced from volunteers with no history of gastrointestinal abnormality, after the ingestion of one of three liquid and semi-solid test meals; meal A, (mineral water), meal B (low fat liquid meal) and meal C (high fat semi-solid meal).

The detection of statistically significant differences in the quantitative values produced by the software and qualitative changes in the signals between the three meal types, which can be justified by established physiological explanations, will demonstrate that EIE is able to identify subtle differences in the gastric response to different meals. This will indicate that EIE can potentially contribute to the measurement of gastric dysmotility and that this technique merits further research to develop the system into a useful clinical tool.

2 GASTRIC ANATOMY AND PHYSIOLOGY

2.1 The gastrointestinal system

2.1.1 The process of digestion

The role of the gastrointestinal system is to process food in order to separate and absorb nutrients into the body and dispose of waste products safely. The gastrointestinal tract is a long passage (approximately 8 metres) extending from the mouth to the anus. The major sections are the mouth, pharynx, oesophagus, stomach and the small and large intestines. The small intestine is divided into three sections: the duodenum, jejunum and ileum. The large intestine has five sections: the ascending colon, the transverse colon, the descending colon, the rectum and the anus (Fig. 2.1).

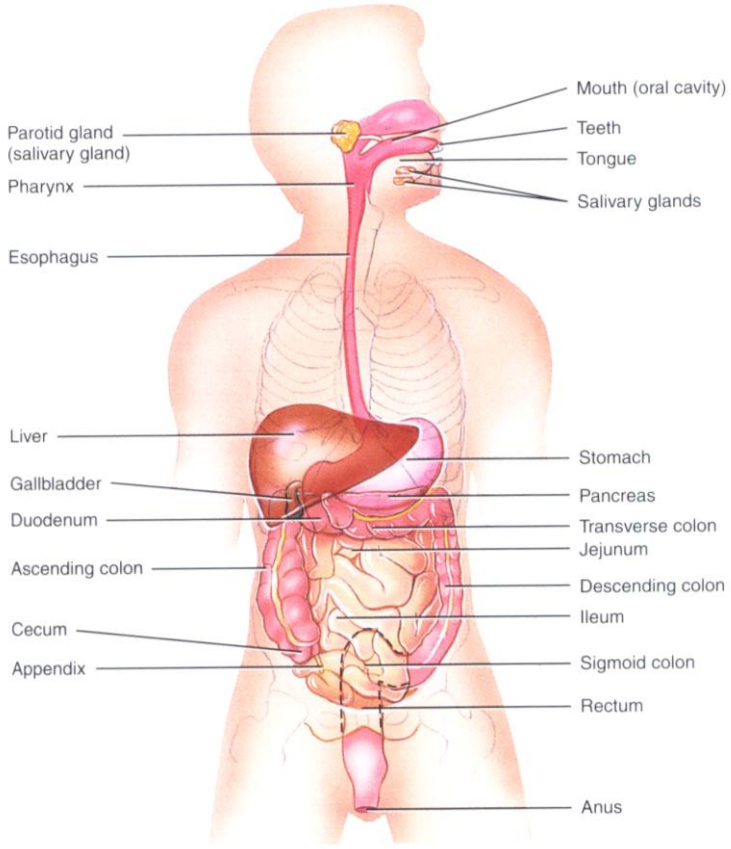

Fig. 2.1 The gastrointestinal system [Reproduced from Tortora GJ, 2000]

The technique for breaking down food so that it may be absorbed into the bloodstream may be divided into four distinct, but interrelated processes: motility, secretion, digestion and absorption. Motility refers to the mixing of the gastric contents in the stomach with the gastric juices (mucous, water, electrolytes and enzymes) secreted by glands and specialised cells in the stomach wall and the propulsive movement of chyme through the gastrointestinal tract. Digestion is the chemical process in which large particles of food disintegrate resulting in nutrient molecules small enough to permeate across the wall of the gastrointestinal tract. The absorption process is the method by which the nutrient molecules are taken into cells in the gastrointestinal tract so that they can enter the bloodstream.

As food enters the mouth it is mixed with saliva produced from three salivary glands: the parotid in the cheek, the submandibular near the frenulum of the tongue and the sublingual found below the tongue. In addition to water, mucous and electrolytes, saliva contains an enzyme called amylase, which breaks down starch. The tongue compresses the food against the hard palate to form a soft bolus and it is forced into the oropharynx. The deglutition reflex takes over so that respiration is inhibited as the epiglottis closes off the larynx. The bolus enters the oesophagus, which passes it into the stomach by the process of peristalsis. The stomach then mixes the bolus with various gastric secretions (section 2.3). As the chyme passes through the gastrointestinal tract, the useful nutrients are absorbed into the blood while the waste products are allowed to pass through until they are expelled through the anus by defecation.

2.1.2 The anatomy of the gastrointestinal tract

The wall of the gastrointestinal tract consists of a number of different layers that vary in structure and function from region to region. The first and innermost layer is the mucosa, which consists of three components: the epithelium, the lamina propia and the muscularis mucosae. The epithelium comprises of a single layer of specialised cells which line the lumen of the entire gastrointestinal tract. The lamina propia is essentially connective tissue made from collagen (a class of proteins, primarily glycine that form inelastic fibres with large tensile strength) and elastin fibrils (another class of proteins whose fibres are highly elastic). There are also several glands, lymph nodules and capillaries that pervade the lamina propia. The muscularis mucosae is the thin layer of smooth muscle that forms part of the motile system in the gastrointestinal tract.

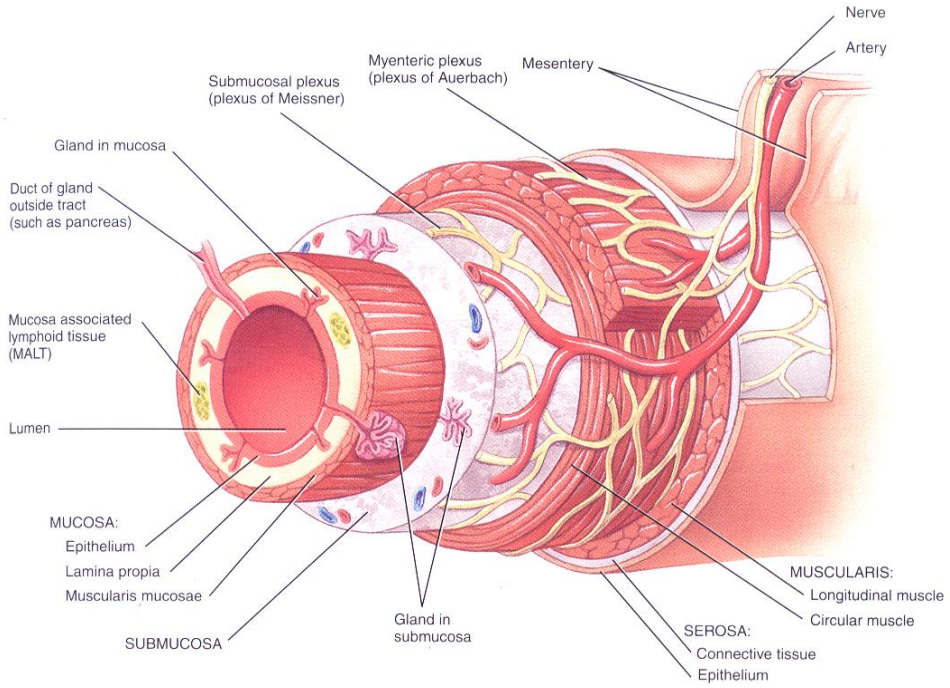

Fig. 2.2 The four layers that are found throughout the wall of the GI tract [Reproduced from Tortora GJ, 2000]

The submucosa also comprises mainly of collagen and elatsin fibrils that make up the connective tissue and includes larger nerves and blood vessels. The muscularis is composed of two extensive layers of smooth muscle: an inner circular layer and outer longitudinal layer. It is the contractions of these smooth muscle layers that mix chyme in the stomach and propel it along the gastrointestinal tract. The outermost layer is the serosa and consists of connective tissue layer surrounded by an epithelium that contains squamous mesothelial cells.

2.1.3 Location and structure of the stomach

Essentially the stomach is an enlargement of the gastrointestinal tract between the oesophagus and duodenum. It primarily lies in the epigastric region of the abdomen on the left hand side, beneath the diaphragm. There are four anatomical regions of the stomach that are distinctive from a morphological, histological and physiological perspective: The cardia, fundus, body and pylorus. In the muscularis, the circular muscle layer is more prominent than the longitudinal layer, but the primary difference between these regions is the variation of the total thickness. The muscularis is fairly thin in the fundus and body but thickens towards the pylorus. However, the oblique layer of muscle is only complete in the fundic region.

The pylorus is divided into two sections: the pyloric antrum and the pyloric canal which leads to the duodenum. The pyloric sphincter which separates the stomach from the duodenum, coordinates and regulates gastric emptying and mixing (section 2.6). The rugae are large folds in the mucosa that are visible when the stomach is in the fasting state. As the stomach fills the stomach wall stretches and the rugae disappear.

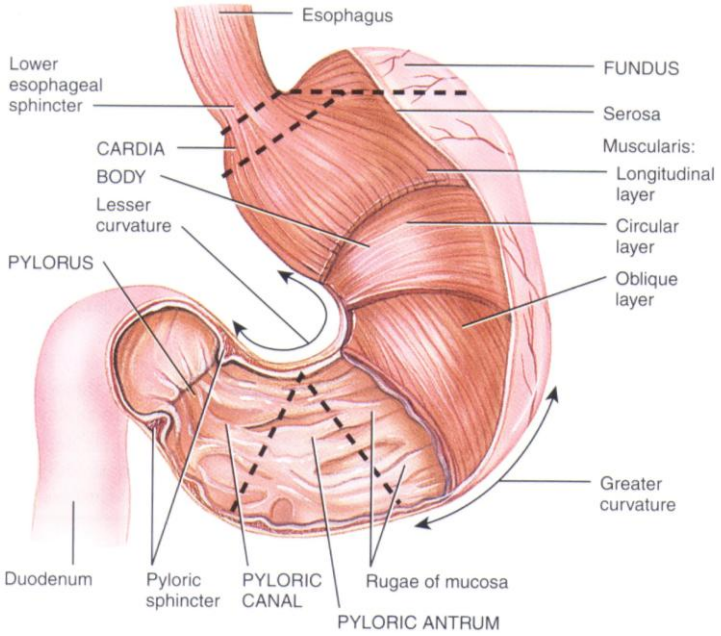

Fig. 2.3 Internal and external anatomy of the stomach showing the four regions; the cardia, the Fundus, the body and the pylorus [Reproduced from Tortora GJ, 2000]

2.1.4 The role of the stomach in the digestive process

The stomach plays a multifaceted role in the digestive process. Since it is possible to eat a meal more quickly than the time needed for the digestion and absorption processes, the stomach acts as a reservoir for the ingested food. While the food is held in the stomach it is mixed with a variety of gastric secretions which are essential in the digestive process (section 2.3), while some substances are absorbed. The gastric contractions (section 2.4) mix ingested food with the various gastric secretions to produce chyme while physically breaking down larger particles into smaller molecules.

2.2 Control mechanisms of the gastrointestinal system

2.2.1 Neural control systems

There are two subdivisions of the nervous system: the central nervous system (CNS) consisting of the brain and spinal chord and the peripheral nervous system (PNS) made up of the cranial and spinal nerves, ganglia and sensory perceptors. The PNS has three components. The first is the somatic nervous system (SNS) that consists of sensory receptors that convey information to the CNS from the head, body and limbs together with motor neurons for skeletal muscle. The second is the autonomic nervous system (ANS) contains sensory neurons and motor neurons that control smooth muscle, cardiac muscle, glands and adipose tissue. The ANS has sympathetic and parasympathetic divisions that control function by opposing one another.

The third is the enteric nervous system (ENS), which directly controls the motor and secretory functions of the gut, describes all of the neural elements in the gastrointestinal system. It is an element of the autonomic nervous system (together with the sympathetic and parasympathetic nervous systems) and consists of two dense networks of neurons called the submucosal plexus (Meissner's plexus), located in the submucosa and the myenteric plexus (Auerbach's plexus), located between the circular and longitudinal muscle layers. The ENS is considered as an independent integrative nervous system that has anatomical and physiological properties similar to that of the CNS [Wood JD, 1987]. Fig. 2.4 shows how the ENS is integrated into the general nervous system of the body and the role it plays in controlling the function of the gut.

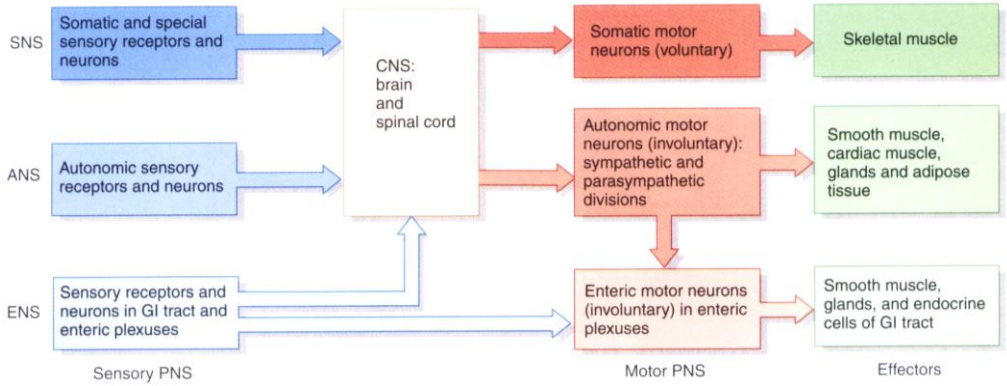

Fig. 2.4 The organisation of the nervous system showing the integration of the ENS and the control pathways to the gastrointestinal system [Reproduced from Tortora GJ, 2000]

2.2.2 Endocrine and paracrine control systems

An endocrine control describes the process whereby a stimulus triggers the secretion of a hormone that is transported through the bloodstream in order to interact with a target to cause a response. Paracrine mediated responses are those in which the chemical signal released by the cell is a local mediator acting only on those cells in the immediate locality. Endocrine and paracrine cells line the entire gut secreting a variety of peptides. The primary peptides that affect gastric function are given below.

Gastrin is contained in G-cells located mainly in the gastric antrum and also in the beginning of the duodenum [Greider, 1972]. Gastrin is directly stimulated from G-cells by amino acids, peptides (formed from amino acids) and calcium. The neural mechanism for gastrin release is facilitated by the vagus nerve brought about by the thought, sight, smell, and taste of food (cephalic phase). Additionally, the distension of the stomach detected via the ENS and ANS and also has a stimulatory effect on gastrin secretion. Gastrin has a number of important effects on the stomach. In physiological doses, gastrin enhances the frequency of pacemaker potentials as well as the number of pacemaker potentials that result in antral contractions [Strunz UT, 1979].

Cholecystokinin (CCK) is an important neuropeptide that is stimulated by lipids in the intestine and causes secretions from the pancreas that are high in digestive enzymes while inhibiting gastric secretions. It also triggers the gall bladder to contract while relaxing the hepatopancreatic ampullar sphincter leading to the release of bile into the small intestine. There has been considerable interest in the physiological role of CCK in the control of gastric acid secretion and gastric emptying and the consequential effects on appetite and satiety. However, there is also evidence that suggests that CCK has far reaching effects on cardiovascular and respiratory function, body temperature, seizures, cancer cell proliferation, sleep and memory [Crawley JN, 1994].

Secretin is stimulated by the acidity of chyme released into the duodenum and intraluminal fatty acids. Its effects are to inhibit gastric secretions and gastric emptying, stimulate pancreatic secretions that are high in bicarbonate ions and increase the rate of bile and intestinal mucous secretion.

Somatostatin concentrations increase with fat and protein in the intestine and with acidification of the gastric antrum and duodenum. The effects of somatostatin with respect to the stomach are that it inhibits the secretion of secretin and CCK and also inhibits motility. Gastric inhibitory peptide (GIP) is produced in the duodenum and proximal jejunum and is also triggered by lipids. Its primary effects are to inhibit gastrin release and gastric acid secretion.

Motilin producing cells are found in the mucosa of the upper small intestine. Motilin is released during the fasting state and at the initiation of fasting contractions known as migrating motor complexes (section 2.4.3). It has consequently been suggested that motilin regulates the fasting contractions, particularly in the stomach and duodenum [Walsh JH, 1987].

Histamine is an essential nonpeptide paracrine mediator that stimulates HCl secretion by interacting with histamine-H_2 receptors on the cell. Histamine-H_2-antagonists such as cimetidine inhibit gastric acid secretions.

2.3 Gastric secretions

2.3.1 Histology of the gastric mucosa and the role of gastric secretions

The gastric mucosal lining is covered with simple columnar epithelial cells with numerous tubular gastric glands that open at the surface of the mucosa through holes called gastric pits. Their role is to secrete mucous and an alkaline fluid to protect the stomach wall from physical damage and gastric acid. The mucosa is interspersed with gastric pits that are the opening of the gastric glands. They have the effect of significantly increasing the surface area of the stomach.

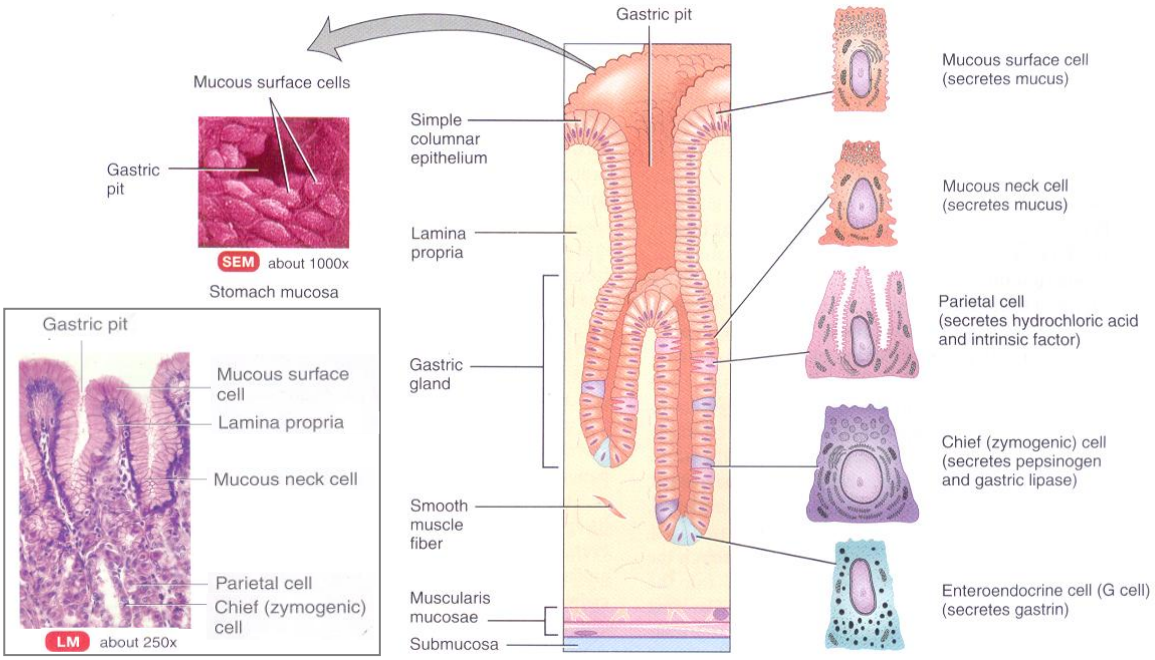

Fig. 2.5 Histology of the gastric mucosa showing the specialised gastric glands and the types of cell that produce gastric secretions [Reproduced from Tortora GJ, 2000]

A variety of chemicals are released from the gastric mucosa into the lumen to facilitate the digestion of ingested food. Gastric secretions include mucous, hydrochloric acid (HCl), gastric intrinsic factor and pepsinogen (the inactive form of pepsin which is an enzyme for digesting proteins).

The surface mucous cells and mucous neck cells secrete a viscous alkaline mucous that coats the surface of the epithelial cells with a thickness 1.0 to 1.5 mm. This layer of mucous protects the epithelial cells from the acidic chyme and lubricates the stomach wall. Additional mucosal secretion is stimulated by irritation of the stomach wall. The parietal cells, found particularly in the pyloric region, secrete intrinsic factor that is a glycoprotein (a protein that contains a carbohydrate group) that binds to vitamin B_{12} so that it can be absorbed in the ileum[1].

Hydrochloric acid (HCl) has a minor digestive effect on the ingested food but is primarily responsible for lowering the pH of the chyme to between 1 and 3 in order to kill the bacteria that are digested together with the food. Pathogenic bacteria that have an outer coat may avoid digestion in the stomach by resisting the acidic effect. The acidic nature of the stomach also deactivates the salivary amylase, consequently stopping the digestion of carbohydrates and denatures protein so that proteolytic enzymes can break the protein down.

Pepsinogen, secreted from chief (zymogenic) cells is activated and converted into pepsin by the HCl secreted from the parietal cells for the digestion of proteins. Gastric lipase is also released by chief cells and splits short chain triglycerides into fatty acids and monoglycerides. The enteroendocrine or gastrin producing cells (G cells) secrete the hormone gastrin that stimulates the parietal and chief cells to secrete HCl and pepsinogen respectively.

In general the stomach secretes approximately 2 to 3 litres of fluid per day and depending on the types of ingested food, approximately 700mL is secreted at each meal. The secretions are triggered by three overlapping phases (section 2.3.2) regulated by neural and hormonal pathways. Neural pathways involve primary reflexes in the medulla oblongata and regional stimulation from the myenteric and submucosal plexuses. The hormones responsible for regulation secretion are gastrin, secretin, cholecystokinin and gastric inhibitory peptide.

[1] Vitamin B_{12} is improtant in the production of deoxyribonucleic acid (DNA) and red blood cell formation.

2.3.2 The phases of gastric secretion

The first phase of gastric secretion (the cephalic phase) occurs when the stomach begins to secrete chemicals for digestion into the lumen with the thought, sight, smell, and taste of food. Gastrin is produced (mediated by the vagus nerve and myenteric and submucosal plexuses) and carried through the bloodstream to other parts of the stomach where it stimulates the secretion of HCl and pepsinogen from parietal cells.

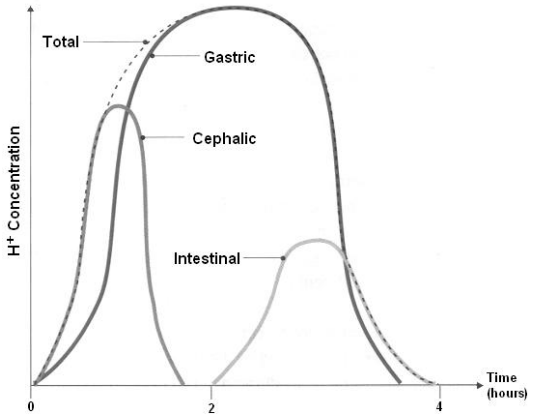

Fig. 2.6 Diagram of phases of gastric secretion [Redrawn from Cheshire E, 1998]

The largest volume of secretion occurs during the second (gastric) phase triggered by gastric distension and the presence of gastric peptides and amino acids in the ingested food. Mechanoreceptors detect the stretching of the smooth muscle wall initiating reflexes that result in the secretion of mucous, HCl, pepsinogen, intrinsic factor and gastrin. This increase in secretion is limited by negative feedback that blocks secretion when the pH of the chyme falls below 2. HCl secretion from parietal cells is activated by the amino acids (organic compounds that contain at least one from the amino and carboxyl groups) and peptides (formed from amino acids in which the amino group from one is joined to the carboxyl group of another), both of which are products of the pepsin-facilitated protein digestion.

The third (intestinal) phase is controlled by the entry of acidic chyme into the duodenum. This activates neural and hormonal responses that either inhibit or stimulate gastric secretions depending on the acidity of the chyme. When the pH is above 3, the stimulatory response prevails and gastrin released in the duodenum is carried in the blood stream to the stomach, increasing the rate of secretion. When the pH of the chyme falls below 2, the inhibitory response predominates through the release of secretin, GIP and CCK. There are also neural reflexes in the myenteric and submucosal plexuses, which slow the rate gastric secretion.

2.4 Gastric motility

2.4.1 Electrical properties of gastric smooth muscle as the basis for gastric motiltiy

The gastrointestinal tract comprises of autorhythmic visceral smooth muscle that possesses an intrinsic electrical rhythm that may be observed both *in vivo* and *in vitro*. The interconnecting neural plexuses and the close contact between the cells establishes the physiological connections between the individual smooth muscle cells.

The autorhythmic properties of the smooth muscle in the stomach induce action potentials known as slow waves, in a region situated high on the greater curvature in the corpus called the pacemaker region as shown in Fig. 2.7. In humans the frequency of the gastric slow waves is approximately three per minute. From an electrophysiological perspective the pacemaker region may be considered as the smooth muscle that produces a high frequency of spontaneous firing of action potentials with respect to the rest of the gastric smooth muscle.

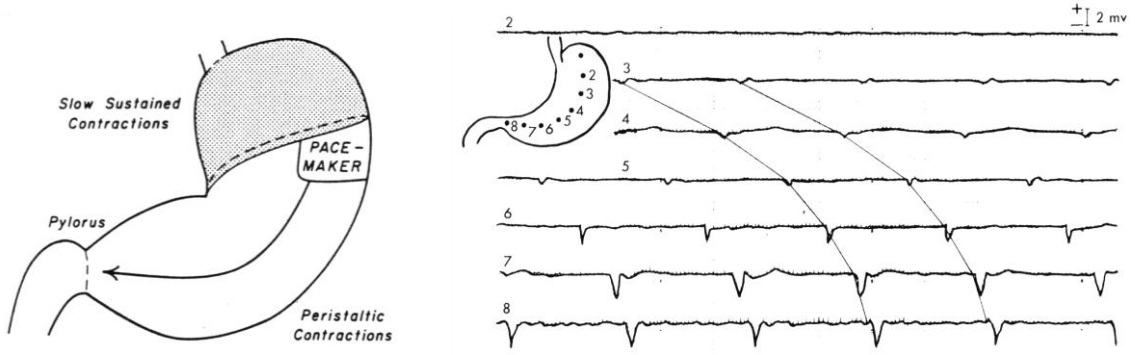

Fig. 2.7 Proximal (shaded) and distal gastric motor regions of the human stomach [Reproduced from Kelly KA, 1981] and recording of the canine gastric and duodenal electrical activity illustrating velocity of caudad conduction of gastric pacemaker potential. Velocity, indicated by the slope of lines connecting a cycle as it was detected in sequence by electrodes placed at equal intervals on the surface of the stomach, increases as the pacemaker potential approaches the pylorus [Reproduced from Kelly KA, 1969].

The proximal area shown exhibits few changes in electrical activity whereas the area distal to the pacemaker region shows cyclic changes in potential that ultimately cause the tonal contractions. The slow waves propagate distally from the pacemaker zone towards the pylorus. When the wave reaches the pylorus, another is generated from the pacemaker zone [Kelly KA, 1969]. The speed of the wave's propagation increases from 0.1 to 0.2 cms^{-1} in the pacemaker zone to 4.0 cms^{-1} in the antrum [Carlson HC, 1966].

The electrical activity of the smooth muscle varies throughout the regions of the stomach. Fig. 2.8 illustrates these differences by showing the changes in the electrical properties of gastric smooth muscle in the canine stomach [Szurszewski JH, 1987]. The spikes in the plateau regions of the gastric action potentials increase in number and amplitude moving towards the pylorus and are clearly defined from the orad terminal antrum to the pyloric ring. The same is true for the human stomach and is shown in Fig. 2.9.

The fact that gastric action potentials increase in amplitude and develop larger and more frequent action potential spikes in the plateau region may indicate that the contractile force progressively increases from the pacemaker region in the corpus until it reaches the terminal antrum. This concept will be examined in detail in section 2.3.2.

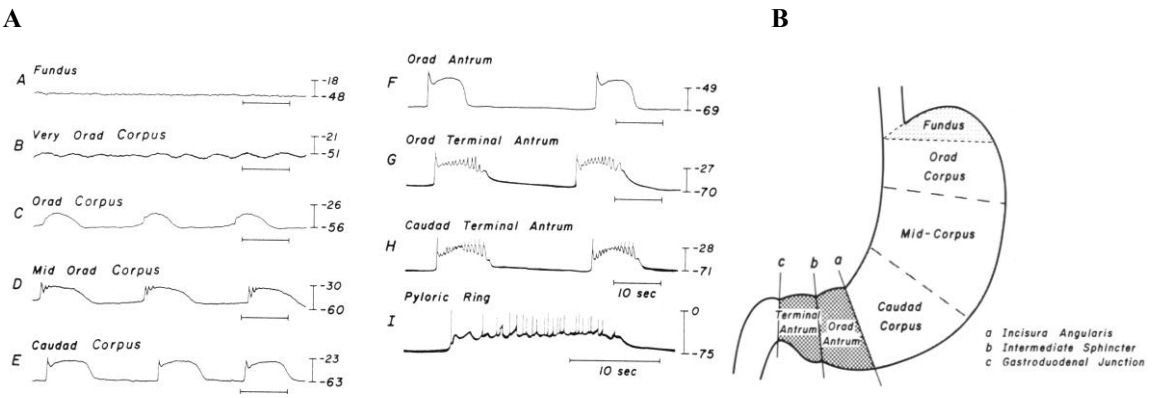

Fig. 2.8 **A** Intracellular resting potentials and spontaneous action potentials in different regions of the canine stomach. **B** schematic diagram of the canine stomach [Reproduced from Szurszewski JH, 1987].

Despite the paucity of information regarding the electrophysiological properties of human visceral smooth muscle, the regional differences found in canine stomachs are similar to

those found in human stomachs. Circular muscle cells in the fundus demonstrate little or no electrical activity, whereas the circular muscle cells of the orad antrum and terminal antrum generate spontaneous potentials. Figure 2.9 illustrates that the changes in intracellular potential of human gastric smooth muscle cells are similar to those obtained from the canine stomach.

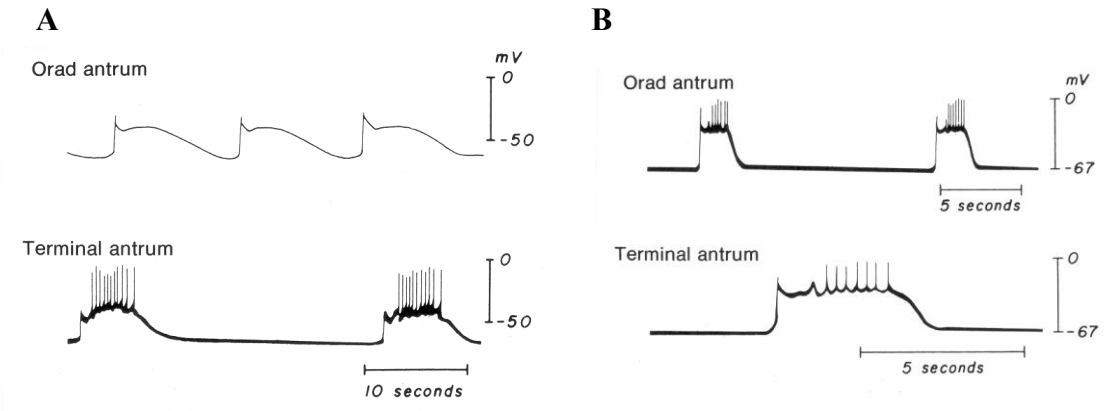

Fig. 2.9 Intracellular muscle activity recorded using electromyography from circular muscle cells in the orad antrum and terminal antrum (6cm proximal to the gastroduodenal junction) from **A** a human stomach and **B** a canine stomach [Redrawn from Szurszewski JH, 1987].

2.4.2 The contractile response to the electrical properties of gastric smooth muscle

The continuous pacemaker action potentials described in section 2.3.1 rarely produce direct the tonal contractions of the smooth muscle. Contractions are generated when the slow wave action potential exceeds a threshold level (Fig. 2.10A).

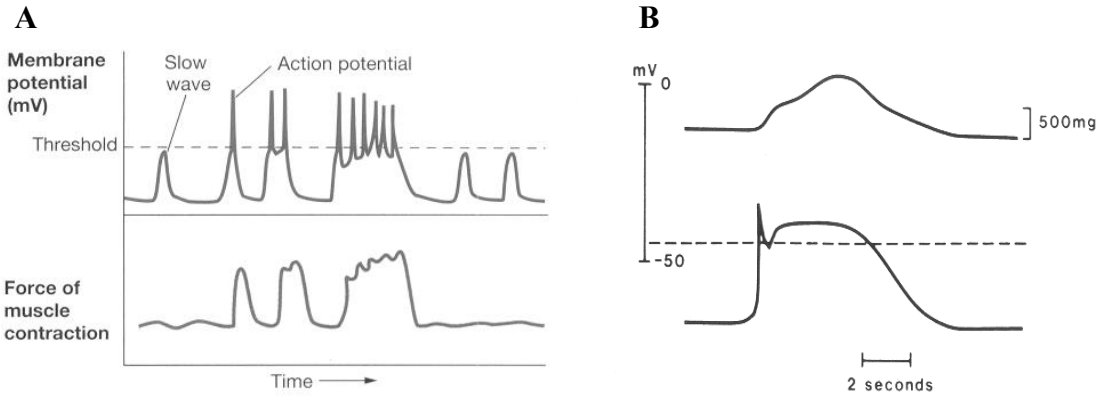

Fig. 2.10 **A** Action potentials fire when the gastric slow waves exceed threshold, producing muscular contractions. The force and duration of the muscle contraction is related to the amplitude and number of action potentials [Silverthorn DU, 2001]. **B** The relationship between intracellular slow waves and the contraction of canine smooth muscle. The dashed line is the electrical threshold for contraction [Redrawn from Szurszewski JH, 1987].

Fig. 2.10B shows that the gastric slow waves in smooth muscle are biphasic. There is a sharp depolarisation causing an increase in the resting potential of the smooth muscle, immediately followed by an equally abrupt partial repolarisation (phase 1), followed by a sustained plateau in the membrane potential (phase 2). Contraction occurs when the depolarising phase exceeds the threshold for contraction (dashed line). The amplitude and duration of this plateau is directly related to the smooth muscle contractions. The greater the depolarisation and the longer the muscle cell remains above threshold, the greater the force of the contraction. However, in the presence of action potential spikes during the plateau region, the contractile force is even greater.

Factors that affect whether the sweeping pacemaker potentials cause a plateau in the membrane potential which would result in a contraction, depends on the stretch of the muscularis, release of neurotransmitters and the presence of hormones or paracrine substances. However, if a plateau is triggered, the frequency, duration and character vary with position along the stomach's axis.

The signals recorded from a canine stomach in Fig. 2.11 illustrate the electrical and mechanical differences found in physiologically different sections of the stomach.

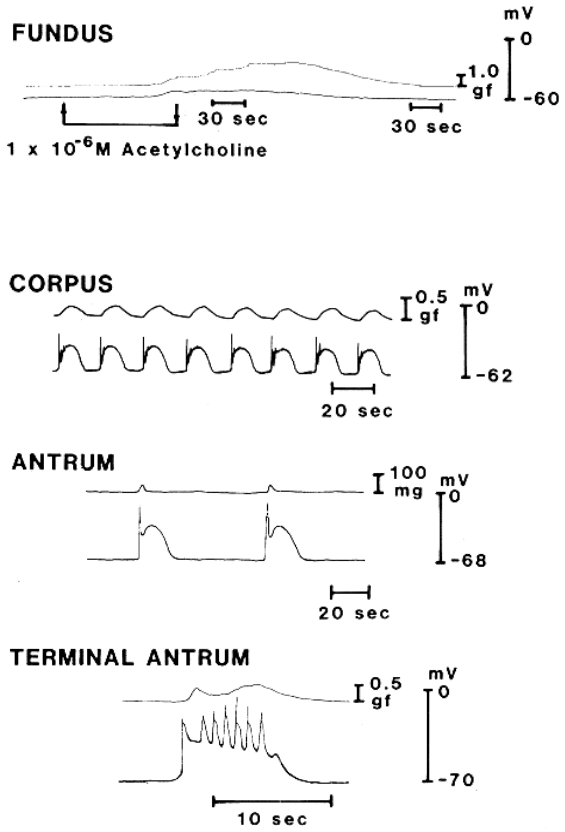

Fig. 2.11 Mechanical activity (top signal) and electrical activity (bottom signal) recorded simultaneously from the circular muscle layer in four different regions of the canine stomach: the fundus, corpus (body), antrum and terminal antrum [Reproduced from Szurszewski JH, 1987].

In the fundus there is usually no electrical or contractile activity. However, the effect of artificially increasing the levels of acetylcholine on fundal tissue is to trigger a small sustained depolarisation that results in a continuous tonal contraction. In the corpus (or body) the gastric action potentials at three cycles per minute produce biphasic contractions; one phase is the upstroke and the second is the plateau region. The upstroke is caused by the initial increase in potential whereas the plateau region initiates the contraction of the smooth muscle. In the antrum the upstroke of the action potential produces a rapid contraction unless the potential exceeds a certain threshold, in which case a second contraction occurs. In the terminal antrum the gastric action potentials demonstrate spike action potentials during the plateau region that are responsible for phasic contractions.

Neural and hormonal processes control the amplitude and frequency of gastric contractions. The neurotransmitter acetylcholine has a stimulatory effect while gastrin and cholecystokinin increase the amplitude of the contraction. The effects of gastrin and acetylcholine are given in Fig. 2.12 below.

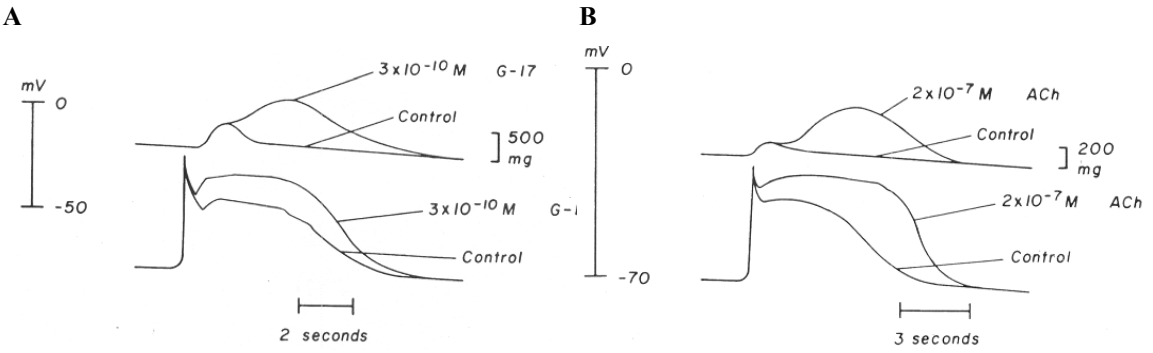

Fig. 2.12 The effects of **A** gastrin (G-17) and **B** acetylcholine (ACh) on the mechanical activity (top signal) and electrical activity (bottom signal) in the orad antrum of the canine stomach [Reproduced from Szurszewski JH, 1987].

2.4.3 The Migrating Motor Complex (MMC)

Invasive electrogastrography has been used for decades to measure the electrical activity of the entire gastrointestinal tract. The technique was employed by Szurszewski to analyse the electrical activity of the small bowel in fasted dogs over a period of 18-21 hours.

The results showed a caudedly-moving band of intense action potential activity, sweeping the GI tract in recurring cycles of approximately 90–180 minutes [Szurszewski JH, 1969]. Code and Martlett later demonstrated that the activity front is part of a complex (the migrating motor complex, MMC) that starts in the pyloric antrum and sweeps through the small intestine every 90-120 minutes [Code CF, 1975]. Four distinct phases in the MMC were identified.

Phase I is a period of quiescence lasting for 45–60 minutes. Although pacemaker potentials are generated in the antrum during this phase, they do not exhibit spike potentials and consequently few contractions are observed. This means that there is little or no movement of gastric contents.

Persistent or random spike potential marks the beginning of the phase II. During this phase there are intermittent contractions that initially occur at one per minute. These increase in frequency and amplitude for a period of 30 minutes and occur together with simultaneous bursts of duodenal contraction [Houghton LA, 1988]. During phase II there is some mixing of the gastric contents but little propulsion.

Phase III comprises of a period of high electrical activity, between 5 and 15 minutes in duration. Each potential is followed by a contraction that sweeps down the pyloric antrum and small intestine. The frequency of the contractions in the pyloric antrum and canal are between 2.5 and 3.5 cycles per minute (cpm). Conversely, the contractions in the duodenum are more frequent at 10–12 cpm [Houghton LA, 1988].

These contractions lead to the propulsion of chyme, thus clearing out the GI tract. Phase IV is identified by the abrupt and rapid decrease in incidence and intensity of the spike potentials, returning to phase I activity within a few minutes. The MMC may be responsible for producing the hunger pangs that we feel during the fasting period, especially when we first awake in the morning.

Although the MMC is generally associated with the intestinal section of the alimentary canal, Code and Martlett attempted to investigate the repercussions of the MMC on gastric motility in the canine stomach. Twelve electrodes were sewn onto the serosa of the stomach and duodenum to measure the myoelectrical activity. They found that the MMC activity starts in the pylorus of the stomach and the duodenum before progressing through the GI tract [Code CF, 1975].

Subsequently, Itoh established that the fundus and body of the stomach also contract in association with the pyloric antrum during the MMC [Itoh Z, 1978]. This was confirmed by further research carried out in 1983 [Itoh Z, 1983] shown in Fig. 2.13.

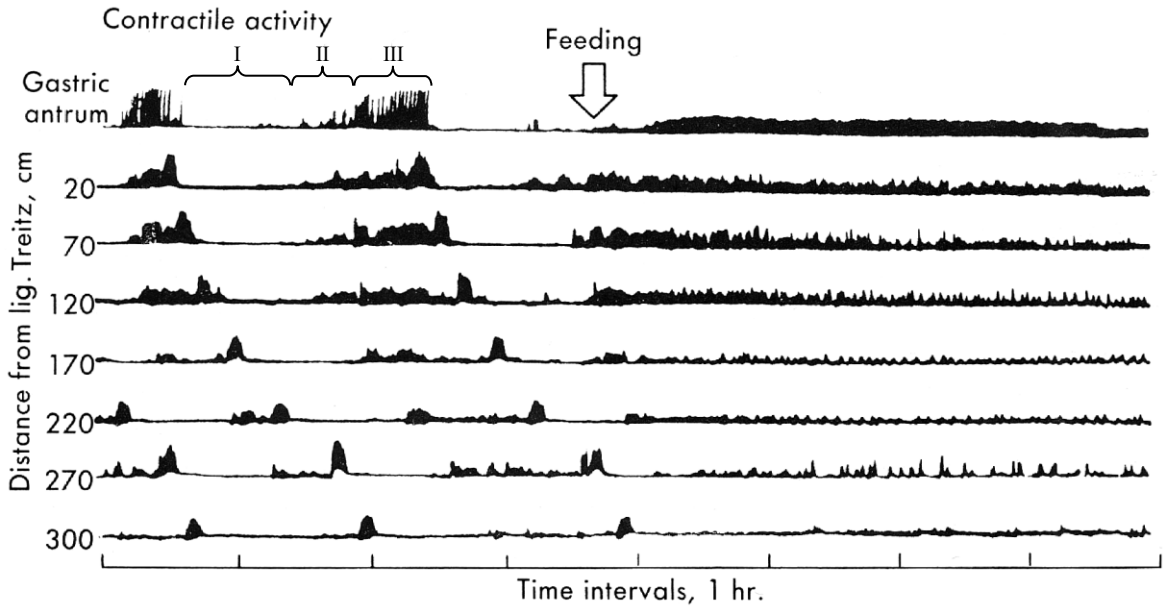

Fig. 2.13 Contractile activity in the stomach and small intestine of an initially fasted canine in which periodic migrating myoelectric complexes are present. Note that the MMCs are abolished following feeding and contractile activity is continuous [Redrawn from Itoh Z, 1983].

Non-invasive electrogastrography has been used simultaneously with gastric intraluminal pressure recordings. It was concluded that the gastric myoelectrical frequency is less stable during motor activity than during periods of quiescence, particularly during phase III of the MMC.

There was a consistent 4% drop in gastric myoelectrical frequency during the transition from phase I (quiescence) to phase II and an increase in the power by at least a factor of two of frequencies in the gastric bandwidth (0.04 to 0.06 Hz or 2.4 to 3.6 cpm). Additionally the study found that out of 21 recorded MMC activity fronts in ten volunteers, 16 (73%) originated in the stomach. Table 2.1 gives a summary of their results [Geldof H, 1986a].

Table 2.1 Comparison of findings during different phases of the MMC

IMC	*Phase I*	*Phase II*	*Phase III*
		Stomach (n=16)	
Gastric frequency (Hz)	0.049	0.047	0.048
	0.043-0.052	0.041-0.052	0.041-0.056
Standard deviation	0.0019	0.0029	0.0042
	0.0014-0.0023	0.0021-0.0043	0.0024-0.0060
Power increase		2.61†	0.76‡
		2.06-5.20	0.05-3.95
		Duodenum (n=5)	
Gastric frequency (Hz)	0.050	0.050	0.050
	0.049-0.051	0.048-0.051	0.049-0.053
Standard deviation	0.0022	0.0024	0.0023
	0.0018-0.0026	0.0020-0.0029	0.0020-0.0026
Power increase		1.17†	0.81‡
		1.02-2.18	0.46-1.04

Values represent medians and ranges. †Power increase at the changeover from phases I to II. ‡Power increase at the changeover from phases II to III. [Reproduced from Geldof H, 1986a].

2.4.4 The regulation of gastric emptying

Gastric emptying is the process by which chyme is periodically released from the stomach into the duodenum. The emptying rate is moderated by neural and hormonal reflexes as shown in Fig. 2.14 in order to ensure that the flow of chyme into the duodenum is at a rate suitable for optimal nutrient absorption. The emptying rate must be sufficiently low in order to maintain the correct levels of intestinal pH and osmolarity [Wingate DL, 1994].

The rate of gastric emptying increases with distension of the stomach and the presence of protein, alcohol and caffeine. These trigger gastrin secretion and produce parasympathetic impulses in the vagus nerves. There is subsequently an increase in gastric motility, the contraction of the lower oesophageal sphincter and the relaxation of the pyloric sphincter resulting in the movement of gastric chyme into the duodenum.

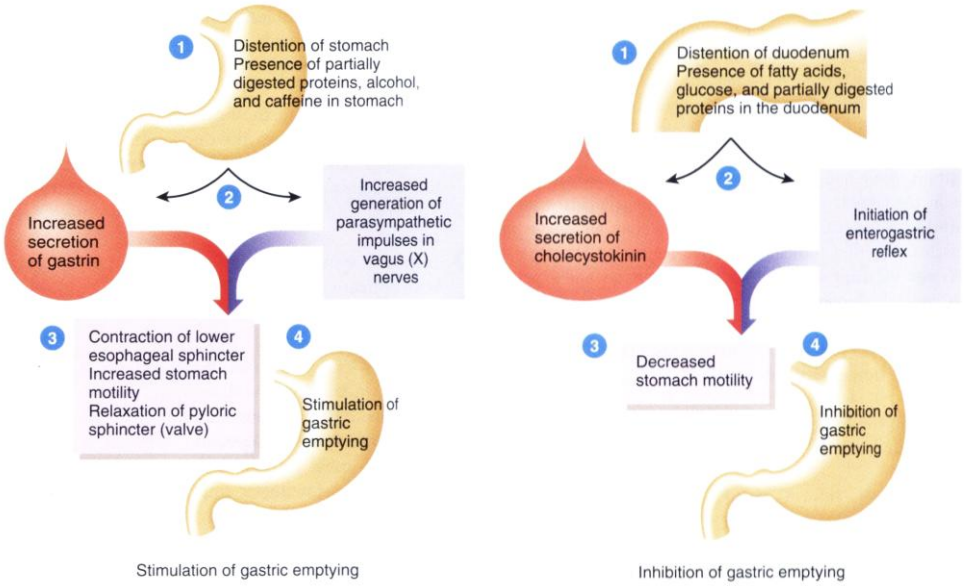

Fig. 2.14 Basic neural and hormonal regulation of gastric emptying [Reproduced from Tortora GJ, 2000]

Conversely, neural and hormonal reflexes also ensure that the stomach does not empty too quickly so that the duodenum cannot process the chyme. There is much evidence to suggest that duodenal chemoreceptors and mechanoreceptors play a vital role in feedback regulation of gastric emptying [Kelly KA, 1981]. Duodenal distension and the presence of fatty acids, glucose and proteins in the duodenum begin to inhibit gastric emptying by initiating the enterogatsric reflex. The duodenum then sends messages via nerve impulses to the medulla oblongata in the brain to inhibit parasympathetic stimuli and promote sympathetic activity that releases CCK.

A number of studies have shown that the blocking of CCK with loxiglumide (a CCK antagonist which blocks CCK receptors) reverses the delay in gastric emptying brought about by the presence of nutrients in the small bowel [Fried M, 1991]. Other research using Loxiglumide successfully demonstrated that CCK exerts a potent inhibitory action on gastric secretions and gastrin release [Konturek JW, 1993]. Another study validated these findings and proved that CCK also has a key function in the control of gastric emptying, delaying the emptying rate of chyme into the duodenum in response to a fatty meal [Konturek JW, 1994].

It is a well established physiological phenomenon that incorporating fat into a meal will delay gastric emptying from the feedback mechanisms described above. The mechanisms are activated in order to mix the chyme with a variety of gastric secretions. Further studies have shown that in aqueous meals mixed with fat in both human and canine models, the aqueous part of the meal emptied rapidly while the intra and extracellular fat emptied in parallel after a lag time. However, it was also shown that the majority of intracellular fat emptied within the solid food phase while most of the extracellular fat emptied as oil [Meyer JH, 1986].

All of the studies related to research into the effects of lipids and CCK on gastric emptying rates are of prime importance to the study of satiety, particularly with respect to dyspepsia (section 3.2.4). Many patients complain of unpleasant abdominal cramps and bloated feelings after eating meals with a high fat content [Stanghellini V, 1994]. Some studies have suggested that the presence of lipids in the duodenum may induce sensations of early satiety or symptoms of nausea [Drewe J, 1992].

There has also been interest in identifying a relationship between the calorific value of the chyme and the rate of emptying. Work by Hunt and Stubbs, shown in Fig. 2.15 demonstrates that the rate of delivery of calories to the duodenum is relatively constant [Hunt JN, 1975].

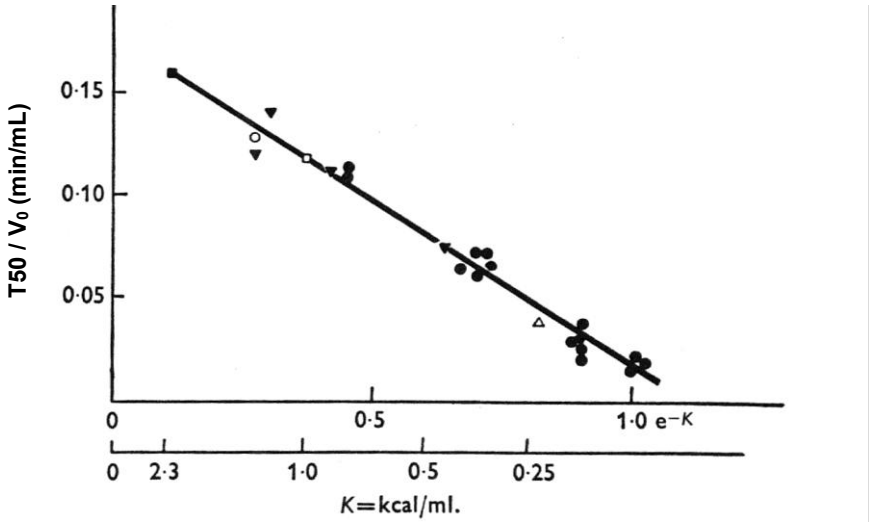

Fig. 2.15 Relationship between ratio of T_{50}/volume of original meal and e^{-K}, where K=kcal/mL of meal. $T_{50}/V_0=0.1797-0.167e^{-K}$ (sem.±0.005), V_0(mL) ● 750, □ 550, ○ 500, ■350, ▼300, △ 200 [Reproduced from Hunt JN, 1975].

McHugh and Moran showed that by doubling the volume of saline infused into unanaesthetised male *Macaca Mulatta* (a genus of monkey), the emptying rate increased so that the time taken to empty half of the volume (T50) remained constant (15 minutes). However, glucose meals emptied more slowly than saline progressively and linearly more slowly with increasing concentrations.

Doubling the volume of the glucose meal did not change the emptying rate as it had with saline verifying the work of Hunt and Stubbs to show that rate of delivery of calories into the duodenum is constant. They calculated that the emptying rate in kcal per minute for glucose was approximately 0.4 kcal/min. The tests were repeated with medium triglyceride oil meals with similar results [McHugh PR, 1979].

There is also evidence that suggests that the osmolarity of the chyme in the duodenum also has an effect on gastric emptying rates. Meeroff found that emptying rates were fastest when the duodenal content was isotonic. Non-isotonic chyme slowed emptying but only in the duodenum. That is to say that the osmolarity of chyme in the stomach did not have an effect on the gastric emptying rate. Therefore, there are osmoreceptors which slow gastric emptying located in the duodenum, but not in the stomach or jejunum [Meeroff JC, 1975].

2.5 Post prandial gastric contractility

2.5.1 Gastric contractility of the fed stomach

The stomach exhibits a number of mechanical functions following the consumption of a meal required for digestion and emptying. There are generally at least several seconds between each bolus of food entering the stomach, as effective swallowing would be impossible at a faster rate. Since the stomach is in essence a muscular bag, it possesses a reservoir function that means that it can expand in volume at a rate of at least 100mL/min from approximately 50mL in the fasted state to 1500mL or more in the fed state [Christensen J, 2001]. The initial effect of swallowing induces a relaxation in the fundic region of the stomach (Fig. 2.3) known as adaptive relaxation.

Azpiroz and Malagelada demonstrated this phenomenon using a barostat and manometer and their results have been reproduced in Fig. 2.16. The barostat consists of a plastic bag tied to the end of a catheter and placed directly into the gut lumen. The air pressure inside the bag is kept constant by feedback control. Pressure increases inside the gut causes a withdrawal of air from the bag and vice versa. Consequently, gastrointestinal contractions are registered as volume decreases and relaxations as volume increases [Kreis ME, 2002].

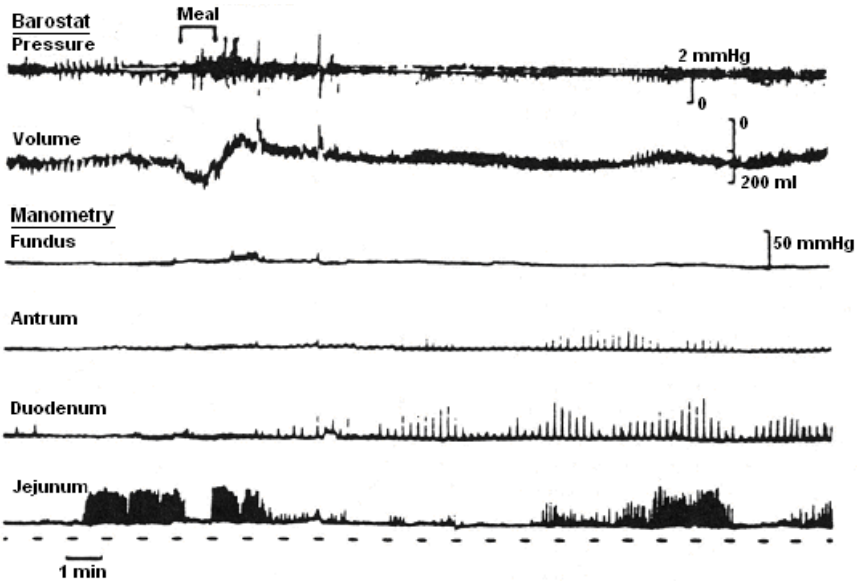

Fig. 2.16 Gastrointestinal motor response to feeding in dogs recorded by barostat, which inversely measures changes in gastric tone and manometry [Redrawn from Azpiroz F, 1985a].

It is clear from the Volume recordings in Fig. 2.16 that the direct consequence of deglutition is to relax the gastric tone in the fundic region. The tone recovers after a few minutes and momentarily increases to assist the emptying of chyme [Azpiroz F, 1985a].

The results from Azpiroz and Malagelada also illustrate the increase in antral contractility following the ingestion of a meal. Fig. 2.13 indicates that gastric contractions begin as soon as food is ingested, following the cessation of any MMC activity. These antral contractions facilitate digestion as the sequence of motor events determines the way chyme is mixed in the stomach and emptied into the duodenum. Cineradiographic studies have provided evidence for the understanding of these events. Carlson studied this in the canine antrum by giving barium sulphate and acquiring pictures at 15 frames per second and tracing every fifteenth frame [Carlson HC, 1966]. Therefore the frames shown in Fig. 2.17 are 1 second apart.

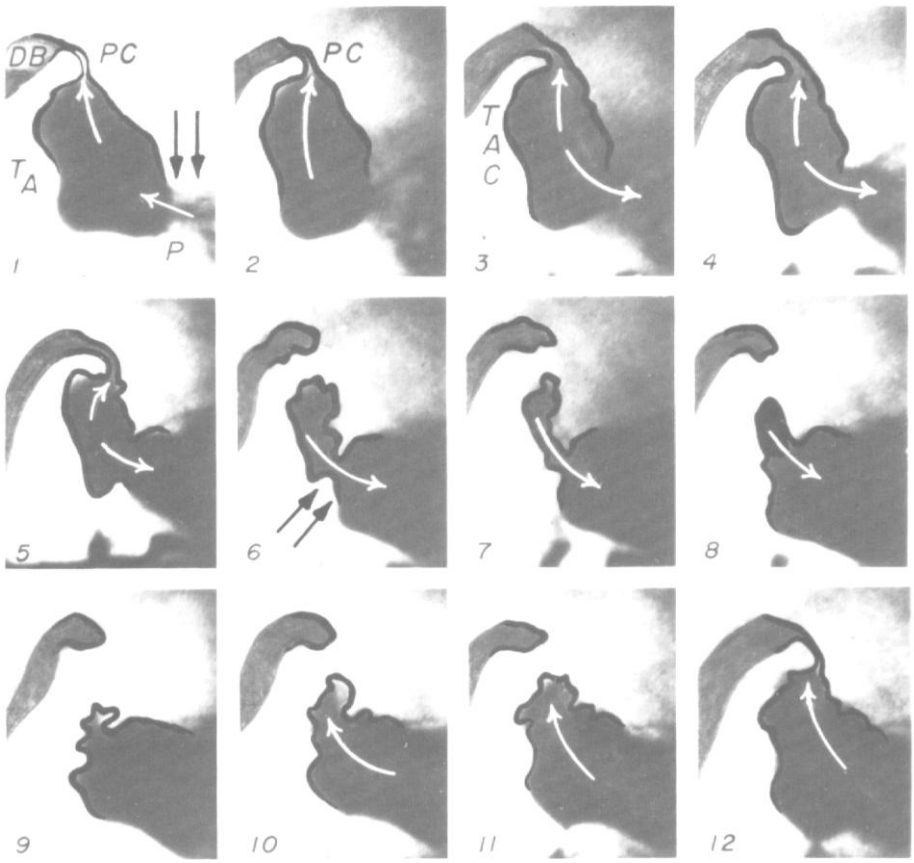

Fig. 2.17 Cineradiographic sequence of pyloric and antral contractions in the stomach of an unanaesthetised dog. DB is the duodenal bulb, PC is the pyloric canal, TA is the position of the terminal antrum and TAC in frame 3 is the terminal antrum contraction [Reproduced from Carlson HC, 1966].

In section 2.3.2 it was explained that gastric action potentials (which trigger changes in muscle tone and bring about tonal contractions) are biphasic; there is an initial depolarisation (phase 1) followed by a plateau period (phase 2). Fig. 2.18 shows the two phases of the action potential that produce a two-component tonal contraction. The first component is caused by phase 1 of the action potential and the second component is caused by phase 2. The strength of the second component depends on the length of the plateau period and the presence of spike activity (Fig. 2.10). It has been suggested that emptying of chyme into the duodenum occurs between the two components of the contraction [Szurszewski JH, 1987]. The duration of the period between the two components is in the range of 2.0 and 3.2 seconds (mean 3.0) and may be seen in Fig. 2.18.

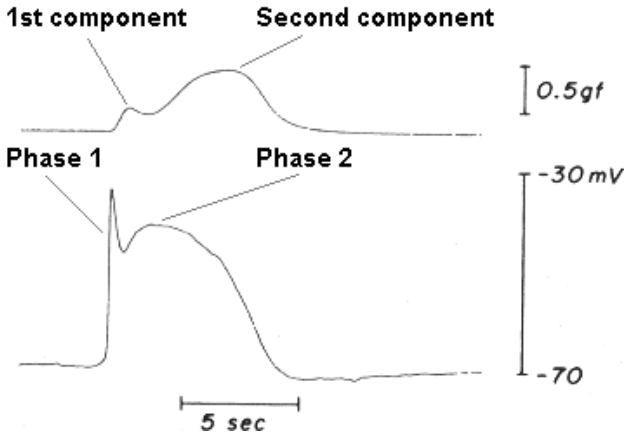

Fig. 2.18 Electrical activity (lower signal) and subsequent tonal contraction (upper signal) in the canine orad antrum clearly showing the biphasic nature of the terminal antrum contraction [Redrawn from Morgan KG, 1981].

Szurszewski's hypothesis states that the characteristics of the two-component contraction govern the coordination between terminal antral contractions and the timing of the opening and closing of the pyloric sphincter. It is reasonable to say that these two factors control gastric emptying rates and in order to understand the procedure properly it is important to consider the sequence of antral contractions shown in Fig. 2.17. Frame 1 shows the presence of an antral peristaltic contraction (P). Double arrows mark the likely location of the second component of the contraction. The first component is too weak to see anywhere except the terminal antrum. In the first five frames the contraction moves from the corpus to the antrum while the pyloric sphincter remains open and tiny amounts of chyme enter the duodenum.

Fig. 2.19 shows that since the leading edge of the action potential is the initial depolarization, as the action potential propagates towards the pylorus, the first component of the contraction closes the pylorus completely and separates the antrum from the duodenum. This can be seen clearly in frame 6 of Fig. 2.17. It is also possible to locate the plateau of the action potential, as it is responsible for the large contraction indicated by the double arrow in Fig. 2.17.

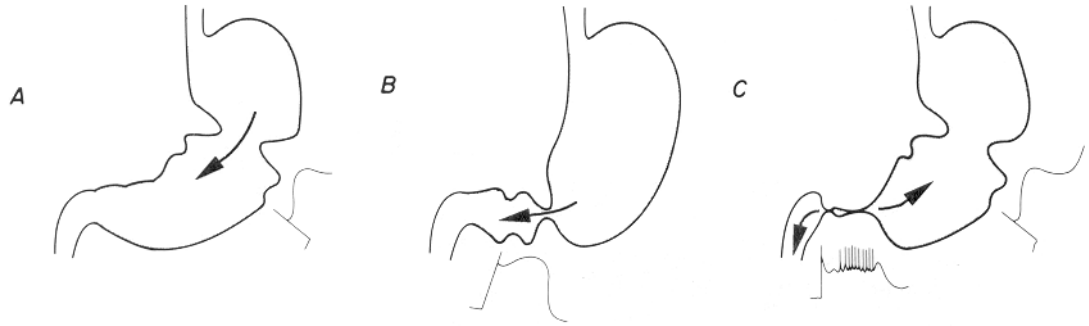

Fig. 2.19 Schematic representation of the relationship between gastric action potentials and contractions during the digestive process. **A** The action potential propagates from the antrum towards the pylorus (compare the shape of the contraction with Fig. 2.18). **B** The magnitude of the plateau region increases which in turn increases the strength of the contraction. **C** As the action potential reaches the pylorus, phase 1 (Fig. 2.18) closes the pylorus completely [Redrawn from Szurszewski JH, 1981].

The pylorus remains closed as the antral contraction caused by the plateau potential continues to propagate towards it, gaining in power. Three seconds after the pylorus has closed the terminal antrum contraction closes the lumen off completely (frame 9 in Fig. 2.17). The time lag corresponds with the time between the first and second components of the contraction caused by the two phases of the biphasic action potential (Fig. 2.18). The pyloric antrum remains closed for the next 4 seconds while the plateau potential progresses into it. During this time the orad antrum relaxes to allow the stomach to fill again (frames 9 to 12 in Fig. 2.17) [Carlson HC, 1966].

It seems that the physiological role of the initial contraction is to close off the pylorus and this would consequently suggest that the pylorus would close regardless of the presence of a second phase in the action potential above threshold level (Fig. 2.10A). Explicitly this means that even if the threshold level for the second phase of the action potential is not reached and accordingly there is little or no antral contractility, the pylorus is still triggered to close and open, allowing passive control of gastric emptying. These pyloric contractions in the absence of antral contractility are called isolated pyloric pressure waves (IPPWs).

When threshold level for the second phase of the action potential is reached, the physiological effect of the subsequent antral contraction is to generate a pressure difference between the antrum and the duodenum. When solid meals (or meals containing solid and liquid) are ingested, the coordination of these contractions with the closure of the pylorus allows the stomach to mix, triturate, sieve and decant the gastric contents as part of the digestive process before emptying can take place (Fig. 2.20).

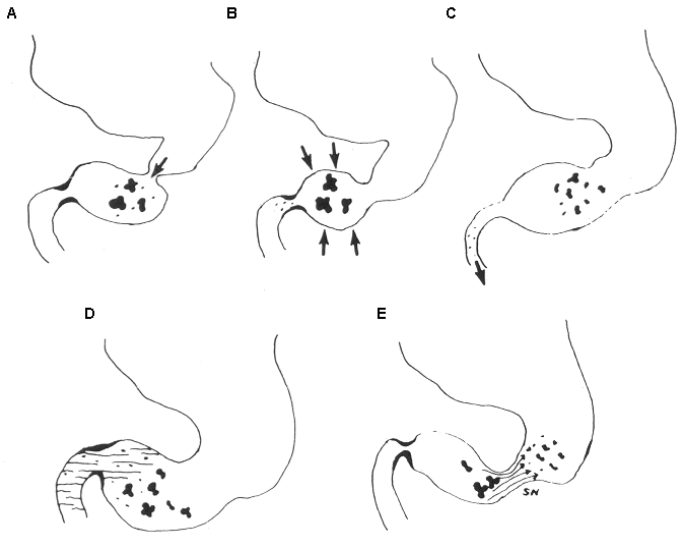

Fig. 2.20 **Gastric sieving: A** Food is swept into the distal stomach where **B and C** the small particles are emptied and the larger particles are retained and broken down further by the contraction. **Gastric decanting: D** Due to the elevated level of the pylorus, the liquid part of the meal is emptied leaving the solid part to be digested further. **E** The closure of the pyloric sphincter at the time when the antral contraction strengthens causes retropulsion of large particles into the antrum grinding and mixing them down [Redrawn from Rao SSC, 1993].

There have been few studies investigating the sieving, grinding and decanting properties of the stomach, probably due to the difficulty in detecting such events. One exception is a study by Marciani L (2001b) using echo-planar magnetic resonance imaging to measure the forces exerted on the gastric contents. Emptying rates were measured for model meals containing agar gel beads (with a diameter of 1.27 mm and a range of fracture strengths from 0.15 to 0.90 Newtons). The meals had either high or low viscosity. Fig. 2.21 illustrates that the effect of increasing the bead strength is to delay their emptying into the duodenum (i.e. increase their residence time in the stomach. There was no significant effect on antral contractility [Marciani L, 2001b].

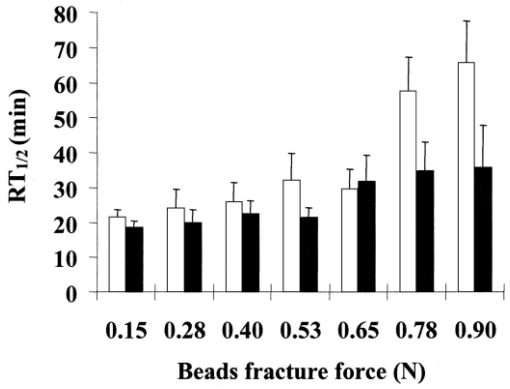

Fig. 2.21 Half-residence time of intact agar gel beads in the gastric lumen for each of the 7 bead breakdown forces and for both low-viscosity (open bars) and high-viscosity (filled bars) meals [Redrawn from Marciani L, 2001b].

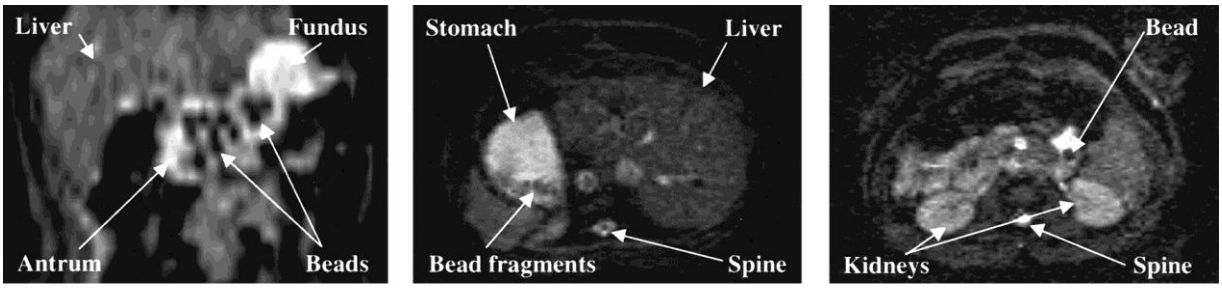

A **B** **C**

Fig. 2.22 Examples of echo-planar magnetic resonance imaging of the gastric lumen of normal volunteers who ingested 500mL of low-viscosity meal together with 15 spherical agar gel beads. The meal appears bright and the beads dark in the images. **A** Intact beads in the antrum in a coronal view reconstruction. **B** Fragments of broken-down beads in fundus. **C** An intact bead in the duodenum in transverse view [Redrawn from Marciani L, 2001b].

2.5.2 The effect of fat on the emptying of liquid meals

When liquid meals are ingested there is great interest into the effect of the fat content on gastric contractility and motility (sections 2.3.1 and 2.3.4). There is little doubt that the presence of fat in the meal causes gastric emptying rates to lengthen. It is likely that the slowing of transit from the stomach is necessary for mixing of the chyme with various gastric secretions that enter the lumen that are required for the digestion of fat (Fig. 2.23). Low-calorific meals such as water do not need digesting and so they are allowed to empty more quickly.

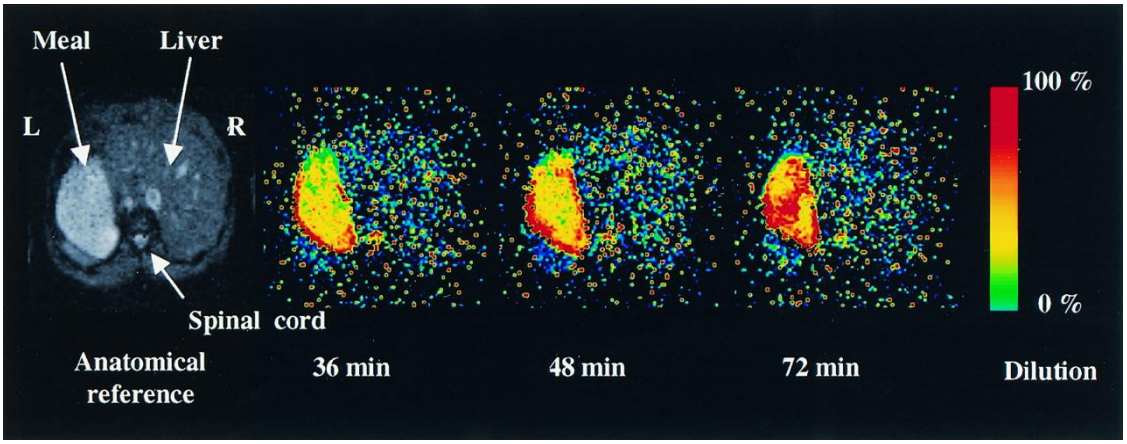

Fig. 2.23 MRI colour-coded dilution maps showing the mixing of chyme with gastric secretions. Images were acquired after the volunteer ingested 500mL of viscous locust bean gum meal. Gastric secretion made the outer boundaries of the meal more diluted (red) at an early time, whereas the inner bolus remained undiluted (green) for longer. As time progressed, the meal became more diluted and mixed [Reproduced from Marciani L, 2001a].

There has been extensive research into the effect of fat on the emptying and motility of liquid meals. The cause of the fat-induced reduction in gastric emptying rates appears to be highly complex. Nevertheless, research into this area has focussed on investigating the coordination between contractility in the gastric antrum, pylorus and duodenum.

2.6 Gastro-pyloro-duodenal coordination after the ingestion of liquid meals

2.6.1 The structure and function of the gastroduodenal junction

The interrelationship between contractile events in the gastric antrum, pylorus and duodenum is known as gastro-pyloro-duodenal coordination and it has been recognised as playing a vital role in controlling gastric motility and mediating gastric emptying rates. It is therefore important to understand the structure of the gastroduodenal junction and its function in gastric motility.

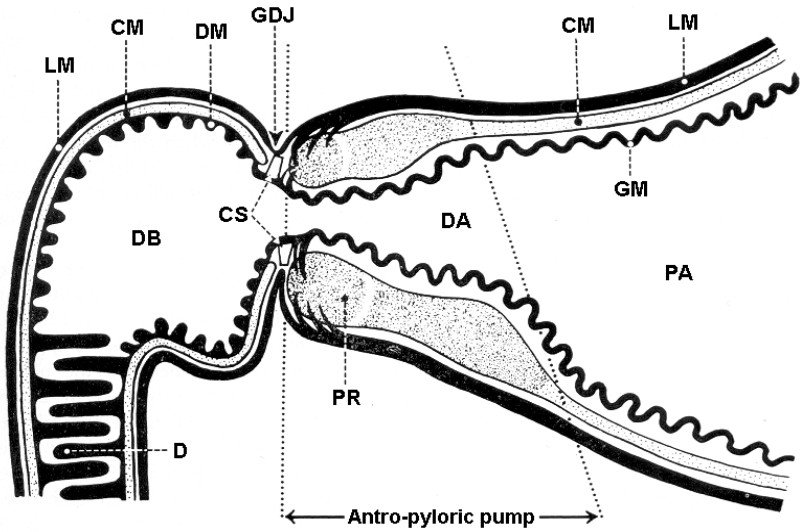

Fig. 2.24 Diagram of the anatomy of the human gastroduodenal junction. **DA** Distal antrum (pyloric canal). **PA** Pyloric antrum. **GDJ** Gastroduodenal junction. **CM** Circular muscle fibres. **LM** Longitudinal muscle fibres. Note that three quarters end at the GDJ and the remaining fibres continue into the duodenum. **CS** Connective tissue septum that separates the circular muscle fibres of the stomach with those of the duodenum. **DM** Duodenal mucous membrane. **GM** Gastric mucous membrane. **DB** Duodenal bulb. **D** Duodenum showing the circular folds of mucous membrane and submucosa. [Redrawn from Edwards DAW, 1968].

The pylorus contains circular smooth muscle layers that form two ring shaped thickenings (distal and proximal muscle loops) followed by a ring of connective tissue that isolates the duodenum from the pylorus. This section of the stomach acts as a sphincter and is fundamental in controlling transpyloric flow.

2.6.2 Postprandial changes in antro-duodenal pressure

Transpyloric flow occurs through two possible processes: either by local increases in the pressure difference between the antrum and duodenum caused by propagating gastric contractions in the presence of constant pyloric resistance, or by a sustained antro - duodenal pressure difference caused by tonic changes in the antral smooth muscle together with the independent opening and closing of the pylorus. The former is referred to as the peristaltic pump and the latter (pressure pump) occurs during periods of peristaltic quiescence. The question is whether the method used by the stomach depends on the fat content of the meal and if so, whether this is responsible for the delay in gastric emptying.

Hausken investigated the transpyloric flow of a low-calorie liquid meal (meat soup) using Duplex ultrasound and manometry [Hausken T, 2002]. The soup contained 0.9g protein, 0.9g fat and 0.9g carbohydrate with a total energy content of 37.7 kJ. The results showed that antroduodenal pressure differences were significantly lower during non-peristaltic-related emptying than during peristaltic-related emptying (Fig. 2.25).

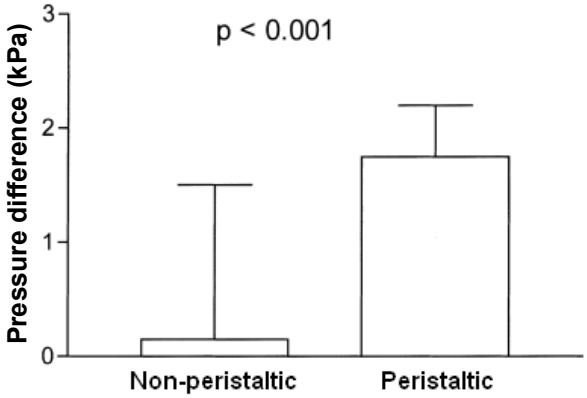

Fig. 2.25 Antroduodenal pressure differences of non-peristaltic and peristaltic antral contractions (mean ± range). [Redrawn from Hausken T, 2002].

Hausken reported that considerable flow was observed without peristalsis and that despite lower antroduodenal pressure differences the duration of those emptying episodes that occurred without peristalsis were longer than those with peristalsis (6.5s [3.0s – 8.7s] and 4.4s [2.0s – 6.0s] respectively). Hausken concluded that this was probably due to a decrease in pyloric resistance. These findings demonstrated that gastric emptying of a low-calorie liquid meal occurs during both peristaltic and non-peristaltic antral contractility [Hausken T, 2002].

Indireshkumar investigated the effects of intraduodenal nutrient infusion (4.6kJmL^{-1} at the rate of 2mLmin^{-1} from 30 minutes before scanning until the end of the experiment) on gastric volume, pressure and contractility following the ingestion of non-nutrient saline using MRI and intraluminal manometry. The results indicated that four out of the seven subjects exhibited propagating high pressure events (between 7.1% and 31.5% of the examination time) whereas the other three subjects (who exhibited no propagating high pressure events) had longer periods of quiescence (98±2.8% vs. 76±9.4%). Non-propagating high pressure events occurred in all seven subjects and were not significant.

The maximum antral pressure was calculated by multiplying the mean antral pressure with the duration of the high pressure event. The gastric emptying was generally higher in groups that exhibited *low* maximum antral pressure, based on propagating *and* non-propagating high pressure antral events (Fig. 2.6). This implied that fast emptying was associated with the pressure pump mechanism (sustained antro - duodenal pressure difference together with the independent opening and closing of the pylorus).

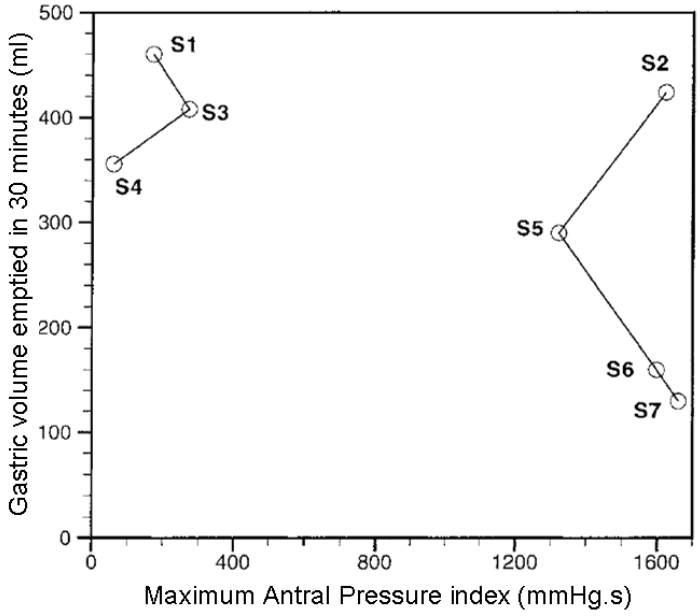

Fig. 2.26 Level of antral pressure against gastric emptying rate expressed as volume of gastric content emptied in 30 minutes [Indireshkumar K, 2000].

The correlation coefficient was calculated as -0.65 between the gastric emptying rate and level of antral pressure. However, Indireshkumar acknowledged that the number of samples was not sufficient for this to be statistically significant.

The pyloric motility was also investigated and Indireshkumar noted that in periods of quiescence in the antral pressure correlated with periods of quiescence in the pyloric region suggesting that transpyloric flow was taking place by the pressure pump mechanism. Furthermore, in those subjects that exhibited a high proportion of propagating high pressure events, pyloric resistance increased as the propagating antral pressure waves moved towards it, suggesting the action of the peristaltic pump.

Indireshkumar demonstrated that the peristaltic pump did not play a dominant role in gastric emptying. This hypothesis was strengthened by the fact that differences in antral pressure were not significant across the seven subjects despite the fact that the emptying rate varied between 4.3 $mLmin^{-1}$ to 15.3 $mLmin^{-1}$. If the emptying rate had correlated with a reduction in intragastric pressure, it would imply that the stomach is a simple elastic bag.

However, since the emptying rate was not correlated with a reduction in intragastric pressure, it seems that that tonic increases in the gastric smooth muscle occurred independently of contractile activity in the antrum. Indireshkumar concluded that counter intuitively, fast emptying is the result of pressure pump activity in which the gastric content is emptied by the pressure difference between the antrum and duodenum in conjunction with lower pyloric resistance whereas reductions in gastric emptying rates prompted by the presence of fat in the duodenum are caused by increased pyloric contractility triggered by propagating antral pressure waves (Fig. 2.19) [Indireshkumar K, 2000].

2.6.3 Postprandial changes in the flow of chyme

Boulby used MRI to analyse the flow of chyme in the gastric antrum following the ingestion of 5% glucose, 10% glucose and an isotonic high calorie nutrient meal (Fresubin®) with energy content of 4.2 $kJmL^{-1}$. The results showed an increase in forward and backward antral flow events in the Fresubin meal compared to the 5% glucose meal. The peak flow velocities varied between 1.9 and 5.8cms^{-1} but did not differ significantly between meals [Boulby P, 1999]. Fig. 2.27 shows the detection of retrograde flow in the body of the stomach caused by an antral pressure wave with MRI. The volume of chyme emptied into the duodenum largely depends on the magnitude of the contraction.

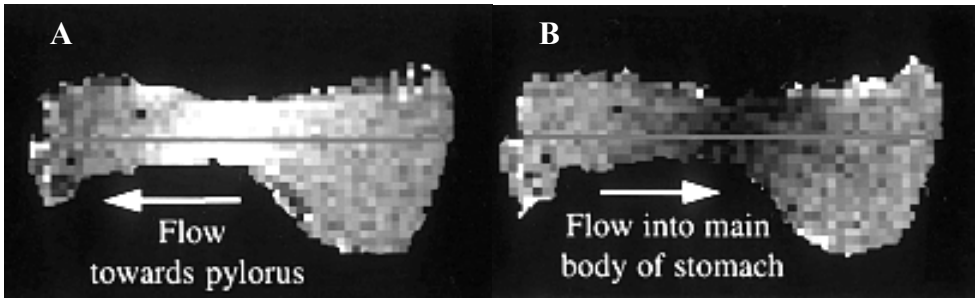

Fig. 2.27 Two images where **A** flow towards the pylorus and **B** flow away from the pylorus was observed. [Redrawn from Boulby P, 1999].

It seems clear from Figs. 2.18 and 2.19 that the physiological role of the first phasic contraction is to close the pylorus. The antral contraction seems to facilitate the propulsion of the gastric content towards the closed pylorus by creating a pressure difference thus forcing most of the chyme back into the stomach, while allowing some to enter the duodenum. The main finding from this study was that flow activity was greater 35 minutes after the ingestion of the high fat Fresubin meal than the 5% glucose solution, despite the delayed gastric emptying.

2.6.4 Postprandial changes in the contractile power

Ferdinandis studied the effects of various carbohydrate meals on gastric myoelectrical activity using electrogastrography (EGG). There were large differences recorded in the dominant power between fasting and fed states for solid meals (7.4%) and semi solid meals (5.3%). However, liquid meals did not trigger a statistically significant increase the postprandial power [Ferdinandis TGHC 2002].

2.6.5 Duodeno - gastric exchange and retropulsion

King used ultrasound to investigate the transpyloric flow movements of dilute orange juice and bran [King PM, 1984]. Bran was included so that it would clearly show the movement of the chyme on the ultrasound and the particle size was small enough to regard the mixture as a liquid. Results from 4 of the 15 subjects are shown in Fig. 2.28. The findings indicated that emptying of the juice (a low-calorie liquid meal) through the pylorus occurred in 2 to 5 second bursts predominantly when the antrum, pylorus and duodenum were relaxed. This brief period was sometimes followed by retrograde flow.

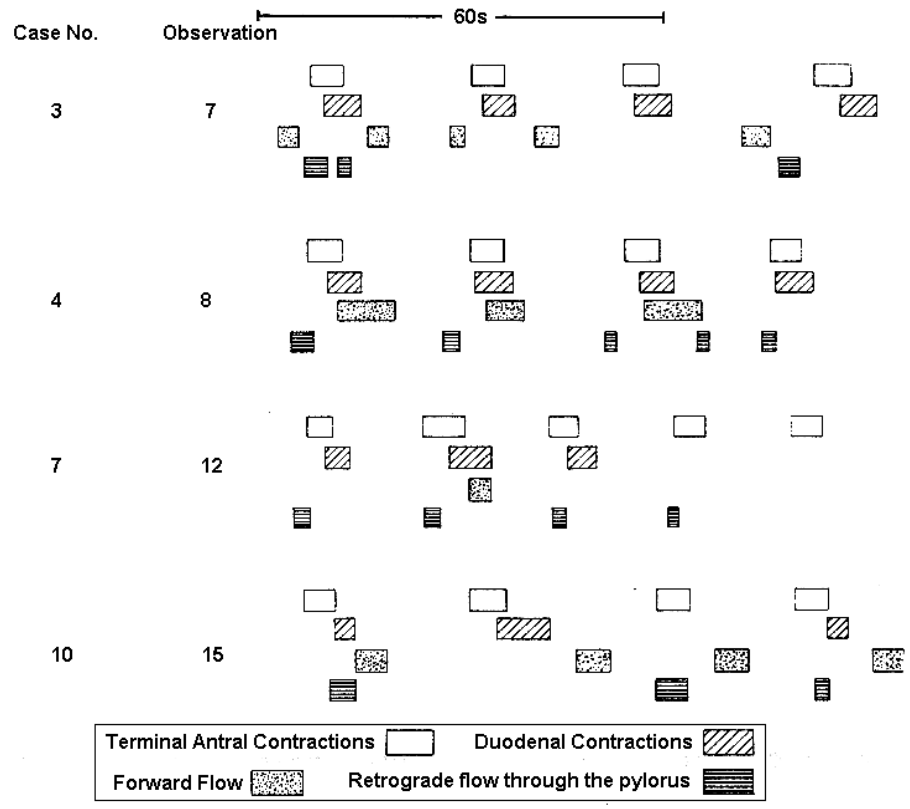

Fig. 2.28 Approximate timings and duration of terminal antrum contractions, duodenal contractions and episodes of forward and retrograde flow through the pylorus from four different subjects [Redrawn from King PM, 1984].

Pressure differences are prerequisite for the movement of fluids and therefore, the transpyloric flow described above would require rapid pressure fluctuations in the pylorus. Backpressure from duodenal contractions must also be considered as a significant source of resistance to transpyloric flow, together with pyloric pressure.

However, the duodenal contractions may generate a backpressure, which either promotes or inhibits gastric emptying, depending on the size of the pressure. There has been extensive research that clearly demonstrates that not only is the gastric content repelled back into the body of the stomach by the closure of the pylorus and subsequent antral pressure wave, but also that there is coordinated retrograde flow through the pylorus implying a continual exchange of chyme between the stomach and the duodenum. The purpose of exchanging gastric chyme is that the duodenum consists of many receptors (measuring chemical makeup, osmotic pressure, acidity and stretch of the muscle wall), which form part of the feedback mechanism that controls gastric motility.

However, retrograde flow from the duodenum to the stomach may have clinical consequences. The gastric mucosa is specialised so that it is resistant to the gastric acid secretions and therefore does not digest itself. However, bile (that contains acids, water, pigments and electrolytic chemicals) secreted in the duodenum by the liver to aid the digestion of fats, is harmful to the gastric mucosa. In contrast, the mucosa of the duodenum is resilient to bile but damaged by the gastric acid secretions. Consequently, if the stomach empties the gastric contents too quickly, there is an increased risk of duodenal ulceration. Conversely, persistent duodenal retropulsion of chyme that contains high levels of bile increases the risk of gastric ulceration.

3 GASTRIC PATHOPHYSIOLOGY

3.1 Current methods of investigating gastric emptying rates and contractility

3.1.1 Diagnostic techniques

The following list shows the most common diagnostic techniques for determining gastric emptying rates and contractility. Many of these methods are not used clinically and there is a constant discussion between clinicians as to the value of each technique.

1 Aspiration techniques (ASP)
2 Absorption techniques (ABS)
3 Breath tests (BRT)
4 Scintigraphy (SCT)
5 X-ray radiology (RAD)
6 Ultrasound (U/S)
7 Manometry and Barostat (M&B)
8 Magnetic Resonance Imaging (MRI)
9 Electromyography and Electrogastrography (EGG)
10 Applied Potential Tomography (APT) and Electrical Impedance Tomography (EIT)

The advantages and disadvantages of these techniques have been summarised in the next section together with a comparison with Electrical Impedance Epigastrography (EIE).

3.1.2 Summary of the characteristics of the techniques for measuring gastric function

The table below outlines the techniques for measuring gastric function.

Table 3.1 Summary of gastric measuring techniques

	Gastric emptying technique (see section 3.1.1)										
	ASP	ABS	BRT	SCT	RAD	U/S	M&B	MRI	EGG	APT	EIE[1]
A	●	●	●	●	●	●		●		●	●
B				○	●	●	●	●	○	●	●
C	●			●				●		●	○
D							○	●	○		●
E				●	●	●		●	○	●	●
F				●	●	●		●	○	●	●
G	●	●	○			●	○	●	●	●	●
H	●	●	●				●				
I	●	●	●	○	○	○	○				
J	●	●	●	●	●	●		●	●	○	
K	●	●	●			●			●	●	●
L						●			●	●	●
M										●	●
N			●			○			○	●	●
O	●	●	●	○	●		●	○			
P				●		●		●			

A Measures gastric emptying rates
B Measures contractility
C Measures gastric secretions
D Measures the velocity of gastric contractions
E Non-invasive
F Percutaneous
G Does not use ionising radiation
H Position of subject is not important
I Not sensitive to motion artefacts
J All types of test meal available (solid, semi-solid and liquid)
K Does not require expensive equipment
L Does not require specialist hospital department (e.g. nuclear medicine department)
M Does not require specialist technician (e.g. Radiologist)
N May be performed in outpatients department, local clinic or GP's surgery
O Obese subjects are not excluded
P Measures gastro oesophageal reflux

● Strongly applies to this technique

○ Applies in some ways to this technique

[1] The advantages and disadvantages of EIE will be discussed at length in Chapter 5.

3.2 Gastric dysmotility

3.2.1 Vagotomy and pyloroplasty

Vagotomy (severing of the vagus nerve supplying the stomach) and pyloroplasty (removal of part of the pylorus) were often performed on patients with gastric ulcerative disorders in order to reduce gastric secretions, as adequate medication was not available. However, since the improvement of medication for the reduction of gastric secretions, particularly omeprazole, the procedure is never performed today. Vagotomised and pyloroplastised patients often exhibited accelerated gastric emptying because the ability of the stomach to accommodate the ingested meal was impaired. Therefore, in vagotomised and pyloroplastised patients the intragastric pressure becomes abnormally high following the ingestion of a meal since the accommodation reflex is lost as a result of vagotomy. Consequently, there is a rapid emptying of the liquid phase of the meal.

3.2.2 Gastric dysrhythmia

During failure of the specialised smooth muscle located in corpus of the stomach known as the pacesetter zone (see section 2.4.1 and Fig. 2.7), cells of lower firing frequency take on the pace setting role. This results in abnormally slow waves of electrical propagation, known as bradygastria. Furthermore, it is possible that competing cells with a faster frequency may dominate the pacesetting function resulting in abnormally fast waves of electrical propagation, known as tachygastria. The normal pacemaker may also fire intermittently giving rise to gastric arrhythmia. These electrical malfunctions of the gastric smooth muscle inevitably have detrimental effects on the contractility. Contractions are poorly coordinated and may in fact exhibit retrograde properties. Action potentials that manage to exceed threshold rarely possess action potential spikes during the plateau region, meaning that contractions in the antrum are impaired consequently triggering antral hypomotility leading to delayed gastric emptying.

3.2.3 Diabetes mellitus

The primary underlying cause of gastrointestinal dysfunction caused by diabetes appears to be autonomic neuropathy, which causes gastroparesis (deterioration in the function of the stomach). The most common symptoms reported are nausea, vomiting, dyspepsia, early satiety and anorexia although these tend to occur intermittently.

There have been a number of studies into diabetes induced gastric dysfunction. The earliest studies showed that gastric contractions were weaker, slower and ineffective as they died out quickly [Ferroir J, 1937]. Blood glucose concentration plays an important role in diabetes induced gastric dysmotility. Gastric emptying is slower in states of hyperglycaemia and accelerated during hypoglycaemia [Horowitz M, 2001]. Accelerated gastric emptying has been found in only a tiny number of Type I diabetic patients [Lipp RW, 1997] but in contrast there is a fair amount evidence that patients with 'early onset' type II diabetes frequently exhibit accelerated gastric emptying [Frank JW, 1995]. This may be significant in the counter regulation of hypoglycaemia; accelerated gastric emptying will facilitate the return to normal blood glucose concentrations. One of the most common complications presented in diabetic patients is the abnormal distribution of the meal in the stomach, with increased retention of food in both the proximal and distal parts [Jones KL, 1995]. Retention in the proximal region may also explain the high incidence of gastro oesophageal reflux among diabetics [Lluch I, 1999].

The leading hypothesis for the aetiology of reduced gastric efficiency, caused by diabetes mellitus is neuropathy of the Vagus nerve, which mediates gastric function. However, impairment of acid secretion brought about by hyperglycaemia may indicate that the blood glucose concentration plays an important role in gastric function. Changes in blood glucose concentration have an acute affect on gastric motility in both diabetic patients and non-diabetic subjects [Schvarz E, 1997].

It is not clear however, that the lengthening of gastric emptying rates during states of hyperglycaemia (blood glucose concentration 16-20 mmol/l) is directly proportional to the gastric emptying rate of a given patient during states of euglycaemia (blood glucose concentration 5-8 mmol/l). What is apparent is that a change in the gastric emptying rates of diabetic patients (particularly those who are insulin dependant) has a marked effect on post prandial insulin requirements and general treatment planning. Type-I diabetic patients with gastroparesis require less insulin to maintain normal blood glucose concentrations following a meal compared to those with normal gastric emptying [Ishii M, 1994]. It is important to note that in many cases the delay in gastric emptying may be modest and distinction should be made between delayed gastric emptying and diabetic gastroparesis, which describes a more severe delay in gastric emptying [Horowitz M, 2001].

3.2.4 Non Ulcerative (Functional) Dyspepsia (NUD)

A significant number of patients complain of non-specific postprandial symptoms such as indigestion, early satiety, nausea, pressure like abdominal pain and vomiting without any specific cause on diagnostic evaluation or any medical or surgical history. Thirty to fifty percent of patients referred to tertiary medical centres presenting with those symptoms do not show signs of any abnormalities following upper endoscopy and ultrasound scans of the gallbladder and pancreas but do exhibit delayed gastric emptying [Lin HC, 1991]. Those patients often report intolerance to specific foods, usually containing liquid fats such as oily foods or milk that have a fast initial emptying [Lin HC, 1994]. The term given to this condition is Non Ulcerative (Functional) Dyspepsia (NUD).

The cause of NUD is not clear; the duodenal load of particular fats may trigger symptoms. Since the load of nutrients into the small intestine regulates gastric emptying (see section 2.4.4) one possible cause of NUD is a breakdown in the normal intestinal feedback response to nutrients leading to a delay in gastric emptying. Solid fats do not cause the same problem because the antral trituration (see section 2.5.1 and Fig. 2.20) process naturally impedes the gastric emptying rate restricting the nutrient load entering the duodenum per unit time. Prokineteic agents such as metoclopramide may have unpredictable effects; symptoms could be exacerbated as accelerated emptying of chyme into the duodenum would lead to an even larger nutrient load causing greater inhibitory feedback resulting in an even slower gastric emptying rate [Lin HC, 1994]. Despite this, there is evidence that patients do often benefit from treatment [Cucchiara S, 1992].

There has been extensive research into the causes of NUD using a number of the techniques described in section 3.2. However, there has been little proof of a specific cause of NUD; a number of studies have found a lack of correlation between individual symptoms and motility disorders found by various tests. Malegalada found no correlation between NUD symptoms and dysmotility using manometry [Malegalada JR, 1985] and Jian found no relationship between symptoms and gastric stasis [Jian R, 1989]. An extensive multifactorial study by Waldron identified a range of abnormal gastrointestinal functions in patients with NUD but could not prove unequivocally that these directly caused the symptoms of NUD and were therefore forced to conclude that they could have been related to other gastrointestinal disorders. [Waldron B, 1991].

Nevertheless, there is a general agreement that a cluster of pathological signs appears to be related to NUD despite a lack of hard proof that they are the underlying cause. Gastric dysrhythmia characteristically implies gastroparesis and delayed gastric emptying. However, the link between abnormal contractility and delayed emptying is not absolute; delayed emptying cannot necessarily be used as a predictor for abnormal contractility and gastric dysrhythmias have been recorded in dyspeptic patients with normal gastric emptying rates [Koch KL, 1992].

Dyspepsia patients also have a lower tolerance to fundal distension despite the fact that barostat experiments have shown that fundal compliance is normal [Mearin F, 1991]. Furthermore, the fundus fails to relax in response to duodenal distension after the emptying of the meal. This suggests an abnormality in the neurogastric pathways causes a hypersensitivity to gastric distension. Troncon investigated the hypothesis that patients with symptoms of early satiety and severe postprandial bloating are likely to exhibit an abnormal distribution of food in the proximal stomach caused by fundoparesis. The study showed that emptying rates of NUD patients and normal controls were similar. Fig. 3.1 shows how food in the control group tended to remain in the proximal stomach and distribute to the distal half slowly whereas in NUD patients, significantly less food remained in the proximal stomach after ingestion and passed directly to the distal stomach [Troncon LEA, 1994].

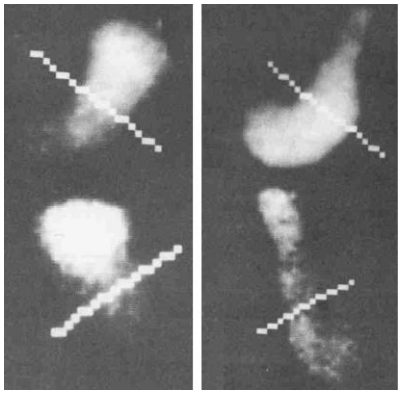

Fig. 3.1 Gamma camera images taken immediately after ingestion of 415ml of chicken soup labelled with ^{99m}Tc. The left images are from a normal volunteer and the right images are from an NUD patient. In both cases the top images are anterior bottom images are posterior. The line shown on each image divides the proximal and distal regions [Adapted from Troncon LEA, 1994].

All of these pathological findings imply that NUD patients have gastric electrical dysrhthmia resulting in a variety of neuromuscular dysfunctions. A study by Lin with using multichannel EGG demonstrated that NUD patients exhibit an abnormally low percentage of slow-wave propagation (58.0% in NUD vs. 89.9% in normals), irregular slow wave frequency and power (Fig. 3.2A) and intermittent statistically significant reductions in the dominant frequency (Fig. 3.2B) and power (Fig. 3.2C) [Lin X, 2001].

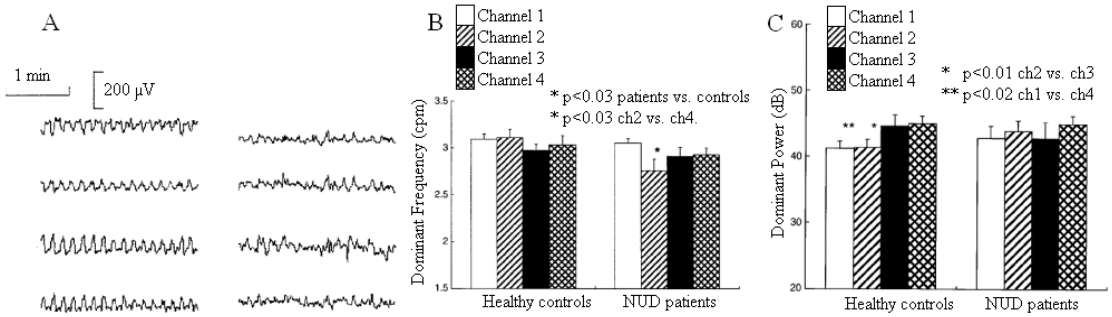

Fig. 3.2 **A** Multichannel EGG from a healthy subject (*left*) and a patient with NUD (*right*). **B** Dominant frequency in patients and healthy controls over four channels showing a significant decrease in channel 2 and **C** Dominant power in patients and healthy controls over four channels showing a significant decrease in channels 1 and 2 [Reproduced from Lin X, 2001].

Despite the fact that gastric electrical abnormality, gastric dysrhythmia and gastro- and fundoparesis are related to dyspepsia, direct causes of these abnormalities have not been clarified. Oba-Kuniyoshi recently conducted a study that disproves the hypothesis that gastric electrical dysrhthmias cause the symptoms of NUD. The study concluded that dysmotility (caused by abnormal gastric myoelectrical rhythms) may be an effect of gastric distension. A meal of yoghurt (150ml) was given to fourteen NUD patients and thirteen healthy volunteers. Ten NUD patients reported postprandial symptoms but only one exhibited an abnormal EGG signal. Furthermore, with a higher volume meal (300ml) only seven NUD patients complained of symptoms and all EGG signals recorded were normal. No significant differences were found between the NUD group and control group [Oba-Kuniyoshi, 2004]. Additionally, there is evidence to show that gastric distension elicits changes in the gastric myoelectrical activity, which may explain the detection of abnormal EGG signals in NUD patients [Ladabaum U, 1998].

3.2.5 Motion sickness

Unfamiliar or uncontrolled motion, whether simulated or real will cause motion sickness. The characteristic symptoms are nausea and vomiting but in severe cases there may be salivation, pallor and sweating. Everyone experiences motion sickness as seasickness or travel sickness but the susceptibility of individuals varies but is most common in children under 2 years old and in adults above the age of 50.

Motion sickness is caused by a mismatch between converging sensory signals regarding vision, static and dynamic equilibrium and awareness of position [Takeda N, 2001]. People who have lost function in their otolithic organs, inner ear or vestibulocochlear (8^{th} cranial) nerve do not experience motion sickness and it is therefore apparent that the afferent pathways from the vestibular organs to the vomiting centre are the principal cause of motion sickness.

Investigations into the effects of motion sickness on gastric myoelectrics and contractility predictably show that the response is similar to other emetic stimuli. However, motion sickness is not caused by one specific motor or myoelectrical event [Lang IM, 1999]. Many researchers have shown that motion sickness causes a range of gastrointestinal responses; decreased oesophageal sphincter tone, decreased gastric contractility, slower emptying rates, increased intestinal motility and gastric myoelectical dysrhythmia [Stanghellini V, 1983, Thompson DG, 1982 and Muth ER, 1996]. However, while it seems that motion sickness elicits dysrhythmic myoelectrical activity, EGG results have shown large inter-subject variations and it is therefore difficult to consider the pathologies discussed as reliable and robust indicators of motion sickness.

3.2.6 Stress

Stress is a broad term used to describe a variety of conditions that may affect gastric function. These include external effects such as extremes of temperature, emotional distress, clinical depression and conditions that cause anxiety and tension such as migraine. The generic symptoms of stress on gastrointestinal function are impaired gastric emptying and the stimulation of colonic motility. The tachygastric dysrhythmias described in section 3.3.1 may also be caused by experimentally induced mental stress. This may explain the ‘butterflies in the stomach’ sensation experienced by people in anxious or nervous situations.

4 BIODIELECTRICS AND BIOIMPEDANCE

4.1 Dielectrics

4.1.1 Introduction to dielectrics

Electrical conductors contain free charge carriers that are able to move in response to an applied electric field, producing a flow of charge. The conductivity, σ (S ≡ $\Omega^{-1}m^{-1}$) of a material is a measure of the ease with which free charge carriers move in response to an external electric field. It is defined as the current density, J (Am^{-2}) produced by each unit of applied electric field, E (Vm^{-1}).

$$J = \sigma E \tag{4.1}$$

Dielectric materials consist of bound electrons, confined to their respective atoms and are therefore unable to produce charge flow in an electric field. However, charges will move very slightly in a dielectric material in response to an electric field without leaving their atoms. Positive charges move in the direction of the field and negative charges in the opposite direction, creating an electric dipole. Therefore, the dielectric becomes polarised, generating an electric field in the opposite direction to the applied field, thus reducing the total field.

The total permittivity, ε (see equation 4.2) of a material indicates the extent to which the external electric field affects local charge distributions. The charge density due to an applied electric field in a vacuum is the permittivity of free space, ε_0 (8.854×10^{-12} Fm^{-1}) and the relative permittivity is a ratio between the capacitance of the dielectric medium to the capacitance of the in a vacuum (equation 4.3).

$$\varepsilon = \varepsilon_0 \varepsilon_r \tag{4.2}$$

where

$$\varepsilon_r = \frac{C_{dielectric}}{C_{vacuum}} \tag{4.3}$$

Fig. 4.1A shows an ideal conductor and an ideal insulator with a surface area of A and thickness of x. The conductivity of the slab is σ and the conductance of the slab, G is given by equation 4.4.

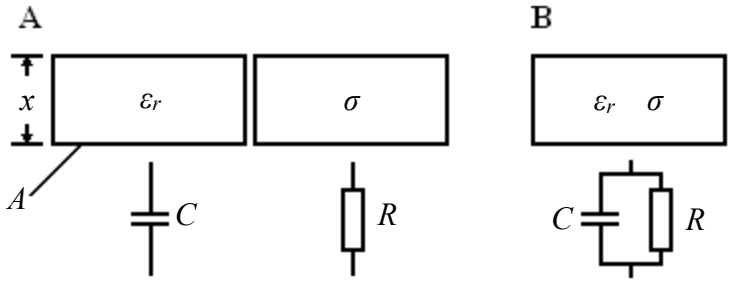

Fig. 4.1 **A** Ideal insulator represented by a capacitor (*left*) and ideal conductor represented by a resistor (*right*). **B** The equivalent circuit for biological tissue showing both capacitive and resistive properties.

Equation 4.5 states that resistance, R is the reciprocal of conductance. If the dielectric has a relative permittivity of ε_r then the capacitance, C of the slab is given by equation 4.6.

$$G = \frac{\sigma A}{x} \tag{4.4}$$

$$R = \frac{1}{G} \tag{4.5}$$

$$C = \frac{\varepsilon_0 \varepsilon_r A}{x} \tag{4.6}$$

4.1.2 Biodielectrics

Biological tissue however (Fig. 4.1B), contains both free and bound charge carriers and therefore simultaneously possesses both conductive and dielectric properties. The model presented above describes the static conductance (equation 4.4) and capacitance (equation 4.6), i.e. when frequency = 0. When an alternating voltage is applied the conductivity and relative permittivity are a function of frequency.

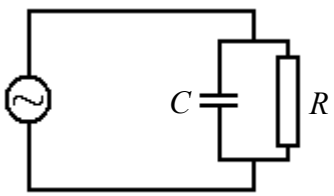

Fig. 4.2 Equivalent circuit for biological tissues with an alternating voltage source.

In this case the voltage source begins to deposit positive charge to one plate of the capacitor and negative charge to the other. Half a cycle later and the polarity of the voltage source reverses and so does the current. Therefore, the current now removes all charges from the plate and deposits inverted charges. This reversal repeats every half cycle. With $R = 0$, if the instantaneous voltage across the capacitor, V_c is defined in terms of the charge, Q and the capacitance, C shown in equation 4.7.

$$V_c = \frac{Q}{C} \tag{4.7}$$

If the electromotive force of the voltage source (emf) is $\mathcal{E}$, with a maximum voltage of $\mathcal{E}_{max}$ then according to Kirchoff's law

$$\mathcal{E} - \frac{Q}{C} = 0 \tag{4.8}$$

Since $$\mathcal{E} = \mathcal{E}_{max} \cos \omega t \tag{4.9}$$

rearranging 4.8 gives $$Q = C\,\mathcal{E} \tag{4.10}$$

$\therefore$ 4.9 yields $$Q = C\,\mathcal{E}_{max} \cos \omega t \tag{4.11}$$

The current flowing in the circuit, I is the rate of change of charge given by equation 4.12.

$$I = \frac{\Delta Q}{\Delta t} \tag{4.12}$$

From equation 4.11 it is clear that I is related to the rate of change of $\cos\omega t$. Therefore, to find I it is necessary to differentiate $\cos\omega t$.

The chain rule states $$\frac{dy}{dt} = \frac{dy}{dz}\frac{dz}{dt} = f'(z) \cdot g'(t)\,,$$

Let $$y = \cos z \text{ and } z = \omega t\,,$$

$\therefore$ $$f'(z) = \omega \text{ and } g'(t) = -\sin z$$

$\therefore$ $$\frac{d}{dt}\cos\omega t = -\omega \sin \omega t \tag{4.13}$$

Therefore, from 4.11, 4.12 and 4.13

$$I = -\omega C\,\mathcal{E}_{max} \sin \omega t \tag{4.14}$$

Equation 4.14 shows that the current and the emf are out of phase by π/2 radians. Therefore, when $R = 0$, effectively the equivalent circuit in Fig. 4.2 becomes a capacitor in series with the current leading the voltage by π/2 radians. If $C = 0$ the equivalent circuit becomes a simple resistance and the current and voltage synchronise into phase. In the dc circuits in Figs. 4.1A and B, the terms to describe the properties of a material with respect to current flow are resistance and conductivity. With ac circuits, capacitive effects must be considered and the equivalent terms are impedance, *Z* and admittance, *Y*. From equation 4.5 the relationship between the impedance and admittance is expressed in equation 4.15.

$$Z = \frac{1}{Y} \tag{4.15}$$

The complex admittance, Y^* of the dielectric is therefore shown in equation 4.16. Permittivity can also be expressed in complex form, ε^* shown in equation 4.17 where ε' is the real part and ε'' is the imaginary part.

$$Y^* = G + j\omega C \tag{4.16}$$

$$\varepsilon^* = \varepsilon' - j\varepsilon'' \tag{4.17}$$

Expressions for ε' and ε'' can be found by combining equations 4.4, 4.6 and 4.16.

$$Y^* = \frac{A}{x}(\sigma + j\omega\varepsilon_0\varepsilon_r) \tag{4.18}$$

By analogy with the relation $C = \frac{y}{j\omega}$ for an ideal capacitor, we define the complex capacitance as $C^* = \frac{Y^*}{j\omega}$. Similarly, by analogy with equation 4.6, we define $\varepsilon^* = \varepsilon_r - j\frac{\sigma}{\omega\varepsilon_0}$.

$$\varepsilon' = \varepsilon_r \text{ and } \varepsilon'' = \frac{\sigma}{\omega\varepsilon_0} \tag{4.19a and b}$$

Therefore, the real part ε' is simply the relative permittivity and the imaginary part $j\varepsilon''$ is the dielectric loss, which is proportional to the energy absorbed by the material from the applied electric field and is related to the resistive properties of the dielectric.

4.2 The basis for impedance measurements

4.2.1 The composition of biological tissue

The four most abundant atoms in the human body are hydrogen (65.0%), oxygen (18.5%), carbon (9.5%) and nitrogen (3.2 %) [Tortora GJ, 2000]. The majority of solid matter in the human body is made from proteins, carbohydrates or lipids all of which consist of carbon, hydrogen, oxygen and nitrogen. Since biological tissue contains both free and bound charges it has both conductive properties described in terms of the conductivity, σ and dielectric properties described in terms of relative permittivity, ε_r. Subsequently, when a voltage, V is applied between opposite faces of a cube (Fig. 4.3), a conduction current (I_c) caused by free charge carriers and a displacement current (I_d) caused by bound electrons will flow.

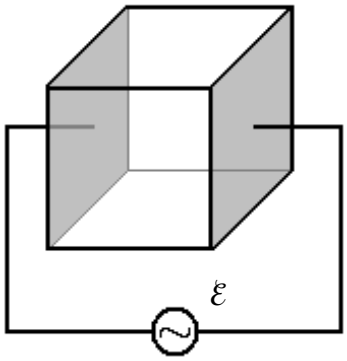

Fig. 4.3 Potential, $\mathcal{E}$ applied to a cube of biological material with conductivity, σ and relative permittivity, ε_r.

Both the conduction and the displacement currents are a function of frequency and are defined in equations 4.20 and 4.21 respectively.

$$I_c = \mathcal{E}(t)\sigma(\omega) \tag{4.20}$$

$$I_d = \left(\frac{d\mathcal{E}(t)}{dt}\right)\varepsilon_0\varepsilon_r(\omega) \tag{4.21}$$

If $\mathcal{E}$ is a sinusoid $$I_d = \mathcal{E}\,\omega\varepsilon_0\varepsilon_r \tag{4.22}$$

$\mathcal{E}(t)$ is the applied voltage, t is the time, ω is the angular frequency, $\sigma(f)$ is the conductivity of the material (S), ε_r is the permittivity of the material (Fm^{-1}) and ε_0 is the permittivity of free space (8.854×10^{-12} Fm^{-1}).

4.2.2 Current flow in biological tissues

Fig. 4.4 shows the relationship between the conduction and the displacement currents with frequency. It is clear that at low frequencies (below 100kHz) the effect of I_d is negligible and so tissue conductivity depends largely on the existence of free charge carriers (electrons).

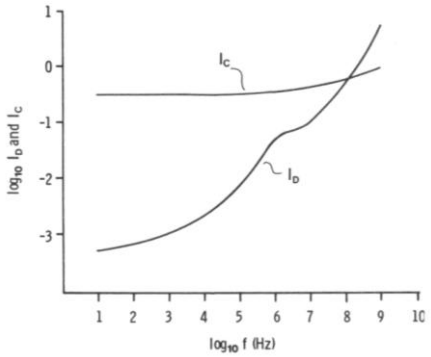

Fig. 4.4 Variation of conduction and displacement current with frequency in biological tissues [Redrawn from Brown BH, 1983].

Biological tissue contains many electrolytes and is therefore predominantly an electrolytic conductor supporting the active transport of ions and so there is no separate flow of electrons in biological tissue; all of the electrons are bound to their ionic charge carriers and so tissue dc currents are ionic rather than electronic. This is why it is not possible to use low frequency currents (below 0.1Hz) for physiological measurements, as electrolytic effects would be induced and the patient would experience a stinging sensation at the electrode site. At higher frequencies these effects disappear although neural effects may occur if the electrodes are placed over major nerves.

4.2.3 Effects of volume change on impedance

In order to investigate the effects of volume change on impedance, it is necessary to consider the following model. The impedance Z between the faces of a homogenous cylinder with length L and cross sectional area A (Fig. 4.5) is given in equation 4.23 below.

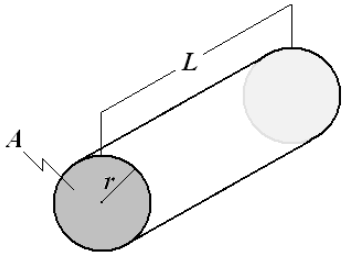

Fig. 4.5 Cylinder representing a homogenous medium with length, L.

Electrical impedance measurements are affected by two factors; primarily the volume that is bound by the electric field, v and the conductivity, σ which is equal to the reciprocal of resitivity, ρ.

$$Z = \frac{\rho L}{A} \equiv \frac{\rho L^2}{AL} \tag{4.23}$$

Since $AL=v$

$$Z = \rho \frac{L^2}{v} \tag{4.24}$$

Taking derivatives of Z with respect to v in equation 4.24 yields an expression for the change in impedance with respect to a change in volume.

From equation 4.24 $Z = \rho L^2 v^{-1}$

$$\therefore \quad \frac{dZ}{dv} = \rho L^2 (-v^{-2}) = -\frac{\rho L^2}{v^2}$$

$$\therefore \quad dZ = -\frac{\rho L^2}{v^2} dv \tag{4.25}$$

From equation 4.24

$$v = \frac{\rho L^2}{Z} \tag{4.26}$$

Substituting 4.26 into 4.25 $dZ = -\frac{Z^2}{\rho L^2} dv$

$$\therefore \quad dv = -\frac{\rho L^2}{Z^2} dZ \tag{4.27}$$

Equation 4.27 shows that changes in the volume of the cylinder are directly proportional to changes in impedance, provided that the conductivity remains constant [Baker LE, 1971]. However, varying ionic compositions will also affect the measured impedance. In addition, the conductive heterogeneities found in biological tissue mean that it is difficult to predict the exact shape of the electric field. These factors are therefore important when attempting to relate impedance changes to volume.

4.3 The origin of epigastrographic signals

4.3.1 The electrophysiological basis for epigastrographic signals

In order to establish the field patterns that will be produced by a system, it is important to consider the geometry of the electrode – skin interface, as there are many factors that determine important characteristics of the electrical field produced that will ultimately influence the characteristics of the recorded signal. Fig. 4.6 shows an electrode in contact with the skin surface with current *I*, radius *r*. The distance from the electrode surface is *x*.

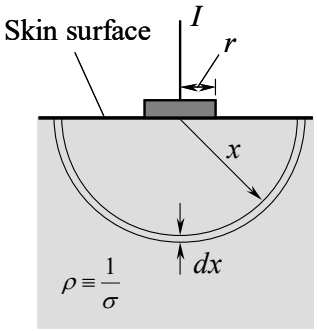

Fig. 4.6 Diagram of an electrode placed in contact with a volume of tissue with homogenous conductivity [Redrawn from Brown BH, 1999].

The electrical field vector **E** is related to the scalar potential ϕ by equation 4.28 where ∇ is the gradient operator and **i**, **j** and **k** are unity vectors in a Cartesian coordinate system.

$$\mathbf{E} = -\nabla\phi \tag{4.28}$$

where $$\nabla = \frac{\partial}{\partial x}\mathbf{i} + \frac{\partial}{\partial y}\mathbf{j} + \frac{\partial}{\partial z}\mathbf{k}$$

From Ohm's law $$\mathbf{J} = \sigma\,\mathbf{E} \tag{4.29}$$

J is the current density and σ is the conductivity (a scalar quantity as the volume is assumed to have isotropic conductivity). By considering the single electrode in Fig. 4.6, the current source density, I_v will be given by the divergence of the current density **J**.

$$I_v = \nabla \bullet \mathbf{J} \tag{4.30}$$

where $$\mathbf{J}(x,y,z) = f(x,y,z)\mathbf{i} + g(x,y,z)\mathbf{j} + h(x,y,z)\mathbf{k}$$

and $$\nabla \bullet \mathbf{J} \equiv \text{div}\,\mathbf{J} = \frac{\partial f}{\partial x} + \frac{\partial g}{\partial y} + \frac{\partial h}{\partial z}$$

By substituting 4.28 into 4.29 and then into 4.30, it is possible to obtain an equation for the divergence of **J** with respect to the conductivity σ, potential ϕ and Laplacian operator, ∇^2.

$$\nabla \bullet \mathbf{J} = I_v = -\sigma \nabla^2 \phi \tag{4.31}$$

where the Laplacian operator, $\nabla^2 \phi = \nabla \bullet \nabla \phi = \frac{\partial^2 \phi}{\partial x^2} + \frac{\partial^2 \phi}{\partial y^2} + \frac{\partial^2 \phi}{\partial z^2}$

For a region with homogenous conductivity and current source I_v equation 4.31 simplifies to equation 4.32, also known as Poisson's equation.

$$\nabla^2 \phi = -\frac{I_v}{\sigma} \tag{4.32}$$

Poisson's equation for a single current source can be written in integral form.

$$\phi = \frac{1}{4\pi\sigma} \int \frac{I_v}{x} dV \tag{4.33}$$

As the spread of current density will be radial for $x \approx r$, by considering the electrode in Fig. 4.6, with a current *I*, the current density can be expressed as equation 4.34.

$$J = \frac{I}{2\pi x^2} \tag{4.34}$$

The hemisphere of tissue in Fig. 4.6 has a thickness of *dx* and a radius of *x*. The potential drop across *dx* is therefore given in equation 4.35.

$$dV = \frac{I\rho}{2\pi x^2} dx \tag{4.35}$$

With one electrode, the current must flow to ground and so the potential at infinity is zero. Therefore, the potential at any radius *x* (Fig. 4.6) is given by equation 4.37.

$$V(x) = I \int_x^\infty \frac{\rho}{2\pi x^2} dx \tag{4.36}$$

$$\therefore \quad V(x) = \frac{\rho I}{2\pi x} \tag{4.37}$$

4.3.2 Geometrical analysis of electric field in Electrical Impedance Epigastrography

In Electrical Impedance Epigastrography (EIE) the current is passed through two electrodes placed on the skin surface, shown in Fig. 4.7.

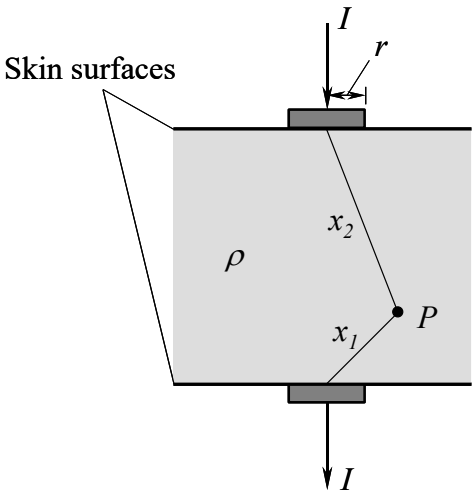

Fig. 4.7 Diagram of two electrodes in contact with a volume of tissue with homogenous conductivity and placed opposite each other so that a current, I may be passed through. Note that $r \ll x_1$ and $r \ll x_2$. P is an arbitrary point at which the voltage is measured.

With two current injecting electrodes, the integral limits in equation 4.36 are the distances from point P to each electrode, x_1 and x_2. Therefore the equation becomes the following.

$$V_P(x) = I\int_{x_2}^{x_1}\frac{\rho}{2\pi x}dx$$

$$\therefore \quad V_P(x) = \frac{\rho I}{2\pi x}\Big|_{x_2}^{x_1} = \frac{\rho I}{2\pi x_1} - \frac{\rho I}{2\pi x_2}$$

$$\therefore \quad V_P(x) = \frac{\rho \mathrm{I}}{2\pi}\left(\frac{1}{x_1} - \frac{1}{x_2}\right) \tag{4.38}$$

This equation describes the potential at an arbitrary point in a homogenous, isotropic medium caused by a positive and negative point current source with magnitude *I*. Witsoe cautioned that the possible effects of high current densities near the electrode surface due to the assumption of point electrodes and local heterogeneities caused large errors when using equation 4.38 experimentally for measurements of resistivity with four equally spaced electrodes; two outer current injecting and two centre voltage measuring [Witsoe DA, 1967].

Therefore, Witsoe used an equation he had derived earlier which allowed for circular disk electrodes with radius *r*, rather than point electrodes. This equation (4.39) for zero potential at infinity reduces the errors caused by high current densities [Brown BH, 1983].

$$V_P(x) = \frac{\rho I}{2\pi r}\left(\sin^{-1}\frac{r}{x_1} - \sin^{-1}\frac{r}{x_2}\right) \tag{4.39}$$

Three pairs of electrodes are used in EIE. Each pair has an anterior electrode and a corresponding posterior electrode that mirrors its position. The Epigastrograph contains digital multiplexing electronics that allows each pair of electrodes to apply current *and* measure voltage. Consequently, six signals are recorded, each generated by four electrodes; two current injecting-electrodes (one pair) and two voltage-measuring electrodes (the other pair). This means that the results obtained in section 4.3.1 may be used to predict the field patterns expected in EIE. The nomenclature for labelling the signals depends on which pair of electrodes was injecting the current and which was measuring the voltage. The electrode pairs are colour-coded yellow (Y), red (R) and black (B) so for example, if the red pair is injecting the current and the yellow pair is measuring the voltage, the signal label would be Y, i(R). The geometrical configuration of the electrodes is shown in Fig. 4.8 the two-dimensional plane that the signal is generated from.

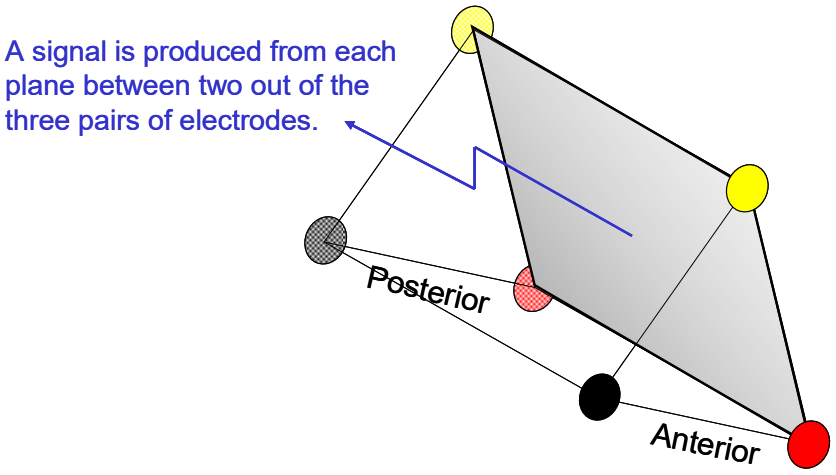

Fig. 4.8 Basic geometrical configuration of the electrodes in EIE. The signal is produced from a volume that lies on the plane between the current injecting electrodes and measuring electrodes. Here the yellow pair are the current injecting electrodes and the red pair are the measuring electrodes, R, i(Y).

The model presented in Fig. 4.8 is helpful for visualising the direction in which the field lines act. The abdominal region may be modelled as a perfect homogenous elliptical cylinder, shown in Fig. 4.9A so that the field distribution can be approximated.

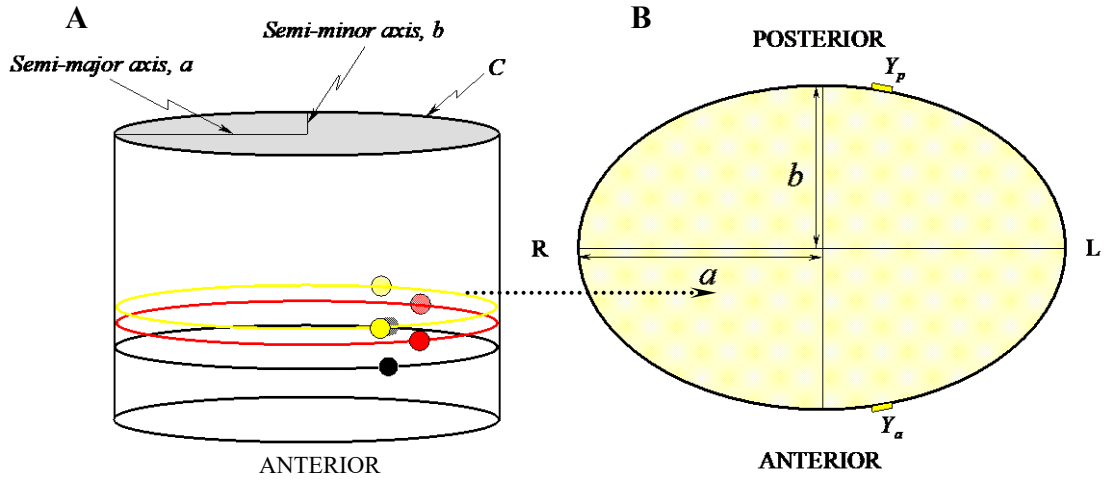

Fig. 4.9 **A** Elliptical cylindrical model of the abdomen. The electrode planes are ellipses that join the paired electrodes. **B** The electrode plane for the yellow pair shows that each electrode plane has the same dimensions as the cross section.

It is convenient to align the three-dimensional axes used in EIE with the body axes (sagittal, transverse, and longitudinal axes). The rectangular coordinate system used together with the convention for measuring angles is illustrated in Appendix A. Fig. 4.10 demonstrates that two pairs of electrodes form a circumferential line and the plane produced within the cylinder will be another ellipse called the field plane.

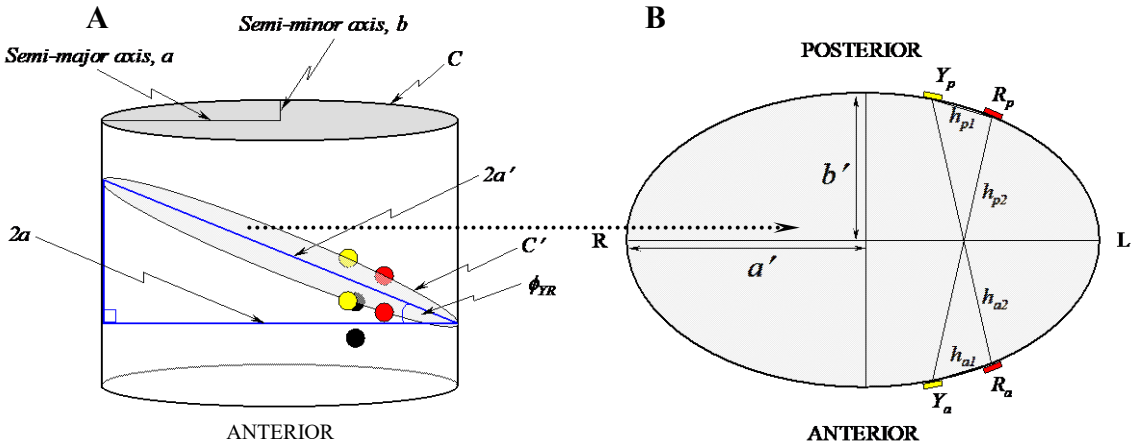

Fig. 4.10 **A** Modelling of the abdominal region by a perfect homogenous elliptical cylinder. The electrodes are shown and the yellow and red pairs form an ellipse. **B** The ellipse formed between the red and yellow pairs of electrodes (YR plane) where $a' = a(\cos\phi_{YR})^{-1}$.

Despite geometrical variations in the human torso and conductive heterogeneities, the cylindrical model is a valuable tool in estimating the field distribution in EIE. The ellipse shown in Fig. 4.10B is generated by the field plane through two selected electrode pairs (the yellow pair applying current and the red measuring potential difference). The potential difference measured between the red electrodes, V_R is calculated by solving equation 4.39 for each electrode potential, R_a and R_p.

Potential at R_a:
$$V_{Ra} = \frac{\rho I}{2\pi r}\left(\sin^{-1}\frac{r}{h_{a1}} - \sin^{-1}\frac{r}{h_{a2}}\right) \tag{4.40}$$

Potential at R_p:
$$V_{Rp} = \frac{\rho I}{2\pi r}\left(\sin^{-1}\frac{r}{h_{p1}} - \sin^{-1}\frac{r}{h_{p2}}\right) \tag{4.41}$$

Ohm's law states that $V(t) = I(t)Z(t)$ and so the impedance for the signal R, i(Y) is given by the two equations 4.42 and 4.43 which represent the anterior and posterior measurements.

$$Z_{Ra} = \frac{\rho}{2\pi r}\left(\sin^{-1}\frac{r}{h_{a1}} - \sin^{-1}\frac{r}{h_{a2}}\right) \tag{4.42}$$

$$Z_{Rp} = \frac{\rho}{2\pi r}\left(\sin^{-1}\frac{r}{h_{p1}} - \sin^{-1}\frac{r}{h_{p2}}\right) \tag{4.43}$$

4.3.3 Calculating the distance between electrodes using the elliptical model

It is now possible to estimate the equipotentials for each electrode combination by finding a relationship between the subject's girth and electrode positions using the elliptical model. The equation for the ellipse shown in Fig. 4.11 is given in equation 4.44.

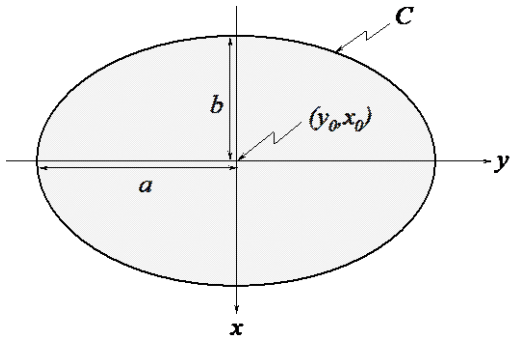

Fig. 4.11 The ellipse representing the cross section of the elliptical cylinder (Fig. 4.10A) with semi-major axis a, semi-minor axis b, circumference C and centre point (y_0,x_0).

$$\frac{(y-y_0)^2}{a^2} + \frac{(x-x_0)^2}{b^2} = 1 \tag{4.44}$$

According to Snyder the dimensions of the human torso are defined as an ellipse with semi-major axis of 30cm and semi-minor axis of 20cm [Snyder WS, 1975]. Therefore, the ratio of semi-major axis to semi-minor axis in the human torso defined in Fig. 4.9 is 0.33. However, given that the ellipse formed in the electrode plane depends on the angle between electrodes, θ_{YR} (see Fig. 4.10A) the ellipse will be elongated in the direction of the semi-major axis. Therefore $a \Rightarrow a'$ and $b \Rightarrow b'$. Since the semi-minor axis does not change, $b = b'$. Therefore, the relationship between a' and b is given by equation 4.46.

$$a = \frac{3}{2} b$$

$$a' = \frac{a}{\cos\phi_{YR}} \tag{4.45}$$

$$\therefore \quad a' = \frac{3b}{2\cos\phi_{YR}} \tag{4.46}$$

The exact formula for the circumference of an ellipse is an infinite series that converges very quickly and is given in equation 4.47.

$$C = \pi(a+b)\left\{1 + \sum_{n=1}^{\infty}\left[\frac{(2n-2)!}{(n!\left[n-1\right]!\,2^{2n-1})}\right]^2 x^{2n}\right\} \tag{4.47}$$

However, a number of approximations have been proposed. In the Mathematical Tables from the Handbook of Chemistry and Physics the following solution in equation 4.48 can be found. It uses the formula for the circumference of a circle, $2\pi r$ with r being the root mean square of the semi-major and semi-minor axes.

$$C \approx 2\pi\sqrt{\frac{(a^2+b^2)}{2}} \tag{4.48}$$

More accurate approximations are available but since the most accurate measurements of girth are likely to be ± 0.5cm, equation 4.48 will suffice.

Therefore, by combining equations 4.46 and 4.48 and by measuring the girth of a person (corresponding to the circumference, C of the ellipse in Figs. 4.9, 4.10 and 4.11) an estimate for the lengths a and b can be found. This assumes that equation 4.46 remains constant in every individual. Clearly, this will be progressively inaccurate with increasing body mass index (BMI). Nevertheless, since a BMI over 30 would exclude a subject from EIE (see section 5.3.3), the assumption is justified.

From equation 4.48 $$2\left(\frac{C}{2\pi}\right)^2 = a^2 + b^2$$

$$\therefore \quad a^2 = 2\left(\frac{C}{2\pi}\right)^2 - b^2$$

From equation 4.46 $$a^2 = 2\left(\frac{C}{2\pi}\right)^2 - \frac{2}{3}a^2$$

$$a^2 + \left(\frac{2}{3}a\right)^2 = 2\left(\frac{C}{2\pi}\right)^2$$

$$a^2 + \frac{4}{9}a^2 = 2\left(\frac{C}{2\pi}\right)^2$$

$$\frac{13}{9}a^2 = 2\left(\frac{C}{2\pi}\right)^2$$

$$\therefore \quad a = \sqrt{\frac{18}{13}\left(\frac{C}{2\pi}\right)^2}$$

From equation 4.45 $$a' = \frac{\sqrt{\frac{18}{13}\left(\frac{C}{2\pi}\right)^2}}{\cos\phi_{YR}} \tag{4.49}$$

From equation 4.46 $$\frac{3b}{2\cos\phi_{YR}} = \frac{\sqrt{\frac{18}{13}\left(\frac{C}{2\pi}\right)^2}}{\cos\phi_{YR}}$$

$$b = \frac{2}{3}\sqrt{\frac{18}{13}\left(\frac{C}{2\pi}\right)^2}$$

$$\therefore \quad b' \equiv b = \sqrt{\frac{8}{13}\left(\frac{C}{2\pi}\right)^2} \tag{4.50}$$

By defining the centre of the ellipse as the origin, $y_0 = 0$ and $x_0 = 0$, equation 4.44 is simplified to equation 4.51. Consequently, by combining equations 4.49, 4.50 and 4.51, an expression for each x and y point that lies on the ellipse may be found.

$$\frac{y^2}{a'^2} + \frac{x^2}{b'^2} = 1 \tag{4.51}$$

$$\therefore \quad \frac{y^2}{\frac{18}{13}\left(\frac{C}{2\pi}\right)^2 (\cos\phi_{YR})^{-1}} + \frac{x^2}{\frac{8}{13}\left(\frac{C}{2\pi}\right)^2} = 1$$

$$\therefore \quad x = \pm\sqrt{\left\{1 - \frac{y^2}{\frac{18}{13}\left(\frac{C}{2\pi}\right)^2 (\cos\phi_{YR})^{-1}}\right\}\frac{8}{13}\left(\frac{C}{2\pi}\right)^2} \tag{4.52}$$

During the EIE experiment, precise measurements of the electrode positions relative to the xiphisternum and the midline (an imaginary line between the xiphisternum and umbilicus) are recorded so that the electrodes can be placed in exactly the same positions on future tests, eliminating experimental errors (see section 5.2.2). Therefore, the positions of the electrodes on the ellipse (electrode plane) in Fig. 4.9B can be calculated from their measured positions on the subject and the subject's girth, equal to the circumference of the ellipse, C. In order to calculate the coordinates of the electrode in the xy plane it is necessary to consider the two planes that cross each anterior and posterior electrode pair; the electrode plane and the field plane. Fig. 4.12A shows the red electrode plane crossing the red-yellow field plane.

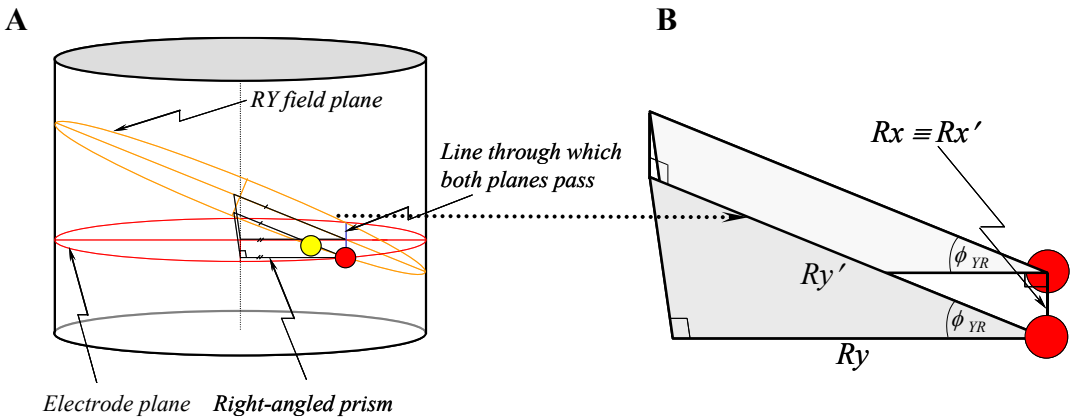

Fig. 4.12 **A** Red electrode plane and red-yellow field plane crossing to produce a right-angled prism. **B** Diagram of the right-angled prism with angle ϕ_{YR}.

Fig. 4.13 illustrates that the measurements taken in the y-direction for the position of the electrodes are an arc of the ellipse from the midline to the electrode.

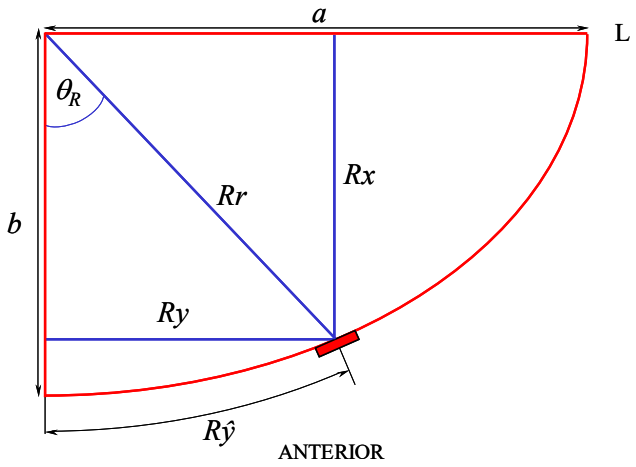

Fig. 4.13 Anterior left quarter of the red electrode plane showing the position of the electrode and $R\hat{y}$ that would have been measured immediately following EIE.

The calculations of the angle θ_R and the length Rr are not simple as there is no specific equation for the length of the arc of an ellipse.

Equation 4.48 approximates the circumference of an ellipse using the equation for the circumference of a circle and applying a radius equal to the root mean square of the semi-major and semi-minor axes. It may therefore be possible, to take the equation for the length of an arc of a circle (equation 4.53) with the radius of the root mean square of the semi-major and semi-minor axes of the ellipse to calculate the arc length of an ellipse.

Arc of a circle: $\hat{y} = r\theta_{(RADIANS)}$

$$\therefore \quad \hat{y} = r\theta^{\circ}\left(\frac{\pi}{180}\right) \tag{4.53}$$

For an ellipse $r \approx \sqrt{\left(\frac{a^2+b^2}{2}\right)}$

$$\therefore \quad \theta^{\circ} \approx \frac{180\hat{y}}{\pi\sqrt{\left(\frac{a^2+b^2}{2}\right)}} \tag{4.54}$$

However, Fig. 4.14 demonstrates that while the errors in equation 4.48 are small due to the rapid convergence of equation 4.47, the error in estimating the angle subtended by a given arc length of an ellipse using the above approximation is significant. Consequently, a different method for estimating the angle subtended by a given arc length of an ellipse must be found.

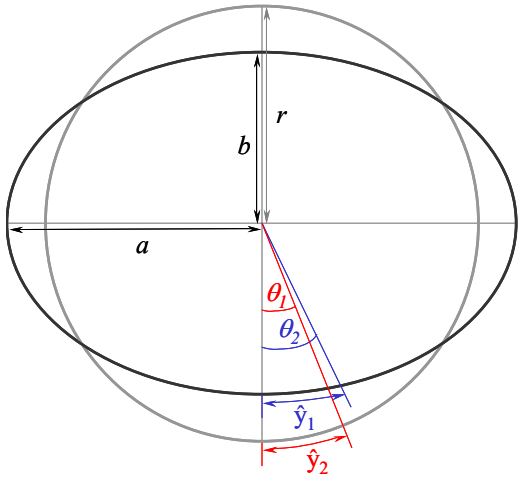

Fig. 4.14 Diagram of an ellipse and the corresponding circle with radius, r equal to the root mean square of a and b demonstrating the inaccuracy in the estimation of angle θ where $\hat{y}_1 = \hat{y}_2$ and $\theta_1 \neq \theta_2$.

It is possible to estimate the angle θ_R by dividing the quarter ellipse into individual 1° segments as shown in Fig. 4.15 below. The equation for the length of the radius of an ellipse at a given angle is shown in equation 4.55[1], where $r(\theta)$ is the radius of the ellipse at angle θ.

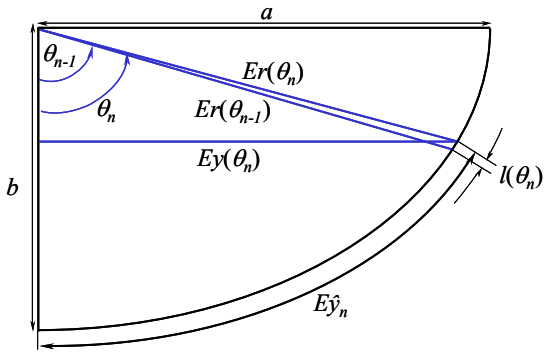

Fig. 4.15 Arbitrary 1° segment subtended by angles θ_{n-1} and θ_n.

$$Er(\theta)^2 = \frac{b^2 a^2}{b^2 \sin^2\theta + a^2 \cos^2\theta} \tag{4.55}$$

[1] For a derivation of this formula please see Appendix B.

By using equation 4.55 it is possible to calculate the length of each radius at increasing angles of θ_R with an increment of 1° for given semi-major and semi-minor radii, a and b. If $r(\theta_n)$ is the radius at angle θ_n and $r(\theta_{n-1})$ is the radius at the angle θ_{n-1} then the length l_n may be approximated from equation 4.56 by assuming that it is a straight line (see Fig. 4.15). Note that n = 0°, 1°, 2° … 90° beginning from the semi-minor towards the semi-major axis.

$$l(\theta_n) \approx \sqrt{[r(\theta_n) - r(\theta_{n-1})\cos 1]^2 + [r(\theta_{n-1})\sin 1]^2} \qquad (4.56)$$

Calculating the cumulative value of $l(\theta)$ for every angle from 0° to 90° and interpolating the results for the desired length $\hat{y}_n$ gives an estimate for the angle θ_n subtended by the arc. The technique is shown in Fig. 4.16 and the equation is given in equation 4.57.

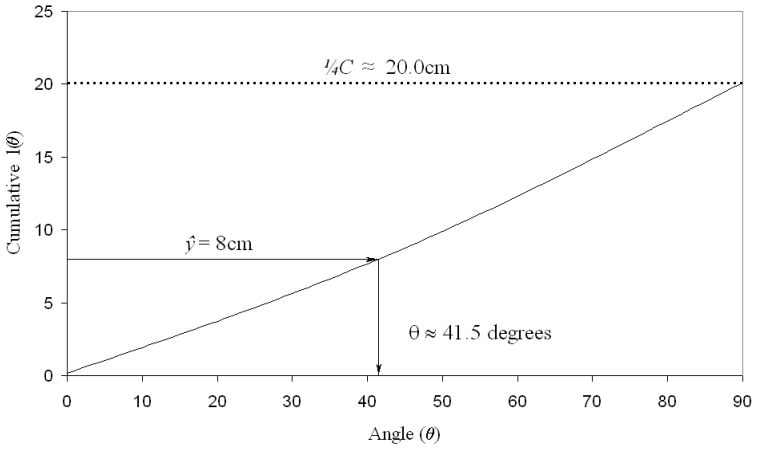

Fig. 4.16 Cumulative length $l(\theta)$ versus angle θ for the interpolation of $\hat{y}$ to estimate the angle θ for typical reference man [Snyder, 1975] where the semi-major axis a is 15cm, semi-minor axis b is 10cm and circumference $C \approx 80.1$cm.

From the estimate of angle θ_R the lengths R_y and R_x shown in Fig. 4.12B can be found using equations 4.57 and 4.58. Since the field plane crosses the electrode plane of the two pairs of electrodes that produce the field, the coordinates for the electrodes found in the electrode plane are the same as those in the field plane. Fig. 4.17 shows a detailed diagram of Fig. 4.10A viewing the anterior of the subject in the frontal plane.

$$Ey(\theta_R) = Er(\theta_R)\sin\theta_R \qquad (4.57)$$

$$Ex(\theta_R) = Er(\theta_R)\cos\theta_R \qquad (4.58)$$

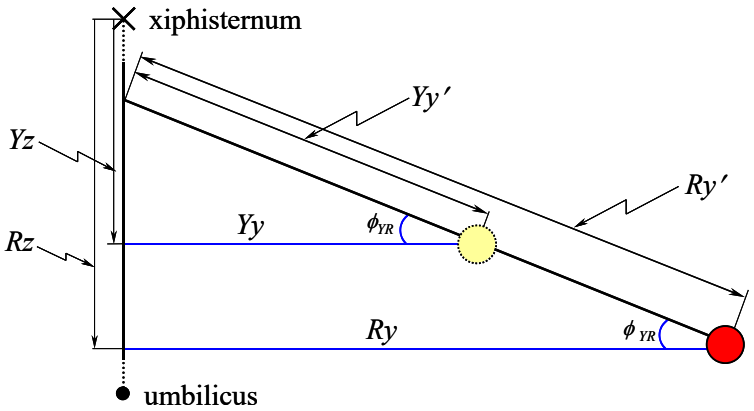

Fig. 4.17 Frontal view showing electrode positions and measurements for the YR electrode plane from 4.12B. Note that the yellow electrode does not lie on this plane due to the curvature of the ellipse (see Fig. 4.10B).

It is obvious that simple trigonometry can be used to calculate Yy' and Ry'. The formulae are given below. The angle ϕ_{YR} can be calculated using the equation 4.59.

$$\phi_{YR} = \tan^{-1}\left(\frac{Rz - Yz}{Ry - Yy}\right) \tag{4.59}$$

$$Ry' = \frac{Ry}{\cos\phi_{YR}} \tag{4.60}$$

$$Yy' = \frac{Yy}{\cos\phi_{YR}} \tag{4.60}$$

Rx' and Yx' can now be found using equation 4.52 by substituting Ry' and Yy' respectively for y and calculating the circumference, C' using equation 4.48 and substituting it for C. It is important to note that two numbers are obtained corresponding to positive and negative values of the same magnitude, which are the coordinates for the posterior and anterior electrodes respectively, since the posterior electrodes mirror the anterior electrodes. Consequently, equations 4.42 and 4.43 may be simplified as follows.

Since $h_{a1} \equiv h_{p1} = h_1$ and $h_{a2} \equiv h_{p2} = h_2$

$$\therefore \quad Z_R = Z_{Ra} = Z_{Rp} = \frac{\rho}{2\pi r}\left(\sin^{-1}\frac{r}{h_1} - \sin^{-1}\frac{r}{h_2}\right) \tag{4.62}$$

The lengths h_1 and h_2 can be calculated from the coordinates of the electrodes: (Ry', Rx') for the red electrode, (Yy', Yx') for the yellow electrode and (By', Bx') for the black electrode.

$$h_1 = \sqrt{(R_a y' - Y_a y')^2 + (R_a x' - Y_a x')^2} \equiv \sqrt{(R_p y' - Y_p y')^2 + (R_p x' - Y_p x')^2} \tag{4.63}$$

$$h_2 = \sqrt{(R_p y' - Y_a y')^2 + (R_p x' - Y_a x')^2} \equiv \sqrt{(R_a y' - Y_p y')^2 + (R_a x' - Y_p x')^2} \tag{4.64}$$

Equation 4.62 can be written in general form where E = Y, R or B (yellow Y, red R or black B).

From 4.62 $$Z_E = \frac{\rho}{2\pi r}\left(\sin^{-1}\frac{r}{h_1} - \sin^{-1}\frac{r}{h_2}\right) \tag{4.65}$$

The lengths h_1 and h_2 can be found using the following set of generic equations.

From 4.63 and 4.64 $$h_1 = \sqrt{(-E1y' + E2y')^2 + (E1x' - E2x')^2} \tag{4.66}$$

$$h_2 = \sqrt{(-E1y' - E2y')^2 + (E1x' - E2x')^2} \tag{4.67}$$

From 4.60 $$E1y' = \frac{E1y}{\cos\phi_{E1E2}} \tag{4.68}$$

From 4.61 $$E2y' = \frac{E2y}{\cos\phi_{E1E2}} \tag{4.69}$$

From 4.59 $$\phi_{E1E2} = \tan^{-1}\left(\frac{E2z - E1z}{E2y - E1y}\right) \tag{4.70}$$

From 4.57 $$Ey = Er\sin\theta_E \tag{4.71}$$

From 4.58 $$Ex = Er\cos\theta_E \tag{4.72}$$

From 4.52 $$E1x' = \pm\sqrt{\left\{1 - \frac{E1y'^2}{\frac{18}{13}\left(\frac{C'}{2\pi}\right)^2(\cos\phi_{E1E2})^{-1}}\right\}\frac{8}{13}\left(\frac{C'}{2\pi}\right)^2} \tag{4.73}$$

$$E2x' = \pm\sqrt{\left\{1 - \frac{E2y'^2}{\frac{18}{13}\left(\frac{C'}{2\pi}\right)^2(\cos\phi_{E1E2})^{-1}}\right\}\frac{8}{13}\left(\frac{C'}{2\pi}\right)^2} \tag{4.74}$$

4.3.4 The shape of field lines and equipotentials

Field lines are graphical representations of a vector at any given point whose magnitude and direction are those of the electric field at that point. Equipotentials are lines in which the electrical potential is constant. The general principle is that the equipotentials are perpendicular to the field lines. Fig. 4.18 shows the field lines and equipotentials for a finite surface.

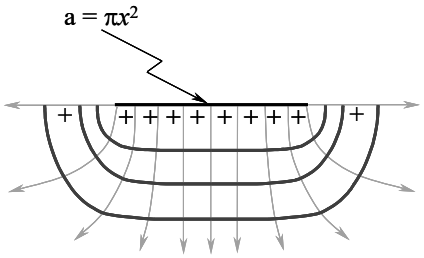

Fig. 4.18 Field lines (grey) and equipotentials (black) produced by a finite surface charge.

A program was written in LabVIEW (see section 6.1.3) to plot the equipotentials generated by a single pair of electrodes used in EIE using equations 4.65 to 4.74. The result for a person with a girth of 80.10 cm is shown in Fig. 4.19A.

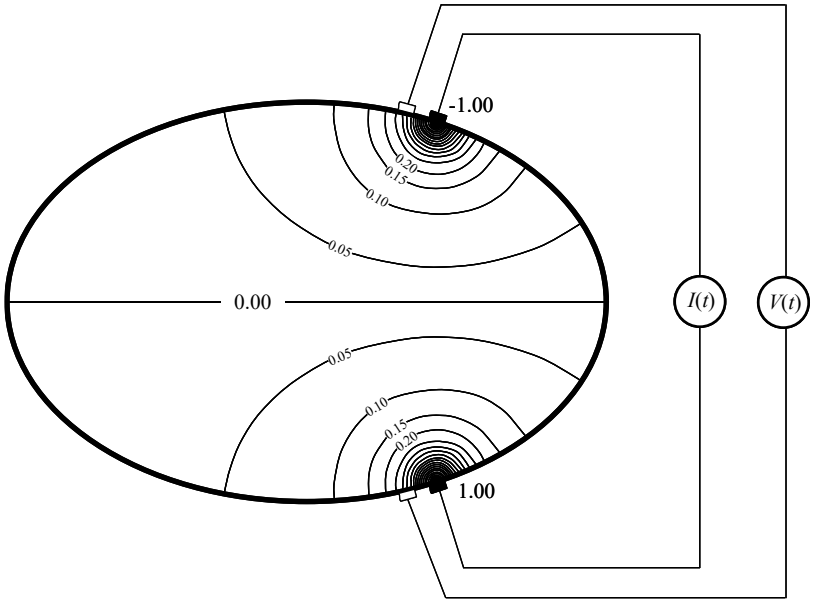

Fig. 4.19 Equipotentials produced by EIE in a homogenous elliptical model of the human abdomen with semi-major axis = 15cm and semi-minor axis = 10cm. The electrodes are positioned at $\hat{y} \approx 7$cm. $I(t)$ is the alternating current source and the voltage is measured at $V(t)$. The potential has been normalised.

4.3.5 Current density and sensitivity

The relative sensitivity of the EIE system with respect to volume change is simply a function of the local current density at a particular point. Large current densities result in greater sensitivity in response to volume changes and vice versa. The current density, J may be calculated from the measured impedance, Z_m and the predicted voltage V_p using ohm's law.

$$I = \frac{V_p}{Z_m} \tag{4.75}$$

Fig. 4.20 shows the variation of current density with depth by using equation 4.39 and 4.75. The electrode radius, r is 0.5cm (see section 5.1.3), the resistivity, ρ is 5 Ωm, (see section 5.4.3) and the applied current, I is 2.5mA.

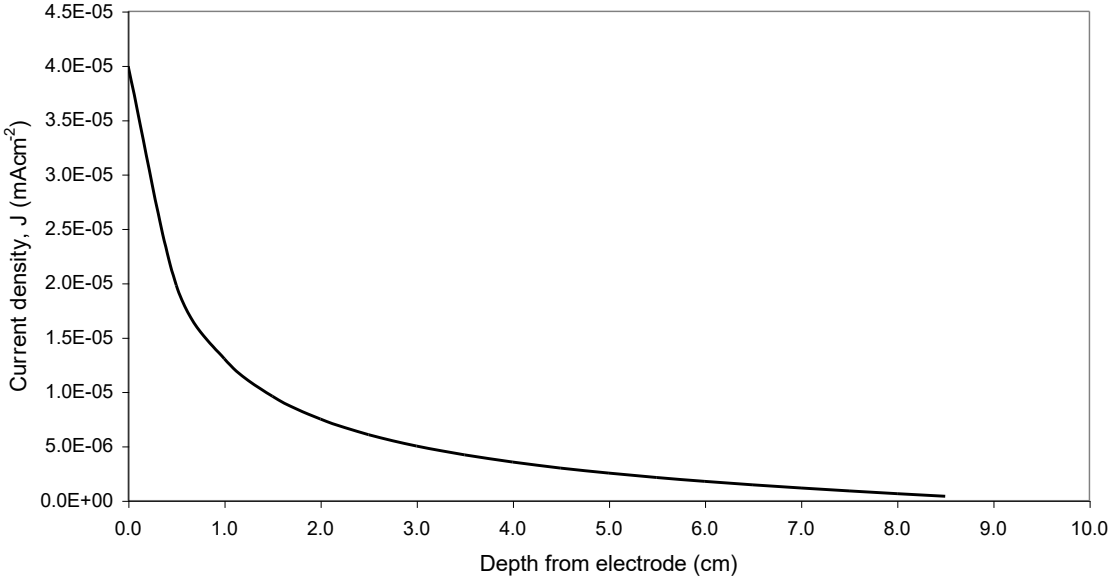

Fig. 4.20 The variation of current density with tissue depth assuming that the conductivity is homogenous.

Fig. 4.20 indicates that since the current density decreases rapidly with depth, the signal is highly sensitive to volume changes near to the electrode surface. Furthermore, there is significantly less sensitivity to internal volume changes. Fig. 4.21 shows the variation in current density with surface distance, $\hat{y}$ when the current is passed between the two electrodes that are 20cm apart.

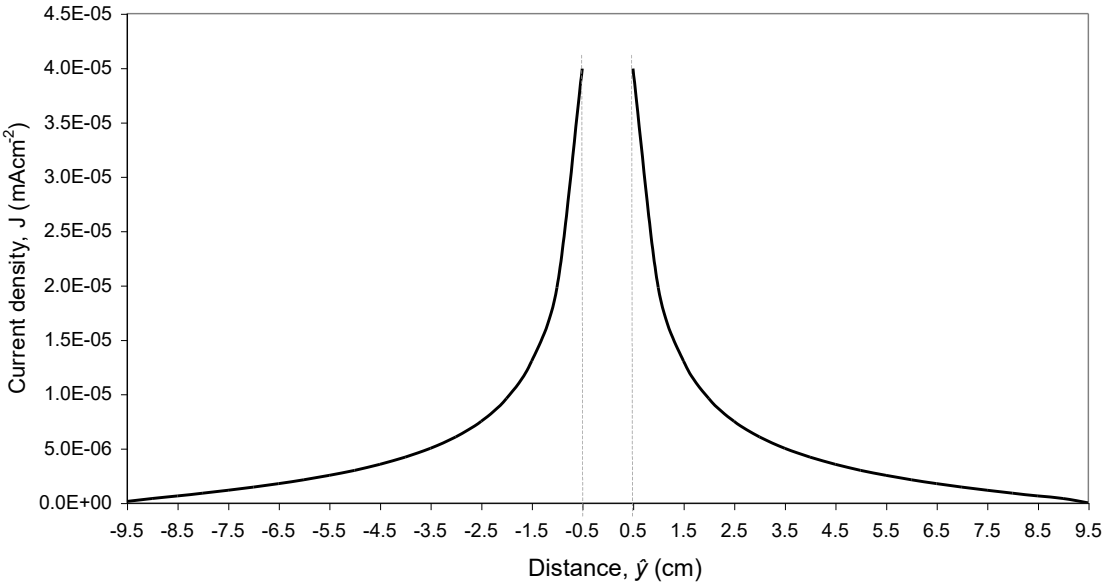

Fig. 4.21 Graph showing the change in current density, J with surface distance, $\hat{y}$ calculated from equations 4.39 and 4.75.

5 ELECTRICAL IMPEDANCE EPIGASTROGRAPHY (EIE)

5.1 Introduction to EIE

5.1.1 The principle of Electrical Impedance Epigastrography (EIE)

Section 3.2 described the leading techniques currently used for measuring gastric emptying rates and contractility. Electrical Impedance Epigastrography (EIE) is a relatively new method that has been proposed as a potentially valuable technique for measuring gastric emptying rates and contractility. EIE involves applying an AC electrical current, $I(t)$ via surface electrodes placed over the epigastric region and measuring the potential difference, $V(t)$. The impedance, $Z(t)$ is calculated using Ohm's law stated in equation 5.1.

$$V(t) = Z(t)I(t) \tag{5.1}$$

where $$Z = R + jX \tag{5.2}$$

and $$X = \frac{1}{\omega C} \tag{5.3}$$

Figure 4.4 demonstrated that at frequencies below 100kHz, the capacitive effects of the biological tissue are negligible, meaning that the impedance is essentially a measure of the simple resistance. Nevertheless, since the name of the technique under investigation is Electrical *Impedance* Epigastrography, the term impedance will be retained for further calculations. From equation 4.23 it follows that since $V = LA$, then

$$Z = \frac{\rho L^2}{V} \tag{5.4}$$

Since the stomach is essentially a muscular bag, the resistivity, ρ of the epigastric region can be altered through the ingestion of a meal that has a different resistivity to the stomach and surrounding tissues. Equation 5.4 shows that with constant resistivity, the measured impedance is proportional to the macroscopic volume. This is primarily affected by the content of the stomach. A low resistivity meal will lead to relatively low impedance signal and vice versa.

5.1.2 The Epigastrograph

The device responsible for taking EIE measurements is called an Epigastrograph. It works by applying an AC current through three pairs of surface Ag/AgCl$^-$ electrodes (three posterior and three anterior) over the epigastric region. Three electrode pairs were originally used to ensure that a good signal was obtained. The excitation current applied to the electrodes is a 32kHz sinusoidal with amplitude of 1 to 4 mA rms. Digital multiplexing means that for each data point, the Epigastrograph switches the application of the current between each electrode pair while the other two pairs measure the voltage. Consequently, six combinations of signal are acquired. The electrode pairs (each pair having one anterior and one posterior electrode opposite one another) are colour coded, yellow, black and red.

The hardware (shown in Fig. 5.1) consists of three components; the mains powered PC interface unit (PCIU), the battery powered subject interface unit (SIU) and the laptop computer (PC). The PCIU is powered by mains and is responsible for passing data and information between the SIU and the PC. It has two connector ports; one is a 9 pin serial port for the PC interface and the other is the socket for the optical fibre lead, required to electrically isolate the subject from mains electricity. The optical fibre connects the PCIU to the optical port of the battery powered SIU (which contains the epigastrograph electronics). Two sockets on the opposite side of the unit are for the two electrode leads (one lead is for the anterior electrodes and the other is for the posterior electrodes). It does not matter which socket is used for the anterior and which is used for the posterior electrodes.

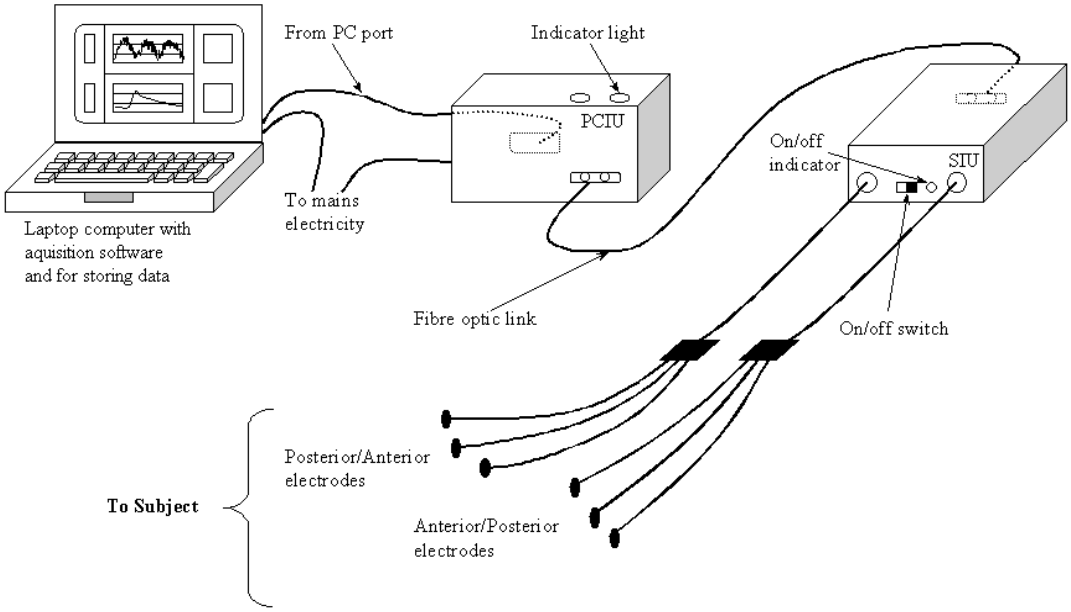

Fig. 5.1 The EIE hardware [Reproduced from Freedman MR, 2001].

5.1.3 Ag/AgCl Electrodes

The electrical connection between a medical electronic device and the surface of the skin is crucial in minimising noise and recording useful signals. The interface is made via surface electrodes that are essentially transducers with the ability to detect or apply electrical currents from an electronic system (the device) to an ionic system (the patient). One of the most commonly used surface electrodes is the metal plate silver/silver chloride (Ag/AgCl) electrode. It has the advantage of being easy to manufacture while being highly effective and relatively noise free. In addition, these electrodes are manufactured with an electrolyte gel that acts as a mediator between the metal disk applying the electrical current and the skin that requires an electrolytic current, to enhance their performance. It also reduces motion artefact by acting as a flexible contact between the electrode and the skin. The electrode reacts with the tissue by the reaction given in equation 5.5.

$$Ag + Cl^{-} \Leftrightarrow AgCl + e^{-} \qquad (5.5)$$

The double arrow indicates that this is a reversible reaction. There are also irreversible effects that generate potentials across the electrode known as polarisation potentials and are a source of noise in electrical measurements. Ag/AgCl electrodes minimise this unwanted effect are readily available at very low cost making them a desirable choice for many physiological measurement devices.

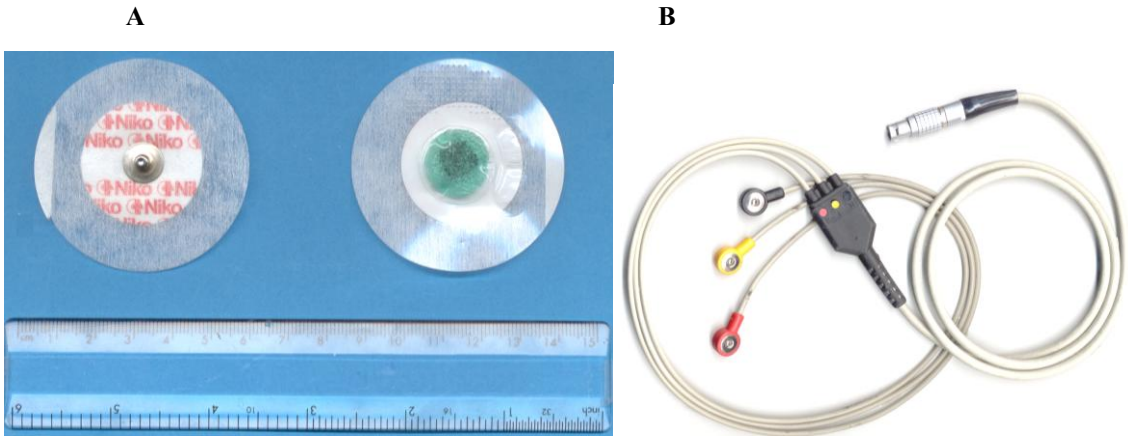

Fig. 5.2 **A** Front and back of the ECG electrode showing the button connection for the leads **B** The ECG connection leads used in EIE. Two leads are required, one anterior and one posterior.

The pre-gelled ECG electrodes used for all studies shown in Fig. 5.2 were manufactured by Niko™ (reference number 4060). The electrode was covered with Micropore™ surgical tape pad that kept the electrodes attached to the skin without causing discomfort. The area of the interface between the active electrode and the skin was 0.79 cm^2 (radius = 0.50 cm).

5.2 Methodology in acquiring EIE signals

5.2.1 Volunteer preconditions

Volunteers are asked to complete a questionnaire prior to the test regarding anthropomorphic measurements, lifestyle and eating habits. The reverse of the form included an explanation of the EIE test and experimental procedure. These forms were given to all volunteers some time before the experiment was to be carried out to ensure that they were satisfied with the experimental procedure. The volunteers were asked to sign the form as proof of their consent. The forms can be seen in Appendix C. All data was treated in the strictest confidence; each subject referred to with a unique confidential code number.

The inclusion criteria were as follows:

(i) Healthy subjects between the ages of 18 and 65 of either sex.
(ii) Refrained from food or drink (except water) 6 hours prior to the test.
(iii) Refrained from water 2 hours prior to the test.
(iv) Their last meal was a light, low fat snack.
(v) Refrained from strenuous exercise from the night before the test.
(vi) Refrained from alcohol, nicotine based products (including patches and gum) and spicy foods from the night before the test.

The exclusion criteria were as follows:

(i) The volunteer has a medical condition that may affect GI tract function.
(ii) The volunteer takes regular medication that may affect upper GI tract function.
(iii) The volunteer has a body mass index above 30.
(iv) The volunteer has a history of alcohol or drug abuse.
(v) The volunteer cannot understand or comply with the requirements of the protocol.
(vi) The volunteer cannot give written informed consent.

5.2.2 Application of the electrodes

The interface between all medical electronic devices and the human body is very important, not only with respect to safety, but also in terms of loss of signal through bad contact. Therefore, the skin surface must be cleaned with non-alcohol wipes and shaved if necessary prior to the application of the electrodes in order to minimise the electrode-skin impedance. Three anterior electrodes (pre-gelled Ag/AgCl) are placed onto the skin of the volunteer or patient, over the epigastric region of the abdomen (see Fig. 5.3).

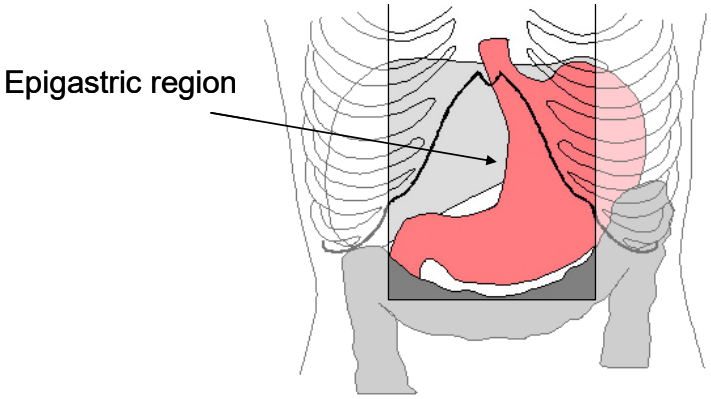

Fig. 5.3 Position of the epigastric region according to Tortora [Tortora GJ, 2000] with respect to the human torso [Redrawn from Pansky, B 1975].

As with all non-invasive techniques (excluding those that image the stomach such as MRI), the internal region of interest must be located using surface anatomy. By placing the electrodes at set distances from particular anatomical markers, which are present in all humans and visible from the skin surface, the region of interest can be located with reasonable accuracy and for all individuals of varying height and girth.

Fig. 5.4A shows the positions of the anatomical features used to locate the stomach with the equivalent internal anatomy. The anatomical features are the xiphisternum, which is flat point of cartilage at the base of the sternum, the umbilicus and the costal margin (end-point ribs marking the beginning of the intercostal space). The distance between the xiphisternum and umbilicus (XU) is measured and divided into half.

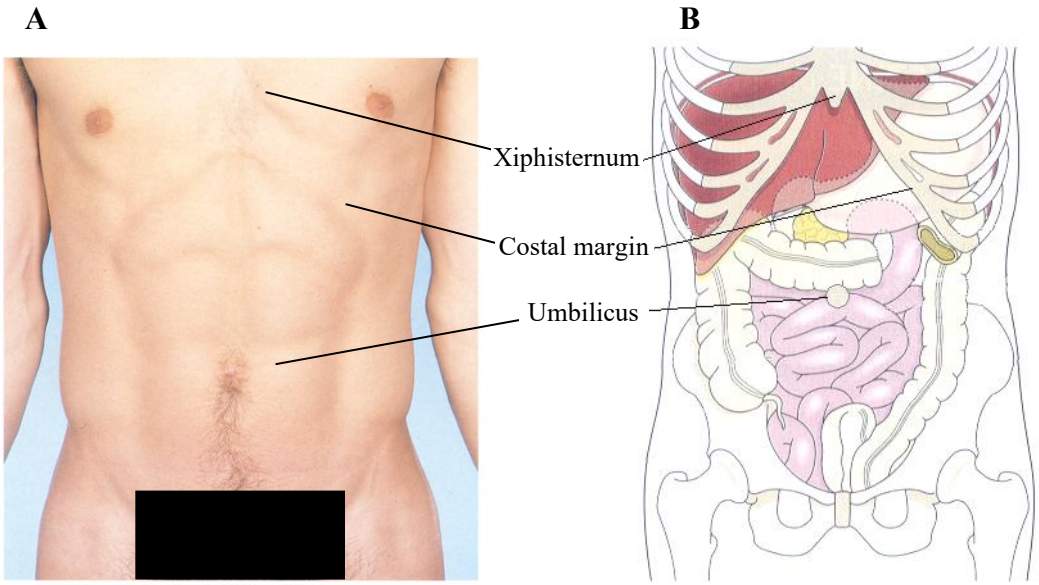

Fig. 5.4 **A** Surface anatomy of the human torso used for the location of the electrodes in EIE with associated anatomical features [Redrawn from Lumley JSP, 1996] **B** Diagram showing the location of the stomach with respect to internal organs [Redrawn from Waugh A, 2001].

The fist anterior electrode (yellow) is placed just inside the intercostal margin at a distance of half XU. The lower right electrode (black) is placed approximately 3cm from the midline so that the angle between it and the first electrode is between 30° and 50°. The third electrode (red) is then placed with its edges touching the other two, to form a triangle with the other two electrodes. The three anterior electrodes are then placed on the back in corresponding positions, so that each of the posterior electrode mirrors their anterior equivalent. The electrode positions are shown in Fig. 5.5.

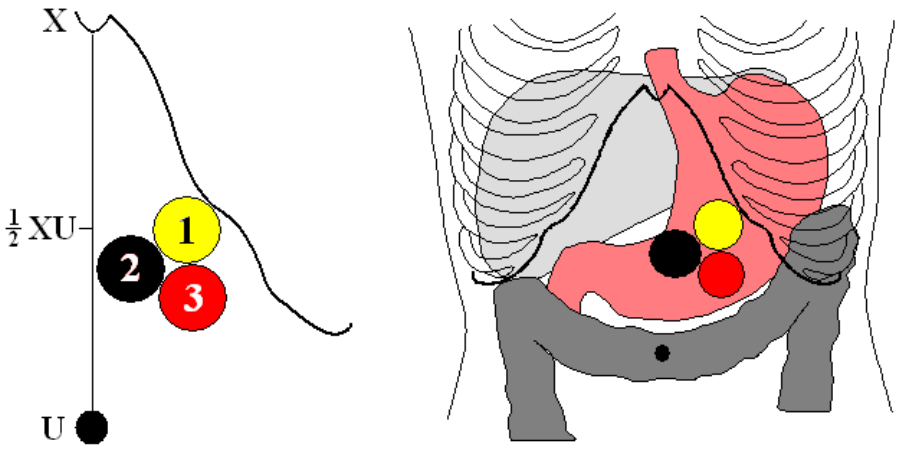

Fig. 5.5 Electrode positions and surface anatomy with corresponding internal organs [Right hand picture redrawn from Pansky B, 1975].

5.3 Advantages and limitations of EIE

5.3.1 Practical advantages

The primary advantages of EIE is that the technique is percutaneous, meaning that it does not penetrate the skin in any way and non-invasive indicating that it does not affect the medium in a way that is likely to change the physiological processes being measured. Unlike the standard techniques for measuring gastric function such as scintigraphy, EIE does not use ionising radiation, which means that it can be used repeatedly on patients and volunteers without any risk from the potential stochastic hazards related to ionising radiation exposure. This is particularly pertinent with regards to children, females of childbearing age and pregnant women.

The equipment is relatively inexpensive; the cost of the EIE monitor is approximately £3000, (excluding laptop computer) and when considering the several hundreds of thousands of pounds spent on imaging equipment such as MRI scanners and gamma cameras that are currently used for gastric motility studies, there are clear financial benefits particularly as the cost of maintenance and upkeep is negligible. There are practical advantages too. Unlike several techniques mentioned in section 3.2, EIE does not require much training to use. This means that not only does EIE not need to rely on specialised hospital departments, it could be used in a small district hospital, outpatients department, clinics or doctors surgeries and since the equipment is small, it is portable and could be moved from clinic to clinic as required.

5.3.2 Efficacy in measuring gastric function

EIE is a very sensitive technique and so the signals recorded detect not only the gastric emptying rates but also the tiny fluctuations in gastric volume caused by the contractile events in the stomach [McClelland GR, 1985]. Attempts have also been made to measure gastric secretions using a simultaneous acquisition of EIE and scintigraphy. This principle works using the fact that EIE measures both the volume changes caused by emptying and contractility but also the temporal changes in gastric pH related to the concentration of gastric secretions.

Therefore, since only the ingested meal is detected by scintigraphy, the emptying rate measured only provides an estimate of the volume of the meal remaining (without gastric secretions). Consequently, by subtracting the normalised scintigraphic analysis of the emptying rate from that measured by EIE an approximation of the changes in gastric pH during the digestion of the meal can be found [Giouvanoudi A, 2002].

Previous research has indicated that the measurement of gastric emptying rates by EIE is comparable to dye dilution methods [McClelland GR, 1985], paracetomol absorption [Sutton JA, 1989], single scanner scintigraphy [Sutton JA, 1985], dual headed gamma camera scintigraphy [Giouvanoudi A, 2000] and Applied Potential Tomography (APT) [Mangnall YF, 1988]. Studies have shown that EIE can detect changes in gastric emptying due to varying the content of the test meals [McClelland GR, 1985], by changing the physical position of the subject [Rainbird AL, 1987] and pharmacologically induced changes such as the effect of morphine [Murphy DB, 1996] and metoclopromide [McClelland GR, 1985].

5.3.3 Limitations and complications

The most significant limitation of EIE is undoubtedly related to the fact that fat has a relatively high resistivity in the region of 2.00 kΩcm for frequencies between 1 and 100kHz [Brown BH, 1999]. Since a large proportion of potential is therefore lost across fatty tissue layers, the sensitivity at gastric depths is greatly diminished in obese subjects resulting in a signal that lacks any useful gastro-physiological information. This explains why the third exclusion criterion cited in section 5.2.1 is a BMI above 30. Studies have shown (Fig. 5.6) an inverse relationship between impedance deflection and body weight, which confirms the need excluding obese volunteers.

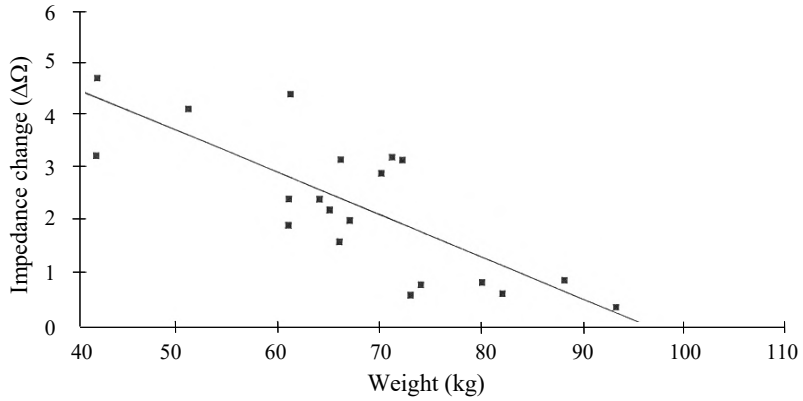

Fig. 5.6 The effect of body weight on the resulting maximum impedance change by 600ml of water [Redrawn from Spyrou NM, 1993].

Furthermore, section 4.3.5 illustrated that since current density decreases exponentially with depth, EIE is most sensitive near to the skin's surface. This means that not only is the majority of the signal's sensitivity lost to dermal fat layers but that small movements near to the electrode caused by subject motion result in large rapid changes in impedance that cause large spikes in the signal, thus corrupting the data. Section 6.2.2 discusses the signal processing techniques that can be employed to reduce the effects of these motion artefacts. Nevertheless, it is necessary for the subject to remain as still as possible during the test (which may last for up to a 90 minutes) to minimise the incidence and extent of motion artefacts. Motion artefacts are not exclusive to EIE and present greater problems with other techniques.

Problems with locating internal organs are inherent to non-invasive, percutaneous measurements. However, failure to correctly locate the stomach with the method described in section 5.2.2 becomes apparent by little or no deflection in the EIE signal upon meal ingestion.

Measurements taken *in vitro* (Fig. 5.7) confirm that changes in resistivity measured by EIE and APT were directly proportional to the radius of a glass rod [Mangall YF, 1988].

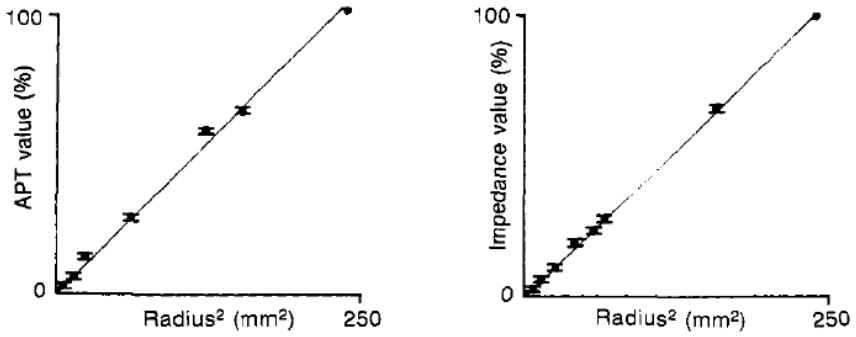

Fig. 5.7 Diameter of a glass rod placed in the centre of a saline filled Perspex tank versus APT and EIE values. Results are mean ± sem of 5 experiments for EIE and 10 experiments for APT [Reproduced from Magnall YF, 1988].

The linear relationship between glass rod diameter and signal deflection shown in Fig. 5.7 is for a homogenous system implying that the electrical field travels in straight lines. Measurements taken in vivo also make this assumption and therefore presuppose a linear relationship between the volume ingested and the deflection in impedance.

However, this assumption has been tested by a number of studies including Fenlon (Fig. 5.8) who used a two-channel impedance-measuring device. Despite a linear correlation the standard deviation shown in Table 5.1 implies large variations in individual results.

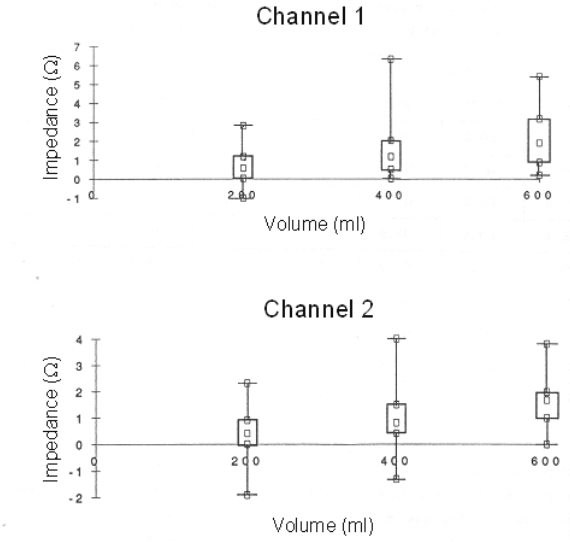

Fig. 5.8 Medians and interquartile ranges for the impedance deflection of different meal volumes given to 28 subjects [Redrawn from Fenlon TJ, 1992].

Table 5.1 The mean, standard deviation and standard error of the mean for impedance deflections with varying meal volumes [Reproduced from Fenlon TJ, 1992].

		Channel 1			*Channel 2*		
		200ml	400ml	600ml	200ml	400ml	600ml
Mixed	Mean	0.7Ω	1.5Ω	2.4Ω	0.5Ω	1.0Ω	1.7Ω
	STDEV	0.8Ω	1.2Ω	1.4Ω	0.7Ω	0.9Ω	0.9Ω
	sem	0.1Ω	0.2Ω	0.3Ω	0.1Ω	0.2Ω	0.2Ω
Male	Mean	0.5Ω	1.5Ω	2.3Ω	0.4Ω	0.8Ω	1.5Ω
	STDEV	0.8Ω	1.4Ω	1.4Ω	0.7Ω	0.8Ω	0.8Ω
	sem	0.2Ω	0.3Ω	0.3Ω	0.1Ω	0.2Ω	0.2Ω
Female	Mean	1.0Ω	1.4Ω	2.3Ω	0.8Ω	1.4Ω	2.0Ω
	STDEV	0.8Ω	1.0Ω	1.4Ω	0.7Ω	1.1Ω	1.2Ω
	sem	0.2Ω	0.3Ω	0.4Ω	0.2Ω	0.3Ω	0.3Ω

5.4 The choice of test meal

5.4.1 Liquid and semi-solid versus solid meals

Many of the studies into gastric emptying and motility advocate the use of solid meals for gastro-physiological investigations. However, solid meals have a significantly longer emptying rate and so extracting results is far more time consuming. Longer examination times increase the inconvenience and irritation to the subject under investigation, which in turn increases the temptation for the subject to fidget causing motion artefacts.

The criticism of liquid meals is that they are not believed to be physiologically significant meaning that the stomach does not utilise all of the gastro-physiological processes to digest liquids in the way that solid meals are digested. Previous research into gastric function using electrical impedance methods has only ever used liquid and semi-solid meals with great success. It seems that not only do the established test meals result in successful results with acquired signals providing a rich source of gastro-physiological information, but that using conventional test meals will allow comparisons to be made with previous work.

5.4.2 Composition of the test meals

Three test meals were chosen that had been used extensively in previous studies. The composition and physicochemical properties of those meals are given in table 5.2. The volume of each meal administered was 500ml. The simplest meal used (type A) was Volvic™ mineral water that contains a variety of minerals listed in table 5.3. The other two meals (type B and C) contained fixed quantities of fat in the form of double cream (see table 5.4) and carbohydrate in the form of spray-dried maltodextrin (see table 5.5), a complex carbohydrate used in sports drinks to lower the osmolarity making the drink isotonic and in the process of making low-alcohol or alcohol free beer to compensate for lack of body. It is obtained through a process of the enzymatic conversion of starch. Meal types B and C were therefore considered ‘complex’ meals.

Table 5.2 Composition and physicochemical properties of the test meals [Values are taken from Giouvanoudi A, 2000].

Meals	*Ingredients*								*Physicochemical properties*		
	Volvic™		Maltodextrin		Double cream		Flavouring		Energy	Resistivity	pH
	(ml)	(kJ)	(g)	(kJ)	(g)	(kJ)	(g)	(kJ)	(kJ)	(kΩcm)	-
A	500	0	0	0	0	0	0	0	0	6.25	7.00
B	*	0	50	834	8	148	20	334	1316	3.45	5.37
C	*	0	50	834	92	1707	20	334	2875	2.63	4.90

* Exact quantities are unknown.

Table 5.3 Analysis of minerals found in Volvic™ mineral water [values taken from the label of a Volvic™ mineral bottle].

Mineral composition		*Physicochemical properties*		
Mineral	Weight (mgl^{-1})	Dry residue	Resistivity	pH
Bicarbonates	71.0	@180°C (mgl^{-1})	(kΩcm)	-
Silica	31.7	130	6.25	7.0
Chlorides	13.5			
Sodium	11.6			
Calcium	11.5			
Sulphates	8.1			
Magnesium	8.0			
Nitrates	6.3			
Potassium	6.2			

Table 5.4 Nutritional values of Sainsbury's™ double cream [values taken from the label of Sainsbury's™ double cream].

Ingredient	*Value per 100ml*
Protein	1.70g
Total carbohydrate (sugars)	2.60g
Total Fat	47.50g
of which - Saturates	29.70g
of which - Monounsaturates	13.80g
of which - Polyunsaturates	1.40g
Cholesterol	0.13mg
Sodium	0.05g

Table 5.5 The composition of spray-dried maltodextrin [values taken from Cerestar™ technical information sheet].

Carbohydrate composition		*Physicochemical properties*		
Dextrose	1.0	Sulphur dioxide	Moisture	pH
Maltose	6.0	($mgkg^{-1}$)	(%)	-
Maltotriose	9.0	6.0	4.0	4.5
Higher saccharides	84.0			

Care was taken during the production of the two complex meals to dissolve the dry ingredients with Volvic™ mineral water before combining them in order to avoid agglomeration. An electronic whisk was used to mix the wet ingredients while adding more Volvic™ mineral water to increase the total volume to 500ml. Consequently, the exact volume of Volvic™ mineral water used in meals B and C is unknown.

5.4.3 Typical results

Since it is possible to maintain the volume of each meal at 500ml, the most important property of the meal with respect to the signal produced by EIE is the resistivity. It is self-evident from equation 4.72 that increases in the resistivity over the gastric region will increase the measured impedance. The resistivity of the gastric region of a fasting individual has been estimated to be in the region of 0.18 kΩcm ± 1.0 at 37ºC [Giouvanoudi A, 2000].

Since the test meals in table 5.2 all have a resistivity above 0.18 kΩcm they are considered to be non-conductive with respect to the gastric region. Consequently, a positive deflection in the signal obtained by EIE on the ingestion of each test meal is expected. Additionally, volume changes that occur in the stomach during emptying due to gastric contractility manifest themselves in the following way. Contractile events manifest themselves as decreases in impedance and the subsequent increase in impedance indicates the end of the contraction.

Fig. 5.9 shows a typical signal for a water test meal. The arrows mark the beginning and end of meal ingestion. It is clear that the introduction of 500ml of Volvic™ mineral water results in an increase in impedance of approximately 1Ω.

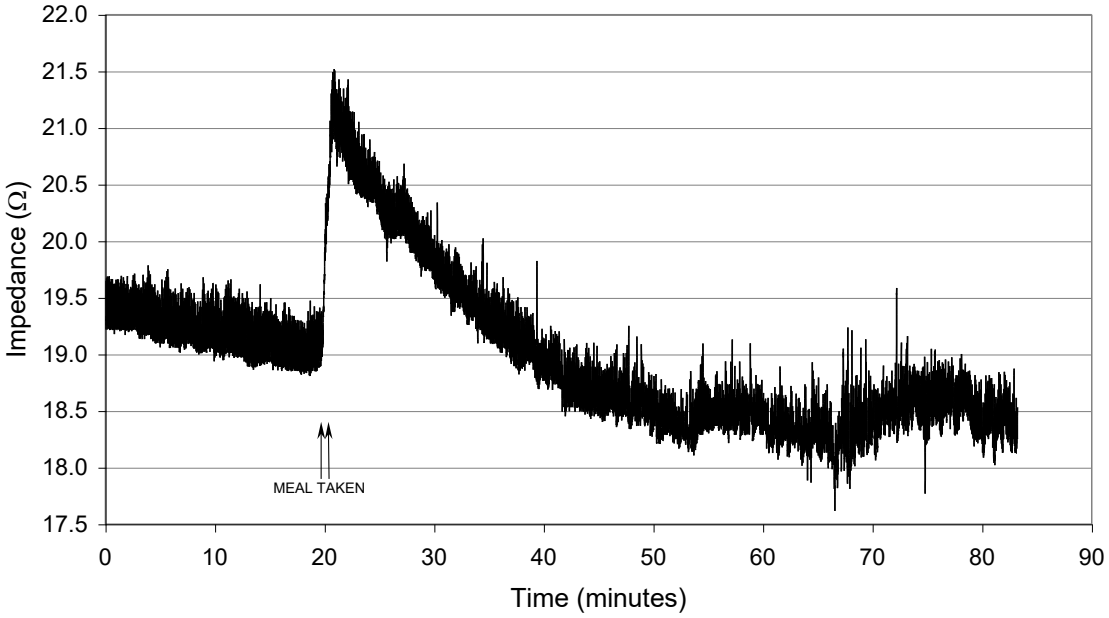

Fig. 5.9 Typical signal obtained for a 500ml Volvic™ mineral water test meal.

The example of an EIE signal for a non-conductive meal shown in Fig. 5.9 clearly shows an emptying pattern expected for a meal of 500ml of Volvic™ mineral water. However, there is more gastro-physiological information hidden within EIE signals that can be extracted using a number of mathematical and signal processing techniques. These techniques will be discussed in chapter 6.

6 ANALYSIS SOFTWARE

6.1 Introduction to EIE analysis software

6.1.1 The need for a comprehensive EIE analysis software package

Electrical Impedance Epigastrography has existed as a technique designed for the analysis of gastric function since the mid-1980s. A number of research projects have investigated the use of signal processing and analysis to extract gastrophysiological information from EIE signals. However, despite these attempts there has never been a comprehensive software package that processes and analyses EIE signals to produce quantitative results that can differentiate between gastric function and dysfunction. The need for such a software package is paramount if EIE is to progress from a simple research tool with great potential to being a serious complementary or even alternative technique to existing diagnostic methods in gastroenterology.

6.1.2 The requirements for the analysis package

There are a number of important prerequisites of the software analysis package for EIE signal analysis. From a scientific perspective, the software should be able to deal with every potential type of EIE signal with the ability to remove all the possible unwanted signals such as noise from motion artefacts, respiratory signals or mains interference. The analysis must be as thorough and as wide-ranging as possible in order to extract as much gastro-physiological information as possible while remaining user friendly. Current techniques for analysing gastric function are almost exclusively mono-factorial; they only measure one specific gastro-physiological variable such as half emptying time (T50) or contractility but rarely both (see section 3.2). Consequently, these techniques do not figure as serious diagnostic systems because although research studies using these techniques often demonstrate differences between control and abnormal groups, there is usually a large overlap between normal and abnormal subjects (see Fig. 6.1). Therefore, the immediate problem with using these techniques for diagnostic purposes is that in the clinical environment the number of data samples (i.e. patients) is always one. If the gastro-physiological variable investigated by a particular diagnostic technique cannot absolutely differentiate between normal and abnormal patients without any possible overlap between normal and abnormal groups, it is impossible to decide if the result obtained is normal or abnormal, without some margin of error.

The results in Fig. 6.1 highlight the problem of using a single gastro-physiological variable to attempt to differentiate between control and abnormal groups: although the difference between mean values is significant, there is a considerable overlap between the two groups, meaning that it is impossible to set a boundary between normal and abnormal using the solid meal gastric half emptying time. Therefore, this particular gastro-physiological variable cannot be relied on independently to make a definite diagnosis.

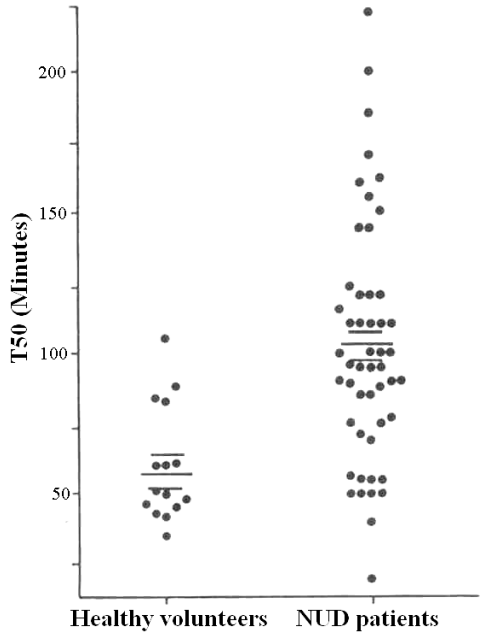

Fig. 6.1 Gastric half emptying times using scintigraphy (T50 with mean and SEM) from a study investigating dysmotility in Non-Ulcerative Dyspepsia (NUD) [Redrawn from Waldron B, 1991].

A technique that is not able to distinguish between normal and abnormal groups means that when individual patients are tested, the results can never be conclusive and so there is little benefit to the clinician or diagnostic process. Although it may never be possible to differentiate between normal and abnormal groups using one gastro-physiological parameter, it may be possible to separate clinical cases with a multifaceted approach that simultaneously produces quantitative measures of a variety of gastro-physiological variables. It is obvious that the more gastro-physiological information that is obtained, the more chance there is of being able to differentiate between gastric function and dysfunction successfully. Therefore, the primary aim of the software package is to extract as much information as possible in order to build a multidimensional picture of gastric function so that a more reliable diagnosis can be made.

6.1.3 The base language

There are a number of computer languages that software can be written in. The vast majority employ top-down programming methods that involve code written line by line. The package that was used for the acquisition software written at the time of the construction of the current EIE system used a package called LabVIEW, manufactured by National Instruments. This package is based on the concept of data flow so that instead of the program following a consecutive number of instructions (as in traditional top-down programming shown in Fig. 6.2A and B), the package uses graphical representations that correspond to blocks of source code that have specific functions from simple mathematical operations such as addition and subtraction, to complex signal processing algorithms (shown in Fig. 6.2C).

A

Fortran program

```
program addition;
var
          A, B, C : real;
begin
write('Enter the first number');
readln(A);
write('Enter the second number');
readln(B);
C := A + B;
writeln ('The sum is ', C)
end
```

B

C program

```
/* A program to read in two numbers and print their sum */

main()
{
          float     A,B; /* A and B are the two inputs */
          printf("Enter A ");
          scanf("%d",&A);
          printf("Enter B ");
          scanf("%d",&B);
          printf ("The sum of A and B was %d\n",A+B);
}
```

C

LabVIEW program

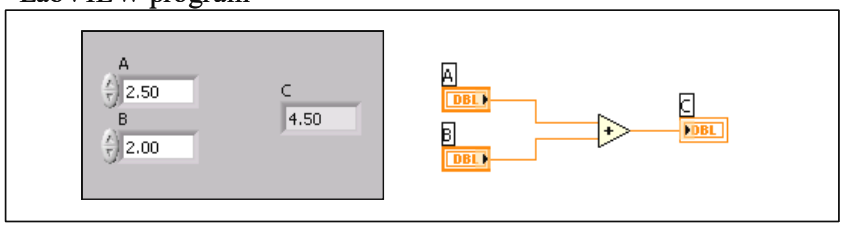

Fig. 6.2 **A** Fortran program for adding two real (floating point) numbers. **B** The equivalent C program and **C** The LabVIEW program showing the 'front panel' on the left which is the operator interface and the program on the right showing the graphical representation and data flow (flowing from left to right).

LabVIEW has many advantages over conventional top-down programming; since the block diagram shows the programmer how data is passed and modified from beginning to end, fault finding and de-bugging is simplified. Furthermore, the package allows the instant production of ready-to-use executable files from the source code. Consequently, LabVIEW was chosen as the preferred language in which to write the software. Appendix D has flow charts that represent each function of the EIE software and how they interact with one another.

6.2 Design and functions of the EIE analysis software

6.2.1 Introduction

The following sections describe the functions of the software developed for analysing EIE signals. The software was called ACCESS (Analysis, Characterisation and Classification of Epigastrographic SignalS) because the ultimate aims were threefold: (i) to extract physiological information by means of a thorough, qualitative and quantitative analysis (ii) to characterise Epigastrographic signals by revealing and explaining patterns and features that are physiologically and pathophysiologically significant and (iii) to classify each EIE signal based on those characteristics. Appendix D contains a user manual for ACCESS (version 2.40). This chapter deals with the purpose of each function and details the theory behind the signal processing and analysis tools employed while discussing their efficacy in fulfilling the objectives outlined above.

The operator is presented with fourteen different pages that control different aspects of the processing and analysis. Although the aim of the software was to extract as much quantitative and qualitative physiological information as possible from EIE signals, it was also necessary to make it accessible and uncomplicated for other researchers using EIE. Therefore, some features are designed to make ACCESS more user-friendly. For example, many of the pages have information boxes (with an italic '*i*' next to them) to denote information about the signal processing and analysis methods related to that page. In addition, since results and calculated data are used by the software for subsequent signal processing and analysis, upcoming pages are initially greyed out so that the operator is forced to work through each function in the correct order and activate all of the required procedures. When a page is activated it turns light blue and when the software has finished loading or processing the information for that page it turns dark blue.

6.2.2 Time domain processing

Subject movements will cause spikes in the signal because a significant amount of current density is concentrated close to the skin surface (see section 4.3.5). These artifacts invariably cause positive or negative spikes in the signal [Gaitanis A, 2003 and Freedman MR, 2005]. Fig. 6.3 illustrates that spikes are composed of a large range of frequencies. It is therefore necessary to remove these artifacts in the time-domain signal *before* any frequency domain signal processing. If left in the signal the spikes would contribute the power density over a large frequency range leading to false positive results; suggesting the presence of gastric contractility when there was none, or exaggerating the magnitude of real events [Freedman MR 2005].

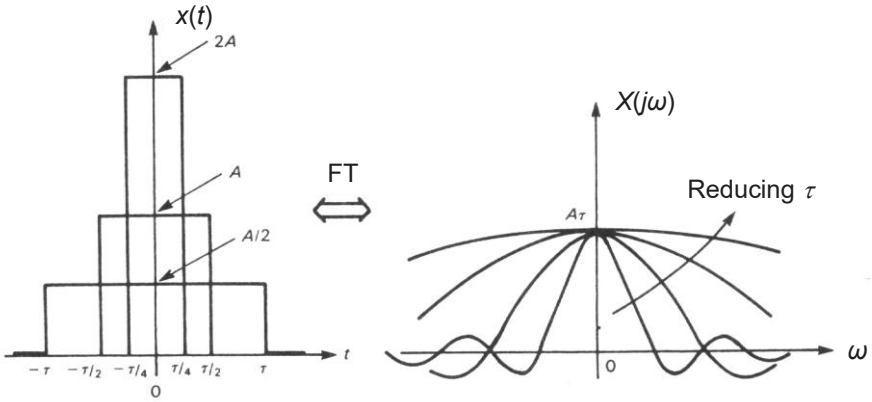

Fig. 6.3 Fourier transforms of a square wave graduating to a unit impulse [Adapted from Meade ML, 1997]

A motion artifact rejection algorithm (MARA) was designed to remove the motion artifacts in the time domain. MARA works by splitting the signal into small epochs and applying a statistical threshold to eliminate statistically significant values. The statistical threshold is based on the Normal distribution and is calculated from the mean, μ and standard deviation, σ for each epoch [Crawshaw J, 2001].

If the input signal is $x[i]$ where $i = 0, 1, 2, \ldots, [T_s\text{-}1]$ and T_s is the total length of the signal (in data points) and the epoch number is m where $m = 0, 1, 2, \ldots, [T_m\text{-}1]$ and T_m is the total number of epochs, then each epoch can be expressed as $x_m[k]$ where $k = (mT_e + 0), (mT_e + 1), (mT_e + 2), \ldots, (mT_e + [T_e\text{-}1])$ and T_e is the total length of the epoch (in data points) which must be selected by the operator (the minimum is 500 points). If the epoch length, T_e does not divide exactly into the signal length, T_s (which is very likely) the total number of epochs is rounded up to the nearest integer (equation 6.1).

$$T_m = \left\lceil \frac{T_s}{T_e} \right\rceil \tag{6.1}$$

Consequently, the length of the last epoch $T_{e_{(T_m-1)}}$ is less than T_e.

$$T_{e_{(T_m-1)}} = T_s \bmod T_e \text{ where } x \bmod y = x - \left\{ y \left\lfloor \frac{x}{y} \right\rfloor \right\} \tag{6.2}$$

Therefore, the mean and standard deviation of each epoch can be expressed as follows.

$$\mu_m = \frac{\sum_{k=mT_e}^{(mT_e+[T_e-1])} x_m[k]}{T_e} \tag{6.3}$$

$$\sigma_m = \sqrt{\frac{T_e \cdot \sum_{k=mT_e}^{(mT_e+[T_e-1])} x_m[k]^2 - \left\{ \sum_{k=mT_e}^{(mT_e+[T_e-1])_e} x_m[k] \right\}^2}{T_e(T_e-1)}} \tag{6.4}$$

Statistically significant values exceed $\mu \pm a\sigma$ where a may be varied to alter the size of the threshold. Consequently, the protocol for MARA was that any point of the signal outside the range $\mu \pm a\sigma$, was considered artifactual. Points that are deemed artifactual are suppressed to the mean value of the epoch in order to minimise their contribution to the signal. After the signal has been processed once, the procedure may be repeated in an iterative fashion. Therefore, the algorithm may be expressed as follows ($\vee$ means logical OR).

$$x_{m_{MARA}}[k] = \begin{cases} x_m[k] & \left(\mu_m - a\sigma_m\right) \le x_m[k] \le \left(\mu_m + a\sigma_m\right) \\ \mu_m & x_m[k] < \left(\mu_m - a\sigma_m\right) \quad \vee \quad x_m[k] > \left(\mu_m + a\sigma_m\right) \end{cases} \tag{6.5}$$

The complete MARA processed signal, $x_{MARA}[i]$ is produced by the computational concatenation of each processed epoch. An example of the effect of MARA on a pseudo EIE signal is shown in Fig. 6.4.

It is also clear that spikes in the time-domain signal contain a large range of frequencies that affect the bandpass filtered signal which is used for gastric contractile analysis. These are successfully removed by MARA and the bandpass filtered signal is restored.

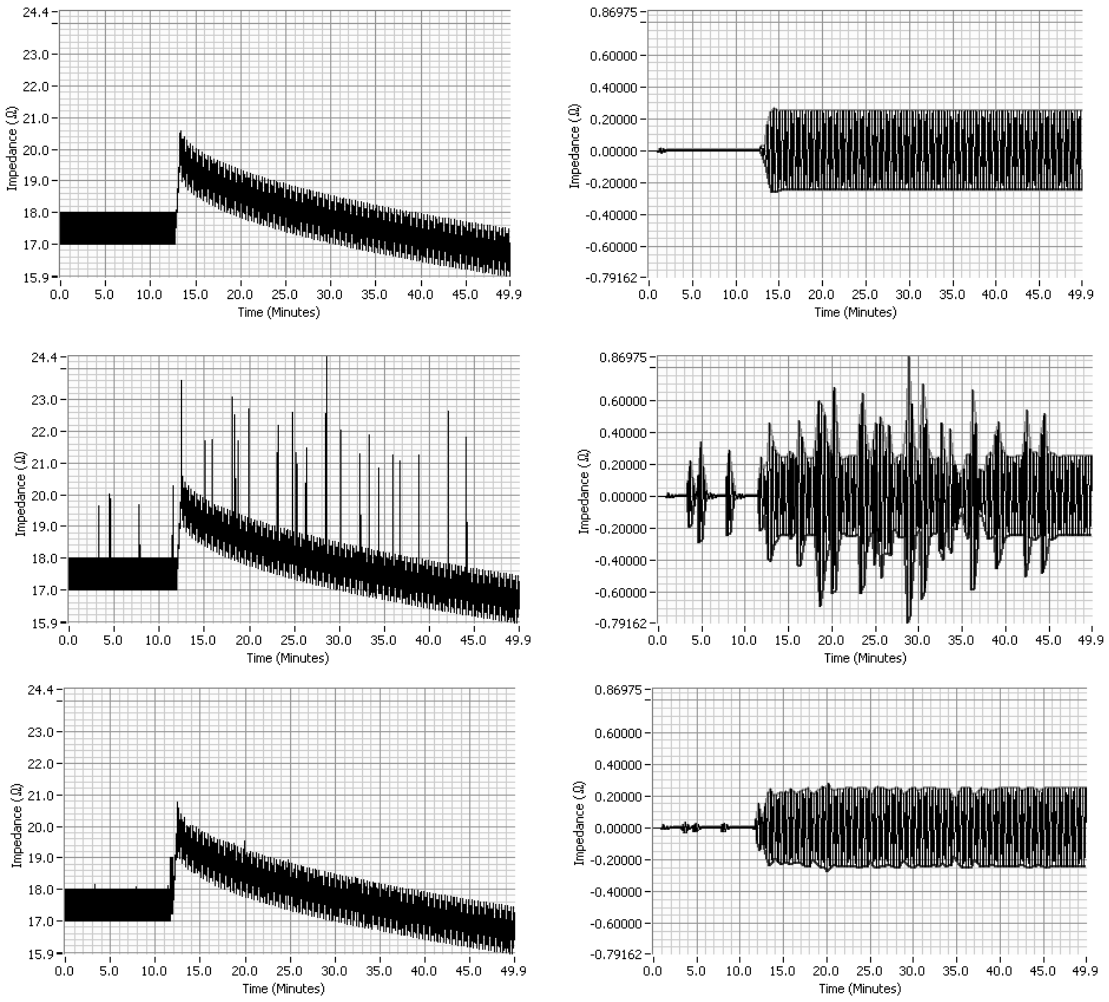

Fig. 6.4 The top two graphs show a pseudo EIE signal (see chapter 7) without artifacts with resultant band pass filtered signal (0.04 to 0.06 Hz). The middle two graphs show the pseudo EIE signal with artifacts added and the bottom two graphs show the same signal after MARA processing to remove the artifacts with variables set as listed above.

The other time domain signal processing algorithm designed was the spike rejection algorithm (SRA). SRA operates in a similar way to MARA. The operator sets an upper and lower impedance threshold for the entire signal. The signal is split into epochs of *n* points (corresponding to the window length) and any points in the epoch that are outside the threshold are suppressed to the mean of that epoch.

Visual inspection is necessary to determine the threshold and different thresholds may be set for each of the six channels. The SRA is needed because large spikes are not always removed by MARA alone because the rejection threshold in MARA is based on the mean of each epoch. Therefore, large spikes (which increase the mean of the epoch) reduce the efficacy of the MARA threshold.

For that reason, SRA was designed to remove very large spikes before MARA was applied so that the mean of the epoch in which those spikes occur is reduced, thus lowering the MARA rejection threshold. The spike shown in the first image in Fig. 6.5 was caused by the subject yawning. The second image shows that MARA has not removed the spike completely. With the SRA set to an upper threshold of 24.5Ω and a lower threshold of 0, the spike disappears completely (the spike at approximately 63.6 minutes is in fact a genuine physiological event).

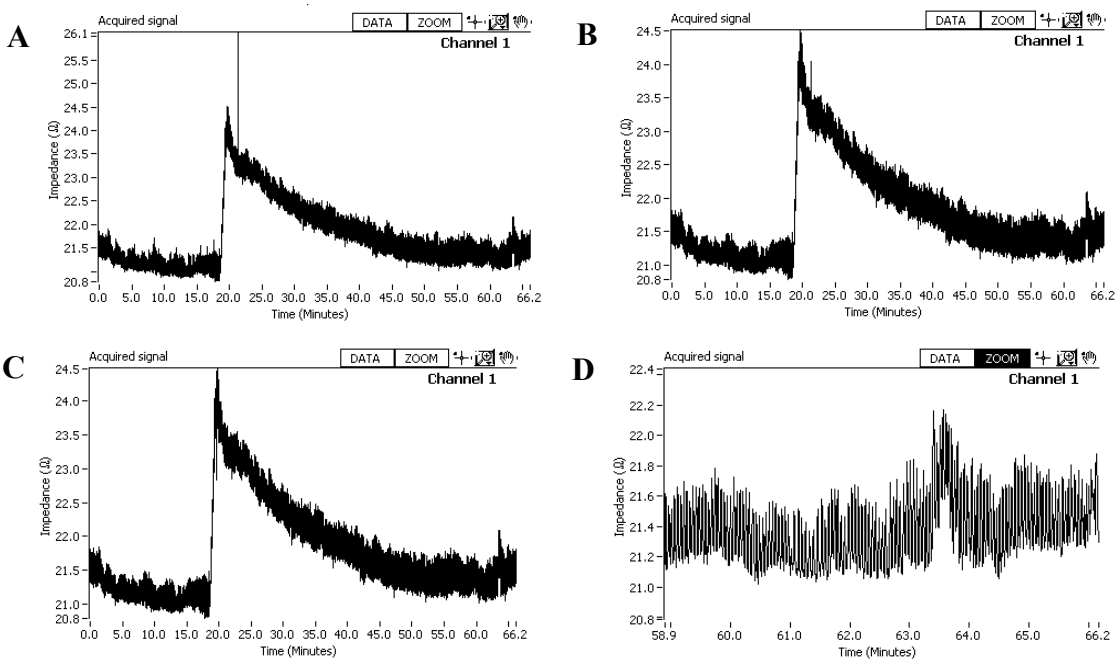

Fig. 6.5 The use of the spike rejection algorithm (SRA). **A** The original signal with motion aritfact. **B** The application of the MARA without the SRA. **C** The total removal of the spike with MARA and SRA applied. **D** The apparent artifact at 63.6 minutes that is in fact a gastric contraction.

6.2.3 Creation of a modelled emptying period

The second function of the ACCESS is to model the acquired EIE. The modelling is performed by dividing the signal into three sections; preprandial, ingestion and postprandial. The preprandial period is modelled using a linear fit and one of three non-linear fits (polynomial, exponential or moving average) is used for the postprandial period. These sections are determined from the event markers activated during the experiment at the beginning and end of meal ingestion. If either the event markers were not activated or more than two were triggered, the software informs the operator and recommends that the ingestion period is separated by observation of the rise in impedance caused by the ingestion of a meal that is non-conductive with respect to the conductivity of the stomach, or by the drop in impedance caused by the ingestion of a meal that is conductive with respect to the conductivity of the stomach.

The preprandial linear fit (L_i) uses equation 6.6 where m is the gradient and c is the y-intercept. One of the methods for the postprandial fit is selected by the operator with the necessary variables to minimise the error if applicable. The equation for the polynomial fit, P_i is shown in equation 6.7. The optimal polynomial order, m is 4 and this was used for the analysis of all EIE experiments[1]. The equation for the exponential fit, E is shown in equation 6.8. The parameters a, b and c are found using a nonlinear Levenberg-Marquardt algorithm[2]. The equation for the moving average fit, A_i is shown in equation 6.9. The ideal number of points, n was 500[3] where $i = 1, 2, ..., n-1$ and j is an integer.

$$L_i = mx + c \tag{6.6}$$

$$P_i = \sum_{j=0}^{m} a_j x_i^j \tag{6.7}$$

$$E_i = a \exp^{(bx_i)} + c \tag{6.8}$$

$$A_i = a_1, a_2, ..., a_{n-1} \quad \text{where} \quad a_i = \frac{1}{n} \sum_{j=i-\left(\frac{n}{2}\right)}^{i+(n-1)} x_j \tag{6.9}$$

[1] The explanation for using the fourth order polynomial is discussed in Appendix E.

[2] The nonlinear Levenberg-Marquardt algorithm is described in Appendix E.

[3] A moving average of 500 data points was used because it equals a period of 100 seconds, meaning that all frequencies above 0.6cpm are averaged out so that the fit only represents the *trend* of the emptying curve.

Fig. 6.6 illustrates the three different postprandial fit algorithms together with R^2, the coefficient of determination[4]. The curves are fitted to the low pass filtered signal but have been displayed with the acquired signal (The R^2 values are also calculated with respect to the low pass filtered signal).

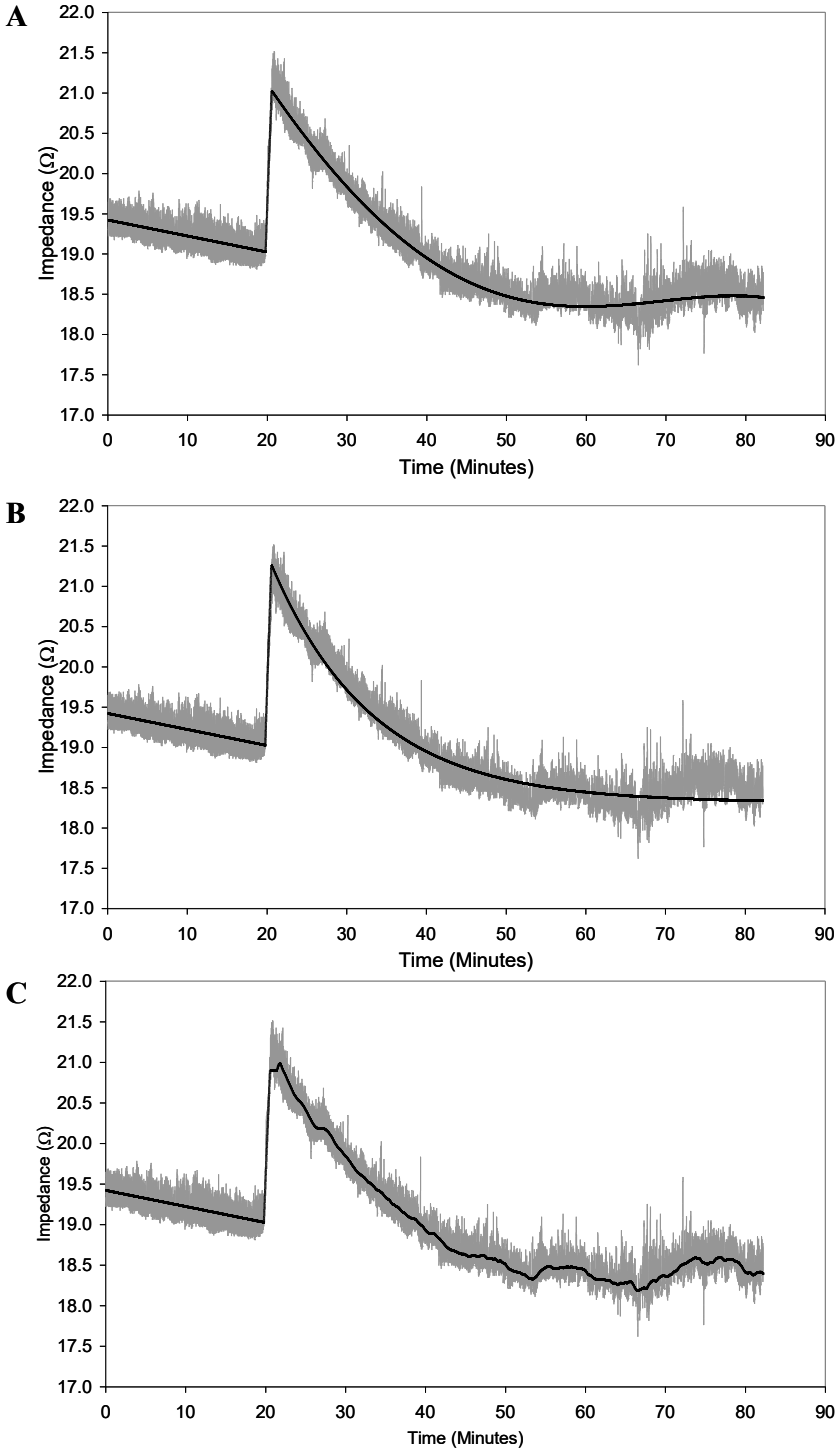

Fig. 6.6 The three emptying curve fits: **A** The 4th order polynomial fit ($R^2 = 0.98$), **B** exponential fit ($R^2 = 0.97$) and **C** 500-point moving average ($R^2 = 0.99$).

[4] The coefficient of determination, R^2 is defined in Appendix E.

The values for R^2 are typical for most EIE signals. Although the exponential fit gives an accurate representaion, not all EIE signals have exponential shaped emptying curves and so fitting an exponential curve to them would be inappropriate (Fig. 6.7A). However, the exponential fit was included in the software to allow the user to compare results to those obtained by other research studies that have favoured the exponential fit for gastric emptying curves. The 500-point moving average gives the best correlation but has a tendency to highlight details that are undesirable for modelling the general trend of the emptying curve. These details may be eliminated by increasing the number of points used to 1500 data points (5 minutes). However, significant inaccuracies occur at the beginning of the moving average due to the averaging method (Fig. 6.7B). Increasing the number of points of the moving average can smooth the fit obtained but this can result in errors at the beginning of the signal due to the averaging method. This effect is demonstrated in Fig. 6.7B.

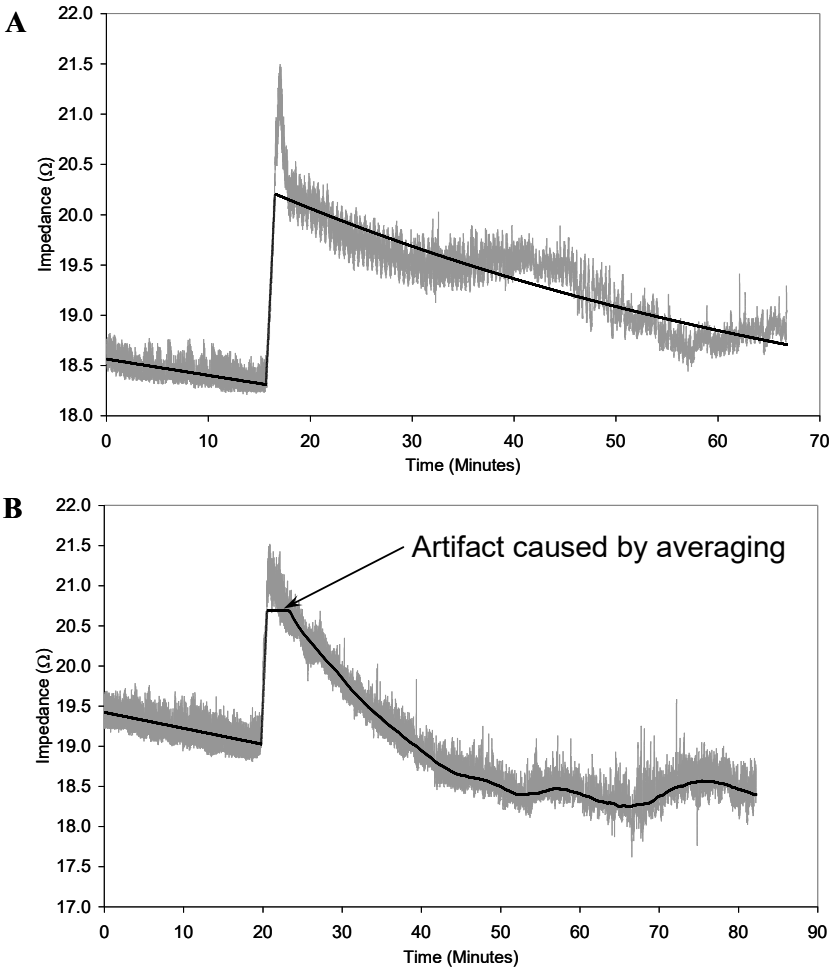

Fig. 6.7 **A** EIE signal with a nonlimear emptying curve with an attempt to fit an exponential curve (R^2 = 0.86) and **B** artifact caused by averaging with a 1500-point moving average fit (R^2 = 0.99).

6.2.4 Calculation of half emptying times

Gastric half emptying times (T50) may be calculated from the modelled emptying period using nine different methods. The first eight methods use a combination of one of four baselines together with one of two calculation methods.

The four baselines are defined as follows: (i) zero gradient baseline from the last preprandial point, (ii) zero gradient baseline from the last postprandial point, (iii) pre- to postprandial baseline connection and (iv) preprandial baseline drift. The two methods for calculation of the half emptying time are the deflection midline method and the equal area method.

The deflection midline method calculates the midpoint of the impedance deflection caused by ingestion and extrapolates a line towards the emptying curve parallel to the baseline. The T50 is measured from the beginning of the postprandial period to the point at which the emptying curve crosses the midline. The equal area method calculates the area enclosed by the emptying curve and the midline. The T50 is the time between the beginning of the postprandial period and the point at which the area enclosed by the emptying curve and baseline is half of the total area.

The ninth method is used for very slow half emptying times in which the experiment has been stopped before the meal has fully emptied. It operates by selecting two points, shown as crosses in Fig. 6.8 and calculates the equation for the straight line drawn between them using $y=mx+c$. The T50 (x_{T50}) is calculated from equation 6.10.

$$x_{T50} = \frac{y_{T50} - c}{m} \tag{6.10}$$

where

$$y_{T50} = \frac{(y_1 - y_0)}{2}$$

$$c = y_1 - mx_1$$

$$m = \left(\frac{y_2 - y_1}{x_2 - x_1} \right)$$

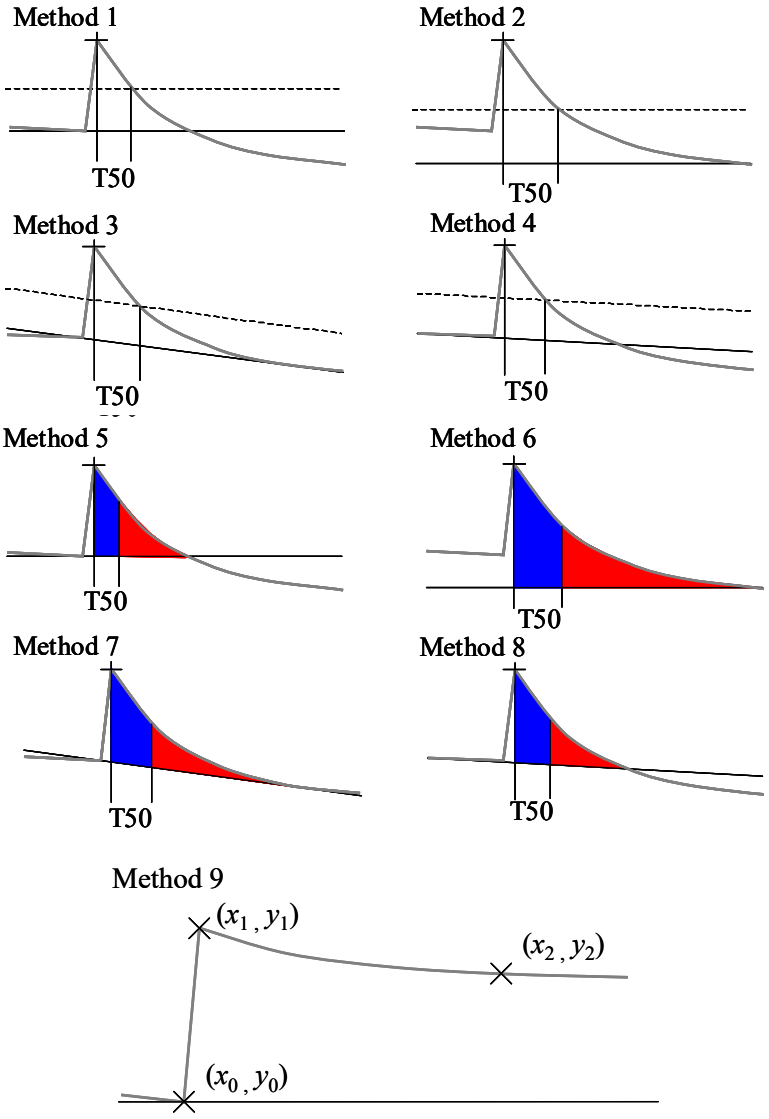

Fig. 6.8 The nine methods of calculating the half emptying time (T50) from pseudo EIE signals. In methods 5 to 8, the blue area equals the red area.

Appendix H analyses the measurement of the half emptying rate (T50) using each of the nine methods. The results (Table H8) demonstrated that there are significant differences between using the deflection baseline method (Methods 1 to 4) or the equal area method (methods 5 to 8) for the analysis. The equal area method underestimated the T50 by approximately 61% whereas the deflection baseline method overestimated the T50 by approximately 5%. Methods 1 and 2 only take into account the preprandial and postprandial baselines respectively thus rejecting the possibility that the other baseline is significant in any way. Method 4 uses the natural drift of the preprandial baseline.

However, this drift is likely to have a physiological cause because it did not occur during experiments using resistor phantoms [Freedman MR, 2000]. Consequently, the assumption that the drift continues without changing during the whole experiment can not be justified. Method 9 was designed to only be used as a last resort if the meal emptied so slowly that the operator had stopped the experiment before the emptying period had finished. Method 9 was not used for the measurement of T50 in any of the experiments described in chapter 8.

Therefore, the method that was selected for the calculation of the T50 for all experimental work was method 3. This method considers both the pre- and postprandial baselines and uses the deflection baseline method, which has been shown to be the most accurate at calculating the T50.

The calculation of the T50 (and subsequent analysis of the dominant power and frequency of the contractile range) was only performed on one of the six signals obtained from EIE. The signal was chosen had the largest impedance deflection caused by the ingestion of the meal, indicating that it was the most sensitive to changes in conductivity.

6.2.5 Band pass filtering

EIE signals contain a number of unwanted frequency components caused by a variety of factors. Motion artifacts that generate spikes in the time-domain signal have been discussed in section 6.2.2. However, there are a number of continuous processes that are detected by the Epigastrograph which cause unwanted sinusoidal signals (such as the breathing of the subject and mains interference) and random noise (for example from the heating of the electronics inside the equipment) to be superimposed onto the gastric signal.

Filtering is one of the most commonly used signal processing techniques and describes the process in which the signal is altered to remove unwanted frequencies called noise. There are many sources of noise; the 50Hz signal from mains electricity often corrupts signals, particularly in a hospital environment in which there is a concentration of medical electronic devices that are powered by mains electricity. Other sources may be physiological processes that produce signals that are detected by the measuring device and superimposed onto the signal, consequently obscuring the data of interest.

The frequency ranges attenuated by the filter are called stop bands and the permitted frequency ranges are called pass bands. The gain of an ideal filter would therefore be zero in the stop band and one in the pass band. However, in reality there is a finite transition region between each pass band and stop band. Furthermore, the pass bands may exhibit small variations in gain called pass band ripple and in addition the stop band attenuation is not constant. The gastric frequency range is defined as 2.4 to 3.6 cpm (0.04 to 0.06 Hz) based on clinical definitions for bradygastria (1.0 – 2.4 cpm) and tachygastria (3.6 – 9.9 cpm) given by Koch [Koch KL, 1993]. Fig. 6.9 shows a practical bandpass filter with its transition period, pass band ripple and stop band attenuation.

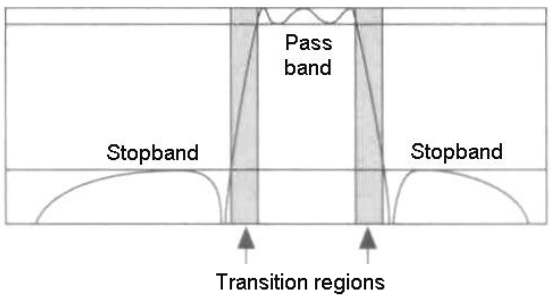

Fig. 6.9 The frequency response of a band pass filter with transition periods, pass band ripple and stop band attenuation [Redrawn from Chugani ML, 1998].

Filters are often classified by their impulse response. The FFT of a filter's impulse response is called the frequency response, which describes the gain of the filter with respect to frequency. If the impulse response continues indefinitely the filter is known as an Infinite Impulse Response (IIR) filter. Conversely, if the impulse response falls to zero after a finite time, the filter is known as a Finite Impulse Response (FIR) filter. IIR filters require fewer coefficients and are therefore faster. However, their phase response is non-linear and so since the phase information is important, an FIR filter was used. Fig. 6.10 shows the effect of band pass filtering on an EIE signal.

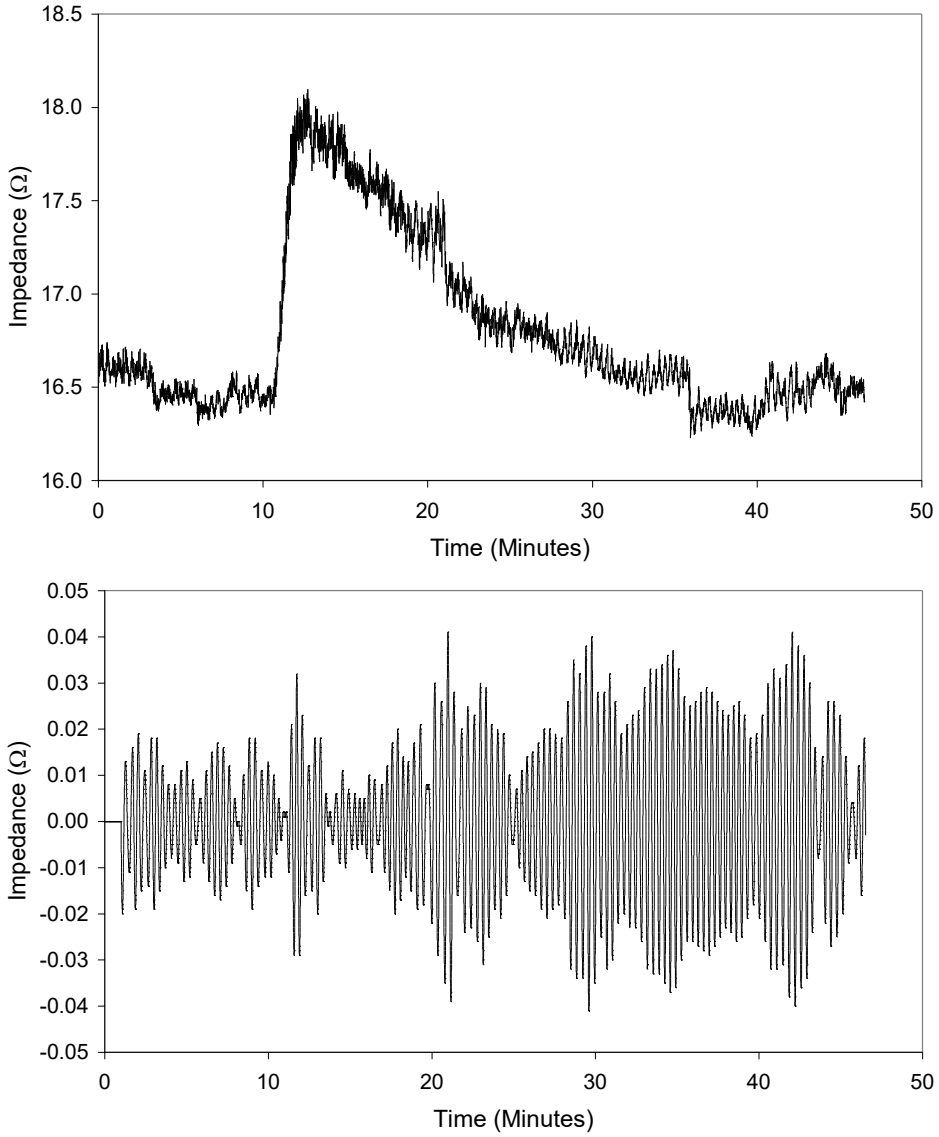

Fig. 6.10 **A** Original time-domain signal before band pass filtering. **B** Post band pass filtering (BPF) for the detection gastric contractilty. **Note the increase in the BPF signal after ingestion.**

6.2.6 Analysis of the power spectrum

Fourier theory states that complex waveforms may be reduced to a series of simple sinusoidal functions with a specific amplitude, frequency and phase. Fig. 5.9 showed an example of an epigastrographic signal produced after the ingestion of 500ml of Volvic™ mineral water. The signal is expressed as a function of time and is therefore described as the 'time domain signal'. However, although useful gastro-physiological information is obtainable from the time domain signal, much of the useful information can be found by extracting the sinusoidal functions that constitute the time domain signal. Consequently it is possible to plot the variation in amplitude of these sinusoidal functions with their frequency thus expressing the data as a function of frequency rather than time and is therefore described as the 'frequency domain signal'.

The Fourier transformation of discrete signals is achieved using the Discrete Fourier Transform (DFT). If a sampled signal with N samples is $x[n]$, where $0 \le n \le N-1$ and $n \in \square$, then the output from the DFT in equation 6.11 is $X[k]$, where $0 \le k \le N-1$ and $k \in \square$.

$$X[k] = \sum_{n=0}^{N-1} x[n]\, e^{\frac{-j2\pi nk}{N}} \tag{6.11}$$

Since N samples were obtained for the time-domain signal then the DFT will also contain N samples. Given that Δt is the sampling period which is the inverse of the sampling frequency, f_s, the actual duration of the signal, T_0 may be expressed as equation 6.12. Equation 6.13 shows that the frequency resolution of $X[k]$ is therefore the reciprocal of T_0. Equation 6.14 demonstrates that the maximum frequency, $f_{\max}$ (the centre value of $X[k]$ due to the symmetrical properties and sampling constraints) is determined by the sampling period Δt.

$$T_0 = \Delta t N \tag{6.12}$$

$$\Delta f = \frac{1}{\Delta t N} \text{ (Hz)} \tag{6.13}$$

$$f_{\max} = \left(\frac{N}{2}\right) \cdot \left(\frac{1}{\Delta t N}\right) = \frac{1}{2\Delta t} \text{ (Hz)} \tag{6.14}$$

The main difficulty with the DFT algorithm is that with N data points, there are N^2 arithmetic operations to make and so there are practical problems in computation time, particularly with large values of N. The Fast Fourier Transform (FFT) reduces the number of calculations that must be made to $N\log_2 N$. For example, if $N = 2048$ the FFT algorithm requires 22,528 mathematical operations whereas the DFT algorithm would require over 4 million. Equation 6.11 shows $X[k]$ will always be complex. This signifies that there are two pieces of information available from the DFT; the magnitude and phase. The power spectrum, $P[k]$ is shown in equation 6.15 and is defined as the squared magnitude of the Fourier transform.

$$P[k] = \left|X[k]\right|^2 \tag{6.15}$$

Fig. 6.11A shows the power spectrum of the acquired EIE signal in Fig. 6.10A. The lower frequency peaks are primarily caused by low frequency changes in the emptying curve (at around 1 cpm) and baseline drift. Fig. 6.11B demonstrates the effect of band pass filtering on the power spectrum and the removal of low and high frequency artifacts.

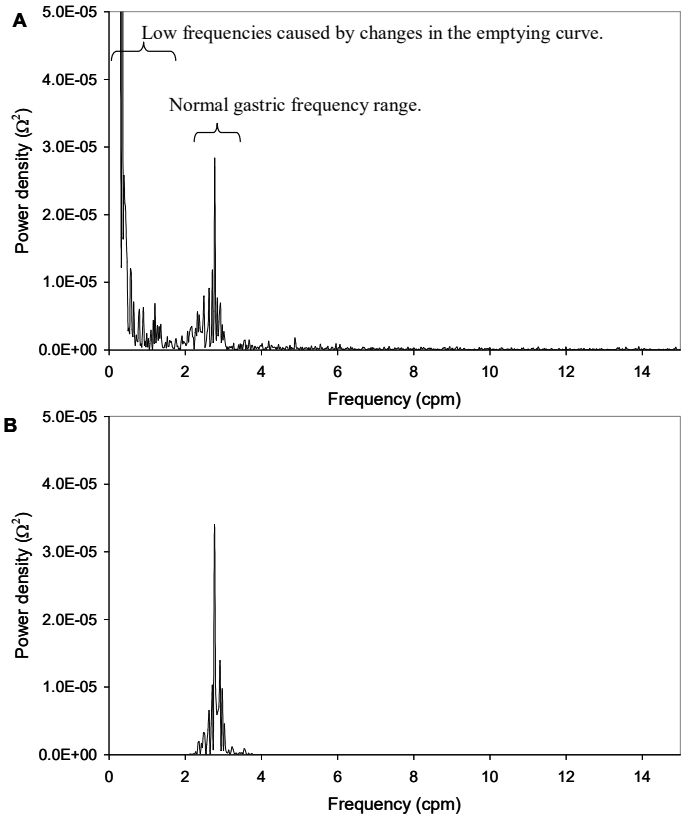

Fig. 6.11 **A** The power spectrum of the time domain signal in showing a peak between 2 and 3 cycles per minute (the gastric frequency range) and **B** of the band pass filtered signal.

6.2.7 Application of the Joint Time-Frequency Transform (JTFT)

Since the basis functions for Fourier transforms are infinitely long complex sinusoid functions (see equation 6.11), Fourier transforms have zero time resolution. Power spectra calculated from the square of the real part of the Fourier transform algorithm are only able to indicate the average power at discrete frequencies of the original data (Fig. 6.11) and so DFT and FFT algorithms are only useful in analysing data that is stationary. However, physiological signals are not stationary. Moreover, physiological and pathophysiological processes may reveal themselves in the acquired signal as small, temporal deviations in frequency and amplitude. The Fourier Transform can only separate different frequencies from the entire time-domain signal but it is not able to locate a particular frequency characteristic in time. Hubbard noted that, *'the Fourier transform is poorly suited to very brief signals, or signals that change suddenly and unpredictably; yet in signal processing, brief changes often carry the most interesting information'* [Hubbard BB, 1998].

The purpose of Joint Time Fourier Transform (JTFT) algorithms is to produce a three dimensional representation of a signal showing the variations in the magnitude of each frequency over time. The JTFT algorithm operates by segmenting the time-domain signal into short sections of time called epochs so that each epoch contains a stationary section of the original signal. A window function (usually a Hanning window) $w[n-\ell]$ is applied to each epoch to reduce spectral leakage and the FFT is calculated to produce frequency spectra. These frequency spectra are subsequently presented in chronological order to reveal the variations in frequency over time, exposing frequency changes that may indicate important physiological or pathophysiological events.

The discrete JTFT spectrogram is defined in equation 6.16. The original signal is $x[n]$, N is the number of frequency bins and k is the frequency index. ΔM is the time sampling interval and m is the time index and $\ell = m\Delta M$. The windowing function is $w[n - \ell]$ where n is the current data point and L is the total number of data points in $x[n]$.

$$X[\ell,k] = \left| \sum_{n=0}^{L-1} x[n]w[n-\ell]e^{\left(\frac{-j2\pi kn}{N}\right)} \right|^2 \qquad (6.16)$$

Fig. 6.12 shows the process of obtaining the JTFT spectrogram by windowing the original time-domain data and calculating the power spectra of each epoch. The spectra are stacked in chronological order to produce a three-dimensional 'waterfall' spectrum that clearly shows changes in the power of each frequency over time.

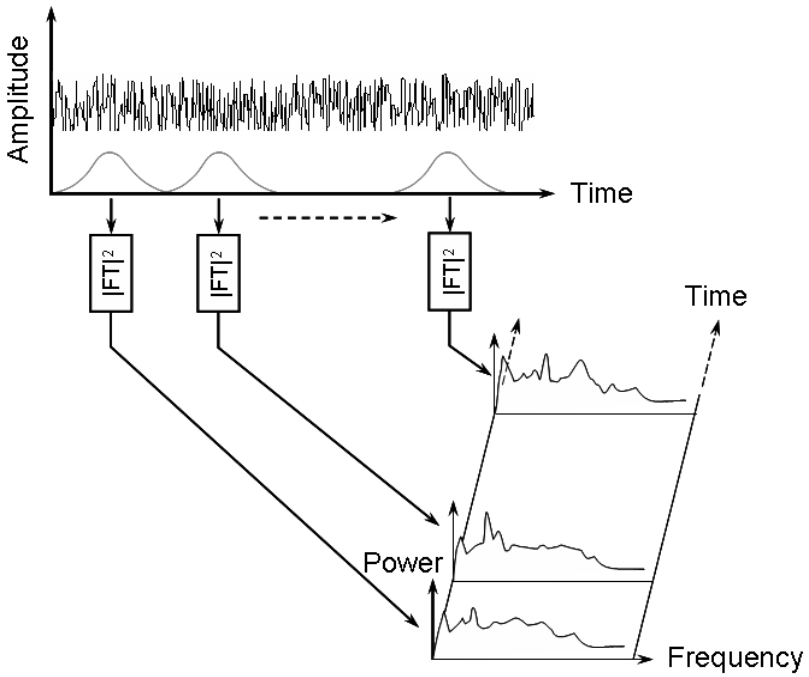

Fig. 6.12 The JTFT spectrogram technique showing the time-domain signal at the top with windowed epochs. These individual epochs are considered stationary signals so that the power spectrum can be calculated. The Frequency-Power spectra are then plotted in a waterfall spectrum in chronological order.

The most significant drawback of the JTFT is that the time and frequency resolution depend on the size of the epoch chosen. With a long epoch, the joint time-frequency spectrum has high frequency resolution but poor time resolution and conversely with a short epoch, the time-frequency spectrum has poor frequency resolution but high time resolution. This problem is called the windowing effect and it concerns all JTFT algorithms. The windowing effect means that the ability of the JTFT spectrogram is limited; after the length of the window is selected, the time and frequency resolutions are fixed. One method of improving the time resolution without affecting the frequency resolution is to overlap the epochs. This does mean however, that since data will be counted more than once, frequency characteristics will be smeared over the time domain. Fig. 6.13 shows the JTFT for the band pass filtered signal in Fig. 6.10B

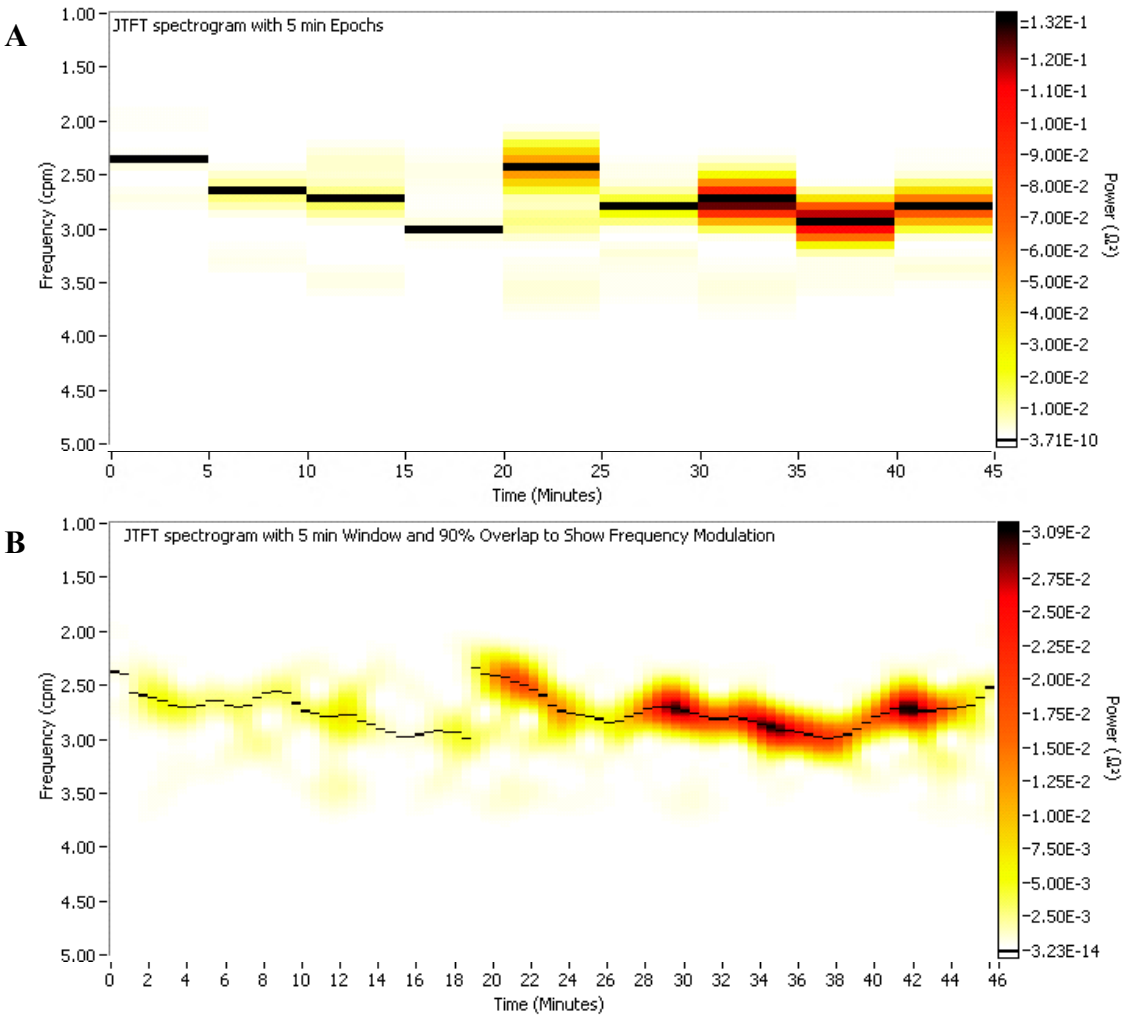

Fig. 6.13 **A** The JTFT spectrogram using epochs of 5 minutes with no overlap and **B** the JTFT spectrogram using epochs of 5 minute with a 90% overlap.

Figs. 6.13A and B illustrate the effect of overlapping the 5 minute epoch. The time resolution is improved by overlapping the epochs. However, the maximum power is reduced in Fig. 6.13B. This is caused by the overlapping process that results in the smoothing of information across the time axis. This effect can be seen in Appendix H (Fig. H52 and H53).

6.2.8 Application of the Wavelet Transform

Section 6.2.6 explained that during the process of Fourier transformation, Fourier coefficients are calculated that measure the similarity of the time domain signal to each basis function. However, section 6.2.7 noted that since the basis functions are infinitely long complex sinusoids (see equation 6.11) Fourier transforms are good at representing stationary signals but cannot represent the important temporal characteristics of non-stationary signals such as those generated from physiological processes. However, the Wavelet transform uses basis functions that are finite waveforms (called wavelets) with a specific central frequency meaning that they can be located in frequency *and* time. Fig. 6.14A shows the Morlet wavelet and Fig. 6.14B illustrates that this wavelet is made from a Sine wave (grey line) multiplied by a Gaussian envelope (dashed line).

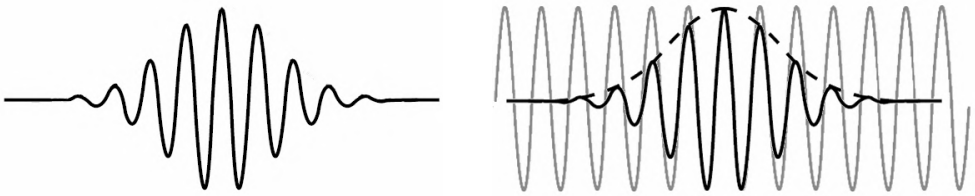

Fig. 6.14 **A** The Morlet wavelet of arbitrary width and amplitude where the x-axis is time and the y-axis is magnitude. **B** Construction of the Morlet wavelet with a Sine curve (grey) modulated by a Gaussian function (dashed).

Furthermore, the nature of the wavelets means that they may be used to overcome the problem of the window effect. After establishing the optimal window type in JTFT analysis, the time and frequency resolutions are fixed. However, since the frequency of a waveform is simply the reciprocal of the time period waveforms always exhibit a long time period at low frequencies and a short time period at high frequencies. This implies that it would be more effective for the window applied to have a high time resolution at high frequencies and a low time resolution at low frequencies. Consequently, a more efficient analysis can be achieved through an analytical process that has a frequency dependant resolution.

Multiresolution (MRA) analysis using wavelets gives good time resolution and poor frequency resolution at high frequencies and good frequency resolution and poor time resolution at low frequencies. The Continuous Wavelet Transform (CWT) algorithm is used to implement MRA.

The formula for the CWT, $\Psi(\tau,s)$ is given in equation 6.17 where the original time-domain signal, $x(t)$ is decomposed into a set of wavelet basis functions, $\psi_{s,\tau}(t)$. The * denotes the complex conjugate.

$$CWT[x(t)] = \Psi(\tau,s) = \int_{-\infty}^{+\infty} x(t)\cdot\psi^*_{\tau,s}(t)\,dt \tag{6.17}$$

The basis functions are generated from a single basic wavelet called the mother wavelet. The $s^{-½}$ factor ensures that the total power of the scaled wavelet remains constant.

$$\psi_{\tau,s}(t) = \frac{1}{\sqrt{s}}\psi\left(\frac{t-\tau}{s}\right) \tag{6.18}$$

The values τ and s are the translation and scale respectively. Translation refers to the position of the wavelet in time. Scale is a similar concept to the scale used in map reading; large scales mean analysis of the general trend of the signal while small scales mean analysis of the details. Therefore scale is inversely proportional to frequency. The technique of the CWT implements MRA by modifying the scale of the mother wavelet to produce a family of wavelets that are each shifted along the signal by incrementing τ. At each position the CWT is calculated and plotted. Fig. 6.15 illustrates the respective sampling grids.

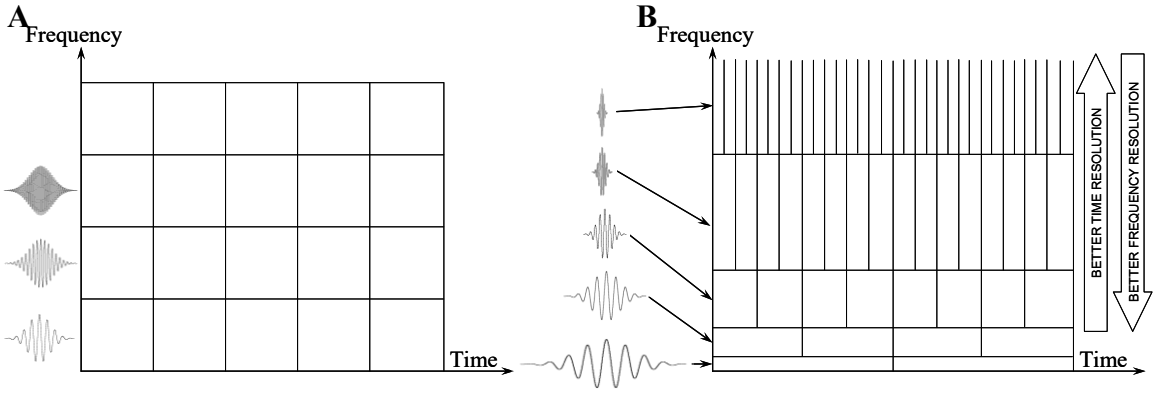

Fig. 6.15 **A** The JTFT sampling grid showing equal time and frequency resolution across all frequencies. The window function (on the left of the grid) remains unchanged with increasing frequency. **B** The CWT sampling grid showing multiresolution analysis with a constant Q value. The frequency and duration of the wavelet changes with frequency

However, equations 6.17 and 6.18 express the *continuous* wavelet transform. Real world applications in which all physical variables are sampled, require discrete analysis and so the CWT must be adapted so that it can be used with discrete systems. The equivalent algorithm used for discrete signals is known as the Discretised Continuous Wavelet Transform (DCWT). The scale, s and translation, τ are discretised as shown in equations 6.19 and 6.20. In these equations the notation always uses j as an integer and it should not be confused with the j uses for the imaginary solution to $\sqrt{-1}$. The original mother wavelet function (equation 6.18) may therefore be modified to give the mother wavelet function used in DCWT, shown in equation 6.21.

$$s = s_0^{-j} \tag{6.19}$$

$$\tau = k s_0^{-j} \tau_0 \tag{6.20}$$

$$\psi_{j,k}(t) = s_0^{(j/2)} \psi\left(s_0^{j} t - k\tau_0\right) \tag{6.21}$$

Since fewer samples are needed at high scales, sampling steps of τ depend on s. If s_0 is close to one and τ_0 is close to zero the sampling grid obtained is very fine and the DCWT is similar to the CWT. Dyadic sampling (octave by octave) is achieved by selecting $s_0 = 2$ and $\tau_0 = 1$. Therefore, equation 6.17 may be rewritten as 6.22 and equation 6.18 may be rewritten as 6.23 where $j,k \in \mathbb{Z}$ and j represents scale and k represents translation. This is known as the Dyadic Wavelet Transform (DyWT). The scalogram, $E(j,k)$ (also known as the wavelet power spectrum) is defined in equation 6.24 describes the contribution to the signal power at a given scale and time [Addinson PS, 2002].

$$DyWT[x(t)] = \Psi(j,k) = \int_{-\infty}^{+\infty} x(t) \cdot \psi_{j,k}^{*}(t)\, dt \tag{6.22}$$

$$\psi_{j,k}(t) = 2^{j/2} \psi\left(2^{j} t - k\right) \tag{6.23}$$

$$E(j,k) = \left|\Psi(j,k)\right|^2 \tag{6.24}$$

The DyWT for the band pass filtered signal in Fig. 6.10B is shown in Fig. 6.16.

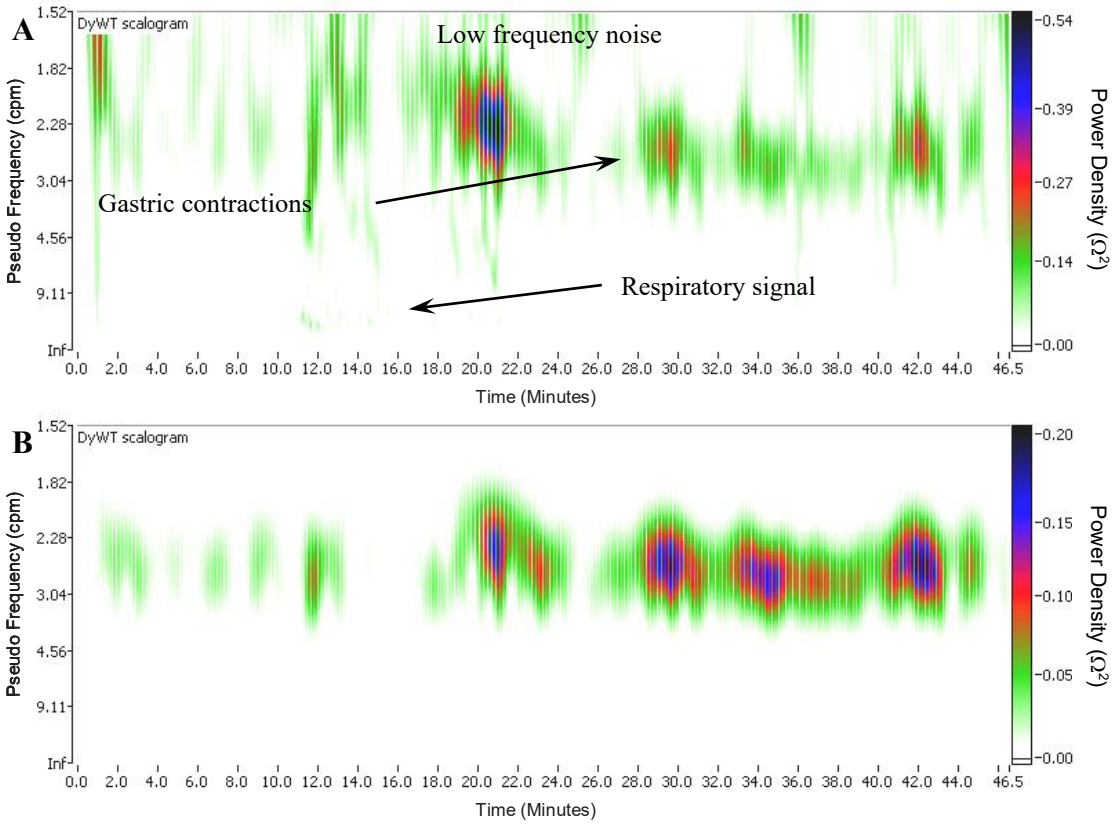

Fig. 6.16 **A** The DyWT scalogram of the unfiltered time-domain signal in Fig. 6.10A with high levels of noise caused by high magnitude low frequencies. **B** The DyWT scalogram of the band pass filtered signal in Fig. 6.10B demonstrating the removal of noise and respiratory artifacts.

Since the wavelet equivalent of frequency is scale, it is necessary to convert the values of scale into 'pseudo' frequency in order to compare measurements with the other Fourier based algorithms such as the Joint-Time Fourier Transform. The pseudo frequency, f_{PSEUDO} is calculated from the scale using equation 6.25 where f_c is the centre frequency of the mother wavelet. It is calculated by taking the peak frequency of the FFT of the mother wavelet. f_s is the sampling frequency of the signal (5 Hz) and s is the scale, defined in equation 6.19.

$$f_{PSEUDO} = \frac{f_c f_s}{s} \tag{6.25}$$

6.2.9 Triangulative Impedance Mapping (TrIM) for measuring velocity

Sections 4.3.1 to 4.3.4 discuss the origin of epigastrographic signals and the field patterns generated by each pair of electrodes. Triangulative Impedance Mapping (TrIM) is a technique developed exclusively for EIE signal analysis. The objective of TrIM is to use the values for the impedance from each signal to build a map of the impedance over a region of interest (ROI) that covers the three electrode pairs and is centred on the orthocentre of the triangle created by the three electrodes. The impedance map provides a four dimensional representation of impedance which can be used to examine the propagation velocity of gastric contractions. The four dimensions are the impedance (x), the position in the area of the ROI, lateral (y) and longitudinal (z) and time, (t). Fig. 6.17 shows the anterior and posterior view in the frontal plane (see Appendix A) of a typical electrode arrangement.

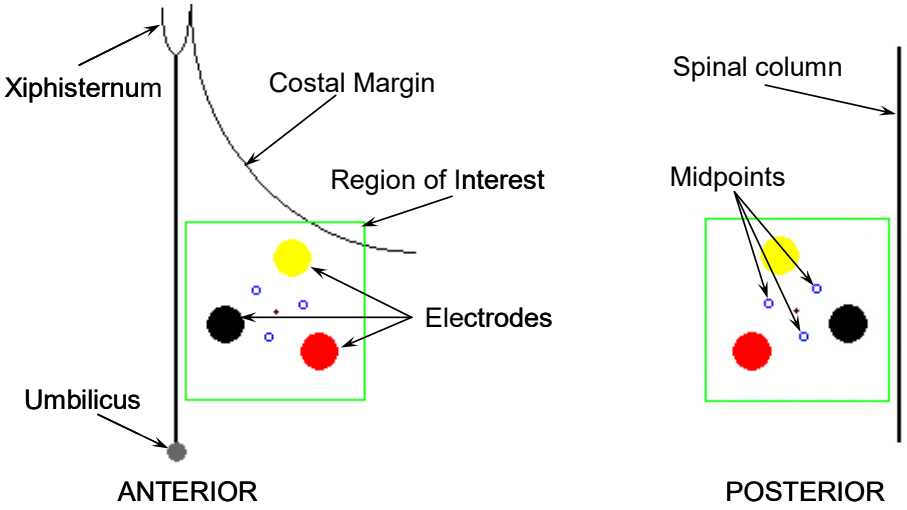

Fig. 6.17 The anterior and posterior views of a typical electrode arrangement in EIE.

The format of the EIE signals (recorded as *.eie files) is shown in table 6.1 where the following nomenclature is used: Y,i(R) means that the red (R) pair of electrodes is applying the current and the yellow (Y) pair is measuring the voltage.

Table 6.1 The format of *.eie files. A tab separates each column and the data is in ASCII (American Standard Code for Information Interchange) format.

Time (s)	**Y,i(R)**	**B,i(R)**	**R,i(Y)**	**B,i(Y)**	**R,i(B)**	**Y,i(B)**	**Mean**	**Event**
x-axis	YR1	RB1	YR2	BY1	RB2	BY2	Mean of all six signals	Event markers

The theory of reciprocity has previously been used to show that Y,i(R) ≈ R,i(Y), B,i(R) ≈ R,i(B) and B,i(Y) ≈ Y,i(B) [Freedman MR, 2000]. Therefore, since the signal obtained from one pair of electrodes applying the current with the second pair of electrodes measuring the voltage is very similar to the signal from the second pair of electrodes applying the current and the first of electrodes pair measuring the voltage, the corresponding signals are averaged resulting in three signals YR, RB and BY defined in equations 6.26, 6.27 and 6.28 respectively.

$$YR = \frac{\left(Y,i(R) + R,i(Y)\right)}{2} \tag{6.26}$$

$$RB = \frac{\left(R,i(B) + B,i(R)\right)}{2} \tag{6.27}$$

$$BY = \frac{\left(B,i(Y) + Y,i(B)\right)}{2} \tag{6.28}$$

Triangulation (or trilateration) is used by Global Positioning Systems (GPS) to locate an object or person based on the signal strength of signals transmitted from three known locations (in the case of GPS, three satellites). Fig. 6.18 illustrates that the location can be found by assuming that the relative distance from each transmitter is inversely proportional to its signal strength. The point at which all three dashed circles meet reveals the location.

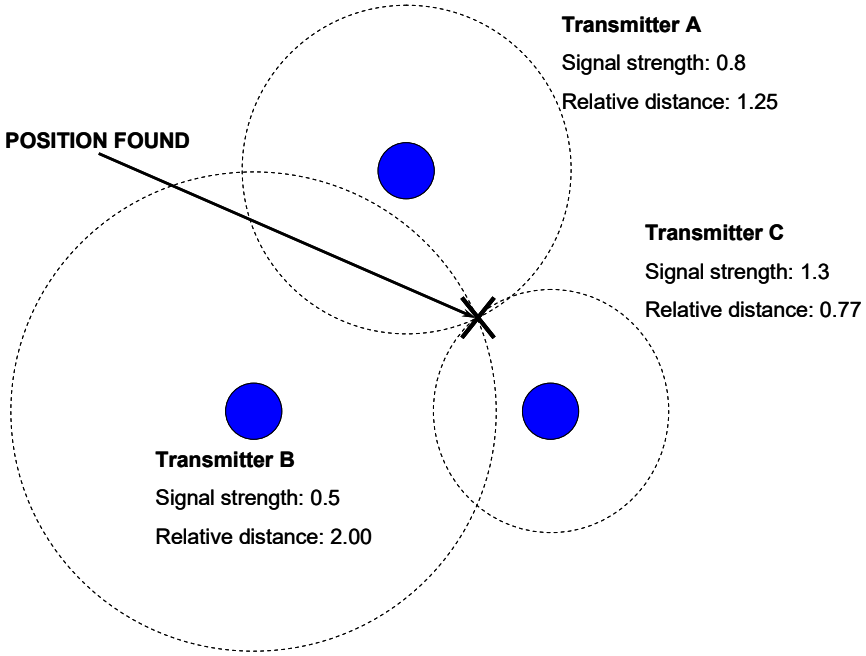

Fig. 6.18 The principal of positional triangulation using three transmitters.

The technique of TrIM is a tentative method for mapping the impedance in a region of interest over the three electrodes. It exploits the fact that since the three pairs of electrodes produce three signals, each can be considered as a 'transmitter' at the midpoint between the two relevant pairs of electrodes (shown as blue circles in Fig. 6.17)[5]. The triangulation used in GPS uses a known signal strength to locate an unknown position. TrIM uses the locations of pixels on an imaginary grid covering the region of interest (ROI) and calculates the signal strength for each pixel based on the strengths of the three signals. Fig. 6.19 shows the grid used by TrIM. The size selected for each pixel was 0.5cm by 0.5cm [6].

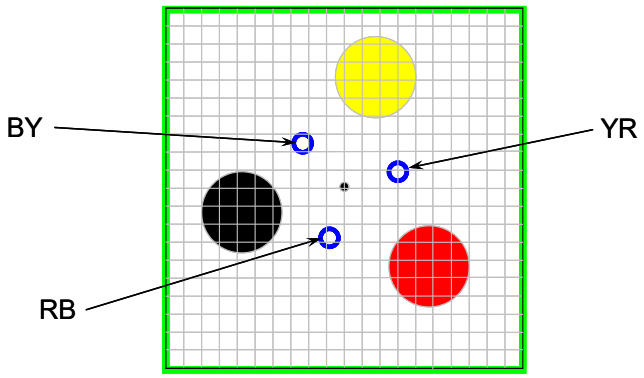

Fig. 6.19 The pixel grid for the region of interest employed in TrIM. The size of each pixel is 0.5cm × 0.5cm and the grid size is 20 × 20 pixels.

The signal strength is calculated using equation 6.29 where Z_{YR}, Z_{RB} and Z_{BY} correspond to the impedance measured by equations 6.26, 6.27 and 6.28 respectively (from the band pass filtered data). l_{YR}, l_{RB} and l_{BY} correspond to the Euclidian distance between the pixel and each of the three midpoints, YR, RB and BY respectively. Fig. 6.20 displays a sequence of TrIM frames representing one gastric contraction from the signal in 6.10B. Each frame lasts for 1s and the blue pixels indicate high impedance and the red pixels indicate low impedance. Contractions which reduce the volume of the stomach cause a decrease in impedance whereas the subsequent relaxation causes an increase in impedance[7].

$$\frac{1}{3}\left\{\left(\frac{Z_{YR}}{l_{YR}}\right)+\left(\frac{Z_{RB}}{l_{RB}}\right)+\left(\frac{Z_{BY}}{l_{BY}}\right)\right\} \tag{6.29}$$

[5] Electrode positions were saved in a special file format (*.elc) so that they could be recalled for subsequent studies.

[6] See Appendix H for justification of pixel size choice.

[7] See section 9.3.2 for a full discussion of the origins of impedance change in EIE.

The sequence shows the contraction (red pixels) moving from the top right towards the bottom left because of the position of the stomach (Fig. 2.3) and the direction of the contractions towards the pylorus.

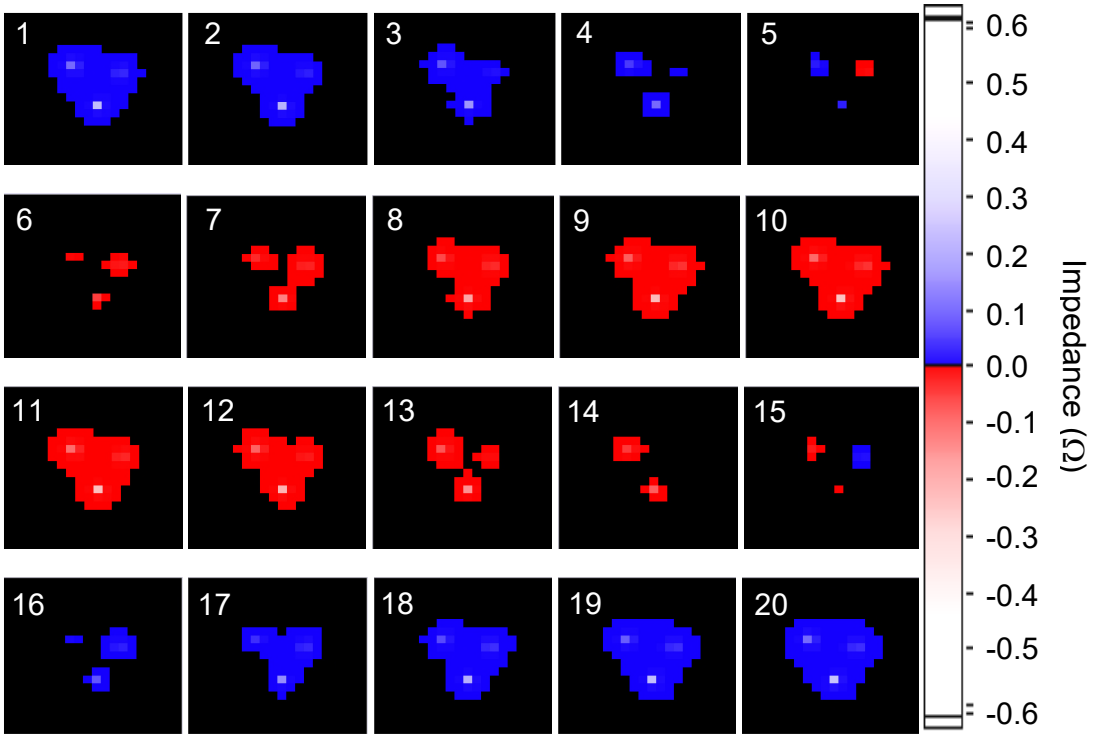

Fig. 6.20 A sequence of impedance maps showing the propagation of one contraction. Each frame lasts for 1 second (due to the down-sampling used in TrIM) and since the frequency of gastric contractions is 3cpm, the total period of one contraction is approximately 20 seconds.

In order to extract the useful information from the impedance maps, three cross sections are taken at lines equal to $y = z$, $y = 10$ and $z = 10$. Since the map is made from a grid of 20 by 20 pixels, 10 is assumed to be the midline in the lateral (y) and longitudinal (z) directions.

Fig. 6.21A shows one frame from TrIM. Fig. 6.21B illustrates the three cross sections that are fitted with a 7^{th} order polynomial curve so that the peaks and valleys can be found using differentiation to locate local maxima and minima. The position of the valley (corresponding to the point of contraction) is plotted under the impedance map in Fig. 6.21A to illustrate the displacement and impedance of the contraction with time in the $y = z$ plane. Since velocity is equal to displacement divided by time, the variation of velocity with time can be found by taking the derivative of a displacement – time graph.

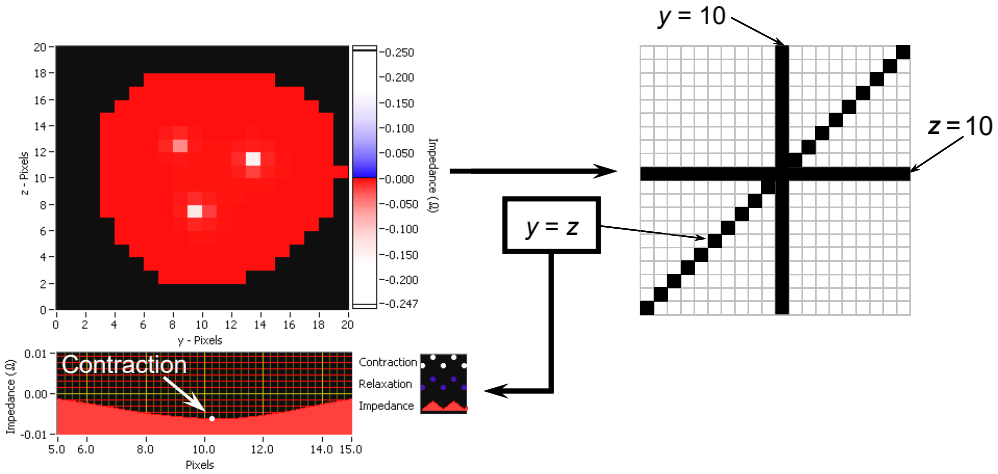

Fig. 6.21 The three cross sections used to calculate the velocity from the impedance maps. The impedance map (top left) is analysed by three cross sections (top right). The $y = x$ is fitted with 7th order polynomial fit and the peaks and troughs (corresponding to the contraction) are identified (bottom left).

Fig. 6.22 shows the displacement – time and velocity – time graphs computed from the TrIM sequence calculated from the band pass filtered signal in Fig. 6.10B.

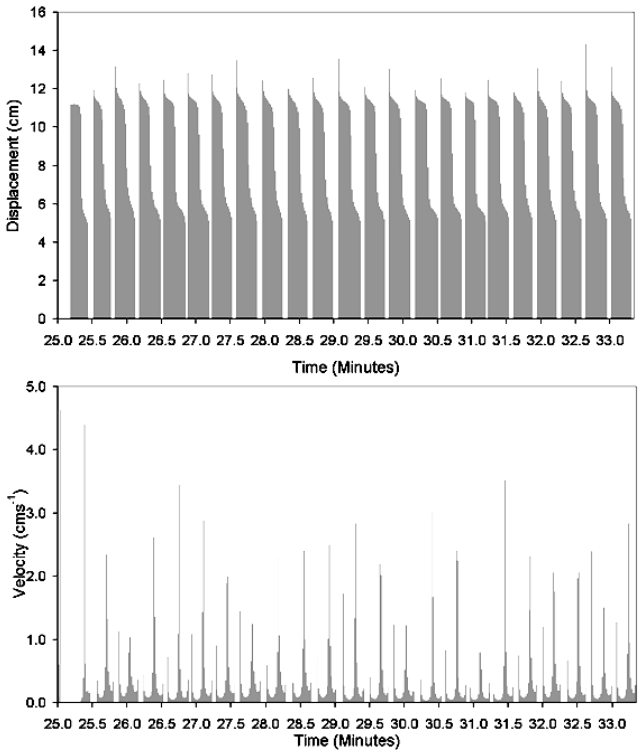

Fig. 6.22 Sections of the displacement – time and corresponding velocity – time graphs for the signal in Fig. 6.10B measured in the $y = z$ plane.

The measurements for each contraction show significant variations in velocity. Therefore, the mean velocity is calculated. However, since the velocities are calculated in the $y = z$ plane with a fixed angle of 45°, if the true velocity is not at an angle of 45°, the velocity measurements only represent a component of the true velocity. To rectify the mean velocity measurement taken in the $y = z$ plane, the cosine of the difference between the mean measured angle, $\bar{\theta}$ and the cross section $y = z$ (45°) is used to correct the mean velocity. The mean velocities calculated from the graph in Fig. 6.22 are shown in Fig. 6.23.

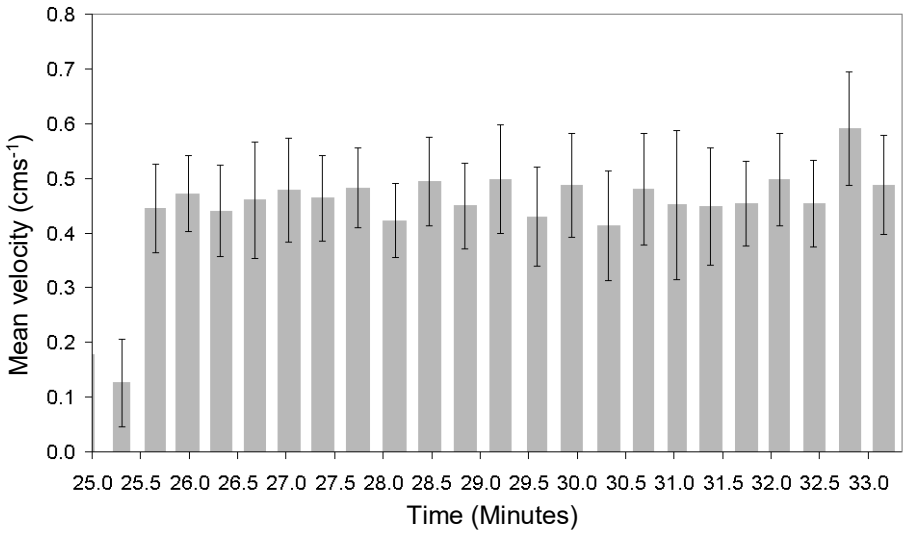

Fig. 6.23 The mean velocity measured by TrIM with σ_M for the velocity measurements in Fig. 6.22.

The mean angle at which the contraction propagates may be estimated from the other two cross sections, $y = 10$ and $z = 10$ using simple geometry. It is calculated using equation 6.30 where y_i is the y cross section, z_i is the z cross section and N is the number of data points in the contraction and i is a positive integer together with the standard error of the mean, σ_M (equation 6.31) where σ is the standard deviation and N is the number of points in the contraction. The result is shown in Fig. 6.24A with the classification for the angles.

$$\bar{\theta} = \frac{1}{N}\sum_{i=0}^{N} \tan^{-1}\left(\frac{y_i}{z_i}\right) \tag{6.30}$$

$$\sigma_M = \frac{\sigma}{\sqrt{N}} \text{ where } \sigma = \sqrt{\frac{\sum\left(x-\bar{x}\right)^2}{\left(N-1\right)}} \tag{6.31}$$

A

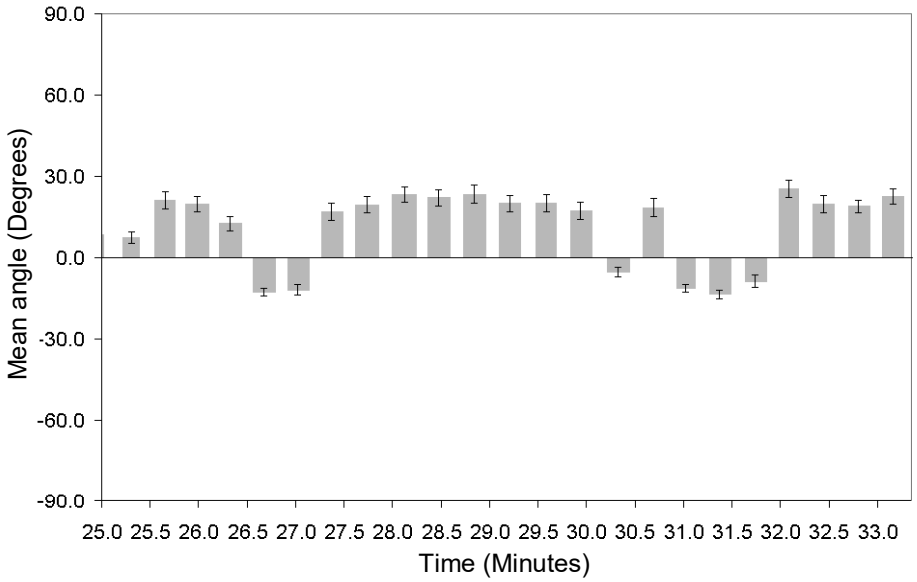

B

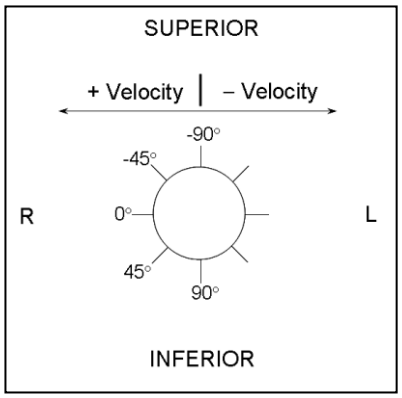

Fig. 6.24 **A** The mean angle with σ_M for the velocity measurements in Fig. 6.22. **B** The classification for the angles and velocity measurements. Superior means towards the head and inferior means towards the feet. R and L are the right and left sides of the subject.

6.2.10 Velocity vector analysis for measuring velocity

The alternative method for extracting information regarding the propagation velocity of gastric contractions from EIE signals is known as vector velocity analysis. It operates by analysing the time differences between the peak of each contraction at the three electrode midpoints. After the peak values have been found for each of the three signals (see Table 6.1) they are plotted in an intensity graph shown in Fig. 6.25.

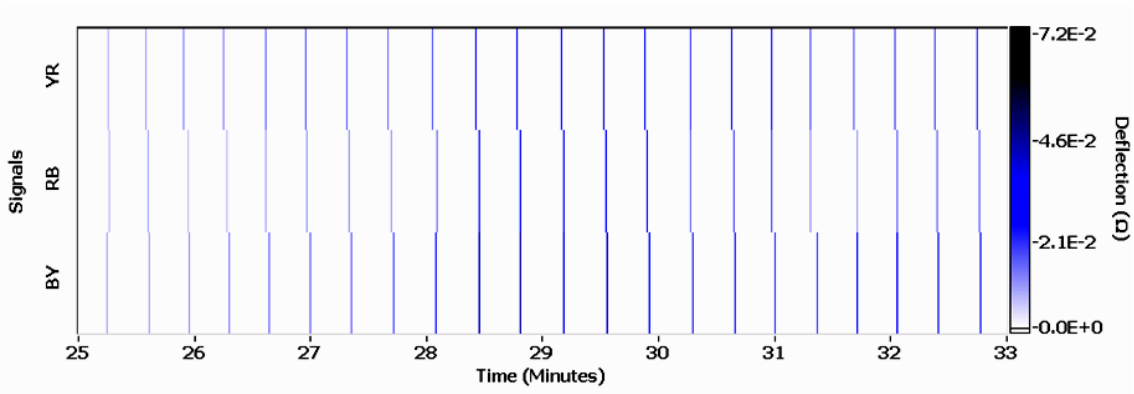

Fig. 6.25 The magnitude of the peak of each contraction detected in the same EIE signal shown in Fig. 6.10B. BY is the signal obtained between the Black and Yellow electrode, RB is the signal obtained between the Red and Black electrode and YR is the signal obtained between the Yellow and Red electrode. This graph is calculated before down-sampling so the time resolution is 0.2s.

Since the distances between the midpoints BY, RB and YR are known, the velocities between these points may be calculated from the time differences between the peaks of each contraction. The coordinate system used for the vector velocity analysis is shown in Fig. 6.26. The lengths and angles between the midpoints are calculated from their positions (recorded at the time of the experiment). Fig. 6.26A shows that the coordinates of the midpoints (blue circles) are p (between B and Y), q (between Y and R) and r (between R and B). The lengths between them are shown in Fig. 6.26B and the positions of the relevant angles are illustrated in Fig. 6.26C.

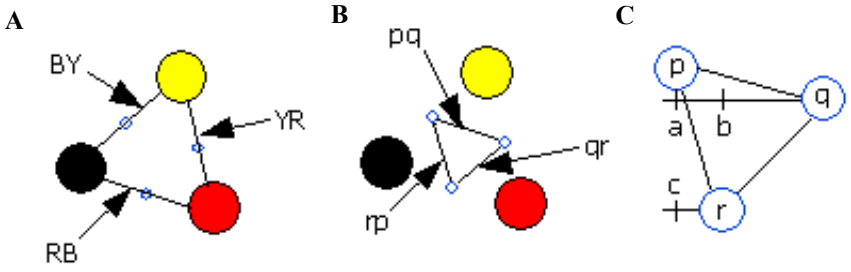

Fig. 6.26 **A** The electrodes B (Black), Y (Yellow) and R (Red) and lengths between them. **B** The midpoints where $p \equiv$ BY, $q \equiv$ YR and $r \equiv$ RB and the three connecting lines between them; *pq*, *qr* and *rp*. **C** Points a, b and c for calculation of the angles between the midpoints.

The three velocities calculated are v_{pq}, v_{qr} and v_{rp}. The y and z components (see Appendix A) are found from each of these vectors. The overall angle of propagation may be found by simple vector addition of the y and z components followed by the application of an adapted version of equation 6.30, given in equation 6.32.

$$\theta_t = \tan^{-1}\left(\frac{y_{pq} + y_{qr} + y_{rp}}{z_{pq} + z_{qr} + z_{rp}}\right) \tag{6.32}$$

The calculation of the magnitude of the velocity is more complicated. Vector addition is not applicable because to simply add the y and z components of the three planes would imply that those three velocities are contributing to the total velocity. In reality there is one true velocity measured in three different planes.

The angles subtended by the lines connecting the midpoints and the y-axis, (180−$\angle prc$), $\angle rqb$ and (180−$\angle pqa$) are calculated and compared with the propagation angle θ_t. Two of the midpoint connecting lines (from pq, qr and rp) are selected by choosing the two angles that give the closest matches to θ_t. The magnitudes of the velocities measured between the two connecting lines are weighted by the difference between the angle of the connecting line and the overall angle of propagation, θ_t and the total velocity, v_t is then calculated from the mean of these two weighted velocities. The expression for this is given in equation 6.33 and an example is illustrated in Fig. 6.27.

$$v_t = 0.5\left\{v_A\left(\angle A - \theta_t\right) + v_B\left(\angle B - \theta_t\right)\right\} \tag{6.33}$$

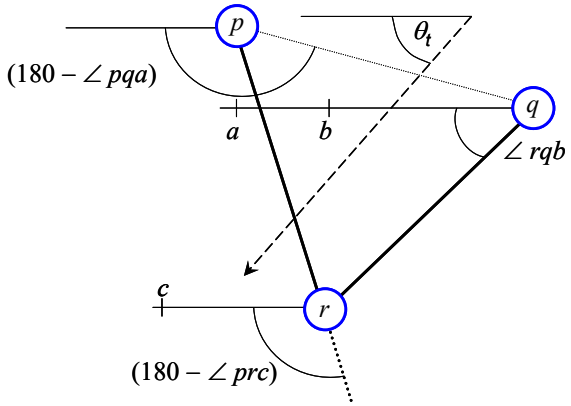

Fig. 6.27 The vector velocity at the propagation angle (dashed arrow) with the two selected midpoint connecting lines (qr and rp) shown as thicker lines.

The vector velocity analysis of the same section of signal shown in Fig. 6.23 is given in Fig. 6.28. Note that there are large differences (±6.5cm^{-1}) in the magnitude of the velocity between the velocity measurements calculated using the TrIM method (Fig. 2.23). However, there appears to be some correlation between the angle measured by vector velocity and TrIM (compare with Fig. 2.24).

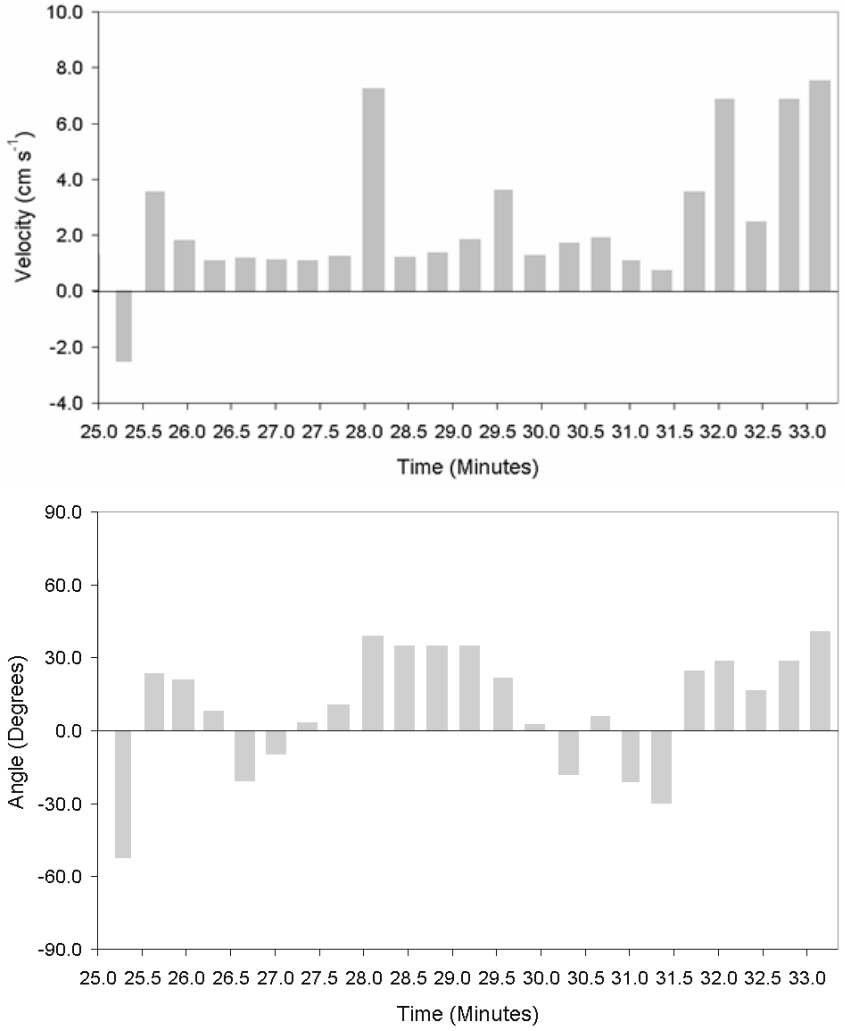

Fig. 6.28 The velocity and angle measurements for the vector analysis applied to the same section of signal shown in Figs. 6.23 and 6.24.

There are clearly significant differences between the results for the propagation velocity and angle measurements using impedance mapping and the vector method. However, by examining the contractions from ten EIE studies, it is possible to ascertain whether there is any correlation between the two techniques and more importantly, whether there are any patterns that can explain the nature of the differences between the measurements taken by the two methods.

6.2.11 Correlation of TrIM and vector velocity methods

During the ten EIE signals studied, a total of 2686 individual contractions were recorded with both TrIM and the vector method. By plotting the values of the velocity and angle, measured by both methods for each contraction, it is possible to examine any possible correlation or pattern. The results are shown in Fig. 6.29.

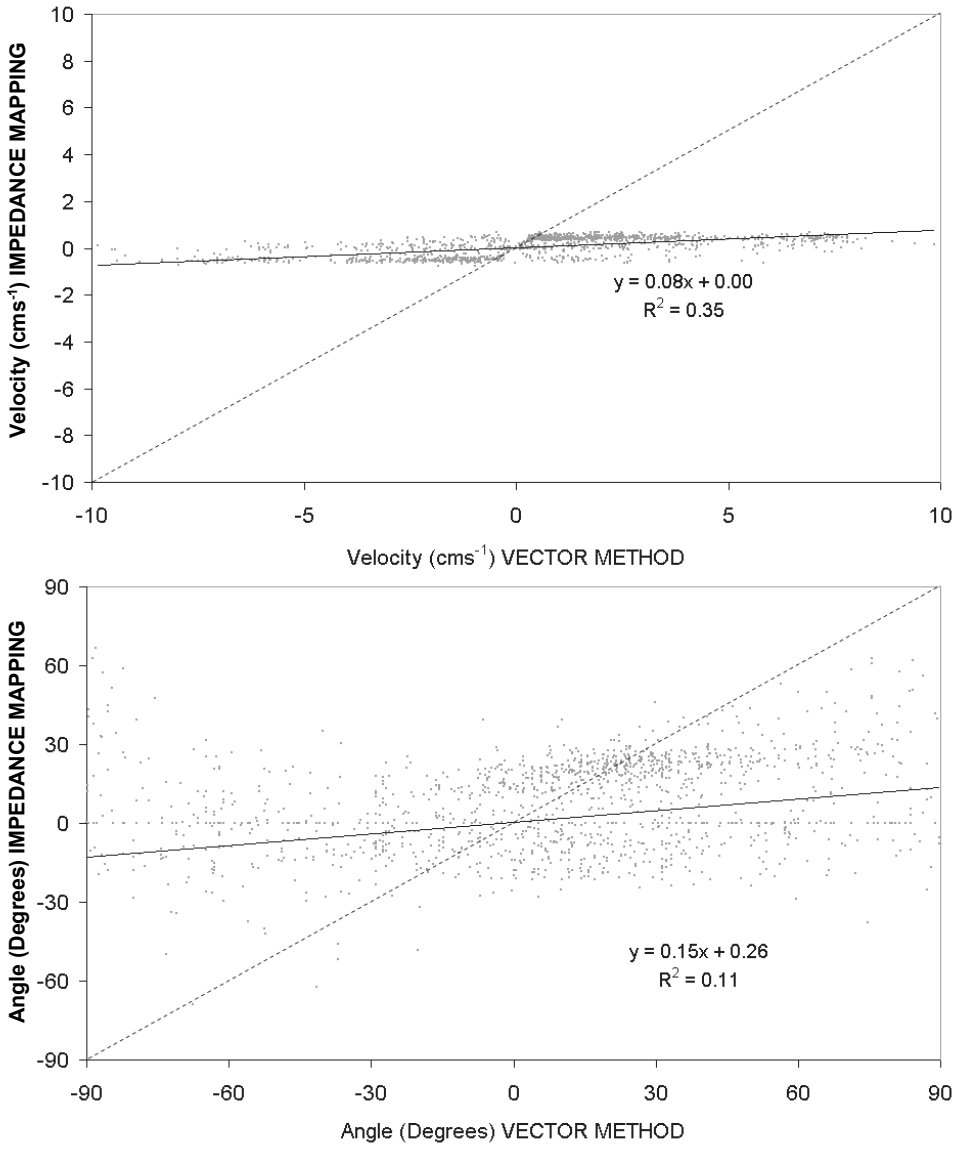

Fig. 6.29 The comparison between velocity and angle measurements calculated with TrIM and vector analysis.

It is clear that there is no direct correlation between the measurements of velocity and angle calculated with TrIM and vector analysis. However, closer examination of the results shows that there are concentrated clusters in the velocity measurements and to a lesser extent in the angle measurements.

Fig. 6.30 shows a section of the top graph in Fig. 6.29 centred on the origin. It is apparent that two clusters appear either side of the $y = x$ line (shown as the blue dashed line). However, the most striking pattern illustrated in Fig. 6.29 and 6.30 is that the TrIM method does not calculate any of the contractions to be above approximately 0.7cms^{-1}.

It seems that there are factors related to TrIM that preclude it from measuring contractions above 0.7cms^{-1} and if so, this would explain the cluster of results on both sides of the origin; assuming that the vector velocity calculations are accurate, contractions with a velocity above 0.7cms^{-1} would be plotted along a line $y = \pm 0.7$. The positive cluster is denser because the majority of contractions are positive (see Fig. 6.24B).

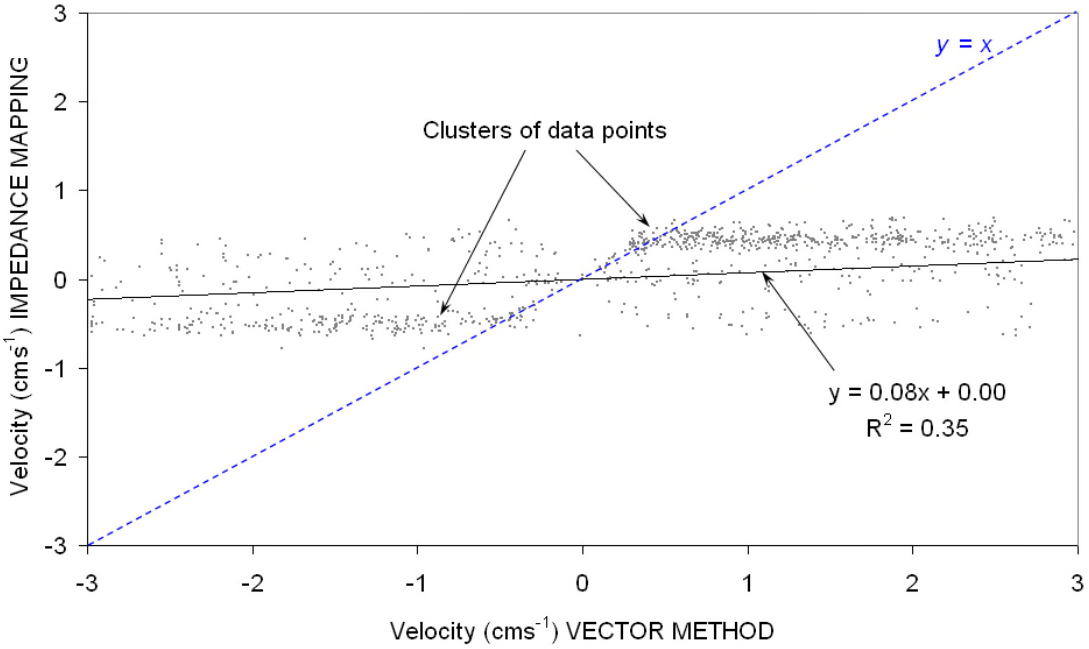

Fig. 6.30 Examination of the two clusters in the velocity analysis in Fig. 6.29.

In order to confirm this theory, it is necessary to verify that the vector analysis method is calculating the correct velocity. In order to test this, test signals (chapter 7) with known velocities and angles were analysed. Velocities from 0.0cms^{-1} to 5.0cms^{-1} were analysed in 0.1cms^{-1} steps at an angle of 86.82° over a five minute period. The mean velocity with the standard deviation is shown in Fig. 6.31A. The mean vector velocities correlate with the line $y = x$ for velocities in the range 0.3 to 2.0 ($R^2 = 0.99$) and furthermore, the trend line is almost exactly $y = x$. However, in the range of 2.0 to 5.0, the trend line deviates and the correlation weakens ($R^2 = 0.92$). This is shown in Fig. 6.31B and 6.31C.

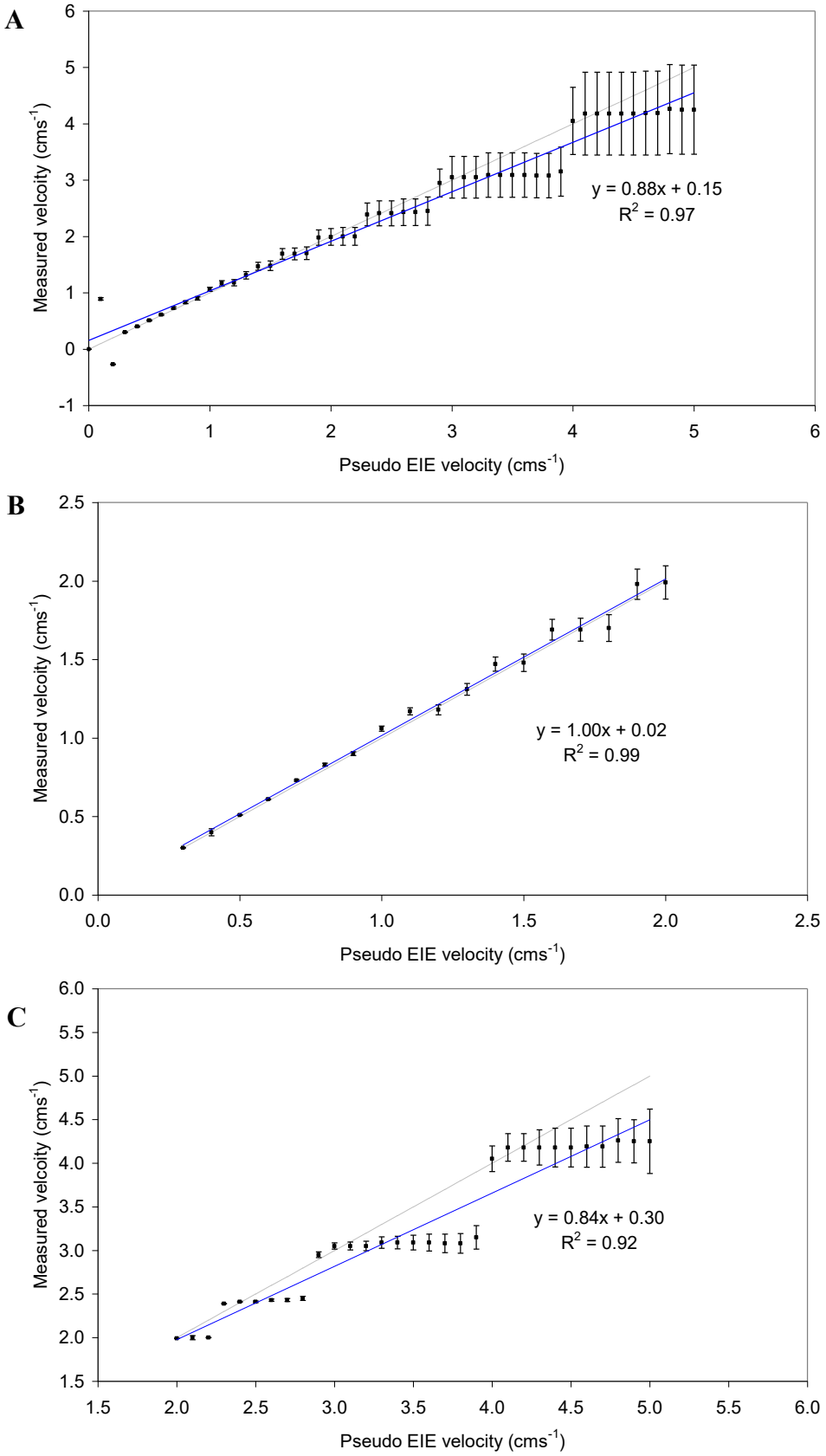

Fig. 6.31 **A** The mean vector velocity measurements of Pseudo EIE signals showing the standard deviation. **B** Period from 0.3-2.0cms^{-1}. **C** Period from 2.0-5.0cms^{-1}. The grey lines represent $y = x$ and the blue lines show the linear trend.

The reason for these differences is more apparent when examining Fig. 6.31C. The vector analysis appears to be unable to differentiate between clusters of velocity measurements at 2.0 – 2.2cms^{-1}, 2.3 – 2.8cms^{-1}, 2.9 – 3.9cms^{-1} and 4.0 – 5.0cms^{-1}. The inability to distinguish 0.1cms^{-1} changes in velocity at relatively high velocities is caused by the deterioration of vector velocity resolution. This is due to the fact that since the velocity is calculated from time differences in the peak of the contraction measured over known, fixed distance, small time differences result in large velocities and so the vector velocity resolution is inversely proportional to the time resolution. It is also important to note in Fig. 6.31A that the magnitude of the measured vector velocities at 0.1 and 0.2cms^{-1} are wrong. The reason is that since the time differences are large, the software mistakes the lagging peak for the leading peak of the next contraction.

Fig. 6.32 illustrates the variation in vector velocity resolution with vector velocity and explains why it becomes increasing difficult to resolve velocities accurately. Note that in Fig. 6.31 the problem worsens with each cluster; the first cluster is three data points, the second is six and the third is eleven (the fourth is incomplete because the fastest velocity analysed was 5.0cms^{-1} but is likely to continue until approximately 5.4cms^{-1}). Table 6.2 shows the vector velocity resolution as a percentage of true velocity. It is apparent that the velocity resolution below 2cms^{-1} remains under 20% of the true velocity.

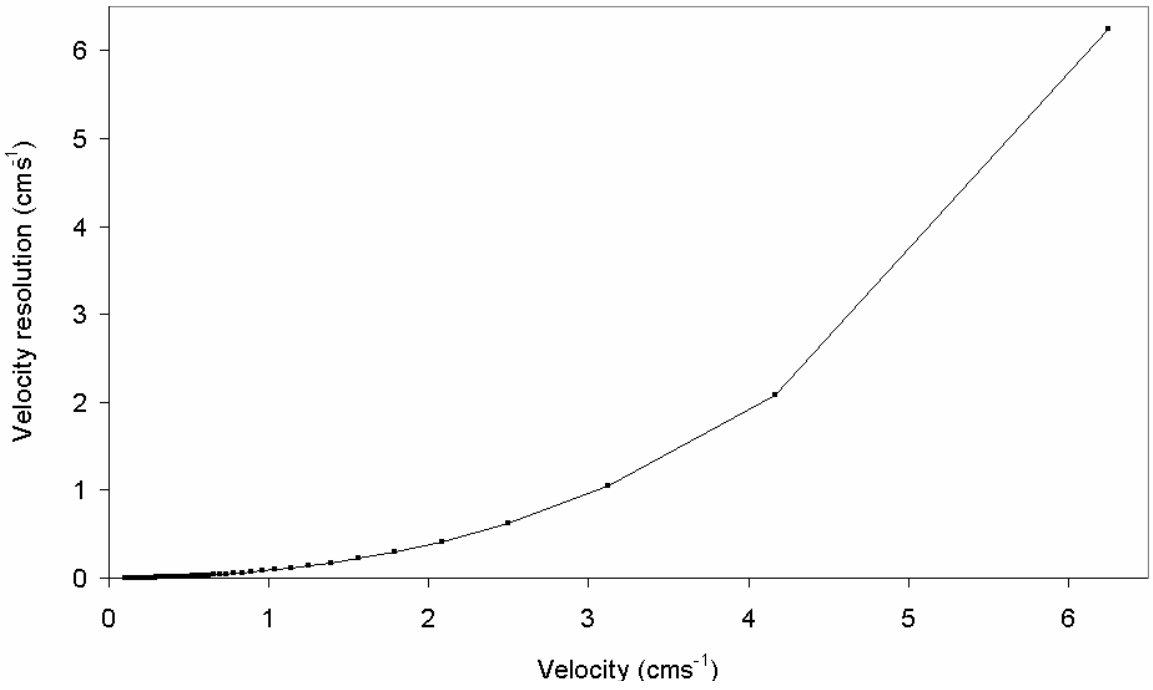

Fig. 6.32 The change in vector velocity resolution with velocity for a distance of 2.5cm.

Table 6.2 Vector velocity resolution as a percentage of true velocity

Velocity (cms^{-1})	Percentage resolution	Velocity (cms^{-1})	Percentage resolution	Velocity (cms^{-1})	Percentage resolution	Velocity (cms^{-1})	Percentage resolution
6.250	100.00	0.379	3.13	0.195	1.59	0.132	1.06
4.167	50.00	0.368	3.03	0.192	1.56	0.130	1.05
3.125	33.33	0.357	2.94	0.189	1.54	0.129	1.04
2.500	25.00	0.347	2.86	0.187	1.52	0.128	1.03
2.083	20.00	0.338	2.78	0.184	1.49	0.126	1.02
1.786	16.67	0.329	2.70	0.181	1.47	0.125	1.01
1.563	14.29	0.321	2.63	0.179	1.45	0.124	1.00
1.389	12.50	0.313	2.56	0.176	1.43	0.123	0.99
1.250	11.11	0.305	2.50	0.174	1.41	0.121	0.98
1.136	10.00	0.298	2.44	0.171	1.39	0.120	0.97
1.042	9.09	0.291	2.38	0.169	1.37	0.119	0.96
0.962	8.33	0.284	2.33	0.167	1.35	0.118	0.95
0.893	7.69	0.278	2.27	0.164	1.33	0.117	0.94
0.833	7.14	0.272	2.22	0.162	1.32	0.116	0.93
0.781	6.67	0.266	2.17	0.160	1.30	0.115	0.93
0.735	6.25	0.260	2.13	0.158	1.28	0.114	0.92
0.694	5.88	0.255	2.08	0.156	1.27	0.113	0.91
0.658	5.56	0.250	2.04	0.154	1.25	0.112	0.90
0.625	5.26	0.245	2.00	0.152	1.23	0.111	0.89
0.595	5.00	0.240	1.96	0.151	1.22	0.110	0.88
0.568	4.76	0.236	1.92	0.149	1.20	0.109	0.88
0.543	4.55	0.231	1.89	0.147	1.19	0.108	0.87
0.521	4.35	0.227	1.85	0.145	1.18	0.107	0.86
0.500	4.17	0.223	1.82	0.144	1.16	0.106	0.85
0.481	4.00	0.219	1.79	0.142	1.15	0.105	0.85
0.463	3.85	0.216	1.75	0.140	1.14	0.104	0.84
0.446	3.70	0.212	1.72	0.139	1.12	0.103	0.83
0.431	3.57	0.208	1.69	0.137	1.11	0.102	0.83
0.417	3.45	0.205	1.67	0.136	1.10	0.102	0.82
0.403	3.33	0.202	1.64	0.134	1.09	0.101	0.81
0.391	3.23	0.198	1.61	0.133	1.08	0.100	0.81

Analysis of the TrIM measured velocity for the same test signals used to analyse the vector velocity method confirmed that the TrIM method was unable to measure velocities above $0.7cms^{-1}$. There are five primary sources of inaccuracy with the TrIM method. Firstly, the band pass filtered signal is down-sampled from 5Hz to 1Hz, meaning that the time resolution is reduced to 1s. Secondly, the dynamic velocity is averaged over each contraction. Thirdly, the cross sectional distance used to measure the movement of the contraction is fixed at 10cm (Fig. 6.21A) so fast contractions may not be detected efficiently. Fourthly, the contraction is detected using a 7^{th} order polynomial fit that smoothes the data which may destroy important information. Fifthly, the TrIM algorithm is simplified from the algorithm derived in sections 4.3.2 to 4.3.4. The TrIM algorithm assumes that the measured impedance is inversely proportional to the distance from each signal to save processing time.

Fig. 6.33 shows the difference in percentage impedance versus distance calculated for the algorithm in section 4.3.4 and the TrIM method.

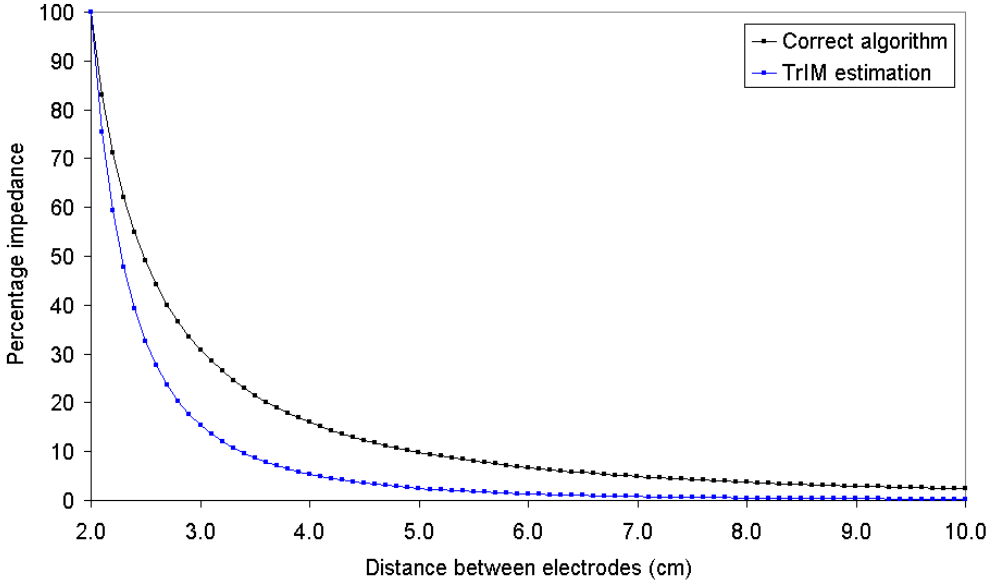

Fig. 6.33 Comparison between the algorithm derived in section 4.3.4 to predict the variation in measured impedance and the TrIM estimation. The advantage of the TrIM estimated algorithm is that it significantly reduces computing time.

Table 6.3 shows the analysis of the comparison between the direction of the velocity and angle measured by both the TrIM and vector velocity methods. Positive velocity implies movement towards the pylorus (anterograde) and negative velocity implies movement away from the pylorus (retrograde). Positive angles are downwards and negative angles are upwards (Fig. 6.24B). Since the correlation is good, it is the calculation of magnitude that is wrong. Nevertheless, the vector velocity is able to detect the correct magnitude with reasonable accuracy between velocities of 0.3 – 2.0cms^{-1} (±3% – ±20%) but with increasingly poor accuracy between velocities of 2.0 –5.0cms^{-1} (±20% – ±75%).

Table 6.3 Comparison between the sign of velocity and angle with vector velocity and TrIM.

Velocity measurements			**Angle measurements**		
Match sign: 83.28%	Different sign: 16.72%		Match sign: 62.78%	Different sign: 37.22%	
–	TV –ve	TV +ve	–	TA –ve	TA +ve
–	8.65%	8.07%	–	18.80%	18.42%

6.2.12 Analysis of gastric frequency changes

The study of the changes in frequency are performed by three algorithms; the JTFT spectrogram using epochs of 5 minutes with no overlap (Fig. 6.13A), the JTFT spectrogram using epochs of 5 minute with a 90% overlap (Fig. 6.13B) and DyWT. The indices of each gastric contraction are found by taking the peak impedance deflection of each contraction during the TrIM algorithm (see Fig. 6.25). The dominant pseudo frequency (see section 6.2.8) is defined at the peak of the scalogram power (see Fig. 6.16). This means that the scalogram (Fig. 6.16B) can be adapted to locate each contraction in time, pseudo frequency and power. Fig. 6.34A shows the dominant pseudo frequency of the signal in Fig. 6.16B. Low power contractions (defined as contractions that are less than 10% of the mean power density) were deemed to be artifactual and are not included in the analysis of frequency modulation[8]. The graph of all peaks together with these statistically significant peaks is shown in Fig. 6.34B.

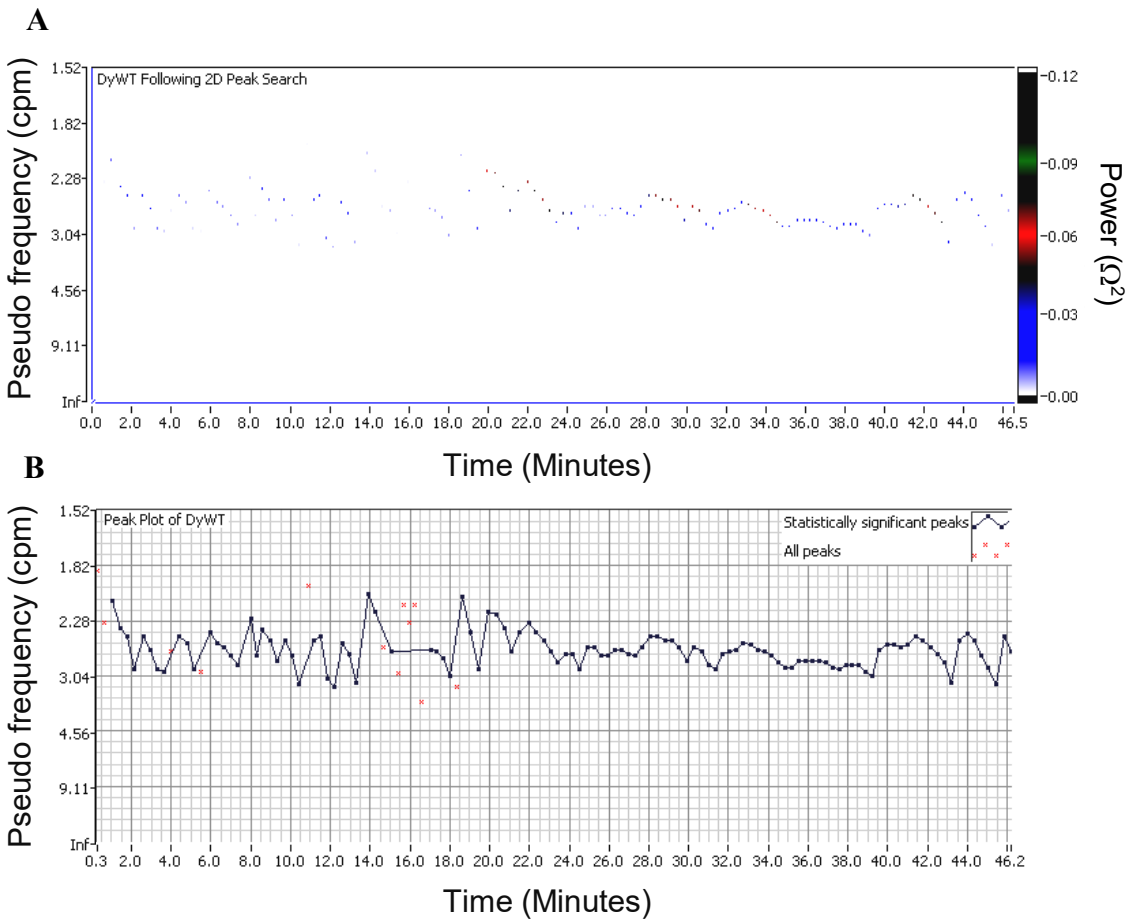

Fig. 6.34 **A** The DyWT following the 2D peak search using the indices for gastric contractions calculated by TrIM. **B** The graph of the peaks with statistically significant peaks (above 10% of the mean power density)[8].

[8] The choice of the 10% mean threshold is expounded in Appendix G.

The purpose of analysing the dominant pseudo frequency is to establish whether there are any reoccurring changes in frequency between different experiments that could indicate a gastro-physiological process. It is possible that changes in the smooth muscle during contractility, ingestion and emptying alter the pacesetter of the stomach (see section 2.4.1) following the ingestion of food. The only documented change in frequency that is not thought to be pathophysiological was discovered by Geldof using Electrogastrography (sections 3.1.1 and 3.1.2) during research into the gastric electrical activity of patients with unexplained nausea and vomiting. Geldof noted that immediately after ingestion of a yoghurt meal (250ml yoghurt and 20g of sugar), the frequency of gastric contractions decreased in all control subjects by approximately 23% and returned to normal after approximately 12 minutes, often overshooting the original fasting state frequency [Geldof H, 1986b]. The greyscale intensity graph in Fig. 6.35 also shows that the power of the EGG signal increases after the frequency shift.

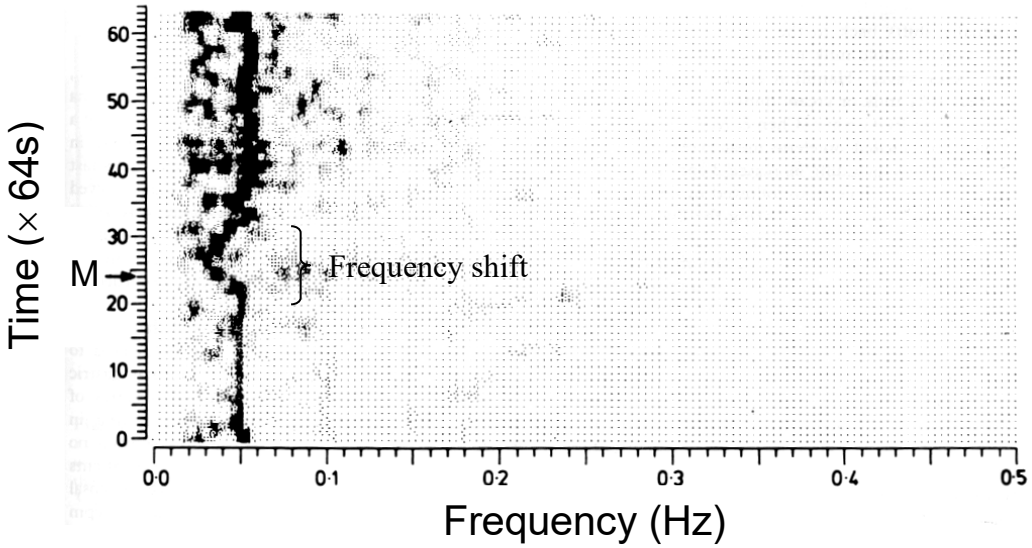

Fig. 6.35 Grayscale plot of the EGG of a control subject following the ingestion (at M) of a yoghurt meal [Redrawn from Geldof H, 1986b].

The frequency modulation shown by Fig. 6.13B is for qualitative analysis although a number of quantitative measurements (section 6.2.16) are calculated for example, the assessment of abnormally fast or slow contractility (section 6.2.13). The software examines the frequency of each epoch in the JTFT spectrogram (Fig. 6.13A) using epochs of 5 minutes to detect the presence of frequency shifts for the calculation of a quantitative measure of frequency modulation defined in section 6.2.16.

6.2.13 Assessment of abnormal gastric frequency

Many studies using EGG have found that gastric irregular gastric frequencies are related to gastric pathophysiology and dysmotility (section 3.2). A normal EGG is characterised by a regular waveform with a frequency of approximately 3cpm and an increase in postprandial power. Abnormal signals show dysrhythmias as tachy- and bradygastrias (Fig. 6.36) with no specific dominant frequency and a lack of postprandial signal power [Parkman HP, 2003].

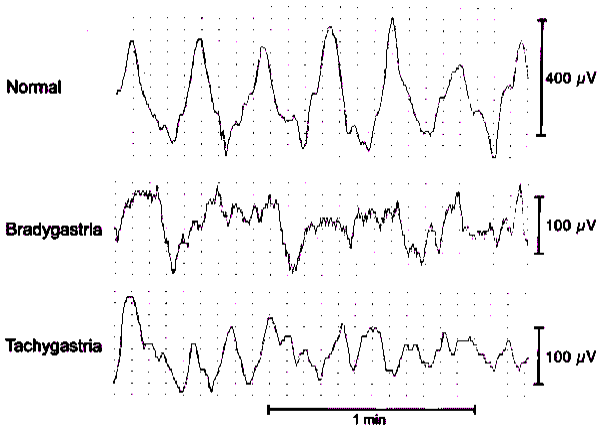

Fig. 6.36 Electrogastrography signals showing normal rhythm, bradygastria and tachygastria [Redrawn from Parkman HP, 2003].

Since EGG has detected abnormal gastric electrical activity in patients with gastric dysfunction, it is reasonable to state that EIE will detect abnormal gastric dominant frequencies. The DyWT scalogram, following the 2D peak search (Fig. 6.34A) can be used to classify the percentage of gastric contractions that fall outside the 'normal' range. Koch defines tachygastrias as gastric contractions in the range of 3.6 to 9.9cpm and bradygastrias in the range of 1.0 to 2.4cpm. Consequently, the normal gastric range is 2.4 to 3.6cpm [Koch KL, 1993]. It is expected that signals from patients with clinical conditions will demonstrate persistently abnormal gastric frequencies. The software measures the percentage of contractions in each frequency band. The results for the signal in Fig. 6.34A are shown in Table 6.4.

Table 6.4 Percentage of gastric contractions in the gastric, brady- and tachygastric ranges.

	Preprandial	Postprandial	Total signal
% Bradygastric*	20.83	11.24	13.27
% Gastric*	79.17	88.76	86.73
% Tachygastric*	0.00	0.00	0.00

6.2.14 Respiratory analysis

Section 4.3.5 demonstrated that the sensitivity of EIE to impedance change is greatest at the skin surface. This is why movements such as yawning or coughing generate motion artifacts in the signal that appear as spikes (see section 6.2.2). However, in addition to sudden transient movements, the action of breathing itself involves the movement of the chest and lower abdomen to some degree. Therefore, this respiratory signal is superimposed onto the EIE signal. Fig. 6.37 shows part of an EIE signal with gastric contractions and respiratory artefact.

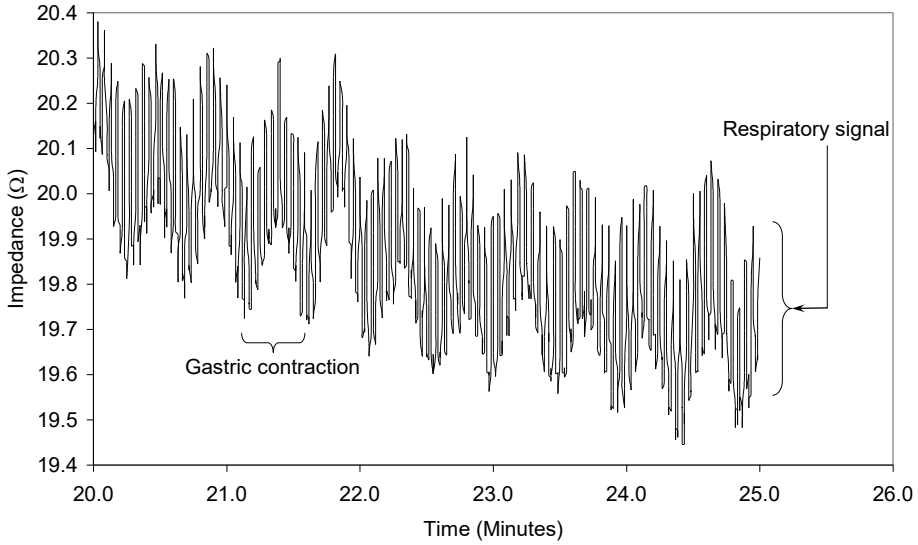

Fig. 6.37 A section of an EIE signal recorded after the ingestion of 500ml of mineral water clearly showing the gastric contractions and respiratory signal.

The respiratory signal can be easily removed using band pass filtering (see section 6.2.5) but it may in fact be of some significance from a gastro-physiological perspective. Since the stomach can expand to hold more than 50 times its fasting volume the volume increase will affect the surrounding organs. Fig. 6.38 illustrates that the stomach is located directly below the diaphragm.

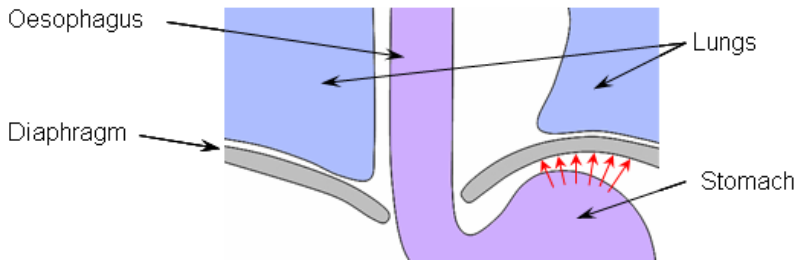

Fig. 6.38 The location of the stomach with respect to the diaphragm and lungs. The red arrows indicate the mechanical force applied on the diaphragm and lungs.

When a meal is ingested, the volume increase exerts a pressure on the diaphragm, altering the breathing; more effort will be required to fill the lungs when the stomach is full and so theoretically, the power of the respiratory signal will increase after ingestion. This explains the mild breathlessness that is often experienced following a large meal. The question is whether there is any *clinical* significance to the postprandial respiratory power increase. It is possible that it would provide information regarding the fullness of the stomach and help to indicate cases of early satiety where the patient feels full after a relatively small meal.

The respiratory signal is extracted from the acquired signal using a band pass Butterworth Filter with a pass band from 10 to 30cpm and processed using the JTFT algorithm described in section 6.2.7 using a window length of 1min and no overlap. The dominant respiratory power for the signal in Fig. 6.10A is shown in Fig. 6.39. There is an increase in power after the meal is ingested (at time M) which gradually decreases until it returns to normal after 15 minutes (t = 26mins).

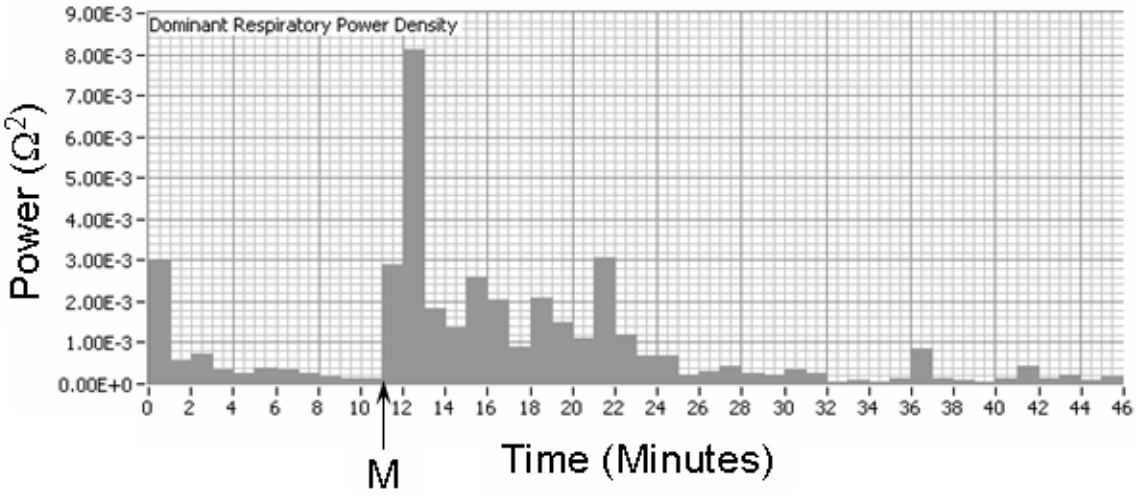

Fig. 6.39 Dominant respiratory power for the signal in Fig. 6.10A.

6.2.15 Classification of the emptying curve

Pattern recognition is the process of extracting specified features from the acquired data and grouping features that share similar properties into classes. However, similarity is not a clearly defined or objective term and depends on the information that is sought. Pattern recognition is something that humans are highly skilled at and do subconsciously on a daily basis, for example distinguishing the face of a friend in a crowd of strangers. However, these tasks are immensely complex and therefore very challenging to implement by computer algorithms.

The term 'feature' in the above definition refers to a variable that is a particular characteristic of a set of data. For example, height is a feature of a population of human beings. A pattern vector may be thought of as an arrangement of features. Equation 6.34 shows a pattern vector **x** (in red) with *n* features (blue).

$$\mathbf{x} = \begin{bmatrix} x_1 \\ x_2 \\ \vdots \\ x_n \end{bmatrix} \tag{6.34}$$

A pattern class is a family of patterns that share some common properties and they are denoted as $\omega_1, \omega_2, \ldots, \omega_M$ where M is the number of classes. After a set of features has been selected the pattern vector produced is all that defines each sample. Each sample is then plotted in n dimensional 'feature space'. The decision-theoretical approach to pattern classification is based on the use of decision functions. For M pattern classes there are M decision functions $d_1(\mathbf{x}), d_2(\mathbf{x}), \ldots, d_M(\mathbf{x})$. If an unknown pattern **x** belongs to the ith pattern class then equation 6.35 will hold. The decision boundary that separates ω_i from ω_j is shown in equation 6.36. If a pattern is in class ω_i then $d_{ij}(\mathbf{x}) > 0$ and if it is in class ω_j then $d_{ij}(\mathbf{x}) < 0$.

$$d_i(\mathbf{x}) > d_j(\mathbf{x}) \qquad \text{where } j = 1, 2, \ldots, M;\ j \neq i \tag{6.35}$$

$$d_{ij}(\mathbf{x}) = d_i(\mathbf{x}) - d_j(\mathbf{x}) = 0 \tag{6.36}$$

In order to define the decision boundary, the pattern vectors of data that are known to belong to each of the specified classes must be mapped onto the feature space. Each class is represented by a mean vector, $\mathbf{m}_j$ calculated from the mean of each feature from all of the pattern vectors in each class (see equation 6.37). N_j is the number of pattern vectors in the class ω_j.

$$\mathbf{m}_j = \frac{1}{N_j} \sum_{\mathbf{x} \in \omega_j} \mathbf{x} \qquad \text{where } j = 1, 2, \ldots, M \tag{6.37}$$

From equation 6.36, the decision boundary based on the minimum distance classifier between two classes ω_i and ω_j can be defined as equation 6.38. A diagram of the formation of the decision boundary between two imaginary features is shown in Fig. 6.40.

$$d_{ij}(\mathbf{x}) = d_i(\mathbf{x}) - d_j(\mathbf{x}) = 0$$

$$\therefore \quad d_{ij}(\mathbf{x}) = \mathbf{x}^T \left(\mathbf{m}_i - \mathbf{m}_j\right) - \frac{1}{2}\left(\mathbf{m}_i - \mathbf{m}_j\right)^T \left(\mathbf{m}_i - \mathbf{m}_j\right) = 0 \tag{6.38}$$

Clearly this technique relies on the optimum feature selection; if the classes are not clearly defined then further calculations are necessary. For two features the boundary is a line, for three the boundary is a plane. If more than three features are used, the feature space becomes impossible to visualise because it requires more than three dimensions.

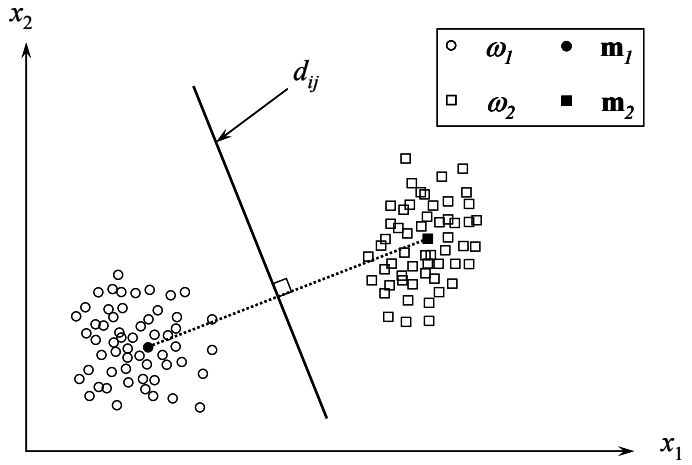

Fig. 6.40 The decision boundary calculated by the minimum distance classifier between two classes. The dotted line is drawn between the two mean vectors.

Pattern recognition algorithms were used by ACCESS to classify the shape of the emptying curve into one of the three classes shown in Fig. 6.41. The decision-theoretical approach was employed by ACCESS to find three continuous features that contribute to the classification of the emptying curve. The first feature was obtained by examining the derivative (rate of emptying) of the signal. The range of the derivative, r_d was able to separate the linear class from the exponential and nonlinear classes (see Appendix F).

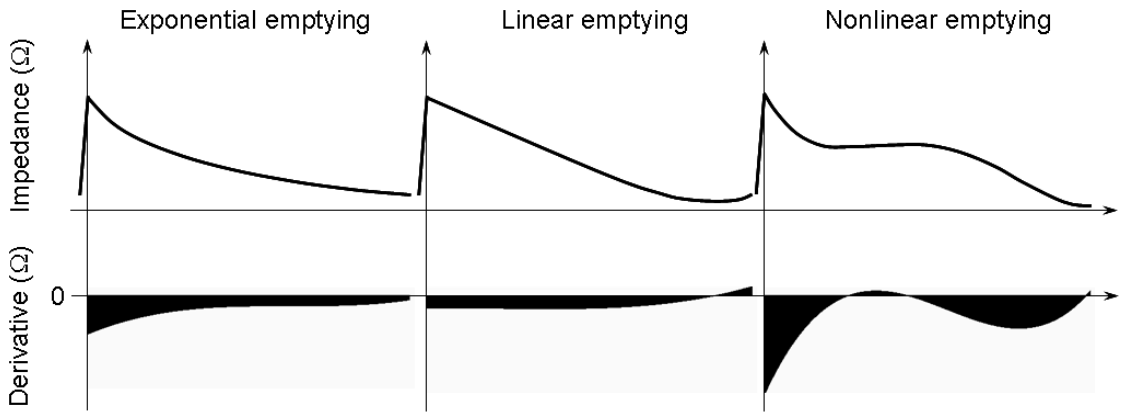

Fig. 6.41 Schematic diagrams of the three classes of emptying curve: exponential, linear and nonlinear together with their derivatives.

The second feature applied a Haar wavelet trend to model the postprandial region resulting in a signal that represented the mean of successive epochs of the polynomial model. An example is given in Fig. 6.42.

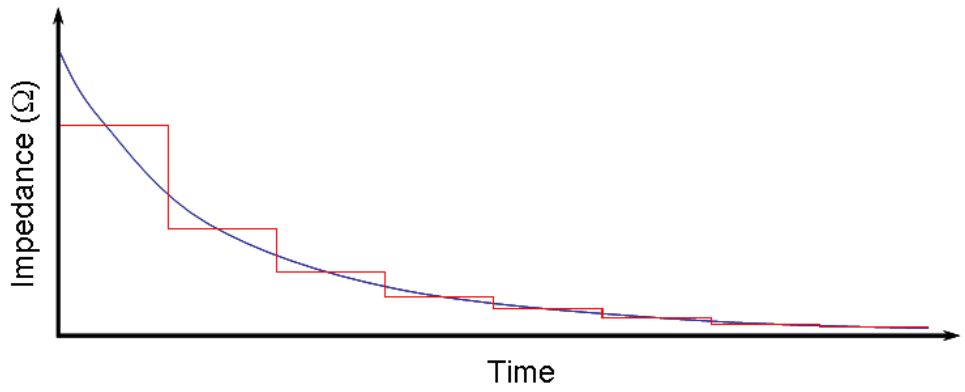

Fig. 6.42 The polynomial model of an exponential emptying curve (blue line) with the Haar wavelet model (red line).

It is clear that for the exponential graph, the differences in impedance for each step of the Haar wavelet model decrease successively. However, this is not the case for the linear and nonlinear emptying curves. Spearman's rank correlation, r_s was applied to the differences in impedance for each step (with their position in time as the rank) to separate the exponential class from the linear and nonlinear classes. High values for r_s implied that the emptying curve was of the exponential class (see Appendix F). The third feature examined the gradient, m_L of the linear fit through the differences in impedance for each step of the Haar model. This value also separated the linear class from the exponential and nonlinear classes (see Appendix F). The above features, r_d, r_s and m_L are examples of continuous features that contribute to the calculation of the decision boundary that can differentiate between exponential and linear classes. Fig. 6.43 shows the feature space for all of the 92 signals tested.

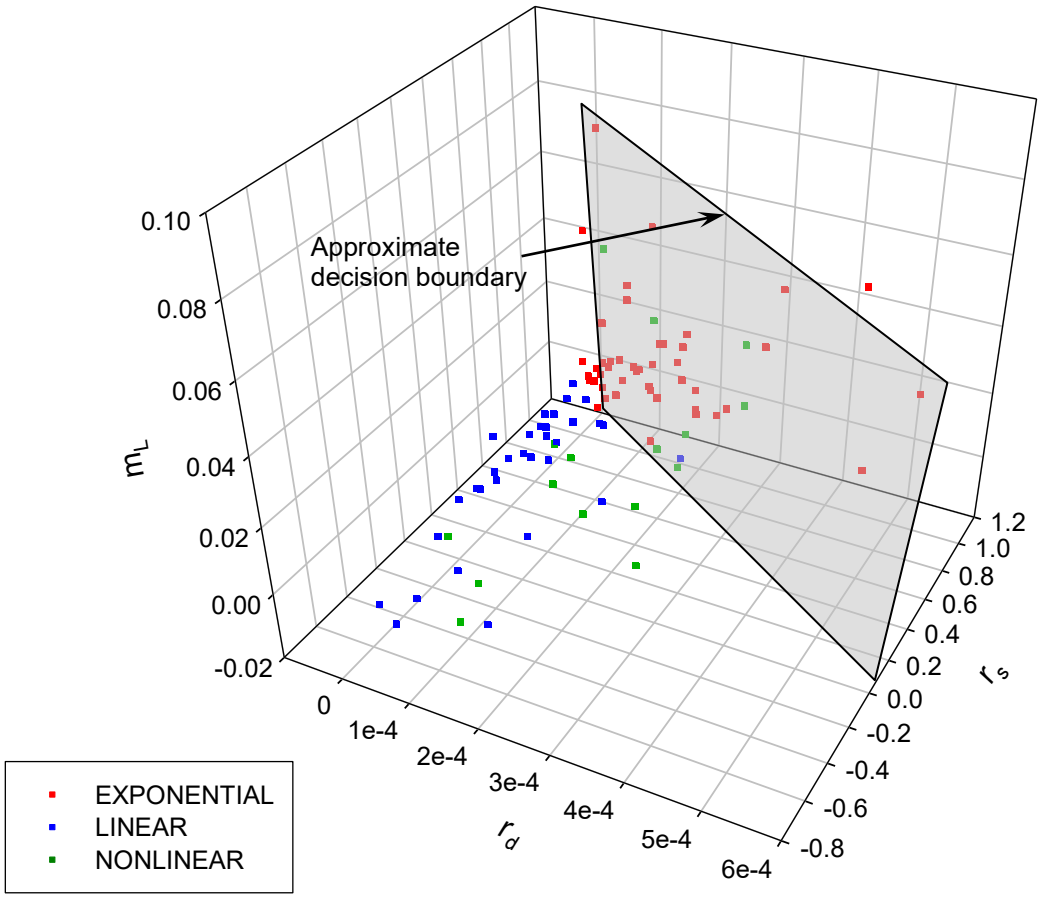

Fig. 6.43 3D Feature space with an approximate decision boundary.

Although this representation illustrates how the decision-theoretical approach operates, it is less complicated and more effective to use 2D feature spaces. In order to do this, it is necessary to compare three distinct 2D feature spaces, each with their own decision boundary (Fig. 6.44).

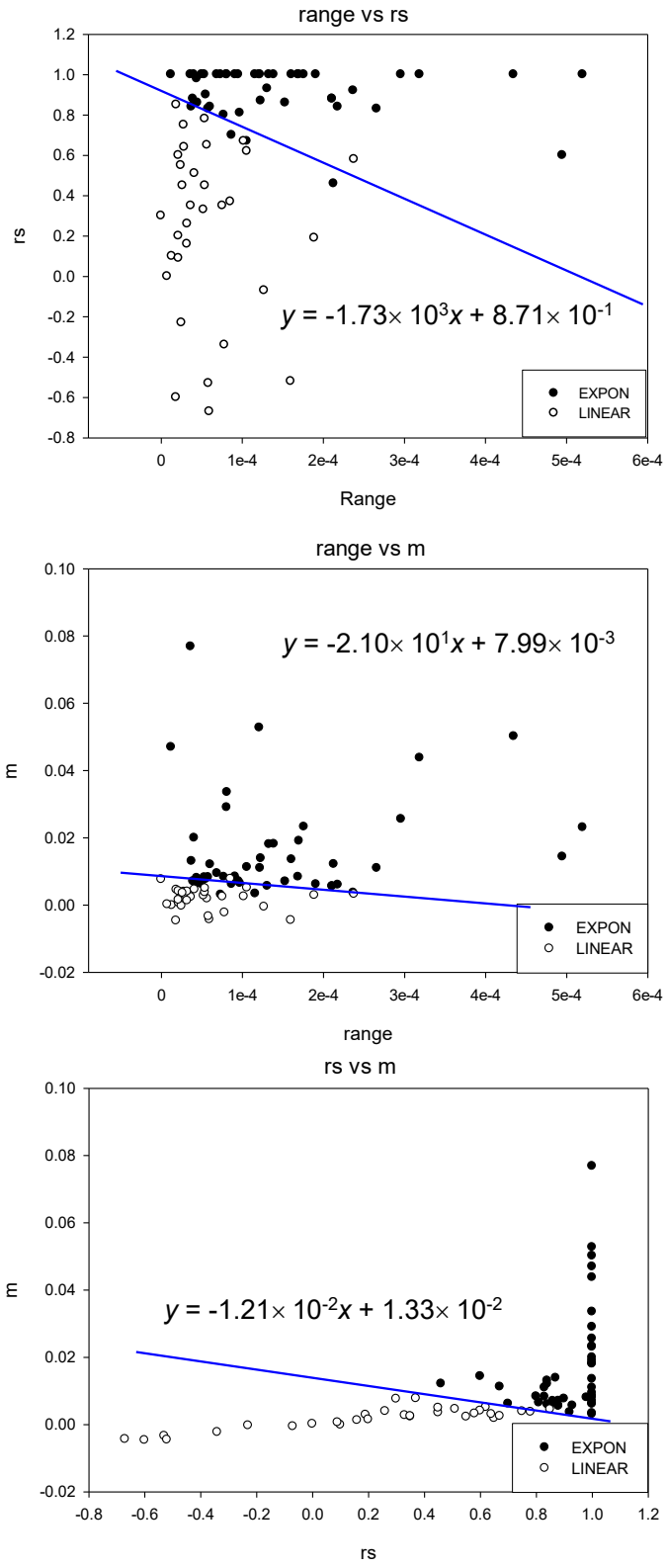

Fig. 6.44 The three two-dimensional feature spaces with their respective feature boundaries (shown in blue) and equations where range is the range of the derivative, m is the gradient of the linear fit through the differences in impedance for each step of the Haar model and rs is the Spearman rank correlation applied to the differences in impedance in the Haar model.

Each signal is classified by its position on the feature space. By inputting the values for range, m and rs, each signal will be placed on either the positive side of the decision boundary (resulting in a linear classification) or on the negative side (resulting in an exponential classification). However, it is possible that the features of a particular signal mean that its classification is not the same on different feature spaces. This problem is solved by attributing different weighting values to each scenario. The position of the signal is converted into either a -1 or 1, depending on whether it falls on the negative or positive side of the decision boundary. Since the data are stored as double-precision floating point numbers[9], it is very unlikely that a data point would fall exactly *on* the decision boundary. However, if this happens, it is given a score of 0 and the classification is based on the proximity of the signal to the decision boundaries in the other two cases. These scores are added giving six possibilities shown in table 6.5.

Table 6.5 Scores for the classification of emptying curves in 2D feature space

2D Feature space score	**Meaning**	**Classification**
-3	All values are negative	High probability exponential
-1	Two are negative one is positive	Moderate probability exponential
3	All values are positive	High probability linear
1	Two are positive one is negative	Moderate probability linear
-2 or 2	The signal falls on the decision boundary in one feature space	Low probability using proximity to the decision boundary in the other two cases

Some features of a particular pattern may not vary continuously. Nominal variables such as gender or the number of humps on a camel consist of named categories with no implied order. In such cases, it is unnecessary to produce feature maps as the features clearly identify which class a given example should fall in; all camels with two humps are Bactrian and all camels with one hump are Dromedary. Since the three continuous features were only able to classify exponential and linear emptying curves, nominal features (referred to as discrete features)[10] were obtained to classify nonlinear emptying curves and aid the classification of exponential and linear emptying curves.

[9] 64-bit IEEE format [IEEE, 1985] with a range of $\pm 4.94\times10^{-324}$ to $\pm 1.79\times10^{308}$.
[10] The term 'discrete' in this instance means that the feature varies by an integer number.

The derivative of the polynomial model of the emptying curve (see Fig. 6.31) was analysed for stationary points. Local maxima, minima and positive and negative inflexions were counted. In total, ten different tests were used to determine the class of the postprandial emptying curve and they are summarised in table 6.6.

Table 6.6 Weights for each test of nominal variables.

No.	Test	α weights	β weights	γ weights
1	Signal is negative in all 2D feature spaces	T = 0.70 F = 0.00	T = 0.00 F = 0.00	T = 0.00 F = 0.00
2	Signal is negative in two 2D feature spaces	T = 0.60 F = 0.00	T = 0.00 F = 0.00	T = 0.00 F = 0.00
3	Signal is positive in all 2D feature spaces	T = 0.00 F = 0.00	T = 0.70 F = 0.00	T = 0.00 F = 0.00
4	Signal is positive in two 2D feature spaces	T = 0.00 F = 0.00	T = 0.60 F = 0.00	T = 0.00 F = 0.00
5a	Test = negative	T = 0.35 F = 0.00	T = 0.00 F = 0.00	T = 0.00 F = 0.00
5b	Test = positive	T = 0.00 F = 0.00	T = 0.35 F = 0.00	T = 0.00 F = 0.00
6	There are maxima in the derivative	T = -0.10 F = 0.03	T = -0.10 F = 0.03	T = 0.25 F = 0.00
7	There are minima in the derivative	T = -0.10 F = 0.03	T = -0.10 F = 0.03	T = 0.25 F = 0.00
8	Positive inflexion	T = -0.10 F = 0.03	T = -0.10 F = 0.03	T = 0.25 F = 0.00
9	Negative inflexion	T = -0.10 F = 0.03	T = -0.10 F = 0.03	T = 0.25 F = 0.00
10	Stationary points in the second derivative	T = -0.20 F = 0.03	T = -0.20 F = 0.03	T = 0.40 F = 0.00

The weights represent the quantitative importance for each test with respect to their class. They were calculated empirically using signals that had not been used for calculation of the three continuous tests. The weights for each class were summed and if the total was more than one it was rounded down to one, and if it was less than zero it was rounded up to zero. These three values represent the probability of the signal falling into each class. The signal is categorised into the class with the largest probability.

The suitability of the classifications made by the pattern recognition algorithm were tested by fitting the empting period of the EIE signals with three different curves (linear, exponential and 4th order polynomial). If the pattern recognition has successfully classified the empting periods into the most appropriate classes, the R^2 values of the fitted curves will vary in a specific way; the exponential curve will only fit the emptying period well if the emptying curve is also exponential and similarly, the linear fit will only fit the emptying curve well if the emptying curve is also linear. However, the 4th order polynomial will be able to represent all three emptying curves, the exponential, linear and nonlinear. Therefore, only the 4th order polynomial will give a good fit to a nonlinear emptying curve. A summary of expected results is shown in Table 6.7.

Table 6.7 Expected R^2 values indicting the quality of fit for three different curves: exponential, linear and 4th order polynomial, for each class of emptying curve: exponential, linear and nonlinear.

Emptying curve	**Exponential fit**	**Linear fit**	**4th order polynomial fit**
Exponential class	VERY GOOD	POOR	VERY GOOD
Linear class	POOR	VERY GOOD	VERY GOOD
Nonlinear class	POOR	POOR	VERY GOOD

Table 6.8 lists the predicted differences in R^2 values between the three types of emptying curve fit (EXP = exponential, LIN = linear and POLY = 4th order polynomial) for each class (exponential, linear and nonlinear) based on Table 6.7.

Table 6.8 Predicted differences in R^2 values between the three types of emptying curve fit for each class where > means R^2 values are significantly greater and < means R^2 values are significantly smaller.

Class	**EXP – LIN**	**EXP – POLY**	**LIN – POLY**
Exponential	EXP > LIN	No change	LIN < POLY
Linear	EXP < LIN	No change	No change
Nonlinear	No change	EXP < POLY	LIN < POLY

6.2.16 Quantitative analysis

Sections 6.1.1 and 6.1.2 stated the need for ACCESS to produce quantitative values that can be compared to determine which are affected by gastro-physiological and pathological characteristics. Therefore, quantitative values were calculated from the data for each part of the total analysis. The following section outlines the calculations of each of the 18 quantitative values listed in Table 6.9.

Table 6.9 Quantitative variables

Emptying curve	
T50 (min)	Half emptying time for selected channel and method
IUV (Ωml^{-1})	Impedance (deflection) per Unit Volume
PPBS (Ω)	Post to Preprandial Baseline Shift
PRC	Pattern Recognition and Classification of the emptying curve
Contractility	
MPR	Mean Power Ratio
JPR	JTFT post to preprandial Power Ratio
GCR	Gastric Contractility Ratio
CIR	Contractile Incidence Ratio
MAR	Maximum frequency Amplitude Ratio
Dominant frequency	
MFR	Mean Frequency Ratio
MFS	Maximum Frequency Shift
% Bradygastric	Percentage of contractions below the normal frequency range
% Gastric	Percentage of contractions in the normal frequency range
% Tachygastric	Percentage of contractions above the normal frequency range
DMI	Dominant frequency Modulation Index
Respiratory analysis	
RPR	Respiratory post to preprandial Power Ratio
RFS (cpm)	Post to preprandial Respiratory Frequency Shift
Velocity	
MVR	Mean Velocity Ratio

The calculation of the T50 (half emptying time) was discussed in section 6.2.4. It is important however, to note that although every T50 for each channel using all nine methods of analysis are documented, the T50 of the signal used for comparison with other signals and statistical analyses in experimental studies is taken from the user-selected channel and T50 calculation method.

The Impedance Deflection per unit Volume, *IUV* (Ωml^{-1}) is calculated to provide a measure of system response to the meal ingestion. *IUV* is defined in equation 6.39 where D_{MAX} is the maximum deflection and *V* is the volume of the meal in millilitres. Note that $D_{MAX} \equiv PPBS$.

$$IUV = \frac{D_{MAX}}{V} \tag{6.39}$$

The Post to Preprandial Baseline Shift, *PPBS* measures the difference in the postprandial and preprandial baselines to detect changes in impedance caused by gastric secretions. *PPBS* is defined in equation 6.40 where $\bar{B}_{POST}$ is the mean postprandial baseline and $\bar{B}_{PRE}$ is the mean preprandial baseline.

$$PPBS = \bar{B}_{POST} - \bar{B}_{PRE} \tag{6.40}$$

PRC is the Pattern Recognition and Classification of the emptying curve and has been discussed in section 6.2.15. The quantitative measures are the class (α, β or γ) and the calculated probability of the emptying curve falling in that class.

The Mean Power Ratio, MPR is the ratio between the postprandial Mean Power Index (MPI_{POST}) and the preprandial Mean Power Index (MPI_{PRE}) calculated as the mean power of all of the contractile peaks (given in Fig. 6.34A). The formula is given in equation 6.41.

$$MPR = \frac{MPI_{POST}}{MPI_{PRE}} \tag{6.41}$$

The JTFT post to preprandial Power Ratio, JPR is defined in equation 6.42 as the ratio between the postprandial and preprandial JTFT mean max Power per minute Indices (JPI_{POST} and JPI_{PRE} respectively). The JPI for each region is calculated by first measuring the maximum power for each epoch. Since the length of one epoch is 5 minutes (see Fig. 6.13A), the maximum power is divided by 5 to obtain the maximum power per minute for each epoch.

There are a number of time-periods; preprandial, postprandial, initial 30 postprandial minutes and after 30 postprandial minutes to the end of the signal. The last two periods are for sham feeding experiments where sham feeding is carried out for 30 minutes after ingestion of the meal. For each time period the values for the maximum power per minute for each epoch are summed and divided by the number of epochs to give a mean value.

$$JPR = \frac{JPI_{POST}}{JPI_{PRE}} \tag{6.42}$$

There are two widely documented measurements of contractility that have been used primarily with gastric or intestinal manometry, known as the gastric contractility index, GCI (also called the motility index) and the contractile incidence index, CII. These are defined in equations 6.43 and 6.44 respectively where N_p is the number of contractions in the time period t (usually expressed in minutes). The index of each contraction is n which is a positive integer so that a_n is the amplitude (power density, Ω^2) of the n^{th} contraction.

$$GCI = \ln\left\{\left(N_p \sum_{n=0}^{N_p} a_n\right) + 1\right\} \tag{6.43}$$

$$CII = \frac{N_p}{t} \tag{6.44}$$

The Gastric Contractility Ratio, GCR is simply the ratio of the postprandial GCI to the preprandial GCI and similarly, the Contractile Incidence Ratio, CIR is the ratio of the postprandial CII to the preprandial CII. All of these values are calculated and tabulated together in ACCESS. In the case of ratios between post and preprandial periods, the ratio is listed in one table and the two indices are listed in a separate table.

The Maximum frequency Amplitude Index, MAI is calculated by measuring the peaks of the preprandial and postprandial power spectra following the band pass filtering of the acquired signal with the passband between 2.4 and 3.6cpm (see Fig. 6.11). The Maximum frequency Amplitude Ratio, MAR is defined in equation 6.45 as the ratio of the postprandial MAI to the preprandial MAI.

$$MAR = \frac{MAI_{POST}}{MAI_{PRE}} \tag{6.45}$$

The Mean Frequency Index, MFI is calculated from the pseudo-frequencies calculated from the DyWT after the 2D peak search (see section 6.2.8 and Figs. 6.34A and 6.34B). The Mean Frequency Ratio, MFR is defined in equation 6.46 as the ratio of the postprandial MFI to the preprandial MFI.

$$MFR = \frac{MFI_{POST}}{MFI_{PRE}} \tag{6.46}$$

The Maximum Frequency Shift, MFS was calculated from difference in frequency between the frequency of peak in the postprandial power spectrum and the frequency of peak in the preprandial power spectrum (see Fig. 6.11). The percentages of contractions in each of the three frequency ranges: Bradygastric; Gastric and Tachygastric, are calculated from the dominant pseudo frequency of the signal (see Figs. 6.34A and 6.34B).

The Dominant frequency Modulation Index, DMI is calculated by analysing the differences between the frequencies of each postprandial epoch in the JTFT (calculated with 5 minute epochs and shown in Fig. 6.13A). The software builds an array of the differences of each epoch; if the two frequencies differ by ±0.2cpm or more, the software adds a +1 or -1 (depending on the direction of the change). If there is no significant change, the software adds a zero to the array. Therefore if each epoch was represented by n, n+1, n+2 … n+N, the comparison is made between the dominant frequencies of n and n+1, and between the dominant frequencies of n+1 and n+2. These differences are labelled d_0, d_1, d_2 … d_{N-1}.

The array of differences is then analysed in a similar way. Each difference is compared to the previous one and a score is given based on the difference between d_n and d_{n+1}. Table 6.10 shows the how the scores are determined for each combination of d_n and d_{n+1}. The DMI is finally calculated by taking the average of the scores. No change ($d_n = dn_{+1}$) is given a score of -1, small change ($|d_n - dn_{+1}| = 1$) is given a score of zero and large change ($|d_n - dn_{+1}| = 2$) are given a score of Table 6.11 illustrates an example of the process.

Table 6.10 Scores given for all combinations of d_n and d_{n+1} for the calculation of the DMI

d	$d+1$	Score = $\|d_n - d_{n+1}\| - 1$
0	0	-1
0	1	0
0	-1	0
1	0	0
-1	0	0
1	1	-1
-1	-1	-1
-1	1	+1
1	-1	+1

Table 6.11 Example of the calculation of the calculation of the DMI

n (cpm)	d	Score
$n_0 = 2.92$	*	*
$n_1 = 2.57$	$d_0 = -1$	*
$n_2 = 2.44$	$d_1 = 0$	0
$n_3 = 2.46$	$d_2 = 0$	-1
$n_4 = 2.43$	$d_3 = 0$	-1
$n_5 = 2.52$	$d_4 = 0$	-1
$n_6 = 2.78$	$d_5 = 1$	0
$n_7 = 2.89$	$d_6 = 0$	0
$n_8 = 2.94$	$d_7 = 0$	-1
TOTAL		-4
$DMI = \frac{-4}{7}$ $= -0.57$		

The DMI therefore ranges from -1 to +1 where a DMI of -1 implies no significant change at all whereas a DMI of +1 implies constant variation in the dominant frequency.

The Respiratory Power Index, RPI is calculated by taking the mean power of the pre- and postprandial regions of the respiratory signal (calculated after the band pass filtering the acquired signal with a passband of 10 to 30cpm). The Respiratory Power Ratio, RPR defined in equation 6.47 is then calculated as the ratio of the postprandial RPI to the preprandial RPI.

$$RPR = \frac{RPI_{POST}}{RPI_{PRE}} \tag{6.47}$$

The Respiratory Frequency Shift, RFS is calculated by subtracting the mean postprandial respiratory frequency from the mean preprandial respiratory frequency, both calculated from the dominant respiratory frequency.

The Mean Velocity Index, MVI is calculated by taking the mean velocity of the pre- and postprandial regions of the vector velocity. The post to preprandial Mean Velocity Ratio, MVR defined in equation 6.48 is then calculated as the ratio of the postprandial MVI to the preprandial MVI.

$$MVR = \frac{MVI_{POST}}{MVI_{PRE}} \tag{6.48}$$

6.2.17 Report generation

After all calculations have been completed, the software offers the user to create a Microsoft Word report containing the subject information and anthropomorphic measurements (which may be saved in a special *.ant file), important quantitative information including all of the measurements in section 6.2.16 and pictures of the graphs. An example report can be seen in Appendix G. Furthermore, the software offers to produce two Microsoft Excel files, one containing the quantitative data and the other containing the graph data so that graphs can be redrawn and compared in Microsoft Excel for different subjects.

7 MODELLING OF THE EIE SIGNALS

7.1 Software Quality Assurance (QA)

7.1.1 The concept of Quality Assurance (QA)

Quality assurance (QA) describes the process of testing equipment or software to ensure that it is performing correctly and giving accurate results. Consequently, it is necessary to perform QA on the final EIE analysis software to eliminate hidden mistakes that may cause incorrect results and assess the accuracy of the various signal-processing procedures. However, the success of the QA depends on the quality and suitability of the tests designed; thorough testing is necessary to ensure that the effects of incorrect operations in the software, which may only manifest themselves in EIE signals with specific characteristics, are identified immediately and subsequently eliminated[1].

7.2 The Pseudo-EIE signal generator for software QA

7.2.1 The pseudo EIE signal generator

The QA for the EIE analysis software employs artificial signals with known, predetermined characteristics to simulate real EIE signals and have been labelled 'pseudo-EIE' signals. A program called *Pseudo EIE* was written in LabVIEW to generate these signals together with simple waveforms known as 'test signals' that also help to assess the performance of the analysis software.

The pseudo-EIE and test signals produced by *Pseudo EIE* are configured in the same format as real EIE signals obtained by the Epigastrograph meaning that they can be saved in the *.eie file format (see section 6.2.9) and loaded into the EIE analysis software. The format of the EIE signals is given in section 6.2.9 in table 6.1.

[1] All Quality Assurance and software testing may be found in Appendix H.

Fig. 7.1 shows the different test signals and the three types of Pseudo EIE signal, exponential, linear and nonlinear (Fig. 7.3) that can be produced by the *Pseudo EIE* program.

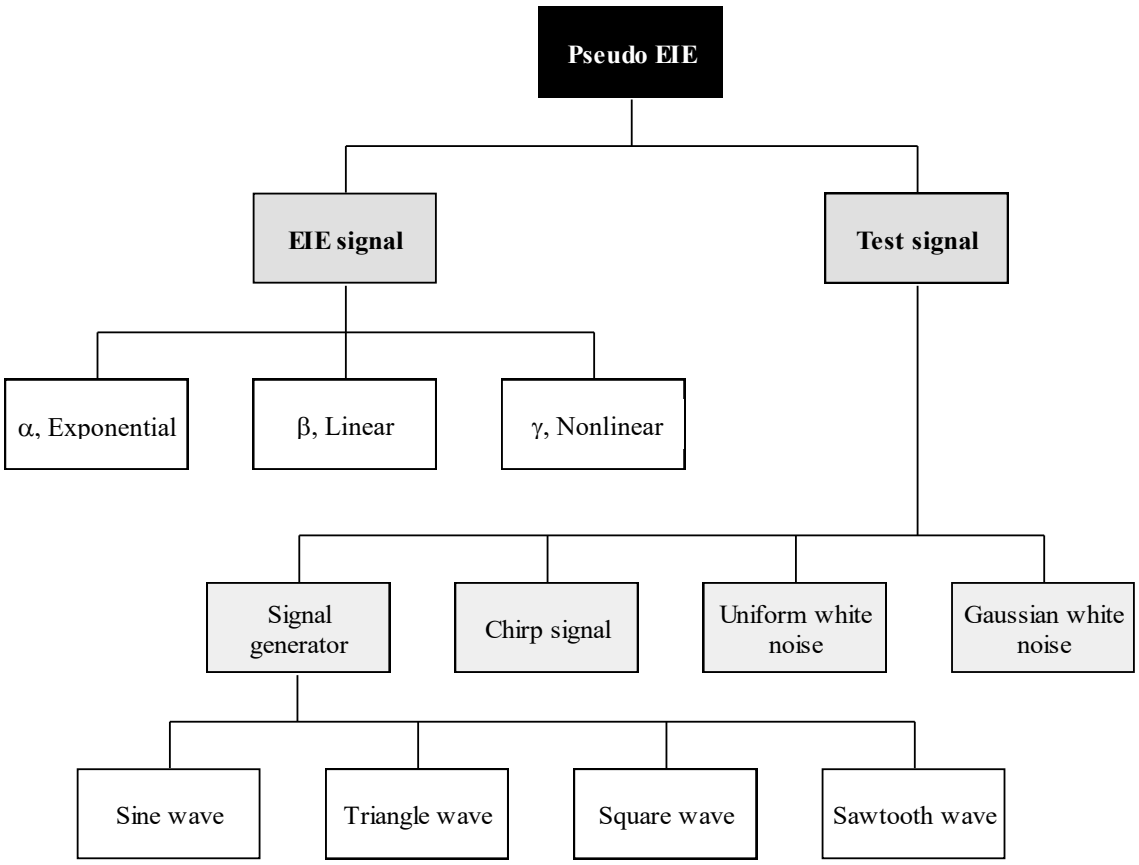

Fig. 7.1 The different signals generated by the *Pseudo EIE* software. Each is explained in detail in the following sections.

There are a number of variables associated for each signal that alter the signal's characteristics, such as length, amplitude and frequency and these will be discussed in the subsequent sections. The opening screen of the Pseudo-EIE program is shown in Fig. 7.2. The default settings are shown and it should be noted that some controls are hidden if they are unrelated to the selected signal type.

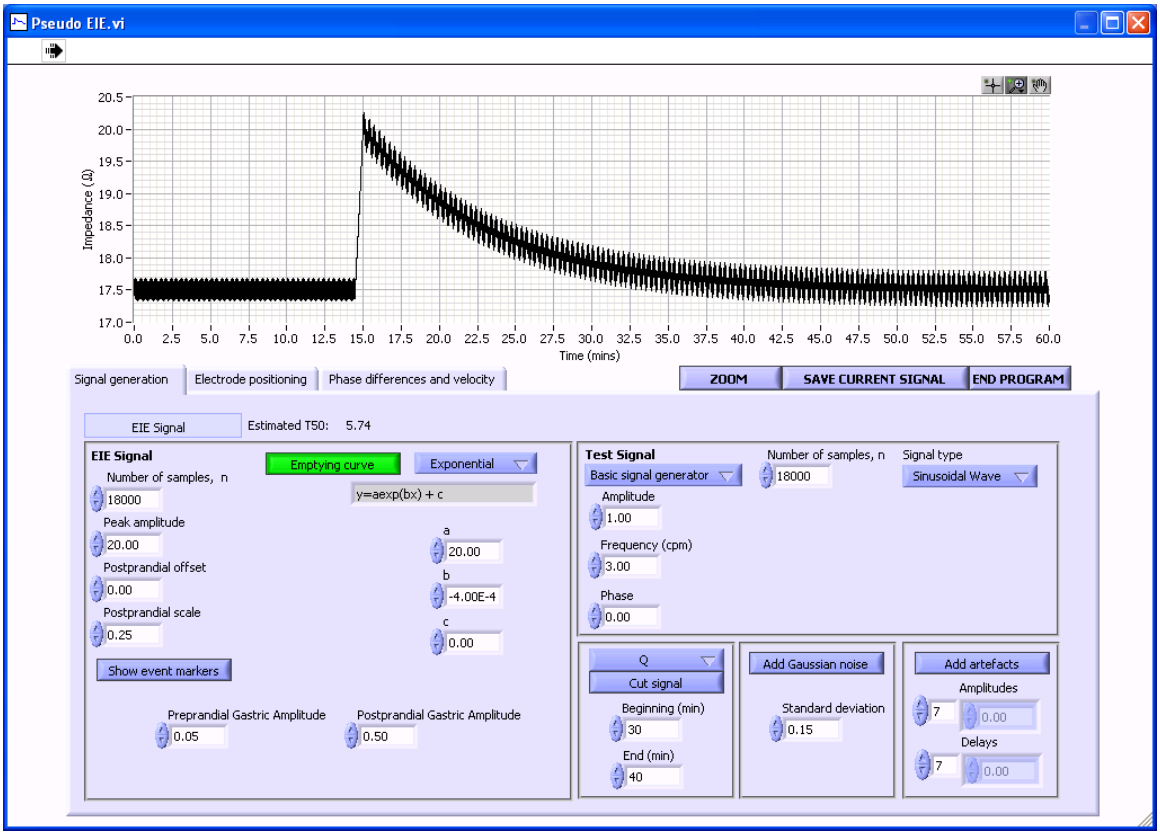

Fig. 7.2 Screen shot of the opening page of the *Pseudo EIE* software.

7.2.2 Pseudo-EIE signal

The two primary sinusoidal frequency components in the EIE signal are respiratory artefact and gastric signal (mains interference has a frequency of approximately 50Hz and is therefore too high to detect with the 5Hz sampling frequency used in EIE studies). The frequency of the respiratory artefact is set to 15cpm while the gastric frequency is set at 3cpm. The amplitude of the respiratory artefact remains constant throughout the pseudo-EIE signal at 0.30Ω but the gastric amplitude may be varied for the preprandial section of the signal and for each of three electrode planes during the postprandial period. The default is 0.50Ω.

The preprandial section of the pseudo-EIE signal has constant amplitude but the meal ingestion period (which is represented by a ramp function) changes the amplitude of the signal. This value represents the change in impedance caused by the ingestion of a non-conductive meal and can be altered by the postprandial offset. The length of the postprandial period is three times that of the preprandial period (the total length of the signal depends on the total number of points selected, *n*).

One of three different algorithms may be selected to generate the emptying curve; alpha, beta and gamma. The alpha curve represents an exponential empting curve often produced by simple meals such as water (see equation 7.1). The beta curve is a linear gradient until the preprandial impedance is reached, at which point the curve flattens to zero gradient. This type of emptying has been detected with both simple and complex meals (see equation 7.2). The gamma curve is non-linear and is produced by superimposing two sine waves (see equation 7.3). This type of emptying occurs when there is a mixing (plateau) period followed by a sharp emptying rate and has been detected predominantly with complex meals. The three emptying curves can be seen in Fig. 7.3.

$$f(x)_{\alpha} = a\exp(bx) + c \tag{7.1}$$

$$f(x)_{\beta} = \begin{cases} mx + c & \text{for } p \le x \le q - z \\ 0 & \text{for } x > q - z \end{cases} \tag{7.2}$$

$$f(x)_{\gamma} = d_1 \sin\left(\frac{2\pi k_1}{n} + \frac{\pi\phi_1}{180}\right) + d_2 \sin\left(\frac{2\pi k_2}{n} + \frac{\pi\phi_2}{180}\right) \tag{7.3}$$

Where (7.1) a = 20, b = -4.00×10^{-4} and c = – peak amplitude (see Fig. 7.2)[2]

(7.2) $p = 0.25n$, $q = 0.75n$, m and c are determined by n, $z = 3000$

(7.3) d = amplitude, k = number of cycles and ϕ = phase

The values for d_1, d_2, k_1, k_2, ϕ_1 and ϕ_2 may be varied by the operator but are usually set to the following: d_1 = 5.00, d_2 = 14.00, k_1 = 1.24, k_2 = 0.50, ϕ_1 = 180 and ϕ_2 = 122. From Fig. 7.2 it is possible to see that there are a number of variables that alter the characteristics of the signal. The peak amplitude simply adjusts the impedance of the highest point of the signal; it does not affect the nature of the signal itself. The postprandial offset and scale change the value of the postprandial period by equation 7.4.

$$f(x) = (\text{scale} \times x) + \text{offset} \tag{7.4}$$

Changing the postprandial offset will alter the deflection of the signal representing the ingestion of the meal while changing the scale will alter the emptying rate of the signal.

[2] The c variable is offset by the peak amplitude so the equation becomes $y = 20\exp\left(-4\times10^{-4}\right) - 20$.

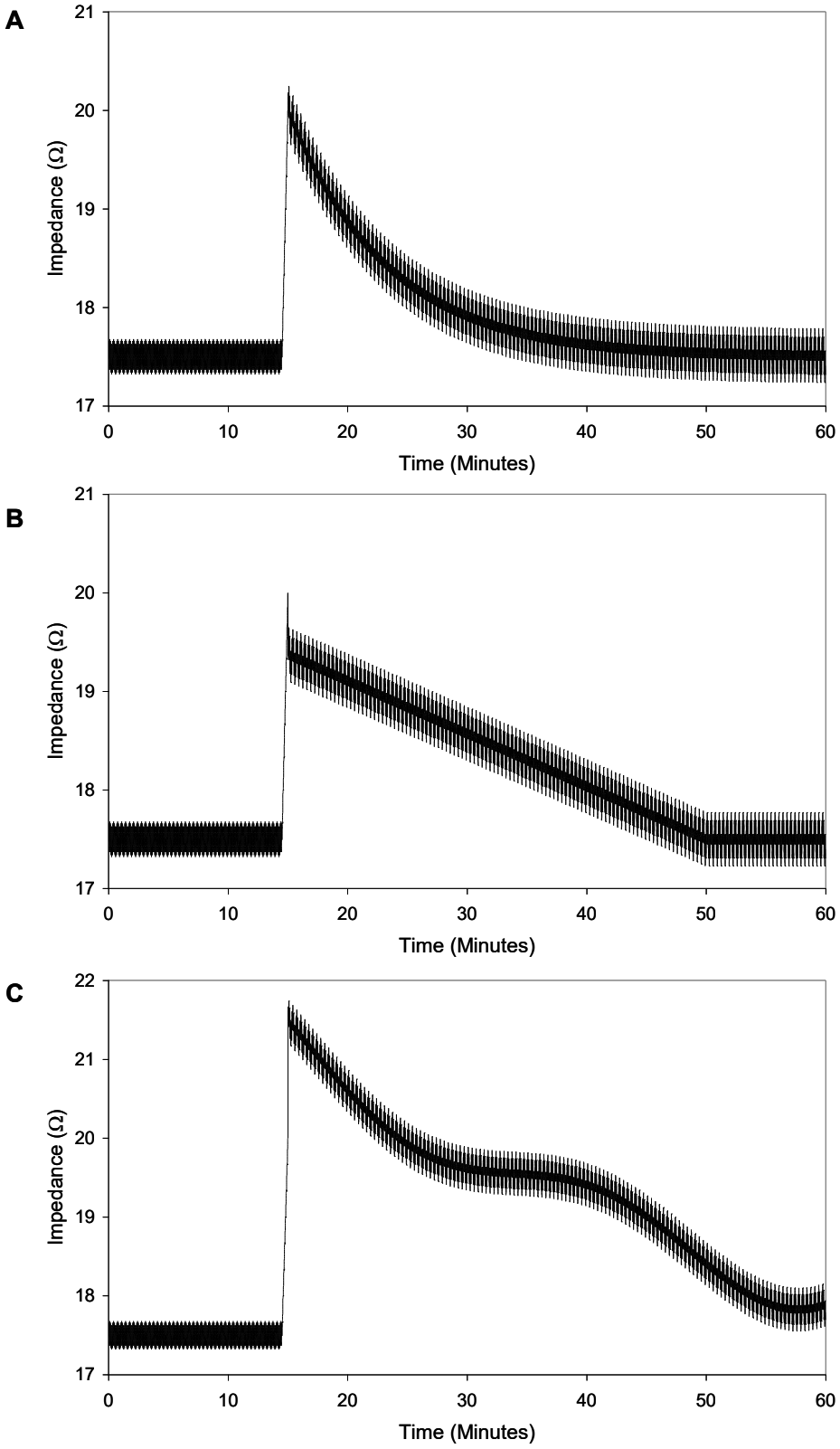

Fig. 7.3 **A** Pseudo-EIE signal representing exponential emptying. **B** Pseudo-EIE signal representing linear emptying. **C** Pseudo-EIE signal representing non-linear emptying.

7.2.3 Test signals

In the test signal window on the right hand side of the screen (see Fig. 7.2), it is possible to generate all of the signals in Fig. 7.1. The basic signal generator produces sinusoidal, square triangular and saw-tooth signals with the option of varying the number of points, phase, amplitude and frequency. These are shown in Fig. 7.4 and their formulae are given as follows.

The sinusoidal signal is represented by equation 7.5 where a = amplitude, i = 0, 1, 2,…, n-1, n is the number of samples and f = the normalised frequency (cycles per sample).

$$f(x)_{sinusoid} = a \cdot \sin\left(\text{phase}[i]\right) \tag{7.5}$$

where $$\text{phase}[i] = \text{phase} + \left(f \cdot 360 \cdot i\right)$$

The triangle wave is represented by equation 7.6 where a = amplitude, i = 0, 1, 2,…, n-1, n is the number of samples and f = the normalised frequency (cycles per sample).

$$f(x)_{triangle} = a \cdot \text{tri}(\text{phase}[i]) \tag{7.6}$$

where $$\text{tri}(\text{phase}[i]) = \begin{cases} \dfrac{p}{90} & 0 \le p < 90 \\ 2 - \dfrac{p}{90} & 90 \le p < 270 \\ \dfrac{p}{90} + 4 & 270 \le p < 360 \end{cases}$$

$$p = \text{phase}[i] \bmod 360$$

$$\text{phase}[i] = \text{phase} + \left(f \cdot 360 \cdot i\right)$$

The modulo function is expressed as follows.

$$x \bmod y = x - \left\{ y \cdot \text{floor}\left(\frac{x}{y}\right)\right\}$$

where floor(r) rounds r down, giving the lowest integer nearest to r, meaning that $r \in \mathbb{R}$, floor(r) $\in \mathbb{Z}$ for example floor(2.9) = 2 and floor (-2.3) = -3.

The square wave is represented by equation 7.7 where a = amplitude, i = 0, 1, 2,…, n-1, n is the number of samples and f = the normalised frequency (cycles per sample).

$$f(x)_{square} = a \cdot square(\text{phase}[i]) \tag{7.7}$$

where

$$square(\text{phase}[i]) = \begin{cases} 1.0 & 0 \le p < \left(\frac{\text{duty}}{100} \cdot 360\right) \\ -1.0 & \left(\frac{\text{duty}}{100} \cdot 360\right) \le p < 360 \end{cases}$$

$$p = \text{phase}[i] \bmod 360$$

$$\text{phase}[i] = \text{phase} + (f \cdot 360 \cdot i)$$

Duty refers to the duty cycle, which is the desired ratio (expressed as a percentage) of the duration of the phase of the pulse to the period of one cycle (1/frequency). This means that a duty cycle of 50% will result in a square wave.

The saw tooth wave is represented by equation 7.8 where a = amplitude, i = 0, 1, 2,…, n-1, n is the number of samples and f = the normalised frequency (cycles per sample).

$$f(x)_{sawtooth} = a \cdot sawtooth(\text{phase}[i]) \tag{7.8}$$

$$sawtooth(\text{phase}[i]) = \begin{cases} \frac{p}{180} & 180 \le p < 180 \\ \frac{p}{180} & 0 \le p < 360 \end{cases}$$

$$p = \text{phase}[i] \bmod 360$$

$$\text{phase}[i] = \text{phase} + (f \cdot 360 \cdot i)$$

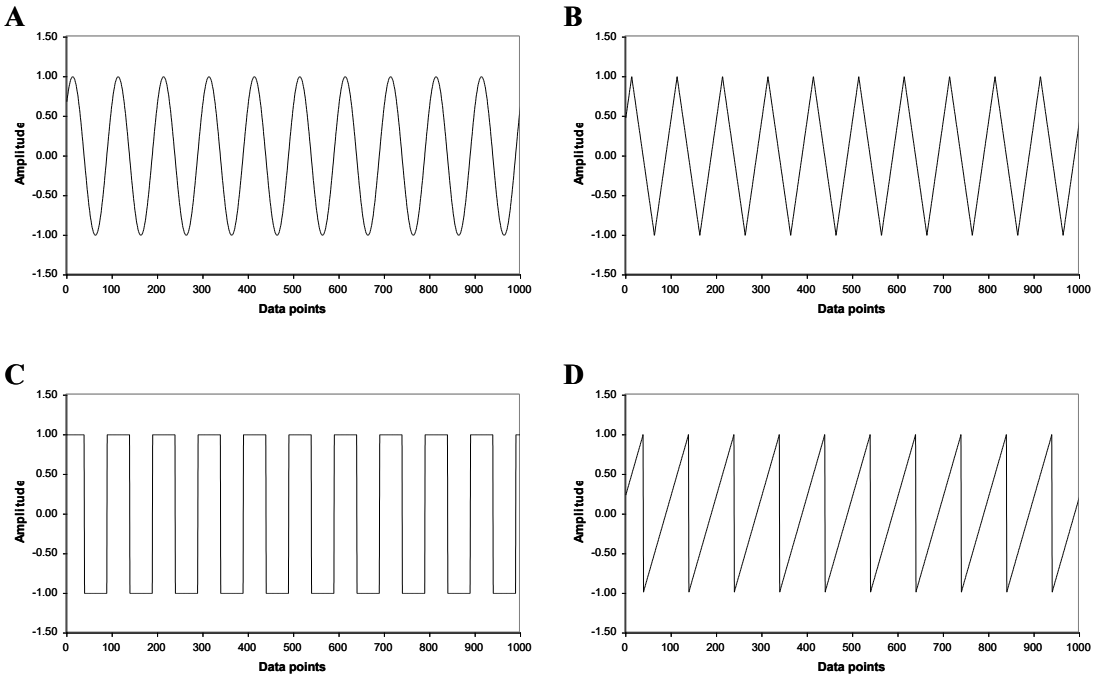

Fig. 7.4 **A** Sinusoidal signal **B** triangle signal **C** square wave and **D** saw tooth signal.

The chirp signal (Fig. 7.5) is essentially a sinusoid with varying frequency and is generated using the equation 7.9 where a = amplitude, i = 0, 1, 2,…, n-1, f_1 is the start frequency in normalized units of cycles/sample, f_2 is the end frequency in normalized units of cycles/sample and n is the number of samples. An example is given in Fig. 7.12.

$$f(x)_{chirp} = a\sin\left\{\left(\frac{A}{2i+B}\right)i\right\} \tag{7.9}$$

where $$A = \frac{2\pi(f_2 - f_1)}{n} \text{ and } B = 2\pi(f_1)$$

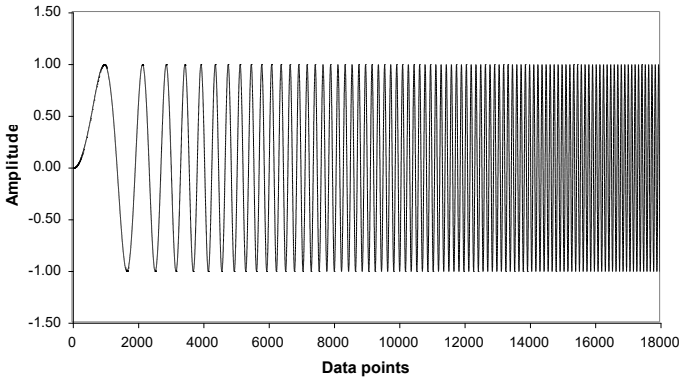

Fig. 7.5 Chirp signal with f_1 = 0 and f_2 = 3cpm.

The Pseudo EIE software can also generate two types of white noise signals; uniform white noise and Gaussian white noise (see Fig. 7.6). The equation for uniform white noise is given in equation 7.10 and the equation for Gaussian white noise is given in equation 7.11. Both uniform white noise and Gaussian noise algorithms generate a pseudorandom sequence (with a uniform or Gaussian distribution respectively) using a modified version of the Very-Long-Cycle random number generator algorithm [Wichman B, 1987].

The pseudorandom sequence produces approximately 2^{90} samples before the pattern repeats itself. The probability density function, $f(x)_{uniform}$, of the uniform white noise is given in equation 7.10 where a is the absolute value of the amplitude.

$$f(x)_{uniform} = \begin{cases} \dfrac{1}{2a} & \text{if } -a \le x < a \\ 0 & \text{elsewhere} \end{cases} \tag{7.10}$$

The probability density function, $f(x)$ of the Gaussian-distributed Gaussian Noise is given in equation 7.11 where s is the absolute value of the standard deviation.

$$f(x)_{Gaussian} = \frac{1}{s\sqrt{2\pi}} e^{-\left(\frac{1}{2}\right)\left(\frac{x}{s}\right)^2} \tag{7.11}$$

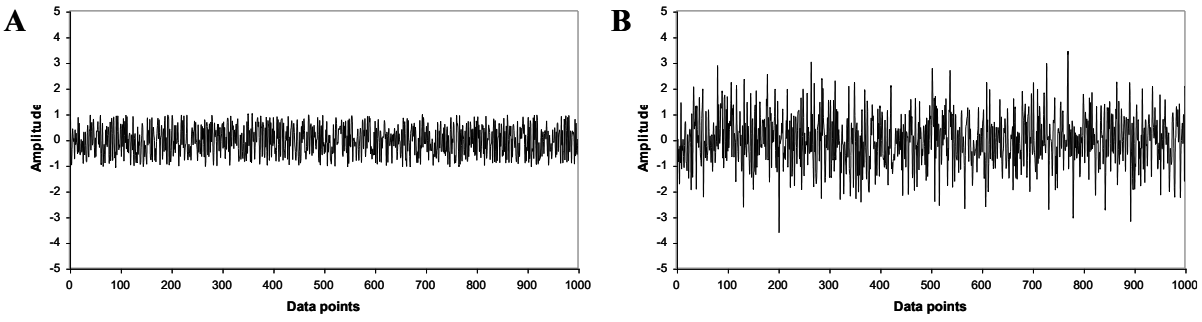

Fig. 7.6 **A** Uniform white noise and **B** Gaussian distributed white noise.

7.2.4 Artefacts

Fig. 7.2 shows that Gaussian noise can be added to the pseudo EIE or test signal to simulate the random noise found in real EIE signals (see Fig. 7.7A). However, motion artefacts (see section 5.3.3) often manifest themselves as positive or negative spikes in the signal, which have a detrimental effect on the results following signal processing [Freedman MR, 2005]. The signal processing techniques employed to remove these artifacts are discussed in section 6.2.2. Spikes can be added to the pseudo EIE signals (Fig. 7.7B) so that the efficacy of the algorithms designed to remove them can be tested.

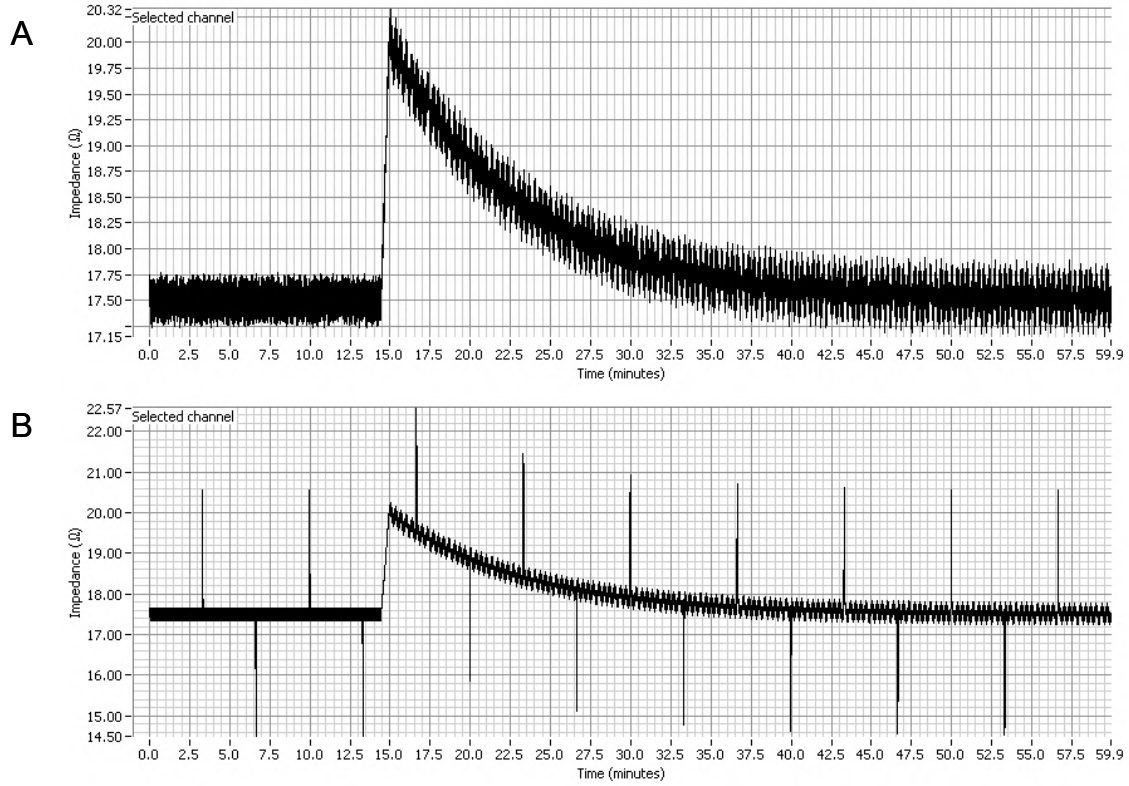

Fig. 7.7 **A** Pseudo EIE signal with uniform white noise. **B** Spikes representing motion artifacts have been added.

7.2.5 Electrode positioning

The second page of the software is entitled 'Electrode positioning' (see Fig. 7.8) and it allows the user to enter imaginary electrode positions for the pseudo-EIE signal. The software calculates the distances and angles between the three electrode midpoints (shown as blue circles).

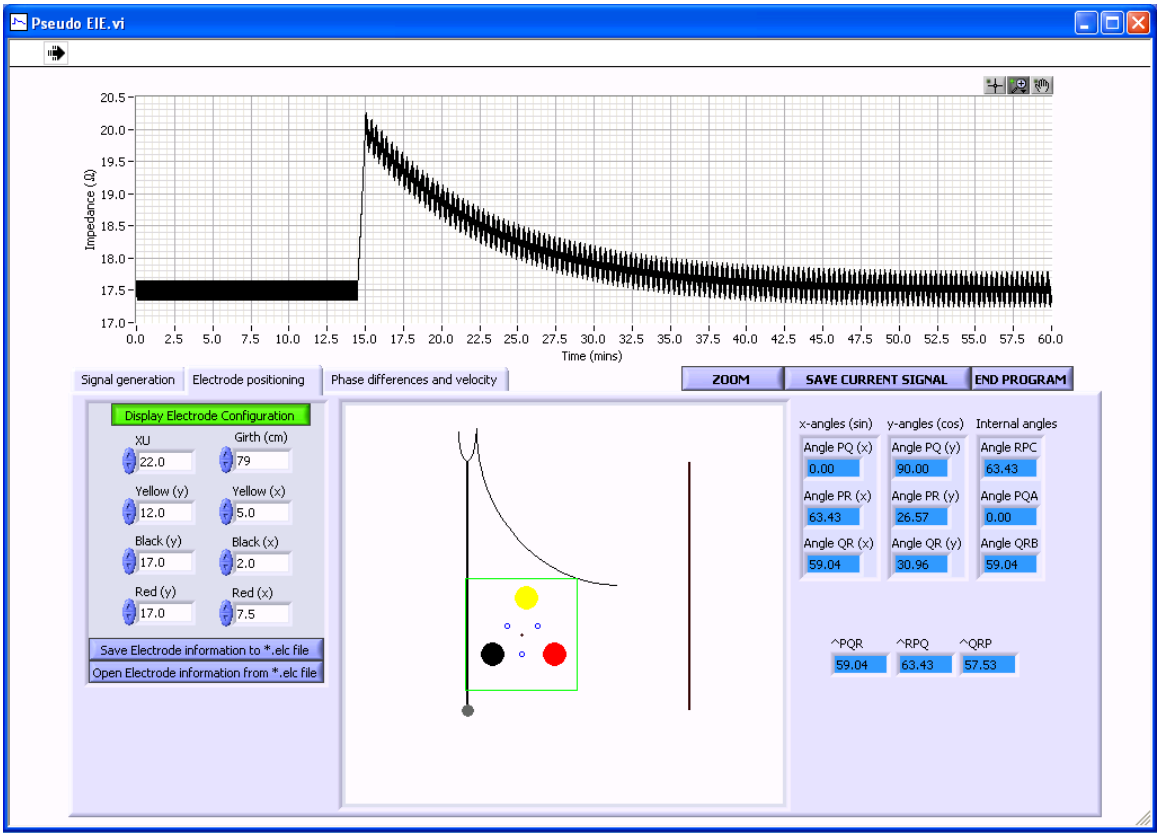

Fig. 7.8 Screen shot of the electrode placement page.

The coordinate system used for the mid points between electrodes is shown in Fig. 7.9. The notation used is as follows: the midpoint between the black and yellow pairs of electrodes is referred to as point P with coordinates (g,h), the midpoint between the yellow and red pairs of electrodes is referred to as point Q with coordinates (i,j) and the midpoint between the red and black pairs of electrodes is referred to as point R with coordinates (k,l).

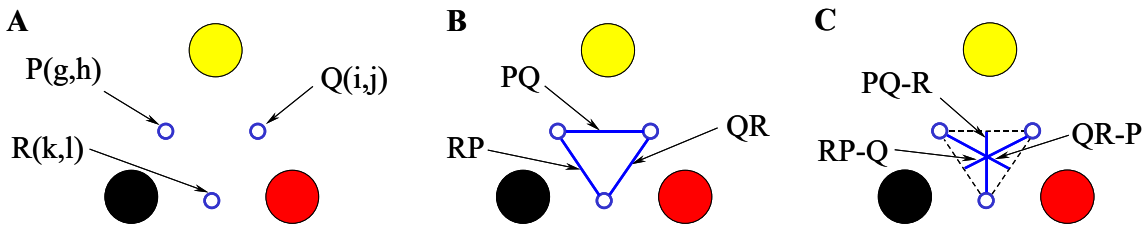

Fig. 7.9 **A** Coordinate system for the midpoints (P, Q and R) of each electrode pair. **B** Connecting lines (PQ, QR and RP) between the midpoints of each electrode pair. **C** Perpendicular distances from two midpoints to the third.

7.2.6 Phase differences for the simulation of velocity

The next stage in pseudo signal generation is altering the phase between the signals to simulate the movement of gastric contractile events. Fig. 7.10 is the screen shot for the phase differences that may be introduced and the prospective velocity measurements based on the distances between the midpoints and their respective phase differences. Pseudo signals with phase are differences are used in the EIE analysis software to verify the velocity calculations (see sections 6.2.9 and 6.2.10).

The phase of both signals in each field plane (the plane between two pairs of electrodes) can be adjusted using the controls at the bottom of the pseudo-EIE window. The software converts the units of each phase into time (in seconds) and divides the phase difference between two of the midpoints to calculate the velocity of imaginary gastric contents between each of the field planes.

Since phase is expressed in degrees, the equivalent time difference may be calculated by equation 7.12 where Δt = the phase difference in seconds, $\Delta\phi_d$ = the phase difference in degrees and f_g = the gastric frequency in Hertz (cycles per second).

$$\Delta t = \frac{\Delta\phi_d}{360} \cdot \frac{1}{f_g} \tag{7.12}$$

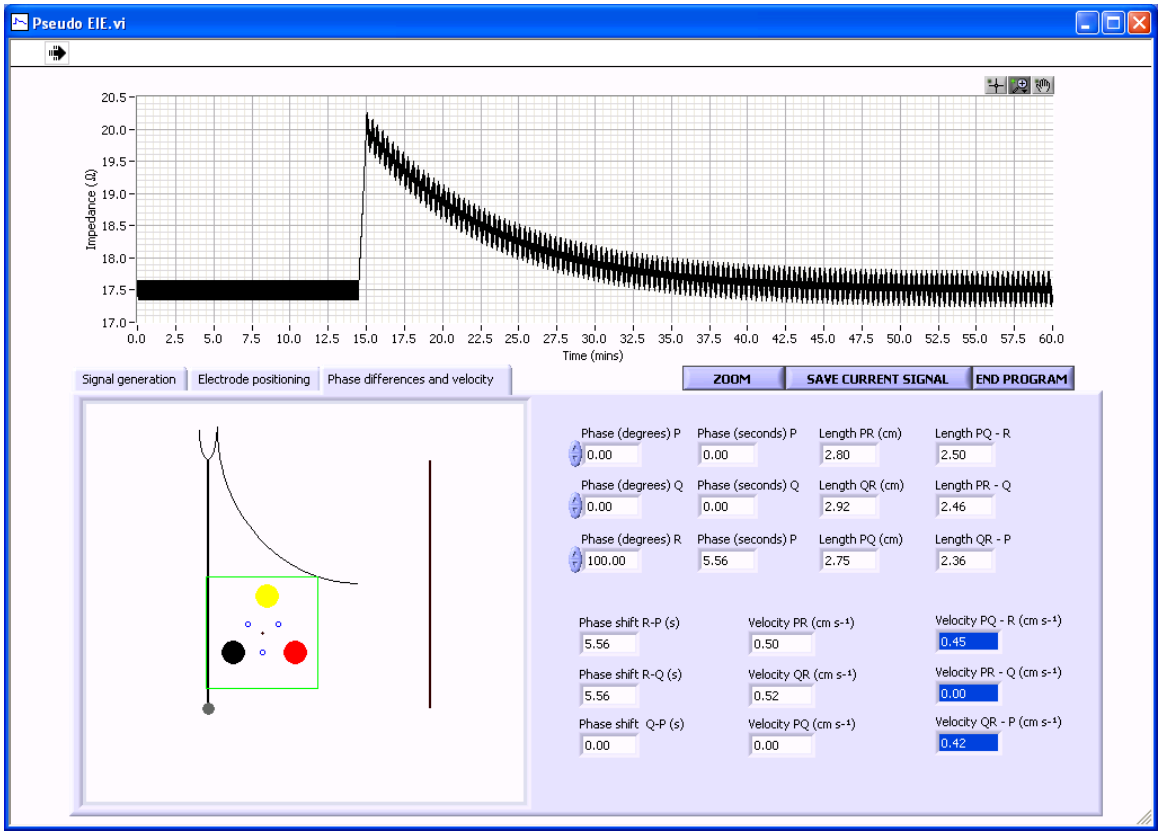

Fig. 7.10 Screen shot of the phase difference and velocity page.

A phase difference in one electrode plane will enable the pseudo signal to simulate the velocity of gastric content by using the simple relationship between velocity, displacement and time given in equation 7.12 where **v** = velocity (vector) and **d** = displacement (vector).

$$\mathbf{v} = \frac{\mathbf{d}}{\Delta\phi_s} \tag{7.13}$$

For example, if the phase of points P and Q is zero and the phase of point R is 102.10° the phase difference in seconds is 5.67s. If the displacement of PQ-R were 2.25cm, then from equation 7.6 the 'pseudo-gastric-content' would be progressing between the midpoint of PQ and R with an expected approximate velocity of 0.40cms^{-1}.

8 RESULTS OF EXPERIMENTAL INVESTIGATIONS

8.1 Analysis of the effects of the fat content of meals on gastric physiology

8.1.1 Hypotheses

The following experiments were designed to test the gastro-physiological effects of the three liquid meals. Table 5.2 detailed these as meal A (Volvic mineral water), meal B (low fat liquid meal) and meal C (high fat semi-solid meal).

Hypothesis 1 (Half emptying time)

The comparison between simple, low fat liquid and high fat semi-solid meals is designed to highlight differences in gastric physiology due to the processing of lipids discussed primarily in section 2.4.4 and illustrated in Fig. 2.15 (also see sections 2.2.2 and 2.3.1). Consequently, the first hypothesis states that the fat content will delay gastric emptying due to the various changes in contractility required for the trituration and emulsification of the fat. This hypothesis also states that the mechanisms that delay gastric emptying with the inclusion of fat in the meal will alter the shape of the emptying curve so that simple exponential emptying is less likely.

Hypotheses 2 and 3 (Antral contractility and gastropyloroduodenal coordination)

There are differences in gastropyloroduodenal coordination between simple, low fat liquid and high fat semi-solid meals based on the fact that fatty meals must be actively mixed with gastric secretions before they can be absorbed by the body (see section 2.5.2 and Fig. 2.23). Since fat-induced delays in gastric emptying are brought about by an increase in pyloric contractility [Boulby P, 1999; Indireshkumar K, 2000] and propagating antral contractions [Indireshkumar K, 2000], measurements of gastric power and velocity should be significantly different between the three meal types. Therefore, the second and third hypotheses state that measurements of contractility and velocity differ significantly between simple, low fat liquid and high fat semi-solid meals.

Hypothesis 4 (Frequency shift)

The changes in the frequency of gastric contractions measured by Electrogastrography (EGG) are usually related to pathological change. However, postprandial reductions in the gastric frequency have been reported in healthy volunteers using EGG. The fourth hypothesis states that if this effect is caused by a physiological process, it will be detected in the EIE signals.

Hypothesis 5 (Anthropomorphic effects)

A number of relationships between anthropomorphic measurements (age, weight, height, body mass index and girth) and selected variables of gastric motility have been investigated. The fifth hypothesis states that anthropomorphic differences will affect (i) gastric function and (ii) the Impedance deflection per Unit Volume (IUV) will be affected by BMI and girth.

Hypothesis 6 (Effects of gender)

There is some evidence that suggests that women empty solid meals more slowly due to the effects of natural hormonal changes caused by the menstrual cycle [Hermansson G, 1996]. It is possible that the same is true for semi-solid liquid meals (but unlikely to be true for simple or liquid meals). The sixth hypothesis states that the gastric half emptying time of semi-solid meals is shorter in men.

Hypothesis 7 (Postprandial respiratory power increase)

Section 6.2.14 suggested that the power of the respiratory contractions will increase following the ingestion of a meal. Therefore, the seventh hypothesis states that the Respiratory post to preprandial Power Ratio will be above 1 in a significant number of experiments.

8.2 Verification of the hypotheses

8.2.1 Experimental method

A total of 54 healthy volunteers (36 men and 18 women) between the ages of 22 and 57 (mean 30.7 and standard deviation of 10.1) with no history of gastrointestinal disorders and with a BMI below 30 (mean 22.2 and standard deviation of 2.7) participated in the following study. Each volunteer took part in one experiment and was given either meal A, B or C. Group A (n = 18) consisted of 12 men and 6 women with an average age (standard deviation) of 28.7 ± 9.5. Group B (n = 18) consisted of 13 men and 5 women with an average age (standard deviation) of 28.2 ± 8.7. Group C (n = 18) consisted of 11 men and 7 women with an average age (standard deviation) of 35.2 ±11.1. The ages across each group were not significant ($P > 0.05$) using the Mann-Whitney U test (M-W test). The majority of the experiments were carried out between the autumn of 2000 and spring of 2004. However, some of the data used came from experiments carried out by other researchers. Ten sets of experiments were carried out by Dr. Nadia Hadi; eight at the Nuclear Medicine Department at Kuwait Cancer Control Centre during the summer of 2003 and two at the University of Surrey during the spring of 2001. Three of the studies were carried out by Dr. Anastasia Giouvanoudi during the spring and summer of 1998. The protocol used for all of the experiments was identical.

The testing of the hypotheses was carried out by the analysis of the quantitative values measured by EIE (section 6.2.16). In addition, the contractions detected for all subjects in each group were analysed for the total number of contractions, the percentage of contractions that registered a power density measured by the dyadic wavelet transform (section 6.2.8) above the 10% mean power density threshold, the percentage of contractions with positive velocity, the percentage of propagating contractions, the percentage of bradygastric and tachygastric contractions together with the contraction length, power, frequency, and velocity were analysed. In total, 1757 contractions were detected from the 18 studies in meal A, 2324 contractions were detected from the18 studies in meal B and 3126 contractions were detected from the 18 studies in meal C.

8.2.2 Hypothesis 1: Gastric half emptying time and emptying curve

The half emptying times for each EIE experiment were calculated using baseline extrapolation and deflection midline (see section 6.2.4). Since the data were not normally distributed, it was not possible to use standard parametric tests to assess statistical significance. Therefore, the M-W test (non-parametric) was used to calculate the statistical significance between two of the three groups, giving a total of the three combinations; A – B, A – C and B – C. The test analyses the sum of the ranks for the two groups separately and when the number in samples is greater than 5, a standard *z*-test approximation may be used (equation 8.1) where *m* and *n* are the sizes of the two groups. The sum of the ranks is calculated for both groups and *U* is defined as the smallest of the two. Statistical significance was defined as $P < 0.05$.

$$z = \frac{U + 0.5 - \left\{ \frac{m(N+1)}{2} \right\}}{\sqrt{\left(\frac{mn(N+1)}{12} \right)}} \tag{8.1}$$

The results in Table 8.1 show that there is a statistically significant difference in all three groups. Predictably however, the difference is greatest between the water and high fat semi-solid meal (A and C), less significant between the low fat liquid and semi-solid meal (B and C) and the least significant between the water and the low fat liquid meal (A and B).

Table 8.1 M-W test of half emptying times

Meal A – Meal B	Meal A – Meal C	Meal B – Meal C
$P < 0.05$	$P < 0.001$	$P < 0.01$

The comparison between the half emptying times for each meal can be seen in the box and whisker plots in Fig. 8.1. In all box and whisker plots the thick line in the centre of the box represents the median and the upper and lower ends of the box represent the upper and lower quartiles (25^{th} and 75^{th} percentiles respectively). Outliers are defined as values that fall between 1.5 and 3.0 box lengths while far outliers exceed 3.0 box lengths. The whiskers represent the smallest and largest values that are not outliers.

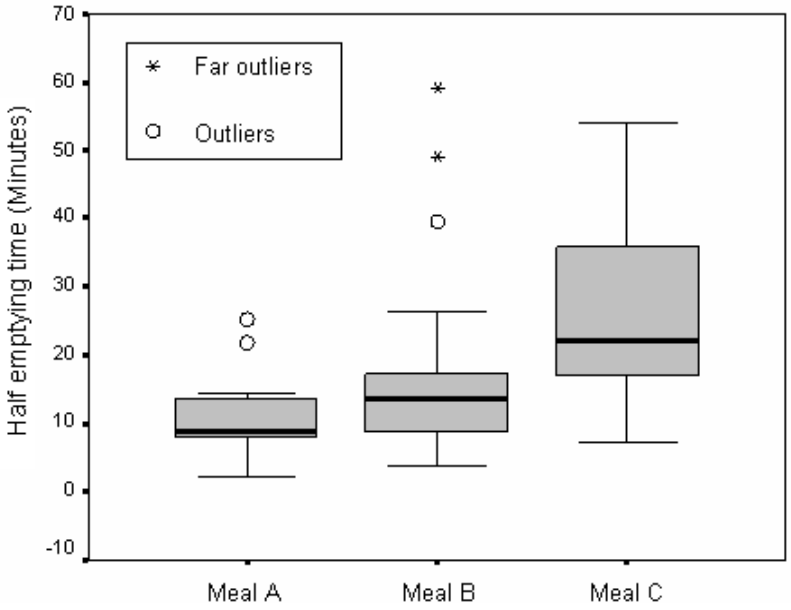

Fig. 8.1 Box plots for the half emptying times of each meal type.

Colleagues have felt that the processing of the low fat liquid meal (meal B) is highly variable and volunteer dependent. To be precise, the gastro-physiological parameters recorded are likely to vary greatly because sometimes the low fat liquid meal is processed as a simple meal whereas with other subjects the gastro-physiological parameters resemble those of a high fat semi-solid meal [Hadi NA, 2001]. This explains the large range of meal B (55.5 minutes) compared to meal A (23.3 minutes) and meal C (46.8 minutes).

Analysis of the class of emptying curve (see section 6.2.5) was carried out for each group by calculating the percentage of each class (exponential, linear and non-linear). The hypothesis implies that gastric emptying by sustained antral pressure in conjunction with pyloric relaxation (see section 2.6.2) produces an exponential emptying curve whereas the need to mix low fat liquid and high fat semi-solid meals with gastric secretions produces a linear or nonlinear emptying curve.

Consequently, the hypothesis implies that a higher proportion of linear and non-linear emptying curves will occur in the B and C meal groups. The proportion of exponential emptying curves in the meal A and B groups is 55.6% and in the meal C group is 38.9%. Although the proportion of linear emptying curves remains fairly constant (27.8%, 22.2% and 27.8% in groups A, B and C respectively), the incidence of nonlinear emptying curves increases from 44.4% in groups A and B to 61.1% in group C.

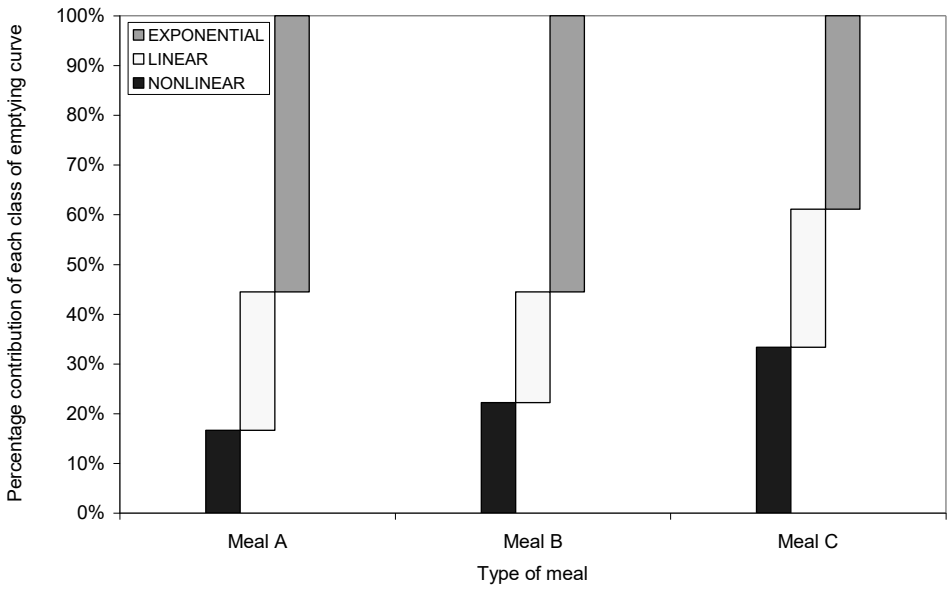

Fig. 8.2 Proportion of each class of emptying curve versus the meal type

To test the statistical significance of the difference between exponential and non-exponential emptying, χ^2 tests (with Yates' correction since there is only one degree of freedom) were used between meals A and B, A and C and B and C (see Table 8.2). The results indicate that the rise in non-exponential emptying curves in the meal C group was not significant ($P > 0.05$) using the χ^2 test with Yates' correction.

Table 8.2 χ^2 tests between exponential and non-exponential emptying

Observed values

MEAL	EXP	NONEXP	TOTAL
A	10	8	18
B	10	8	18
	20	16	36

MEAL	EXP	NONEXP	TOTAL
A	10	8	18
C	7	11	18
	17	19	36

MEAL	EXP	NONEXP	TOTAL
B	10	8	18
C	7	11	18
	17	19	36

Expected values

MEAL	EXP	NONEXP	TOTAL
A	10	8	18
B	10	8	18
	20	16	36

MEAL	EXP	NONEXP	TOTAL
A	8.5	9.5	18
C	8.5	9.5	18
	17	19	36

MEAL	EXP	NONEXP	TOTAL
B	8.5	9.5	18
C	8.5	9.5	18
	17	19	36

Meal A – Meal B	Meal A – Meal C	Meal B – Meal C
NS	*NS*	*NS*

Three different curves (linear, exponential and 4th order polynomial) were fitted to the empting period of the EIE signals to test the suitability of the classifications made by the pattern recognition algorithm (see section 6.2.15). Fig. 8.3 shows three box plots of the R^2 values for each of the three curves of best fit over the three classes.

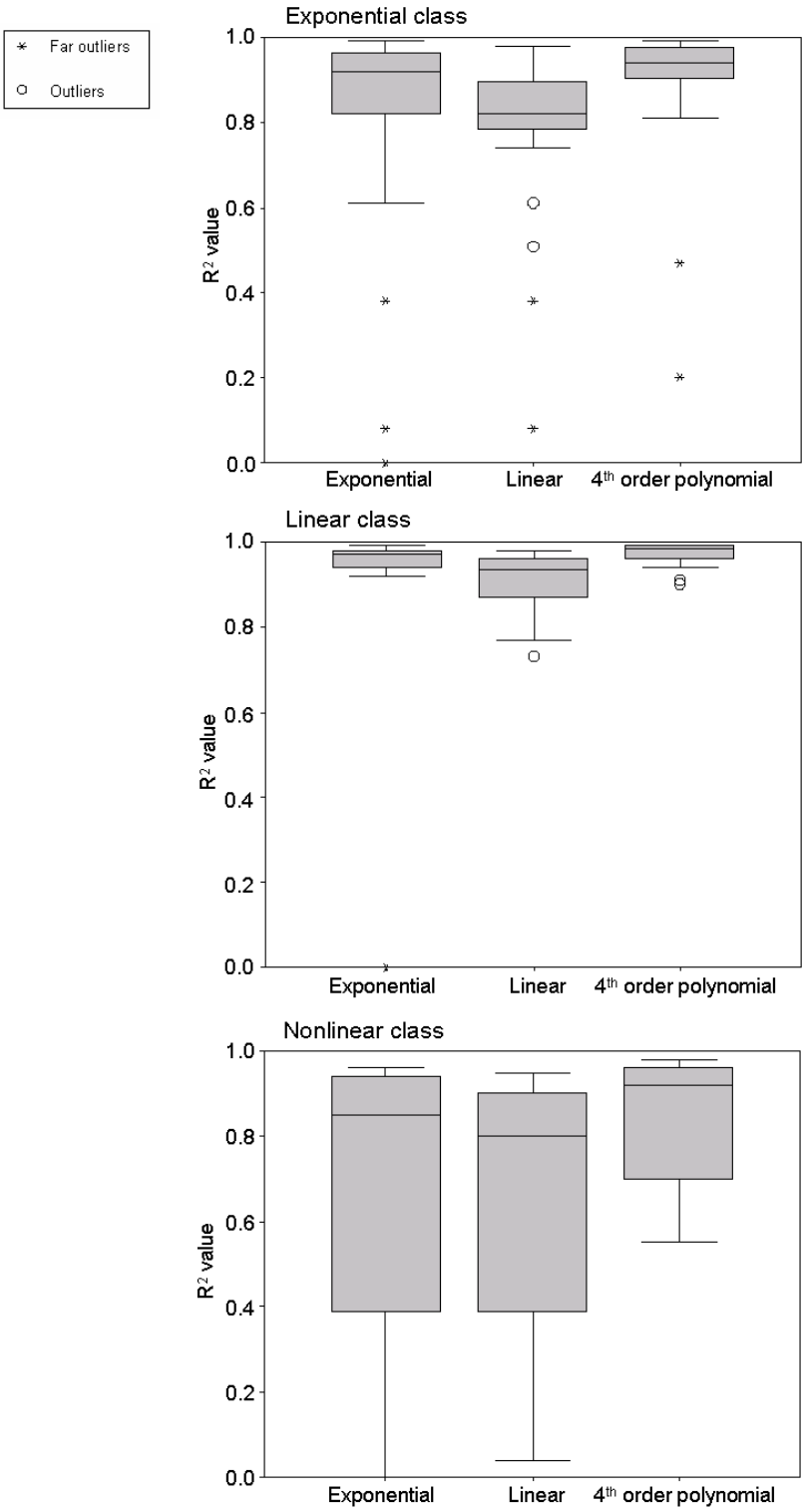

Fig. 8.3 Box and whisker plots of the R^2 values (see Appendix E) of the three types of curve fitting for all three classes, classified by the pattern recognition.

Table 8.3 shows the statistical significance between the three curve fits (linear, exponential and 4th order polynomial) was tested using the Mann – Whitney U test. These results indicate that the changes in the R^2 values between the different types of emptying curve for each of the three classes shown in Fig. 8.3 were significant.

Table 8.3 Significant differences in R^2 values between the three types of emptying curve fit (EXP = exponential, LIN = linear and POLY = 4th order polynomial) for each class (exponential, linear and nonlinear).

Class	**EXP – LIN**	**EXP – POLY**	**LIN – POLY**
Exponential	EXP > LIN ($P < 0.05$)*	*NS* *	LIN < POLY ($P < 0.0001$) *
Linear	EXP > LIN ($P < 0.05$)†	*NS* *	LIN < POLY ($P < 0.005$) †
Nonlinear	*NS* *	EXP < POLY ($P < 0.05$) *	LIN < POLY ($P < 0.05$) *

* Equivalent to the predictions made in Table 6.8.

† Contrary to the predictions made in Table 6.8 due to the variability in R^2 for the polynomial fit (Fig. 8.3).

Further analysis of the pattern recognition classification was performed by comparison to human classification of the emptying curves. The acquired signals of all 54 experiments were shown to one other colleague, Dr. Nadia Hadi who was asked to intuitively classify the emptying curves into exponential, linear or non-linear classes. The procedure was repeated by myself. The percentage agreement between the classifications made by the computer (PC), myself (MF) and Dr. Nadia Hadi (NH) are given in Table 8.4.

Table 8.4 Percentage agreement in the classification of emptying curves between computer (PC), myself (MF) and Dr. Nadia Hadi (NH)

	PC - MF	PC - NH	MF - NH	PC - MF - NH
Percentage agreement	61.11	44.44	72.22	42.59

The number of emptying curves classified into exponential and non-exponential (linear and nonlinear) groups by the computer, myself and Dr. Nadia Hadi are shown in Fig. 8.4.

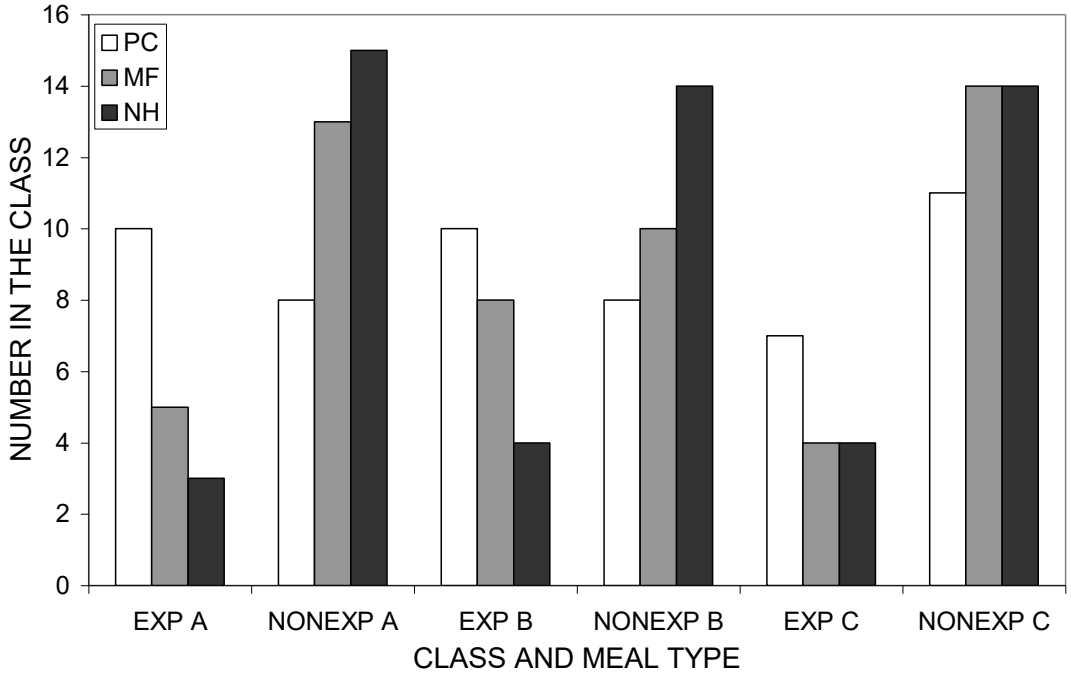

Fig. 8.4 Number of emptying curves classified into the exponential class (EXP) and non-exponential class (NONEXP) by the computer (PC), myself (MF) and Dr. Nadia Hadi (NH) for each meal type, A, B and C.

8.2.3 Hypotheses 2 and 3: Antral contractility and gastropyloroduodenal coordination

The relative postprandial increase in gastric contractile power with respect to the five preprandial power indices are: the Mean Power Ratio (MPR); JTFT Power Ratio (JPR); Gastric Contractility Ratio (GCR); Contractile Incidence Ratio (CIR); and the Maximum frequency Amplitude Ratio (MAR). However, no statistical significance was found using the M-W test with any of the gastric contractility ratios for any of the meal combinations except for the GCR between meals A and B (table 8.10).

The flaw in analysing the increases in postprandial contractility is that during the fasting state the stomach may be involved in the contractile phases of an MMC (section 2.4.3). Furthermore, if highly contractile phases of the MMC are interrupted by ingestion it is possible that the gastric contractility will decrease (Fig. 8.5). Additionally, the ingestion of water may not abolish the MMC contractions leading to ambiguous results.

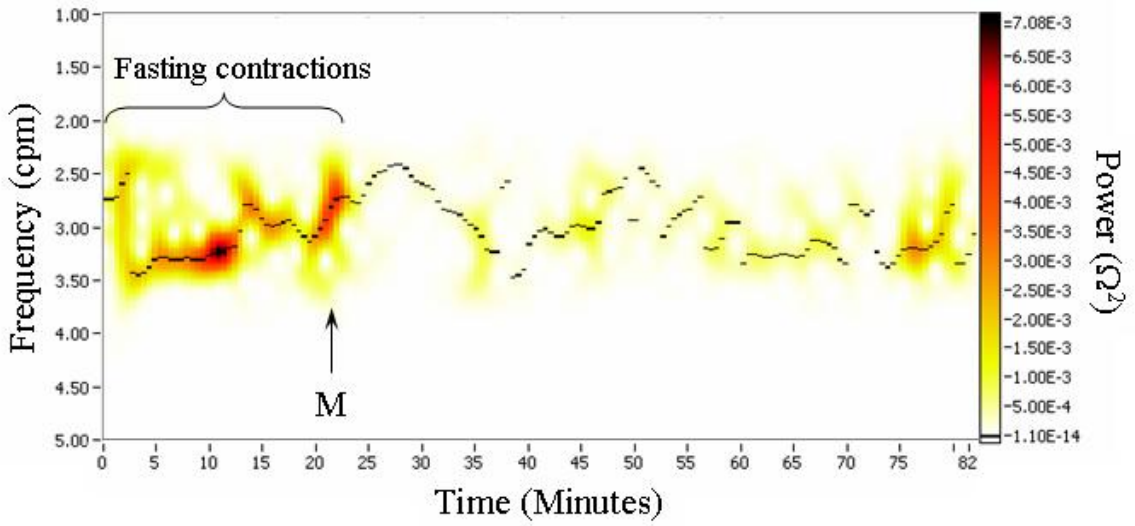

Fig. 8.5 Termination of the MMC contractions after the ingestion of meal C. The MPR was 0.33, the JPR was 0.11, the GCR was 0.40 and the CIR was 0.78.

There are five quantitative values in ACCESS that measure the power of gastric contractility: the Mean Power Index (MPI); JTFT Power Index (JPI); Gastric Contractility Index (GCI); the Contractile Incidence Index (CII); and the Maximum frequency Amplitude Index (MAI). No statistically significant increase was found in any of the five measurements between simple and semi-solid meals except for the GCI between meals A and C ($P < 0.05$). The graph of GCI versus meal energy in Fig. 8.6 shows that there is a decrease in GCI with meal fat content.

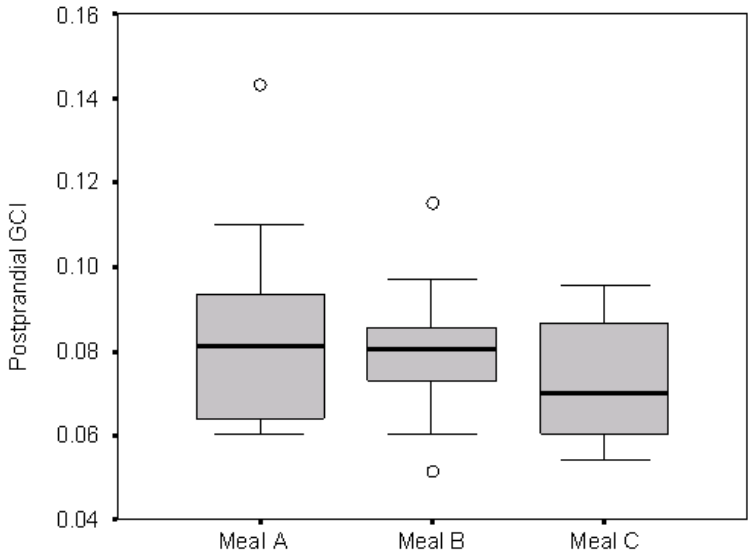

Fig. 8.6 The change of GCI with meal type (open circles are outliers).

Analysis of all recorded contractions in each meal type with a power density above the 10% mean power density threshold revealed that the percentage of contractions above the power threshold was not significantly different (83.44% in meal A, 85.33% in meal B and 82.98% in meal C). By analysing the mean power (mean ± sem) for all contractions above the 10% mean power density in each meal type, the power increases with meal energy density (Fig. 8.7). Nonetheless, at first glance it is clear that the error bars indicate large variations in power between the three groups. Application of a 2-tailed unequal variance t-test confirmed that despite an apparent trend, there is no significance between the pairs of groups.

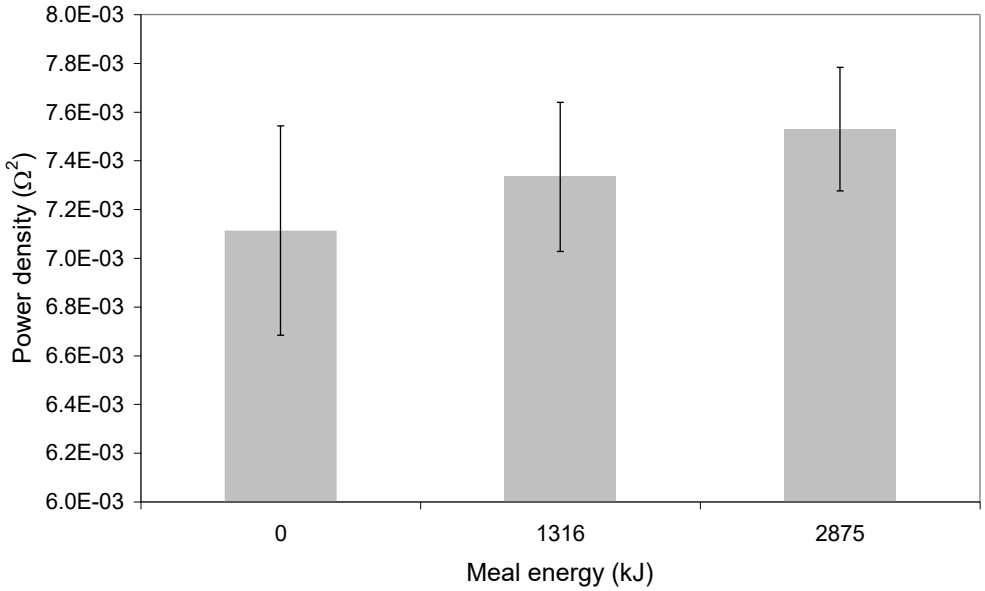

Fig. 8.7 Mean power density (Ω^2) against meal energy (kJ)

The measurement of the Mean postprandial Velocity Index (MVI) also yielded a positive result with the MVI being greater for the type C meal group compared to that of the type A and type B groups. The results are shown in the box and whisker plot in Fig. 8.8 and in Table 8.5. The ratio of the postprandial to the preprandial MVI (MVR) was not significant. This is likely to be related to unpredictability of contractile patterns in the preprandial period outlined in section 8.1.4.

Table 8.5 M-W test for the Mean Velocity Index (MVI) and Ratio (MVR).

	Meal A – Meal B	Meal A – Meal C	Meal B – Meal C
MVI	*NS*	$P < 0.005$	$P < 0.05$
MVR	*NS*	*NS*	*NS*

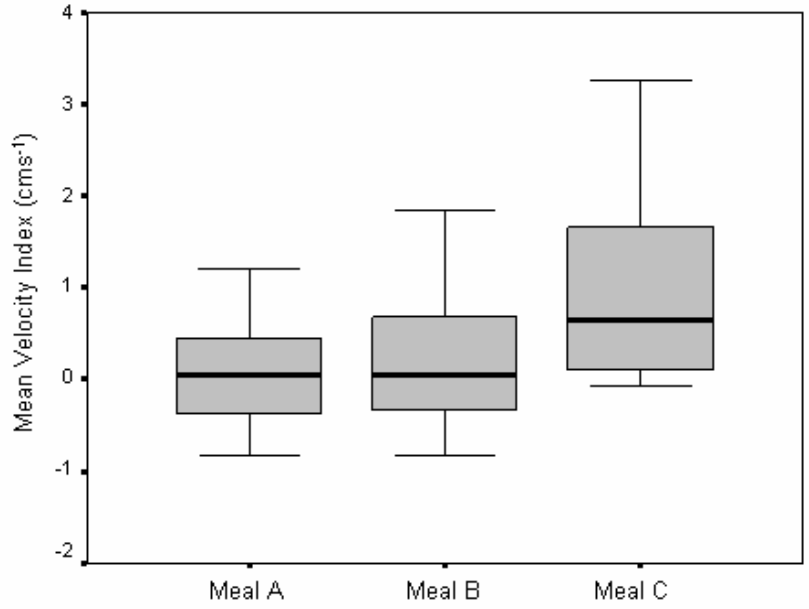

Fig. 8.8 Box and whisker plots showing the MVI for each meal type

Analysis of the individual contractions in each group showed that the mean velocity increased significantly with the energy of the meal (Fig. 8.9). Application of a 2-tailed t-test confirmed that there was a highly significant difference between all three groups (Table 8.6).

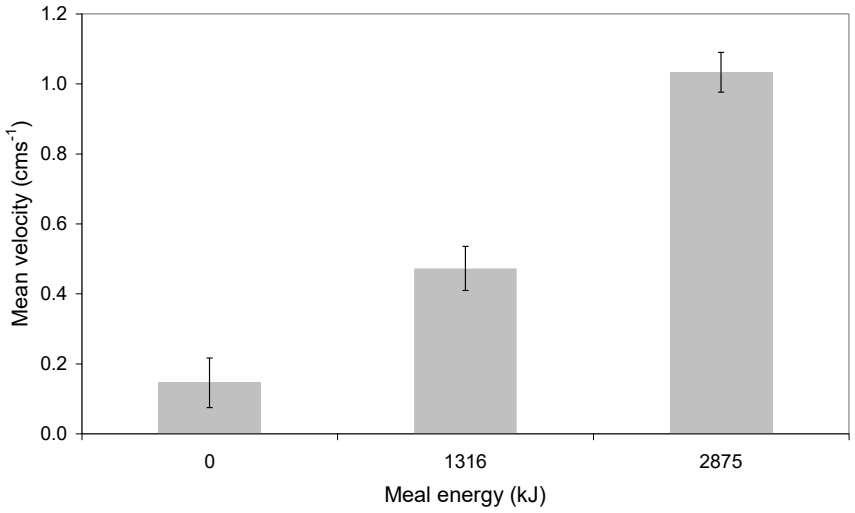

Fig. 8.9 Mean velocity vs. meal energy for all contractions above threshold

Table 8.6 T-test for mean velocity measured for all contractions above threshold

	Meal A – Meal B	Meal A – Meal C	Meal B – Meal C
Mean velocity	*P < 0.005*	*P < 0.001*	*P < 0.001*

Comparisons between the GCI, MVI and T50 for each meal type reveal a significant positive correlation using Spearman's rank correlation between the GCI and MVI in the meal type A group. No significant correlation was found in types B or C (Table 8.7).

Table 8.7 Spearman's rank correlation between GCI, MVI and T50

	Meal A	Meal B	Meal C
GCI – MVI	*0.51**	*0.33*	*0.36*
GCI – T50	*0.27*	*0.14*	*-0.22*
MVI – T50	*0.07*	*0.02*	*-0.10*

* $P < 0.05$

The duration of the each contraction was measured using the vector velocity analysis. The graph in Fig. 8.10 indicates a negative trend between the mean duration of contractions and the meal energy. Table 8.8 shows the application of a 2-tailed unequal variance t-test confirmed that there was a significant difference between all three groups.

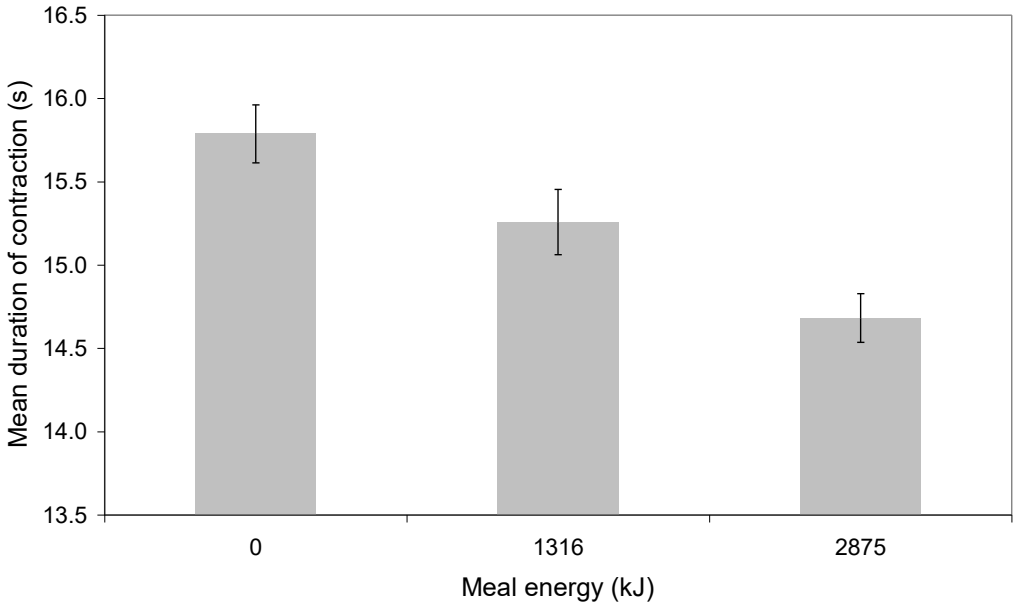

Fig. 8.10 Mean contractile duration vs. meal energy for all contractions above threshold.

Table 8.8 T-test for contractile duration measured for all contractions above threshold.

	Meal A – Meal B	Meal A – Meal C	Meal B – Meal C
Mean duration	*P < 0.05*	*P < 0.001*	*P < 0.05*

8.2.4 Hypothesis 4: Frequency shift

Section 6.2.12 discussed the measurement of changes in frequency during the postprandial region of the signal. Fig. 6.25 gave an example from EGG in which the frequency had decreased immediately after the ingestion of the meal. There is a physiological explanation for this frequency shift: distension of the gastric smooth muscle slows the frequency of the slow waves emanating from the pacesetter region (Fig. 2.7). A number of studies have confirmed this including Ladabaum who induced bradygastric contractions in subjects with nausea by inflating a intragastric balloon. The cutaneous EGG (Fig. 8.11) was recoded before and after inflation [Ladabaum U, 1998].

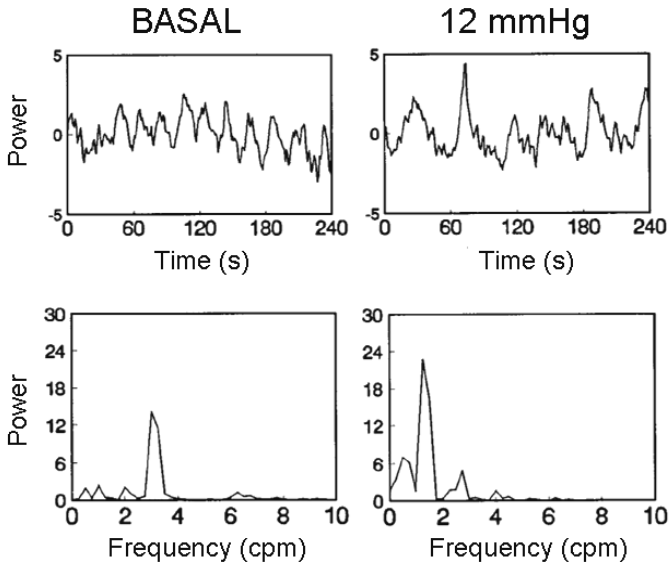

Fig. 8.11 Induction of bradygastria with distal gastric distension in a nauseated subject. Baseline EGG shows normal slow waves at 3.0cpm. Distal gastric distension at 12mmHg induces bradygastria of 1.5cpm [Redrawn from Ladabaum U, 1998].

During emptying the distension of the stomach falls and the slow wave frequency returns to normal, leading to the characteristic frequency 'hop'. A shift in the frequency of this nature was found in 38.9% of type A meals, 27.8 type B meals and 50.0% of type C meals.

Analysis of the frequencies of individual contractions in each group revealed that there was a statistically significant increase in contractile frequency between the type C meal and the type A and B meals ($P < 0.001$ in both cases). However, Fig. 8.12 shows that the magnitude of this difference is only +0.04cpm between meal A and C and +0.03cpm between meal B and meal C.

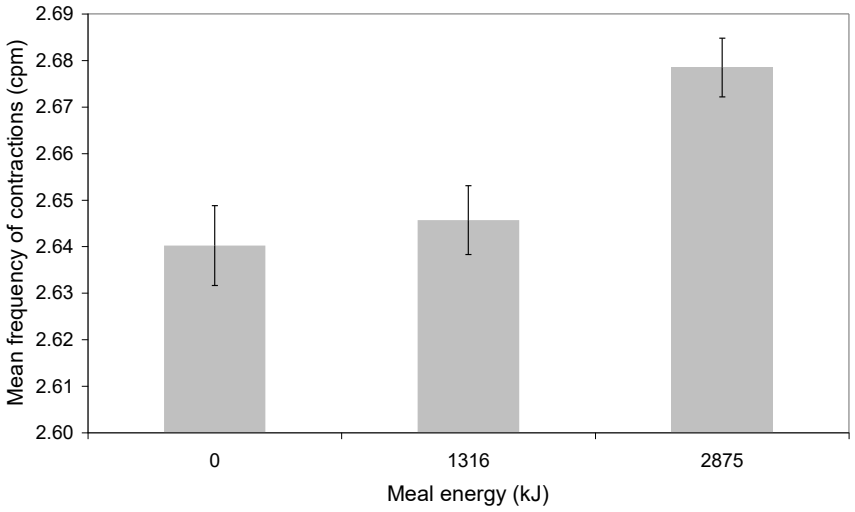

Fig. 8.12 Mean frequency vs. meal energy for all contractions above threshold.

Analysis of the histograms of the frequency of contractions for each group in Fig. 8.13 shows that the skew is more positive in meal types A and B than meal type C. Calculation of the skew confirms this observation (meal A: 0.51, meal B: 0.52 and meal C: 0.13).

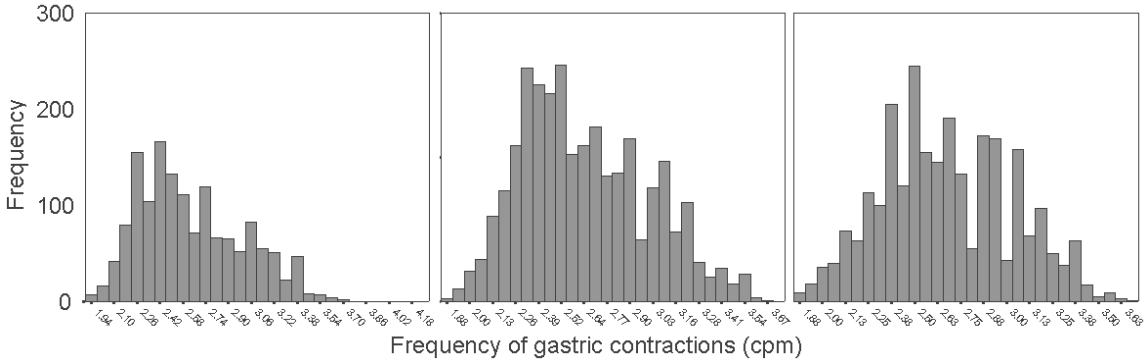

Fig. 8.13 Histograms of the frequency of gastric contractions showing the positive skew in groups A and B and small level of skew in group C. Each histogram contains 30 groups.

The positive skew shown in groups A and B explains the significance of the t-test, despite the fact that the magnitude of the difference is very small. Analysis of the median for each group also reveals an increase of 0.09cpm in the frequency recorded in the type C meal group. The medians for meals A, B and C are 2.56, 2.56 and 2.65 respectively. Analysis of the proportion of brady- and tachygastric contractions (with frequency below 2.4cpm and above 3.6cpm respectively) is given in Table 8.9.

Table 8.9 Percentages of bradygastric, gastric and tachygastric contractions.

	Meal A	Meal B	Meal C
Bradygastric	23.0%	22.8%	17.9%
Gastric	76.7%	77.0%	82.0%
Tachygastric	0.3%	0.2%	0.1%

The mean Dominant frequency Modulation Index (DMI) for each meal type were calculated as (mean ± sem) A: -0.05 ± 0.09; B: -0.23 ± 0.07; C: -0.12 ± 0.05. The difference between meal types A and B was significant ($P < 0.05$; M – W U test) indicating that meal type B causes a greater variation in the dominant frequency. Analysis of the polarity of the DMI revealed that a higher proportion of DMI values were above zero (meaning significant frequency modulation) in meal type A than meal types B and C (A: 44.4%; B: 22.2%; C: 27.8%).

No significance was found between the meal types for the Mean Frequency Ratio (MFR), Maximum Frequency Shift (MFS), postprandial Mean Frequency Index (MFI) or postprandial Maximum Frequency (MF) using the M – W U test (Table 8.10).

8.2.5 Hypothesis 5: Anthropomorphic effects

The age, weight, height, body mass index (BMI) and girth of each subject were measured to investigate whether they affected gastric function and whether the impedance deflection per unit volume (IUV) will be affected by BMI and girth. Each of the anthropomorphic measurements was compared to the T50, the GCI, the MVI and the percentage of propagating contractions. No significant correlations were found between any of these variables and the anthropomorphic measurements. Direct regression between both the BMI and the IUV and between the girth and the IUV did not correlate in either case ($R^2 = 0.20$ and $R^2 = 0.15$). However, after grouping the BMI into seven categories there was a linearly negative relationship between BMI and IUV (Fig. 8.14A). The girth was grouped into nine categories. There was no change in the IUV until approximately the 75 to 80cm category at which point a negative relationship was found (Fig. 8.14B).

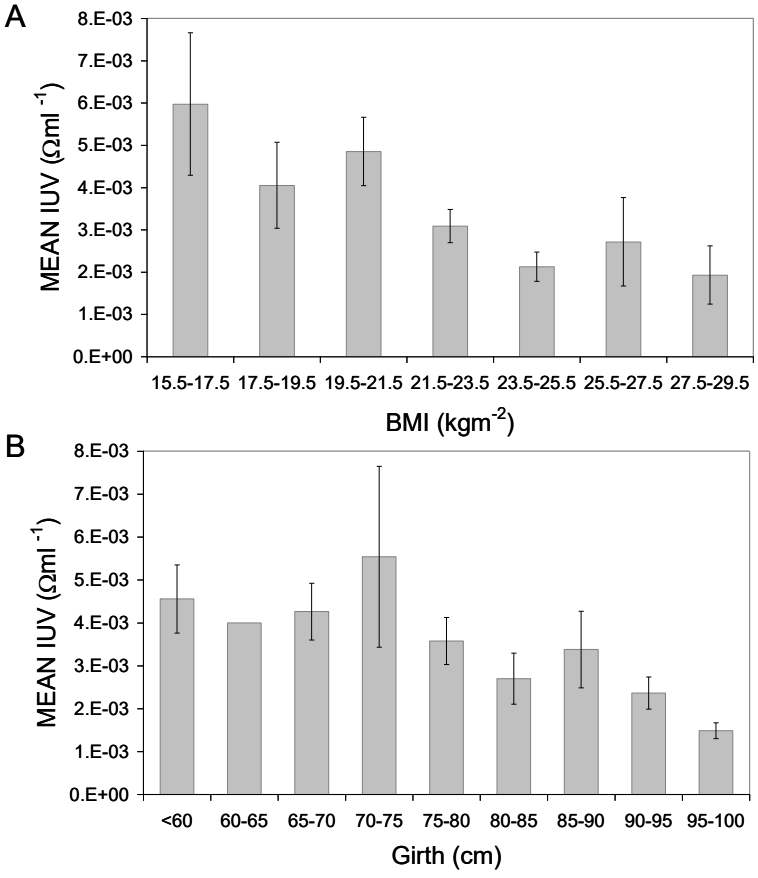

Fig. 8.14 **A** Mean IUV vs. BMI (sem). **B** Mean IUV vs. girth (sem).

The measurement of the IUV is designed to provide an indication of the system's sensitivity to the ingestion of the meal. The two graphs in Fig. 8.14 illustrate that BMI and girth both appear to reduce the sensitivity of the system.

Analysis of the IUV across the three meals is shown in Fig. 8.15. The median (± range) IUV of meal C was greater than meal A and B, (meal A: $2.7\times10^{-3} \pm 6.5\times10^{-3}$; meal B: $2.6\times10^{-3} \pm 8.6\times10^{-3}$; meal C $3.7\times10^{-3} \pm 1.1\times10^{-2}$; the differences were not significant using the M – W U test (A – B: $P = 0.24$; A – C: $P = 0.23$ and B – C: $P = 0.41$).

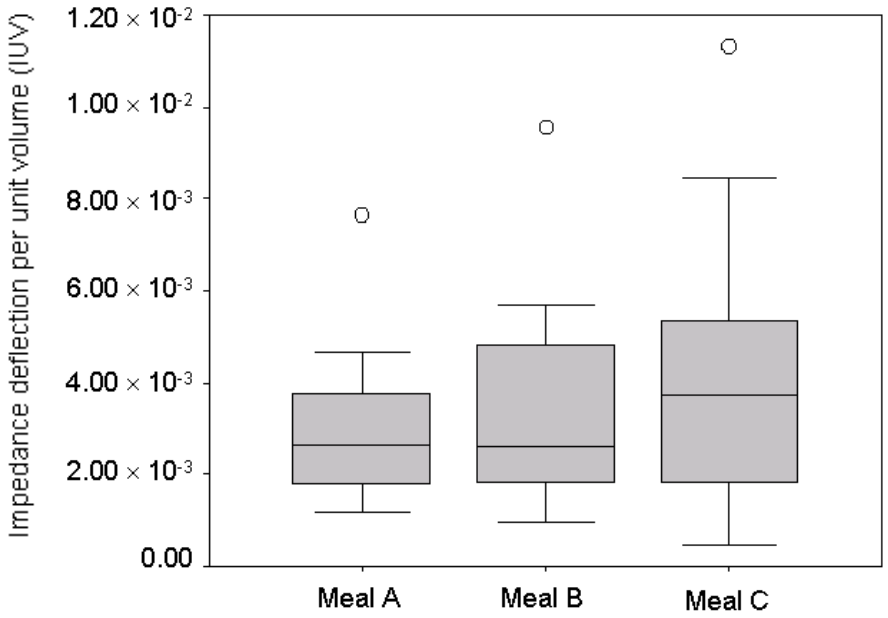

Fig. 8.15 Box and whisker plots of the maximum impedance deflection per unit volume (IUV) for each of the three meals.

8.2.6 Hypothesis 6: The effects of gender on gastric function

This hypothesis tested whether the gastric half emptying time of semi-solid meals is shorter in men than in women, as reported by Hermansson [Hermansson G, 1996]. No significant difference was found between the male and female groups (Table 8.10). However, the protocol did not restrict the participation of women in any of the studies to a particular phase of their menstrual cycle. It is likely that hormonal changes in women are responsible for the differences in gastric function. Therefore, in order to detect these differences it would be necessary to only carry out the experiments on women during the first ten days of their menstrual cycle.

8.2.7 Hypothesis 7: Postprandial respiratory power increase

The analysis of the post- to preprandial respiratory power ratio (RPR) revealed that only 51.9% of signals exhibited an RPR above 1. Linear regression with girth and BMI did not yield a positive correlation. Nevertheless, Fig. 8.16 shows a typical example of the respiratory postprandial amplitude increase observed occurring immediately after the ingestion of the meal and decreasing as the meal is emptied.

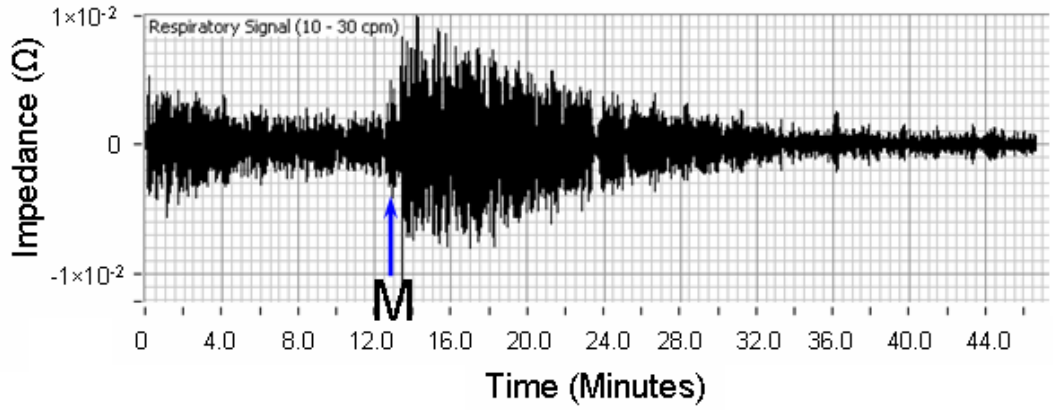

Fig. 8.16 The signal obtained after the application of a band pass filter with a lower cut off frequency of 10cpm and a higher cut off frequency of 30cpm.

It is possible that since the mean of the postprandial amplitude is measured, the effect on the amplitude of the respiratory signal caused by the initial increase in gastric volume following the ingestion of the meal is averaged out as the meal empties and the volume drops. However, there are also examples of respiratory signals that decrease in amplitude following the ingestion of the meal. This may be because in those cases, the volunteer relaxed after the active part of the experiment (the ingestion of the meal) had finished and furthermore, it was also reported in the experimental notes that some volunteers fell asleep after the ingestion of the meal.

Analysis of the Respiratory Power Ratio (RPR) between the three meal types did not reveal any significant differences (Table 8.10) although this may be because the increases in respiratory power do not last for the entire duration of the signal. The mean RFS for each meal type was (mean ± sem) A: -1.10 ± 0.40; B: 0.20 ± 0.34; C: -0.61 ± 0.32 showing no correlation. The mean RFS for meal type B was significantly different from meal type A ($P < 0.05$; M – W U) and from meal type C ($P < 0.05$; M – W U) but there is no obvious physiological reason for this.

8.2.8 Summary of results

Table 8.10 Summary of results where NS = Not Significant

	P values (unless stated)			Statistical significance			Test
	A – B	A – C	B – C	A – B	A – C	B – C	
T50	0.030	0.000	0.006	$p < 0.05$	$p < 0.001$	$p < 0.01$	M – W U
IUV	0.248	0.238	0.431	NS	NS	NS	M – W U
CURVE	0.113†	0.446†	0.446†	NS	NS	NS	χ^2 TEST
PPBS	0.269	0.312	0.481	NS	NS	NS	M – W U
MPR	0.406	0.258	0.248	NS	NS	NS	M – W U
JPR	0.279	0.346	0.279	NS	NS	NS	M – W U
GCR	0.030	0.370	0.192	$p < 0.05$	NS	NS	M – W U
CIR	0.238	0.084	0.071	NS	NS	NS	M – W U
MAR	0.269	0.468	0.301	NS	NS	NS	M – W U
MPI	0.184	0.080	0.229	NS	NS	NS	M – W U
JPI	0.443	0.290	0.248	NS	NS	NS	M – W U
GCI	0.419	0.030	0.071	NS	$p < 0.05$	NS	M – W U
CII	0.100	0.100	0.370	NS	NS	NS	M – W U
MAI	0.301	0.394	0.468	NS	NS	NS	M – W U
POWER*	0.350	0.223	0.325	NS	NS	NS	T-TEST
MVR	0.419	0.394	0.406	NS	NS	NS	M – W U
MVI	0.312	0.004	0.024	NS	$p < 0.005$	$p < 0.05$	M – W U
VELOCITY*	0.001	0.000	0.000	$p < 0.005$	$p < 0.001$	$p < 0.001$	T-TEST
DURATION*	0.032	0.000	0.015	$p < 0.05$	$p < 0.001$	$p < 0.05$	T-TEST
GCI – MVI	0.51§	0.33§	0.36§	$p < 0.05$	NS	NS	SPEARMAN
GCI – T50	0.27§	0.14§	-0.22§	NS	NS	NS	SPEARMAN
MVI – T50	0.07§	0.02§	-0.10§	NS	NS	NS	SPEARMAN
MFR	0.419	0.301	0.089	NS	NS	NS	M – W U
MFS	0.201	0.335	0.062	NS	NS	NS	M – W U
MFI	0.406	0.323	0.468	NS	NS	NS	M – W U
MF	0.468	0.279	0.370	NS	NS	NS	M – W U
DMI	0.024	0.152	0.167	$p < 0.05$	NS	NS	M – W U
FREQ.*	0.329	0.001	0.001	NS	$p < 0.005$	$p < 0.005$	T-TEST
RPR	0.456	0.346	0.406	NS	NS	NS	M – W U
RFS	0.014	0.184	0.048	$p < 0.05$	NS	$p < 0.05$	M – W U
AGE	0.159	0.084	0.066	NS	NS	NS	M – W U
SEX (T50)‡	0.271			NS			T-TEST

* Calculated from the analysis of all contractions above the 10% mean power threshold.

§ Spearman's rank correlation coefficients.

† Chi – squared value.

‡ T50 differences calculated for all men and women regardless of group. Statistical tests could not be applied for separate groups because there were insufficient numbers of subjects of each sex.

9 DISCUSSION AND CONCLUSIONS

9.1 Objective 1: The creation of analysis software for the EIE system

9.1.1 Assessment of ACCESS

Chapter 1 stated that the first objective of this thesis is to develop a software package that can automatically and objectively process and analyse EIE signals in order to extract useful gastro-physiological information revealing changes in gastric function and dysfunction. Section 6.1.1 explained the need for a comprehensive analysis of EIE signals and section 6.1.2 illustrated why a multifaceted approach is necessary. Section 6.2.1 outlined three basic functions of the software: physiological measurement by means of a thorough qualitative and quantitative analysis; characterisation of EIE signals in normal and abnormal states; and to be able to distinguish between normal and abnormal gastric function based on those characteristics.

The software package that has been developed provides qualitative and quantitative information about the half emptying time of a liquid or semi-solid meal in addition to the power, frequency and velocity of each motile event. The possibility that EIE can measure gastric secretions has also been investigated by other researchers and the initial indications are promising [Giouvanoudi A, 2002]. Therefore, EIE in conjunction with ACCESS potentially offers a more comprehensive analysis of gastric function than any other technique outlined in section 3.2 except for MRI.

Since no experiments were carried out on subjects with forms of gastric dysmotility, the second and third requisite functions of ACCESS (defined in section 6.2.1) have only been partly fulfilled. Proof of the hypotheses outlined in section 8.1.1 strengthens the case for EIE as a diagnostic tool because it is clear that EIE is detecting genuine gastro-physiological phenomena caused by changes in fat content of the test meal. Therefore, it follows that comparatively large differences in motility caused by gastric dysfunction are very likely to be detected. Abnormal gastric motility is likely to be characterised by significantly longer half emptying times and a reduction in the magnitude of the gastric contractility index (GCI) and mean velocity index (MVI).

It was essential that despite its complexity, the software remained user-friendly and comprehensible for potential users. The current version of ACCESS (version 2.40) has been successfully used by two colleagues; Dr. Nadia Hadi and Miss Imane Bouallal who have analysed EIE signals for their respective PhD degrees.

9.1.2 Future software development

The results in section 8.2 demonstrate that there are a number of functions in ACCESS that require further development and testing or that are inappropriate for measuring changes in gastric function and other physiological phenomena.

The first stage in the development of the software must ascertain why some quantitative measurements did not produce significant results. There are a number of possible reasons; the measurement may be unable to measure the desired physiological phenomena because of low signal to noise ratio or the method that is used to calculate the quantitative value may be inappropriate. For example, most of the quantitative measurements used in EIE calculate the average of a given parameter, such as frequency, over a time period. It is possible that physiological events trigger important temporal changes in this parameter but that the overall, mean value remains unchanged. Therefore, important physiological information is lost by averaging. Consequently, further investigation into the variation in the magnitude of these parameters is necessary to determine whether they are caused by physiological phenomena.

Further development will be required to simplify ACCESS if the software is to be distributed with the EIE system. It is also necessary to have some idea of 'normal' and 'abnormal' values of the various quantitative parameters. This stage of the development will only be possible after clinical experiments on volunteers with specific gastrointestinal disorders that cause gastric dysmotility. For example, previous research indicates that diabetes [Ferroir J, 1937, Frank JW, 1995, Jones KL, 1995, Lipp RW, 1997, Schvarz E, 1997, Lluch I, 1999, and Horowitz M, 2001] and Non-Ulcerative Dyspepsia, NUD [Lin HC, 1991, Koch KL, 1992, Troncon LEA, 1994, Lin HC, 1994, Ladabaum U, 1998, Lin X, 2001 and Oba-Kuniyoshi, 2004] affect gastric function (see section 3.2 for details).

9.2 Objective 2: Modelling of EIE signals

9.2.1 Pseudo-EIE and test signals

The Pseudo-EIE program successfully modelled certain features of the EIE signals and in addition produced test signals for the assessment and quality assurance of ACCESS (Appendix H). Pseudo-EIE signals were essential for validating the software and examining potential weaknesses and faults (section 9.2.3). The importance and efficacy of the pseudo-EIE and test signals for quality assurance with respect to fault finding in the EIE software is unquestionable. However, *in vitro* testing is necessary to ensure that real velocities are measured correctly.

9.2.2 Analysis of the geometrical field patterns produced by EIE

Section 4.3 investigated the electrical field patterns in EIE by modelling the human abdomen with an elliptical cylinder based on reference man [Snyder WS, 1975]. A set of equations were derived that describe the electrical potential produced by an electrode pair placed on the elliptical cylinder (equations 4.65 to 4.74). The field patterns were calculated by solving these equations using a LabVIEW program that subsequently plotted the equipotentials that would result from a person with a girth of 80.1cm (Fig. 4.19). The analysis of the geometrical field patterns produced by a pair of electrodes facilitated the analysis of current density and sensitivity (section 4.3.5), which clarified the causes of motion artifacts (section 6.2.2) and justified the use of the inverse distance approximation in Triangulative Impedance Mapping (section 6.2.9 and Fig. 6.33). Comparison with work by Fenlon (Fig. 9.1) also shows a concentration of equipotentials near the electrodes [Fenlon TJ, 1992].

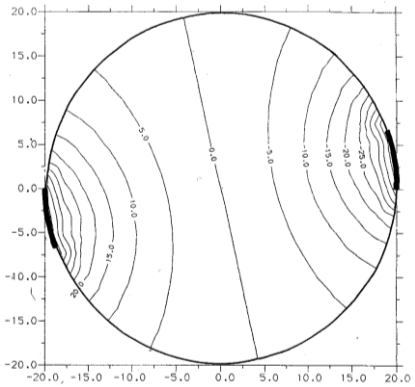

Fig. 9.1 Plot of equipotentials in a resistively homogeneous cylinder [Reproduced from Fenlon TJ, 1992].

9.2.3 Testing of the software for quality assurance

The *Pseudo-EIE* software produced modelled EIE signals and test signals that were able to successfully carry out the quality assurance (QA) of the software. The results of the QA are given in Appendix H. The test signals showed that the Joint Time Fourier Transform (JTFT) and the Dyadic Wavelet Transform (DyWT) functions were performing correctly (see Appendix H, Figs. H1 to H11). The appearance of the DyWT of both test signals and pseudo-EIE signals is affected by interference patterns. These interference patterns are simply caused by a lack of printer resolution. Fig. 9.2A shows a section from the 3cpm sine wave illustrating that in fact the DyWT accurately reflects the wavelet coefficients. However, the wavelet coefficients are squared to obtain the wavelet power (equation 6.24) and so negative coefficients (representing the troughs in the signal) become positive. Consequently, the DyWT appears to display a signal with twice the frequency. This is not a problem because the indices produced by the vector velocity (section 6.2.10) only index the contraction. The intensity graph of the wavelet coefficients (Fig. 9.2B) shows that the frequency is exactly 3cpm and that three cycles can be seen in each minute.

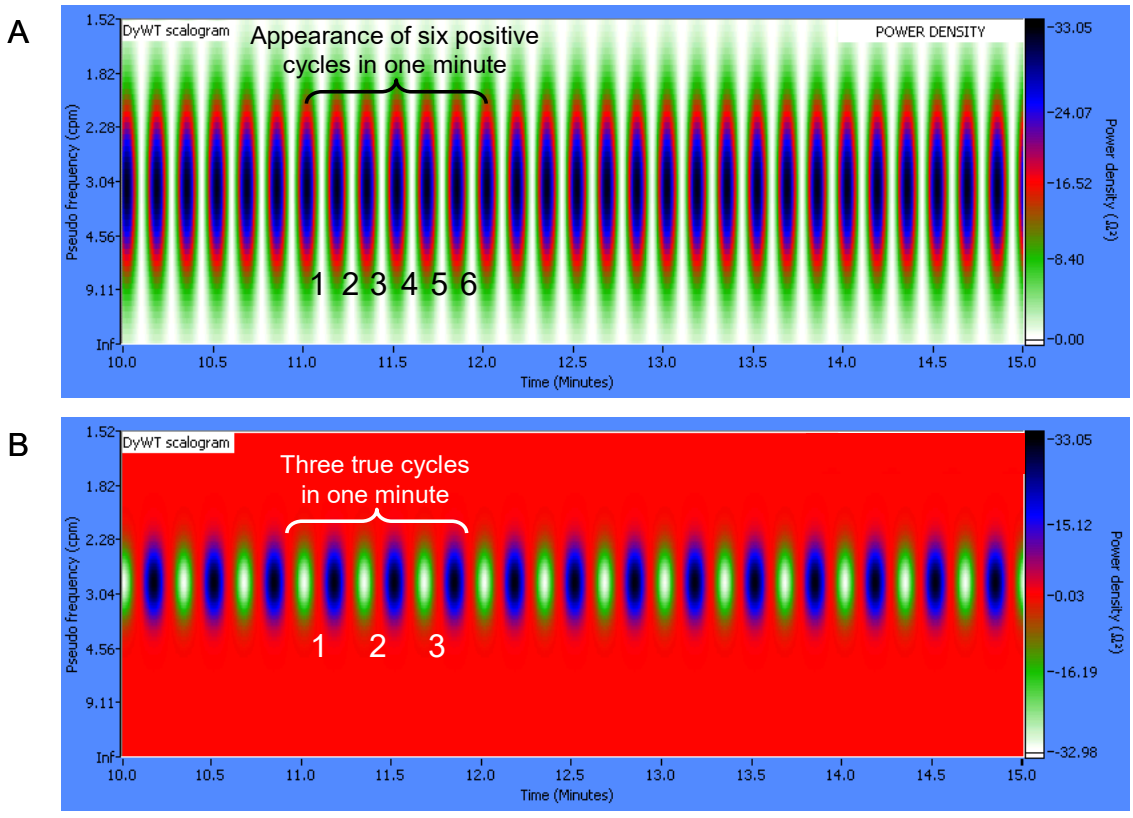

Fig. 9.2 **A** Wavelet power density of the DyWT scalogram. **B** Original wavelet coefficients of the DyWT.

The analysis of Gaussian and white noise test signals demonstrated how both have global effects on the JTFT and DyWT, potentially contributing to the problem of false positive information in the analysis of gastric contractile power (see Appendix H, Figs. H12 to H17). The pseudo-EIE signals provided the means for the thorough testing of the JTFT, DyWT and T50 algorithms (see Appendix H, Figs. H18 to H31). The addition of spikes representing motion artifacts allowed the Motion Artifact Rejection Algorithm (MARA) and spike rejection algorithm (SRA) to be tested with excellent results (see Appendix H, Figs. H32 to H41).

Uniform white noise was superimposed on the exponential signal to investigate whether the software was able to eliminate it. However, since uniform white noise has, by definition a uniform power spectral density the effect of the noise in the time-frequency domain was global. Consequently, the noise was not removed and the maximum recorded power increased by approximately a factor of 2.5. The dominant pseudo frequency was also distorted (see Appendix H, Figs. H42 to H46).

This implies that despite signal processing, sources of interference adversely affect the results producing random increases in the measured contractile power resulting in either false positive results or artifactual amplification of true contractility, while altering the dominant frequency. The application of the 10% mean Gastric Contractility Index (GCI) power threshold demonstrated that although uniform white noise cannot be removed from the signal, the effect can be reduced or even eliminated (see Appendix H, Figs. H47 to H49 and Table H5).

Analysis of the curve fitting algorithms (see Appendix H, Fig. H50) demonstrated that the exponential fit was inappropriate for modelling linear and nonlinear emptying curves and it was not used in the experimental analysis. Nevertheless, the exponential fit may be useful for comparisons to other studies that have adopted the exponential fit for the analysis of gastric emptying times. The R^2 values of the 500-point moving average were comparable to the polynomial fit of the modelled signals (Table H6) but problems with smoothing of real data highlighted in Fig. 6.7B meant that the 4^{th} order polynomial fit was chosen for all analyses.

Analysis of the nine methods for the calculation of the half emptying time (T50) was carried out on a linear pseudo-EIE signal (see Appendix H, Fig. H51). The conclusion reached in section 6.2.4 was that method 3 is the most appropriate method of T50 calculation. Method 3 uses both the pre- and postprandial periods to determine the baseline and uses the deflection baseline method, which testing in Appendix H has shown to be the most accurate at calculating the T50 (see Appendix H, Table H8).

The analysis of the velocity measurements discussed in section 6.2.11 indicates that the vector velocity is able to measure the phase differences and angle of each contraction up to $2cms^{-1}$ very precisely (R^2 – 0.99). However, the precision of the measurement diminishes above $2cms^{-1}$ because the deterioration of velocity resolution with velocity (see section 6.2.11 and Figs. 6.31 and 6.32).

9.3 Objective 3: The detection of physiological phenomena

9.3.1 The detection of the gastric half emptying time and class of emptying curve

The gastric half emptying time has been the most common and dependable measurement of gastric function for many years. Lipid induced delay of gastric emptying is well documented. However, the effects of gastric secretions on the half emptying time are clear; secretions are conductive and since gastric secretions are released in response to the ingestion of a fatty meal, the measured half emptying time would be shorter than the real half emptying time for higher fat meals. Previous studies have investigated the effect of gastric secretions on the EIE signal [Ligris EN, 1997; Hamza AOM, 1999 and Giouvanoudi A, 2000]. Nevertheless, despite the fact that acid suppressant drugs were not given during the experimental investigations, the highly significant differences in the half emptying time shown in Table 8.1 indicate that EIE is highly effective at measuring the changes in gastric emptying brought about by the inclusion of fat in the test meal.

It is not surprising that the levels of significance correlate with the difference in fat content between meals: B – A = 1316 kJ difference, $P < 0.05$; C – B = 1559 kJ difference, $P < 0.01$; and C – A = 2875 kJ difference, $P < 0.001$. This gives even more meaning to the results and confirms that ACCESS is able to objectively measure the gastric half emptying time from EIE signals and detect the fat-induced delay in emptying.

The analysis of the class of the emptying curve for each meal showed an increase in the number of linear and nonlinear emptying curves in the meal C group compared with the meal A and meal B groups, although this was not significant ($P > 0.05$). Investigation into the classifications of the emptying curves made by the pattern recognition algorithm by fitting three different curves (linear, exponential and 4^{th} order polynomial) to the empting period of the EIE signals and measuring the R^2 values, revealed that the classifications made by the pattern recognition are, in general justified (Table 8.3). The results for the exponential and nonlinear classes match the predicted differences in R^2 values between the three types of emptying curve fit for each class in Table 6.8. This indicates that the pattern recognition algorithm is able to classify exponential and nonlinear emptying curves effectively.

However, comparison between Tables 8.3 and 6.8 shows that the R^2 values for the exponential and polynomial fit were both significantly higher than the R^2 values for the linear fit ($P < 0.05$ and $P < 0.005$ respectively). It is likely that this is caused by the fact that emptying curves classed as linear may not remain exactly linear towards the end of the emptying period and deviations in linearity that are fitted well by the 4^{th} order polynomial curve and, to a lesser extent by the exponential curve, cause the reduction in the R^2 value of the linear fit.

The comparison between the classifications made by the computer (PC), myself (MF) and Dr. Nadia Hadi (NH) revealed large differences in the choices made, especially between PC and NH (PC–MF: 61.1%; PC–NH: 44.4%; MF–NH: 72.2% and PC–MF–NH: 42.6%). It is interesting that the greatest agreement is between the two human referees and it is likely that this is because the pattern recognition algorithm is not as sophisticated as our own natural methods of pattern recognition. The significantly higher agreement between PC and MF (61.1%) compared to the agreement between PC and NH (44.4%) is probably caused by MF's biased understanding of how the pattern recognition algorithm classifies the emptying curve.

However, the most revealing difference between PC, MF and NH was the number of curves classified as exponential (PC: 50.0%; MF: 31.5%; and NH: 20.4%). It is possible that the difference is caused by the polynomial fitting of the emptying curve by ACCESS, which may bias the analysis in the favour of exponential classification. Consequently, although the results of the pattern recognition are promising and comparisons to the three types of curve fitting is good, it is necessary to reconsider the features of the emptying curve selected for the pattern recognition, before reinvestigating whether fat affects the shape of the emptying curve.

9.3.2 Effects of fat on the antral contractility and gastropyloroduodenal coordination

Section 2.6.2 discussed the two mechanisms of transpyloric flow; sustained antral pressure in conjunction with pyloric relaxation (pressure-pump) and by propagating gastric contractions in the presence of constant pyloric resistance (peristaltic-pump). Since the inclusion of fat (and other nutrients) in meals B and C triggers a greater release of gastric secretions that require mixing with the chyme (section 2.5.2), there should be differences between the power of gastric contractions measured in each of the meal types.

Fig. 8.5 shows that ratios of post- to preprandial power are subject to errors from the presence of fasting contractions due to migrating motor complexes (section 2.4.3). The significant decrease in the Gastric Contractility Ratio (GCR) between meal types A (water) and B (low fat liquid meal) is likely to have been caused an unusually high number of signals in the type B group that had high preprandial contractility. Closer analysis reveals that 55.6% of measured GCR values are below 0.9 in the type B group compared with 22.2% in the type A group. In addition, the preprandial Gastric Contractility Index (GCI) is higher in the type B group than the type A group, although the difference is not significant $P = 0.089$.

However, comparison between the postprandial measurements of power across the three meal types seems to be a more appropriate method of analysing the power of gastric contractility because it is not subject to variations in preprandial contractility. Nevertheless, the effects of fasting contractions on the postprandial contractility have not been considered and may also be an important factor; it is possible that the phase of the MMC that is interrupted by ingestion of the test meal may influence the gastric contractile response. Although statistical significance was found in the analysis of the postprandial GCI between meals A and C, the trend in postprandial GCI *decreased* with meal fat content as the mean values illustrate (mean ± sem) A: $8.4\times10^{-2} \pm 5.0\times10^{-3}$; B: $8.1\times10^{-2} \pm 3.3\times10^{-3}$; C: $7.3\times10^{-2} \pm 3.3\times10^{-3}$.

Section 2.6.4 discussed research by Ferdinandis using EGG that compared the postprandial rise in the power of the EGG signal (representing the gastric electrical power) with liquid, semi-solid and solid meals [Ferdinandis TGHC 2002]. Ferdinandis found that the EGG power increase was proportional to the solidity of the meal; solid and semi-solid meals produced a relatively large increase in power (7.4% and 5.3% on average respectively), whereas on average the EGG power did not increase at all after the ingestion of liquid meals [Ferdinandis TGHC 2002]. This suggests that the power of the EGG signal is related to the antral contractility of the stomach (section 2.4.2 and Figs. 2.10, 2.11 and 2.12).

It is logical to assume that the process of trituration (needed to mix high fat meals with gastric secretions) would elicit more powerful antral contractility; the propulsion of chyme towards a closed pylorus is a very effective mixing mechanism (Figs. 2.17, 2.19 and 2.23). However, the significance of the decrease in the Gastric Contractility Index (GCI) between meals A (water) and C (high fat semi-solid) shown in Fig. 8.5, disproves that assertion and suggests that, counter intuitively the power of antral contractions decreases with the presence of fat in the test meal.

Studies with duplex Ultrasonography [Hausken T, 2002 and Hveem K, 2001] and manometry [Tougas G, 1992 and White CM, 1983] have indeed demonstrated that there is a reduction in the number of propagating antral contractions with the inclusion of fat in the ingested meal or intraduodenal lipid infusions (Fig. 9.3). Furthermore, the studies describe an increase in pyloric contractility and the number of independent pyloric pressure waves.

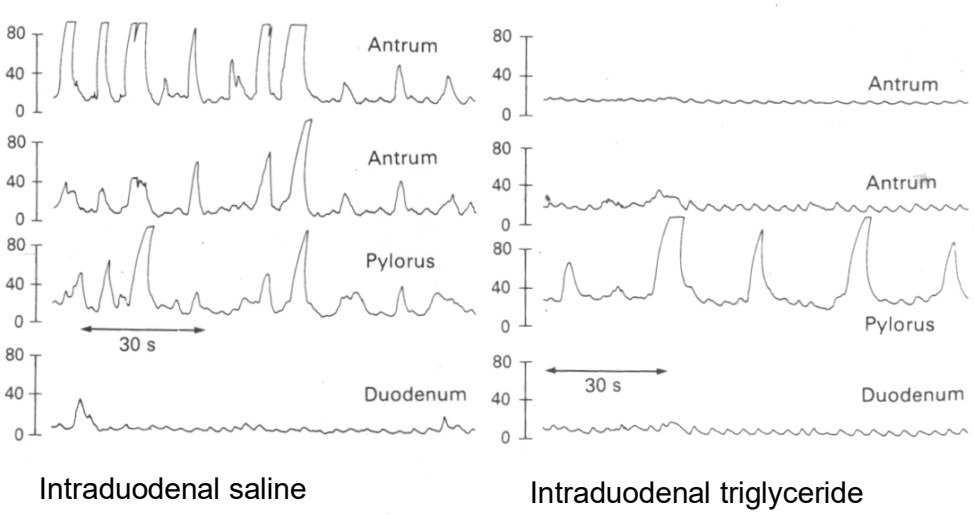

Fig. 9.3 Manometric tracings showing the patterns of antropyloroduodenal motility during duodenal saline and triglyceride infusions [Tougas G, 1992].

There is a connection between the presence of propagating antral contractions and the flow of gastric chyme [Szurszewski JH, 1987] (section 2.51 and Fig. 2.17). Consequently, since the GCI decreases significantly between meal A and C, the measurement of the velocity should also decrease. However, surprisingly this is not the case.

There was a significant *increase* in the velocity between meals A and C ($P < 0.005$) and meals B and C ($P < 0.05$) illustrated by Fig. 8.8. Analysis of the mean velocity for all contractions above the 10% power threshold (Fig. 8.9) corroborated these findings by also indicating a significant increase in the velocity with the inclusion of fat in the meal (A – B: $P < 0.005$; A – C: $P < 0.001$ and B – C: $P < 0.001$).

If the assumption that the velocity measurements computed by analysing the phase difference between contractions, represent changes in the volume of the stomach caused by propagating antral contractions, it follows that the measurements of antral contractile power would also increase with fat content of the three meal types. The overwhelming conclusions reached from previous studies indicating that levels of antral contractility *reduce* with the inclusion of fat in the ingested meal or intraduodenal lipid infusions, lead to the assertion that the measurements of velocity are not detecting volume change. This reasoning necessitates a more detailed analysis to determine exactly what is being detected by EIE.

The resolution of this question calls for careful examination into the origin of EIE signals. Sections 4.2.3 and 4.3.3 describe two models for considering the change in impedance due to volume. The former is derived from the application of a current to each end of a cylinder (Fig. 4.5) and the latter is derived from passing a current between two electrodes either side of an elliptical model of the human torso (Fig. 4.12). It is clear however from the equations that describe the impedance change (equations 4.27 and 4.65) that both volume *and* conductivity contribute to the measured impedance, regardless of the model adopted. Furthermore, studies using Applied Potential Tomography (APT) have shown that the measured conductivity is related to changes in the volume of the stomach and both the acidity and conductivity of gastric chyme [Baxter AJ, 1988]. It is therefore necessary to consider the effect of both changes in volume and conductivity.

Volume changes in the stomach are caused by the ingestion and emptying of the meal and the variation in morphology due to peristaltic contractions and global changes in the tone of the gastric smooth muscle. However, the volume parameter discussed in the two models described in sections 4.2.3 and 4.3.3 and found in equations 4.27 and 4.65 is referring to the total volume of the conductor assuming that the medium is of uniform conductivity.

Gastro-physiological events do not change the total volume of the subject and so variations in the impedance of the EIE signal must be predominantly caused by changes in conductivity in the stomach. Nevertheless, Fig. 9.4 illustrates that *volume* changes in the stomach alter the measured conductivity because the contribution of the lower (intragastric) conductivity, σ_2 to the total conductivity decreases. Consequently, the total conductivity increases (and the measured impedance decreases[1]). Note that $\sigma_2 < \sigma_1$ and in Fig. 9.4A, it is assumed that the conductivity is homogeneous and so $\sigma_0 = \sigma_1$.

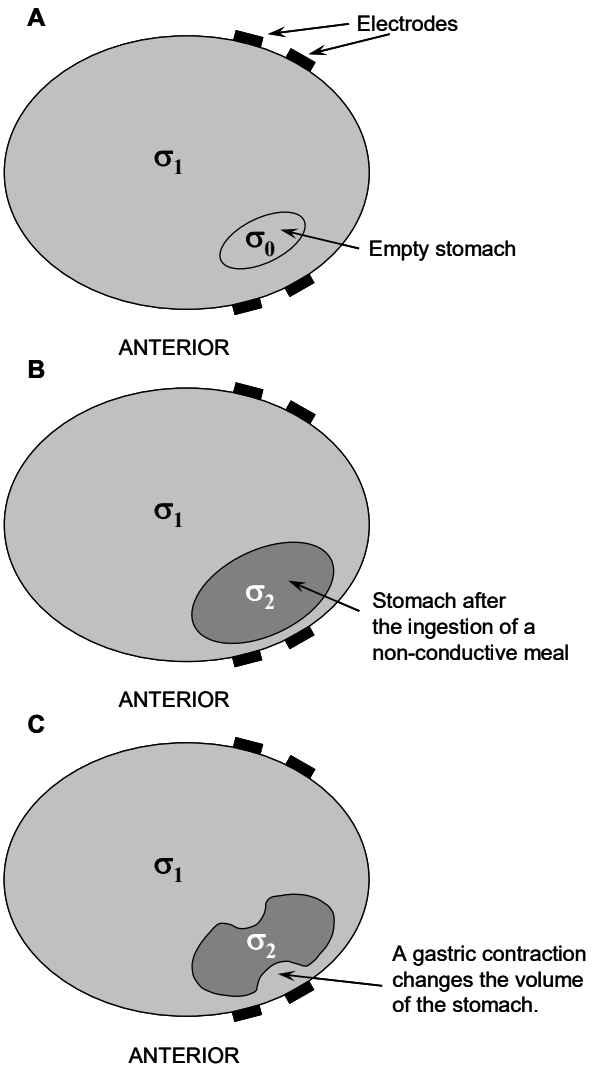

Fig. 9.4 **A** Diagrammatic cross-section of the abdomen over the epigastric region under fasting conditions. **B** Following the ingestion of a non-conductive meal, the abdominal conductivity, σ_1 is greater than intragastric conductivity σ_2. **C** The propagation of a gastric contraction changes the volume of the stomach thus altering the impedance measured between the electrodes.

[1] This is why the *valley* of the band pass filtered signal is taken as the time of gastric contraction for the measurement of gastric contractile power (see section 6.2.9 and Fig. 6.21A).

Previously, studies in EIE have only considered the effects of changes in conductivity caused by gastric secretions (which have a higher conductivity than the meal) on the gastric half emptying time [Giouvanoudi A, 2002]. In addition however, Fig. 9.4C illustrates that volume changes in the stomach caused by antral contractions are in effect, changes in the total conductivity measured between the electrodes.

However, it is reasonable to state that the conductivity of the chyme remains different from the surrounding tissues throughout the postprandial period. Therefore, since the chyme is motile within the stomach, it is critical to consider the potential effects on the EIE signal of the *flow* of chyme as a consequence of both gastric emptying and local changes in the distribution of the gastric content between the proximal and distal parts of the stomach.

Section 4.6.3 described that Boulby used MRI to analyse gastric motility and detected an increase in the number of flow events of chyme from a high fat test meal (Fresubin, 3347.2kJ) than with a 5% glucose meal [Boulby P, 1999]. Since both the Mean Velocity Index (MVI) and the mean velocity of contractions above the 10% mean power threshold increased with meal fat content (Figs. 8.8 and 8.9) it is possible that the velocity measured from the phase differences in the EIE signal is related to the flow of chyme in the stomach.

Investigations by Houghton (shown in Fig. 9.5) into the role of the proximal and distal stomach (Fig. 2.7) during gastric emptying using scintigraphy have shown that the fat induced delay in gastric emptying is partly due to the redistribution of distal stomach content back into the proximal stomach [Houghton LA, 1990].

Furthermore, in addition to a reduction in the number of propagating antral contractions and an increase in pyloric contractility and independent pyloric pressure waves, studies have shown that the inclusion of fat in the ingested meal or intraduodenal lipid infusions triggers a relaxation of the fundus [Dooley CP, 1984 and Azpiroz F, 1985b].

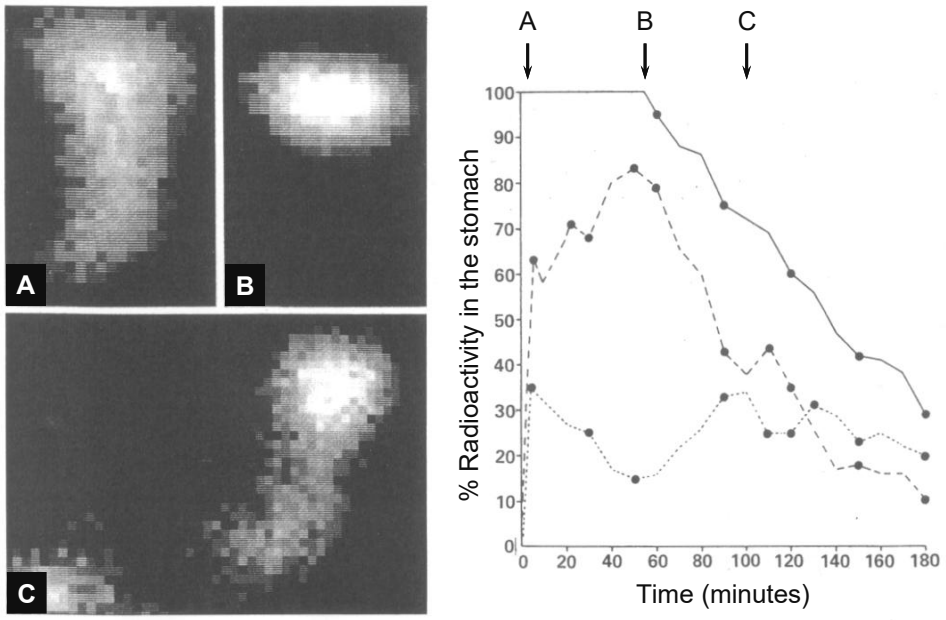

Fig. 9.5 The distribution of a high fat meal using scintigraphy at **A** 4 minutes after ingestion, **B** 54 minutes after ingestion and **C** 100 minutes after ingestion. The emptying profiles on the right are given for the whole (——), proximal (- - - -), and distal stomach (·····). The letters refer to the images on the left [Redrawn from Houghton LA, 1990].

The observation that fatty chyme moves from the distal to the proximal stomach in the first period of emptying may explain the nonlinear nature of some gastric emptying curves measured by EIE (compare the distal stomach signals in Fig. 9.5 with the nonlinear emptying curve modelled in Fig. 7.3C). However, if there is a reduction in the antral peristaltic activity, the question of how chyme held in the proximal stomach is emptied becomes even more obscure.

Hadi has confirmed that the above results from Houghton apply to meal C by comparing meal C with a 10% glucose solution. Fig. 9.6 shows that the distribution of the 10% glucose solution quickly enters the antrum whereas meal C was stored in the proximal stomach for much longer [Hadi NA, 2004]. Furthermore, a low number of counts are recorded in the antrum for meal C despite the fact that activity appears in the intestines. Hadi explained that this is because triturated gastric contents are propelled from the proximal stomach to the antrum and into the duodenum and so the counts are not detected by scintigraphy [Hadi NA, 2004].

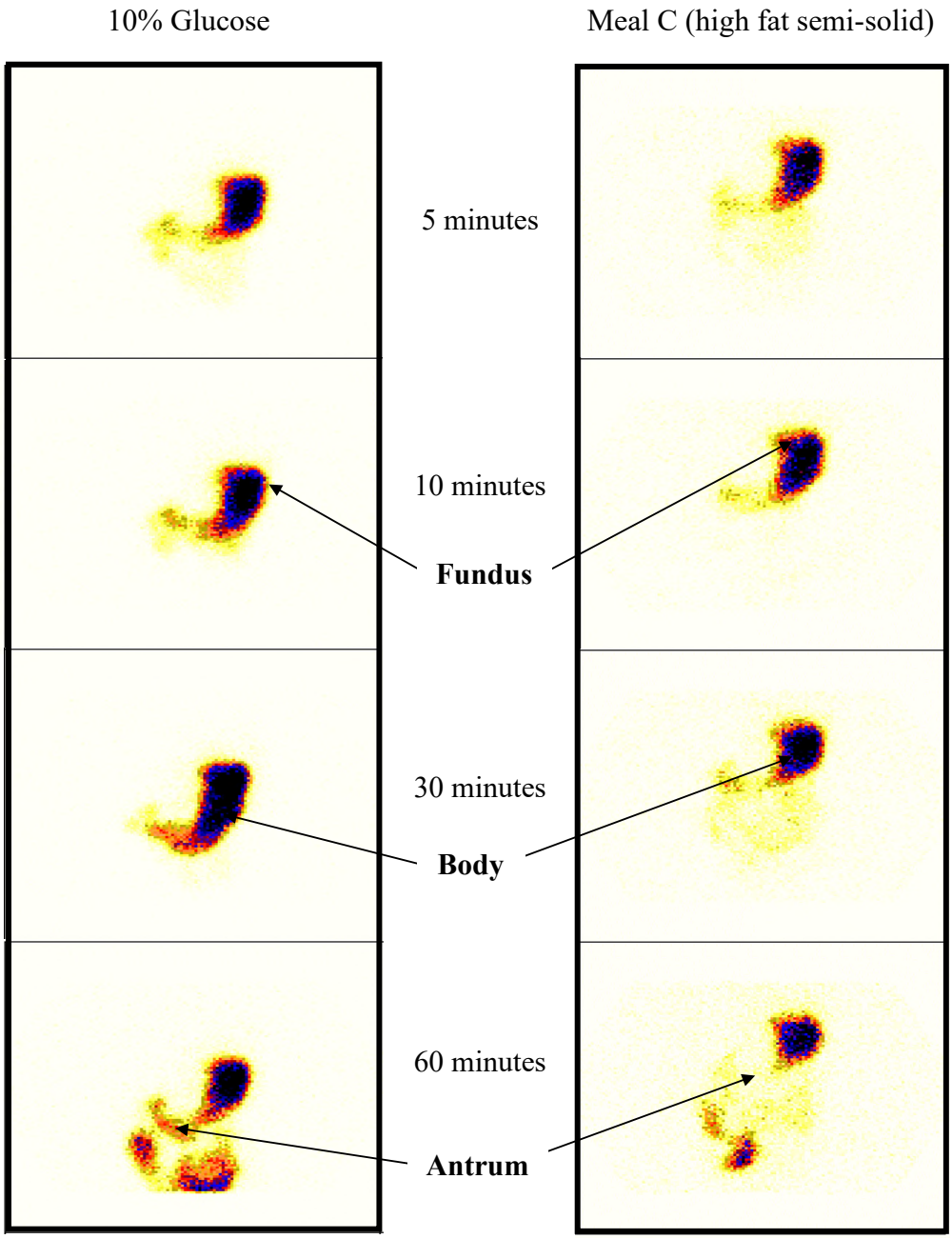

Fig. 9.6 Scintiphotographs showing the distribution of the 10% glucose solution and meal C meal at 5, 10, 30 and 60 minutes [Hadi NA, 2004].

Vassallo investigated the axial forces (along the longitudinal axis of the stomach) using scintigraphy, manometry and an axial force transducer [Vassallo MJ, 1992]. During the emptying of 200ml of skimmed milk (288.7 kJ) he found that axial forces (forces along the longitudinal axis of the distal stomach) were more likely to coincide with increases in *proximal* rather than distal antral pressure. The opposite was true for solid meals. These axial forces were found to vary between subjects.

Fig. 9.7 shows the emptying, axial force and proximal and distal pressure measurements for two subjects after the ingestion of the milk [Vassallo MJ, 1992].

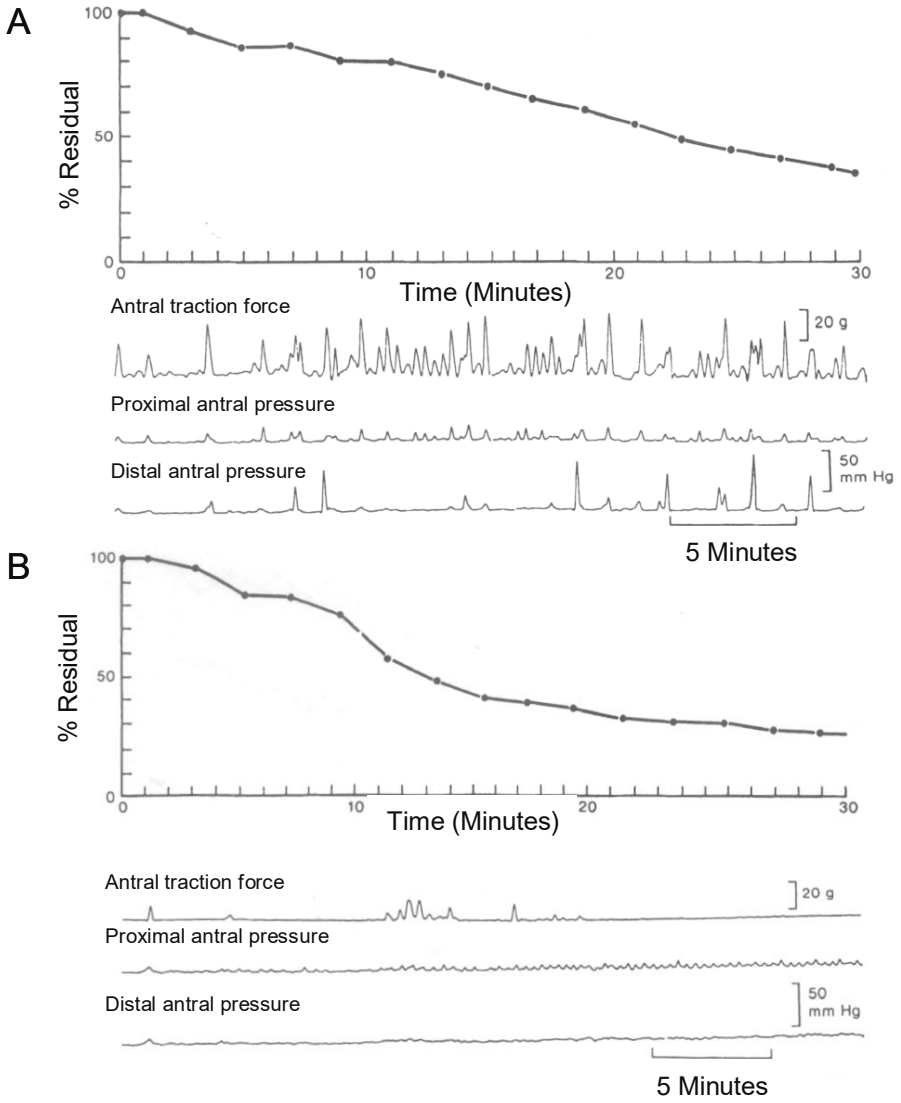

Fig. 9.7 **A** Slow liquid emptying with high antral force measured with a novel axial force transducer. Note that most of the axial forces correlate with proximal antral pressure. **B** Fast liquid emptying with minimal pressure activity. Axial forces occur during the period of fastest emptying [Redrawn from Vassallo MJ, 1992].

Axial forces occurred coincidentally with and independently from proximal and distal antral forces. On average 67% of axial forces coincided with proximal antral pressures during emptying and 47% with distal pressure increases. Fig. 9.8 shows that the axial forces in the antrum occurred a few seconds after the proximal antrum pressure.

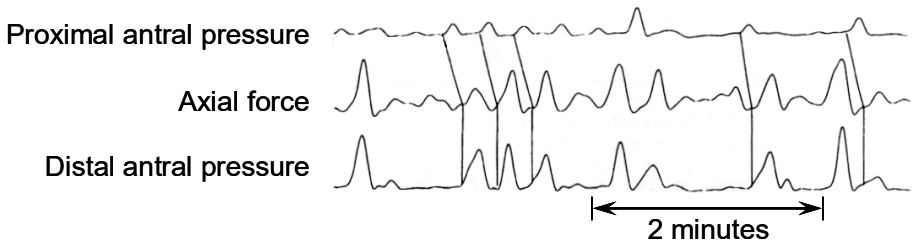

Fig. 9.8 Pressure events recorded with manometry in the proximal antrum and force and pressure events recorded with simultaneous manometry and axial force transducer in the distal antrum [Redrawn from Vassallo MJ, 1992].

These results imply that fatty liquid meals are emptied by contractions in the proximal stomach that force chyme into the distal antrum, towards a closed pylorus with little propagating antral contractility. This does not explain however, why a pulsatile contractile signal is found in EIE signals from fatty meals. If the EIE signal is measuring flow it seems unlikely that it would produce the same type of signal caused by propagating contractions.

Indireshkumar found that increases in gastric wall tone occur independently of contractile activity within the antrum [Indireshkumar K, 2000]. Riddell used fluoroscopy and manometry to study gastric liquid emptying in pigs and found that pulsatile motility of chyme was caused by broad, low amplitude non-lumen occlusive pressure waves which appeared as common cavity rises in pressure when measured by manometry [Riddell P, 1991]. A previous study that analysed the antral wall movements using a force sensor together with conventional manometry confirmed that manometry often fails to detect non-lumen occlusive contractions [Fone DR, 1990]. This implies that previous studies using manometry may have underestimated the contribution made to the processing of fatty chyme by non-occlusive contractions.

Schulze-Delrieu investigated the effects of gastric contractions on the length, diameter, pressure and emptying of isolated cat stomachs (excised and mounted in a Krebs solution bath) using video, ultrasound, force transducer and manometry [Schulze-Delrieu, 1998]. Pressure profiles recorded inside the proximal stomach were found to consist of four phases: (i) steady pressure lasting over several minutes related to gastric accommodation (see Fig. 2.16); (ii) a relatively large pressure wave (mean ± sem duration of 29 ± 2s) superimposed on the initial pressure which terminated with (iii) a pressure peak and (iv) subsequent occurrence of a second smaller and shorter pressure wave (mean ± sem duration of 14 ± 1s).

These studies suggest that proximal contractions generate the pulsatile flow of gastric chyme from the proximal to the distal stomach. However, since the ingested meal is non-conductive, logically it would seem that detection of the flow of gastric chyme in the stomach would cause an *increase* in the impedance of the EIE signal measured. However, ACCESS isolates the *valleys* in the band pass filtered signal, caused by decreases in gastric volume, in order to measure gastric contractility (see Fig. 9.5, section 6.2.9 and Fig. 6.21A). Nevertheless, velocity measurements are calculated by the analysis of phase differences in the signal that are likely to be present in both the valley and the peak of each cycle. Furthermore, the fact that chyme held in the proximal stomach and later propelled into the distal stomach has been mixed with relatively conductive gastric secretions must also be considered. Therefore, it is reasonable to conclude that the phase differences (and therefore measurement of velocity) could be related to either the movement of propagating contractions *or* the flow of chyme.

Nonetheless, these conclusions do not explain why propagating contractions in meal A do not produce the same flow events measured in meal C. Comparison between the GCI and MVI of individual contractions between the three meal groups provides an answer. For type B and C meals, there is no significant correlation between the power (GCI) and velocity (MVI) of motile events (Tables 8.7 and 8.10). However, for type A meals, the Spearman rank correlation is 0.51 ($P < 0.05$). This implies that stronger contractions in the type A group cause a greater flow of chyme towards the relaxed pylorus whereas ‘contractions’ measured in the type B and C groups may in fact be the flow of chyme forced from the proximal stomach to the distal stomach by less powerful non-occlusive contractions. This hypothesis is supported by Schwizer, who also found a decrease in lumen occlusive contractions in 25% glucose, compared with 10% glucose [Schwizer W, 1996].

The differences in the duration of contractions shown in Fig. 8.10 and Table 8.8 may be of physiological importance. However, the mean difference between type A and type C is only in the region of 1 second. The negative trend in Fig. 8.10 may be significant, but since the difference is only approximately 3.2% between types A and B and 3.0% between types B and C, it is likely that as the duration of the motile event is inversely proportional to the measured velocity, the differences in the duration of contractions are simply caused by increases in the velocity of gastric flow.

Qualitative analyses of the acquired signal, JTFT (with maximum power per epoch in black) and velocity measurements of a type C meal (Fig. 9.9) facilitate the investigation into various physiological phenomena. The fasting period of the signal in Fig. 9.9 shows little contractility and the velocity of the contractions measured fluctuates between positive and negative. When the meal is first ingested, there appears to be an initial period of emptying. This may be the effect of chyme entering the duodenum quickly so that the duodenal chemoreceptors and mechanoreceptors (section 2.6.5), can test the chemical composition of the chyme (section 2.4.4). Alternatively, this may be caused by the adaptive relaxation (section 2.5.1 and Fig. 2.16). This phenomenon was detected in 60% of recorded signals.

A period of relative contractile quiescence immediately follows (for approximately 7 minutes) in which the dominant frequency of the contractions falls to 2.4cpm. Around 11 minutes after the ingestion of the meal there is a period of approximately 35 minutes characterised by powerful contractions with forward velocity, implying that following trituration in the proximal stomach, chyme is being propelled towards the pylorus and some of the digested chyme is emptied into the duodenum (see section 2.5.1 and Fig. 2.17).

There are five important events during this period (marked with red dashed lines) related to a ripple in the acquired signal, a reduction in contractile power and frequency and a negative velocity, angle or both. Freedman first noted the significance of ripples in the signal although no conclusions were made as to their origin [Freedman MR, 2000]. It is not clear whether these events are simply the effect of chyme being propelled back into the gastric antrum following the closure of the pyloric sphincter (see Figs. 2.17 and 2.19C) or caused by the contents of the duodenum flowing back into the stomach (duodeno-gastric retropulsion).

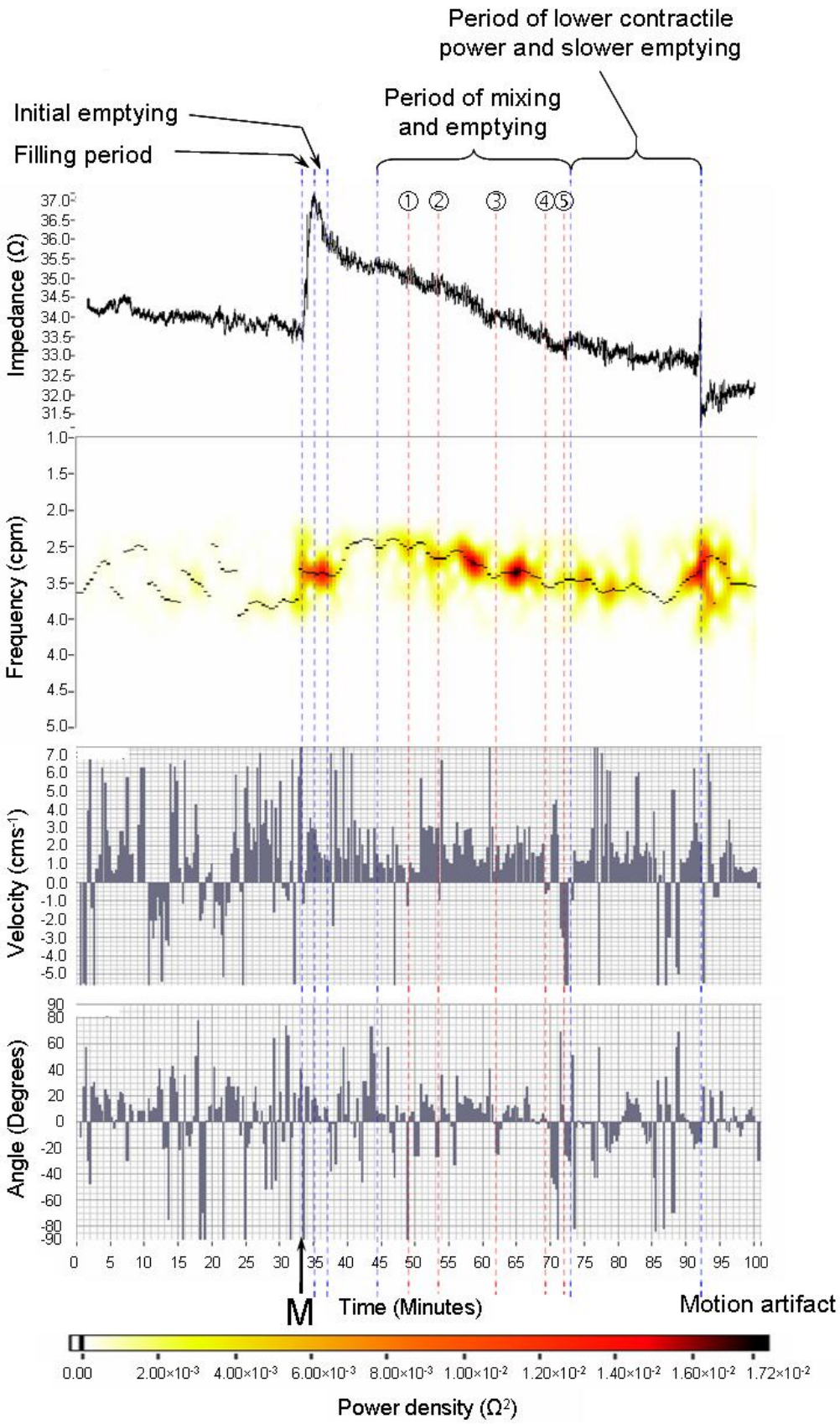

Fig. 9.9 Meal C: The acquired signal (top), JTFT (top-middle), vector velocity (bottom-middle) and the vector angle (bottom) to show the coordinated gastric motile response to a high fat semi-solid meal. Meal taken at time = M.

Boulby found using MRI (Fig. 9.10) that duodenal chyme was propelled back into the stomach along the edge of the lesser curvature [Boulby P, 1999]. This retrograde flow was produced by independent pyloric pressure waves (IPPW) and Hausken measured velocities of retrograde flow up to 60cms^{-1} [Hausken T, 1992]. Qualitative analysis of the acquired signal, power – frequency – time signal and vector velocity indicates that many high magnitude negative velocity events are associated with an increase in frequency. It is possible that these events are caused by retropulsion from the duodenum.

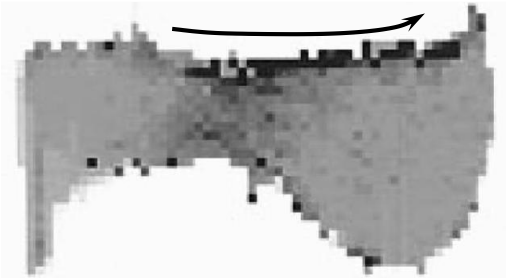

Fig. 9.10 Retrograde flow (dark colours) in the gastric antrum over a 5 minute period shown in the direction of the arrow [Redrawn from Boulby P, 1999].

Hadi used scintigraphy to measure the number of counts in the antrum for both the 10% glucose meal and meal C [Hadi NA, 2004]. Fig. 9.11 shows that while meal C empties continuously, the number of counts in the 10% glucose solution fluctuates. Hadi concluded that this is caused by gastro-duodenal retropulsion brought about by the rapid emptying of the 10% glucose meal [Hadi NA, 2002 and Hadi NA, 2004].

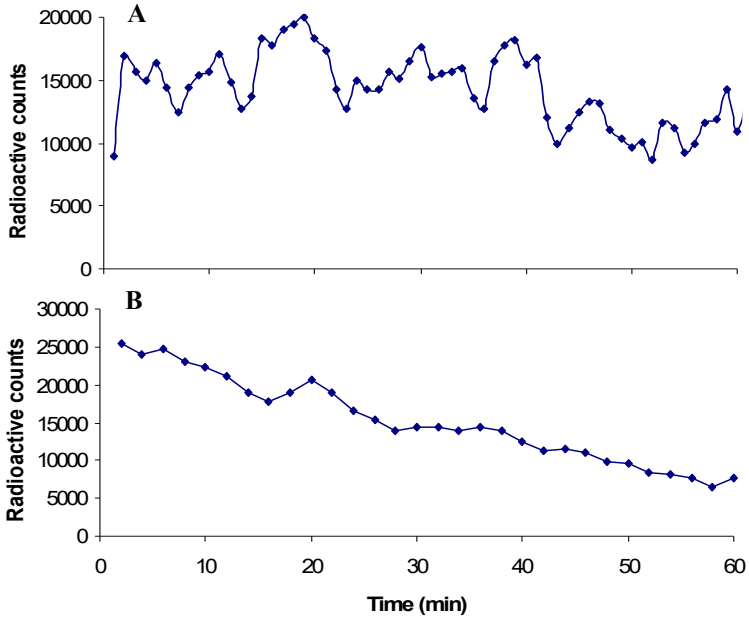

Fig. 9.11 Radioactive counts in the antral region versus time for one subject after the ingestion of **A** 10% glucose meal and **B** meal C [Hadi NA, 2004].

This implies that since simple meals empty more quickly, the duodenum may not be able to deal with the large volume of fluid and so retropulsion occurs. This explains why measurements of velocity exhibit more forward and backward flow in simple meals than complex meals and why measurements of velocity increase with meal fat content (Figs. 8.8 and 8.9).

In the final period of the signal in Fig. 9.9, the power of the gastric contractions is reduced although the velocity remains the same. Consequently, the half emptying time slows. The mean postprandial velocity measured in this signal was 1.7cms^{-1}. The propagation velocity measured by EGG increases from 0.1 to 0.2cms^{-1} in the pacesetter zone to 4.0cms^{-1} in the antrum [Carlson HC, 1966]. The gastric half emptying time for the signal in Fig. 9.13 was 34.5 minutes.

Figs. 9.12 and 9.15 show the same comparison for meal B and A respectively. Once again in the type B meal there is an initial emptying period followed by a period of mixing and emptying in which the characteristic frequency hop appears over approximately a 20-minute period. Marker 1 indicates a change in baseline in the acquired signal, which may indicate pyloric breaking to prevent more chyme entering the duodenum. Marker 2 also denotes a change in baseline together with a frequency shift. The gastric half emptying time for the signal in Fig. 9.13 was 10.7 minutes.

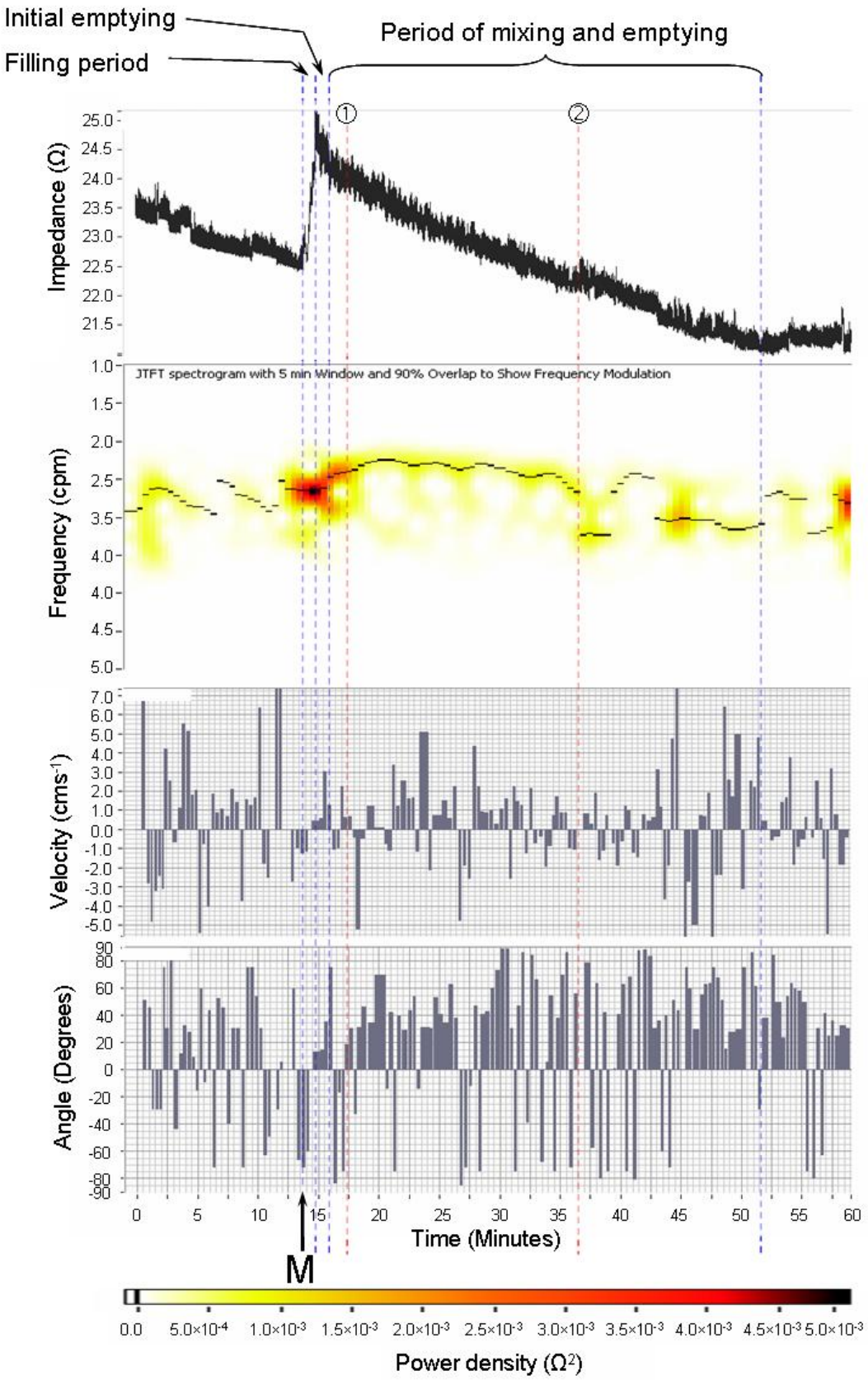

Fig. 9.12 Meal B: The acquired signal (top), JTFT (top-middle), vector velocity (bottom-middle) and the vector angle (bottom) to show the coordinated gastric motile response to a low fat liquid meal. Meal taken at time = M.

Meal A (Fig. 9.14) empties with an exponential curve. The initial drop in impedance recorded in the first three postprandial minutes of the type B and C signals (Figs. 9.9 and 9.12) is not apparent in meal A. This is likely to be because the meal continues to progress from the proximal to the distal stomach. Close inspection of the acquired signal in Fig. 9.14 reveals that a small change in the rate of emptying occurs between the end of the filling period and marker 1 (Fig. 9.13). Markers 2, 3 and 4 show increases in power correlating with increases in velocity.

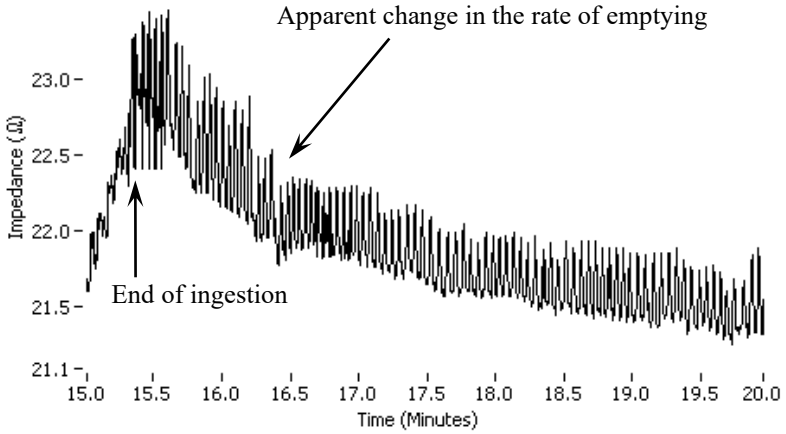

Fig. 9.13 Apparent change in the rate of emptying approximately 1 minute after the end of meal ingestion in the signal in Fig. 9.14.

The most fascinating observation however, is that majority of velocity measurements made have a negative angle (approximately between -20° and -60°). It is also interesting that there is no frequency hop in the water signal, possibly because the meal is not held in the proximal stomach. The gastric half emptying time of the signal in Fig. 9.14 was 5.1 minutes.

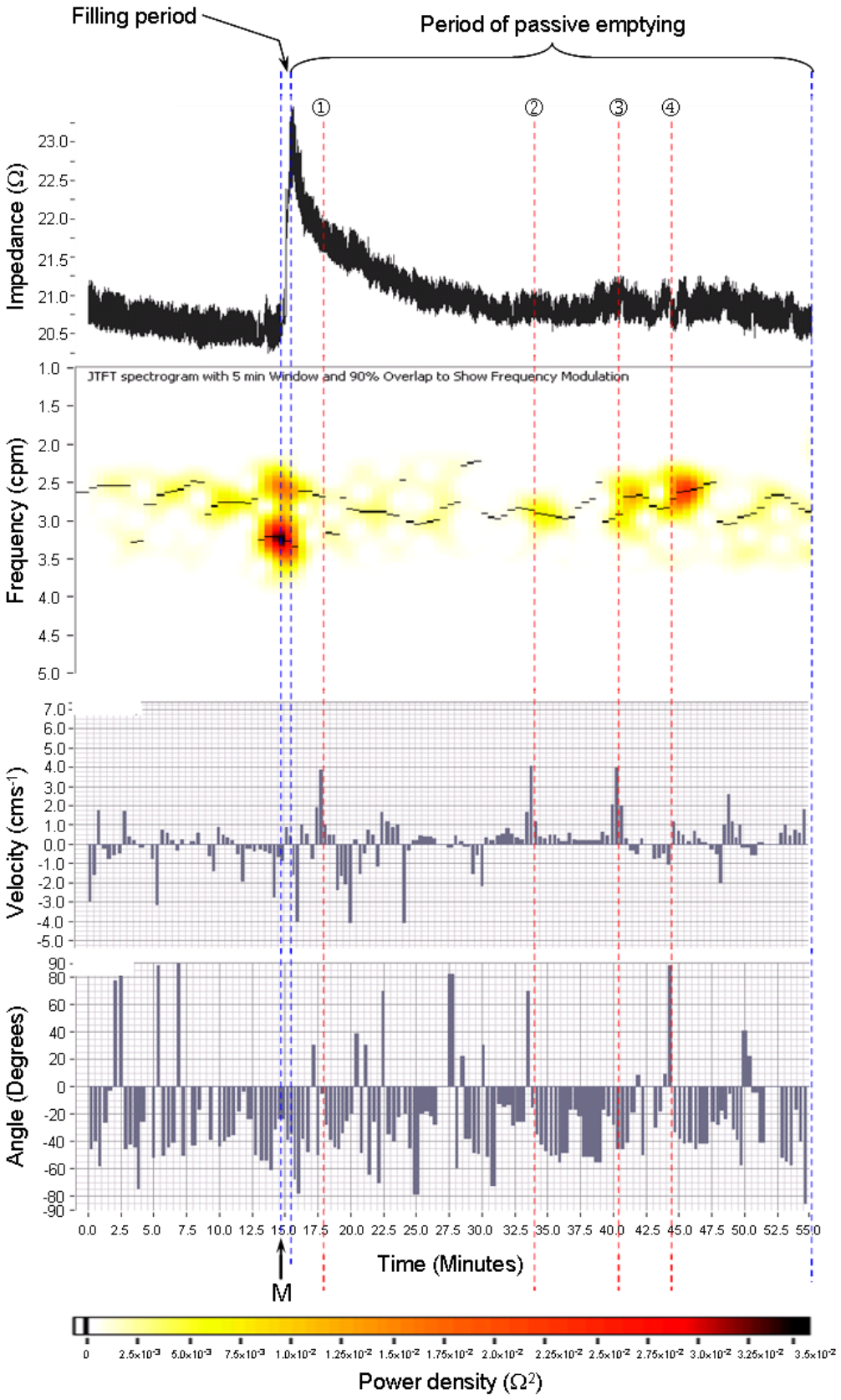

Fig. 9.14 Meal A: The acquired signal (top), JTFT (top-middle), vector velocity (bottom-middle) and the vector angle (bottom) to show the coordinated gastric motile response to a non-calorifc liquid meal. Meal taken at time = M.

Fig. 9.15 gives an example of the emptying of meal A in which not only strong contractility is coordinated with positive velocity, but the emptying curve is nonlinear and contains a number of interesting features. The first three postprandial minutes show the initial empting that appears in Figs. 9.9 and 9.12. This is followed by a period characterised by the frequency change also seen in Figs. 9.9 and 9.12 together with sustained contractility and anterograde velocity. The impedance does not decrease significantly suggesting that little transpyloric flow occurs, but the velocity is primarily positive, suggesting anterograde flow.

Following this period, there is a gradual increase in the impedance in which the power of the contractility increases (particularly at marker 1) and the frequency returns to the initial value shortly after ingestion. The velocity remains predominantly positive. In the third phase, the contractility approximately increases by a factor of six. The peak of this increase occurs at marker 2. The impedance decreases rapidly over a period of 16 minutes indicating transpyloric flow. The velocity of very motile event (except for one) in the third period is positive. During the fourth period, the power decreases, the impedance increases again and the velocity begins to fluctuate between positive and negative values in a similar way to the fasting period.

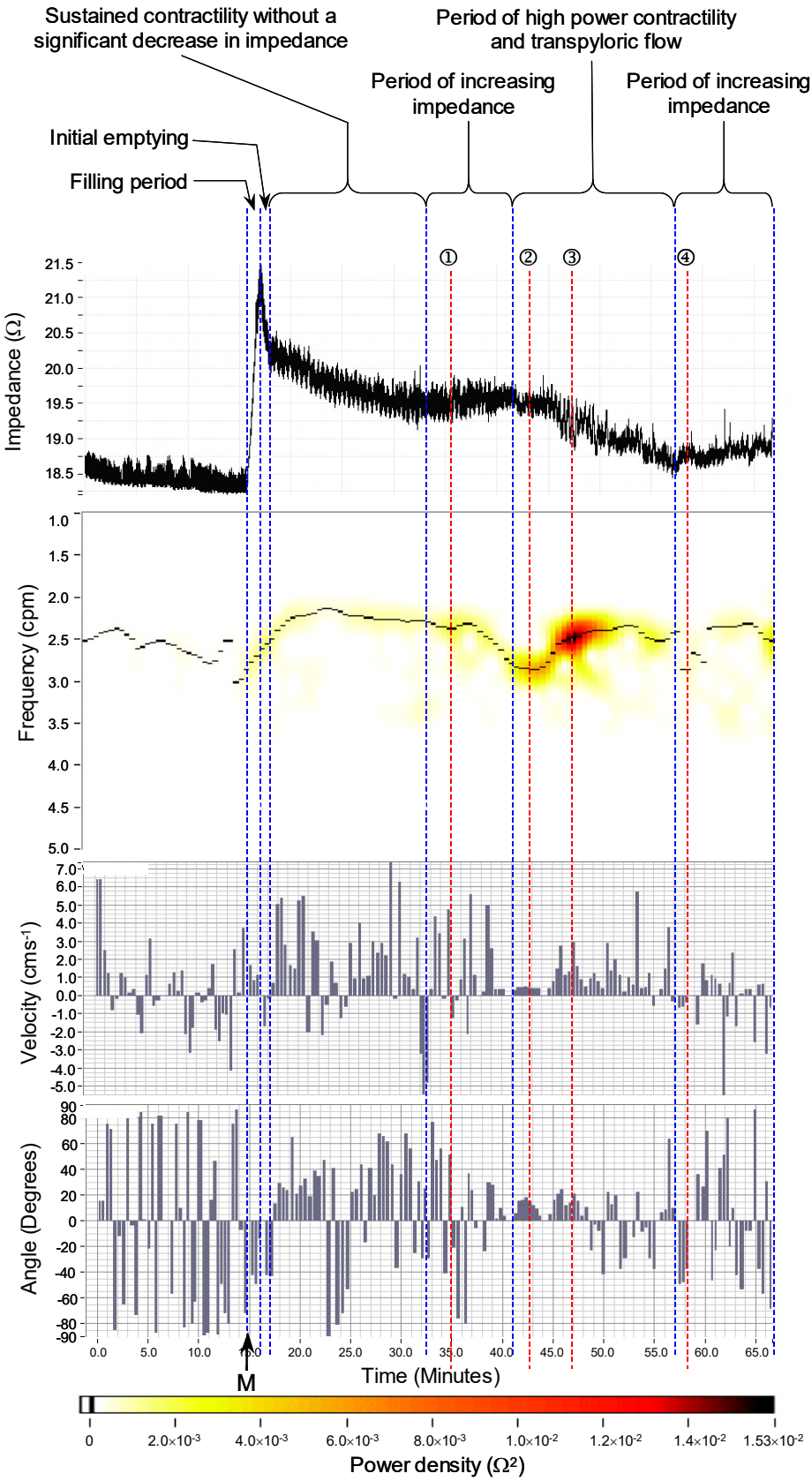

Fig. 9.15 Meal A: The coordinated gastric motile response to a non-calorific liquid meal that demonstrates high antral contractility, especially during periods of transpyloric flow. Meal taken at time = M.

9.3.3 Frequency shifts

The Joint Time – Fourier Transform (JTFT) in Figs. 9.9, 9.12 and 9.15 shows the shift in frequency during the period of mixing and emptying. It is possible that the presence of a frequency hop could be related to the satiety of the subject. Since changes in frequency occur intermittently, single quantitative measures are not appropriate and the statistical analysis of Mean Frequency Ratio (MFR) and the Maximum Frequency Shift (MFS) do not show any statistically significant changes between the three different meal types. This is likely to be because the changes in frequency are not global but more subtle changes caused by physiological processes such as gastroduodenal retropulsion.

Analysis of the Dominant frequency Modulation Index (DMI) revealed very little although it is possible that meal B triggers more frequency modulation than meal A, because although meal B contains fat, there is comparatively very little and so the gastric response is often very variable; sometimes it responds as it were a non-nutrient meal, and sometimes as if it were a complex, high fat meal. It is unclear whether the DMI is a good measure of frequency modulation as the modelled EIE signals could not test this.

9.3.4 Anthropomorphic measurements and effects of gender

Figs. 8.14A and 8.14B showing variations in the impedance deflection per unit volume of ingested meal (IUV) with body mass index (BMI) and girth respectively, confirm previous work by Fenlon that measurements of the maximum impedance deflection are negatively correlated with anthropomorphic measurements [Fenlon TJ, 1992]. Analysis of the slopes of the curves between the maximum impedance deflection and girth and BMI closely match Fenlon's (Table 9.1).

Table 9.1 Linear trendline comparisons in the analysis of impedance deflection per unit ingested volume against BMI and girth between this work and Fenlon TJ, 1992

Freedman 2004		Fenlon 1992	
BMI	*Girth*	*BMI*	*Girth*
$y = -0.18x + 5.60$	$y = -0.05x + 5.56$	$y = -0.24x + 7.70$	$y = -0.05x + 5.91$

Section 8.2.6 explained that in order to study gender effects, experiments on women had to be restricted to the first ten days of their menstrual cycle. This was simply not possible to do.

9.3.5 Respiratory analysis

Section 8.2.7 showed that only just over 50% of signals exhibited a postprandial increase in respiratory power. However, there are a number of possible explanations that are mentioned in section 8.2.7. The value of exploring the application of EIE for detecting respiratory power and frequency have not been fully explored and it is still possible that differences in postprandial breathing patterns exist between normal and abnormal volunteers. For example, since gastric half emptying times are delayed in many gastrointestinal disorders, it is possible that the mechanical effort needed to breathe will be stronger for a prolonged period. In addition, patients with gastric dysmotility may rely on the mechanical effects of breathing to help to mix chyme in the absence of coordinated and effective contractility.

9.4 Conclusions and suggestions for further work

9.4.1 The Neurogastroenterology enigma

Enormous effort and copious research has been focussed towards unlocking the secrets of the mechanisms that control gastriointestinal function. Wingate once compared the various factors that contribute to the management of the gastrointestinal like the playing of a piano; analysis of the pressing of one key is meaningless without an understanding of how that key interacts with the others to produce the music [Wingate DL, 2001].

It is only with a complete knowledge of the sequence of key presses that the music can be reconstructed. Similarly, this work has stressed the need for a comprehensive analysis technique that measures as many gastric physiological phenomena as possible.

The application of Electrical Impedance Epigastrography to the analysis of gastric function has been thoroughly investigated in this thesis. Modelling of the equipotentials produced by the Epigastrograph has highlighted one of the main drawbacks. Concentrations of current density at the site of the electrode and non-uniformity of the electric field mean that the system is very sensitive to changes in impedance at the electrode – skin interface, but less sensitive to changes in conductivity of the stomach related to gastro-physiological events, following the ingestion of non-conductive meals. Consequently, EIE signals are affected by motion artifacts that cause erroneous detection of contractility or exaggerate the power of true contractions after signal processing.

A software package has been produced that provides a comprehensive processing and analysis tool for EIE. The effects of motion artifacts can be reduced significantly by the application of simple algorithms (Motion Artifact Rejection Algorithm, MARA and Spike Rejection Algorithm, SRA). A variety of signal processing techniques have been applied to extract information regarding the power, frequency and dominant frequency changes of gastric contractions. A novel algorithm (Triangulative Impedance Mapping, TrIM) has been developed to map the impedance over a region of interest in order to the display the changes in impedance over the epigastric region caused by gastro-physiological events. Velocity measurements have been calculated from the analysis of the phase differences between contractions measured from the three signals between each pair of electrodes.

A variety of quantitative measurements based on the power, frequency and velocity of gastric contractions have been investigated by experiments on normal volunteers using three test meals; meal A (non-nutrient liquid meal), meal B (low fat liquid meal) and meal C (high fat semi-solid meal). The most significant results demonstrated that the power of gastric contractions significantly decreased with the inclusion of fat while the velocity measurements increased.

Investigations into previous research regarding the effect of fat on the gastric motility of liquid and semi-solid meals has shown that in general, simple meals are emptied by the peristaltic pump (strong propagating contractions towards a relaxed pylorus) whereas the inclusion of fat in the meal means that it is processed by sustained pressure gradients between the antrum an duodenum. Furthermore, the role of the proximal stomach is significant; high fat meals are held in the proximal stomach for longer periods for trituration. Contractions in the proximal stomach propel the high fat and partially digested gastric chyme from the proximal to the distal stomach.

The results from the experiments on healthy volunteers together with the observations made in previous studies indicate that EIE is not only able to measure the half emptying time of a liquid or semi-solid meal, but it can measure the power of gastric contractions and detect the flow velocity and direction of gastric content between the proximal and distal stomach.

9.4.2 Clinical importance of the results

A number of conditions that cause gastric dysmotility are discussed in section 3.2. The results from the experimental studies, together with the conclusions reached by previous researchers reveal important attributes of EIE that have not been previously explored and may help to unlock the mechanisms of gastric dysfunction.

The ability to measure velocity of the flow of gastric content is a significant finding and could be of significant clinical importance regarding the changes in the distribution of gastric chyme in patients with Non-Ulcerative Dyspepsia (NUD). The measurement of gastric contractile efficiency in diabetics by EIE would not only be valuable in assessing the aetiology and nature of diabetic gastroparesis, but could determine whether gastric function is influenced by changes in treatment.

Since EIE can also measure the emptying time and power of gastric contractions it is likely to be able to decipher the nature of dysmotility caused by other conditions such as motion sickness and stress caused by a variety of factors (section 3.2.6). There are also applications in paediatrics and for critically ill patient who can not undergo other examinations.

9.4.3 Modelling of EIE signals for quality assurance and testing of the software

The modelled (pseudo) EIE signals and test signals have facilitated the rigorous testing of the various functions that the software offers. Notably, investigations into the accuracy of velocity measurements have highlighted areas that require improvement and further thought. Comparisons with the velocity vector analysis show that the TrIM algorithm appears to accurately represent the direction of the flow of gastric chyme but that it is ineffective at measuring the magnitude of the velocity.

9.4.4 The advantages of EIE over existing techniques

There is little doubt that EIE has many advantages over existing techniques. From a clinical perspective it is non-invasive, percutaneous and does not use ionising radiation but in addition the small cost, portability and ease of use without the need for a specialist department make EIE a tempting alternative to the techniques mentioned in section 3.1.1 and discussed in section 9.4.

9.4.5 Further work

The tests with meal A, B and C only test a small proportion of the functions of the stomach. Previous pharmacological studies have investigated the ability of EIE to detect the effects of anti-emetic drugs such as metoclopromide that increase contractility [McClelland GR, 1985] and opioid-induced changes in the gastric emptying time such as morphine [Murphy DB, 1996 and Murphy DB, 1997]. Since these studies demonstrated that EIE is able to detect pharmacological changes in gastric function, a repeat of such experiments would valuable in light of the conclusions made in this work.

Experiments *in vitro* to examine the detection of flow by EIE would help to confirm the conclusions reached in section 9.3.2. This would require the production of a stomach phantom that simulated flow from the proximal region to the distal region while also replicating the actions of propagating gastric contractions.

One of the drawbacks mentioned of EIE is the concentration of current density immediately under the electrode which leads to a high sensitivity to motion artifcats (section 4.3.5 and 6.2.2). There have been a number of suggestions made to alter the electrode configuration in order to change the distribution of electrical field. One proposal was to use apply the current to a ring electrode and measure the potential surrounding it [Spyrou NM, 1991]. The idea is to produce a uniform electric field with the sensing electrode as far away from the current applying electrode as possible to minimise the effects of changes in impedance at the skin surface (Fig. 9.16).

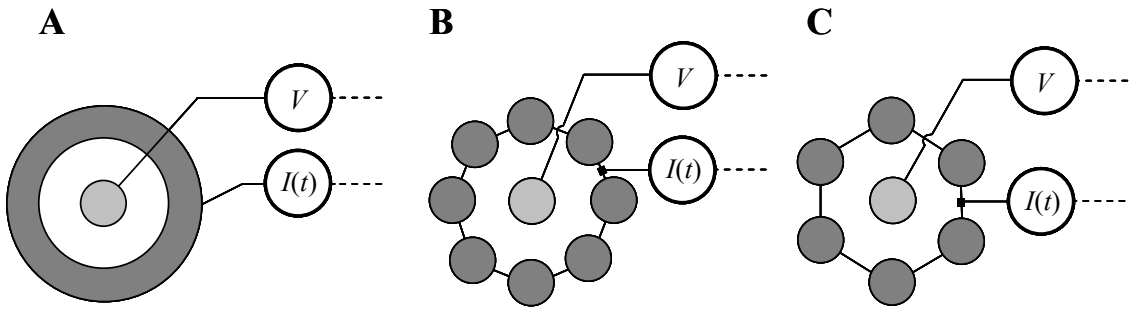

Fig. 9.16 Three possible solutions to the non-uniformity of the electrical field shown in section 4.3.4 (Fig. 4.19) to create a uniform electric field [Spyrou NM, 1991].

The effect of the current injecting electrode surrounding the sensing electrode is to create a uniform electric field. The equipotentials for these configurations have been modelled using the same program that produced the previous analysis of equipotentials shown in Fig. 4.19. Fig. 9.17 illustrates that the eqipotentials are more uniform and that the sensing electrode does not lie over a concentration of eqipotentials.

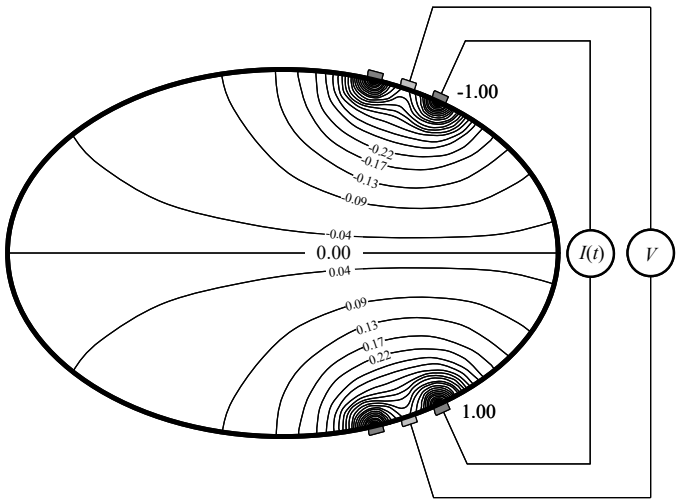

Fig. 9.17 Improvement in the uniformity of the equipotentials using the one of the three configurations suggested in Fig. 9.16.

Analysis of the maximum impedance deflection per unit volume of the meal ingested, has drawn attention to the fact that since the impedance of fat is relatively high, the sensitivity of the EIE system reduces with body mass index and girth. Consequently, the signal to noise ratio is diminished at the depth of the stomach, precluding the detection of gastro-physiological information.

The suggested configuration of electrodes in Figs. 9.16A, B and C may improve the sensitivity of EIE at gastric depths. This is alluded to by comparing the modelling of the equipotentials produced by the suggested configuration in Fig. 9.17 with the modelling of the equipotentials produced by the current EIE system in Fig. 4.19.

Furthermore, in light of the results obtained from the experimental studies carried out during this research, it is my opinion that since the original concept of EIE was only designed to measure half emptying times and the detect contractility, the time has come to redesign the hardware to incorporate the fact that electrical impedance measurements can detect many other gastro-physiological parameters that may be of significant clinical importance. This will also provide the opportunity to test the proposed improvements to enhance sensitivity and resolve the problems highlighted.

9.4.6 The future of EIE

EIE is able to detect important gastro-physiological phenomena and is a very useful research tool for investigating gastric function. Pharmacological and clinical trials will verify whether EIE can detect dysmotility and differentiate between normal volunteers and patients with gastrointestinal disorders. These trials are critical if EIE is going to be accepted by the medical fraternity and take its place as an essential diagnostic tool.

PUBLICATIONS

Giouvanoudi A, Amaee WB, Sutton JA, Horton P, Morton R, Morgan L, **Freedman MR** and Spyrou NM. (2002) 'Physiological interpretation of electrical impedance epigastrography measurements', *Physiological Measurement,* 23: 1-11.

Gaitanis A, **Freedman MR** and Spyrou NM (2003) 'Verification of a simple technique for the removal of motion artefacts in electrical impedance epigastrography signals', *Computational Methods in Sciences and Engineering,* ICCMSE: 179-182.

Freedman MR, Gaitanis A and Spyrou NM (2005) 'Modelling of electrical impedance epigastrography signals to investigate the efficacy of a motion artifact rejection algorithm', Accepted for publication in 2005 in the *Journal of Computational Methods in Sciences and Engineering*.

BIBLIOGRAPHY

Anton H, Bivens I and Davis S (2002) 'Calculus', Seventh edition, John Wiley and Sons.

Banks S (1990) 'Signal processing, image processing and pattern recognition' Prentice Hall.

Bearne RM and Levy MN (1998) 'Physiology', Fourth edition, Mosby publishing.

Binmore K and Davies J (2001) 'Calculus: concepts and methods', Cambridge University Press.

Bland M (1999) 'An introduction to medical statistics', Oxford medical publications.

Brown BH *et al.* (1999) 'Medical physics and biomedical engineering', Institute of Physics Publishing.

Cheshire E (1998) 'Gastrointestinal system', Mosby.

Chugani ML, Samant and Cerna M (1998) 'LabVIEW signal processing', Prentice-Hall.

Crawshaw J and Chambers J (1994) 'A concise course in A-level statistics', Third edition, Stanley Thornes.

Geddes LA (1972) 'Electrodes and the measurement of bioelectric events', John Wiley and Sons.

Geddes LA and Baker LE (1975) 'Principles of applied biomedical instrumentation', Second edition, John Wiley and Sons.

Golten J (1997) 'Understanding signals and sysytems', McGraw Hill.

Gonzalez RC and Woods RE (1992) 'Digital image processing', Addison-Wesley.

Green SB and Salkind NJ (2003) 'Using SPSS for Windows and Macintosh', Third edition, Prentice Hall.

Kirkwood BR (1988) 'Essentials of medical statistics', Blackwell Scientific Publications.

Kumar D and Wingate D (1993) 'An illustrated guide to gastrointestinal motility', Second edition, Churchill Livingstone.

James G (1996) 'Modern engineering mathematics', Second edition, Addison-Wesley.

Lumley JSP (1996) 'Surface anatomy: the anatomical basis of clinical examination', Second Edition, Churchill Livingstone.

Mallat S (1999) 'A wavelet tour of signal processing', Second edition, Academic Press.

Miao GJ and Clements MA (2002) 'Digital signal processing and statistical classification', Artec House.

Neal MJ (1997) 'Medical pharmacology at a glance', Third edition, Blackwell science.

Norman GR and Streiner DL (2000) 'Biostatistics: the bare essentials', Second edition, BC Decker.

Mould RF (1998) 'Introductory medical statistics', Third edition, Institute of Physics Publishing.

Ohanian HC (1994) 'Principles of physics', W. W. Norton and Company.

Peters TM and Williams J (1998) 'The Fourier transform in biomedical engineering', Birkhäuser.

Petersen RD and Myers GG (1976) 'Waveform analysis in medicine: an introduction', Charles C Thomas.

Pethig R (1979) 'Dielectric and electronic properties of biological materials', John Wiley and Sons.

Plonsey R and Fleming DG (1969) 'Bioelectric phenomena', McGraw-Hill.

Seeley RR, Stephens TD and Tate P (1995) 'Anatomy and Pysiology', Third Edition, Mosby.

Teolis A (1998) 'Computational signal processing with wavelets', Birkhäuser.

Webster JG (1998) 'Medical instrumentation: application and design', Third edition, John Wiley and Sons.

REFERENCES

Addinson PS, Watson JN and Feng T (2002) 'Low-oscillation complex wavelets', *Journal of Sound and Vibration,* 254(4): 733-762.

Azpiroz F and Malagelada JR (1985a) 'Physiological variations in canine gastric tone measured by an electronic barostat', *American Journal of Physiology,* 247: 229-237.

Azpiroz F and Malagelada JR (1985b) 'Intestinal control of gastric tone', *American Journal of Physiology Gastrointestinal and Liver Physiology,* 249: G501-G509.

Baker LE (1971) 'Biomedical applications of electrical-impedance measurements', in Watson BW (Ed.), *'IEE Medical Electronics Monographs',* 1: Peregrinus, London.

Bennet EJ (1999) 'Functional gastrointestinal disorders: relations between psychosocial factors, symptoms and sensorimotor disturbance', PhD Thesis, *University of Sydney*.

Baxter AJ, *et al.* (1988) 'Evaluation of applied potential tomography as a new non-invasive gastric secretion test', *Gut,* 29: 1730-1735.

Boulby P, Moore R, Gowland P and Spiller RC (1999) 'Fat delays emptying but increases forward and backward antral flow as assessed by flow-sensitive magnetic resonance imaging' *Neurogastroenterology and Motility,* 11(1): 27-36.

Brown BH *et al.* (1999) 'Medical physics and biomedical engineering' Institute of Physics Publishing, Bristol.

Brown BH (1983) 'Tissue impedance methods', in Jackson DF (Ed.) *Imaging With Non-ionising Radiations,* Surrey University Press.

Carlson HC, Code CF and Nelson RA (1966) 'Motor activity of the canine gastroduodenal junction: A cineradiographic, pressure and electric study' *American Journal of Digestive Diseases,* 11: 155-176.

Castillo FD (1987) 'An investigation into the use of the gastric impedance monitor system for detecting gastric contractions', MSc Dissertation, *University of Surrey*.

Cheshire, E (1998) 'Gastrointestinal system' Mosby, London.

Ching EJ (1992) 'An investigation into the methods of quantifying gastric contractions using epigastric impedance data' MSc Dissertation, *University of Surrey*.

Christensen, J (2001) 'The Motility of the Gastrointestinal Tract' Internally Peer Reviewed.

Chugani ML, Samant AR and Cerna M (1998) 'LabVIEW signal processing', Prentice Hall International.

Code CF and Martlett JA (1975) 'The interdigestive myo-electric complex of the stomach and small bowel of dogs', *Journal of Physiology,* 246: 289-309.

Coffin B, Azpiroz F, Guarner F and Malagelada J-R (1994) 'Selective gastric hypersensitivity and reflux hyporeactivity in functional dyspepsia', *Gastroenterology,* 107: 1345-1351.

Crawley JN and Corwin RL (1994) 'Biological actions of Cholecystokinin', *Peptides,* 15(4): 731-755.

Crawshaw J and Chambers J (2001) 'A concise course in advanced level statistics: with worked examples', Nelson Thornes.

Cucchiara S *et al.* (1992) 'Reversal of gastric electrical dysrhythmias by cisapride in children with functional dyspepsia. Report of three cases.' *Digestive Diseases and Sciences,* 37: 1136-1140.

Dooley CP, Reznick JB and Valenzuela JE (1984) 'Variations in gastric and duodenal motility during gastric emptying of liquid meals in humans', *Gastroenterology,* 87: 1114-1119.

Drewe J, Gadient A, Rovati L and Beglinger C, (1992) 'Role of circulating cholecystokinin in control of fat-induced inhibition of food intake in humans', *Gastroenterology,* 102: 1654-1659.

Edwards DAW and Rowlands EN (1968) 'Physiology of the gastroduodenal junction', in Code CF (Ed.), *Handbook of Physiology,* Section 6: Alimentary canal, Volume IV: Motility, American Physiological Society, Washington DC.

Feinle C *et al.* (1999) 'Scintigraphic validation of a magnetic resonance imaging method to study gastric emptying of a solid meal in humans' *Gut* 44: 106-111.

Fenlon TJ (1992) 'Medical applications of electrical impedance measurements' PhD Thesis, *University of Surrey*.

Ferdinandis TGHC, Dissanayake AS and De Silva HJ (2002) 'Effects of carbohydrate meals of varying consistency on gastric myoelectrical activity' *Singapore Medical Journal,* 43(11): 579-582.

Ferroir J (1937) 'The diabetic stomach', *Thesis in Medicine,* Paris, France.

Fone DR *et al.* (1990) 'Evaluation of patterns of human antral and pyloric motility with an antral wall motion detector', *American Journal of Physiology Gastrointestinal and Liver Physiology,* 258: G616-G623.

Frank JW *et al.* (1995) 'Mechanism of accelerated gastric emptying of liquids and hyperglycemia in patients with type II diabetes mellitus', *Gastroenterology,* 109: 755-765.

Freedman MR, Gaitanis A and Spyrou NM (2005) 'Modelling of electrical impedance epigastrography signals to investigate the efficacy of a motion artifact rejection algorithm' *Journal of Computational Methods in Sciences and Engineering,* Accepted for publication.

Freedman MR (2001) 'Gastric Impedance Measurement System for Electrical Impedance Epigastrography User Manual', *University of Surrey*.

Freedman MR (2000) 'Spectral analysis of Epigastrographic signals for the assessment of gastric motility in humans' MSc Dissertation, *University of Surrey*.

Fried M, *et al.* (1991) 'Role of cholecystokinin in regulation of gastric emptying and pancreatic enzyme secretions in humans. Studies with cholecystokinin antagonist Loxiglumide', *Gastroenterology,* 101: 503-511.

Gaitanis A, Freedman MR and Spyrou NM (2003) 'Verification of a simple technique for the removal of motion artefacts in electrical impedance epigastrography signals', *Journal of Computational Methods in Sciences and Engineering,* International Conference on Computational Methods in Science and Engineering, ICCMSE: 179-182.

Geldof H, Van der Schee EJ and Grashuis JL (1986a) 'Electrogastrographic characteristics of interdigestive migrating complex in humans', *American Journal of Physiology,* 250: G165-G171.

Geldof H, Van der Schee EJ, van Blankstein M and Grashuis JL (1986b) 'Electrogastrographic study of gastric myoelectrical activity in patients with unexplained nausea and vomiting', *Gut,* 27: 799-808.

Giouvanoudi A *et al.* (2002) 'Physiological interpretation of electrical impedance epigastrography measurements', *Physiological Measurement,* 23: 1-11.

Giouvanoudi A (2000) 'Electrical impedance measurements in gastric function investigations', PhD Thesis, *University of Surrey*.

Greider MH, Steinberg V and McGuigan JE (1972) 'Electron microscopic identification of the gastrin cell of the human antral mucosa by means of immunocytochemistry', *Gastroenterology,* 63:572-582.

Hadi NA (2004) 'Impact of different calorific meals and pharmacological blocker agent on the emptying behaviour of the whole stomach and its three regions using simultaneous scintigraphy and electrical impedance epigastrography', PhD Thesis, *University of Surrey.*

Hadi NA (2002) 'Variations in gastric emptying times of three stomach regions for simple and complex meals using scintigraphy', *IEEE transactions on nuclear science*, 49(5): 2328 – 2331.

Hadi NA (2001) Private communication.

Hamza AOM (1999) 'Modelling the effects of stomach secretions in gastric emptying rates', MSc Dissertation, *University of Surrey*.

Hausken T, Mundt M and Samson M (2002) 'Low antroduodenal pressure gradients are responsible for gastric emptying of a low-caloric liquid meal in humans', *Neurogastroenterology and Motility,* 14: 97-105.

Hausken T, Ødegaard S, Knut M and Berstad A (1992) 'Antroduodenal motility and movements of luminal content studied by duplex sonography', *Gastroenterology,* 102: 1583-1590.

Hermansson, G and Sivertsson, R (1996) 'Gender-Related Differences in Gastric Emptying Rate of Solid Meals', *Digestive Diseases & Sciences.* 41: 1994-1998.

Holt S, Cervantes J, Wilkinson AA and Wallace JHK (1986) 'Measurment of gastric emptying rate in humans by real-time ultrasound', *Gastroenterology,* 90: 918-923.

Horowitz M, *et al.* (2001) 'Gastric emptying in diabetes: clinical significance and treatment', *Diabetic Medicine,* 19: 177-194.

Houghton LA, Mangnall YF and Read NW (1990) 'Effect of incorporating fat into a liquid test meal on the relation between intragastric distribution and emptying in human volunteers', *Gut,* 31: 1226-1229.

Houghton LA, *et al.* (1988) 'Motor activity of the gastric antrum, pylorus and duodenum under fasted conditions and after a liquid meal', *Gastroenterology,* 94: 1276-1284.

Hubbard BB (1998) 'The World According to Wavelets', AK Peters, Second Edition, Wellesley.

Hunt JN and Stubbs DF (1975) 'The volume and energy content of meals as determinants of gastric emptying', *Journal of Physiology,* 245: 209-225.

Hveem K, *et al.* (2001) 'Relationship between ultrasonically detected phasic antral contractions and antral pressure', *American Journal of Physiology Gastrointestinal and Liver Physiology,* 281: G95-G101.

IEEE (1985) 'IEEE standard 754 for binary floating point arithmetic, *IEEE publishing*.

Indireshkumar K, *et al.* (2000) 'Relative contributions of "pressure pump" and "peristaltic pump" to gastric emptying', *American Journal of Physiology Gastrointestinal and Liver Physiology,* 278: G604-G616.

Ishii M, *et al.* (1994) 'Altered postprandial insulin requirement in IDDM patients with gastroparesis', *Diabetes Care,* 17: 901-903.

Itoh Z and Sekiguchi T (1983) 'Interdigestive motor activity in health and disease', *Scandinavian Journal of Gastroenterology,* Suppl. 82: 121-134.

Itoh Z, Takayanagi R, Takeuchi, S and Isshiki, S (1978) 'Interdigestive motor activity of Heidanheim pouches in relation to main stomach in conscious dog' *American Journal of Physiology*, 234: E333-E338.

Jones KL *et al.*, (1995) 'Relationships between gastric emptying, intragastric meal distribution and blood glucose levels in diabetes mellitus', *Journal of nuclear medicine,* 35: 2220-2228.

Jian R *et al.* (1989) 'Symptomatic, radionuclide and therapeutic assessment of chronic idiopathic dyspepsia: A double blind placebo controlled evaluation of cisapride', *Digestive Diseases and Sciences,* 34: 657-664.

Kanazawa M, Nomura T, Fukudo S and Hongo M (2000) 'Abnormal visceral perception in patients with functional dyspepsia: use of cerebral potentials evoked by electrical stimulation of the oesophagus', *Neurogastroenterology & Motility,* 12: 87-94.

Kelly KA (1981) 'Motility of the Stomach and Gastroduodenal Junction', In Johnson LR (Ed.), *'Physiology of the Gastrointestinal tract'*, First Edition, Vol.1 Raven press.

Kelly KA, Code CF and Elveback LR (1969) 'Patterns of Canine gastric electrical activity', *American Journal of Physiology,* 219(2): 461-470.

King PM, *et al.* (1984) 'Relationships of human antroduodenal motility and transpyloric flow movement: non-invasive observations with real time ultrasound', *Gut,* 25: 1384-1391.

Koch KL, Medina M, Bingaman S and Stern RM (1992) 'Gastric Dysrhythmia and visceral sensations in patients with functional dyspepsia,' *Gastroenterology,* 102: A469.

Koch KL and Stern RM (1993) 'Electrogastrography', In Kumar D and Wingate D (Eds.), *'An Illustrated Guide to Gastrointestinal Motility'*, Second edition, Churchill Livingstone, Edinburgh.

Koch KL and Stern RM (1996) 'Functional disorders of the stomach', *Seminars in gastrointestinal disease'*, 7:185-187.

Konturek JW *et al.* (1994) 'Role of Cholecystokinin in the control of gastric emptying and secretory response to a fatty meal in normal subjects and duodenal ulcer patients', *Scandanavian Journal of Gastroenterology,* 29: 583-590.

Konturek JW, Stoll R, Konturek SJ and Domschke W (1993) 'Cholecystokinin in the control of gastric acid secretion in man', *Gut,* 34: 321-328.

Laderbaum U, *et al.* (1998) 'Differential symptomatic and electrogastrographic effects of distal and proximal human gastric distension', *American Journal of Physiology Gastrointestinal and Liver Physiology,* 275: G418-G424.

Lang IM, Sarna SK and Shaker R (1999) 'Gastrointestinal motor and myoelectric correlates of motion sickness', *American Journal of Physiology Gastrointestinal and Liver Physiology,* 277: G642-G652.

Ligris EN (1997) 'The effects of stomach secretions in measurement of emptying rates of complex meals', MSc Dissertation, *University of Surrey*.

Lin HC and Hasler WL (1991) 'Disorders of gastric emptying', In Yamada T *et al.* (Ed.), 'Textbook of Gastroenterology', JB Lippincott Company, Philadelphia.

Lin HC (1994) 'Disorders of gastric motility and emptying', In Gitnick G (Ed.), *'Principles and Practice of Gastroenterology and Hepatology'*, Second Edition, Appleton and Lange.

Lin X and Chen JZ (2001) 'Abnormal gastric slow waves in patients with functional dyspepsia assessed by multichannel electrogastrography', *American Journal of Physiology Gastrointestinal and Liver Physiology,* 280: G1370-G1375.

Lipp RW *et al.* (1997) 'Evidence of accelerated gastric emptying in longstanding diabetic patients after ingestion of a semisolid meal', *Journal of Nuclear Medicine,* 38: 814-818.

Lluch I *et al.* (1999) 'Gastroesophageal reflux in diabetes mellitus', *American Journal of Gastroenterology,* 94: 919-924.

Lumley, JSP (1996) 'Surface anatomy: the anatomical basis of clinical examination' Second Edition, Churchill Livingstone, Edinburgh.

Mangnall YF *et al.* (1988) 'Comparison of applied potential tomography and impedance epigastrography as methods of measuring gastric emptying', *Clinical Physics and Physiological Measurement,* 9: 249-254.

Malegalada JR and Staghellini V (1985) 'Manometric evaluation of functional upper gut symptoms', *Gastroenterology,* 88: 1223-1231.

Marciani L *et al.* (2001a) 'Effect of meal viscosity and nutrients on satiety, intragastric dilution and emptying assessed by MRI', *American Journal of Physiology Gastrointestinal Liver Physiology,* 280: G1227-G1233.

Marciani L, *et al.* (2001b) 'Assessment of antral grinding of a model solid meal with echo-planar imaging', *American Journal of Physiology Gastrointestinal Liver Physiology,* 280: G844-G849.

McClelland GR and Sutton JA (1985) 'Epigastric impedance: a non invasive method of the assessment of gastric emptying and motility', *Gut* 6: 607-614.

McHugh PR and Moran TH (1979) 'Calories and gastric emptying: a regulatory capacity with implications for feeding', *American Journal of Physiology,* 236(5): R254-R260.

Meade ML and Dillon CR (1997) 'Signals and systems: Models and behaviour', Chapman and Hall, Second Edition.

Mearin L, Cucala M, Azpiroz F and Malagelada JR (1991) 'The origin of symptoms on the brain-gut axis in functional dyspepsia,' *Gastroenterology,* 101: 999-1006.

Meeroff JC, Go VLW and Phillips SF (1975) 'Control of gastric emptying by osmolarity in of the duodenal contents of man', *Gastroenterology,* 68: 1144-1151.

Meyer JH, Mayer EA, Jehn D, Gu Y and Fink AS (1986) 'Gastric processing and emptying of fat', *Gastroeneterology,* 90: 1176-1187.

Morgan KG, Muir TC and Szurszewski JH (1981) 'The electrical basis for contraction and relaxation in canine fundal smooth muscle', *Journal of Physiology,* 311: 475-488

Murphy DB, Sutton JA and Murphy MB (1996) 'Novel use of an electrical bioimpedance technique to detect opioid-induced changes in gastric emptying', *British Journal of Anaesthesia,* 76: (S2) A45.

Murphy DB, Sutton JA, Prescott LF and Murphy MB (1997) 'Opioid-induced delay in gastric emptying: a peripheral mechanism in humans', *Anesthesiology,* 87: 765 – 770.

Muth ER, Stern RM and Koch KL (1996) 'Effects of vection-induced motion sickness on gastric myoelectric activity and oral-cecal transit time', *Digestive Diseases and Sciences*, 41: 330-334.

Oba-Kuniyoshi AS, Olivera JA Jr, Moraes ER and Troncon LEA (2004) 'Postprandial symptoms in dysmotility-like functional dyspepsia are not related to disturbances of gastric myoelectrical activity', *Brazilian Journal of Medical and Biological Research,* 37: 47-53.

Pansky B (1975) 'Dynamic anatomy and physiology', pg. 423, Macmillan publishing Co., Inc.

Parkman HP, Hasler WL, Barnett JL and Eaker EY (2003) 'Electrogastrography: a document prepared by the gastric section of the American Motiltiy Society Clinical GI Motility Testing Task Force', *Neuroatsroenterology and Motiltiy,* 15: 89-102.

Pickworth MJW (1984) 'Impedance measurements for gastric emptying', MSc Dissertation, *University of Surrey*.

Ploutz-Snyder L *et al.* (1999) 'Gastric gas and fluid emptying assessed by magnetic resonance imaging', *European Journal of Applied Physiology,* 79: 212-220.

Rainbird AL *et al.* (1987) 'Effect of posture and cold stress on impedance measurements of gastric emptying,' *Pharmaceutical Medicine,* 2: 35-42.

Rao SSC and Schulze-Delrieu K (1993) 'The stomach, pylorus and duodenum' In Kumar D and Wingate D (Eds.), *'An Illustrated Guide to Gastrointestinal Motility'*, Second edition, Churchill Livingstone, Edinburgh.

Riddell P, Taylor M, Dent J and Jaimieson GG (1991) 'Origin and mechanical effect of broad gastric pressure waves during liquid gastric emptying in pigs', *Gastroenterology,* 100 (5 part 2): A416.

Schvarz E *et al.* (1997) 'Physiological hyperglycaemia slows gastric emptying in normal subjects and patients with insulin-dependant diabetes mellitus', *Gastroenterology,* 113: 60-66.

Schwizer M, *et al.* (1996) 'Measurement of proximal and distal gastric motility with magnetic resonance imaging', *American Journal of Physiology Gastrointestinal and Liver Physiology,* 271: G217-G222.

Schulze-Delrieu K, Herman RJ, Shirazi SS and Brown BP (1998) 'Contractions move contents by changing the configuration of the isolated cat stomach', *American Journal of Physiology Gastrointestinal and Liver Physiology,* 274: G359-G369.

Silverthorn DU (2001) 'Human physiology: an integrated approach', Second Edition, Pearson Education, Inc.

Snyder WS *et al.* (1975) 'Reference Man: Anatomical, Physiological and Metabolic Characteristics', ICRP Publication 23.

Spyrou NM and Castillo FD (1993) 'Electrical Impedance Measurements', In Kumar D and Wingate D (Eds.), *'An Illustrated Guide to Gastrointestinal Motility'*, Second Edition, Churchill Livingstone, New York.

Spyrou NM, Fenlon TJ and Worpe E (1991) Private communication.

Stanghellini V, *et al.* (1983) 'Stress-induced gastroduodenal motor disturbances in humans: possible humoral mechanism', *Gastroenterology,* 85: 83-91.

Stanghellini V, Borovicka J and Read NW (1994) 'Feedback Regulation and Sensation', *Digestive Diseases and Sciences*, 39(12): 124S-127S.

Strunz UT, Code CF and Grossman MI (1979) 'Effect of gastrin on the electrical activity of the antrum and duodenum of dogs', *Proceedings of the Society of Experimental Biology and Medicine,* 161:25-27

Sutton JA (1987) 'Epigastric impedance: A novel non-invasive method for measuring gastric emptying', MD Thesis, University of London.

Sutton JA, Thompson S and Sobnack R (1985) 'Measurement of gastric emptying rates by radioactive isotope scanning and epigastric impedance', *The Lancet,* 20: 898-900.

Szurszewski JH (1987) 'Electrical Basis for Gastrointestinal Motility', In LR Johnson (Ed.) *'Physiology of the Gastrointestinal tract'*, Second Edition, Vol.1 Raven press.

Szurszewski JH (1969) 'A migrating electric complex of the canine small intestine'*, American Journal of Physiology,* 217:1757-1763.

Takeda N, *et al.* (2001) 'Neural mechanisms of motion sickness', *Journal of Medical Investigation* 48: 44-59.

Talley NJ (2002) 'Dyspepsia: management guidelines for the millennium', *Gut*, 50 (Supplement 4): iv72-iv78.

Thompson DG, Rickelson E and Malagelada JR (1982) 'Pertubation of gastric emptying and duodenal motility through the central nervous system', *Gastroenterology,* 83: 1200-1206.

Tortora GJ and Grabowski SR (2000) 'Principles of Anatomy and Physiology', Ninth Edition, John Wiley and Sons, Inc.

Tougas G *et al.* (1992) 'Relation of pyloric motility to pyloric opening and closure in healthy subjects', *Gut*, 33: 466-471.

Troncon LEA, Bennett RJM, Ahluwalia NK and Thompson DG (1994) 'Abnormal intragastric distribution of food during gastric emptying in functional dyspepsia patients', *Gut,* 35: 327-332.

Vassallo MJ *et al.* (1992) 'Measurement of axial forces during emptying from the human stomach', *American Journal of Physiology Gastrointestinal and Liver Physiology,* 263: G230-G239.

Waldron B *et al.* (1991) 'Evidence for hypomotility in non-ulcer dyspepsia: a prospective multifactorial study', *Gut,* 32: 246-251.

Walsh JH (1987) 'Gastrointestinal hormones', In LR Johnson (Ed.) *'Physiology of the Gastrointestinal tract'*, Second Edition, Vol.2 Raven press.

Waugh A and Grant A (2001) 'Intake of raw materials and elimination of waste', *Anatomy and physiology in health and fitness*, Ninth Edition, Churchill Livingstone, London.

White CM, Poxon V and Alexander-Williams J (1983) 'Effects of nutrient liquids on human gastoduodenal motor activity', *Gut*, 24: 1109-1116.

Wichman B and Hill D (1987) 'Building a Random-Number Generator: A Pascal Routine for Very-Long-Cycle Random-Number Sequences' *BYTE (March 1987)*: 127-128.

Wingate DL, Stacher G and Kreiss C (1994) 'Role and integration of mechanisms controlling gastric emptying' *Digestive Diseases and Sciences,* 39(12): 120S-123S.

Wingate DL (2001) Private communication.

Witsoe DA and Kinnen E (1967) 'Electrical resistivity of lung at 100 kHz', *Medical and Biological Engineering,* 5: 239-248.

Wood JD (1987) 'Physiology of the Enteric Nervous System', In Johnson LR (Ed.) *'Physiology of the Gastrointestinal Tract'* Vol.1, Second Edition, Raven press.

Appendix A The 3D coordinate system

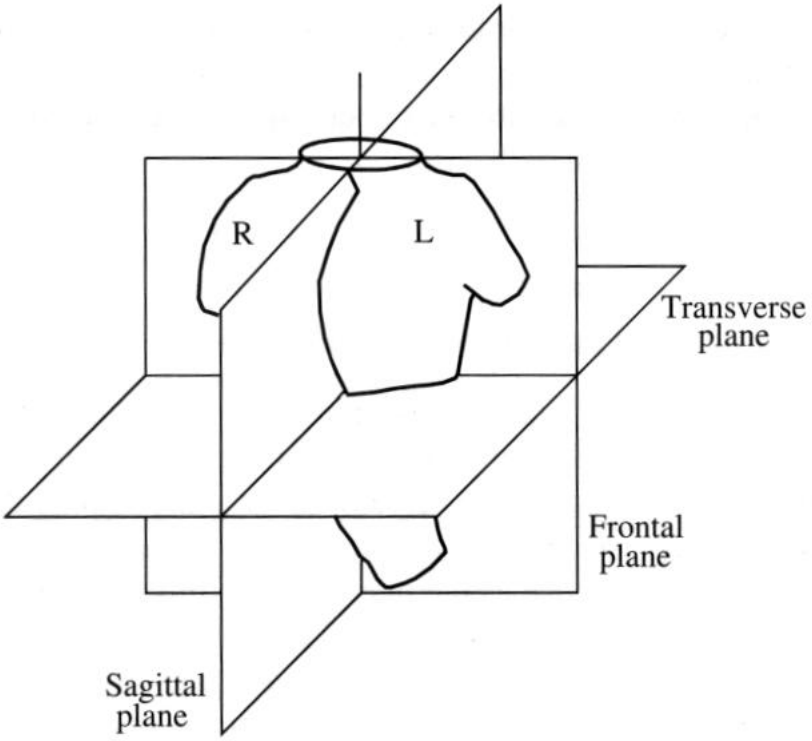

Fig. A1 The three imaging planes; sagittal, transverse and frontal [Reproduced from Brown BH, 1999].

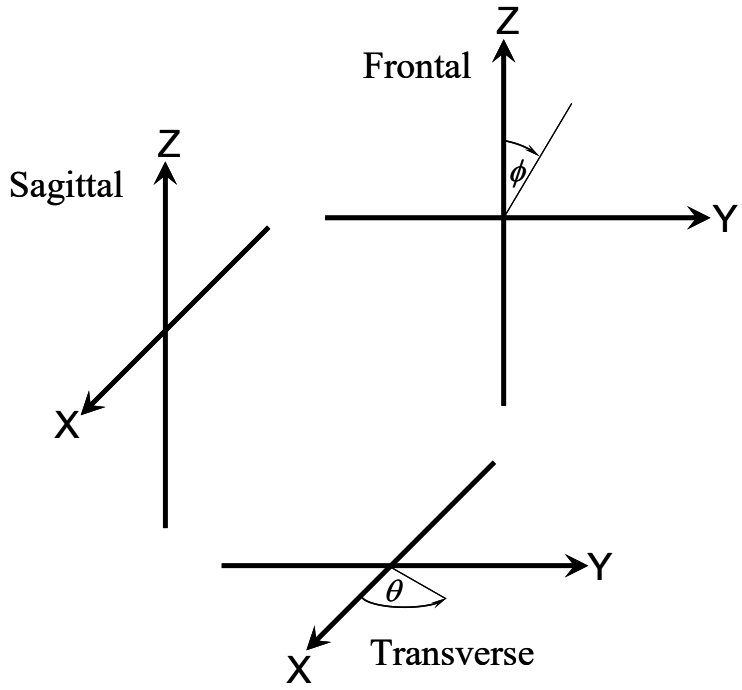

Fig. A2 The 3D coordinate system with respect to the three imaging planes. The (x , y) is the Transverse plane, (x , z) is the Sagittal plane and (y , z) is the Frontal plane.

Appendix B Proof of the equation for the radius of an ellipse

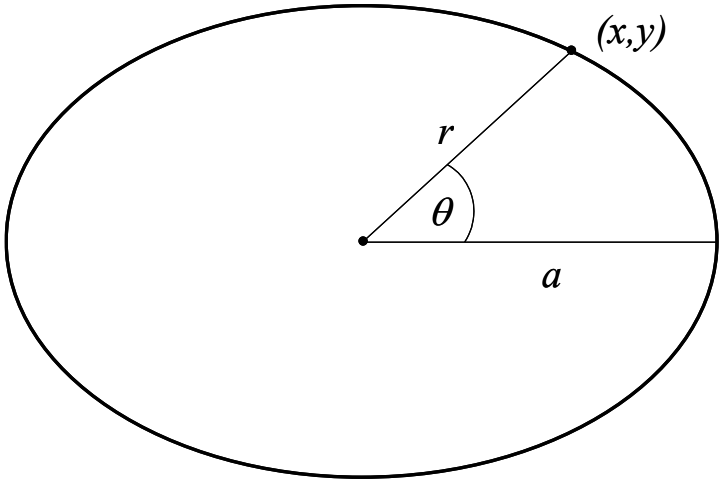

Fig. B1 Ellipse showing semi-minor axis *a* and radius of *r*.

$$\frac{x^2}{a^2}+\frac{y^2}{b^2}=1 \tag{B1}$$

$$x = r\cos\theta \tag{B2}$$

$$y = r\sin\theta \tag{B3}$$

Substituting B2 and B3 into B1.

$$\frac{r^2\cos^2\theta}{a^2}+\frac{r^2\sin^2\theta}{b^2}=1$$

Multiply by b^2 and a^2

$$r^2b^2\cos^2\theta + r^2a^2\sin^2\theta = b^2a^2$$

$$r^2(b^2\cos^2\theta + a^2\sin^2\theta) = b^2a^2$$

$$\therefore \quad r^2 = \frac{b^2a^2}{b^2\cos^2\theta + a^2\sin^2\theta}$$

If the angle is subtended to the semi-minor axis, b then the cosine and sine terms swap.

$$\therefore \quad r^2 = \frac{b^2a^2}{b^2\sin^2\theta + a^2\cos^2\theta}$$

Appendix C Forms used for EIE experiments

FORM 1: Anthropomorphic and volunteer lifestyle questionnaire

To be completed by the demonstrator
No. ……

Full name ……

Sex (M / F) **Age** ….. **Height** …..m **Weight** …...kg **Girth** …...cm[1] **Nationality** …….…….

Do you have any special dietary habits (e.g. Vegetarian)? Please give full details below.

……..

On average, how often do you eat a spicy/'hot' meal?

□ Never □ 1 p month □ 1 p wk □ 2-4 p wk □ 5-7 p wk □ >7 p wk

On average, how many units of alcohol do you drink per week?[2]

□ None □ 1-9 □ 10-19 □ 20-29 □ >30

Which type of alcoholic drink do you take most often?

□ Beer and alcopops □ Cider, wine or weak spirits □ Strong spirits

On average, how many cigarettes do you smoke per day?

□ < 1 □ 1-4 □ 5-9 □ 10-19 □ 20-40 □ > 40

On average, how many times do you deliberately exercise per month?

□ < 1 □ 5-9 ρ 15-20 □ > 20
□ 1-4 □ 10-14

On average, how many caffeinated drinks do you take per day?

□ < 1 □ 1 □ 2 □ 3 □ 4 □ > 4

Which type of <u>caffeinated</u> drink do you take most often?

□ Coffee □ Tea (NOT fruit or herbal) □ Stimulant drinks[3]

Please provide details of any medication you are taking including patches or gum for the delivery of drugs such as nicotine.

……

Do you suffer from any food allergies, food intolerance or gastroenterological complications, e.g. nut allergies, lactose intolerance or irritable bowel syndrome (IBS)?

……

Do you have any <u>objection</u> (on religious grounds etc.) to any of the following…

□ Placement of electrodes by the opposite sex □ Shaving with a razor blade
□ Exposing arms or legs □ Exposing the abdominal region
□ Other relevant religious requirements ……

Is there any other information that you think may be relevant, e.g. Voluntary dieting, other allergies?

……

[1] You should fill this in on the day of the experiment.
[2] One unit equals one measure of spirits, one glass of wine, half a pint of normal strength beer/cider/lager and a third of a pint of strong cider/lager.
[3] Such as Red Bull, Solstis etc.

FORM 2: Electrode placement form

Name:……..……..

Age:……..……..…… Weight:……..……..…kg

Sex: M / F Height:……..……..……..m

Girth:……..…….cm BMI:……..…….....……kgm^{-2}

Date	Measurement	Red	Yellow	Black
	1	cm cm	cm cm	cm cm
	2	cm cm	cm cm	cm cm
	3	cm cm	cm cm	cm cm
	4	cm cm	cm cm	cm cm

XU = ……. cm

NOTES

Girth is measured around the waist with a tape measure positioned over the umbilicus.

The above measurements for electrode placement should be entered in the following format. The first measurement listed should be in the longitudinal (y-direction) and the second measurement should be in the lateral direction (x-direction).

FORM 3: Volunteer information for Electrical Impedance Epigastrography (EIE)

The purpose of the following set of practical experiments is to demonstrate a range of techniques with which this department has been involved and require relatively simple *in vivo* measurements. You will be asked to attend for approximately two and a half hours. It is CRITICAL that you adhere to the agreed times.

Electrical impedance works by passing very small alternating currents (1-4mA) through the body and causes no sensation whatsoever. The technique is totally non-invasive, does not use ionising radiation and is painless. The impedance measured during the test indicates both the emptying rate and motility of the stomach.

Thank you for taking the time to read this. Please note that all personal details given and results taken are treated in the strictest confidence. You will be given a code number, which will be used to refer to you in any publication of the results. Please confirm that you have understood the content and are happy to proceed with the study and comply with the above conditions.

PLEASE READ THIS **BEFORE** YOU SIGN

The purpose of the EIE experiment is to investigate the difference in gastric emptying and motility for three different 500ml liquid meals; mineral water, semi-complex milkshake and complex milkshake. You will be given ONE of the three meals only. **All subjects must refrain from taking any food or drink (excluding water) six hours prior to the test. You must refrain from drinking water two hours prior to the test.** It will be necessary to place three adhesive electrodes to the lower left region of your abdomen (between your ribs and umbilicus) and a further three on the back, to mirror the front. If these areas contain hair it is advisable to shave that area before arriving to ensure that the electrodes remain attached properly.

You will be tested in a semi-supine (half-lying) position and the study will last for approximately 60-90 minutes. During this time you will be asked to drink the 500ml liquid meal through a straw at a constant rate. For the experiment to be successful, it is important to remain quiet and totally relaxed throughout the study while measurements are being taken. It is also necessary for you to adhere to the following conditions:

- **No food or drink (except water) may be taken 6 hours prior to the test.**
- **Water must not be taken 2 hours prior to the test.**
- **The last meal that you have before the study should be a low fat, light snack.**
- **You must refrain from any strenuous exercise starting from the evening prior to the study.**
- **You must refrain from taking any of the following from the evening prior to the study:**

  -Alchohol
  -Caffeine (including coffee, tea, stimulant drinks etc.)
  -Cigarettes or other nicotine based products (including patches and gum)
  -Spicy foods

Signed: _____ Date: _____

APPENDIX D ACCESS 2.40 flow charts and manual

Analysis, Characterisation and Classification of Epigastrographic SignalS: ACCESS 2.40

Each section below will explain the fundamental processing and analysis procedures together with flow charts that describe the underlying program architecture. A key to the flow chart is shown in Fig. D1.

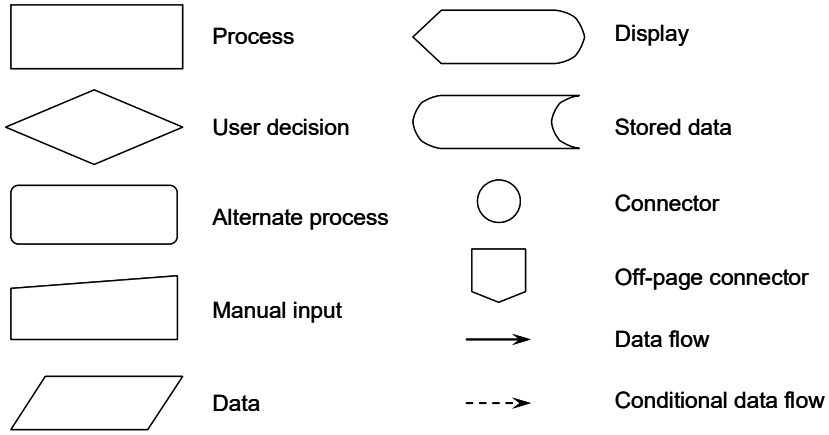

Fig. D1 Key to the flow charts used to describe the architecture of ACCESS 2.40.

Cosmetic functions have been omitted from the block diagrams so ensure that they are not over complicated. These include the ability to save data as ASCII files and graphic operations such as zoom and cursor functions. Auxiliary algorithms designed for user information such as detecting the number of event markers or channel with the greatest deflection are also omitted from the main flow diagram. Flow diagrams that represent the fundamental program architecture are given for each main page in the software numbering from 1 to 14. However, if a main page contains sub pages, these are referred to as a, b, c…etc.

After each flow diagram, there is a screen shot of the page in the software. The function of each control and indicator are explained with a picture to link its position in the software to the relevant flow diagrams. The flow diagram reference to the control or indicator is given in capitals after the title (underlined) and this format is used throughout this Appendix. All graphs in ACCESS constantly update unless the zoom key is pressed. This permits the operator to use the zoom options (). The left key () gives control of any cursors that may be used. The centre key () controls the zoom options and the right key () is a tool for shifting the position of the graph. The data and zoom controls are found on most graphs in ACCESS.

Initial processing and calculation of gastric emptying rates (Pages 1 and 2)

Program architecture of pages 1 and 2

Since the first two pages are intrinsically linked, they will be discussed together. Fig DD shows the block diagram of the software controlled by the first page. The software begins by setting all of the variables used to their preset values. During this operation the screen is disabled and greyed out so that no functions can be used. Once this process is completed, the operator is asked to load a *.eie file (which is the file format generated by the Epigastrograph acquisition software). If the length of the experiment will exceed the maximum acquisition time approximately. In these cases it is necessary for the experimenter to start a continuation file. Consequently, if such a file exists, the operator of ACCESS will be asked to enter the filename. At this stage, the data has been loaded and page 1 is enabled.

Fig D2 shows the block diagram of the software controlled by the first page. This page loads the *.eie file and displays the signal while allowing the user to apply various time-domain processing techniques. It also displays the T50 results and the modelled signal.

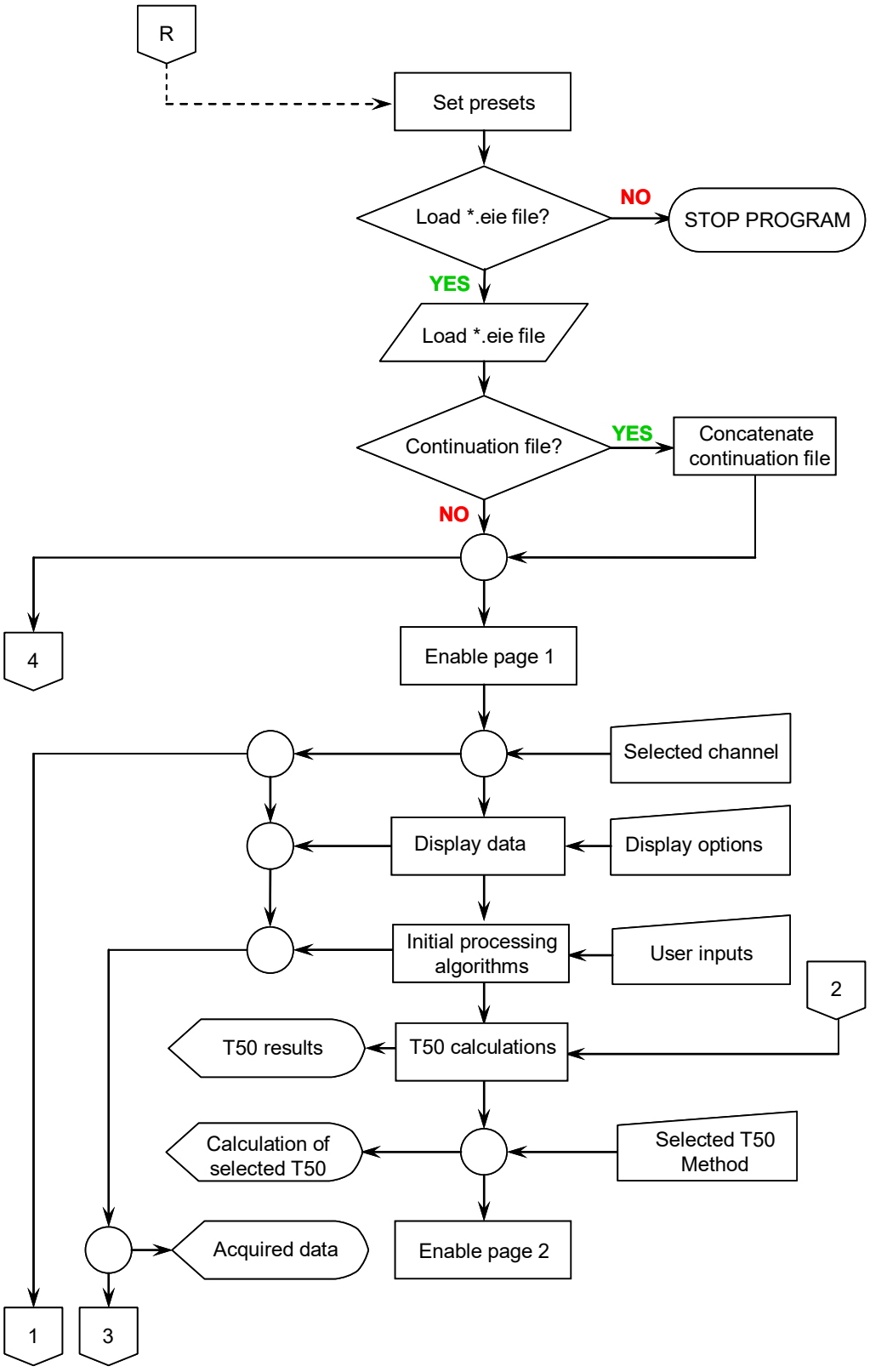

Fig. D2 Block diagram of page 1 of ACCESS 2.40.

Functions for loading the *.eie file and manipulating the signal

Fig. D3 is a screenshot of the first page of ACCESS after the *.eie file has been loaded and T50 method selected.

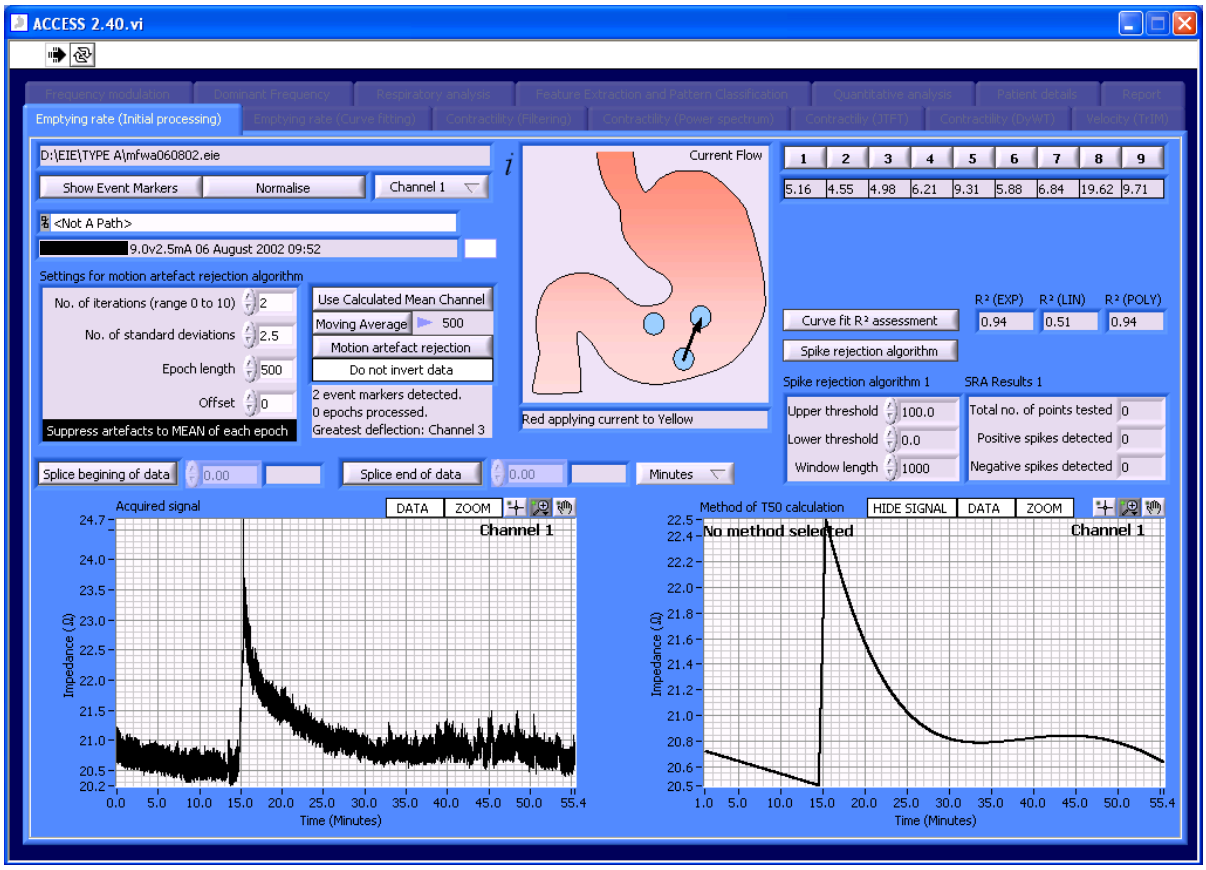

Fig. D3 Screen shot of the first page of ACCESS.

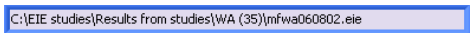

Filename: N/A

Displays the filename and directory path of the selected file.

Select channel: SELECTED CHANNEL

This function allows the operator to select the channel for the analysis. Each channel refers to one of the six signals recorded and saved in the *.eie file. The mean channel is the mean of all six channels and is also recorded by the Epigastrograph.

Show event markers: DISPLAY OPTIONS

Show event markers displays the event markers recorded in the *.eie file.

Normalise: USER INPUTS

This function adjusts the signal amplitude so that the minimum is 0 and the maximum is 1. The software will automatically normalise the data before it is filtered for contractility analysis so the magnitude of the recorded signal has no effect on the power calculations, in order that the power density can be compared between different signals regardless of their original impedance.

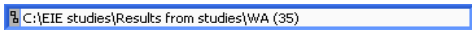

Directory path: N/A

This displays the source directory of the *.eie file. If ACCESS is not shut down, this directory will be opened automatically when ACCESS is run again.

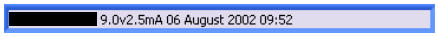

Experiment information indicator: N/A

Displays the text line of the *.eie file containing the subject name, battery voltage, applied date and time recorded before the experiment (the name of the subject has been blacked out).

Use calculated mean: USER INPUT

If the mean channel is corrupted, this allows the calculation the mean programmatically.

Moving average: USER INPUT

This control displays the moving average of the signal on the acquired data graph.

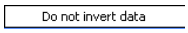

Invert data control: USER INPUT

Data inversion is necessary if a conductive meal has been given as the half emptying time (T50) calculation assumes that a non-conductive meal has been ingested.

Signal splicing: USER INPUT

These controls splice the beginning and end of the signal to remove any unwanted motion artifacts caused by either the subject adjusting themselves at the beginning of the test or by the subject moving at the end, before the operator has finished recording the signal.

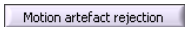

Motion artifact rejection algorithm (MARA): USER INPUT

This control applies the MARA algorithm. The parameter controls are given below.

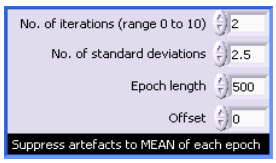

Settings for the MARA: USER INPUT

Apply Spike rejection algorithm (SRA): USER INPUT

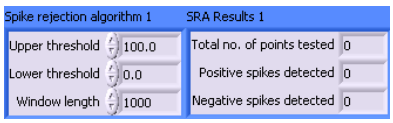

Settings for the SRA: USER INPUT

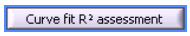

Perform assessment of the R^2 values of each emptying curve type: USER INPUT

EXP = Exponential fit, LIN = Linear fit and POLY = 4th order polynomial fit.

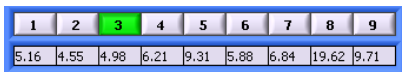

T50 selection: SELECTED T50 METHOD

This control operates like radio buttons; when one is pressed, all the others switch off. There are nine methods available for calculating the T50 and each one is shown in Fig. 6.8. The T50 result for each method applied to the selected channel is shown underneath.

Fig D4 shows the block diagram of the software controlled by the second page. This page governs the creation of a modelled signal using a linear fit for the preprandial period and a variety of fits for the postprandial period; polynomial, exponential and moving average.

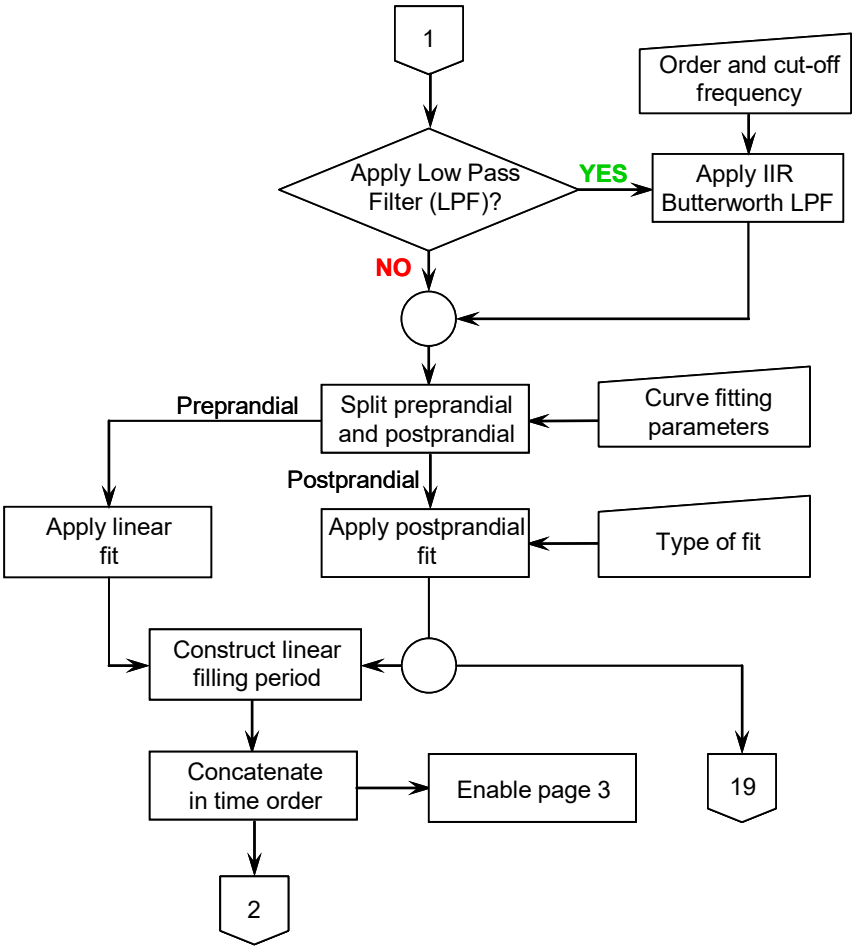

Fig. D4 Block diagram of page 2 of ACCESS 2.40.

The primary functions of pages 1 and 2 are as follows.

- Load *.eie signal from file and signal manipulation.
- Time-domain signal processing for the removal of motion artifacts.
- Low pass filtering for respiratory artifact removal.
- Create ‘fitted’ signal.
- Calculate the half emptying rates (T50).

Functions for curve fitting

The controls for the signal modelling are found in page 2 of the software, shown in Fig. D5.

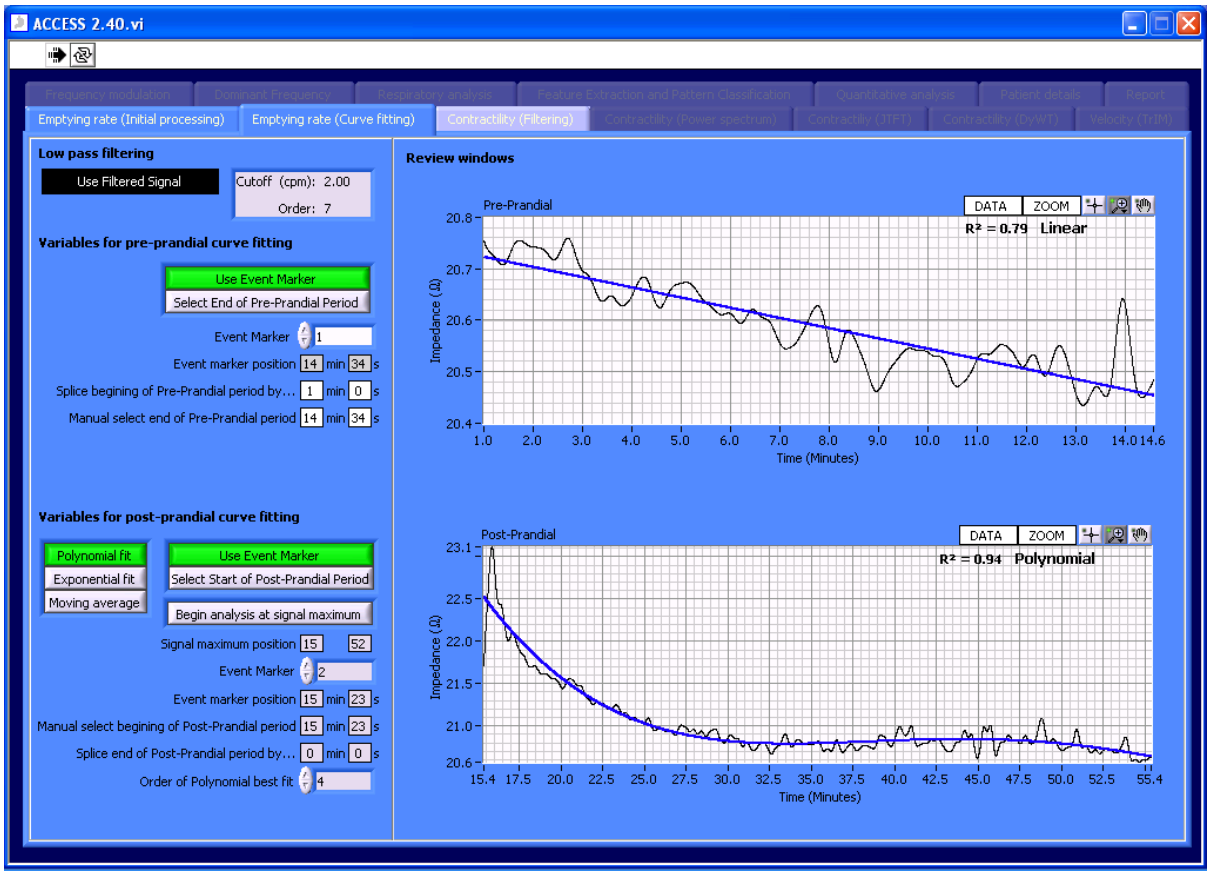

Fig. D5 Screen shot of the second page of ACCESS.

Use Low Pass Filtering: APPLY LOW PASS FILTER (LPF)?

This control allows the operator to use either the unfiltered signal or the low-pass filtered signal to construct the fitted signal. The LPF removes respiratory artifacts from the signal by applying an Infinite Impulse Response (IIR) Butterworth filter. The cut-off frequency is 2 cpm and the order is 7. The response of this filter can be seen in Fig. D6.

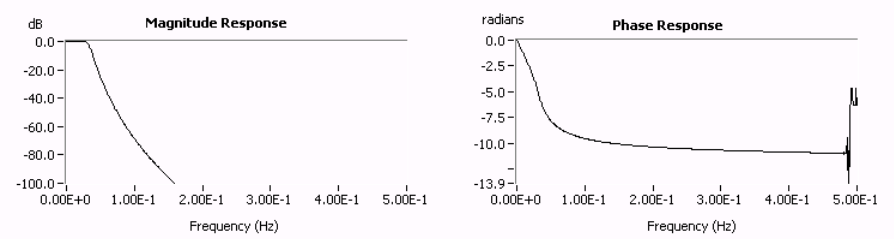

Fig. D6 The magnitude and phase response of a 7th order IIR Butterworth filter with a cut-off frequency of 2cpm.

Modelling the pre and postprandial regions

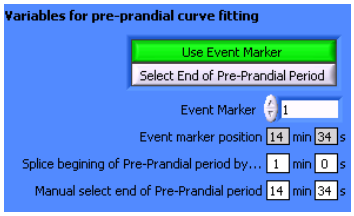

Preprandial curve fitting: CURVE SPLITTING PARAMETERS

Allows the user to use either one of the event markers or manually select the end of the preprandial period. The beginning of the preprandial period may be spliced to remove unnecessary sections of signal at the beginning of the experiment.

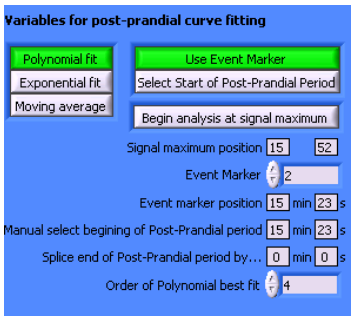

Postprandial curve fitting: CURVE SPLITTING PARAMETERS

Allows the user to use either one of the event markers or manually select the beginning of the postprandial period. The end of the postprandial period may be spliced to remove unnecessary sections of signal at the end of the experiment. Additionally, the type of postprandial fit may be selected from polynomial (recommended), exponential and moving average.

Band pass filtering

Fig D7 shows the block diagram of the software controlled by the third page. This page applies two band pass filters; one is to isolate the frequency range of the gastric contractions while the other is to separate the respiratory artefact for future analysis.

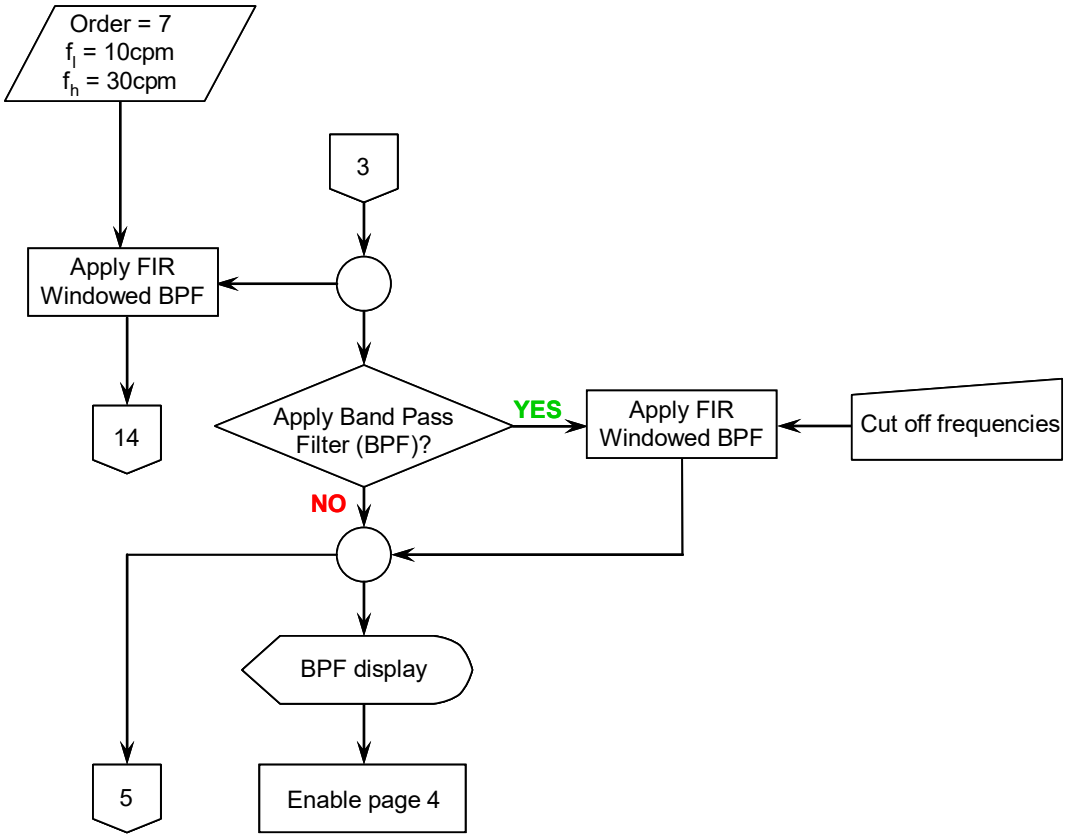

Fig. D7 Block diagram of page 3 of ACCESS 2.40.

Fig. D8 is a screenshot of the third page of ACCESS responsible for band pass filtering.

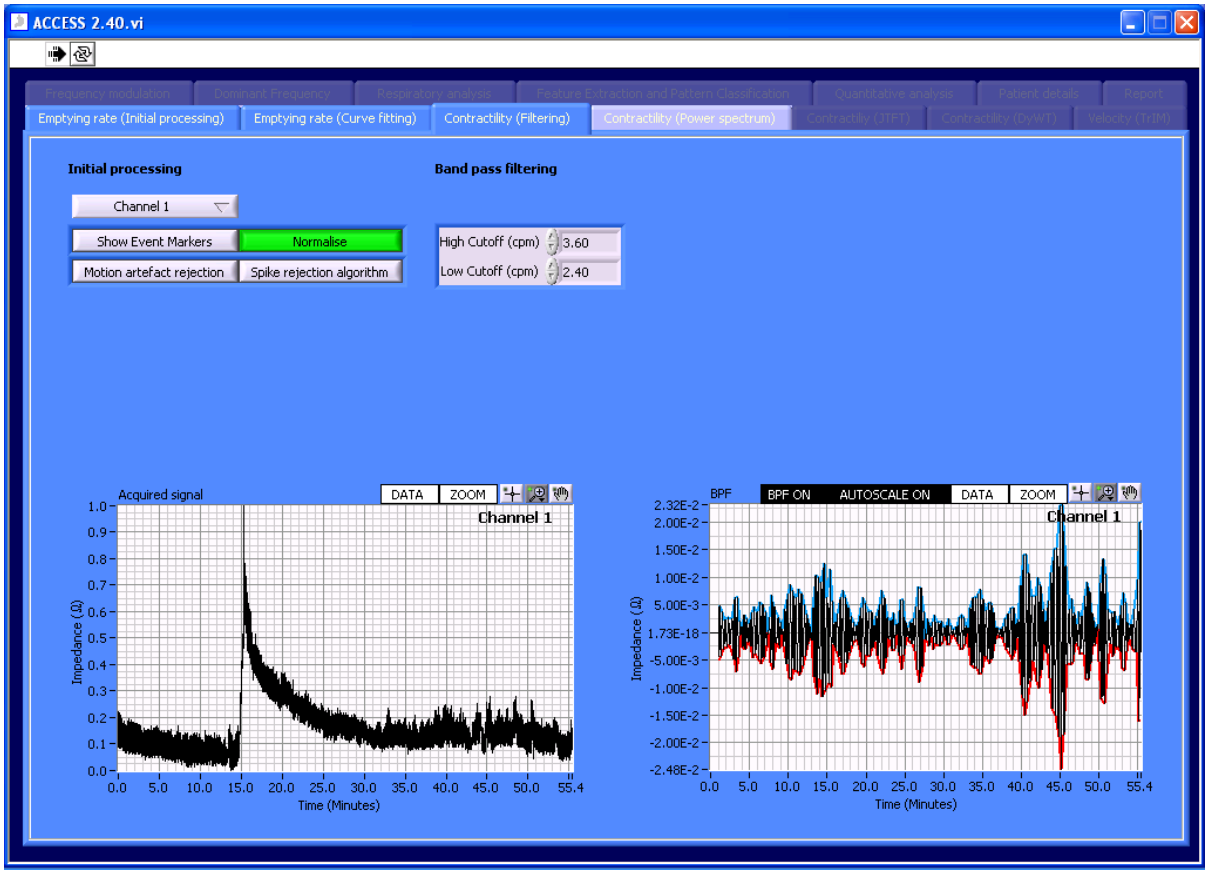

Fig. D8 Screen shot of the third page of ACCESS.

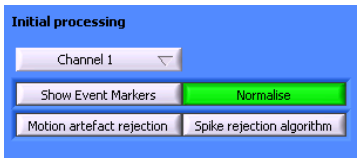

Initial processing: N/A

Allows the user to alter the channel, show the signal event markers, normalise the data, apply the MARA algorithm and spike rejection algorithm in this page to examine the effects on the band pass filtered signal.

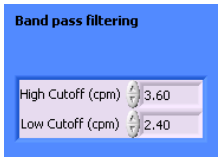

Band pass filter controls: CUT OFF FREQUENCY

These controls allow the user to change the cut off frequencies of the pass band. The default is 2.40 to 3.6 cpm and these are recommended.

Power spectra

Fig D9 shows the block diagram of the software controlled by the fourth page. This page calculates the power spectra for the preprandial and postprandial periods of the band pass signal. The peaks related to the gastric frequencies (gastric peaks) are located in both spectra and the ratio of post- to preprandial power is calculated together with the maximum frequency shift.

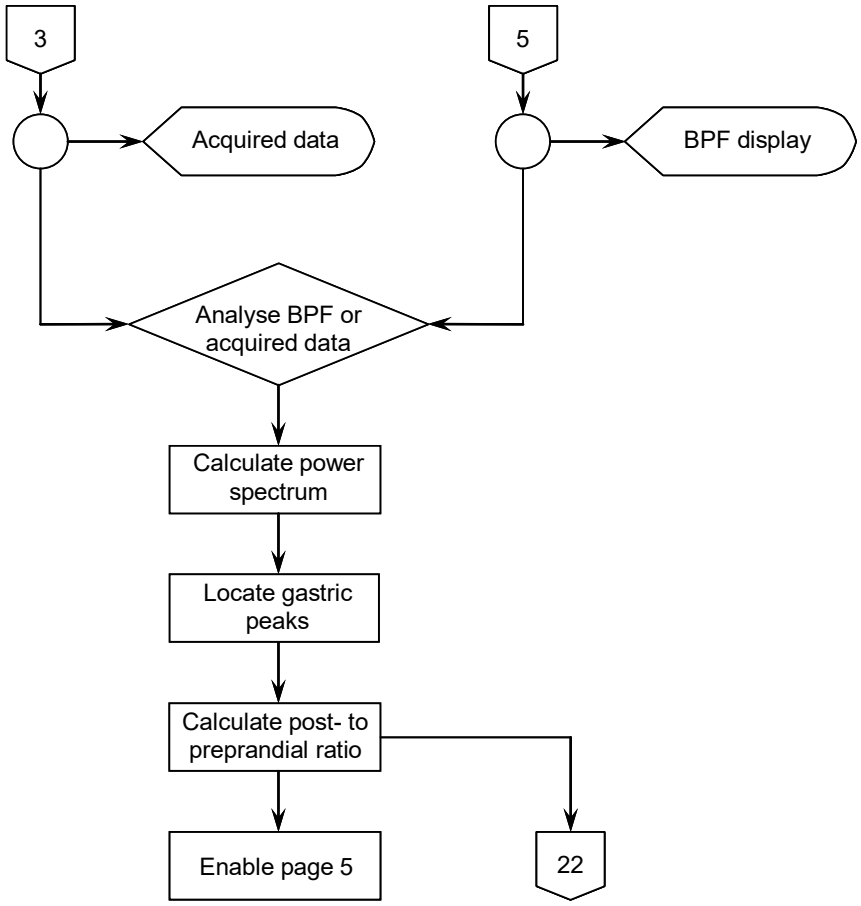

Fig. D9 Block diagram of page 4 of ACCESS 2.40.

Fig. D10 shows a screenshot of page 4 of ACCESS 2.40. This page takes the pre- and postprandial power spectra (after band pass filtering) and analyses the ratio between the powers of the maximum postprandial and preprandial peaks (Maximum Amplitude Ratio, MAR), together with the shift in global frequency (Maximum Frequency Shift, MFS).

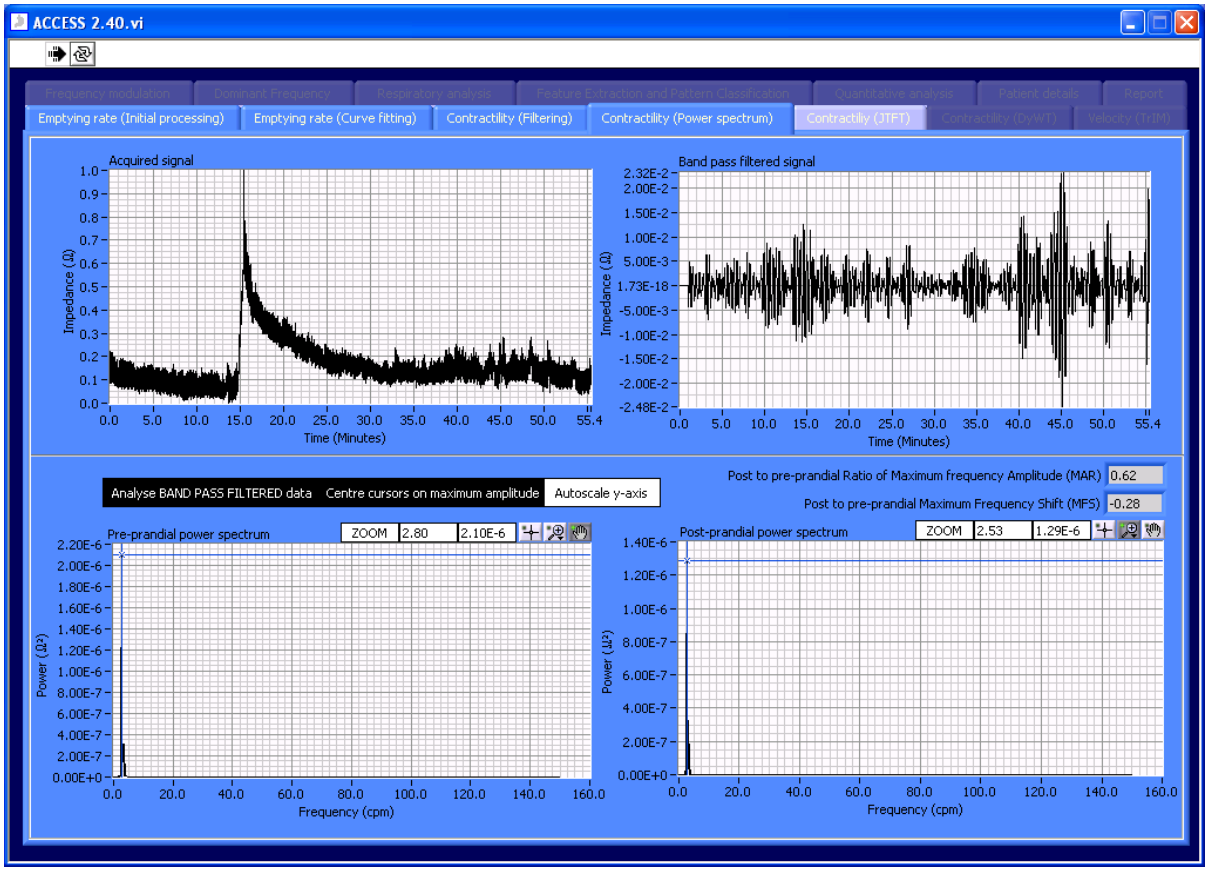

Fig. D10 Screen shot of the fourth page of ACCESS.

Analyse BAND PASS FILTERED data

Analysis control: ANALYSE BPF OR ACQUIRED DATA

This control gives the user the option of analysing the Band Pass Filtered (BPF) data or acquired data.

Centre cursors on maximum amplitude

Lock cursors or allow cursors to move freely: N/A

This control automatically centres the cursors on the maximum peak in the power spectrum. If the acquired data is analysed, it may be necessary to allow the cursors to be moved freely.

Autoscale y-axis

Autoscale power spectra y-axes: N/A

Turns the y-axis autoscale on and off for the power spectra y-axis so that a visual comparison can be made between the two. It is also necessary to switch this off when using the zoom function on either graph.

Joint – Time Fourier Transforms (JTFT)

Fig D11 shows the block diagram of the software controlled by the fifth page. This page calculates the Joint Time Fourier Transforms for gastric, dominant frequency and respiratory analyses. The quantitative values for each investigation are also calculated here.

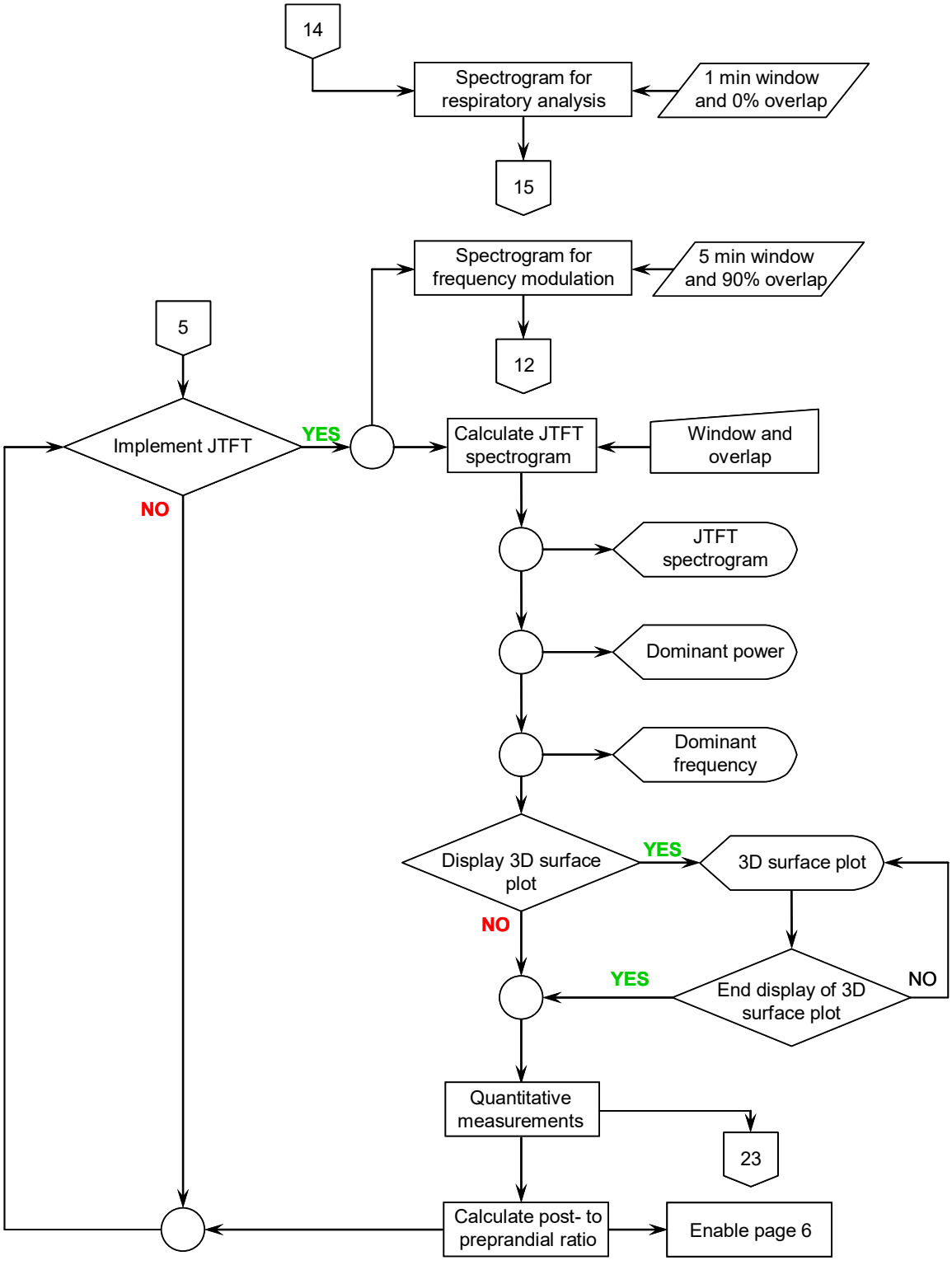

Fig. D11 Block diagram of page 5 of ACCESS 2.40.

Fig. D12 shows the screenshot of the fifth page of ACCESS that controls the Joint-Time Frequency Transform (JTFT) functions.

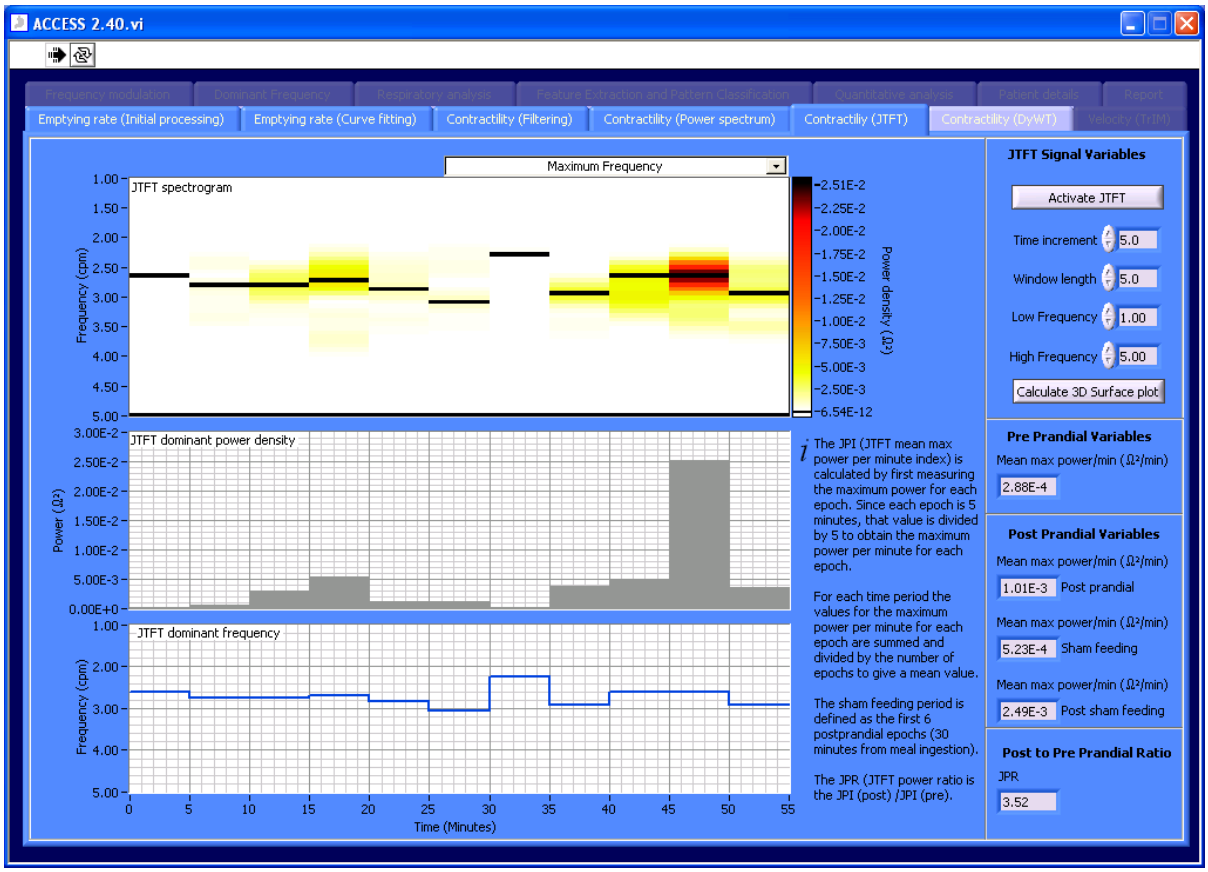

Fig. D12 Screenshot of page 5 of ACCESS 2.40.

Display maximum frequency: N/A

This control displays the maximum frequency over the top of the JTFT. This is necessary for future analysis and must be set as above to enable page 6.

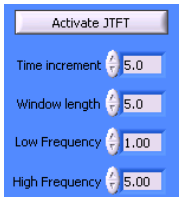

JTFT controls: WINDOW AND OVERLAP

These controls activate the JTFT and control the time increment, window length and the low and high frequencies displayed in the JTFT graph.

Calculate 3D Surface plot

Surface plot control: DISPLAY 3D SURFACE PLOT

This function launches a subroutine that displays the surface plot of the JTFT. This is shown in Fig. D13. The controls modify the display and the button marked 'RETURN TO MAIN PROGRAM' corresponds to the control in the block diagram (Fig. D11).

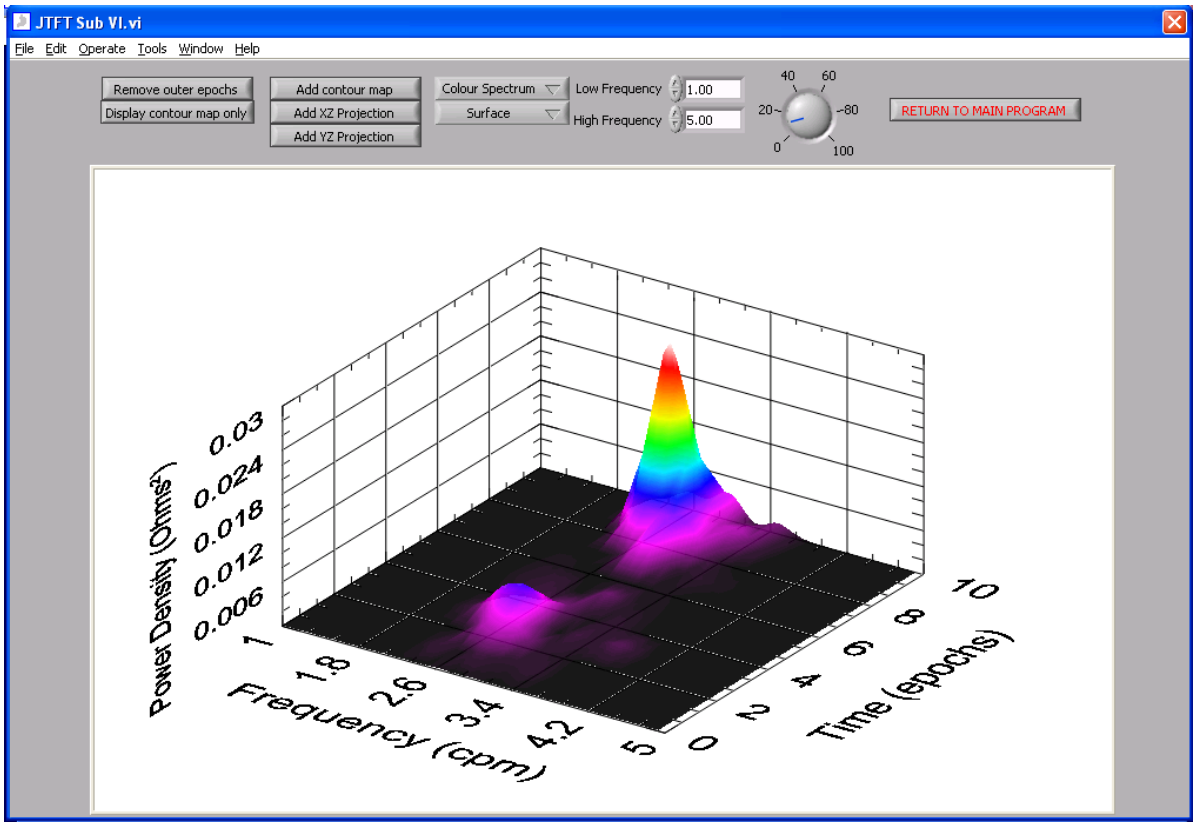

Fig. D13 Subroutine to display the surface plot of the JTFT data.

The Dyadic Wavelet Transform (DyWT)

Fig D14 shows the block diagram of the software controlled by the sixth page. This page calculates the Dyadic Wavelet Transform and calculates the pseudo frequency, power density and position in time for each contraction.

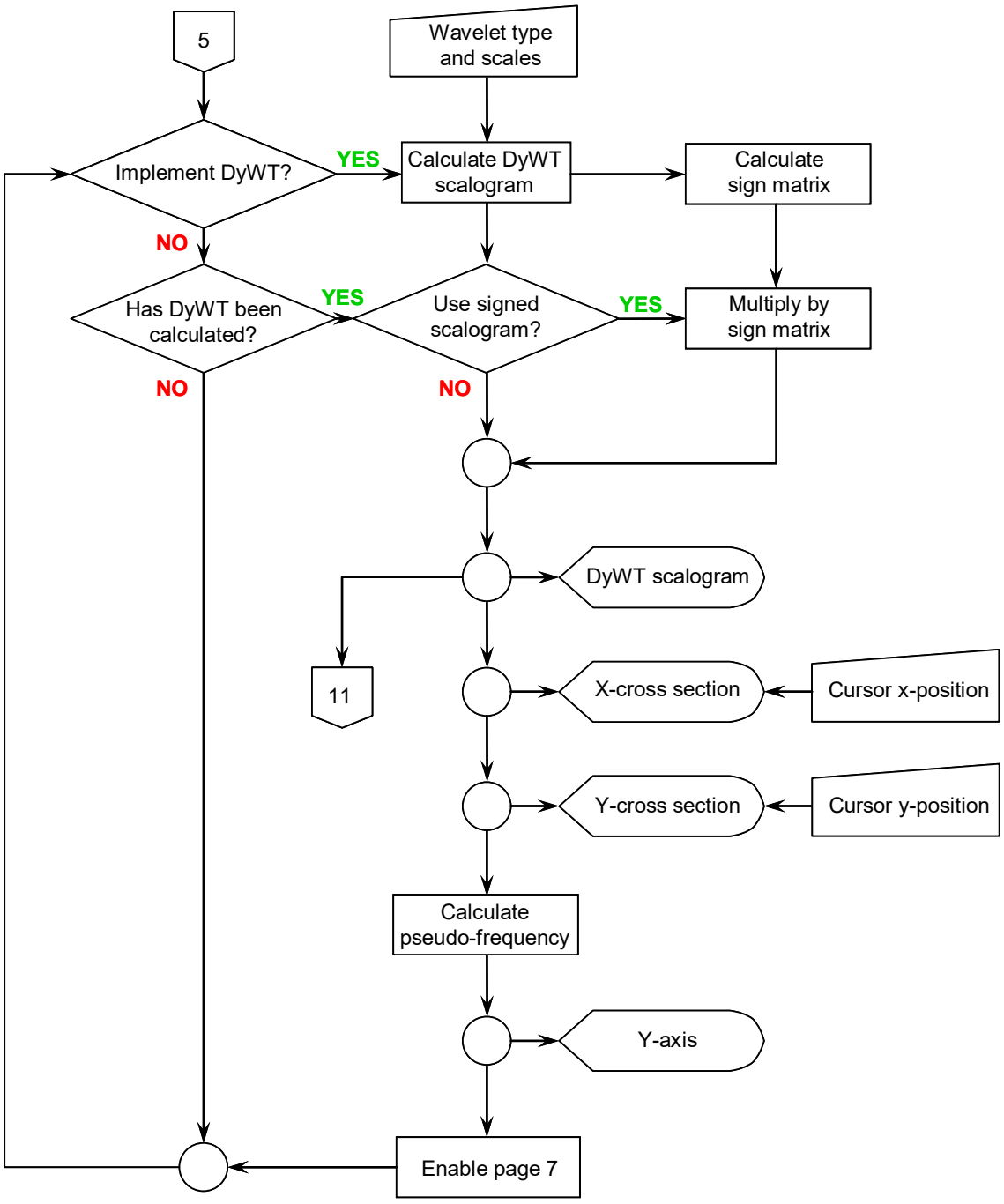

Fig. D14 Block diagram of page 6 of ACCESS 2.40.

Fig. D15 shows the screenshot of the sixth page of ACCESS that controls the Dyadic Wavelet Transform (DyWT).

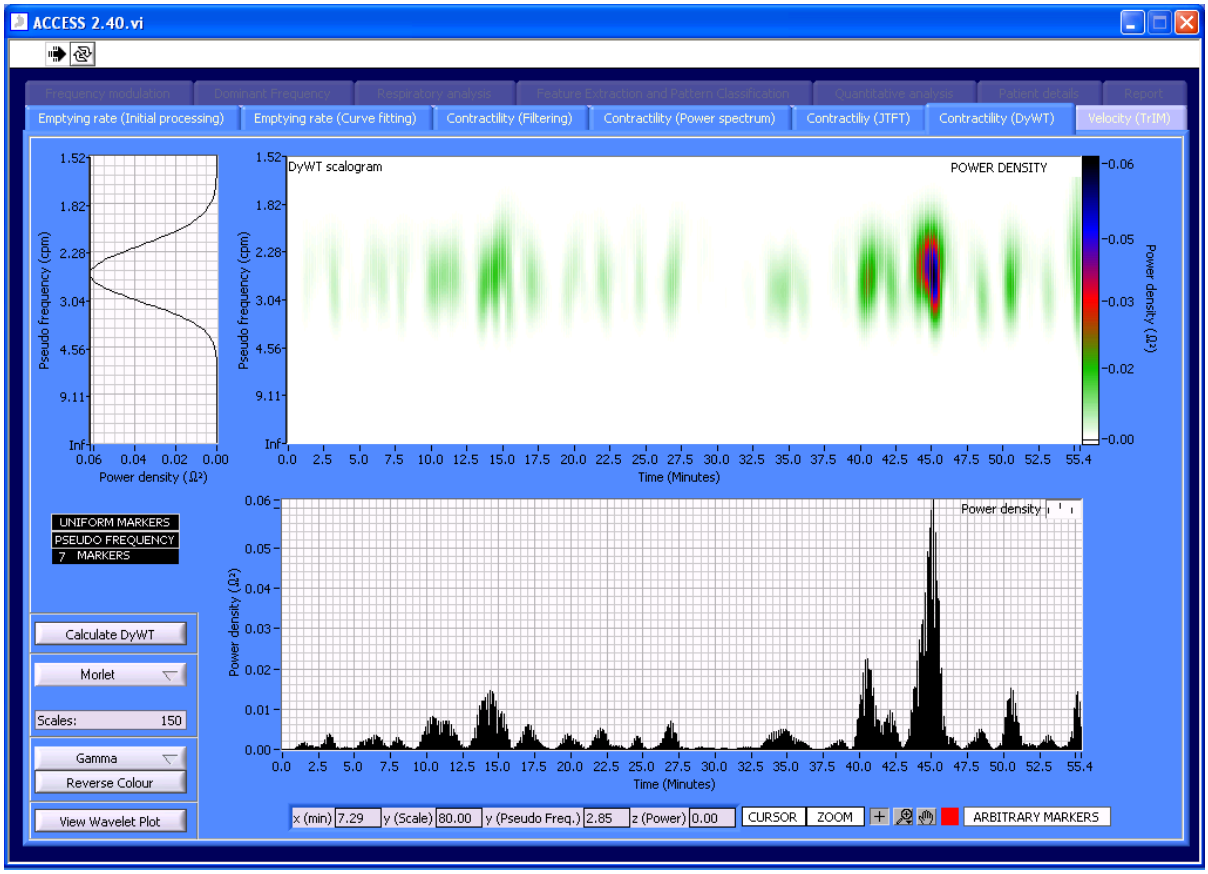

Fig. D15 Screenshot of the sixth page of ACCESS.

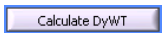

Calculates the DyWT: CALCULATE DYWT SCALOGRAM

Activates the DyWT scalogram calculation.

Selects the type of wavelet to use: WAVELET TYPE AND SCALES

The Morlet wavelet is recommended.

Selects the number of scales: WAVELET TYPE AND SCALES

150 scales are recommended.

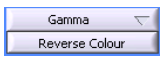

Modifies the colour scheme in the scalogram window: N/A

This control changes the colour of the z-axis in the scalogram window.

View Wavelet Plot

Show mother wavelet: N/A

This control launches a subroutine that displays the mother wavelet. This subroutine can be seen in Fig. D16.

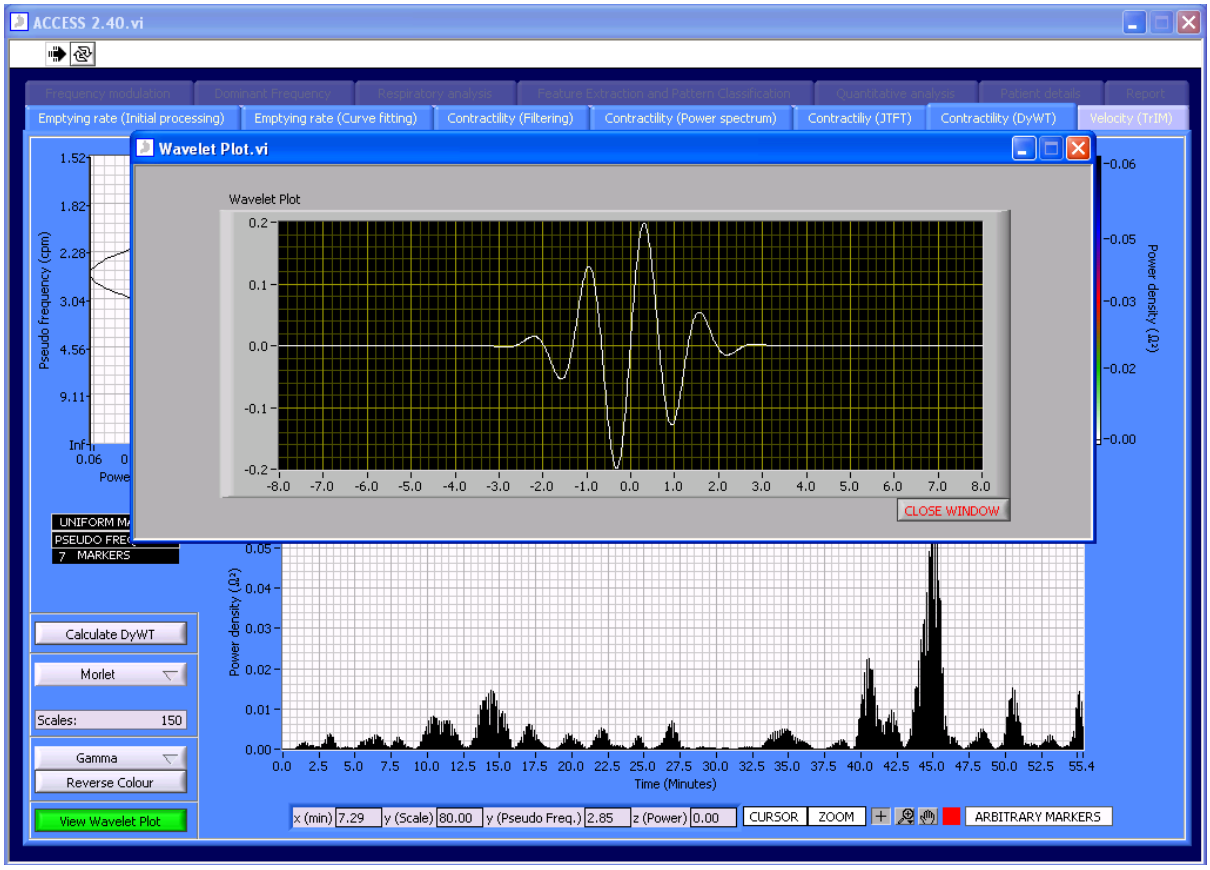

Fig. D16 Running the 'View Wavelet Plot' subroutine showing a Morlet wavelet.

Triangulative Impedance Mapping (TrIM) and Vector Velocity Measurements

Fig D17 shows the block diagram of section a of software controlled by the seventh page. This section loads an *.elc file (unless the user manually inputs the electrode data) and calculates the lengths and angles between each electrode.

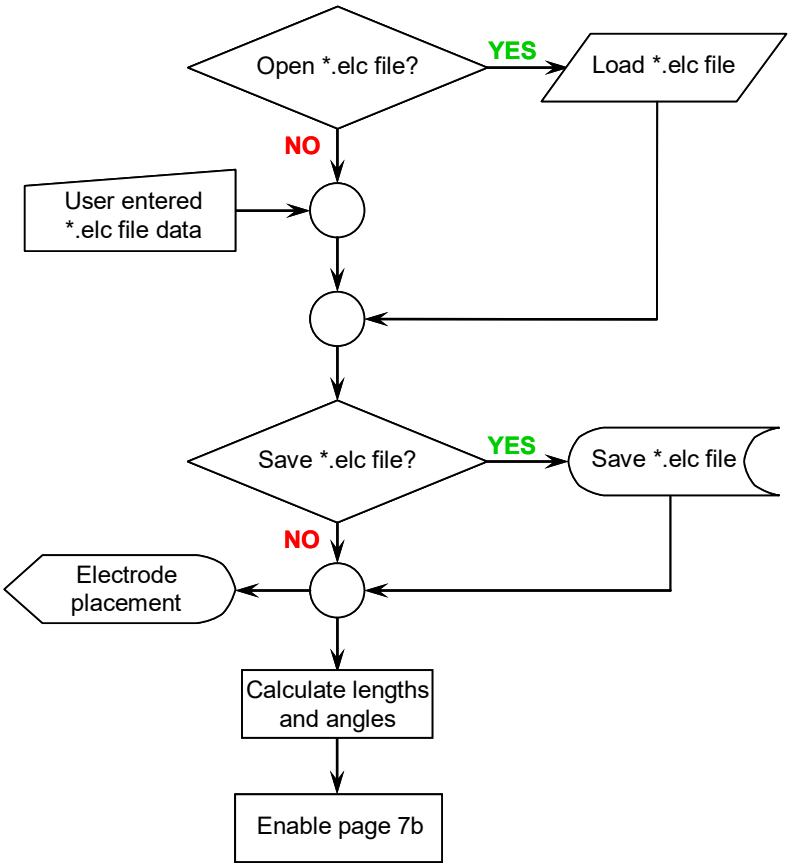

Fig. D17 Block diagram of page 7 (section a) of ACCESS 2.40.

The screen shot of Page 7 (section a) is given in Fig. D18.

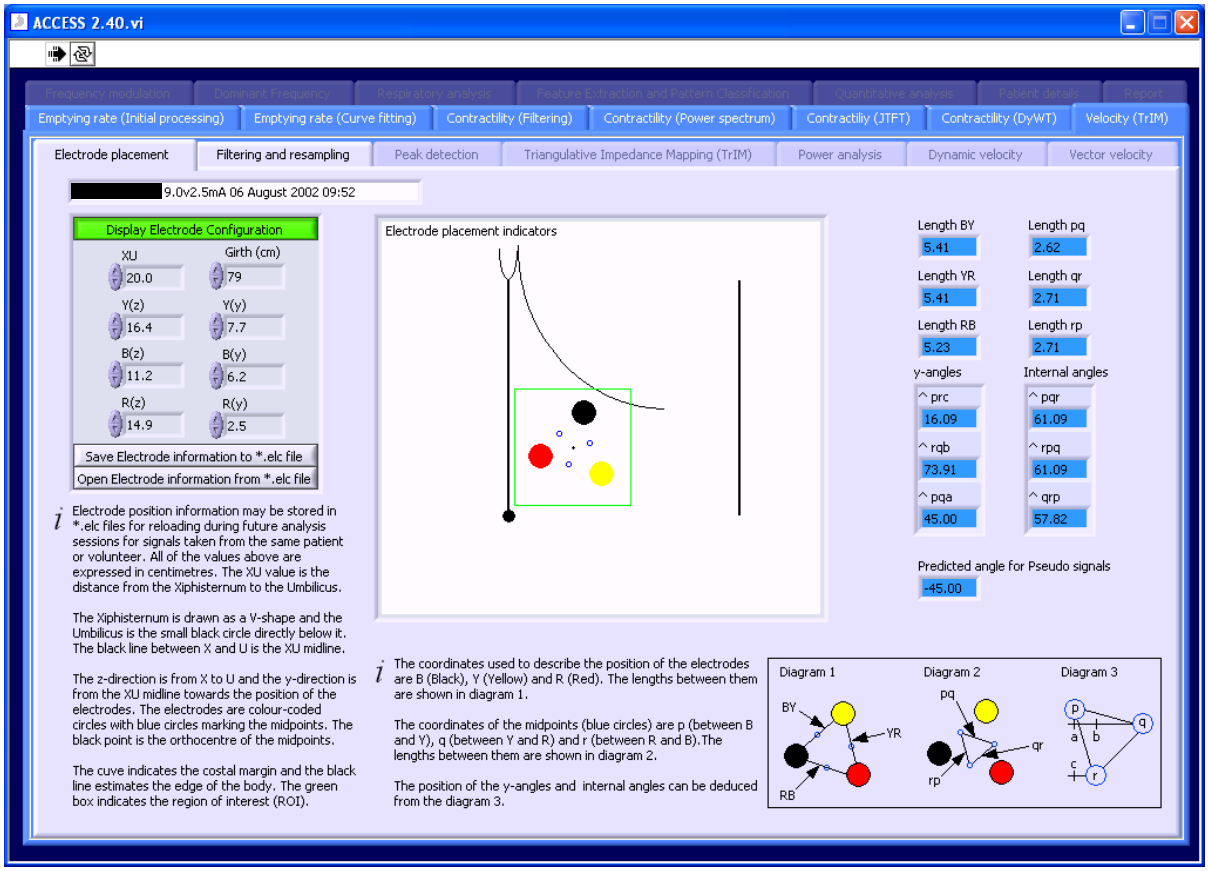

Fig. D18 Screen shot of Page 7 (section a).

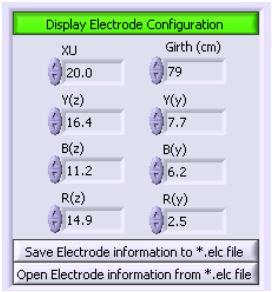

Electrode positional control: OPENED *.elc FILE OR USER ENTERED *.elc FILE DATA. This control manages the positional information of the electrodes which is used to calculate velocity.

Fig D19 shows the block diagram of section b and c of software controlled by the seventh page. Section b down-samples the band pass filtered data to a sampling frequency of 1Hz and section c performs a peak search for each of the three electrode planes.

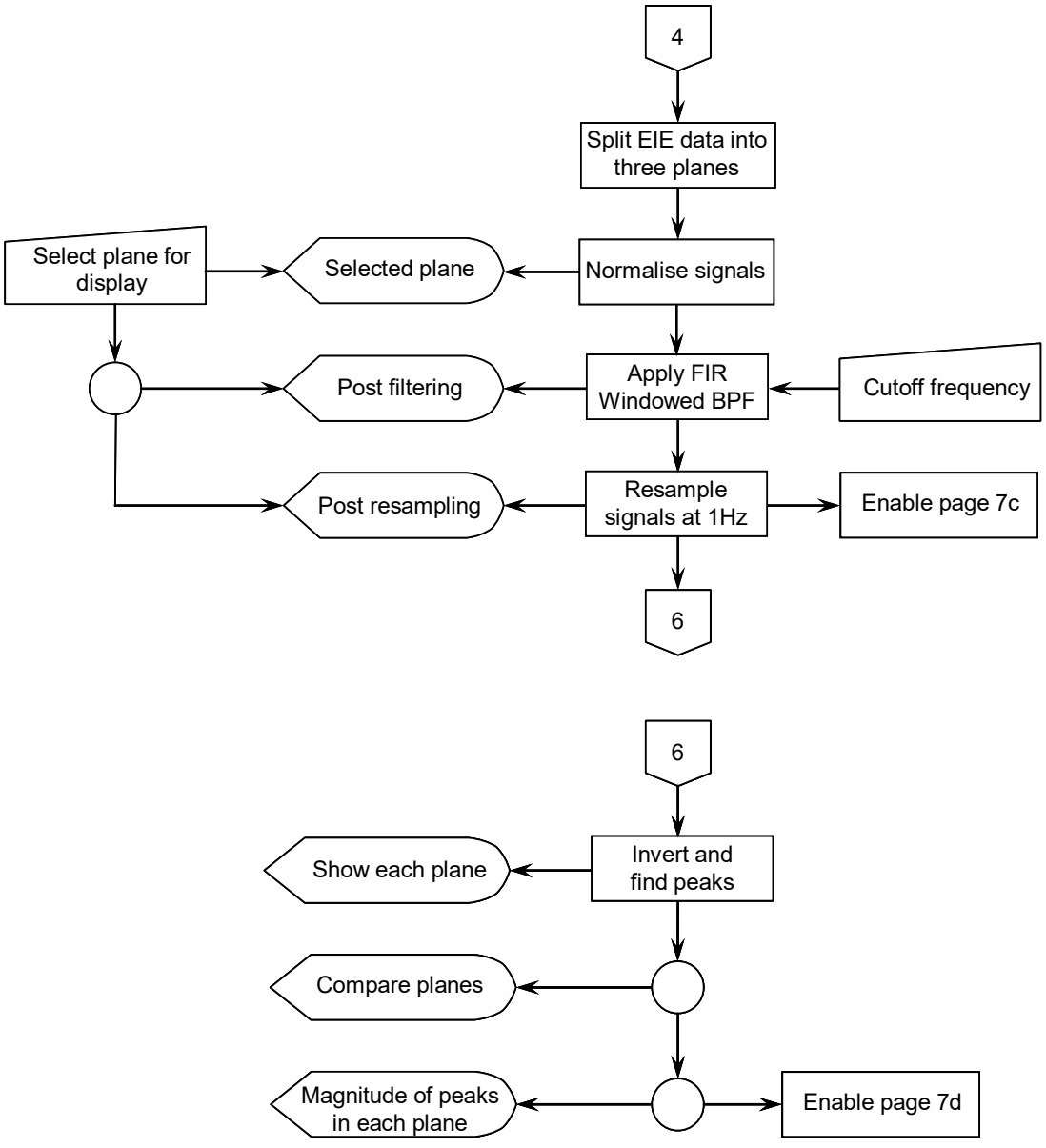

Fig. D19 Block diagram of page 7 (sections b and c) of ACCESS 2.40.

Figs. D20 and D21 show the screen shots of Page 7 (sections b and c respectively).

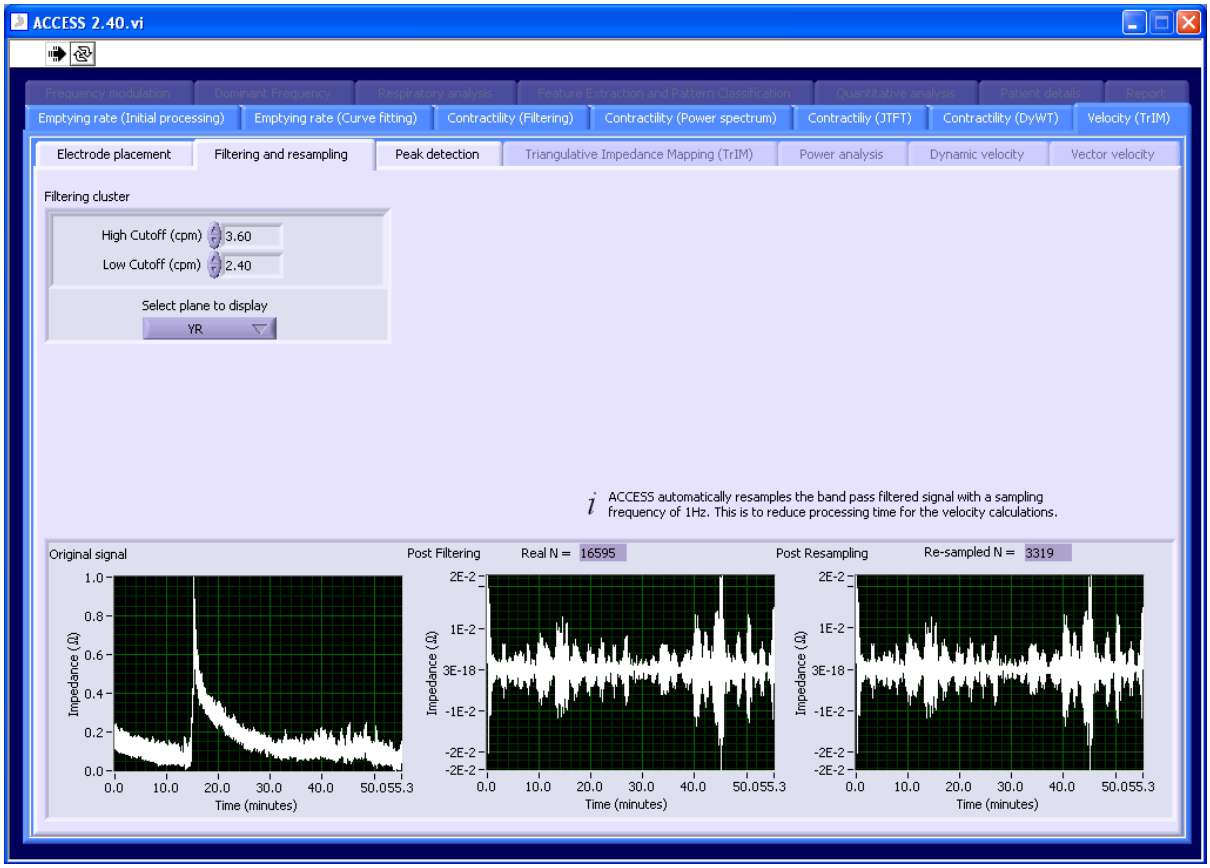

Fig. D20 Screen shot of Page 7 (sections b).

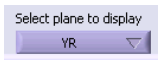

Select plane: SELECT PLANE FOR DISPLAY

Displays the chosen plane: BY (Black – Yellow), YR (Yellow – Red) or RB (Red – Black).

Change cut off frequencies: Cut off frequency

Alters the cut off frequency for the band pass filter.

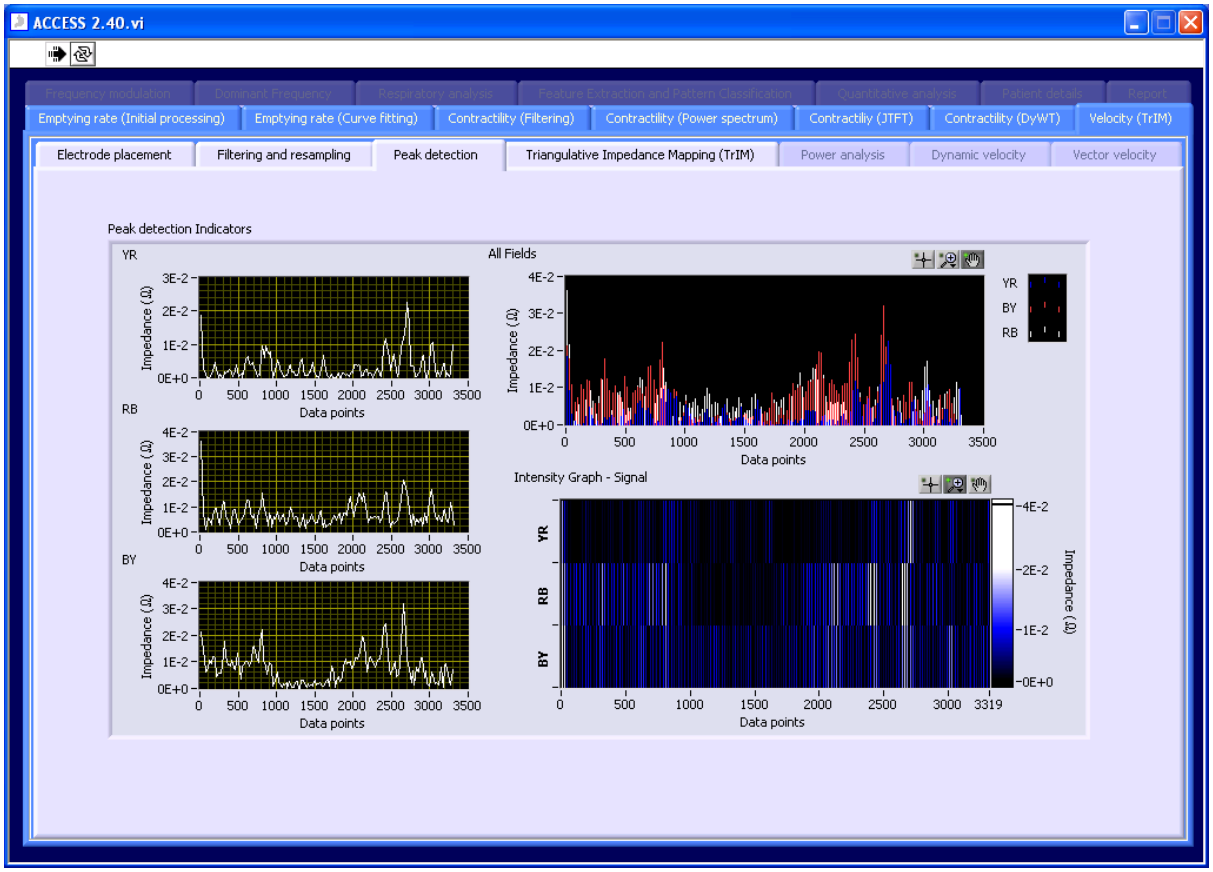

Fig. D21 Screen shot of Page 7 (sections c).

Fig D22 shows the block diagram of section d and e of software controlled by the seventh page. Section d calculates the TrIM algorithm and the TrIM and vector velocity and angle for each contraction. Section e computes the impedance – distance – time graph and the maximum impedance deflection.

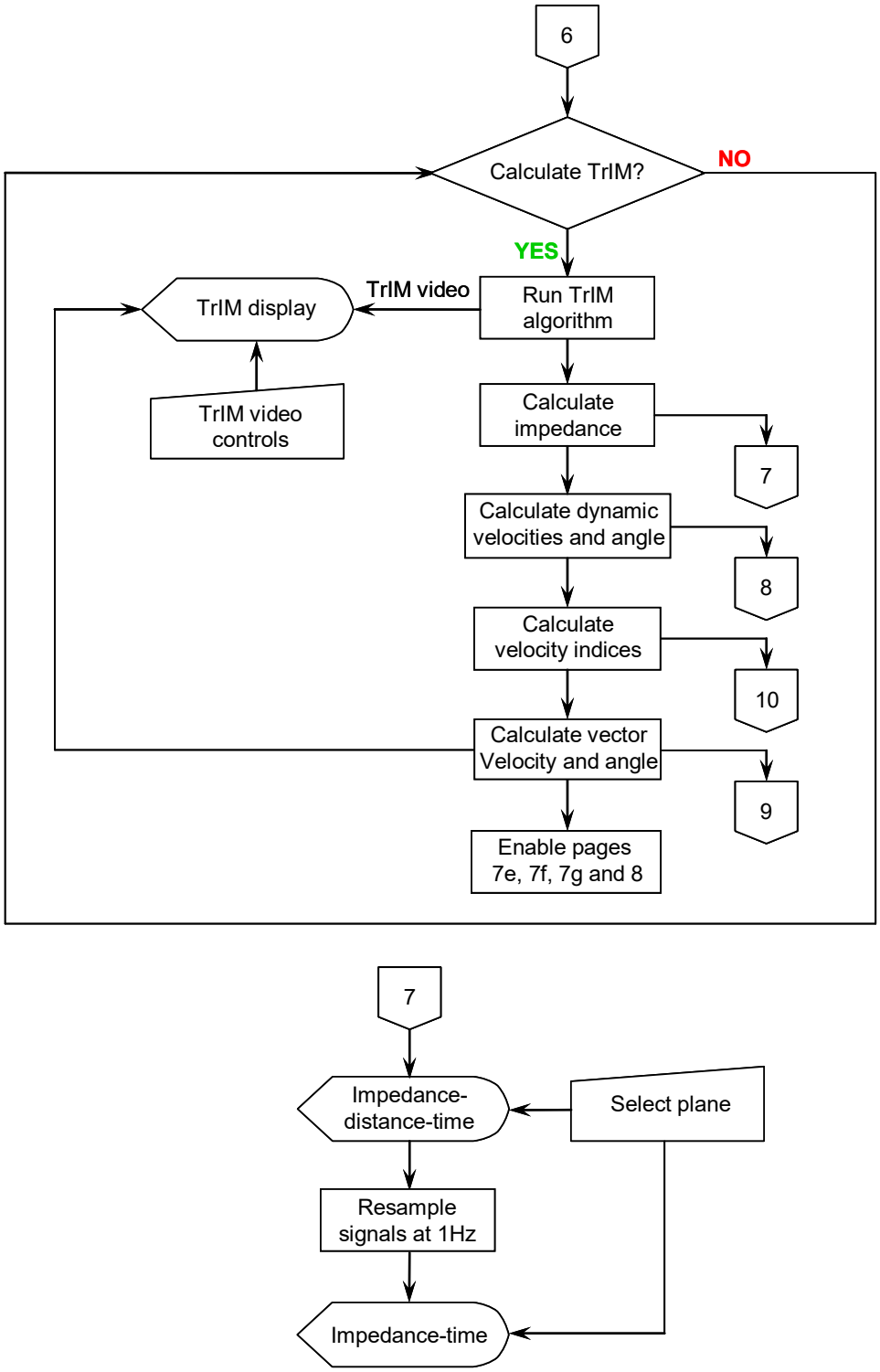

Fig. D22 Block diagram of page 7 (sections d and e) of ACCESS 2.40.

Figs. D23 and D24 show the screen shots of Page 7 (sections d and e respectively).

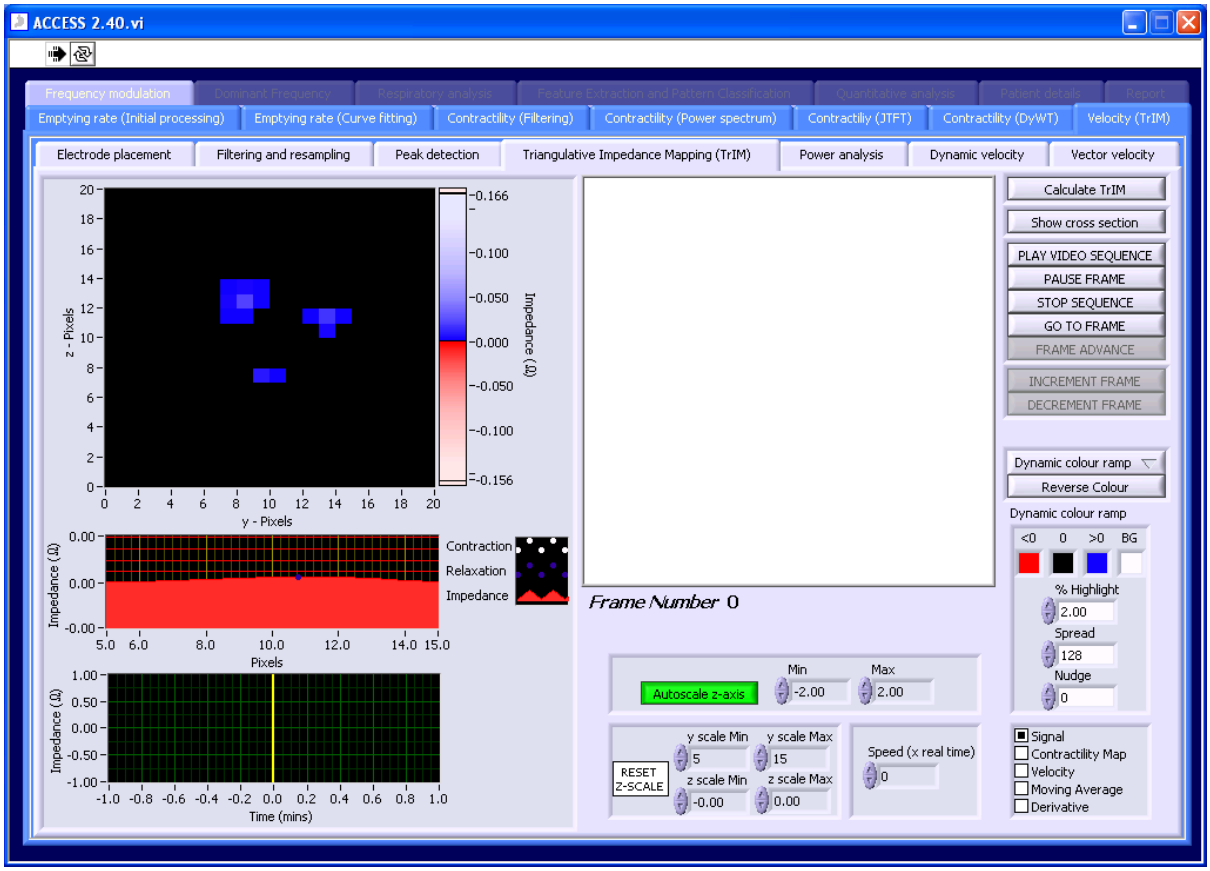

Fig. D23 Screen shot of Page 7 (sections d).

Calculate the Triangulative Impedance Map (TrIM): CALCULATE TRIM?

This control calculates the TrIM. This can only be operated once.

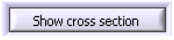

Cross section on graph: N/A

This control displays the line $y = z$ used for theTrIM velocity calculation.

Video controls: TRIM VIDEO CONTROLS

Controls for the TrIM video. Frame advance is greyed out until the TrIM video is played.

Frame increments/decrements: N/A

Advances the TrIM video frame by frame. This is greyed out until the 'Frame Advance' is on.

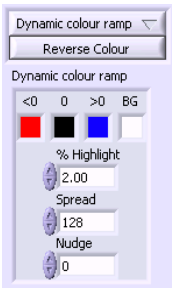

Controls the colour ramp of the TrIM video. The 'dynamic' colour ramp allows the colours and shading to be changed with the control below. <0 is the colour for values below zero, 0 is the colour for zero, >0 is the colour for values above zero and BG stands for background colour. The percentage highlight alters the level of progressive shading, the spread determines how much of the colour ramp is coloured (max = 128) and nudge, alters the zero value and may be positive or negative.

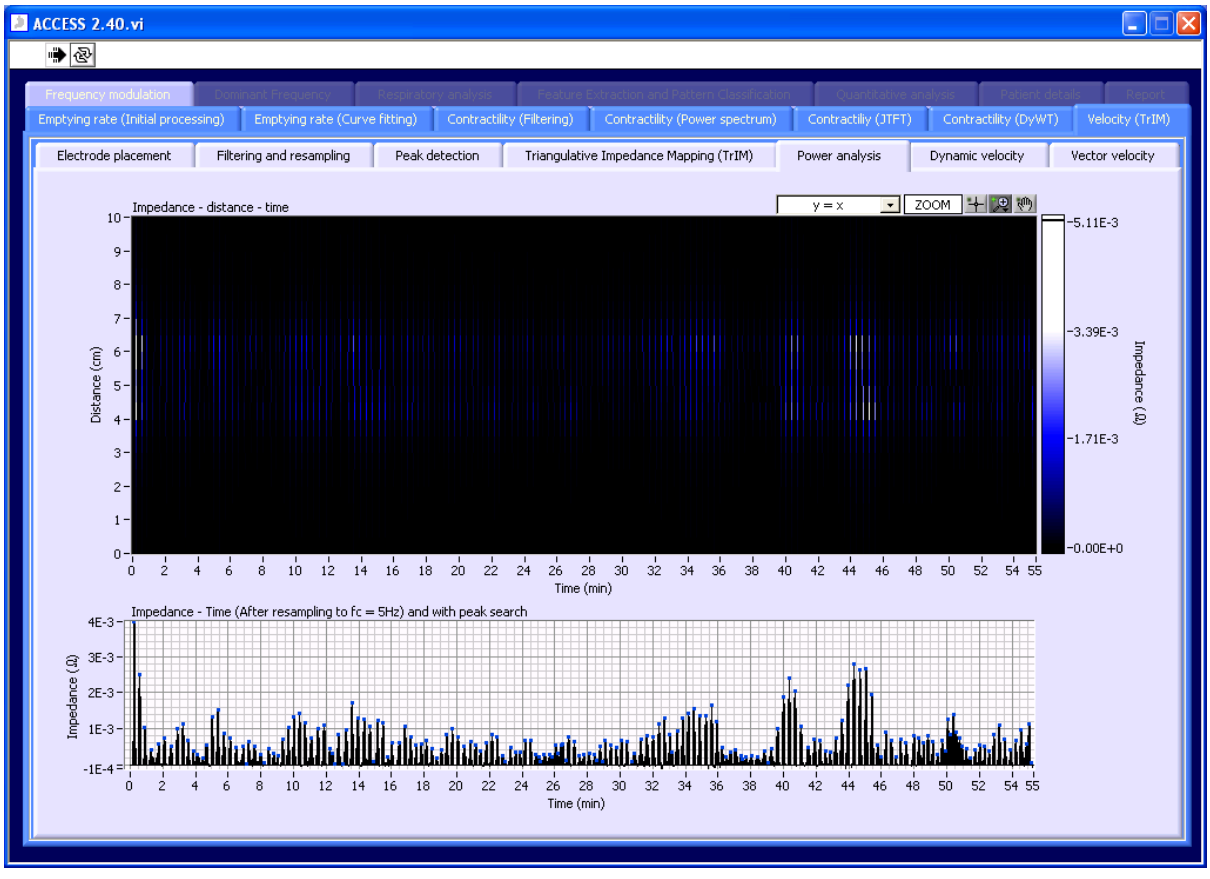

Fig. D24 Screen shot of Page 7 (sections e).

Fig D25 shows the block diagram of section f and g of software controlled by the seventh page. Section f displays the dynamic velocity in the $y = x$ plane, the $x = 10$ plane and the $y = 10$ together with the dynamic angle. Page g displays the velocity vector, angle and the impedance.

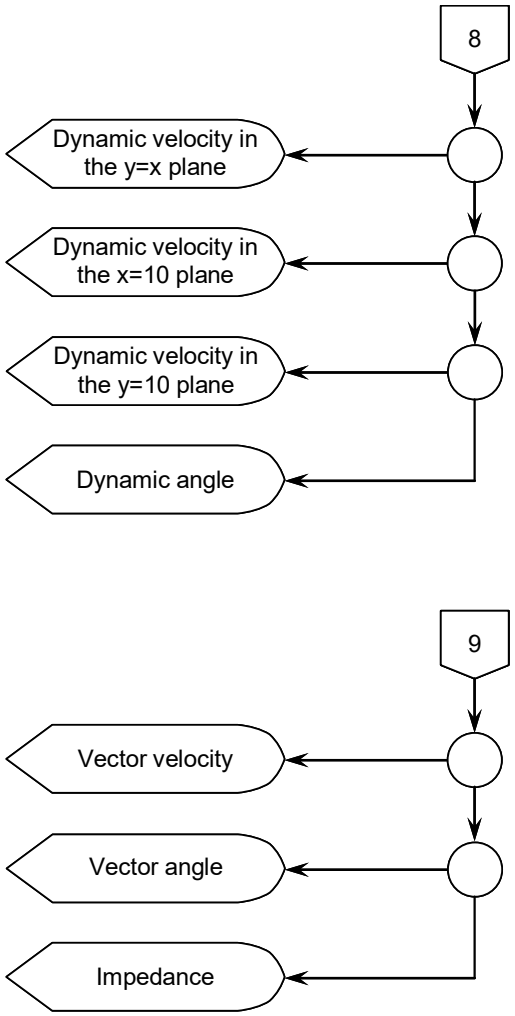

Fig. D25 Block diagram of page 7 (sections f and g) of ACCESS 2.40.

Figs. D26 and D27 show screen shots of sections f and g of page 7. Section f (Fig. D26) displays the mean TrIM velocity (± sem) in the $y = z$ plane, $z = 10$ plane and the $y = 10$ plane and the TrIM angle (± sem). Section g (Fig. D27) displays the vector velocity and angle.

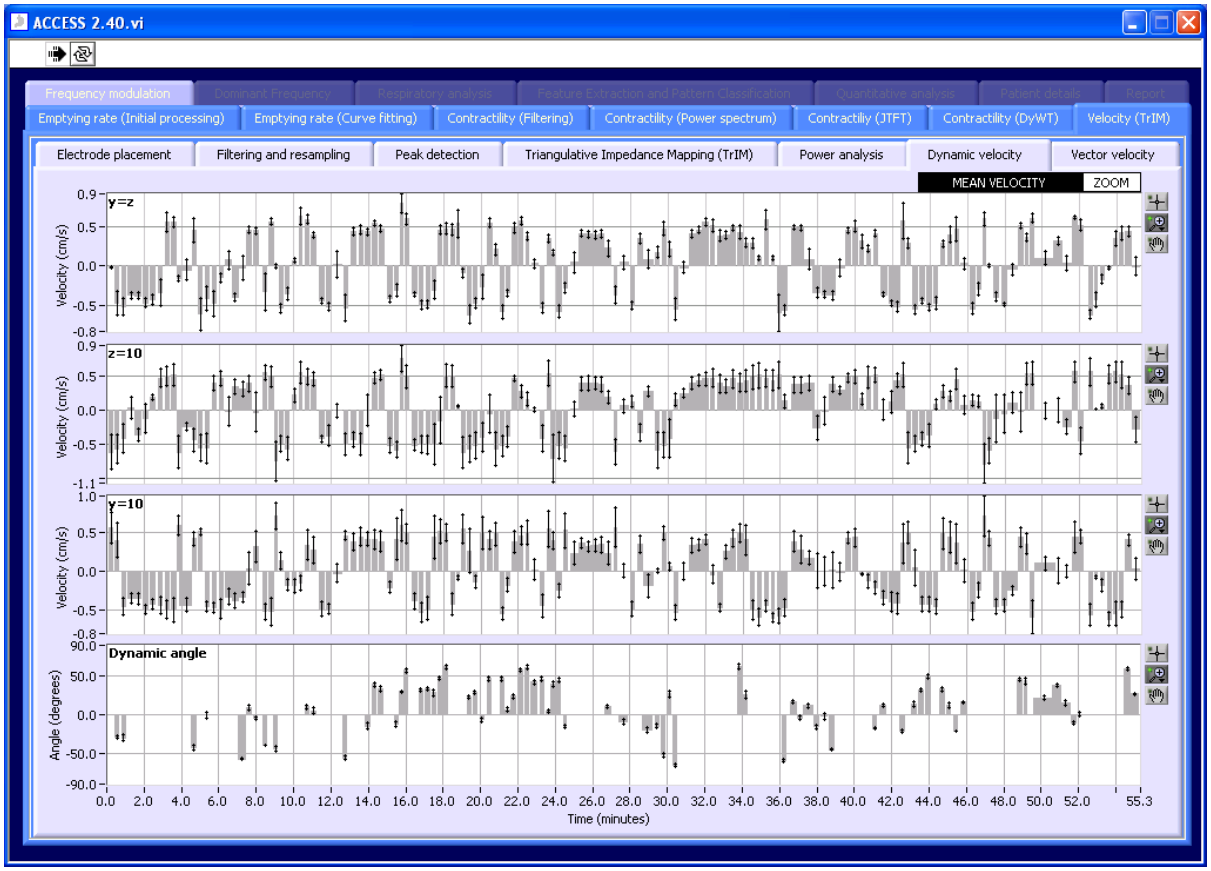

Fig. D26 Screen shot of Page 7 (sections f).

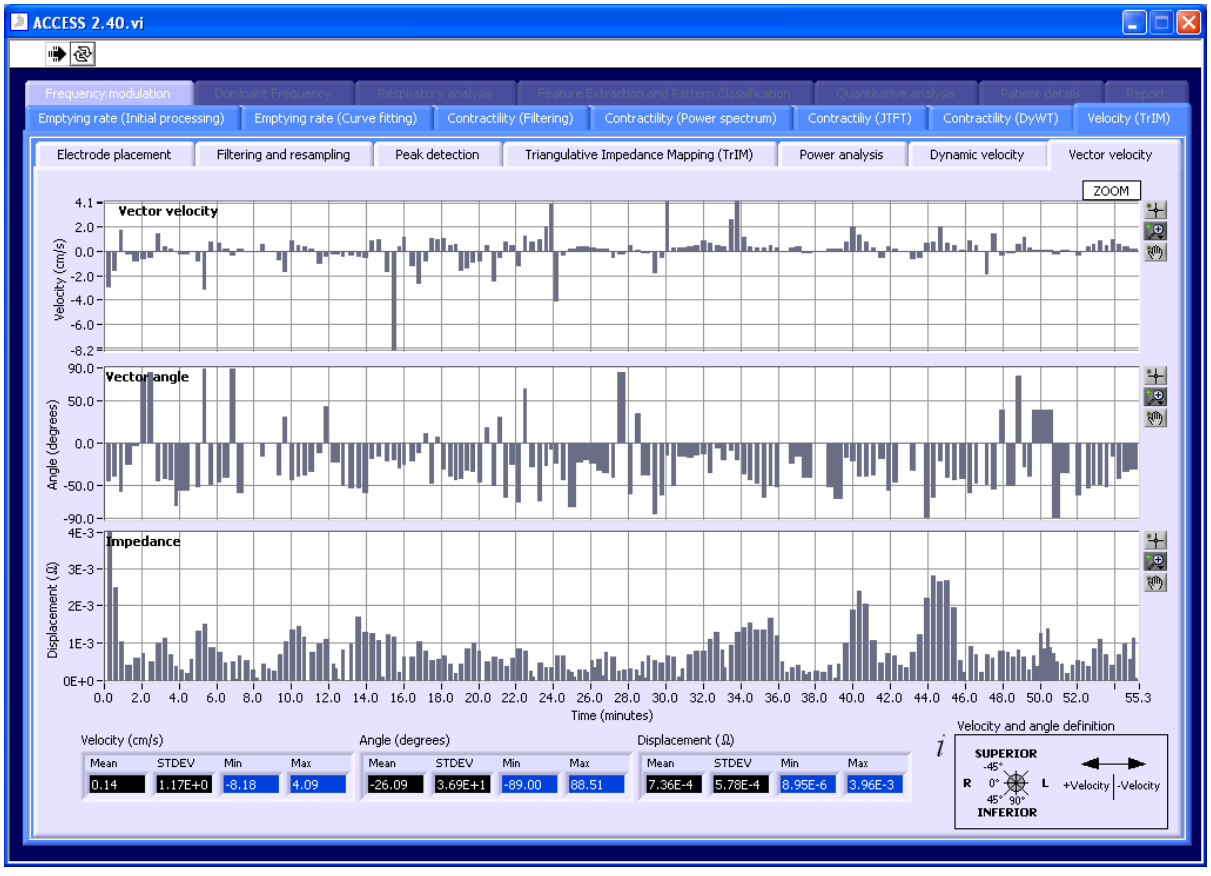

Fig. D27 Screen shot of Page 7 (sections g).

Frequency modulation

Fig D28 shows the block diagram of the software controlled by the eighth page. This page displays the JTFT with a window of 1 minute and a 90% overlap for frequency modulation, the dominant power and the dominant frequency. The qualitative measurements are taken and the DMI is calculated. During this process the velocity indices are used to extract the peaks from the DyWT.

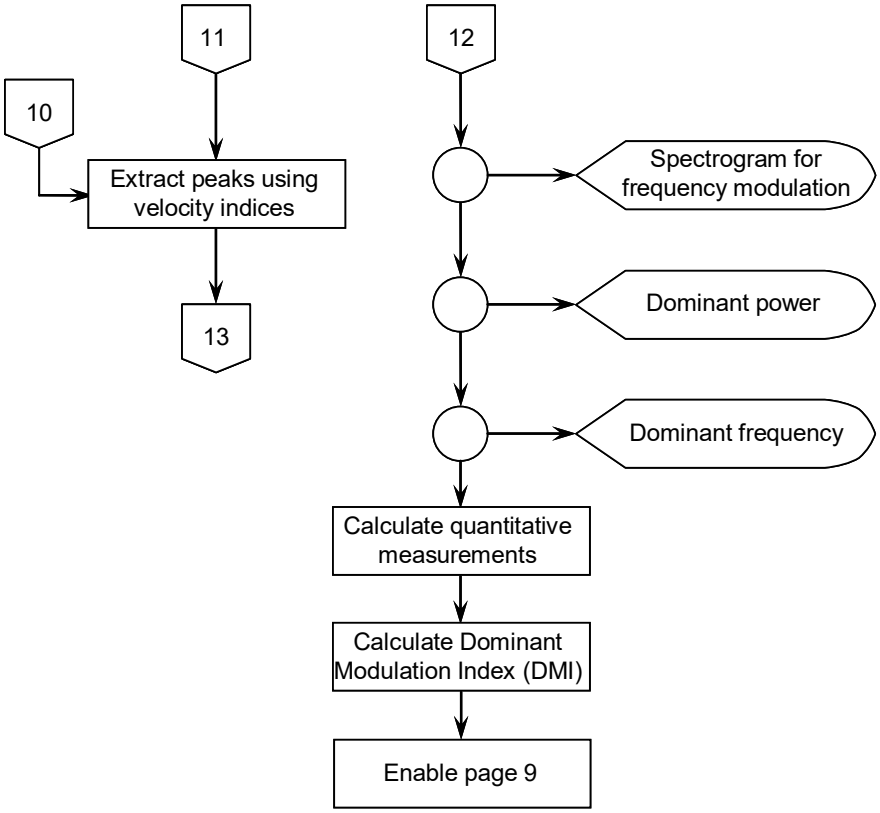

Fig. D28 Block diagram of page 8 of ACCESS 2.40.

Fig. D29 shows a screen shot of page 8 of ACCESS 2.40 showing the JTFT with the maximum power in each epoch (black line). The graph below is the maximum power versus time and the third graph shows the variation in the dominant (maximum power) frequency.

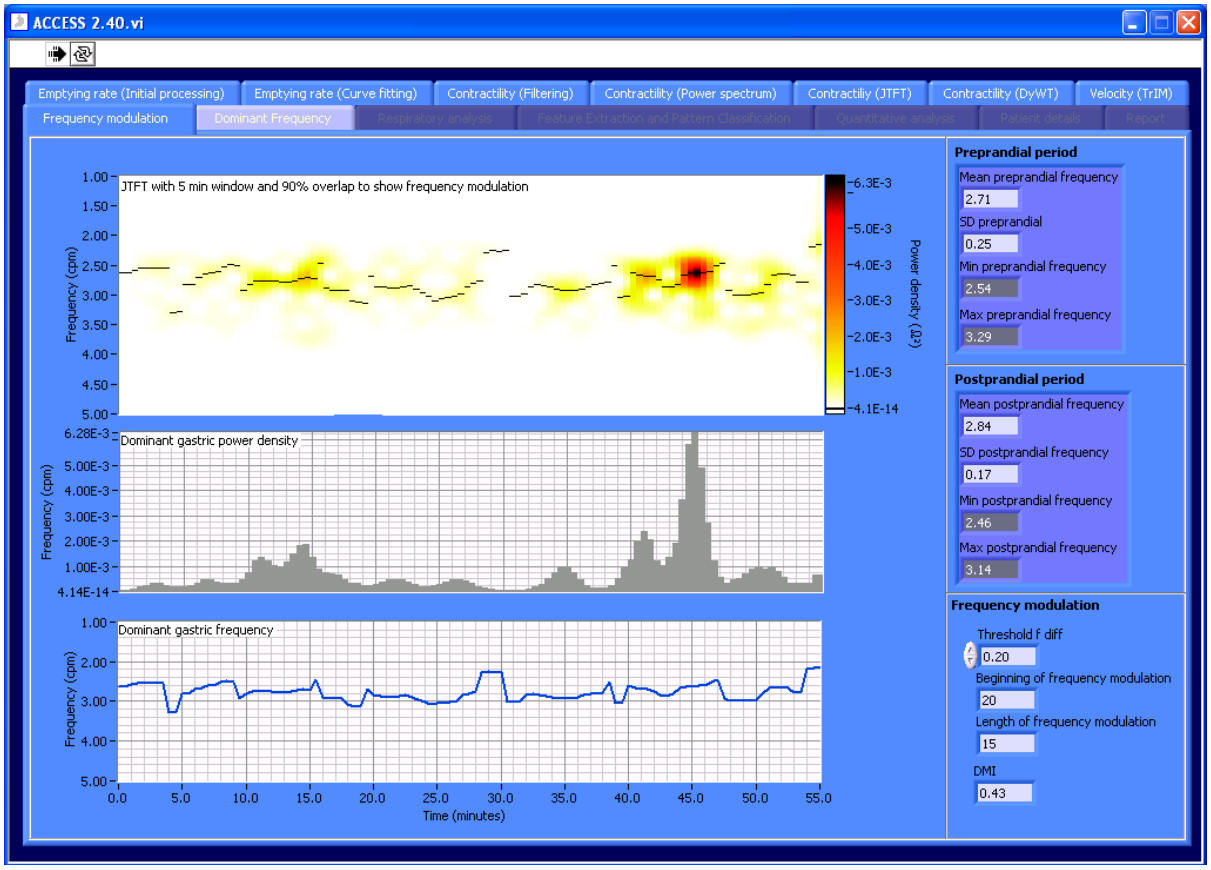

Fig. D29 Screen shot of page 8 of ACCESS 2.40 showing the frequency modulation.

Threshold frequency difference: N/A

This control determines the difference between the frequencies of consecutive epochs in the JTFT using 5 minute epochs on page 5 of ACCESS 2.40. This should always be set to 0.20 to allow a fair comparison between signals.

Dominant frequency

Fig D30 shows the block diagram of the software controlled by the ninth page. This page displays the DyWT following the peak search and the dominant pseudo frequency. The dominant pseudo frequency displays the pseudo frequency of all contractions but marks this with a power above the 10% mean power threshold.

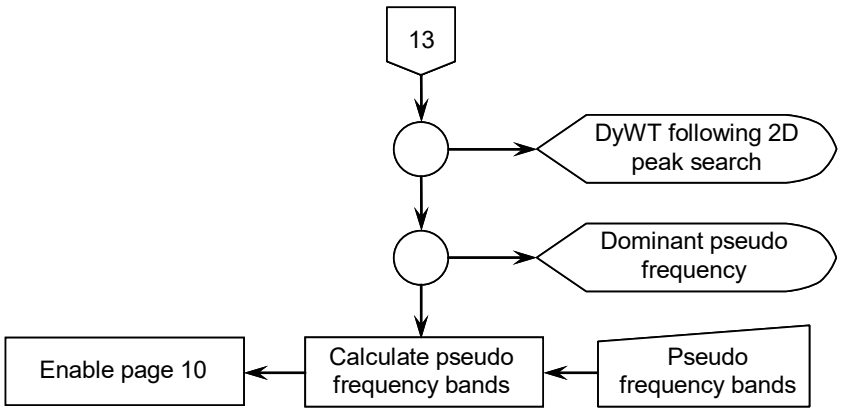

Fig. D30 Block diagram of page 9 of ACCESS 2.40.

Fig. D31 shows a screen shot of page 9 of ACCESS 2.40.

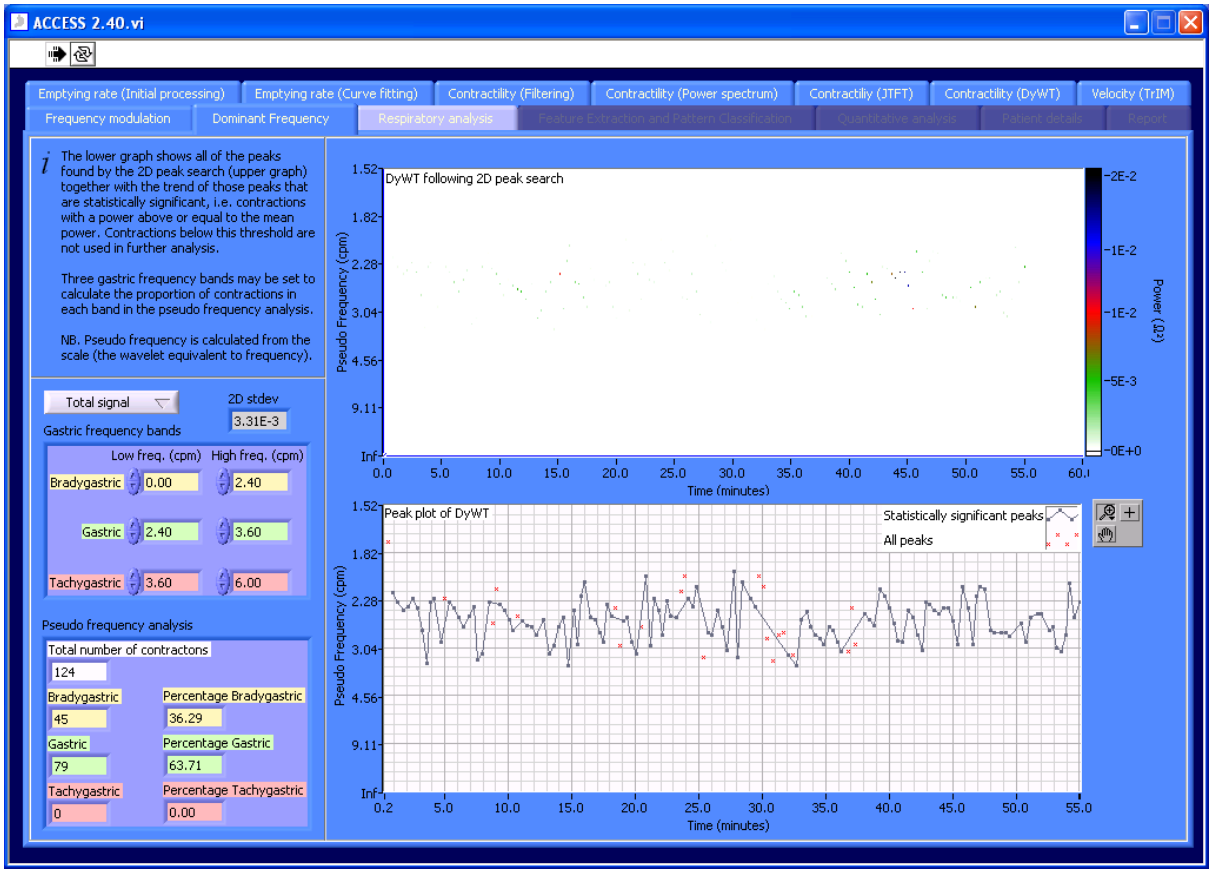

Fig. D31 Screen shot of page 9 of ACCESS 2.40: the dominant frequency analysis.

Period of frequency analysis: PSEUDO FREQUENCY BANDS

Allows the user to choose between analyses of either the preprandial, postprandial or total signal (recommended).

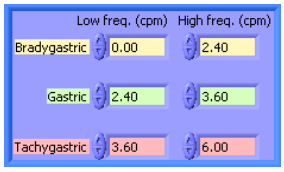

Frequency bands: PSEUDO FREQUENCY BANDS

Determines the threshold for each frequency band.

Respiratory analysis

Fig D32 shows the block diagram of the software controlled by the tenth page. This page displays the respiratory power and frequency. It also calculates the quantitative respiratory variables RPR and RFS together with mean, maximum and minimum pre and postprandial frequencies.

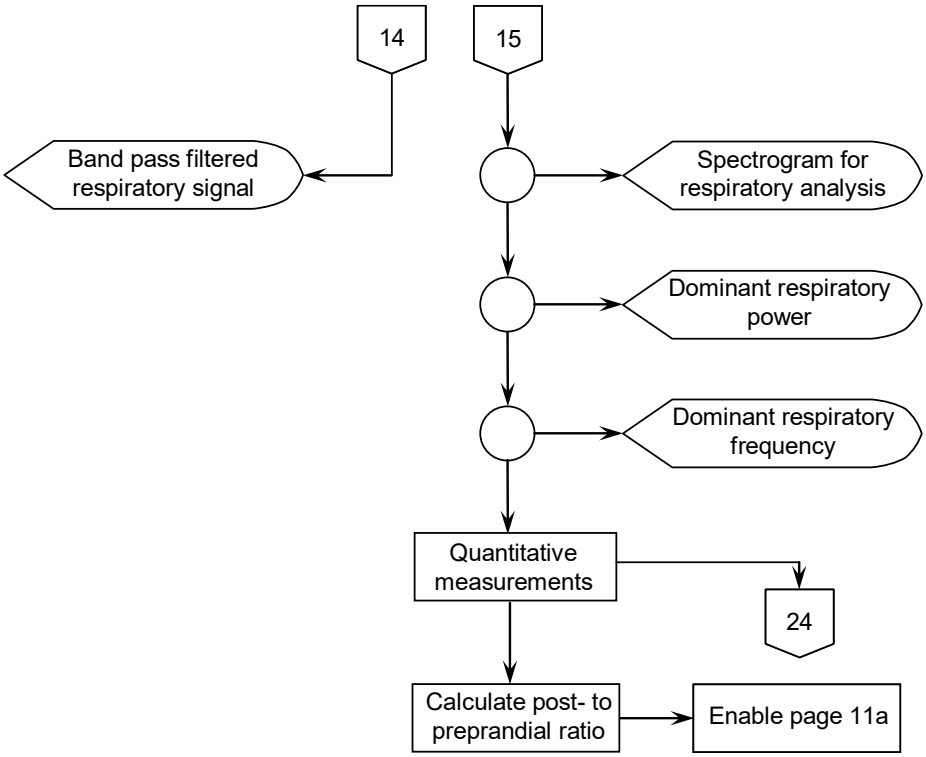

Fig. D32 Block diagram of page 10 of ACCESS 2.40.

Fig. D33 shows a screen shot of page 10 of ACCESS 2.40.

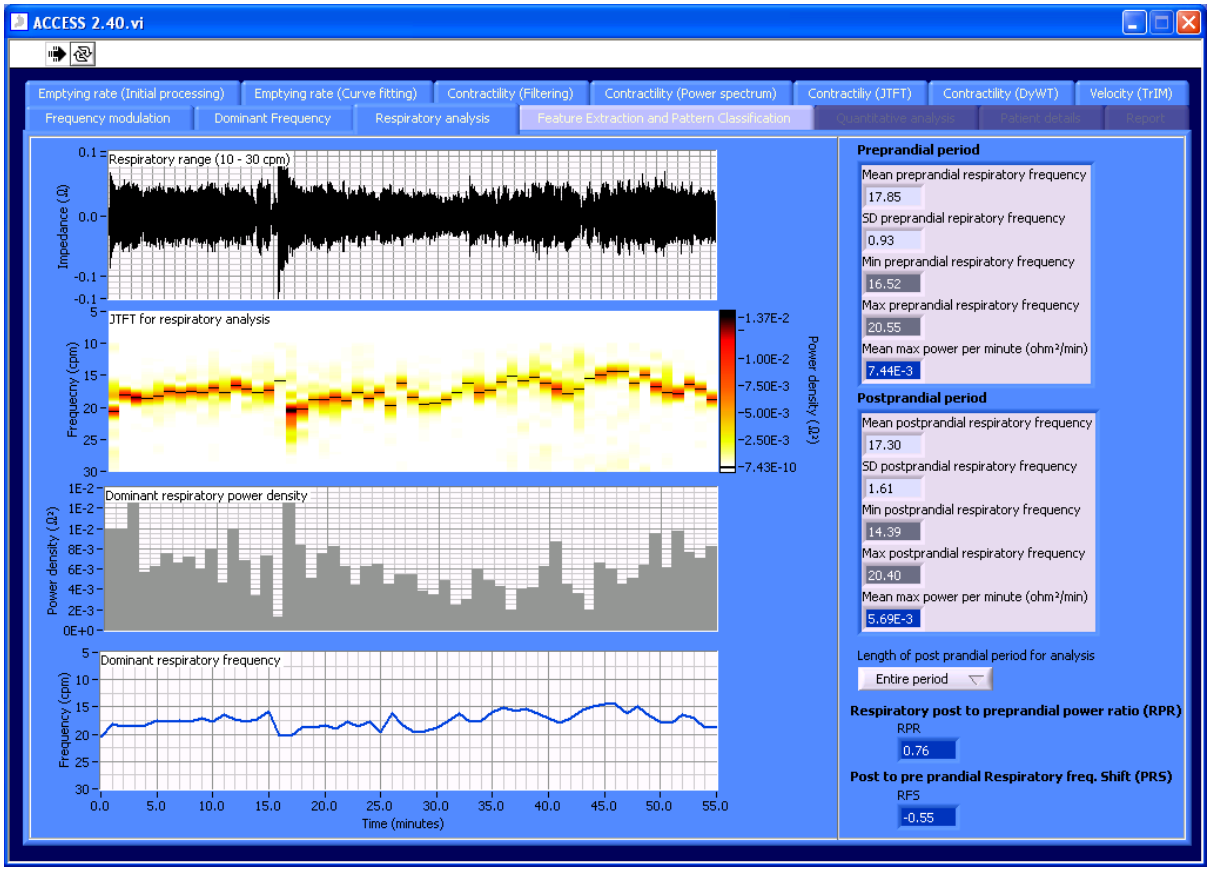

Fig. D33 Screen shot of page 10 of ACCESS 2.40 for respiratory analysis.

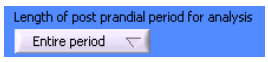

Period of analysis: N/A

Allows the user to choose between analyses of either the entire signal (recommended) or short periods from 10 to 45 minutes in 5 minute steps.

Pattern recognition

Fig D34 shows section a of the block diagram of the software controlled by the eleventh page. This section calculates the Haar wavelet of the emptying curve. Fig. D35 shows a screen shot of page 11 of ACCESS 2.40 and Fig. D36 shows the section b which is the process of calculating the class of emptying curve using the modelled signal.

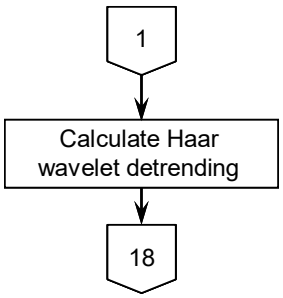

Fig. D34 Block diagram of section a of page 11 of ACCESS 2.40.

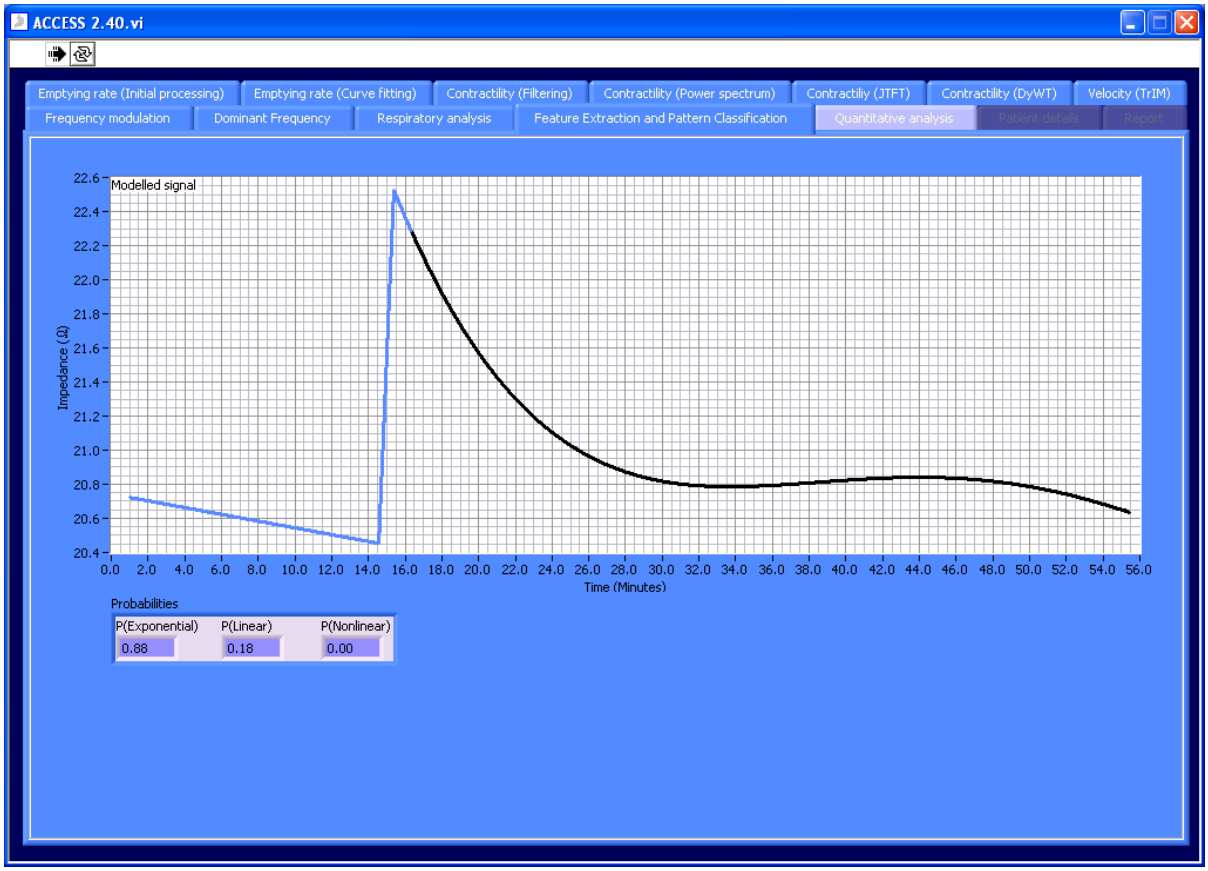

Fig. D35 Screen shot of page 11 of ACCESS 2.40 showing the modelled signal with probabilities of each class of emptying curve. The emptying curve is classified into the class with the highest probability.

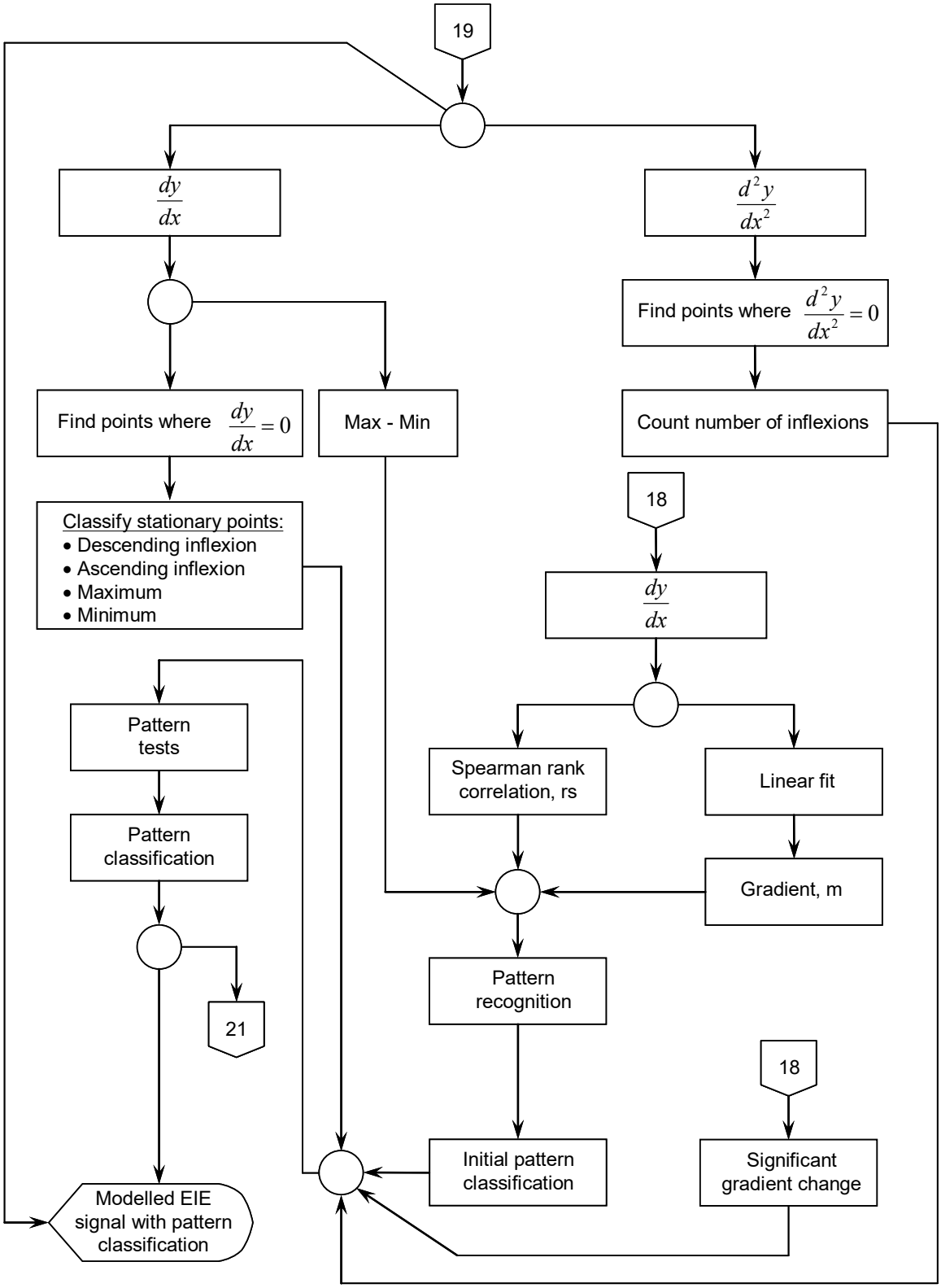

Fig. D36 Block diagram of section b of page 11 of ACCESS 2.40.

Quantitative analysis

Fig D37 shows the block diagram of the software controlled by the twelfth page. This section consolidates the quantitative data and calculates the mean for each epoch (5 minutes) and the whole signal.

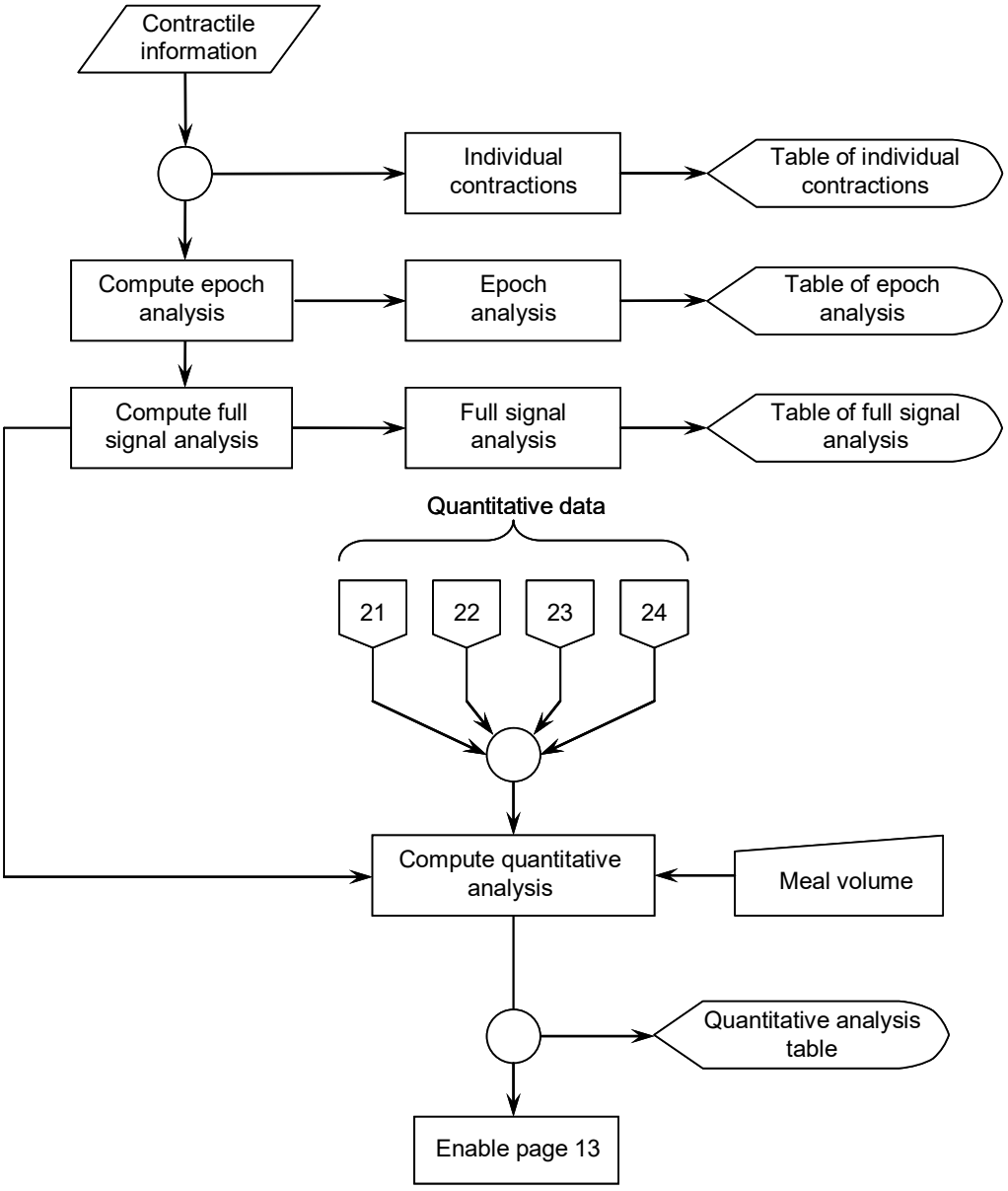

Fig. D37 Block diagram of page 12 of ACCESS 2.40.

Figs. D38 to D41 show screen shots of the sections a, b, c and d of page 12 of ACCESS 2.40 corresponding to the analysis of individual contractions, 5 minute epochs, the total signal and the results table for the quantitative analysis.

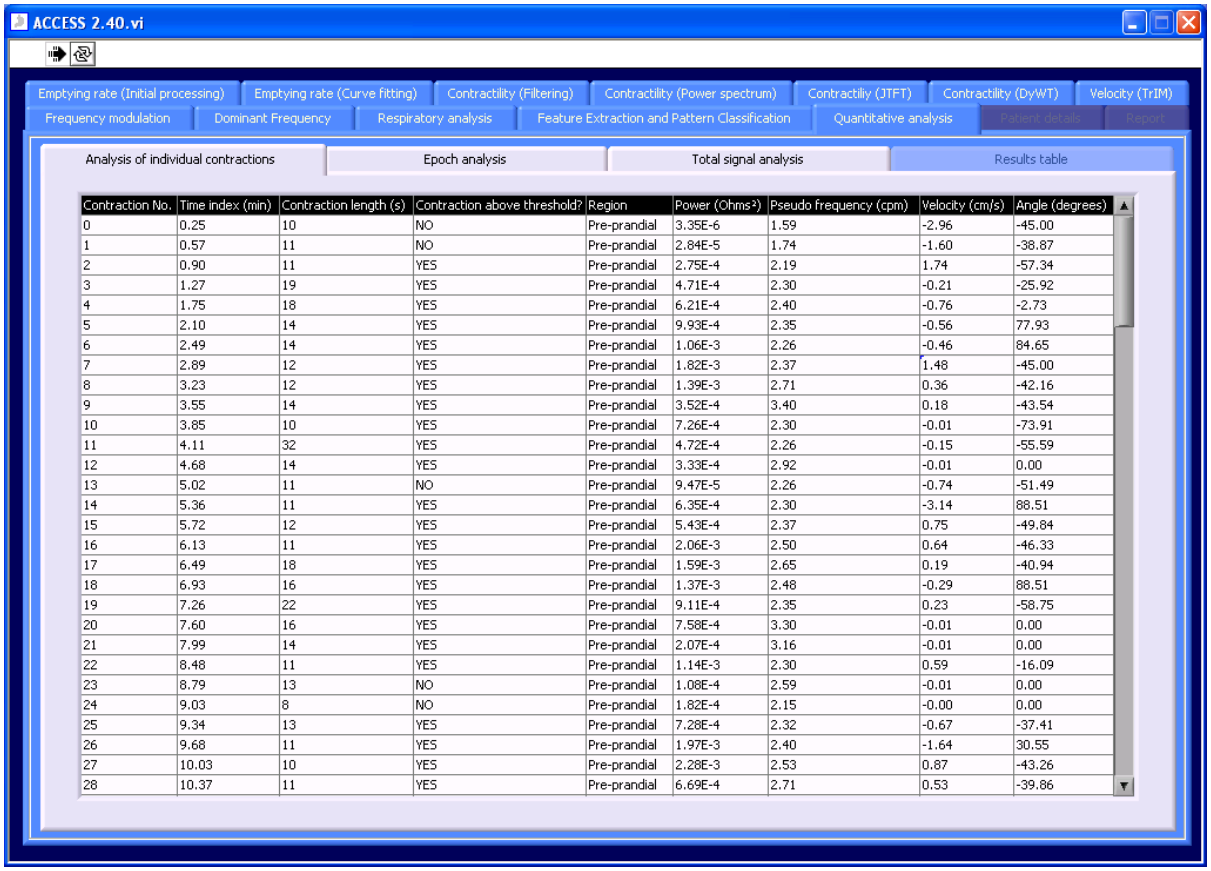

Contraction No.	Time index (min)	Contraction length (s)	Contraction above threshold?	Region	Power (Ohms²)	Pseudo frequency (cpm)	Velocity (cm/s)	Angle (degrees)
0	0.25	10	NO	Pre-prandial	3.35E-6	1.59	-2.96	-45.00
1	0.57	11	NO	Pre-prandial	2.84E-5	1.74	-1.60	-38.87
2	0.90	11	YES	Pre-prandial	2.75E-4	2.19	1.74	-57.34
3	1.27	19	YES	Pre-prandial	4.71E-4	2.30	-0.21	-25.92
4	1.75	18	YES	Pre-prandial	6.21E-4	2.40	-0.76	-2.73
5	2.10	14	YES	Pre-prandial	9.93E-4	2.35	-0.56	77.93
6	2.49	14	YES	Pre-prandial	1.06E-3	2.26	-0.46	84.65
7	2.89	12	YES	Pre-prandial	1.82E-3	2.37	1.48	-45.00
8	3.23	12	YES	Pre-prandial	1.39E-3	2.71	0.36	-42.16
9	3.55	14	YES	Pre-prandial	3.52E-4	3.40	0.18	-43.54
10	3.85	10	YES	Pre-prandial	7.26E-4	2.30	-0.01	-73.91
11	4.11	32	YES	Pre-prandial	4.72E-4	2.26	-0.15	-55.59
12	4.68	14	YES	Pre-prandial	3.33E-4	2.92	-0.01	0.00
13	5.02	11	NO	Pre-prandial	9.47E-5	2.26	-0.74	-51.49
14	5.36	11	YES	Pre-prandial	6.35E-4	2.30	-3.14	88.51
15	5.72	12	YES	Pre-prandial	5.43E-4	2.37	0.75	-49.84
16	6.13	11	YES	Pre-prandial	2.06E-3	2.50	0.64	-46.33
17	6.49	18	YES	Pre-prandial	1.59E-3	2.65	0.19	-40.94
18	6.93	16	YES	Pre-prandial	1.37E-3	2.48	-0.29	88.51
19	7.26	22	YES	Pre-prandial	9.11E-4	2.35	0.23	-58.75
20	7.60	16	YES	Pre-prandial	7.58E-4	3.30	-0.01	0.00
21	7.99	14	YES	Pre-prandial	2.07E-4	3.16	-0.01	0.00
22	8.48	11	YES	Pre-prandial	1.14E-3	2.30	0.59	-16.09
23	8.79	13	NO	Pre-prandial	1.08E-4	2.59	-0.01	0.00
24	9.03	8	NO	Pre-prandial	1.82E-4	2.15	-0.00	0.00
25	9.34	13	YES	Pre-prandial	7.28E-4	2.32	-0.67	-37.41
26	9.68	11	YES	Pre-prandial	1.97E-3	2.40	-1.64	30.55
27	10.03	10	YES	Pre-prandial	2.28E-3	2.53	0.87	-43.26
28	10.37	11	YES	Pre-prandial	6.69E-4	2.71	0.53	-39.86

Fig. D38 Section a of page 12 of ACCESS 2.40: Analysis of individual contractions.

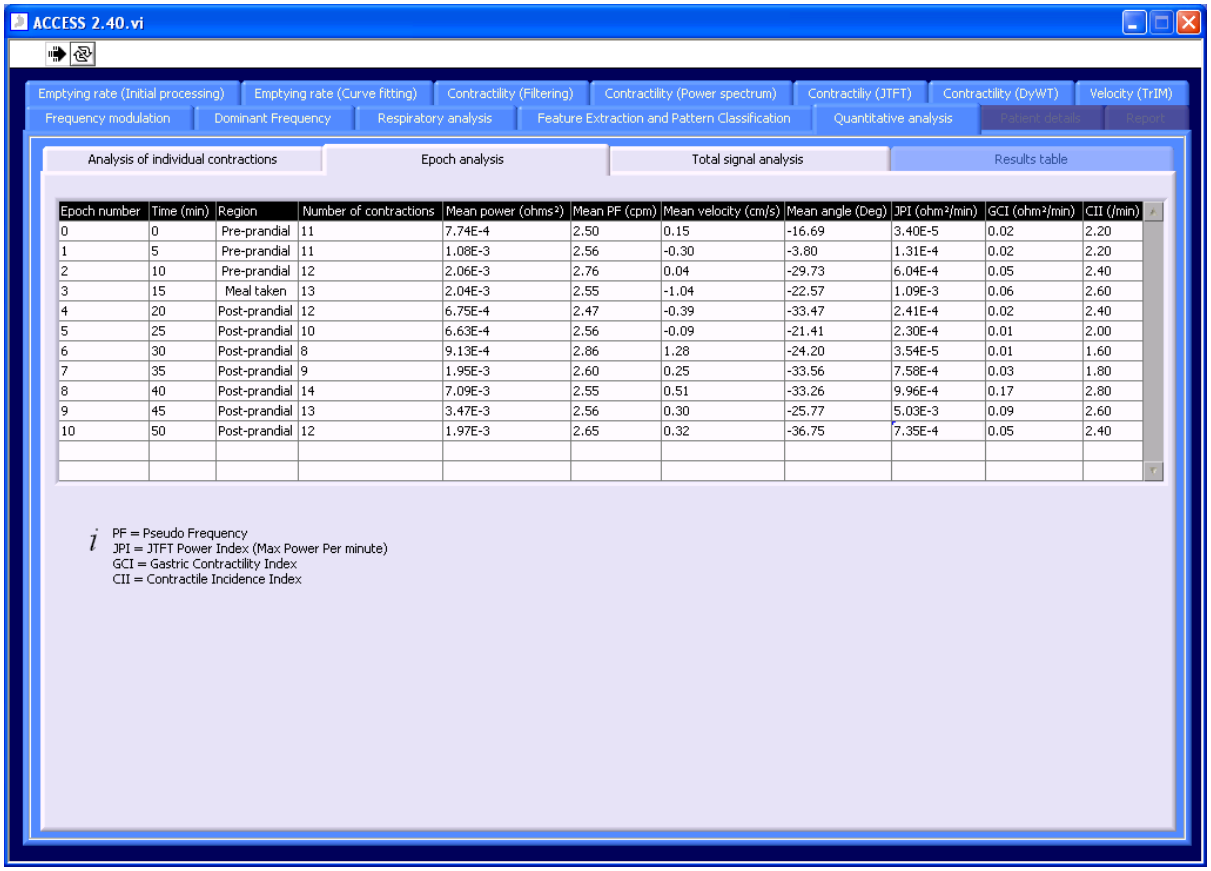

Epoch number	Time (min)	Region	Number of contractions	Mean power (ohms²)	Mean PF (cpm)	Mean velocity (cm/s)	Mean angle (Deg)	JPI (ohm²/min)	GCI (ohm²/min)	CII (/min)
0	0	Pre-prandial	11	7.74E-4	2.50	0.15	-16.69	3.40E-5	0.02	2.20
1	5	Pre-prandial	11	1.08E-3	2.56	-0.30	-3.80	1.31E-4	0.02	2.20
2	10	Pre-prandial	12	2.06E-3	2.76	0.04	-29.73	6.04E-4	0.05	2.40
3	15	Meal taken	13	2.04E-3	2.55	-1.04	-22.57	1.09E-3	0.06	2.60
4	20	Post-prandial	12	6.75E-4	2.47	-0.39	-33.47	2.41E-4	0.02	2.40
5	25	Post-prandial	10	6.63E-4	2.56	-0.09	-21.41	2.30E-4	0.01	2.00
6	30	Post-prandial	8	9.13E-4	2.86	1.28	-24.20	3.54E-5	0.01	1.60
7	35	Post-prandial	9	1.95E-3	2.60	0.25	-33.56	7.58E-4	0.03	1.80
8	40	Post-prandial	14	7.09E-3	2.55	0.51	-33.26	9.96E-4	0.17	2.80
9	45	Post-prandial	13	3.47E-3	2.56	0.30	-25.77	5.03E-3	0.09	2.60
10	50	Post-prandial	12	1.97E-3	2.65	0.32	-36.75	7.35E-4	0.05	2.40

PF = Pseudo Frequency
JPI = JTFT Power Index (Max Power Per minute)
GCI = Gastric Contractility Index
CII = Contractile Incidence Index

Fig. D39 Section b of page 12 of ACCESS 2.40: Analysis of 5 minute epochs.

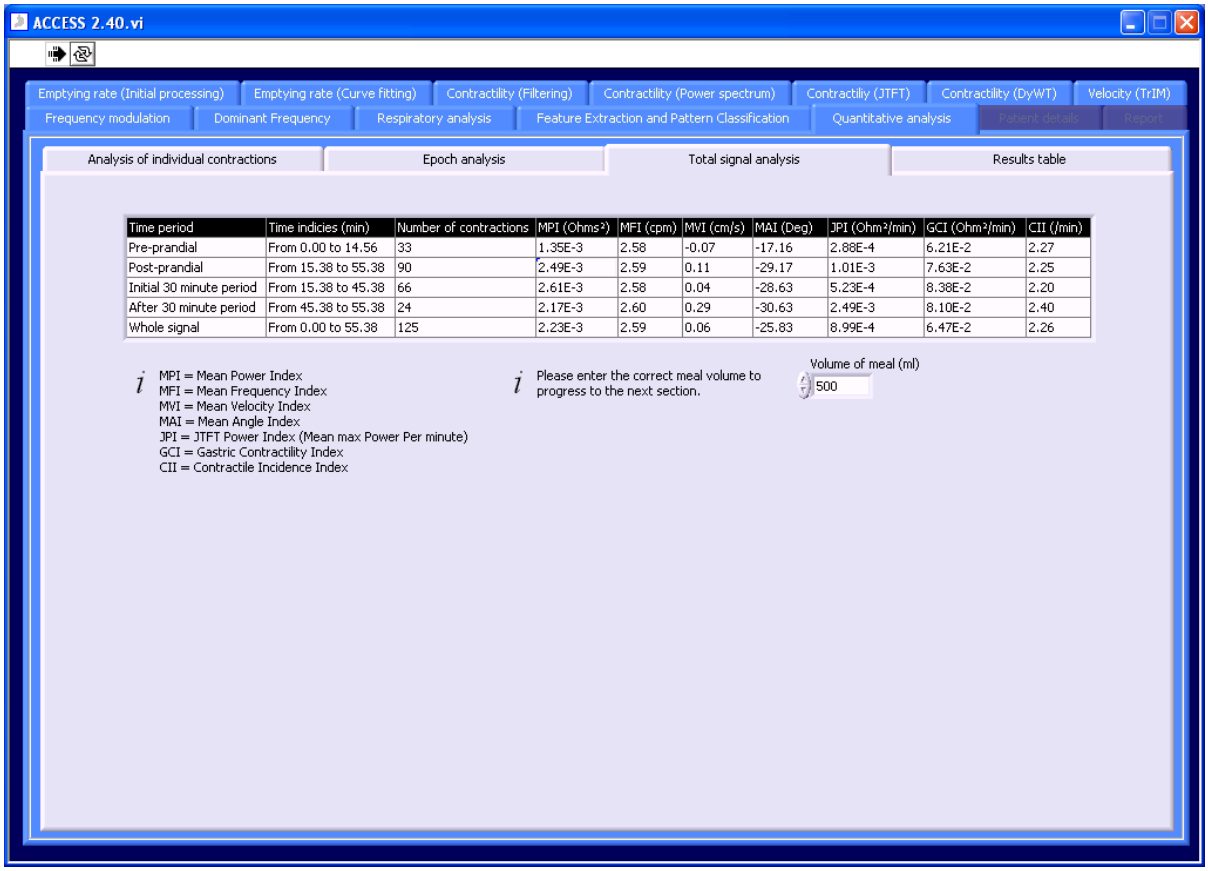

Fig. D40 Section c of page 12 of ACCESS 2.40: Analysis of the total signal.

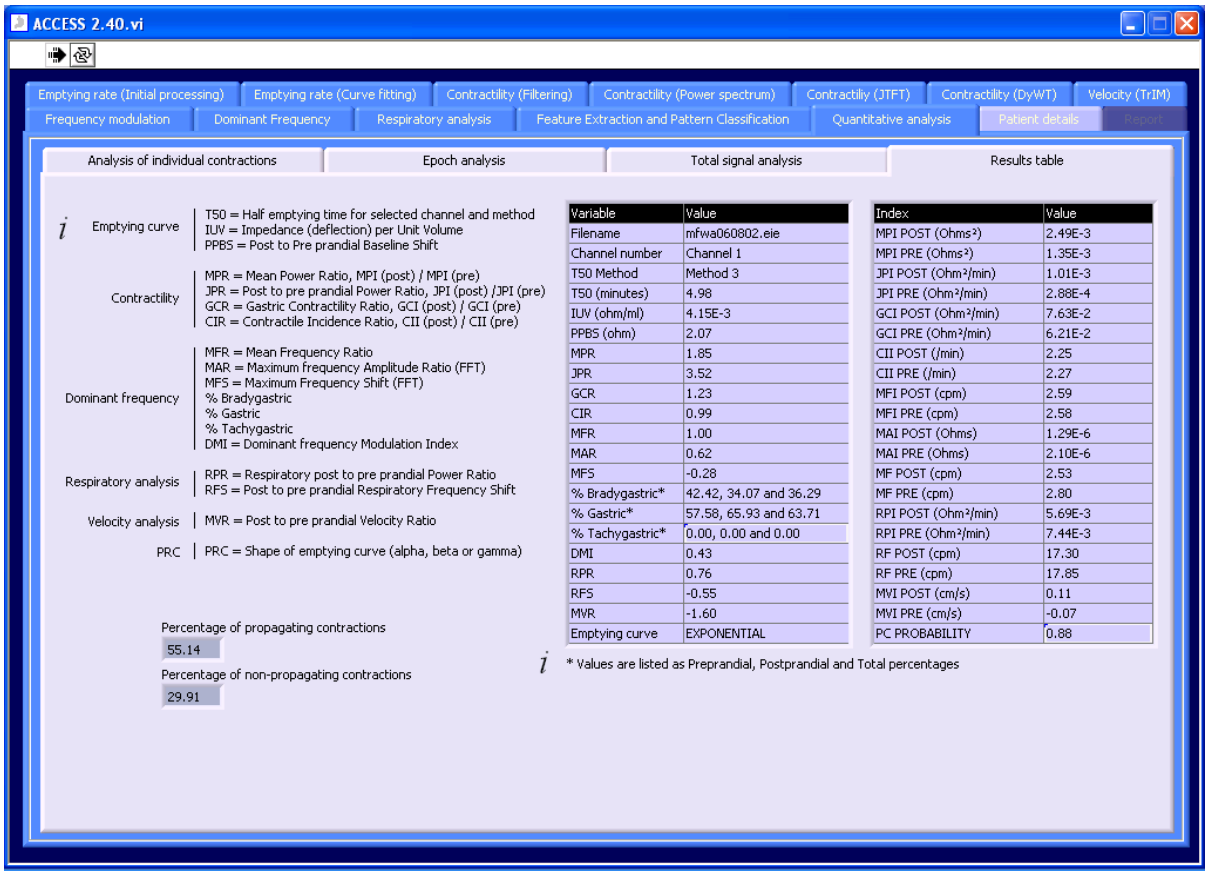

Fig. D41 Section d of page 12 of ACCESS 2.40: Quantitative results table.

Patient details

Fig D42 shows the block diagram of the software controlled by the thirteenth page. This page allows the user to open a *.ant (anthropomorphic) file or enter the anthropomorphic data manually. Subsequently, it is possible to save any measurements entered. Once this is done, the user may compile the report.

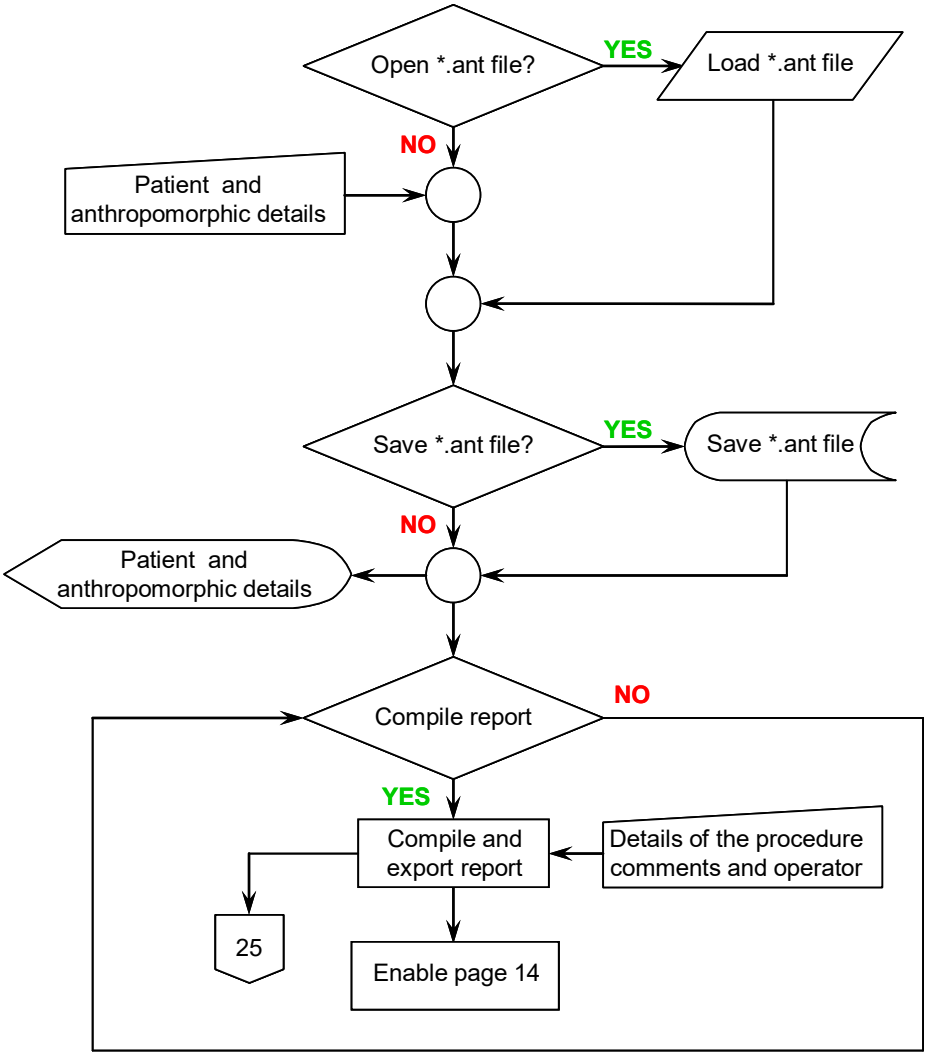

Fig. D42 Block diagram of page 13 of ACCESS 2.40.

Fig. D43 shows a screen shot of page 13 of ACCESS 2.40 after the loading of an *.ant file and during the exportation of the report.

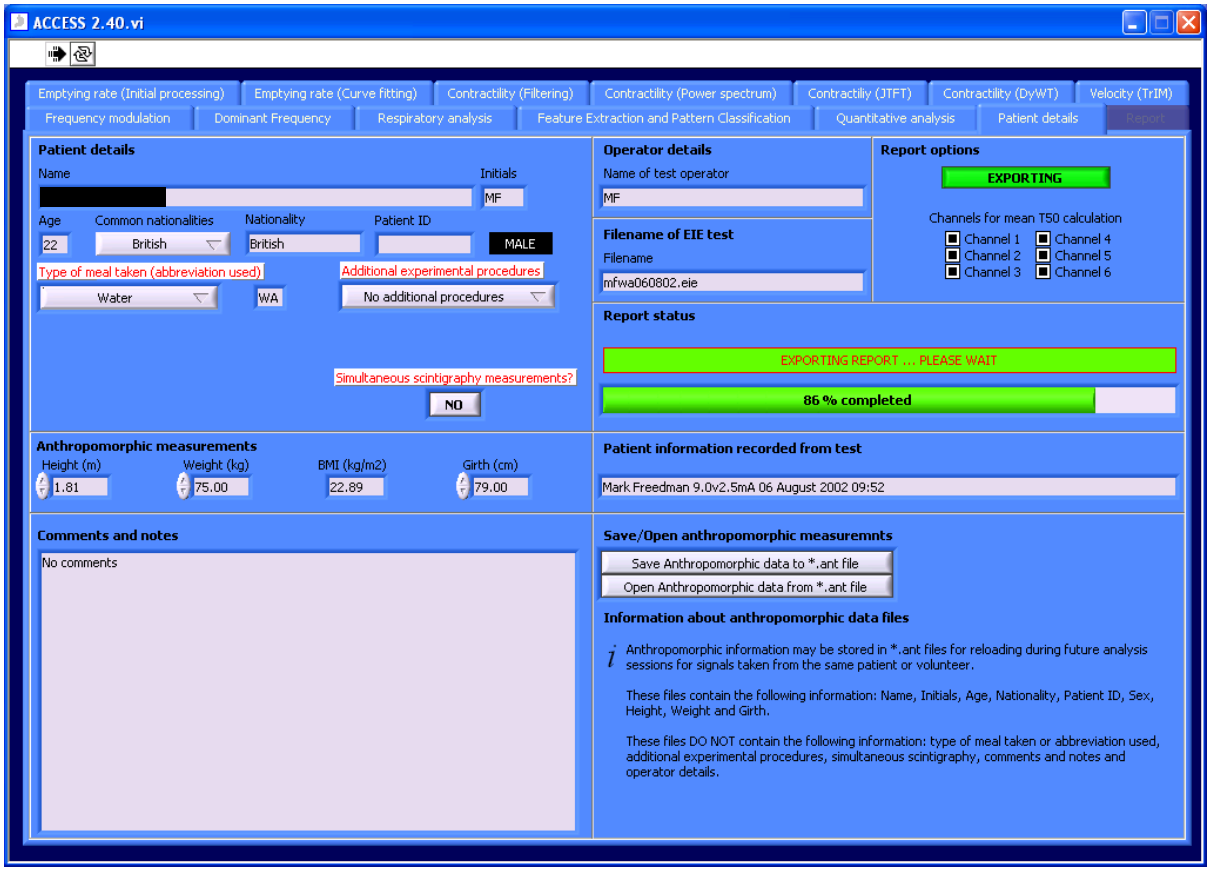

Fig. D43 Screen shot of page 13 of ACCESS 2.40.

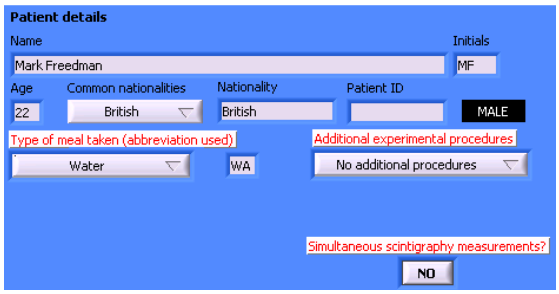

Patient details: PATIENT DETAILS AND ANTHROPOMORPHIC MEASUREMENTS

Name, age, initials, nationality, ID and gender of the volunteer together with the type of meal taken, additional experimental procedures such as sham feeding and whether the test was performed with simultaneous scintigraphy.

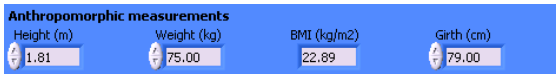

Anthropomorphic data: PATIENT DETAILS AND ANTHROPOMORPHIC MEASUREMENTS

Height in metres, weight in kilograms and girth in centimetres must be entered. The Body Mass Index (BMI) is calculated automatically.

Report generation

Fig. D44 shows the block diagram of the software controlled by the fourteenth page. This page displays the report and allows the user to export it to a Microsoft Word file and two Microsoft Excel files. It is necessary to have Microsoft Office 2000 or above for this to work.

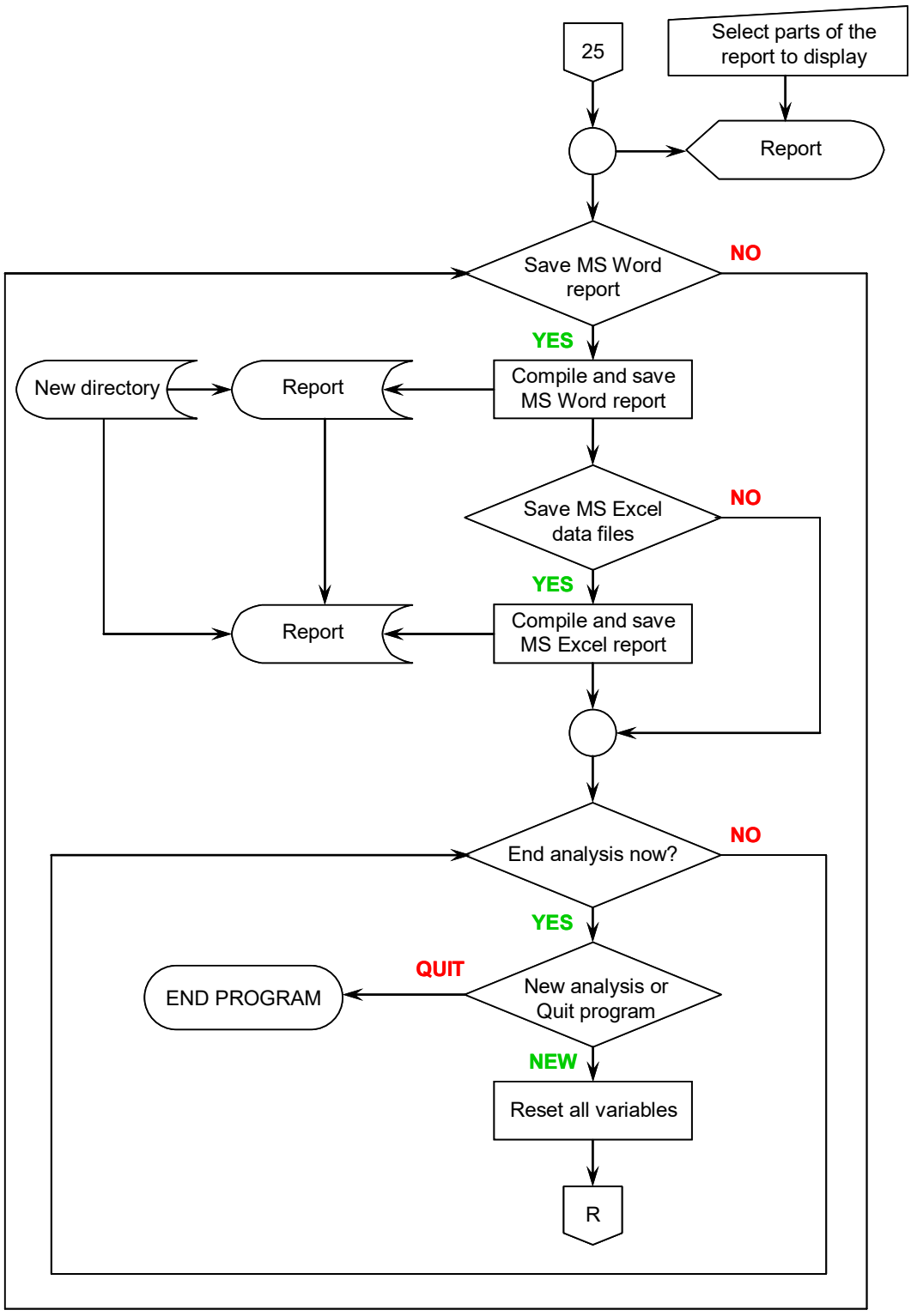

Fig. D44 Block diagram of page 14 of ACCESS 2.40.

Fig. D45 shows a screen shot of page 14 of ACCESS 2.40. Once the report has been saved to a word file, the user is given the option to create two Microsoft Excel files that contain the quantitative analysis results for individual contractions, 5 minute epochs, the total signal and the results table for the quantitative analysis in addition to all of the graph data for further analysis.

These three files are saved in a new directory (automatically created in the same folder as the signal). After all the files have been saved, the user may end the current analysis session and either exit ACCESS completely or re-run the program from the beginning for a new analysis.

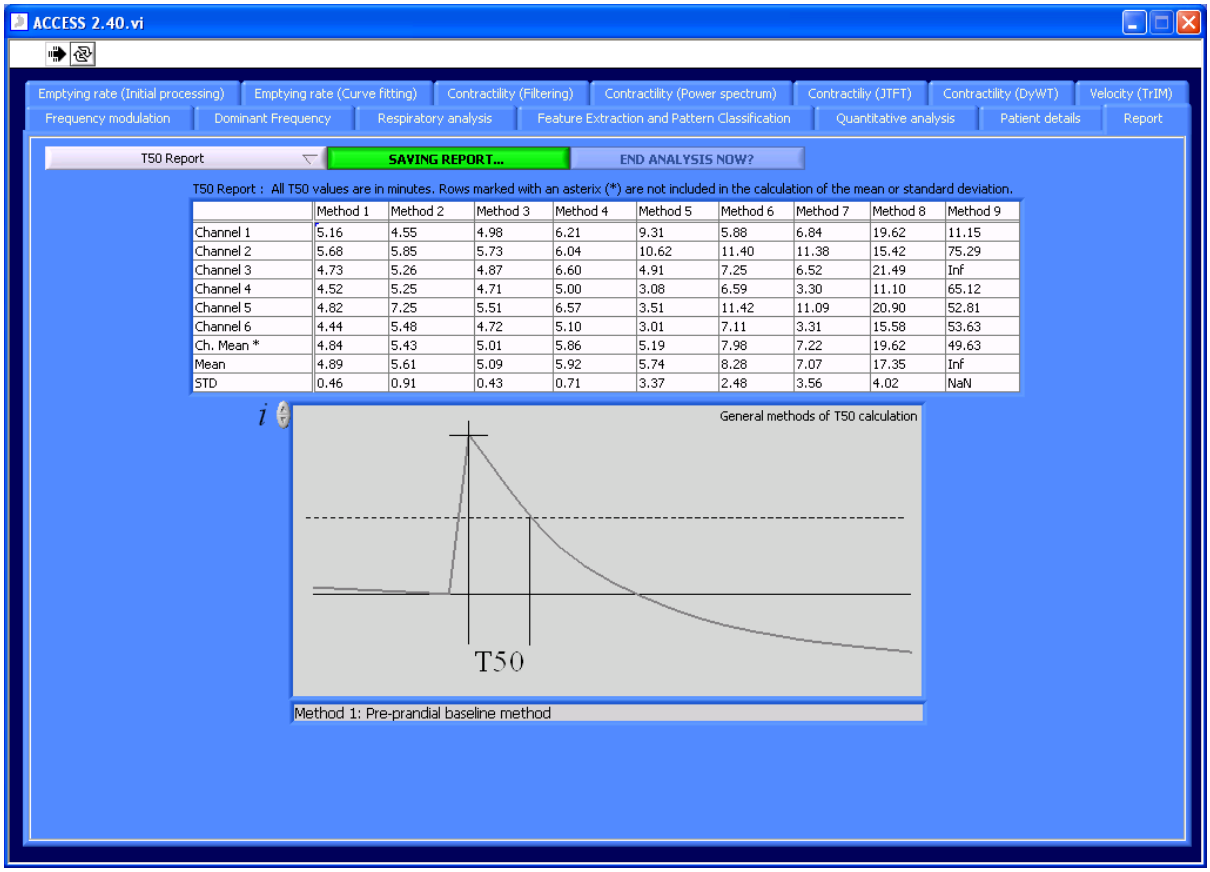

Fig. D45 Screen shot of page 14 of ACCESS 2.40 during the saving of the report to a Microsoft Word file.

Appendix E Curve fitting

The coefficient of determination, R^2 and the calculation of the optimal polynomial order

The coefficient of determination, R^2 expresses the proportion of variance in the fitted curve explained by the original signal. *SS* stands for Sums of the Squares for the data Y containing n data points. The curve fit (polynomial, exponential or moving average) is given as $\hat{Y}$ and the mean of all Y is $\overline{Y}$. SS_{reg} is the sum of the squares (regression) and describes how far the predicted values differ from the mean and SS_{res} is the sum of the squares (residual) and corresponds to the residual variance between the data and fitted curve.

$$R^2 = \frac{SS_{reg}}{SS_{reg} + SS_{res}} \tag{E1}$$

where $$SS_{reg} = \sum_{i=0}^{n}\left(\hat{Y}_i - \overline{Y}\right)^2 \text{ and } SS_{res} = \sum_{i=0}^{n}\left(Y_i - \hat{Y}_i\right)^2$$

The order of the optimal polynomial is determined by analysing the R^2 from 1st to 7th order polynomial curve fits for data from 12 randomly selected EIE signals. Table E1 shows the R^2 values for each of the signals.

Table E1 R^2 values for the EIE signals with a polynomial fit (1st to 7th order).

Signal	1st order	2nd order	3rd order	4th order	5th order	6th order	7th order
1	0.63	0.93	0.95	0.96	0.96	0.96	0.96
2	0.91	0.95	0.95	0.97	0.97	0.98	0.98
3	0.42	0.47	0.72	0.72	0.78	0.83	0.85
4	0.34	0.77	0.77	0.84	0.85	0.86	0.88
5	0.95	0.98	0.99	0.99	0.99	0.99	0.99
6	0.96	0.98	0.99	0.99	0.99	0.99	0.99
7	0.94	0.98	0.98	0.98	0.98	0.99	0.99
8	0.97	0.99	0.99	0.99	0.99	0.99	0.99
9	0.73	0.94	0.94	0.95	0.95	0.96	0.96
10	0.48	0.83	0.86	0.86	0.86	0.86	0.87
11	0.55	0.92	0.95	0.97	0.99	0.99	0.99
12	0.89	0.96	0.96	0.97	0.97	0.97	0.97
Mean	0.73	0.89	0.92	0.93	0.94	0.95	0.95
STDEV	0.24	0.15	0.09	0.08	0.07	0.06	0.05

The table indicates that the R^2 value for the polynomial fit does not significantly improve after the 4th order fit. Significance is defined as a mean difference of more than 0.01 in the R^2 value. Analysis of the differences (Table E2) reveals that the mean difference falls below 0.01 between the 4th and 5th order fit. Therefore, the 4th order polynomial is the most appropriate.

Table E2 Analysis of the differences in R^2 values for increasing orders of the polynomial fit.

Signal	1st to 2nd	2nd to 3rd	3rd to 4th	4th to 5th	5th to 6th	6th to 7th
1	0.30	0.02	0.01	0.00	0.00	0.00
2	0.04	0.00	0.02	0.00	0.01	0.00
3	0.05	0.25	0.00	0.06	0.05	0.02
4	0.43	0.00	0.07	0.01	0.01	0.02
5	0.03	0.01	0.00	0.00	0.00	0.00
6	0.02	0.01	0.00	0.00	0.00	0.00
7	0.04	0.00	0.00	0.00	0.01	0.00
8	0.02	0.00	0.00	0.00	0.00	0.00
9	0.21	0.00	0.01	0.00	0.01	0.00
10	0.35	0.03	0.00	0.00	0.00	0.01
11	0.37	0.03	0.02	0.02	0.00	0.00
12	0.07	0.00	0.01	0.00	0.00	0.00
Mean	1.61×10^{-1}	2.92×10^{-2}	1.17×10^{-2}	7.50×10^{-3}	7.50×10^{-3}	4.17×10^{-3}
STDEV	1.60×10^{-1}	7.05×10^{-2}	1.99×10^{-2}	1.76×10^{-2}	1.42×10^{-2}	7.93×10^{-3}

The Nonlinear Levenberg-Marquardt algorithm

The Nonlinear Levenberg-Marquardt algorithm determines the set of coefficients for a nonlinear best-fit curve (equation E2). However, the algorithm requires *a priori* information regarding the curve in order to provide an initial guess of the coefficients (a_1, a_2, … , a_M). The algorithm then applies an iterative process to minimise the chi-square (χ^2) quantity.

$$\chi^2 = \sum_{i=0}^{N-1} \left(\frac{y_i - f\left(x_i; a_1, \ldots, a_M\right)}{\sigma_i} \right)^2 \qquad \text{(E2)}$$

In equation H1, (x_i, yi) are the input data points, and $f(x_i;a_1...a_M) = f(X, A)$ is the nonlinear function where $a_1...a_M$ are coefficients. Since equation 6.7 shows that the exponential fit has three parameters (a, b and c) $M = 3$.

Appendix F Views of the 3D feature space

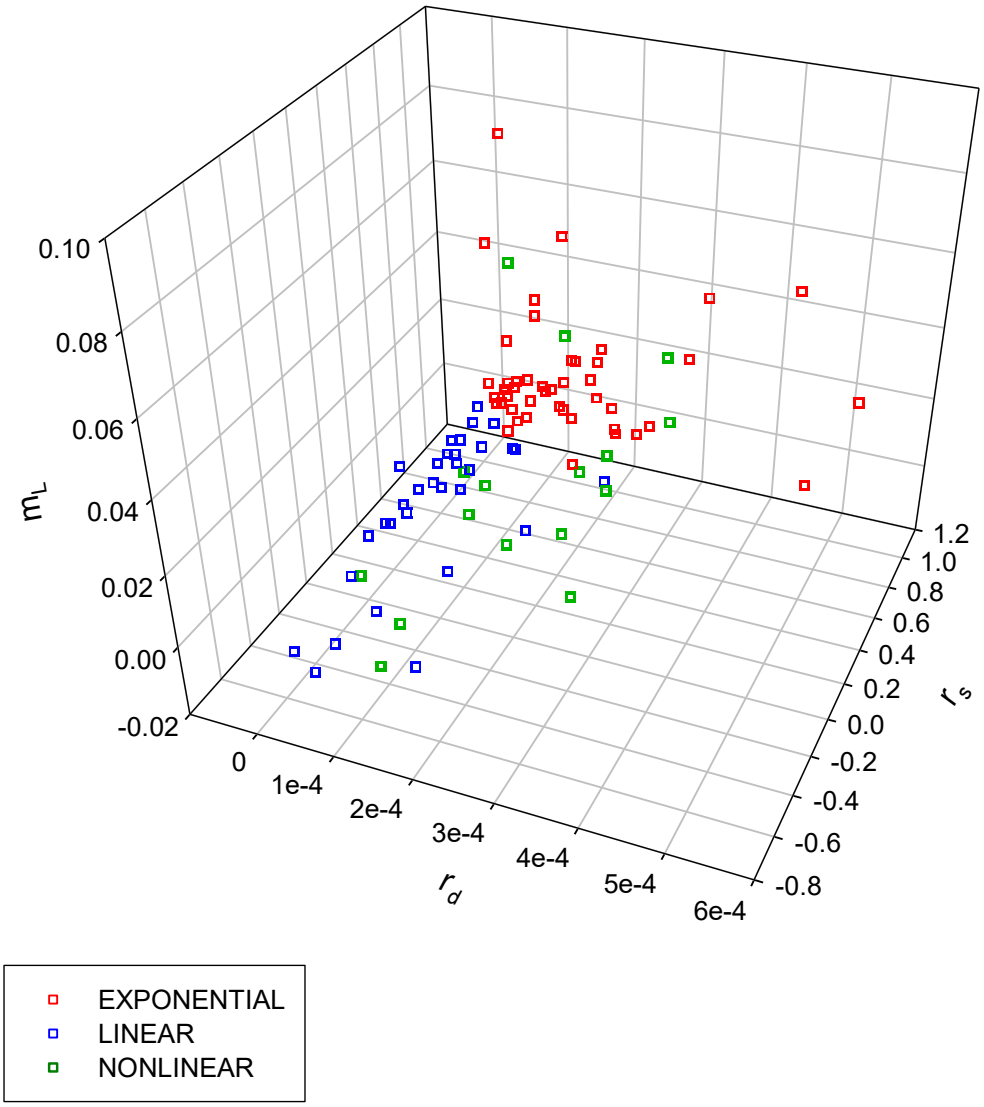

Fig. F1 3D feature space showing the separation of the exponential and linear classes but not the non-linear class. r_d is the range of the derivative, r_s is the Spearman rank correlation and m_L is the gradient of the linear fit through the differences in impedance of the Haar wavelet model.

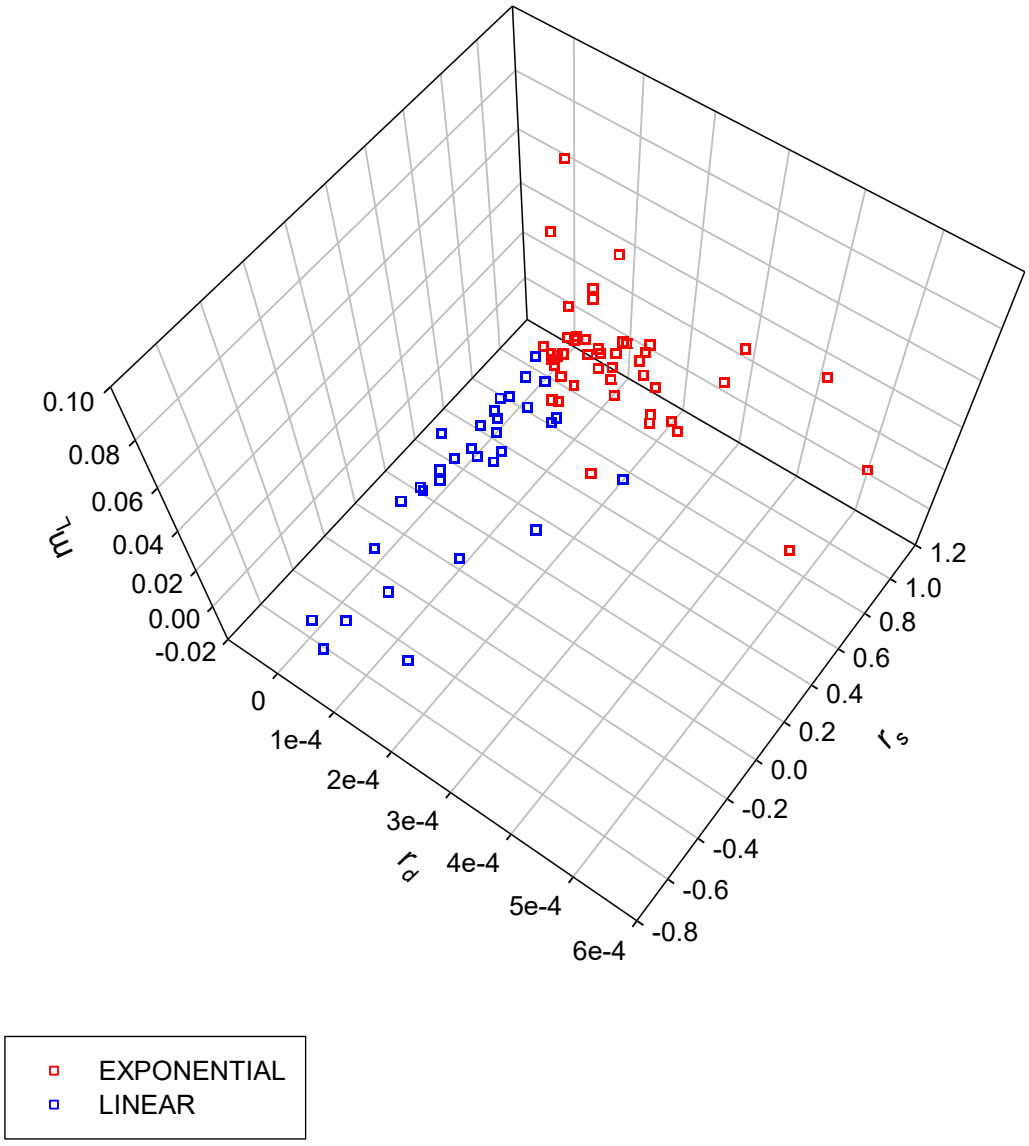

Fig. F2 3D feature space without the non-linear class showing good separation between the exponential and linear classes. r_d is the range of the derivative, r_s is the Spearman rank correlation and m_L is the gradient of the linear fit through the differences in impedance of the Haar wavelet model.

Appendix G Typical report generated by ACCESS

Report for C:\EIE studies\Results from studies\WA\Misc wa (3)\mf01wa24007.eie

Report produced on 22/06/2004 at 12:58 by MF

Signal indices and features

Marker 1:	19.79 min
Marker 2:	20.55 min
End of preprandial:	19.79 min
Beginning of postprandial:	20.55 min
Channel selected:	1

	Current flow	Deflection (Ohms)	Rank
Channel 1	RED to YELLOW	1.98	2
Channel 2	RED to BLACK	1.11	5
Channel 3	YELLOW to RED	2.02	1
Channel 4	YELLOW to BLACK	1.28	4
Channel 5	BLACK to RED	1.08	6
Channel 6	BLACK TO YELLOW	1.37	3

Patient details

Name	#### ########
Nationality	British
Age	22
Sex	MALE
Patient ID	MF
Notes	No comments

Anthropomorphic measurements

Weight (kg)	75.00
Height (m)	1.81
BMI (kg/m²)	22.89
Girth (cm)	79.00

Details of procedure

Simultaneous scintigraphy?	NO
Meal Type	Water
Additional Procedures	No additional procedures

T50 Report

	Method 1	Method 2	Method 3	Method 4	Method 5	Method 6	Method 7	Method 8	Method 9
Channel 1	7.88	10.84	9.33	9.79	5.04	8.28	6.39	13.11	Inf
Channel 2	7.17	9.97	8.37	8.57	4.79	9.06	6.11	12.18	55.65
Channel 3	8.11	10.91	9.58	9.93	5.14	8.76	6.48	13.45	Inf
Channel 4	5.45	10.87	7.17	6.39	3.45	8.71	4.88	4.16	25.11
Channel 5	7.29	9.94	8.43	8.53	4.91	9.11	6.20	6.38	53.59
Channel 6	5.37	11.10	6.94	6.29	3.42	8.98	4.75	4.14	24.96
Ch. Mean *	6.84	10.62	8.40	8.19	4.40	8.56	5.86	5.61	26.01
Mean	6.88	10.60	8.30	8.25	4.46	8.82	5.80	8.91	Inf

Acquired data

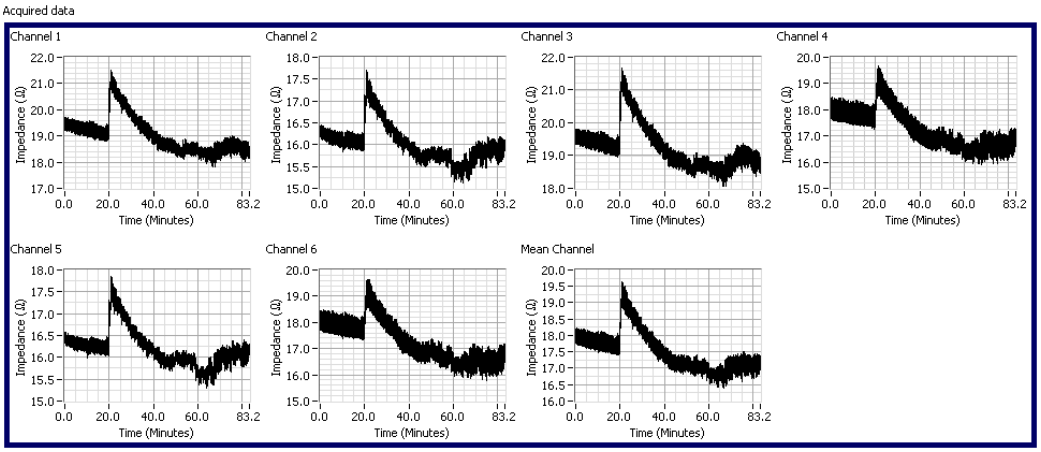

Quantitative data analysis

Variable	Value	Index	Value
Filename	mf01wa24007.eie	MPI POST (Ohms²)	3.39E-3
Channel number	Channel 1	MPI PRE (Ohms²)	8.39E-4
T50 Method	Method 3	JPI POST (Ohm²/min)	9.14E-4
T50 (minutes)	9.33	JPI PRE (Ohm²/min)	1.80E-4
IUV (ohm/ml)	4.08E-3	GCI POST (Ohm²/min)	6.58E-2
PPBS (ohm)	2.04	GCI PRE (Ohm²/min)	2.99E-2
MPR	4.04	CII POST (/min)	2.14
JPR	5.08	CII PRE (/min)	1.57
GCR	2.20	MFI POST (cpm)	2.64
CIR	1.37	MFI PRE (cpm)	2.60
MFR	1.01	MAI POST (Ohms)	1.32E-6
MAR	2.84	MAI PRE (Ohms)	4.64E-7
MFS	-0.32	MF POST (cpm)	2.50
% Bradygastric*	38.71, 30.37 and 31.93	MF PRE (cpm)	2.82
% Gastric*	61.29, 69.63 and 68.07	RPI POST (Ohm²/min)	6.12E-3
% Tachygastric*	0.00, 0.00 and 0.00	RPI PRE (Ohm²/min)	1.01E-2
DMI	0.00	RF POST (cpm)	15.89
RPR	0.61	RF PRE (cpm)	15.34
RFS	0.55	MVI POST (cm/s)	0.56
MVR	-1.15	MVI PRE (cm/s)	-0.49
Emptying curve	EXPONENTIAL	PC PROBABILITY	0.88

* Values are listed as Preprandial, Postprandial and Total percentages

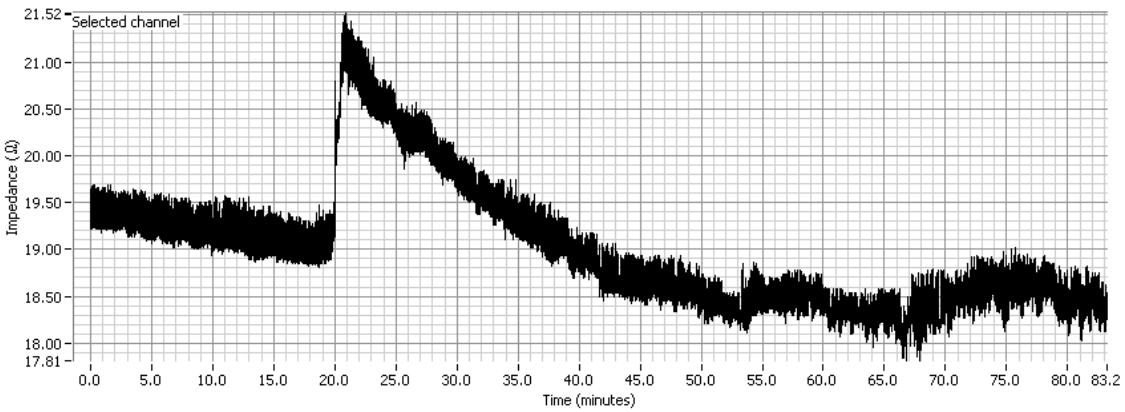

Joint Time Fourier Transform (JTFT)

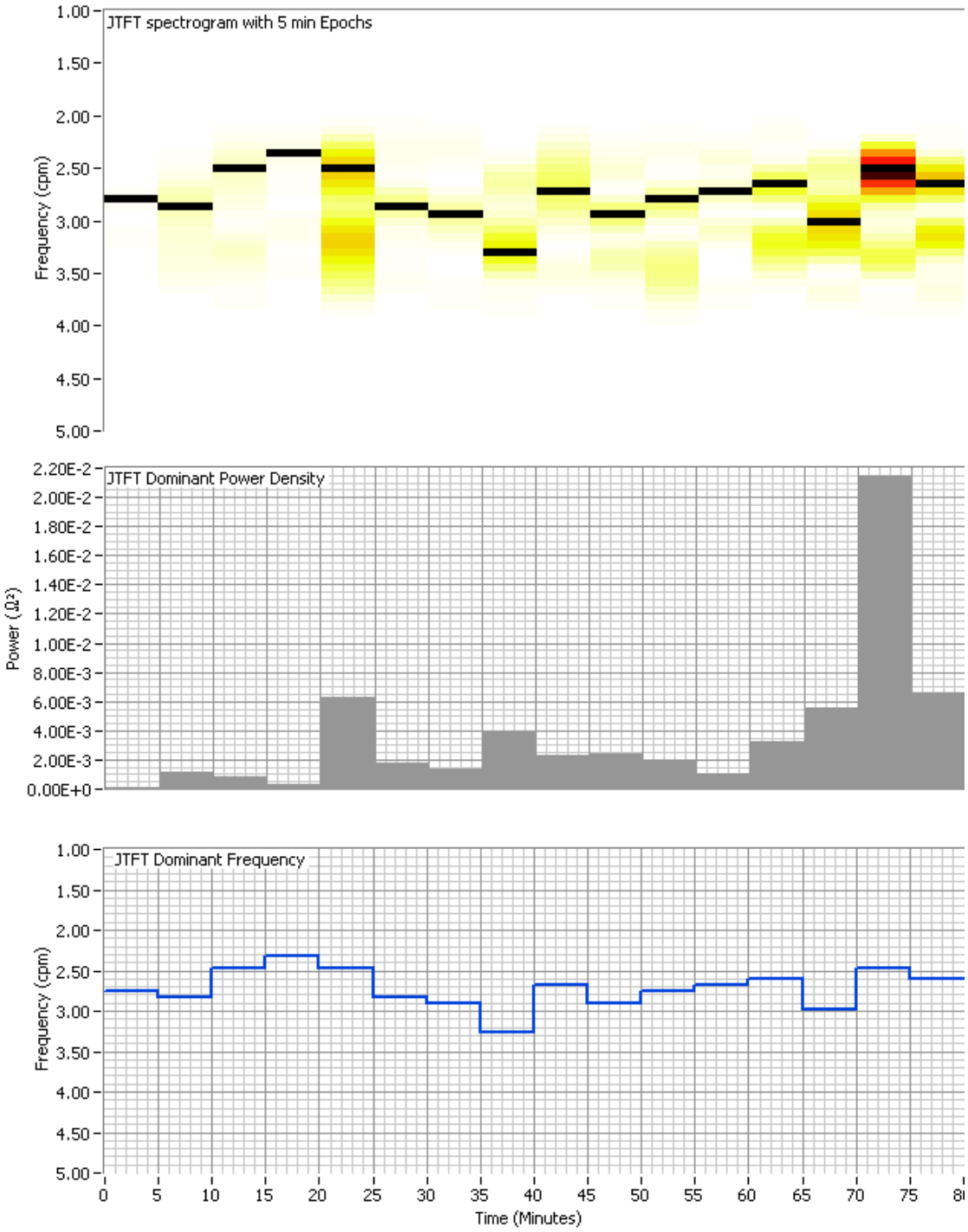

Overlapped JTFT for the analysis of dominant frequency

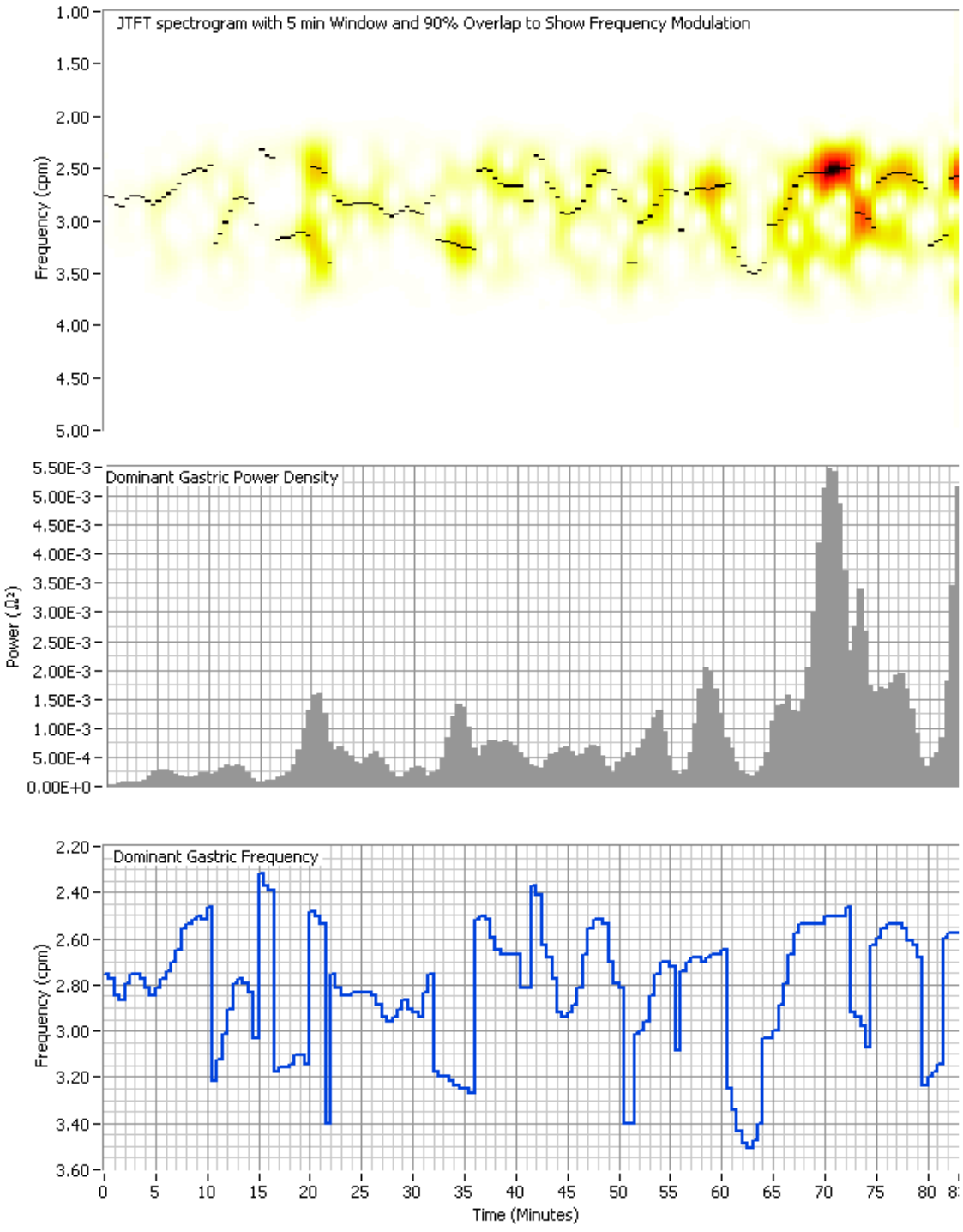

Discretised Dyadic Wavelet Transform (DyWT) for the analysis of dominant frequency

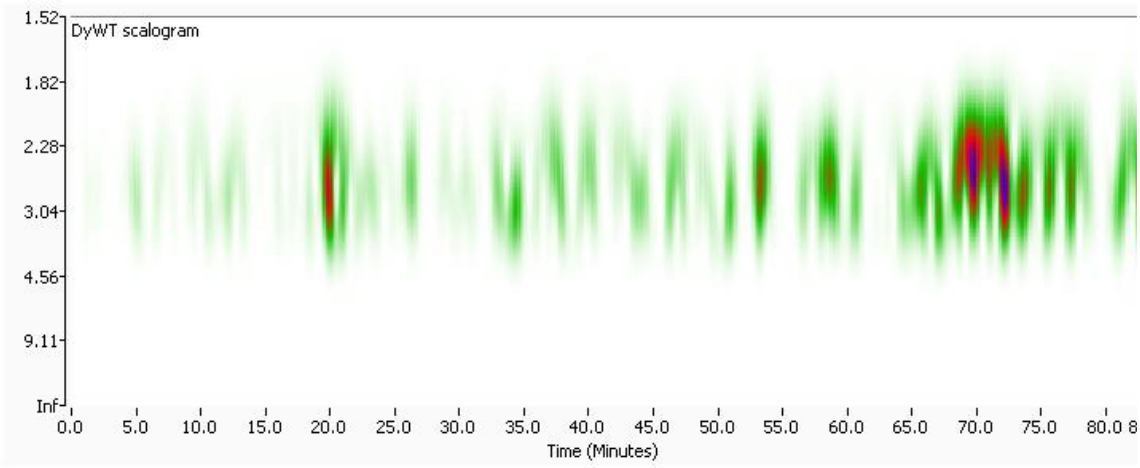

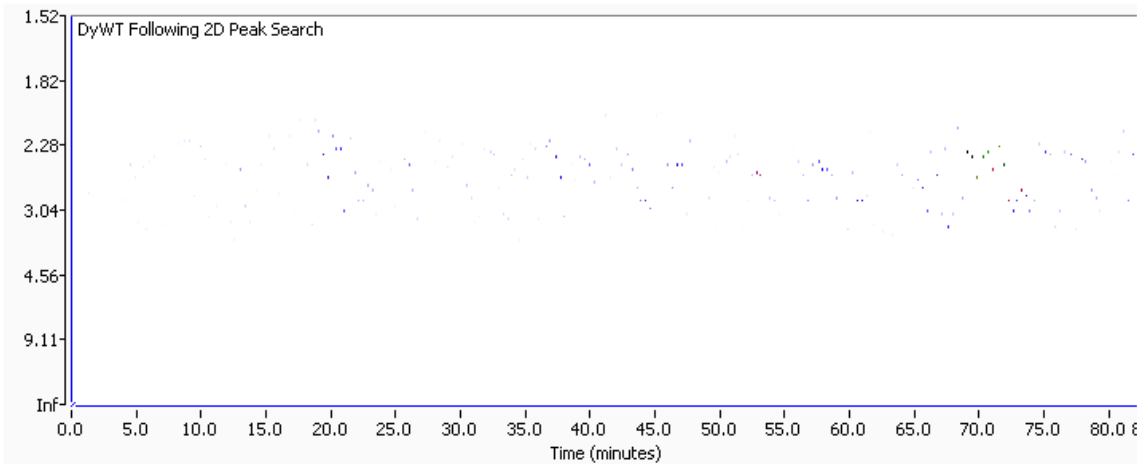

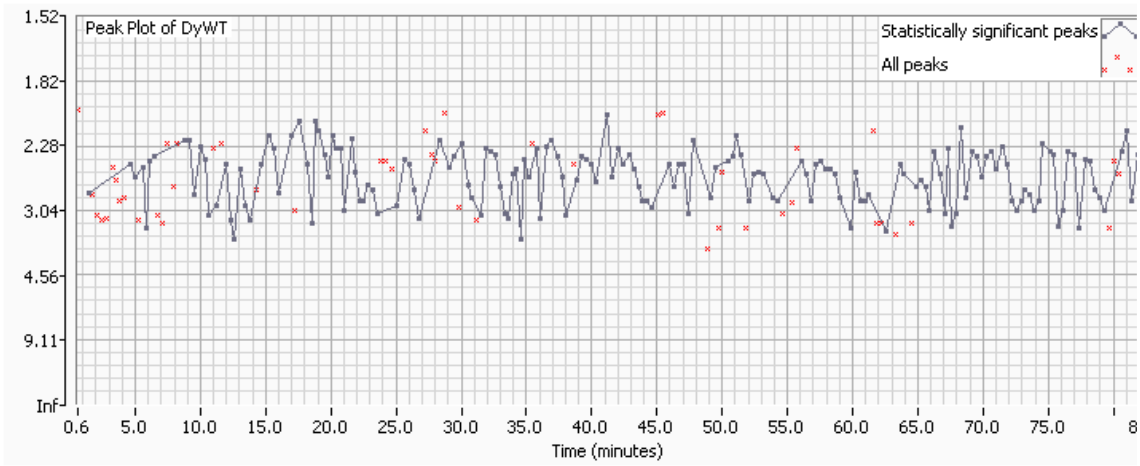

Velocity analysis

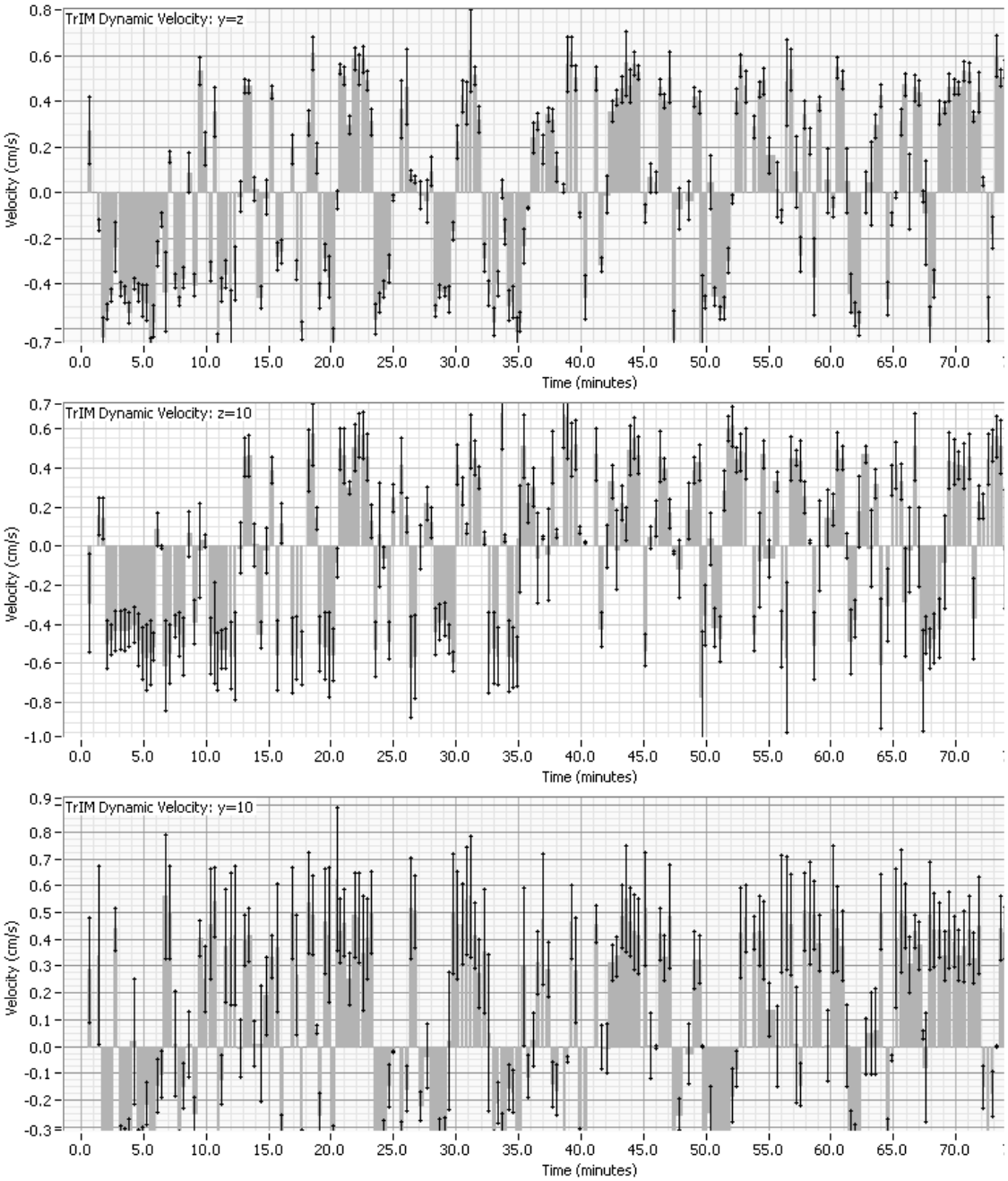

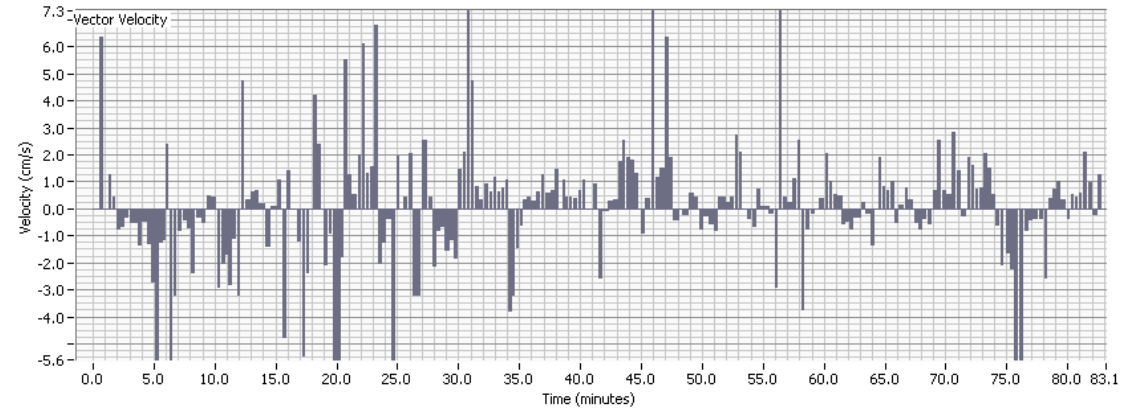

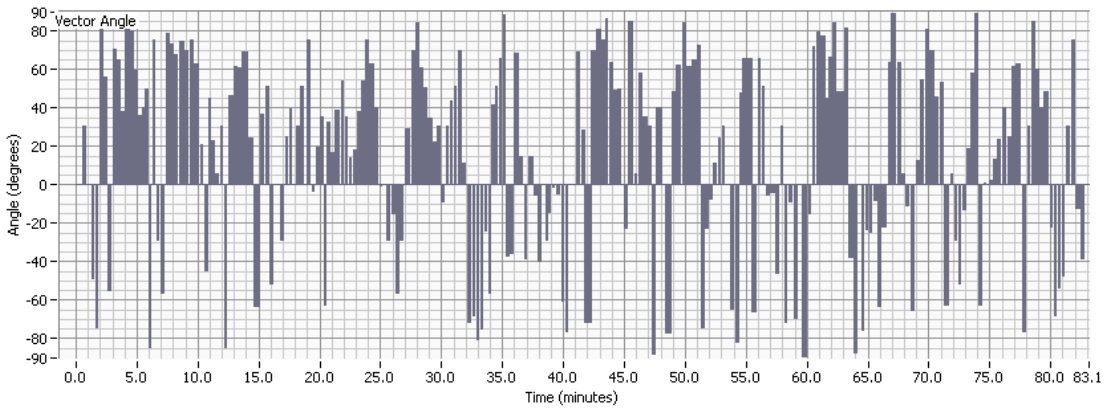

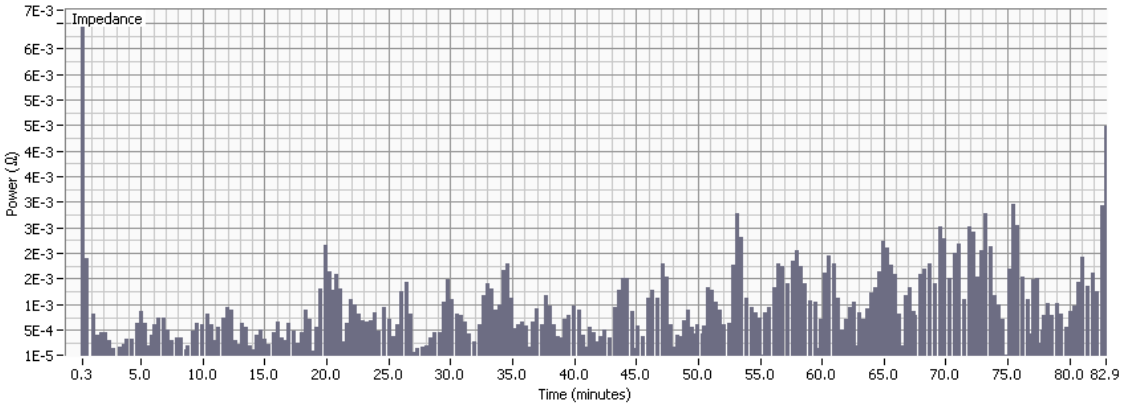

Mean velocity	0.08	Mean angle	19.63	Mean power	9.44E-4
STDEV velocity	2.12	STDEV angle	52.07	STDEV power	7.53E-4
Min velocity	-7.27	Min angle	-89.53	Min power	1.40E-5
Max velocity	9.51	Max angle	89.48	Max power	6.76E-3

Velocity is measured in cm/s, angle is measured in degrees and power is measured in ohms.

Respiratory analysis

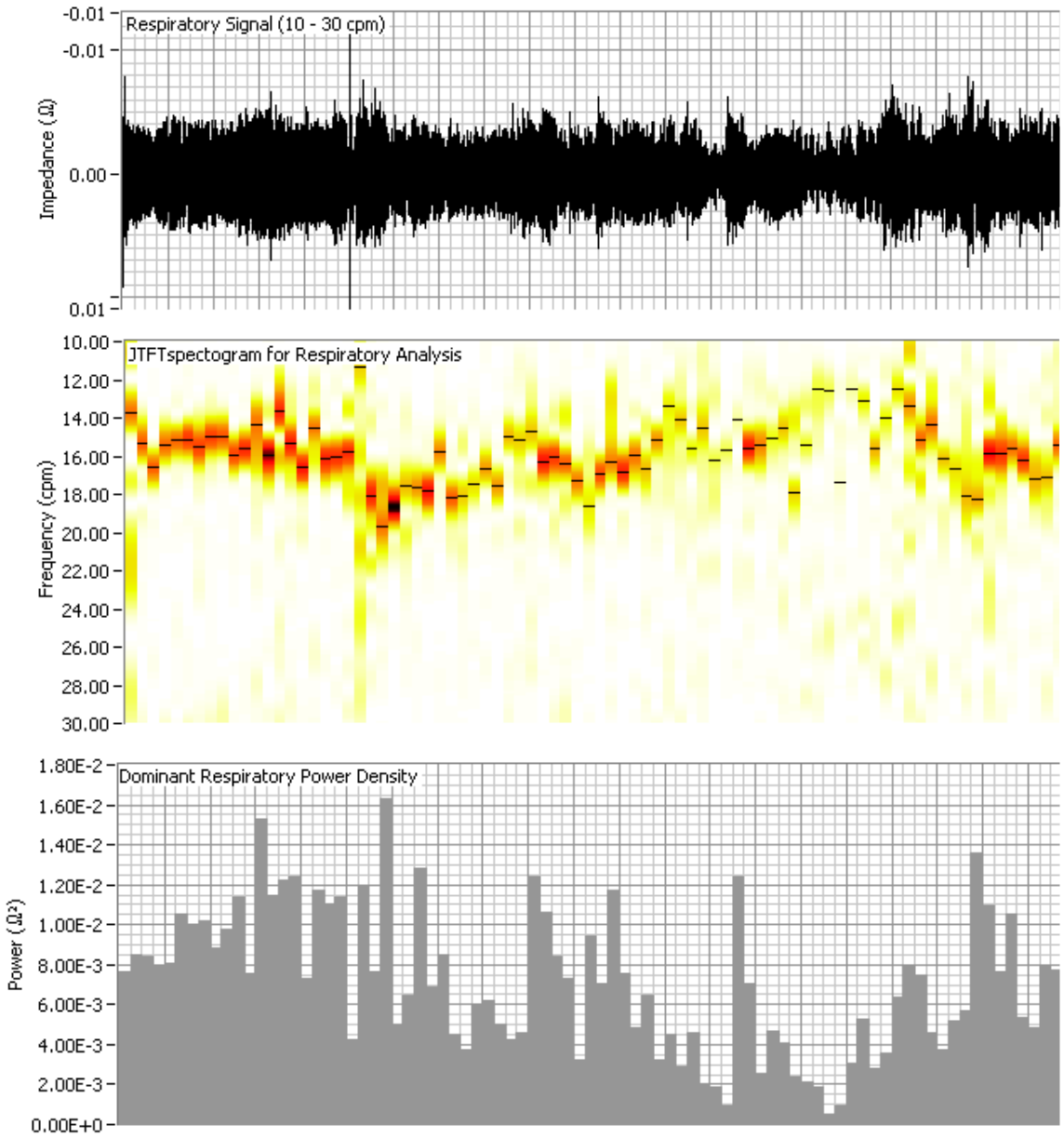

Appendix H Quality assurance and testing of ACCESS

Test signals

Sine wave (3cpm)

Measured pseudo frequency (DyWT): 2.85cpm

Measured frequency (JTFT 5min epochs): 3.00cpm

Measured frequency (JTFT 5min and 90% overlap epochs): 3.01cpm

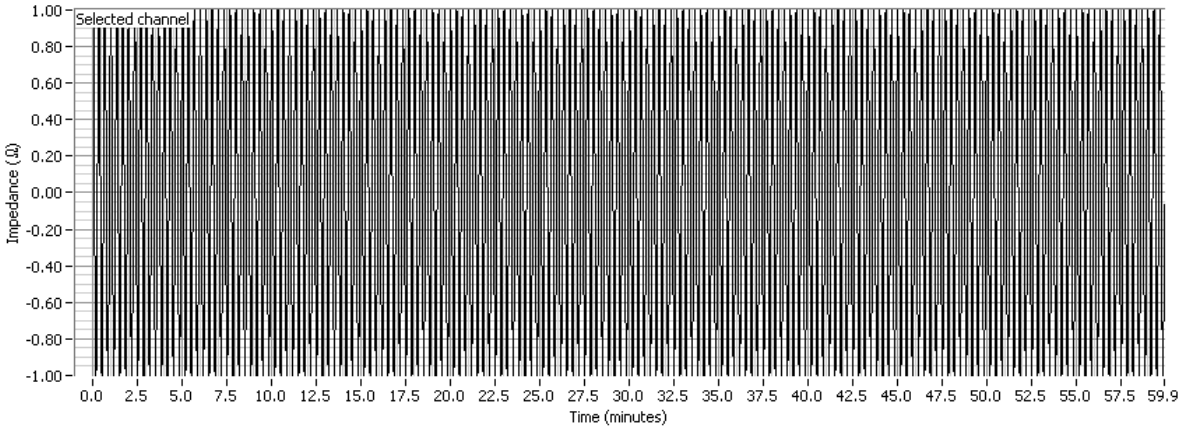

Fig. H1 Sine wave with frequency of 3 cycles per minute (cpm).

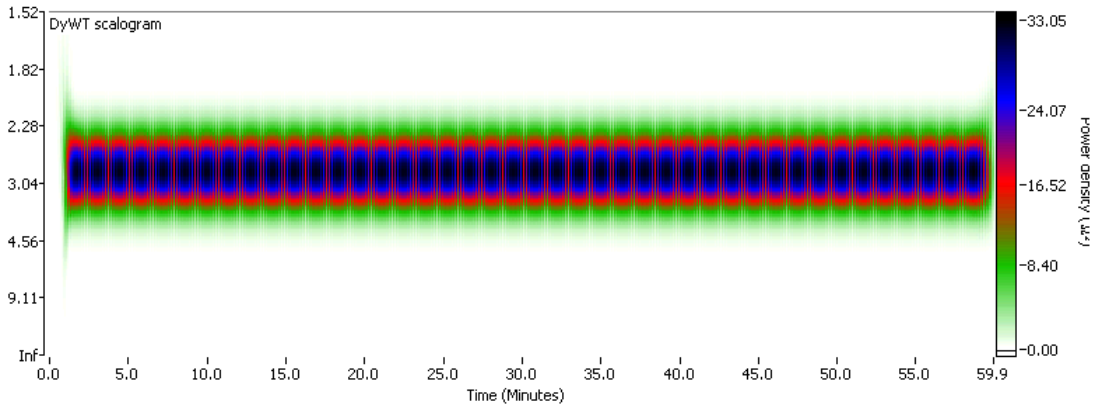

Fig. H2 DyWT scalogram of the sine wave showing the 3cpm frequency component.

Triangle wave (3cpm)

Measured pseudo frequency (DyWT): 2.85cpm

Measured frequency (JTFT 5min epochs): 3.00cpm

Measured frequency (JTFT 5min and 90% overlap epochs): 3.01cpm

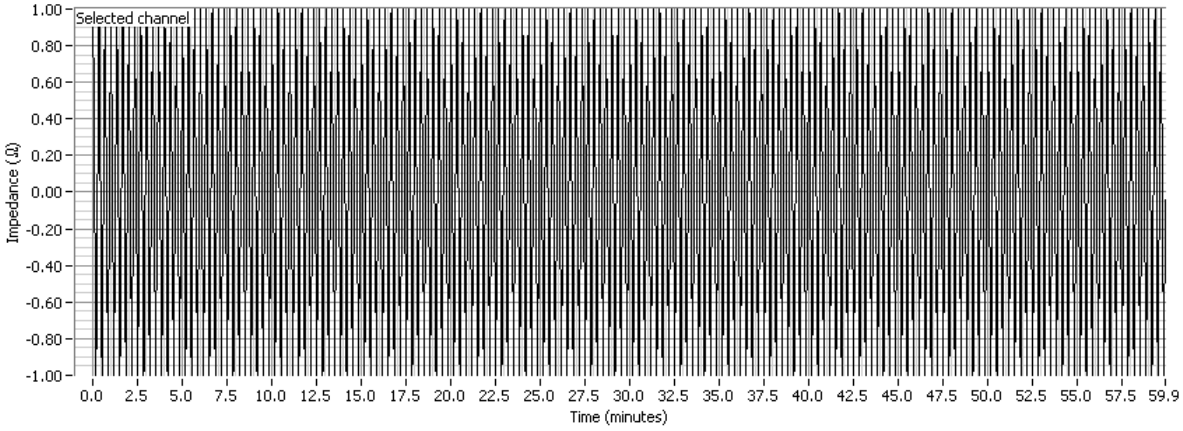

Fig. H3 Triangle wave with frequency of 3cpm.

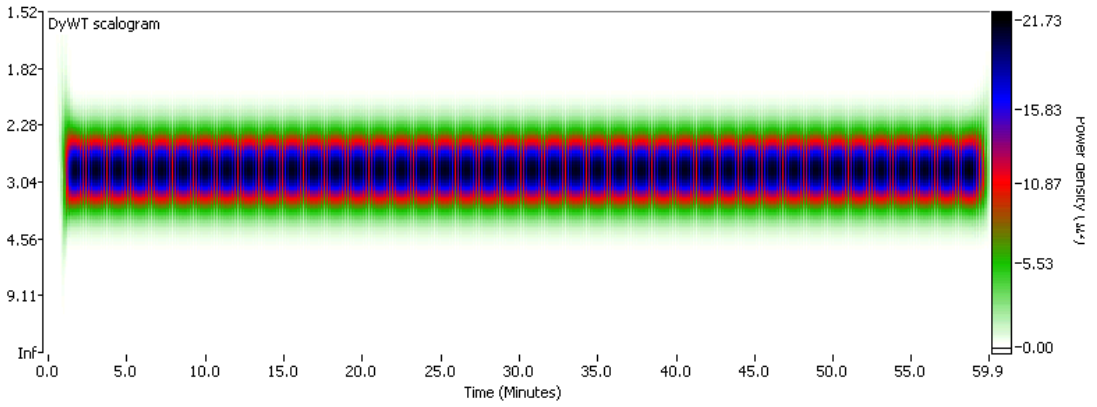

Fig. H4 DyWT scalogram of the triangle wave showing the 3cpm frequency component.

Square wave (3cpm)

Measured pseudo frequency (DyWT): 2.85cpm

Measured frequency (JTFT 5min epochs): 3.00cpm

Measured frequency (JTFT 5min and 90% overlap epochs): 3.01cpm

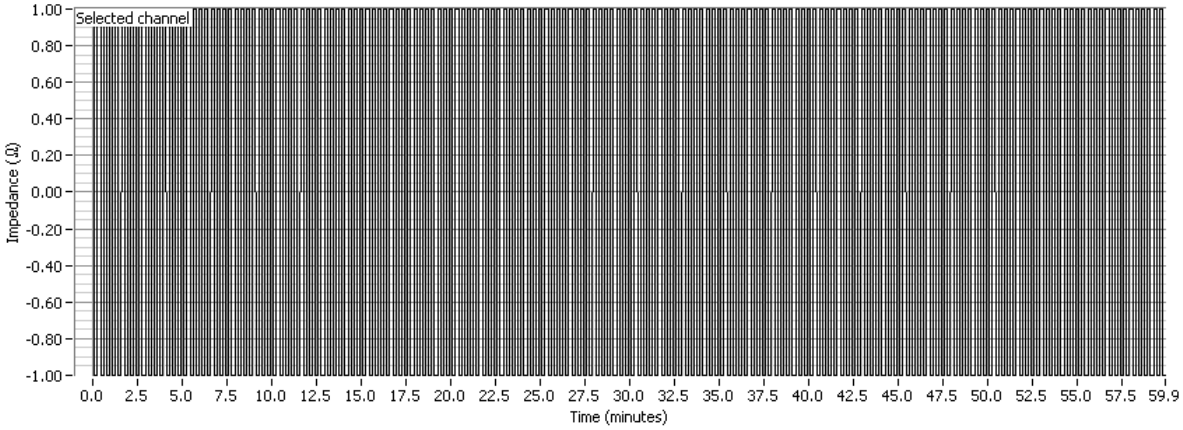

Fig. H5 Square wave with frequency of 3cpm.

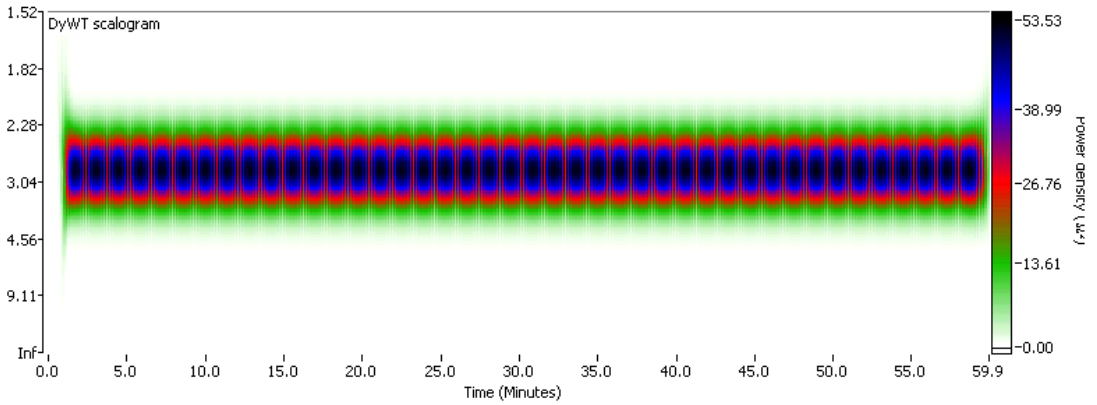

Fig. H6 DyWT scalogram of the square wave showing the 3cpm frequency component.

Sawtooth wave (3cpm)

Measured pseudo frequency (DyWT): 2.85cpm

Measured frequency (JTFT 5min epochs): 3.00cpm

Measured frequency (JTFT 5min and 90% overlap epochs): 3.01cpm

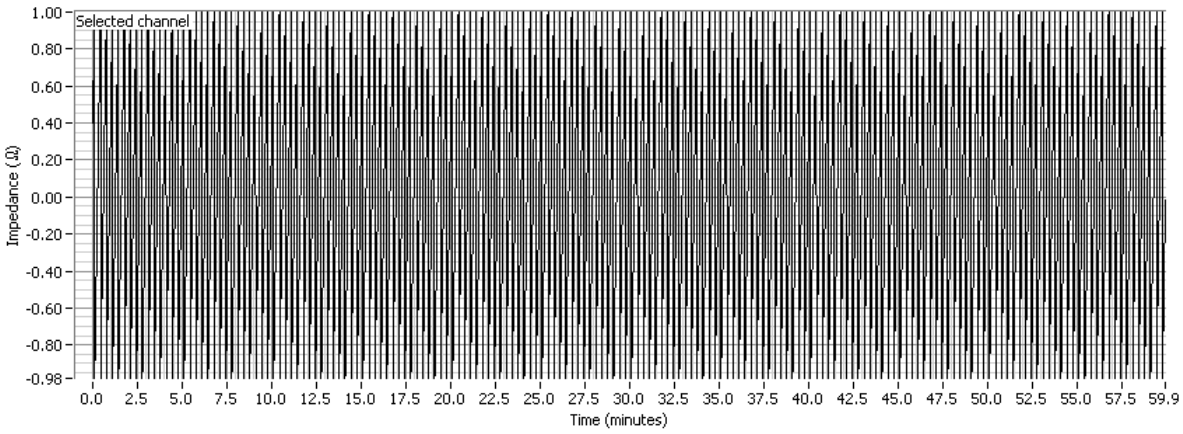

Fig. H7 Sawtooth wave with frequency of 3cpm.

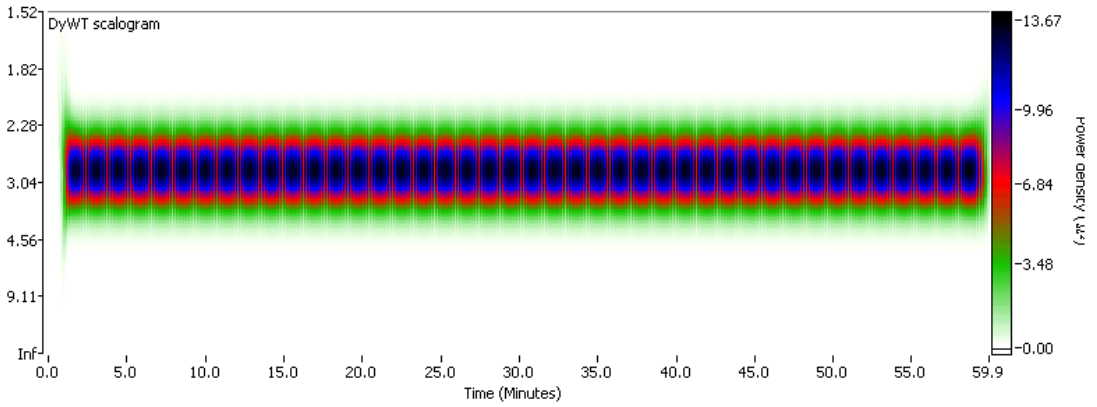

Fig. H8 DyWT scalogram of the sawtooth wave showing the 3cpm frequency component.

Chirp signal (1cpm to 5cpm)

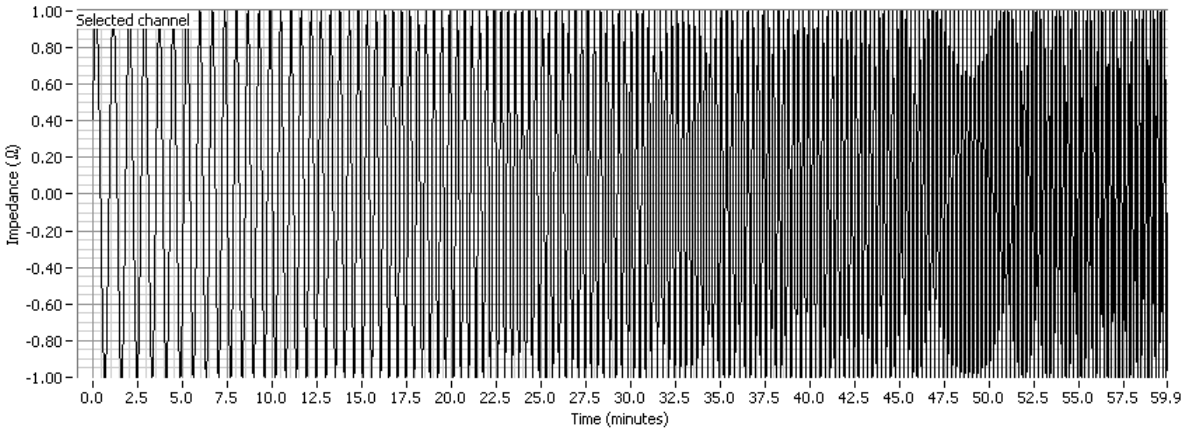

Fig. H9 Chirp with frequency range of 1cpm to 5cpm.

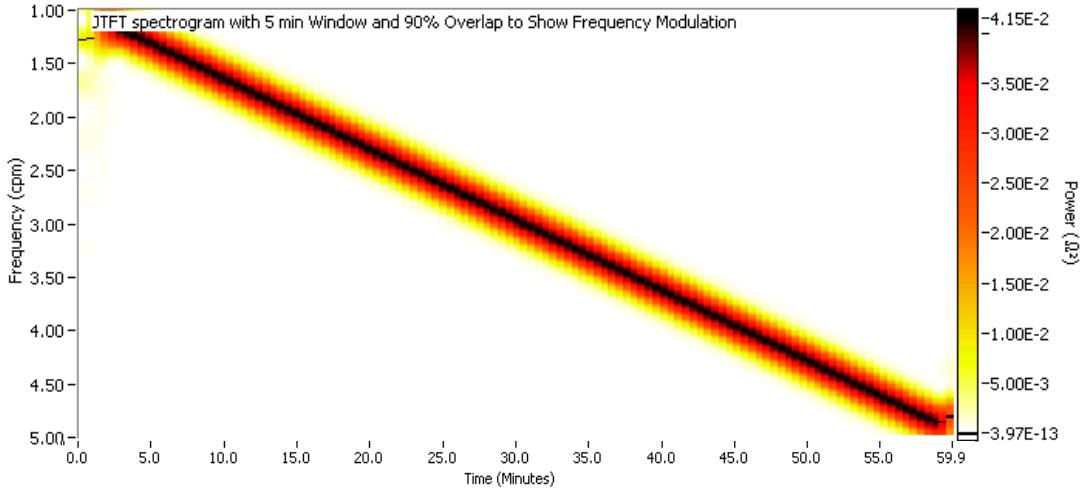

Fig. H10 JTFT of the chirp signal with frequency range of 1cpm to 5cpm.

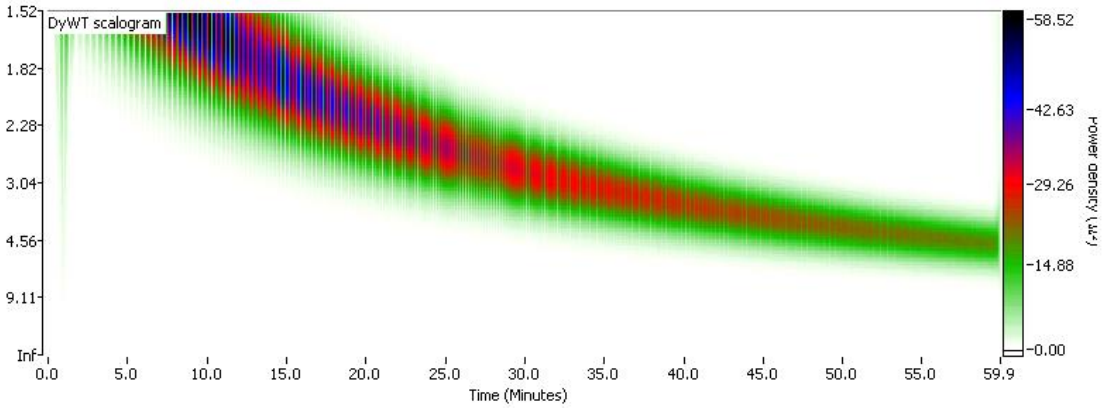

Fig. H11 DyWT scalogram of the chirp signal with frequency range of 1cpm to 5cpm.

Gaussian white noise

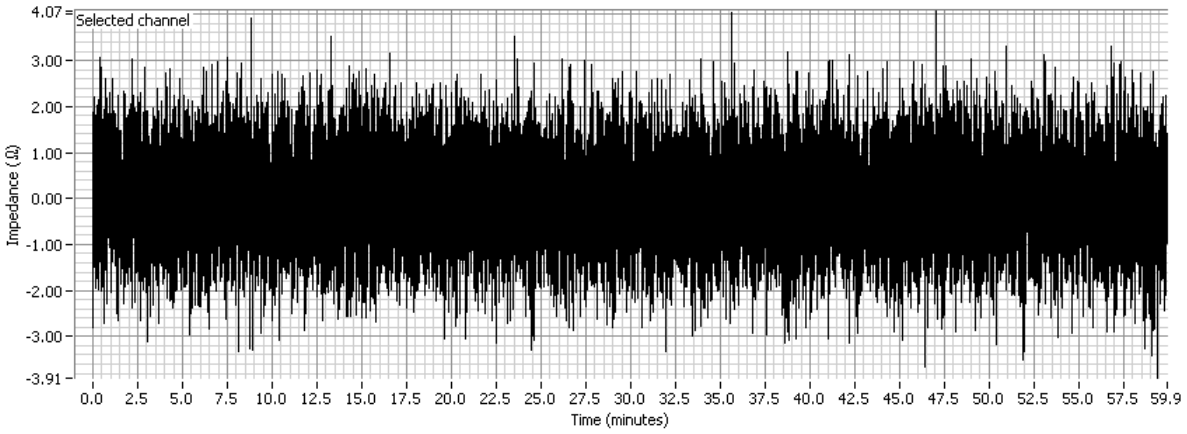

Fig. H12 Gaussian white noise.

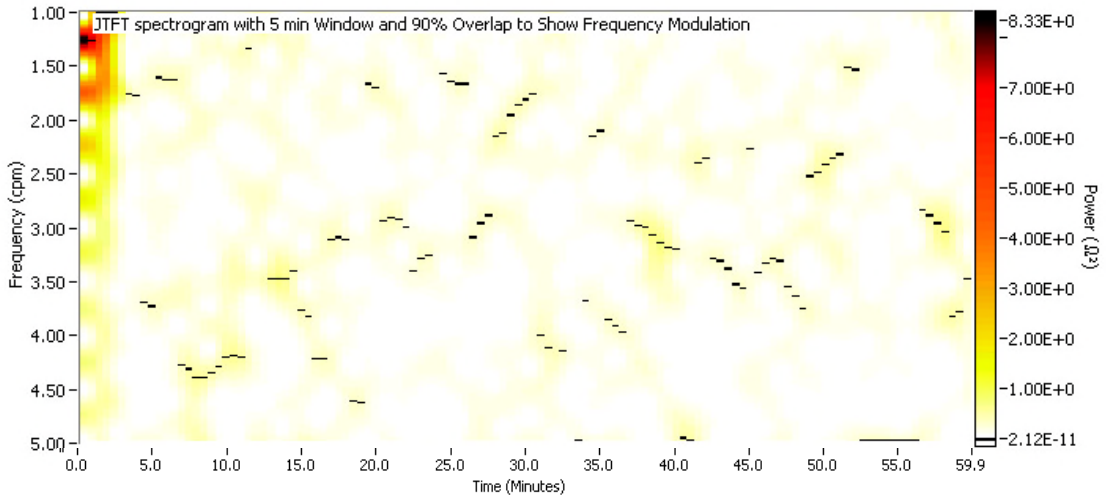

Fig. H13 JTFT of the Gaussian white noise.

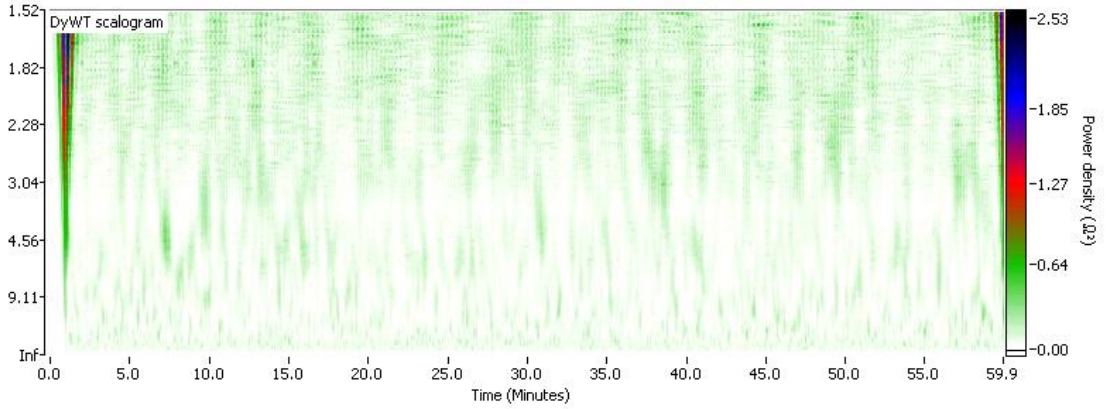

Fig. H14 DyWT scalogram of Gaussian white noise.

Uniform white noise

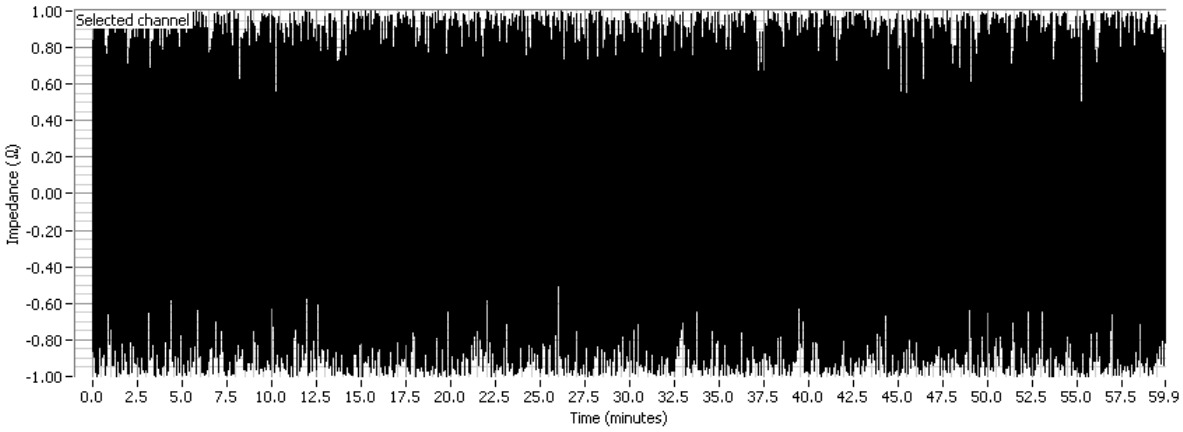

Fig. H15 Uniform white noise.

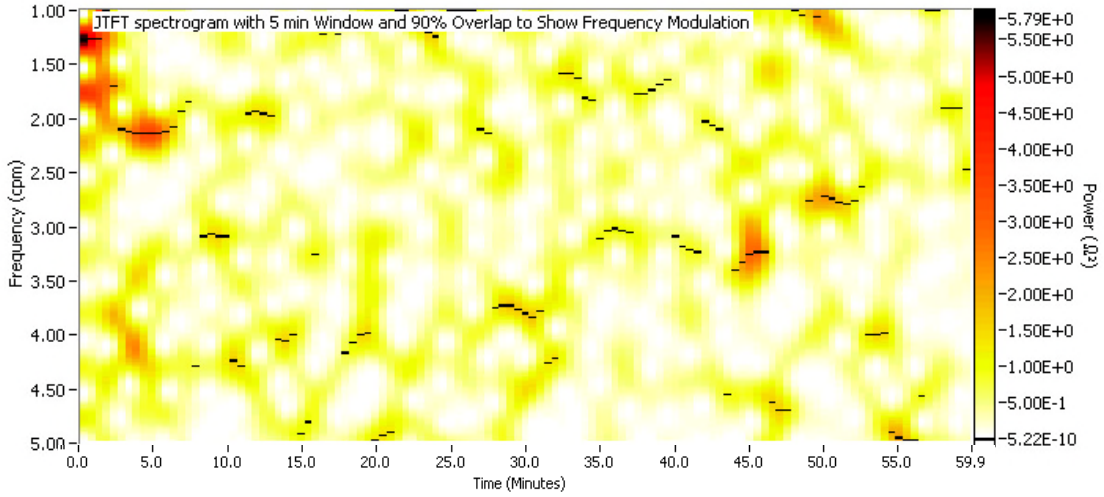

Fig. H16 JTFT of the uniform white noise.

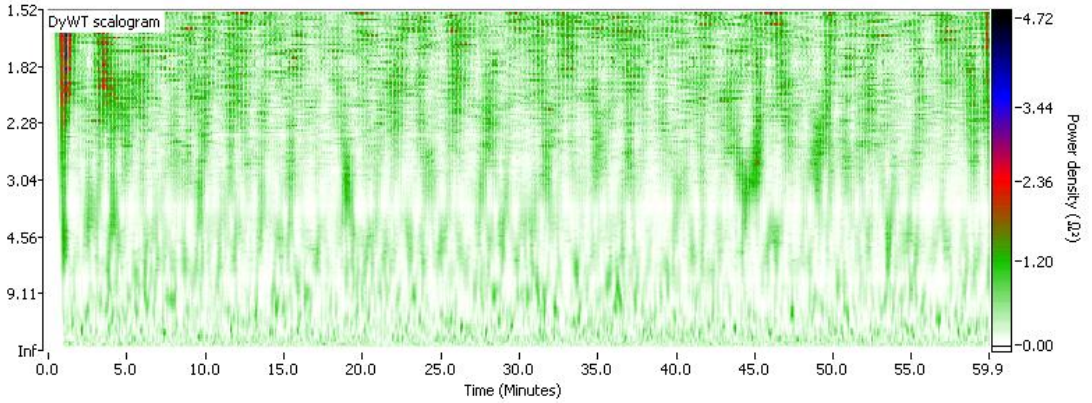

Fig. H17 DyWT scalogram of uniform white noise.

Pseudo-EIE signals

Exponential pseudo-EIE signal

Measured postprandial pseudo frequency (DyWT): 2.85cpm

Measured postprandial frequency (JTFT 5min epochs): 3.00cpm

Measured postprandial frequency (JTFT 5min and 90% overlap epochs): 2.99cpm

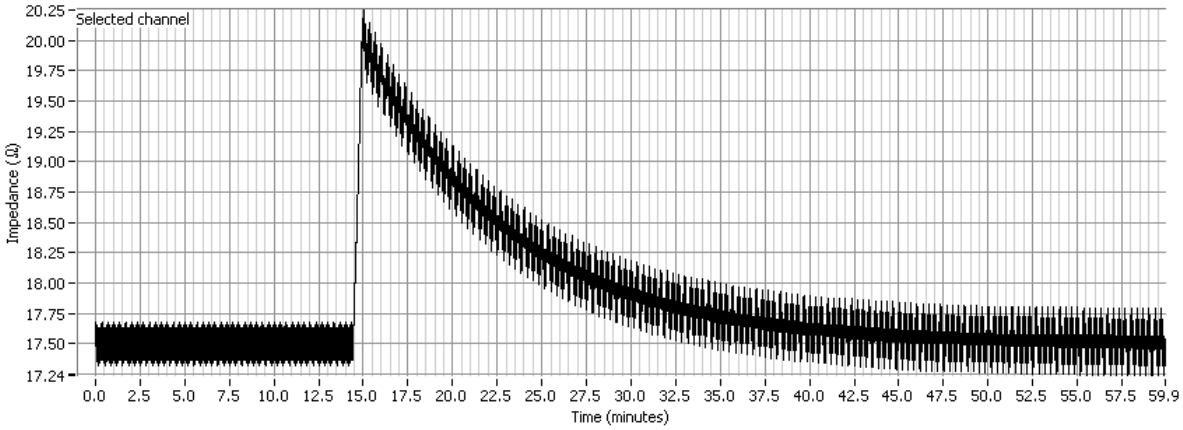

Fig. H18 Exponential pseudo-EIE signal.

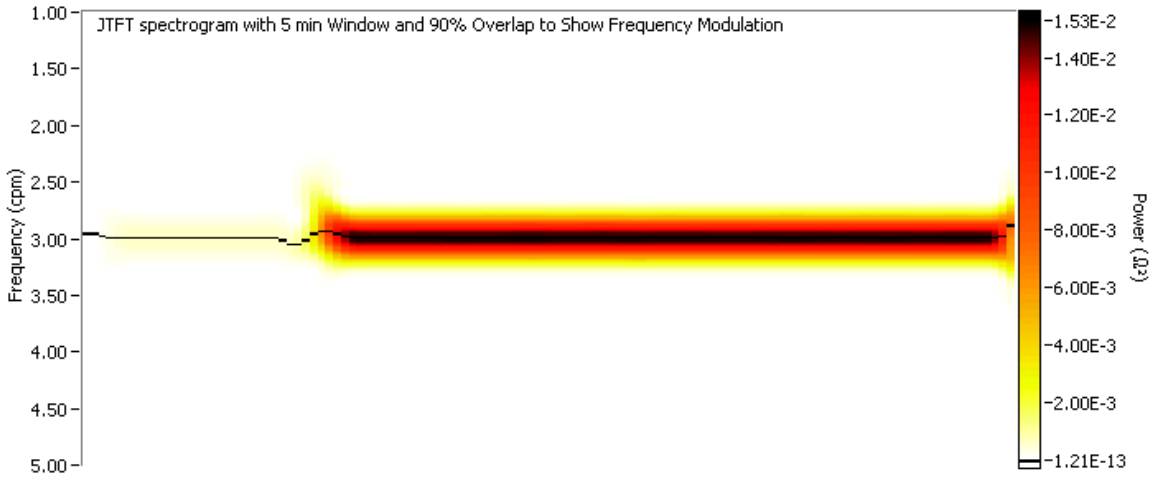

Fig. H19 JTFT of the exponential pseudo-EIE signal.

Table H1 T50 results using the 4th order polynomial of the exponential pseudo-EIE signal.

Method 1	Method 2	Method 3	Method 4	Method 5	Method 6	Method 7	Method 8	Method 9
6.67	6.66	6.67	6.67	5.96	5.91	5.92	5.95	0.15

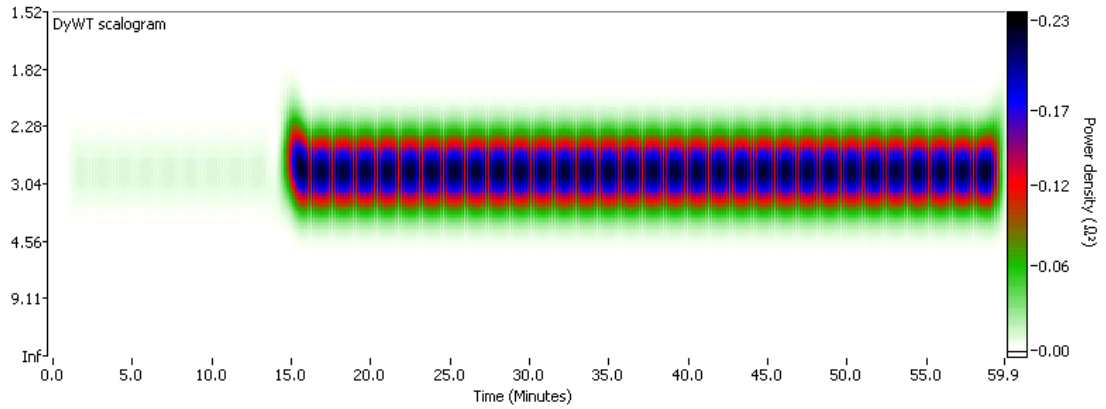

Fig. H20 DyWT scalogram of exponential pseudo-EIE signal.

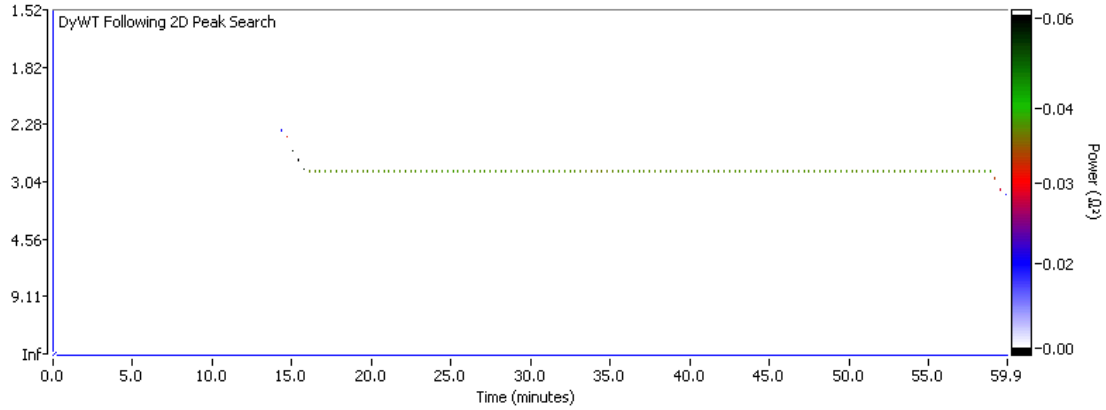

Fig. H21 DyWT scalogram of exponential pseudo-EIE signal after peak search.

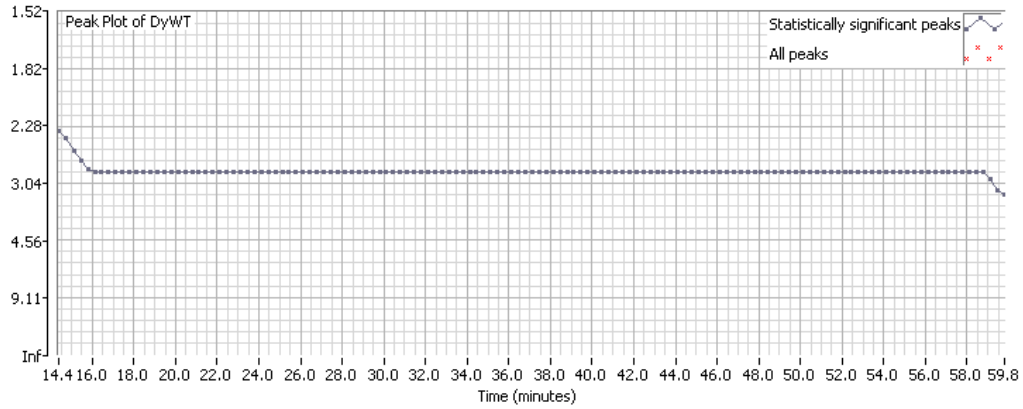

Fig. H22 Plot of statistically significant contractions. For pseudo-EIE signals, all *postprandial* contractions should be above the 10% mean threshold.

Linear pseudo-EIE signal

Measured postprandial pseudo frequency (DyWT): 2.85cpm

Measured postprandial frequency (JTFT 5min epochs): 3.00cpm

Measured postprandial frequency (JTFT 5min and 90% overlap epochs): 2.99cpm

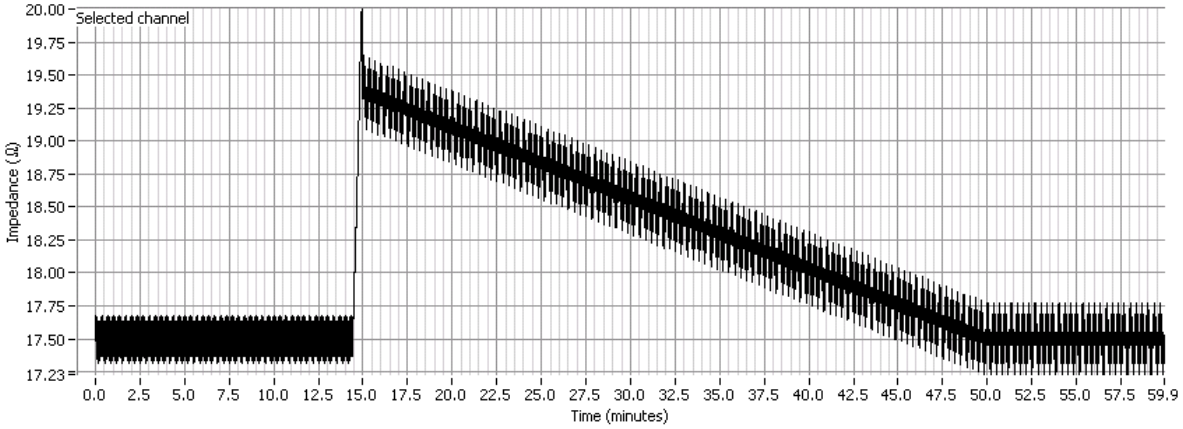

Fig. H22 Linear pseudo-EIE signal

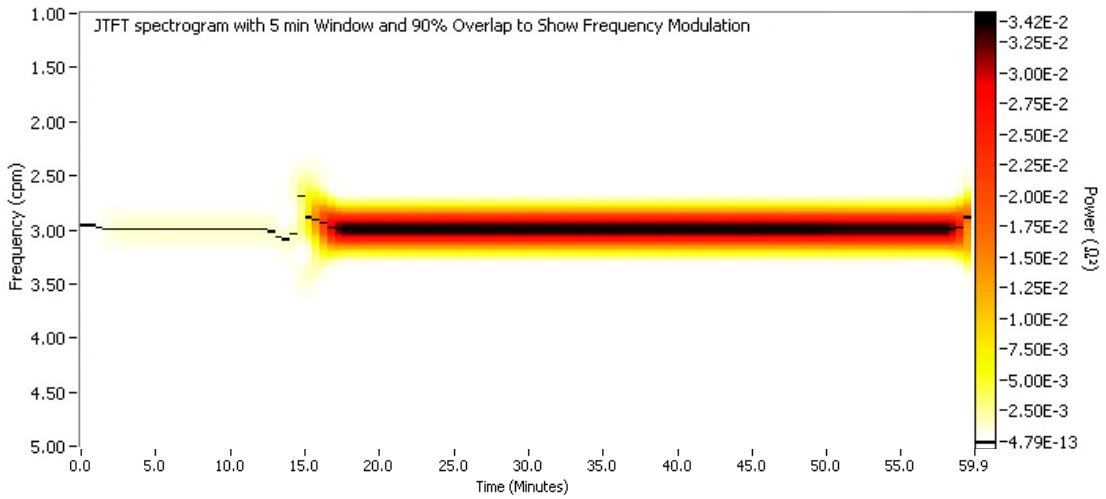

Fig. H23 JTFT of the linear pseudo-EIE signal

Table H2 T50 results using the 4th order polynomial for the linear emptying.

Method 1	Method 2	Method 3	Method 4	Method 5	Method 6	Method 7	Method 8	Method 9
15.98	16.21	16.19	15.96	9.01	9.23	9.17	8.99	33.37

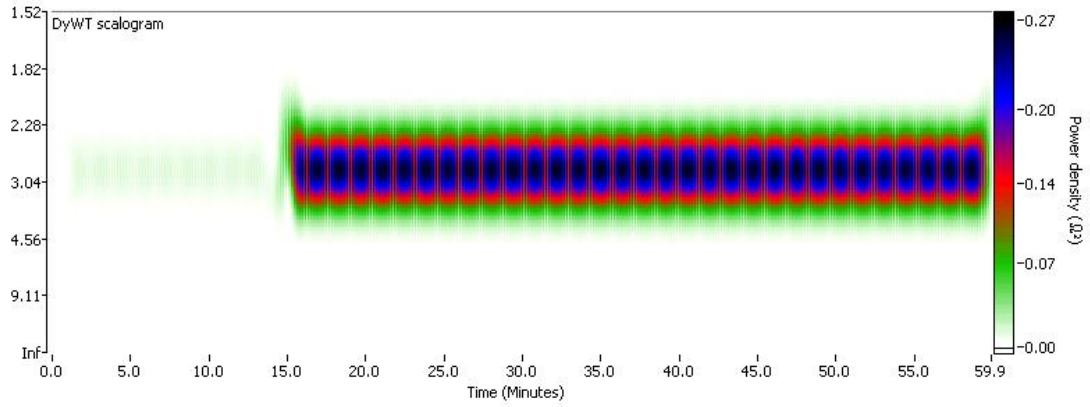

Fig. H24 DyWT scalogram of linear pseudo-EIE signal.

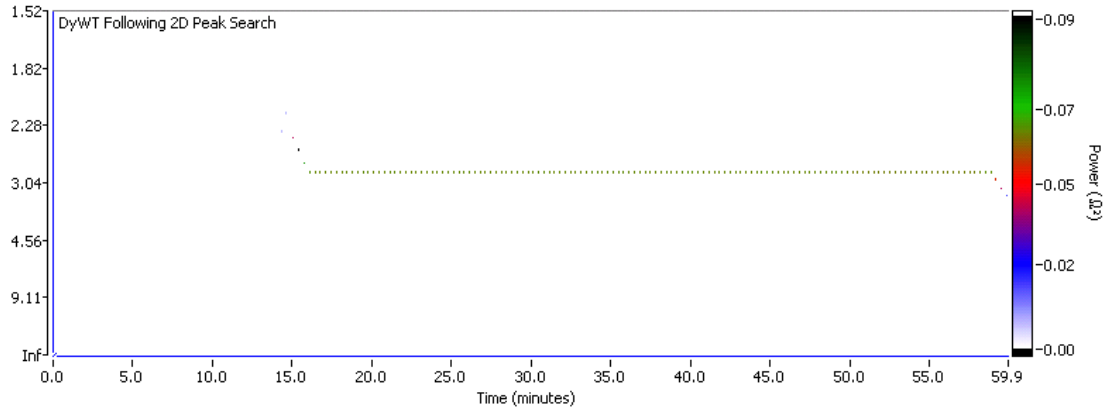

Fig. H25 DyWT scalogram of linear pseudo-EIE signal after peak search.

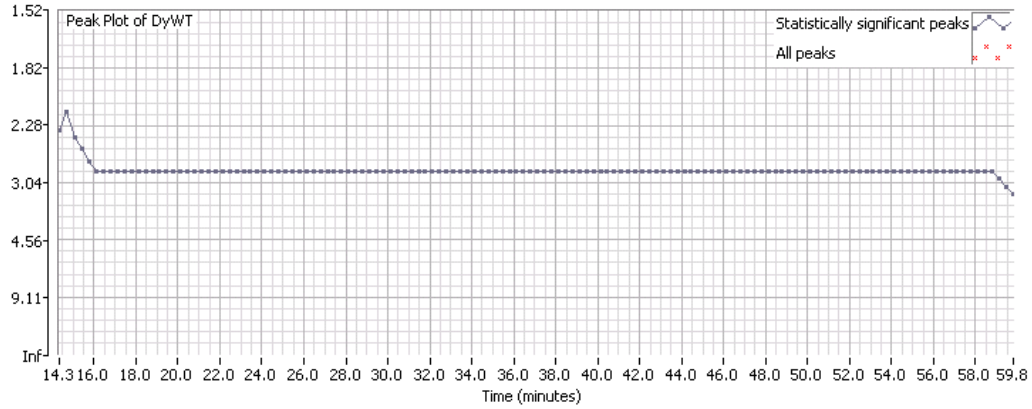

Fig. H26 Plot of statistically significant contractions. For pseudo-EIE signals, all *postprandial* contractions should be above the 10% mean threshold.

Non-linear pseudo-EIE signal

Measured postprandial pseudo frequency (DyWT): 2.85cpm

Measured postprandial frequency (JTFT 5min epochs): 3.00cpm

Measured postprandial frequency (JTFT 5min and 90% overlap epochs): 2.99cpm

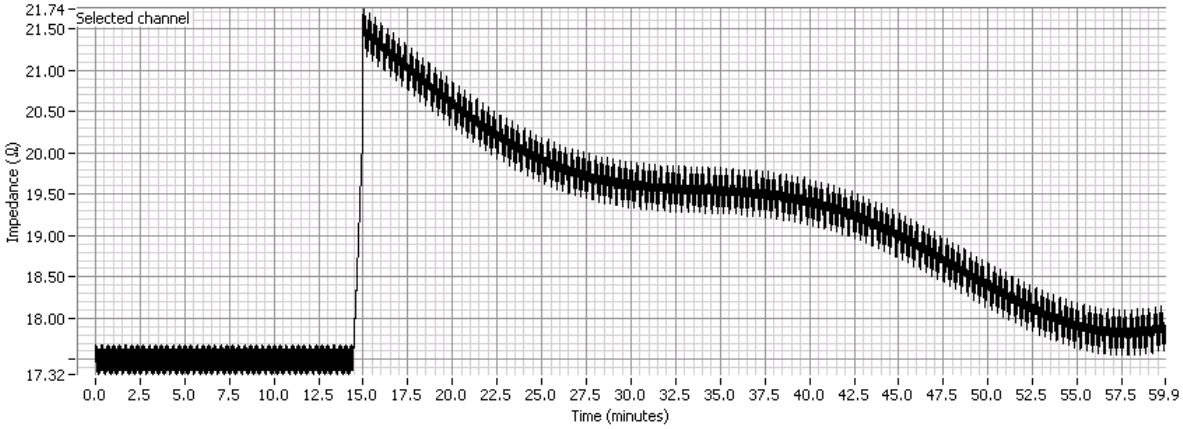

Fig. H27 Non-linear pseudo-EIE signal

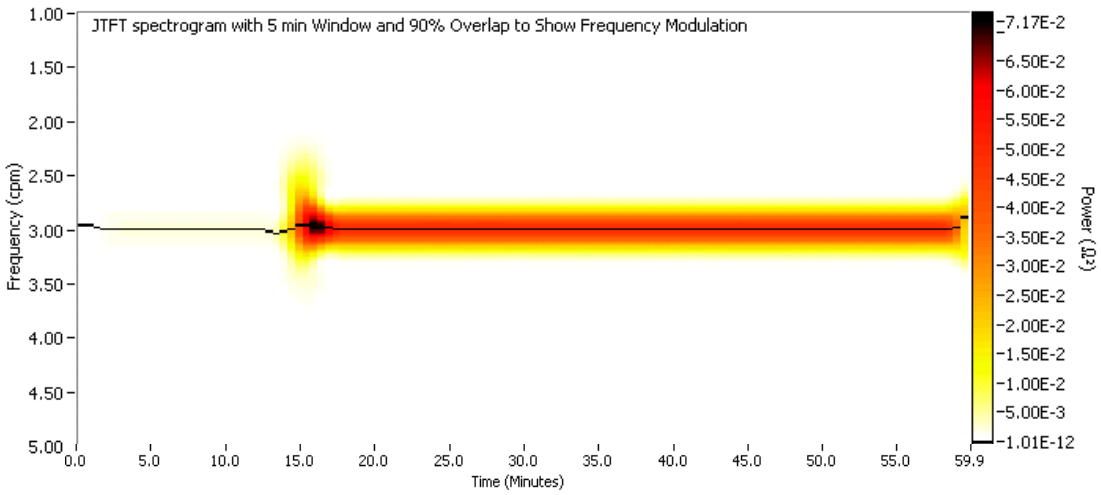

Fig. H28 JTFT of the non-linear pseudo-EIE signal

Table H3 T50 results using the 4th order polynomial for the non-linear emptying.

Method 1	Method 2	Method 3	Method 4	Method 5	Method 6	Method 7	Method 8	Method 9
22.71	24.02	24.28	22.70	13.80	14.22	14.35	13.79	26.35

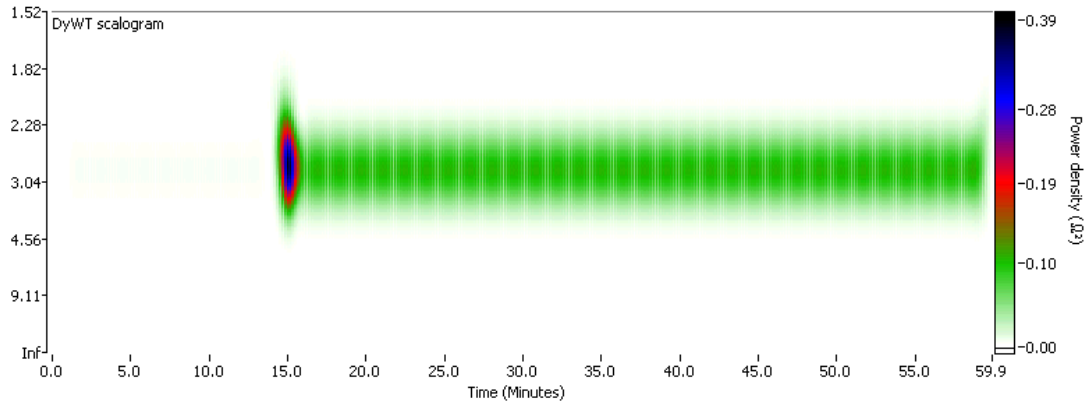

Fig. H29 DyWT scalogram of non-linear pseudo-EIE signal.

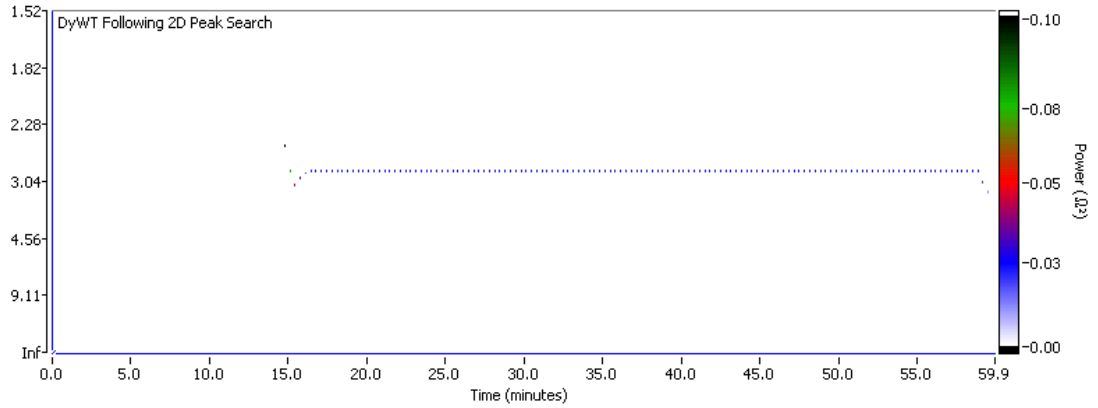

Fig. H30 DyWT scalogram of non-linear pseudo-EIE signal after peak search.

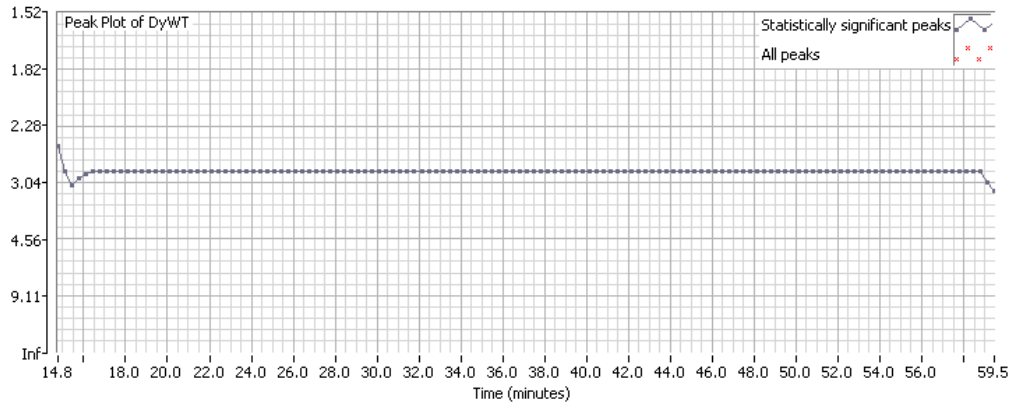

Fig. H31 Plot of statistically significant contractions. For pseudo-EIE signals, all *postprandial* contractions will be above the 10% mean threshold.

Exponential pseudo-EIE signal with motion artefact

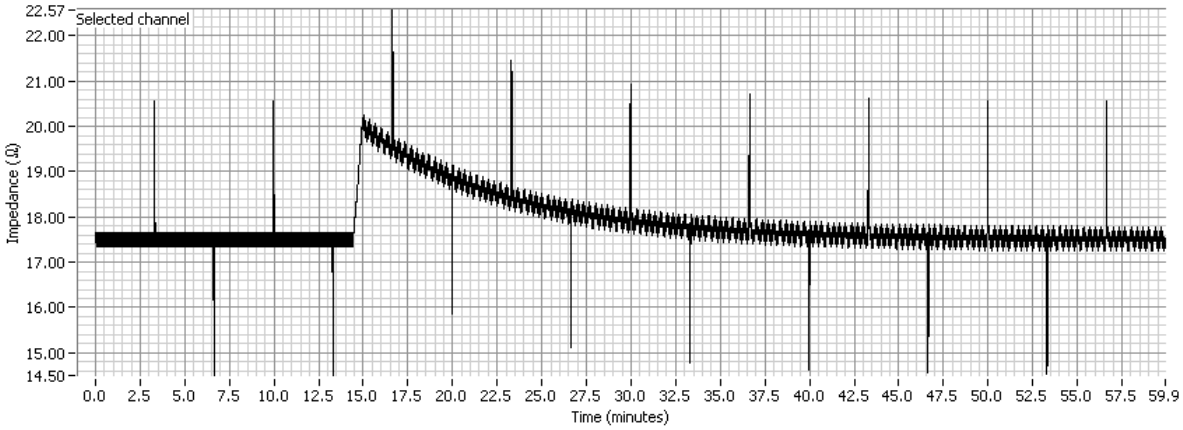

Fig. H32 Alpha pseudo-EIE signal with motion artefacts with amplitude of 3Ω at intervals of 1000 points (3.33 minutes).

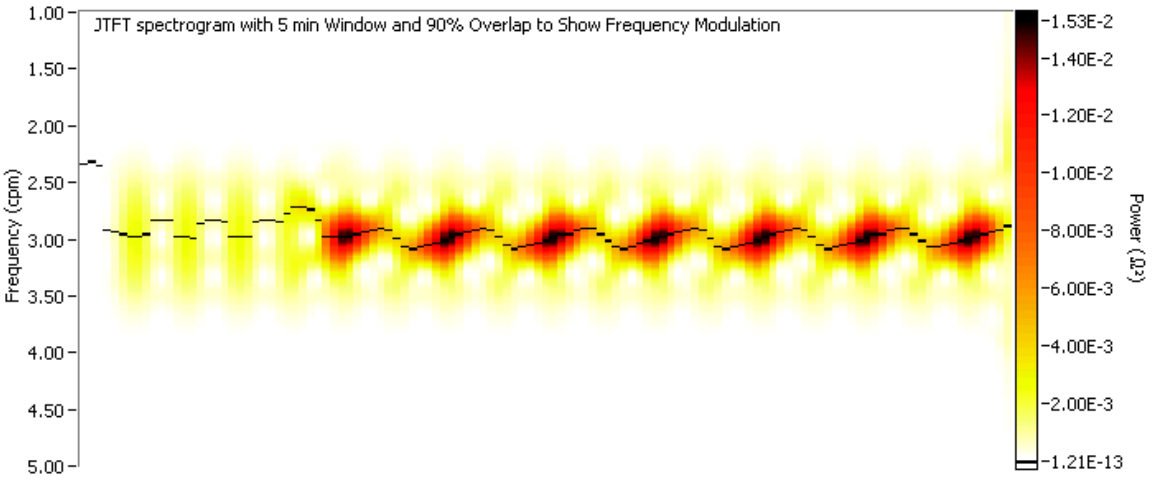

Fig. H33 JTFT of alpha pseudo-EIE signal with motion artefacts showing false positive level of contractile power due to the motion artifacts. The JTFT in Fig. H19 has a maximum power of 1.53×10^{-2}. The artifact has increased the maximum power by more than a factor of 10 (1.59×10^{-1}).

Table H3 T50 results using the 4th order polynomial for the exponential pseudo-EIE signal with motion artefacts. There is little change (±0.6 minutes) between these values and those in for a non-artifactual exponential pseudo-EIE signal in Table H1.

Method 1	Method 2	Method 3	Method 4	Method 5	Method 6	Method 7	Method 8	Method 9
7.73	13.96	10.46	7.74	5.48	11.14	9.60	5.49	Inf

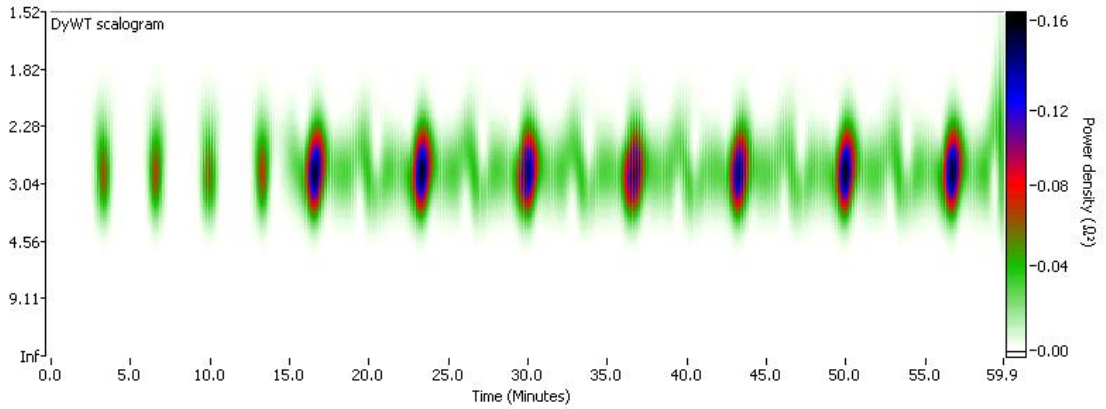

Fig. H34 DyWT of the exponential pseudo-EIE signal with motion artefacts showing the false positive detection of contractility caused by the spikes in the signal.

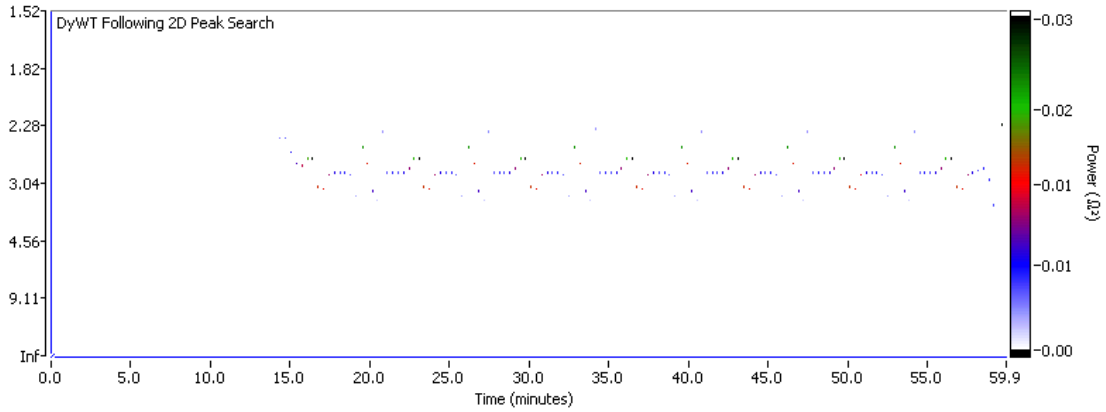

Fig. H35 DyWT scalogram of exponential pseudo-EIE signal with motion artefacts after peak search showing the frequency changes due to the motion artifacts.

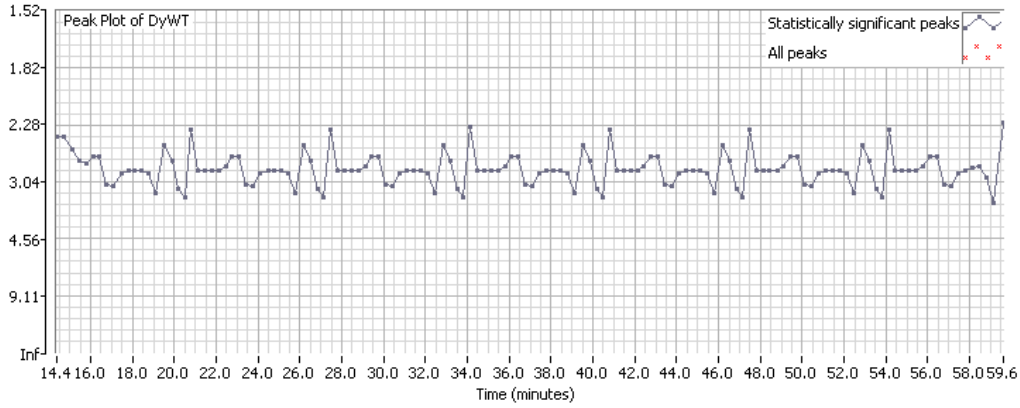

Fig. H36 Plot of statistically significant contractions for the exponential pseudo-EIE signal with motion artefacts after peak search showing the frequency changes due to the motion artifacts.

Exponential pseudo-EIE signal with motion artefact after the application of MARA

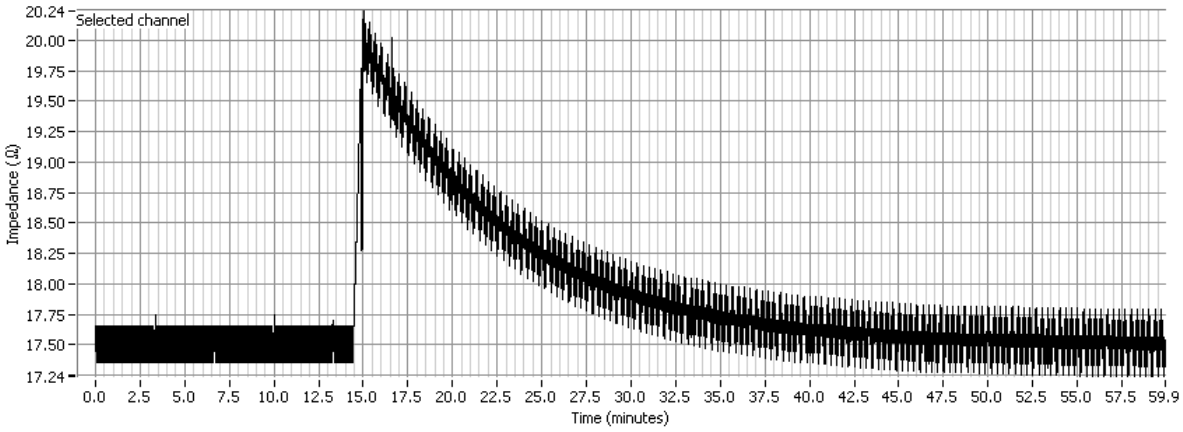

Fig. H37 Alpha pseudo-EIE signal with motion artefacts with amplitude of 3Ω at intervals of 1000 points (3.33 minutes) after the application of the Motion Artifact Rejection Algorithm with an epoch length of 500 data points, standard deviation multiple of 2.5, two iterations and zero offset.

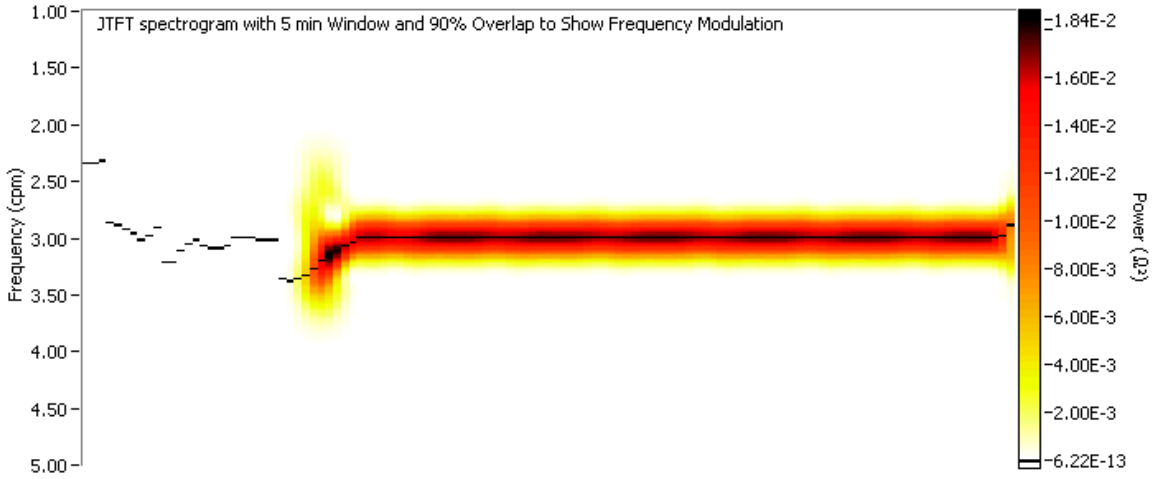

Fig. H38 JTFT of alpha pseudo-EIE signal with motion artefacts showing false positive level of contractile power due to the motion artifacts. The JTFT in Fig. H19 has a maximum power of 1.53×10^{-2} and the artifact increased the maximum power by more than a factor of 10 (1.59×10^{-1}) in Fig. H33. MARA has reduced the effect of the artifact so that there is only a 3.3% increase in the maximum power (1.58×10^{-2}).

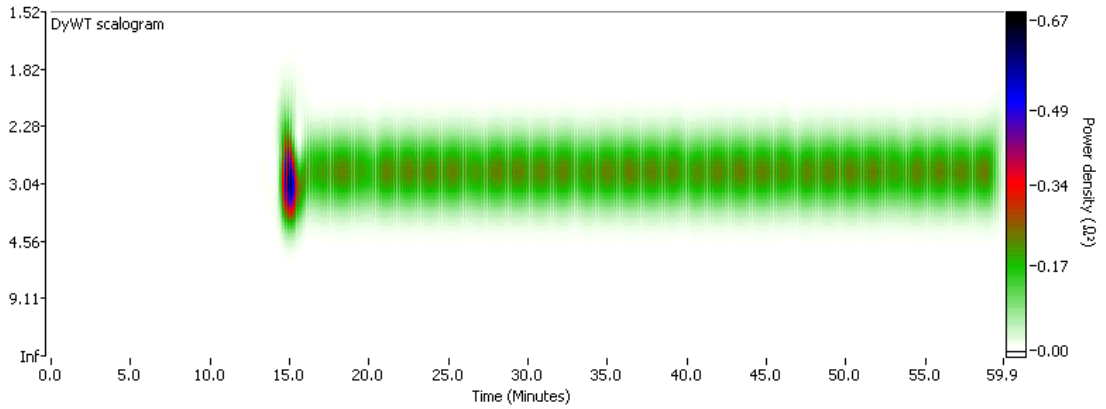

Fig. H39 DyWT of the exponential pseudo-EIE signal with motion artefacts after the application of MARA.

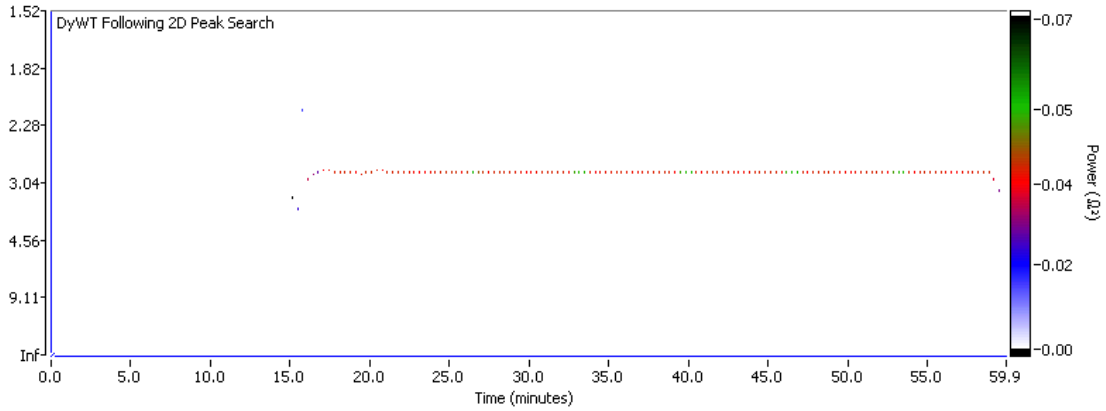

Fig. H40 DyWT scalogram of exponential pseudo-EIE signal with motion artefacts after peak search following the application of MARA. The frequency changes due to the motion artifacts have been eliminated.

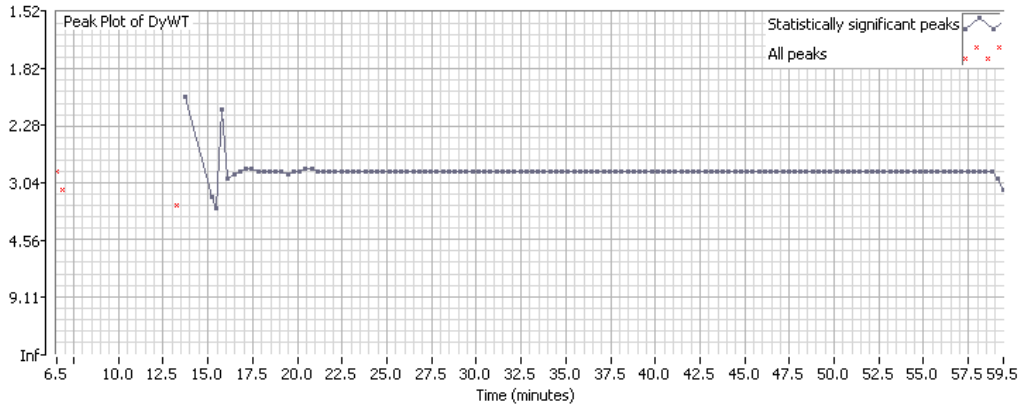

Fig. H41 Plot of statistically significant contractions for the exponential pseudo-EIE signal with motion artefacts after peak search following the application of MARA showing the elimination of frequency changes due to the motion artifacts.

Exponential pseudo-EIE signal with uniform white noise

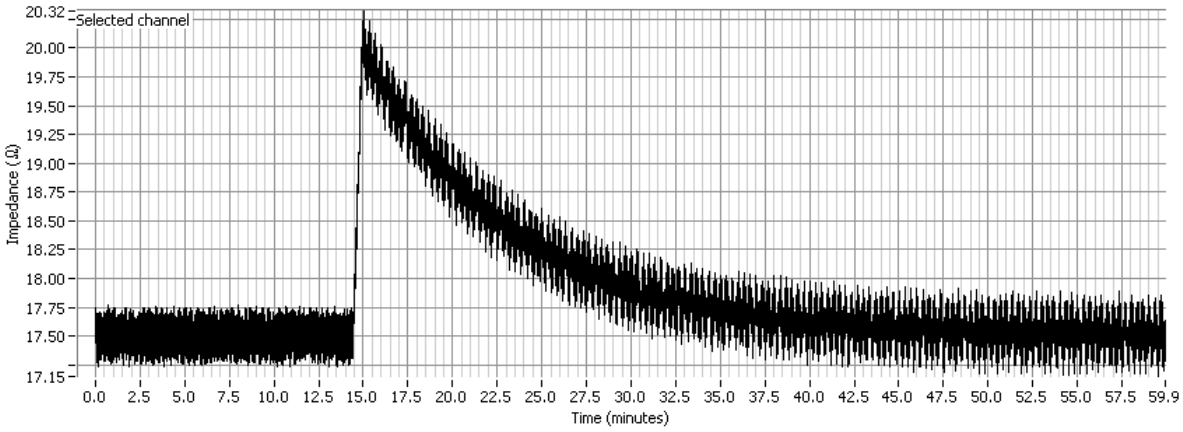

Fig. H42 Exponential pseudo-EIE signal with the addition of uniform white noise.

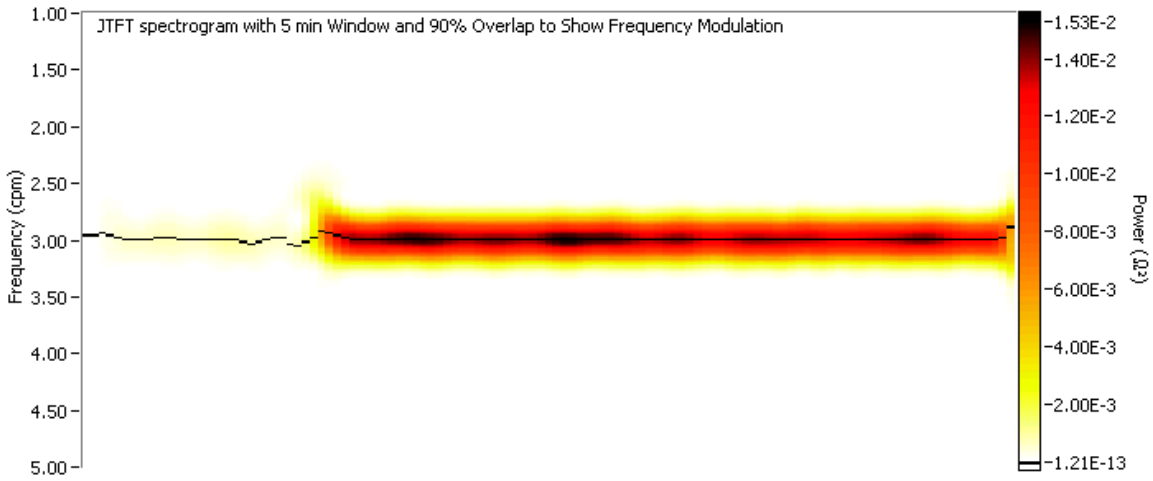

Fig. H43 JTFT of alpha pseudo-EIE signal with uniform white noise showing the false positive contractions due to the noise. The JTFT in Fig. H19 has a maximum power of 1.53×10^{-2}. The noise has increased the maximum power by under a factor of 2.5 (3.68×10^{-1}).

Table H4 T50 results using the 4th order polynomial for the exponential pseudo-EIE signal with uniform white noise. There is little change (±0.5 minutes) between these values and those in for a non-artifactual exponential pseudo-EIE signal in Table H1.

Method 1	Method 2	Method 3	Method 4	Method 5	Method 6	Method 7	Method 8	Method 9
7.71	14.00	10.47	7.70	5.47	11.18	9.65	5.46	Inf

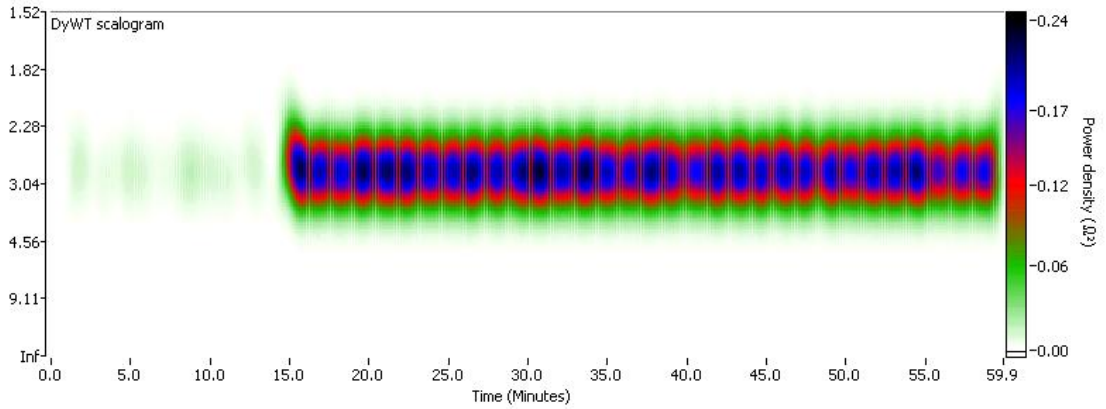

Fig. H44 DyWT of the exponential pseudo-EIE signal with white noise.

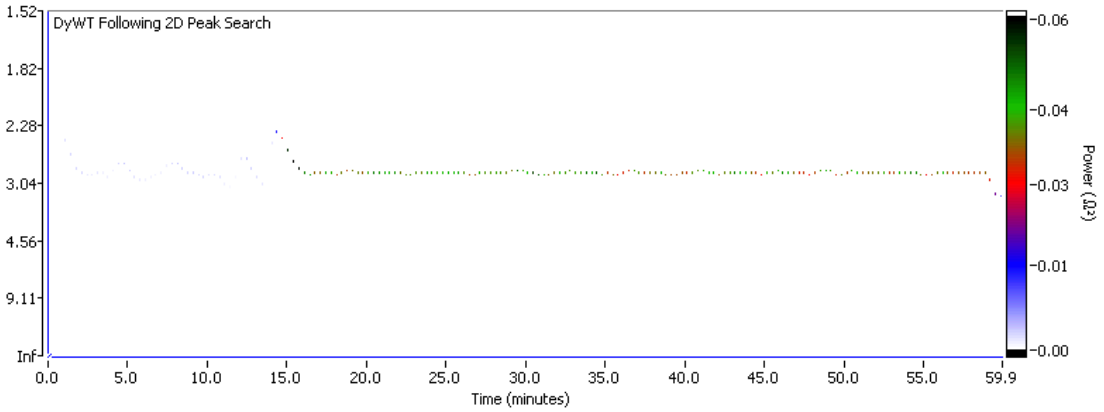

Fig. H45 DyWT scalogram of exponential pseudo-EIE signal with white noise after peak search showing the frequency changes due to the noise.

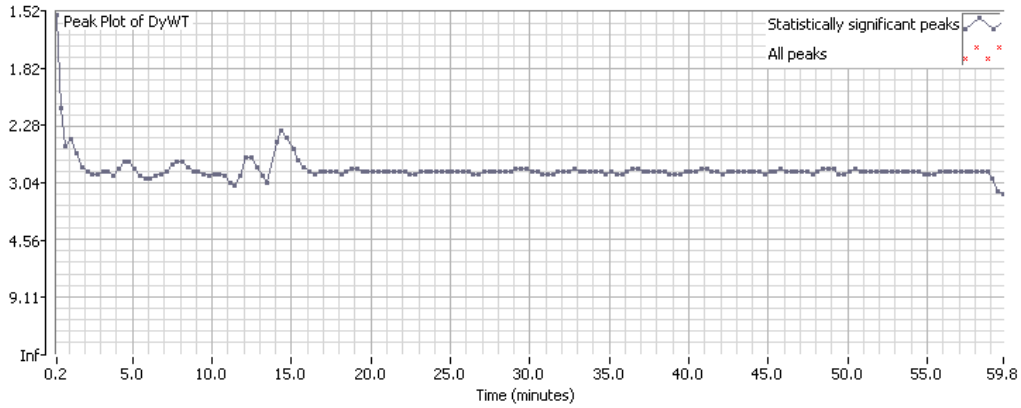

Fig. H46 Plot of statistically significant contractions for the exponential pseudo-EIE signal with white noise after peak search showing the frequency changes due to the noise.

Determination of a fixed power threshold

Figs. H43 to H46 demonstrate that since white noise is comprised of a uniform range of frequencies, when it affects the EIE signal, the power measured in the gastric frequency range increases, potentially causing false gastric contractions and an artifactual increase in the power of genuine gastric contractions. There are a number of sources of noise in EIE signals including the pulsatile motion of the aorta (which passes near to the stomach and the electrodes) and other electrical equipment.

The determination of a fixed power threshold to remove the effects of noise was carried out by adding varying amplitudes of white noise to a pseudo-EIE signal that had no 3cpm (gastric frequency range) signal during the preprandial period and a constant 3cpm signal in the postprandial period. While no contractions were detected during the preprandial period of the original EIE signal, with addition of 0.05Ω of white noise, false contractions appeared in the preprandial period (Fig. H47).

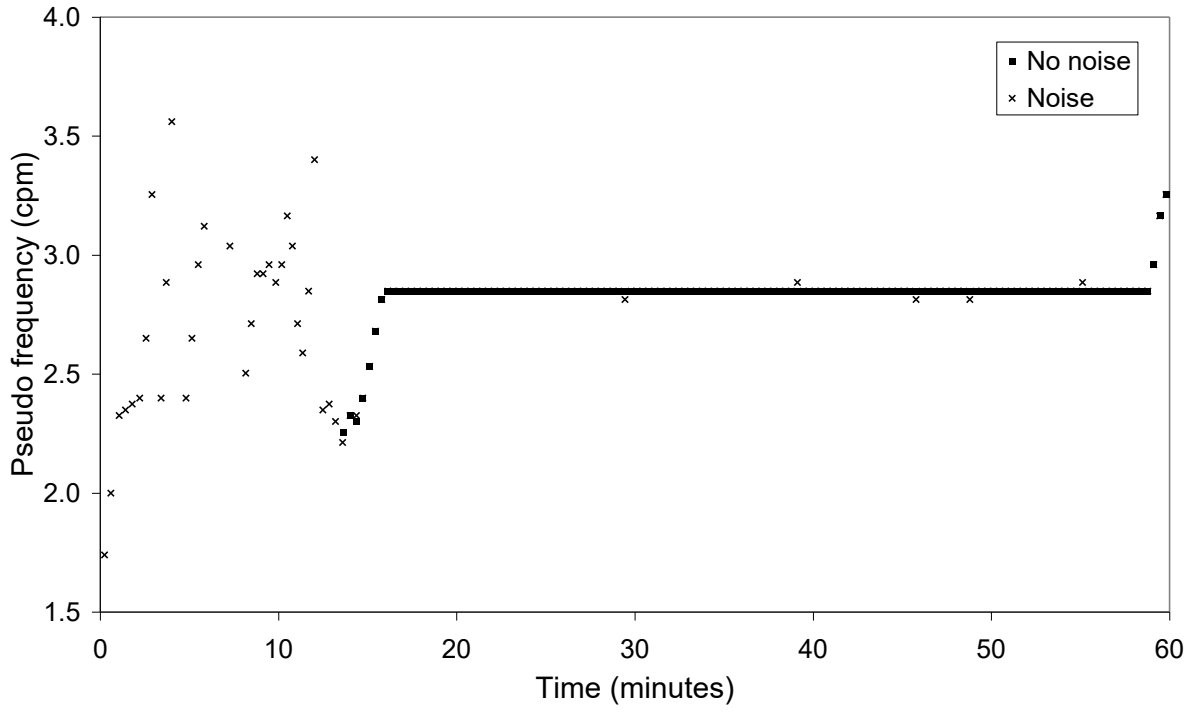

Fig. H47 Contractions measured with pseudo-EIE signal (▪) and in the same signal after the addition of 0.05Ω of white noise (×).

A fixed threshold was proposed to remove the effect of the noise by applying rejecting low power contractions calculated from the DyWT. Two thresholds were tested by adding varying amplitudes of white noise to a pseudo-EIE signal, applying the threshold and comparing the number of artifactual signals. The preprandial period of the pseudo-EIE signal did not contain any 3cpm components and so any preprandial contractions detected were deemed to be false.

Fig. H48 shows the number of false contractions for varying levels of noise and levels of threshold. Noise of 0.30Ω was considered to be higher than any natural noise experienced during EIE experiments. Table H5 indicates that the 10% mean power threshold is effective at removing the majority of the noise, but that the 5% mean power threshold is acceptable for the lower amplitude noise.

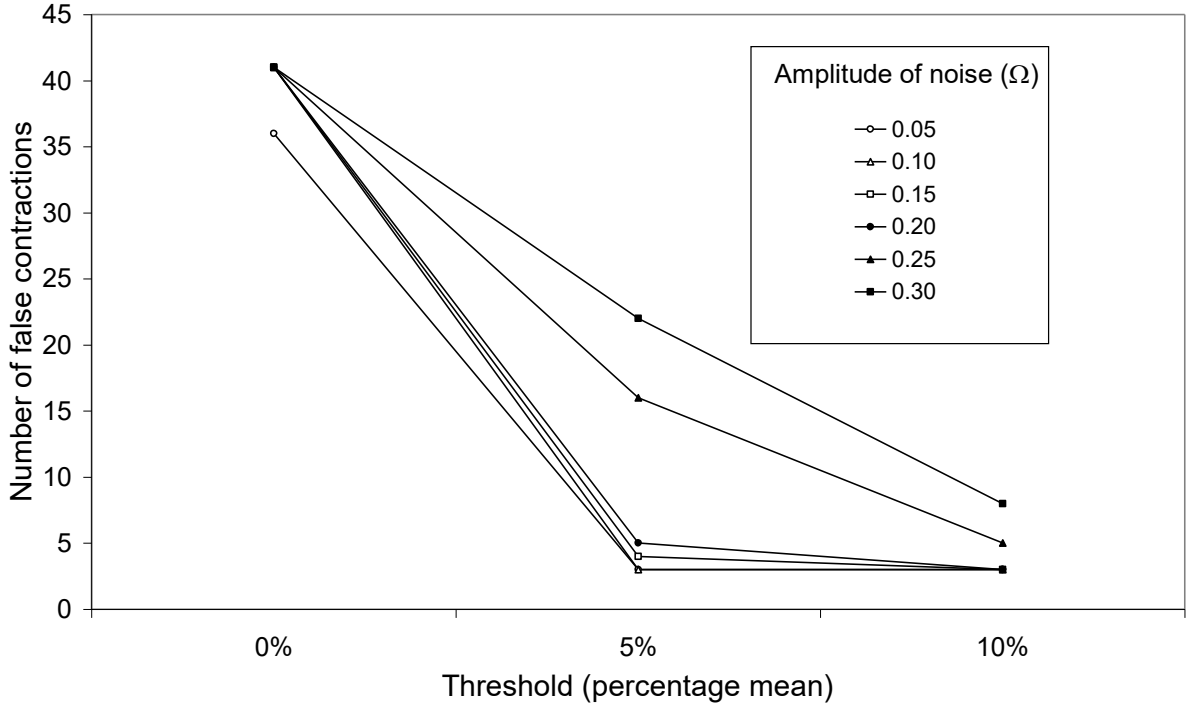

Fig. H48 The number of false contractions detected after the addition of different amplitudes of white noise to an exponential pseudo-EIE signal for (a) no threshold, (b) 5% mean power threshold and (c) 10% power mean threshold.

Table H5 Percentage of false contractions eliminated by the 5% and 10% mean thresholds after the addition of different amplitudes of white noise to an exponential pseudo-EIE signal.

Amplitude of noise (Ω)	Percentage reduction in false contractions	
	5% mean threshold	10% mean threshold
0.05	91.7 %	91.7 %
0.10	92.7 %	92.7 %
0.15	90.2 %	92.7 %
0.20	87.8 %	92.7 %
0.25	61.0 %	87.8 %
0.30	46.3 %	80.5 %

Analysis of the percentage of false contractions remaining after the application of the two thresholds reveals that the while the 5% mean power threshold is successful at removing more than 80% of false contractions up to 0.20Ω amplitude noise, the efficacy of removing false contractions decreases with 0.25Ω and 0.30Ω. However, the 10% mean power threshold maintains its efficacy and removes more than 80% (Fig. H49).

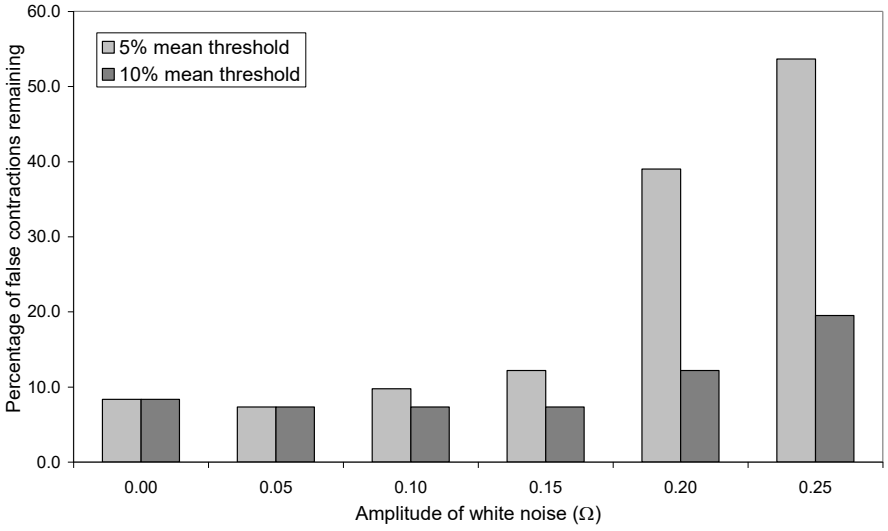

Fig. H49 Percentage false contractions remaining with increasing amplitudes of noise for the 5% mean and 10% mean thresholds.

Neither of the thresholds removed any genuine contractions and since the 10% mean power threshold remove more than 80% of false contractions created by white noise with amplitude of 0.30Ω, it was unnecessary to adopt a higher threshold which in addition may have removed genuine contractions. Therefore, these results indicate that the use of a fixed 10% mean power threshold is acceptable and efficient in removing the majority of false contractions caused by white noise.

Emptying curves

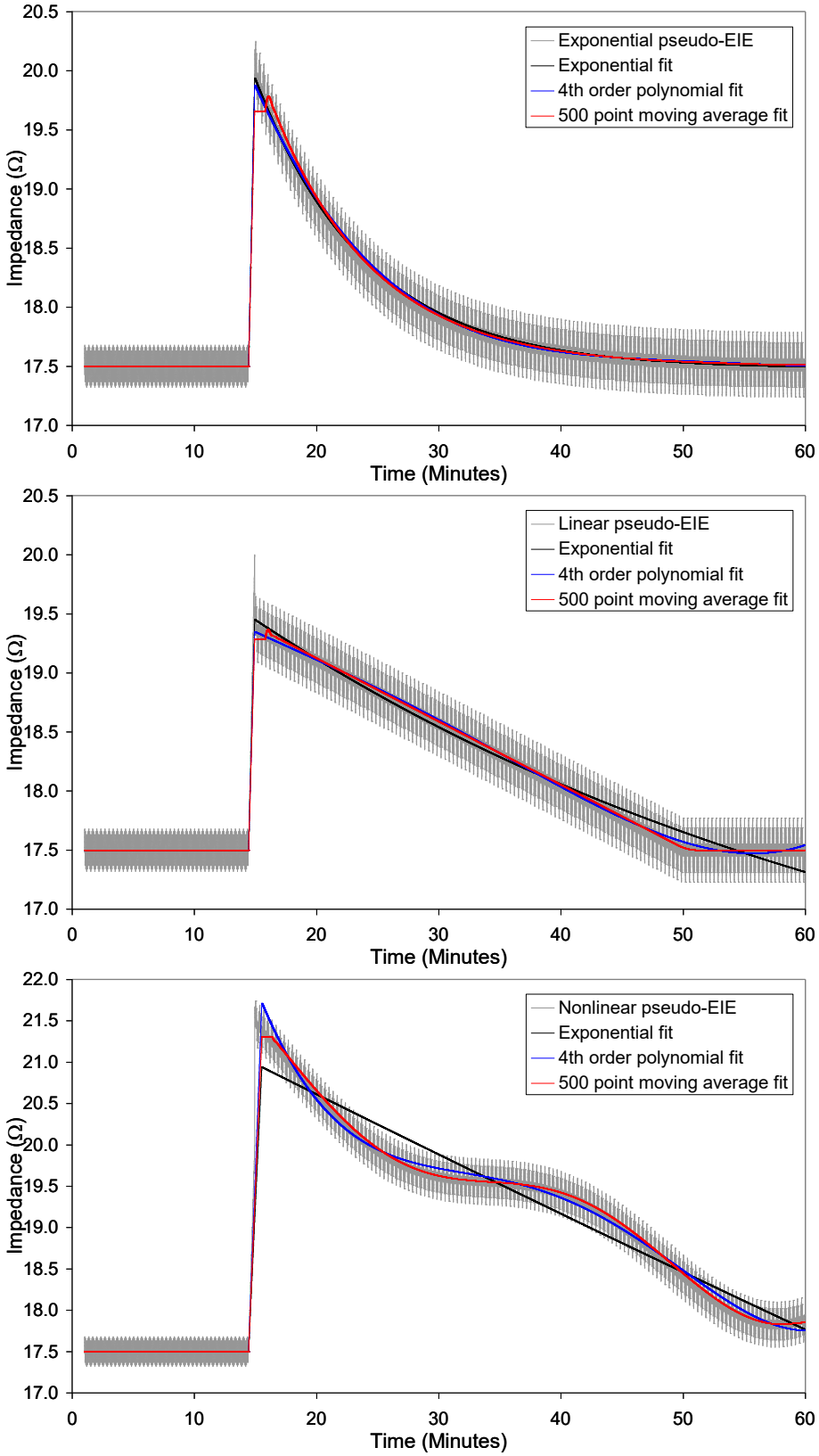

Fig. H50 Emptying curves of exponential, linear and non-linear pseudo-EIE signals. The R^2 values are given in Table H6 on the next page.

Table H6 R^2 values for the polynomial, exponential and 500-point moving average fits used for the exponential, linear and non-linear pseudo- EIE signals. The first number is for the low pass filtered signal, the number in brackets is for the acquired signal.

Pseudo-EIE	4th order polynomial fit	Exponential fit	500-point moving average
Exponential	0.98 (0.95)	0.98 (0.95)	0.98 (0.95)
Linear	0.99 (0.95)	0.98 (0.94)	0.99 (0.95)
Non-linear	0.94 (0.97)	0.95 (0.93)	1.00 (0.98)

Summary of T50 results using the 4th order polynomial

Table H7 Comparison between T50 results using the 4th order polynomial for the three classes of emptying curve.

Method:	1	2	3	4	5	6	7	8	9
Exponential	7.69	13.90	10.40	7.70	5.47	11.13	9.58	5.48	19.20
Linear	15.98	16.21	16.19	15.96	9.01	9.23	9.17	8.99	33.37
Non-linear	22.71	24.02	24.28	22.70	13.80	14.22	14.35	13.79	26.35

Analysis of T50 results using a linear pseudo-EIE signal

A linear pseudo-EIE signal (Fig. H51) was fitted with a 500-point moving average. The equation of the emptying curve was $y = -0.053x + 19.28$. Therefore, the time taken to reach half of the maximum impedance (18.39Ω) calculated from the equation was 16.7 minutes.

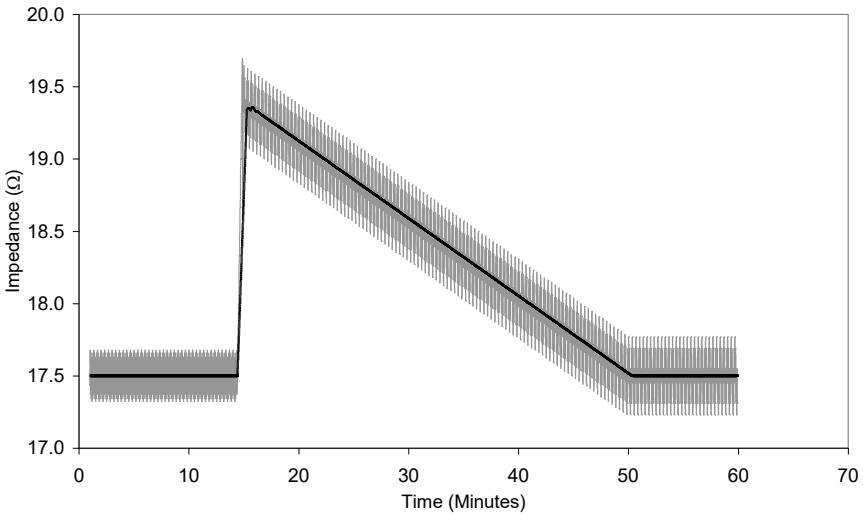

Fig. H51 Linear pseudo-EIE signal with 500-point moving average for T50 analysis.

Since the postprandial baseline of the signal is the same impedance as the preprandial baseline, methods 1 to 4 (using the deflection midline method) should give the same results and methods 5 to 8 (using the equal area method) should also give the same results. The ninth method ought to be accurate since it uses a linear extrapolation. Table H8 shows the T50 times measured using the three different methods.

Table H8 T50 times of a linear pseudo-EIE signal using the nine methods

Predicted	1	2	3	4	5	6	7	8	9
16.7	17.8	17.8	17.8	17.8	10.15	10.15	10.15	10.15	17.6

The results illustrate that the equal area method underestimates the T50 by approximately 61%. However, the deflection midline method measured only a 5% increase demonstrating that the deflection midline method is more accurate at measuring the T50.

Measurements of gastric contractile power change

The pseudo-EIE signal had a postprandial gastric signal with 10 times the amplitude than preprandial. The results in Table H9 demonstrate the comparisons between the four power ratios.

Table H9 Power ratios (post- to preprandial) of pseudo-EIE signals with a factor of 10 post- to preprandial power increase.

Measurement	Unit	Value	Power increase	Difference	% Difference
Impedance change (BPF)	Ω	10.11	10.11	+0.11	1.10
Power spectrum (RMA)	Ω^2	141.88	√141.88 = 11.91	+1.91	19.10
JTFT (JPR)	Ω^2	125.44	√125.44 = 11.20	+1.20	12.00
DyWT (GCR)	Ω^2	186.25	√186.25 = 13.65	+3.65	36.50

Table H9 illustrates that the measurements of power exaggerate the true power. However, since the same measurements are used throughout the analysis, the effect will be uniform and will not change the results of comparisons between meal groups.

The effect of overlapping the JTFT epoch window by 90% was investigated using a signal that contained a single 3cpm cycle (Fig. H52). This signal was processed by ACCESS and the JTFT using 5 minute epochs with (i) no overlap and (ii) 90% overlap were compared.

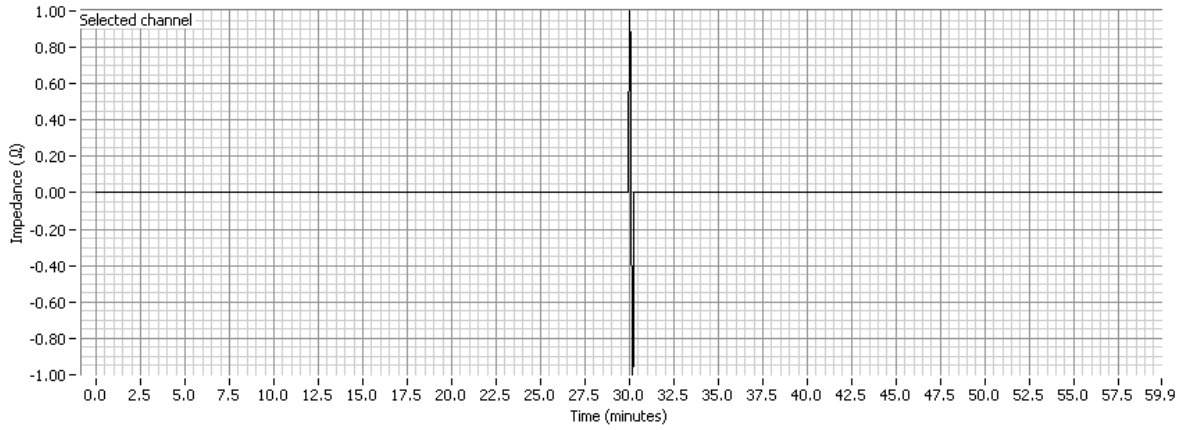

Fig. H52 Signal with one 3cpm cycle for JTFT testing.

The graphs of dominant power in Fig. H53 indicate that the overlapping process smoothes the total power over the 5 minute epoch. This is confirmed by comparing the power measured in 5 minute epoch (no overlap) to the total dominant power measured with overlap. With no overlap the power density is 5.97×10^{-1} and with overlap the total power density is 5.75×10^{-1}. Although small amounts of power have been lost in the overlapping process, the two values are comparable.

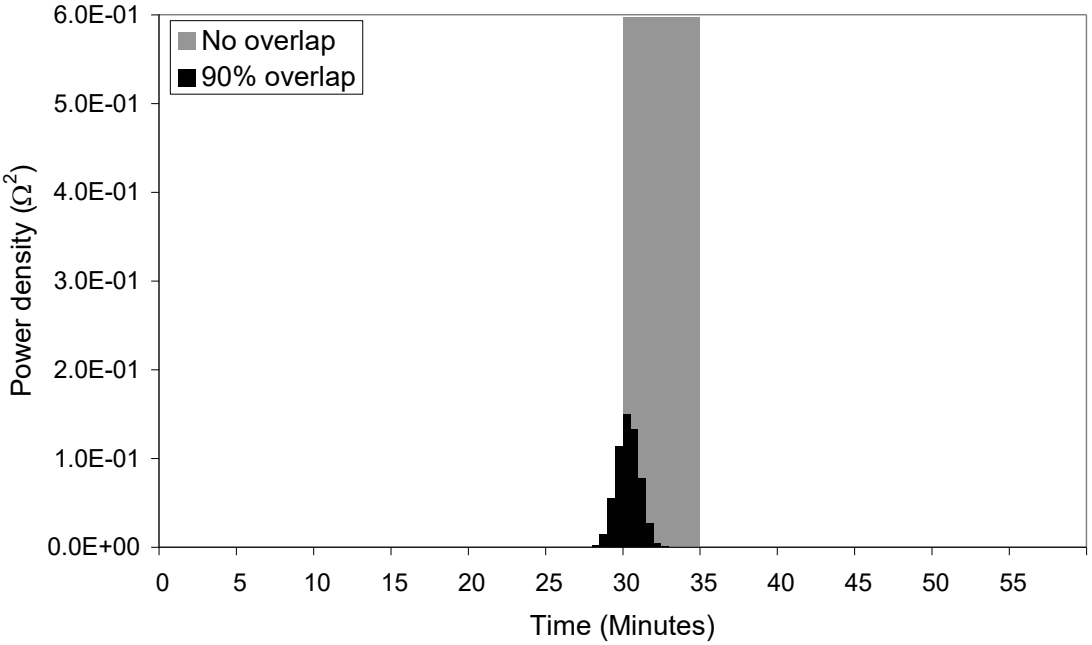

Fig. H53 Dominant power from the JTFT of the signal in Fig. H52 using 5 minute epochs with (i) no overlap (■) and (ii) 90% overlap (■).

Velocity measurements using Triangulative Impedance Mapping (TrIM)

All QA for velocity measurements can be found in chapter 6 (section 6.2.11). The justification for using 0.5cm by 0.5cm pixels in TrIM is demonstrated by plotting the total number of pixels in the region of interest (ROI) for increasing pixel sizes (Fig. H54). Since the relationship between pixel size and the number of pixels in the ROI is an inverse square law, the graph shows that careful selection of the pixel size in necessary to ensure that a fair compromise is found between spatial resolution and computation time (proportional to the number of pixels).

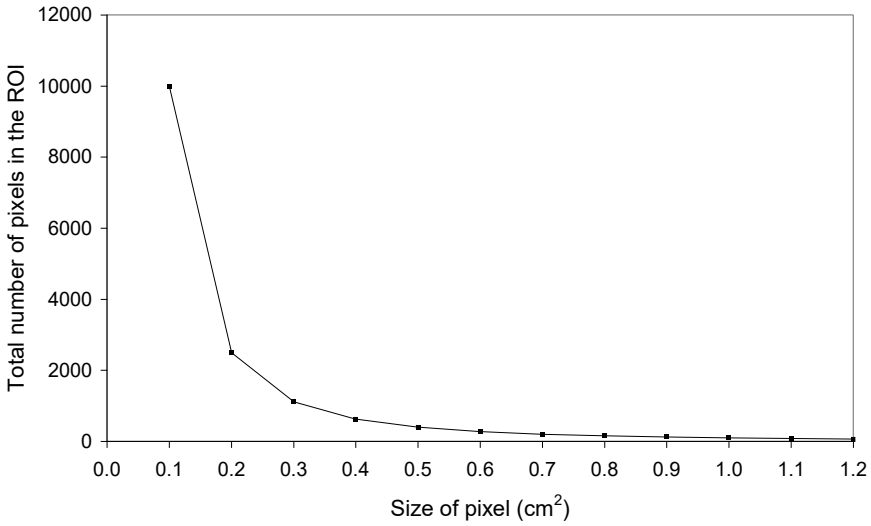

Fig. H54 Change in the total number of pixels in the region of interest (ROI) with pixel size.

The time taken for calculation depends on various characteristics of the computer used such as the processor speed and memory. However, for a computer with an Intel® Pentium® 4 processor with a CPU speed of 3.08GHz and 992 MB (Megabytes) of Random Access Memory (RAM), the time to calculate each pixel was approximately 1.96×10^{-5} seconds. A signal of 90 minutes produces 5,400 data points (after down sampling so that the sampling frequency, fs = 1Hz). Table H8 shows the calculation times for varying pixel sizes with a signal of 90 minutes.

Table H8 Approximate calculation times for pixel sizes from 0.1cm to 1.0cm.

Pixel size	Pixels in ROI	Calculation time (s)	Pixel size	Pixels in ROI	Calculation time (s)
0.1	10000.00	1057.13	0.6	277.78	29.36
0.2	2500.00	264.28	0.7	204.08	21.57
0.3	1111.11	117.46	0.8	156.25	16.52
0.4	625.00	66.07	0.9	123.46	13.05
0.5	400.00	42.29	1.0	100.00	10.57

Quantitative analysis tables

Table H9 Quantitative analysis for exponential pseudo-EIE signal.

Variable	Value	Index	Value
Filename	alpha.eie	MPI POST (Ohms²)	2.90E-2
Channel number	Channel 1	MPI PRE (Ohms²)	7.30E-3
T50 Method	Method 3	JPI POST (Ohm²/min)	2.59E-2
T50 (minutes)	10.46	JPI PRE (Ohm²/min)	8.16E-4
IUV (ohm/ml)	4.19E-3	GCI POST (Ohm²/min)	1.39E-1
PPBS (ohm)	2.09	GCI PRE (Ohm²/min)	5.04E-4
MPR	3.97	CII POST (/min)	2.98
JPR	31.82	CII PRE (/min)	0.07
GCR	275.83	MFI POST (cpm)	2.85
CIR	42.97	MFI PRE (cpm)	2.32
MFR	1.22	MAI POST (Ohms)	2.45E-4
MAR	35.32	MAI PRE (Ohms)	6.92E-6
MFS	0.02	MF POST (cpm)	3.00
% Bradygastric*	100.00, 0.00 and 0.74	MF PRE (cpm)	2.98
% Gastric*	0.00, 100.00 and 99.26	RPI POST (Ohm²/min)	7.52E-3
% Tachygastric*	0.00, 0.00 and 0.00	RPI PRE (Ohm²/min)	8.18E-3
DMI	-1.00	RF POST (cpm)	14.96
RPR	0.92	RF PRE (cpm)	14.94
RFS	0.02	MVI POST (cm/s)	0.46
MVR	-0.12	MVI PRE (cm/s)	-3.84
Emptying curve	EXPONENTIAL	PC PROBABILITY	0.88

* Values are listed as Preprandial, Postprandial and Total percentages

Table H10 Quantitative analysis for linear pseudo-EIE signal.

Variable	Value	Index	Value
Filename	beta.eie	MPI POST (Ohms²)	6.10E-2
Channel number	Channel 1	MPI PRE (Ohms²)	6.83E-3
T50 Method	Method 3	JPI POST (Ohm²/min)	5.37E-2
T50 (minutes)	18.44	JPI PRE (Ohm²/min)	1.72E-3
IUV (ohm/ml)	3.70E-3	GCI POST (Ohm²/min)	1.56E-1
PPBS (ohm)	1.85	GCI PRE (Ohm²/min)	4.72E-4
MPR	8.92	CII POST (/min)	2.98
JPR	31.27	CII PRE (/min)	0.07
GCR	329.57	MFI POST (cpm)	2.84
CIR	42.97	MFI PRE (cpm)	2.32
MFR	1.22	MAI POST (Ohms)	5.08E-4
MAR	35.10	MAI PRE (Ohms)	1.45E-5
MFS	0.02	MF POST (cpm)	3.00
% Bradygastric*	100.00, 0.74 and 1.47	MF PRE (cpm)	2.98
% Gastric*	0.00, 99.26 and 98.53	RPI POST (Ohm²/min)	1.58E-2
% Tachygastric*	0.00, 0.00 and 0.00	RPI PRE (Ohm²/min)	1.57E-2
DMI	-1.00	RF POST (cpm)	14.96
RPR	1.01	RF PRE (cpm)	14.94
RFS	0.02	MVI POST (cm/s)	0.46
MVR	-0.12	MVI PRE (cm/s)	-3.84
Emptying curve	LINEAR	PC PROBABILITY	0.65

* Values are listed as Preprandial, Postprandial and Total percentages

Table H11 Quantitative analysis for non-linear pseudo-EIE signal.

Variable	Value	Index	Value
Filename	gamma.eie	MPI POST (Ohms²)	2.46E-2
Channel number	Channel 1	MPI PRE (Ohms²)	NaN
T50 Method	Method 3	JPI POST (Ohm²/min)	2.21E-2
T50 (minutes)	21.42	JPI PRE (Ohm²/min)	6.75E-4
IUV (ohm/ml)	7.72E-3	GCI POST (Ohm²/min)	1.35E-1
PPBS (ohm)	3.86	GCI PRE (Ohm²/min)	0.00E+0
MPR	NaN	CII POST (/min)	2.96
JPR	32.81	CII PRE (/min)	0.00
GCR	Inf	MFI POST (cpm)	2.85
CIR	Inf	MFI PRE (cpm)	NaN
MFR	NaN	MAI POST (Ohms)	2.07E-4
MAR	36.30	MAI PRE (Ohms)	5.71E-6
MFS	0.02	MF POST (cpm)	3.00
% Bradygastric*	NaN, 0.00 and 0.00	MF PRE (cpm)	2.98
% Gastric*	NaN, 100.00 and 100.00	RPI POST (Ohm²/min)	6.29E-3
% Tachygastric*	NaN, 0.00 and 0.00	RPI PRE (Ohm²/min)	6.13E-3
DMI	-1.00	RF POST (cpm)	14.96
RPR	1.03	RF PRE (cpm)	14.94
RFS	0.02	MVI POST (cm/s)	0.47
MVR	NaN	MVI PRE (cm/s)	NaN
Emptying curve	LINEAR	PC PROBABILITY	0.65

* Values are listed as Preprandial, Postprandial and Total percentages